Modelling ultra-relativistic Heavy Ion Collisions with the quark Molecular Dynamics qMD

Dissertation
zur Erlangung des Doktorgrades
der Naturwissenschaften

vorgelegt beim Fachbereich Physik
der Johann Wolfgang Goethe–Universität
in Frankfurt am Main

von
Stefan Scherer
aus Ottweiler

Frankfurt am Main 2005
(D 30)

vom Fachbereich Physik der Johann Wolfgang Goethe–Universität
als Dissertation angenommen

Dekan	Prof. Dr. Wolf Aßmus
Gutachter	Prof. Dr. Horst Stöcker, Prof. Dr. Carsten Greiner
Datum der Disputation	7. April 2006

Übersicht

Diese Arbeit behandelt das molekulardynamische Simulationsmodell qMD (Quark-Molekulardynamik), das im Zusammenhang mit der Untersuchung der Hadronisierung eines Quark-Gluon-Plasmas zur Berücksichtigung des Farbfreiheitsgrades der elementaren Materie verwendet wird. Das qMD-Modell leistet eine dynamische Beschreibung der Bildung von Hadronen über die Rekombination von Quarks und Antiquarks.

In der Quark-Molekulardynamik qMD werden Quarks und Antiquarks als klassische, relativistische Punktteilchen behandelt, die eine Farbladung tragen und über ein langreichweitiges Cornell-Potential wechselwirken. Diese Potentialwechselwirkung trägt den Gluonfreiheitsgraden Rechnung: Gluonen werden nicht explizit als Teilchen behandelt. Ferner ist die Farbladung kein dynamischer Freiheitsgrad. Sie wird für jedes Quark oder Antiquark als Anfangsbedingung festgelegt und bleibt danach konstant. Der Beitrag der Paarwechselwirkung zwischen zwei Farbladungen zur Gesamtenergie folgt aus aus dem Skalarprodukt der SU(3)-Gewichtsvektoren der Ladungen und kann sowohl positiv als auch negativ sein. Es werden vier verschiedene Quark-*Flavours* (up, down, strange und charm) mit den Strommassen $m_{\mathrm{u}} = m_{\mathrm{d}} = 10\,\mathrm{MeV}$, $m_{\mathrm{s}} = 150\,\mathrm{MeV}$ und $m_{\mathrm{c}} = 1500\,\mathrm{MeV}$ berücksichtigt. Die Unterscheidung zwischen up- und down-Quark wird durch die Isospinquantenzahl beschrieben. Ferner wird jedem Teilchen eine feste Spinprojektion $\pm 1/2$ zugeordnet, die bei der Hadronisierung ausgewertet wird.

Es zeigt sich, daß die dynamische Entwicklung eines Systems von Farbladungen zur Ausbildung farbneutraler Cluster führt. Diese unterliegen trotz der enormen Stärke der Farbpaarpotentiale einer nur noch sehr schwachen Restwechselwirkung und können daher als Hadronen angesehen werden. Hadronisierung kann dann dynamisch beschrieben werden, indem jedem farbneutralen Cluster unter Erhaltung des Viererimpulses und unter Auswertung der Quantenzahlen der beteiligten Farbladungen ein Hadron oder eine hadronische Resonanz zugeordnet wird. Der Zerfall solcher Resonanzen zu den Hadronen des Endzustandes wird von qMD behandelt, nicht aber weitere elastische oder inelastische Streuung der so gebildeten Hadronen.

Im thermischen Gleichgewicht weist das qMD-Modell einen Übergang zwischen einer Phase mit Clusterbildung und Farbeinschluß bei tiefen Temperaturen und einer Phase frei beweglicher Farbladungen bei hohen Temperaturen und/oder Dichten auf, wie er von stark wechselwirkender Materie erwartet wird. An diesem Übergang wird die Zustandsgleichung weich, während Energiedichte und Druck der frei beweglichen Farbladungen ansteigen und sich bei hohen Temperaturen dem Stefan-Boltzmann-Grenzwert eines idealen Gases annähern.

Eigentliches Ziel dieser Arbeit ist die Anwendung des qMD-Modells auf die Beschreibung ultra-relativistischer Schwerionenkollisionen. Der Anfangszustand für die Quarkdynamik wird dabei durch das hadronische Transportmodell UrQMD

bereitgestellt, indem dessen hadronischer Inhalt in seine Valenzquarks zerlegt und in das qMD-Modell eingespeist wird. Das so initialisierte Gas von Farbladungen expandiert und bildet farbneutrale Cluster, die auf Hadronen abgebildet werden. Das qMD-Modell erlaubt einen vollen Zugriff auf die dreidimensionale raumzeitliche Entwicklung des Systems einschließlich der vollständigen Phasenraumverteilungen. Es zeigt sich, daß die dabei ablaufenden dynamischen Prozesse im allgemeinen nicht dem thermischen Gleichgewicht folgen. Dies kommt zum Beispiel in unterschiedlichen Werten der aus Transversalimpulsspektren abgeleiteten Temperaturen der Quarks und Antiquarks gegenüber den aus Teilchenzahlverhältnissen gewonnenen Temperaturen der Hadronen zum Ausdruck. Ein Vergleich von Resultaten der qMD-Simulationen mit Meßdaten für Schwefel-Gold-Kollisionen belegt, daß das qMD-Modell Phasenraumverteilungen der Hadronen im Endzustand der Kollision sehr gut wiedergibt. Er macht aber auch deutlich, daß die in qMD vernachlässigten Streuprozesse in der hadronischen Spätphase der Kollision zu falschen Ergebnissen mancher Teilchenzahlverhältnisse führen, insbesondere für Teilchen mit Seltsamkeit.

Die wirkliche Stärke des qMD-Modells liegt in dem Zugriff auf die Dynamik der Quark- und Antiquarkfreiheitsgrade. Es eignet sich daher hervorragend zur Untersuchung von Fluktuationen in der Quarkphase und deren Schicksal während der Hadronisierung sowie zur dynamischen Beschreibung der Bildung farbneutraler Cluster, einschließlich sogenannter exotischer hadronischer Zustände.

So wird das Problem der ereignisweisen Fluktuationen der elektrischen Ladung als Nachweiskriterium für das Quark-Gluon-Plasma im Rahmen von qMD behandelt. Es zeigt sich, daß die Hadronisierung auf dem Wege der Clusterbildung und Rekombination Fluktuationssignale auslöscht, die eigentlich für ein Quark-Gluon-Plasma erwartet werden. Dies deckt sich mit dem experimentellen Befund, daß auch bei höchsten Energien wider Erwarten anhand der Ladungsfluktuationen kein Hinweis auf die Quarkphase drittelzahliger Ladungen gefunden werden konnte. In der qMD-Simulation steigen die Fluktuationssignale als Funktion der Zeit während der Expansion und Hadronisierung des Systems von dem Wert, der für ein Quark-Gluon-Plasma erwartet wird, auf den des Pionengases, um dann mit dem Zerfall aller Resonanzen wieder zu sinken.

Das Thema exotischer Hadronen hat durch den kürzlichen, wenn auch strittigen Nachweis des Pentaquark-Zustandes Θ^+ großes Interesse erfahren. Ausgehend von der Idee, daß die Hadronisierung eines Quark-Gluon-Plasmas durch die Rekombination von farbneutralen Clustern ein günstiges Umfeld für die Entstehung solcher höherer Multiplett-Zustände liefert, wird die Bildung von Clustern aus bis zu sechs Quarks oder Antiquarks untersucht. Hieraus kann eine Abschätzung für die Zahl der zu erwartenden Zustände gewonnen werden. Für Deuteronen wird ein Wert erhalten, der unter den experimentellen Daten liegt, während für das Pentaquark Θ^+ eine Anzahl gefunden wird, die unterhalb der Erwartungen aus thermischen Modellen liegt. Auch für die exotischen Zustände können vollständige Impulsverteilungen angegeben werden, die als Hilfe bei der experimentellen Suche dienen könnten. Die Verteilung der exotischen Zustände über Seltsamkeit, Isospin und Spin zeigt, daß diese, so sie denn meßbar wäre, einen empfindlichen Sensor für die Thermalisierung und den Verlust von Korrelationen in der Quark-Phase bereitstellen könnte.

Zusammenfassung

Diese Arbeit behandelt das molekulardynamische Simulationsmodell qMD (Quark-Molekulardynamik), das im Zusammenhang mit der Untersuchung der Hadronisierung eines Quark-Gluon-Plasmas zur Berücksichtigung des Farbfreiheitsgrades der elementaren Materie verwendet wird. Das qMD-Modell leistet eine dynamische Beschreibung der Bildung von Hadronen über die Rekombination von Quarks und Antiquarks.

In dieser Zusammenfassung wird zunächst sehr allgemein der physikalische Hintergrund des behandelten Themas skizziert. Es folgen eine Beschreibung des Aufbaus der Arbeit, des verwendeten Modells und seiner Eigenschaften, der wichtigsten Resultate und ein Ausblick auf weitere Anwendungen und Erweiterungsmöglichkeiten.

Hintergrund: Die Suche nach dem Quark-Gluon-Plasma

Hadronische Materie – also Protonen und Neutronen, aus denen Atomkerne aufgebaut sind, Teilchen mit Seltsamkeit wie etwa Hyperonen, hadronische Resonanzen sowie Mesonen wie Pionen und Kaonen – hat nach heutigem Wissen eine Substruktur: Alle Hadronen sind aufgebaut aus *Quarks*, deren Zusammenhalt durch *Gluonen* vermittelt wird. Dies ist die Grundlage der Theorie der starken Wechselwirkung für die elementare Materie. Kombiniert mit der Annahme verschiedener Quarksorten, der sogenannten *Flavours*, liefert dieses Schema nicht nur eine klare Klassifikation der Vielfalt der experimentell nachgewiesenen Hadronen sowie eine schlüssige Erklärung ihrer Eigenschaften. In der Formulierung als quantisierte Eichfeldthorie im Rahmen der Quantenchromodynamik (QCD) gibt es auch dynamische Effekte, wie sie etwa in Streuexperimenten beobachtet werden, richtig wieder. Die Theorie der Quantenchromodynamik ist charakterisiert durch die Wahl der Eichgruppe, in diesem Fall der nicht-abelschen, speziellen unitären Gruppe $\mathrm{SU}(3)$. Dabei werden Quarks mit der dreidimensionalen Fundamentaldarstellung der $\mathrm{SU}(3)$ identifiziert, Gluonen mit der achtdimensionalen adjungierten Darstellung. Konkret bedeutet dies, daß jedes Quark in drei verschiedenen Ladungen, den sogenannten *Farben*, auftreten kann, jedes Gluonen in acht verschiedenen Kombinationen aus Farbe und Antifarbe.

Die Wechselwirkung zwischen Quarks und Gluonen, wie sie durch die QCD beschrieben wird, hat zwei spezielle Eigenschaften, die sie von den übrigen fundamentalen Wechselwirkungen unterscheiden: die *asymptotische Freiheit* und den *Einschluß der Farbladung*. Beides sind Konsequenzen der Tatsache, daß die Austauschbosonen der QCD – anders als die Photonen der Quantenelektrodynamik –

selbst eine Farbladung tragen. Asymptotische Freiheit bedeutet, daß sich Quarks bei Wechselwirkungen mit großem Impulsübertrag oder bei sehr kurzen Abständen wie freie Teilchen verhalten. Der Einschluß der Farbladung ist Ausdruck des experimentellen Befundes, daß in der Natur keine freien Quarks oder Gluonen auftreten. Der Grundzustand der stark wechselwirkenden elementaren Materie bei Temperaturen $T \lesssim 100\,\mathrm{MeV} \approx 1.2 \cdot 10^{12}\,\mathrm{K}$ und nicht zu hoher Dichte $\rho \lesssim 0.16\,\mathrm{Nukleonen/fm^3} \approx 150\,\mathrm{MeV/fm^3} \approx 1.2 \cdot 10^9\,\mathrm{MeV}^4$ besteht vielmehr aus wohldefinierten, farbneutralen Gruppen aus einem Quark und einem Antiquark bzw. aus drei Quarks mit drei verschiedenen Farben – dies sind die Mesonen und Baryonen der hadronischen Materie.

Tatsächlich beinhaltet die Theorie der QCD bei genügend hoher Temperatur oder ausreichender Verdichtung der stark wechselwirkenden elementaren Materie die Aufhebung des Einschlusses der Farbladung in Hadronen. Quarks und Gluonen liegen dann als System frei beweglicher Teilchen vor, das als *Quark-Gluon-Plasma* (QGP) bezeichnet wird. Dieser sogenannte *Deconfinement*-Übergang vom Hadronengas zum Quark-Gluon-Plasma geht einher mit der Wiederherstellung der *chiralen Symmetrie*: Während in Nukleonen gebundene Quarks als *Valenzquarks* aufgrund der Wechselwirkung mit den Gluonen eine sogenannte *Konstituentenmasse* von $\approx m_{\mathrm{Nukleon}}/3$ aufweisen, sind sie in der chiral symmetrischen Phase mit den *Strommassen* von $m_{\mathrm{u,d}} \approx 10\,\mathrm{MeV}$ nahezu masselos. Entsprechendes gilt für alle Baryonen. Ein schematisches Phasendiagramm der QCD als Funktion der Temperatur T und des chemischen Potentials μ der Quarks ist in Abbildung 1 dargestellt. Kernmaterie im Grundzustand ist bei $T = 0$ und $\mu_0 = 308\,\mathrm{MeV}$ zu finden. Bei ausreichend hohem chemischem Potential und tiefer Temperatur kann stark wechselwirkende Materie eine weitere Phase annehmen und farbsupraleitend werden [27]. Die quantitative Erforschung des Phasendiagramms der QCD und die genaue Charakterisierung des Quark-Gluon-Plasmas sowohl mit theoretischen als auch experimentellen Methoden sind Gegenstand der aktuellen Forschung.

In der Natur kommt stark wechselwirkende Materie in anderen Phasen als Kernmaterie im Grundzustand nur unter extremen Bedingungen vor: Ein Quark-

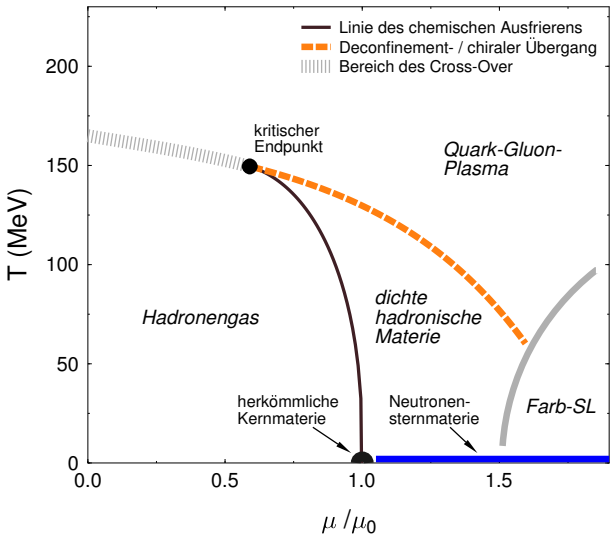

Abbildung 1
Schematische Darstellung des Phasendiagramms der QCD in der (T, μ)-Ebene (siehe auch Abbildung 1.6 auf Seite 13): Die Grenzlinien zeichnen den Verlauf des chemischen Ausfrierens (durchgezogen) und des Deconfinement- bzw. chiralen Phasenübergangs (gestrichelt) nach. Sie enden im kritischen Punkt, der mit der $\mu = 0$-Achse durch die Linie des Cross-Over verbunden ist. Kernmaterie im Grundzustand ist bei $T = 0$ und $\mu = \mu_0$ zu finden. Bei hohem chemischem Potential und tiefer Temperatur kann Farbsupraleitung (Farb-SL) einsetzen.

Gluon-Plasma bei hoher Temperatur $T \gtrsim 200\,\mathrm{MeV}$ und nahezu verschwindendem chemischem Potential $\mu \approx 0\,\mathrm{MeV}$ existierte nach heutigem Wissen in den ersten 10 Mikrosekunden der Geschichte unseres Universums [32]. Dichte, kalte Quarkmaterie mit Temperaturen $T \lesssim 10\,\mathrm{MeV}$ und chemischem Potential $\mu \gtrsim 1.2 - 2\,\mu_0$ tritt möglicherweise im Innern von Neutronensternen auf. Andere Bereiche des Phasendiagramms werden in hochenergetischen Kollisionen schwerer Atomkerne erfaßt: Stoßen zwei Atomkerne mit einer Schwerpunktsenergie $\sqrt{s}_{NN} \gtrsim 8\,\mathrm{GeV}$ zusammen, wird die Kernmaterie derart verdichtet, daß der Farbeinschluß in den Protonen und Neutronen der Kerne aufgehoben und die chirale Symmetrie wiederhergestellt werden kann. Für die kurze Zeit $\Delta t \lesssim 10\,\mathrm{fm}/c \approx 3{\cdot}10^{-23}\,\mathrm{s}$ entsteht dann ein Quark-Gluon-Plasma. Zu solchen ultra-relativistischen Schwerionenkollisionen kommt es zum Beispiel, wenn Eisenkerne der kosmischen Strahlung mit Energien bis zu $10^6\,\mathrm{GeV}/N$ in der Hochatmosphäre auf Argonkerne prallen. Sie können aber auch ganz gezielt an Schwerionenbeschleunigern studiert werden. Solche Beschleuniger sind das SIS an der GSI in Darmstadt, der SPS am CERN, wo Kollisionen von Bleikernen im Target-Modus im Energiebereich von $20 - 160\,\mathrm{GeV}/N$ ($\sqrt{s}_{NN} = 6.4 - 17.4\,\mathrm{GeV}$) untersucht werden, oder RHIC am Brookhaven National Laboratory, wo Goldkerne im Collider-Modus mit Schwerpunktsenergien von $\sqrt{s}_{NN} = 62 - 200\,\mathrm{GeV}$ zur Kollision gebracht werden. Ziel dieser Experimente ist die Erkundung des Phasendiagramms der QCD sowie der Nachweis und die Charakterisierung des Quark-Gluon-Plasmas.

Ein in Schwerionenkollisionen erzeugtes Quark-Gluon-Plasma existiert nur in einem winzigen Bereich der Raumzeit. Es expandiert, kühlt ab und kondensiert wieder in Hadronen. In Teilchendetektoren können immer nur diese Hadronen gemessen werden. Es ist daher von entscheidender Bedeutung, aus den hadronischen Meßdaten Rückschlüsse auf die kurzlebige Zwischenphase der heißen, dichten Materie zu ziehen und Signale zu finden, die eindeutige Belege für die vorübergehende Existenz des Quark-Gluon-Plasmas liefern können [39].

An dieser Stelle kommt die Modellbildung ins Spiel. Sie kann zeigen, welche Auswirkungen ein vorübergehendes Quark-Gluon-Plasma auf hadronische Observablen haben kann. Dazu zählen Teilchenzahlen, Verhältnisse von Anzahlen verschiedener Teilchensorten, Verteilungen in den Phasenraumvariablen Rapidität und Transversalimpuls, Fluktuationen in all diesen Größen und kollektive Variablen wie transversaler und elliptischer Fluß. Im Idealfall lassen sich so eindeutige Kriterien formulieren, die das Quark-Gluon-Plasma von einem dichten und heißen Hadronengas als Zwischenzustand der Kollision unterscheiden. Die Vorgänge, die sich während einer ultra-relativistischen Schwerionenkollision abspielen, sind leider so verwickelt, daß sie bisher nicht unmittelbar aufbauend auf der zugrundeliegenden Theorie der QCD beschrieben werden können.

Es kommt daher darauf an, die relevanten physikalischen Freiheitsgrade in einem Modell zu erfassen. So beschreiben etwa hadronische Transportmodelle die Vorgänge während einer Kollision in den Begriffen von Hadronen und hadronischen Resonanzen. Solche Modelle liefern den Hintergrund, vor dem sich Signale für das Quark-Gluon-Plasma abheben müssen. In der Frühphase der Kollision ist bei höchsten Energien die partonische Substruktur der Nukleonen entscheidend. Diese Freiheitsgrade werden von Partonkaskaden berücksichtigt. Die Expansion und Abkühlung des Quark-Gluon-Plasmas kann durch hydrodynamische Modelle

beschrieben werden. Die abschließende Hadronisierung wird in den verschiedenen Modellen durch Fragmentation von Hadronen, durch Ausfrieren auf Hyperflächen konstanter Temperatur oder durch Rekombination von Partonen modelliert. Verschiedene Befunde von Experimenten am RHIC deuten darauf hin, daß eine zutreffende Formulierung für die Hadronisierung in der Rekombination von Valenzquarks gefunden werden kann.

Genau an dieser Stelle setzt die Quark-Molekulardynamik qMD ein: Sie modelliert das Quark-Gluon-Plasma als ein Gas farbgeladener Quarks, die sich unter dem Einfluß eines den Farbeinschluß erzwingenden Paarpotentials bewegen und unter der daraus folgenden Dynamik farbneutrale Cluster ausbilden, die dann auf Hadronen abgebildet werden können [134]. Damit liegt ein in dieser Form bisher einmaliges Modell vor, das die vollständige Dynamik der Hadronisierung eines expandierenden Quark-Gluon-Plasmas erfassen kann. Die vorliegende Arbeit enthält eine vertiefende Diskussion und Charakterisierung der qMD und wendet sie auf zwei aktuelle Problemkreise an.

Aufbau dieser Arbeit

Die Arbeit ist in vier Teile gegliedert. Teil I behandelt den physikalischen Hintergrund des Themas: die Herausbildung des jetzigen Wissens über den Aufbau der Materie und das Quark-Gluon-Plasma (Kapitel 1, S. 3), die Theorie der QCD und einige Näherungsverfahren, die zu ihrer Behandlung verwendet werden und die für diese Arbeit relevant sind (Kapitel 2, S. 20), sowie die Modelle, die zur Beschreibung von Schwerionenkollisionen verwendet werden (Kapitel 3, S. 39). Teil II stellt das Simulationsmodell qMD vor (Kapitel 4, S. 51), behandelt seine thermischen Eigenschaften (Kapitel 5, S. 74) und beschreibt, wie es zusammen mit dem hadronischen Transportmodell UrQMD zur Simulation von ultra-relativistischen Schwerionenkollisionen verwendet wird (Kapitel 6, S. 98). Teil III behandelt zwei aktuelle Anwendungen des Modells auf das Studium von Ladungsfluktuationen als Nachweiskriterium für das Quark-Gluon-Plasma (Kapitel 7, S. 131) und zur Bildung exotischer Hadronen in Schwerionenkollisionen (Kapitel 8, S. 147). Teil IV liefert eine Zusammenfassung und einen Ausblick auf mögliche Verbesserungen und Erweiterungen des Modells sowie auf weitere Anwendungsmöglichkeiten (Kapitel 9, S. 201). Drei Anhänge behandeln die in qMD propagierten Teilchen (Anhang A, S. 209) sowie die Darstellungstheorien von SU(N) mit Schwerpunkt auf SU(3) (Anhang B, S. 215) und SU(6) (Anhang C, S. 235), die in Kapitel 8 zur Klassifizierung von exotischen Hadronen und speziell Pentaquarkzuständen verwendet werden.

Die Quark-Molekulardynamik qMD

In der Quark-Molekulardynamik qMD werden Quarks und Antiquarks als klassische Punktteilchen behandelt, die eine Farbladung tragen und über ein langreichweitiges Cornell-Potential wechselwirken. Diese Potentialwechselwirkung trägt den Gluonfreiheitsgraden Rechnung: Gluonen werden nicht explizit als Teilchen behandelt. Ferner ist die Farbladung kein dynamischer Freiheitsgrad. Sie wird für jedes Quark oder Antiquark als Anfangsbedingung festgelegt und bleibt danach

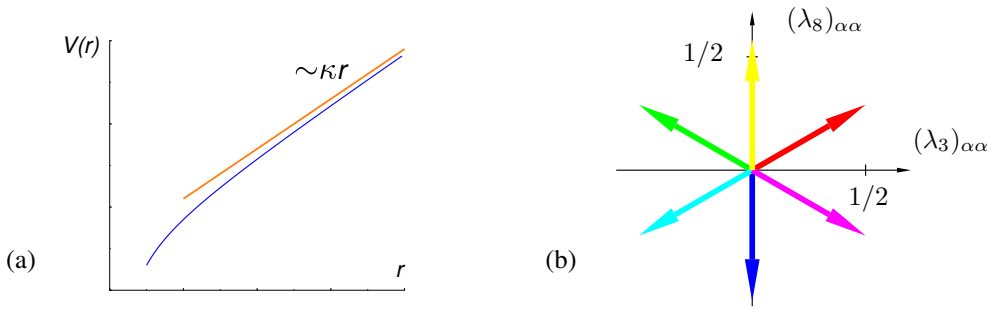

Abbildung 2
In der qMD wird das Cornell-Potential (Teilbild a) verwendet, um die Wechselwirkung zwischen je zwei Farbladungen (Quarks mit den Farben R, G, B oder Antiquarks mit den Farben $\bar{R}$, $\bar{G}$, $\bar{B}$) zu beschreiben. Der relative Beitrag zur Gesamtenergie kann positiv oder negativ sein und ergibt sich aus dem Skalarprodukt der Gewichtsvektoren (Teilbild b), die den Farbladungen zugeordnet sind.

konstant. Die Dynamik eines solchen Systems von Farbladungen folgt aus der Hamilton-Funktion (4.1),

$$\mathcal{H} = \sum_{i=1}^{N} \sqrt{\vec{p}_i^{\,2} + m_i^2} + \frac{1}{2}{\sum_{i,j}}' C_{ij}^{\mathrm{c}} V\left(|\vec{r}_i - \vec{r}_j|\right) \ . \tag{1}$$

Die Summe des Wechselwirkungsterms erstreckt sich über alle Farbladungspaare, und $V(r)$ bezeichnet das Cornell-Potential (Abbildung 2a),

$$V\left(|\vec{r}_i - \vec{r}_j|\right) = -\frac{3}{4}\frac{\alpha_s}{|\vec{r}_i - \vec{r}_j|} + \kappa\ |\vec{r}_i - \vec{r}_j| \ , \tag{2}$$

wobei die Saitenspannung κ jedoch als frei wählbarer Parameter betrachtet wird. Der relative Beitrag der Paarwechselwirkung zwischen zwei Quarks mit den Farbladungen $\vec{w}_i$ und $\vec{w}_j$ folgt aus aus dem Skalarprodukt

$$C_{ij}^{\mathrm{c}} \ = \ -\vec{w}_i \vec{w}_j \tag{3}$$

und kann sowohl attraktiv als auch repulsiv sein. Die zweidimensionalen Vektoren $\vec{w}_i$ beschreiben dabei die SU(3)-Farbladungen der Quarks und Antiquarks im SU(3)-Gewichtsdiagramm (Abbildung 2b). Es werden vier verschiedene Quark-*Flavours* (up, down, strange und charm) mit den Strommassen $m_{\mathrm{u}} = m_{\mathrm{d}} = 10\,\mathrm{MeV}$, $m_{\mathrm{s}} = 150\,\mathrm{MeV}$ und $m_{\mathrm{c}} = 1500\,\mathrm{MeV}$ berücksichtigt. Die Unterscheidung zwischen up- und down-Quark wird durch die Isospinquantenzahl beschrieben. Ferner wird jedem Teilchen eine feste Spinprojektion $\pm 1/2$ zugeordnet, die bei der Hadronisierung ausgewertet wird.

Es zeigt sich, daß die dynamische Entwicklung eines Systems von Farbladungen, das durch die Hamilton-Funktion (1) beschrieben wird, zur Ausbildung farbneutraler Cluster führt (Abbildung 4.4). Diese unterliegen trotz der enormen Stärke der Farb-Paarpotentiale einer nur noch sehr schwachen Restwechselwirkung (Abschnitt 4.1.2) und können daher als Hadronen angesehen werden. Hadronisierung kann also dynamisch beschrieben werden, indem jedem farbneutralen Cluster unter

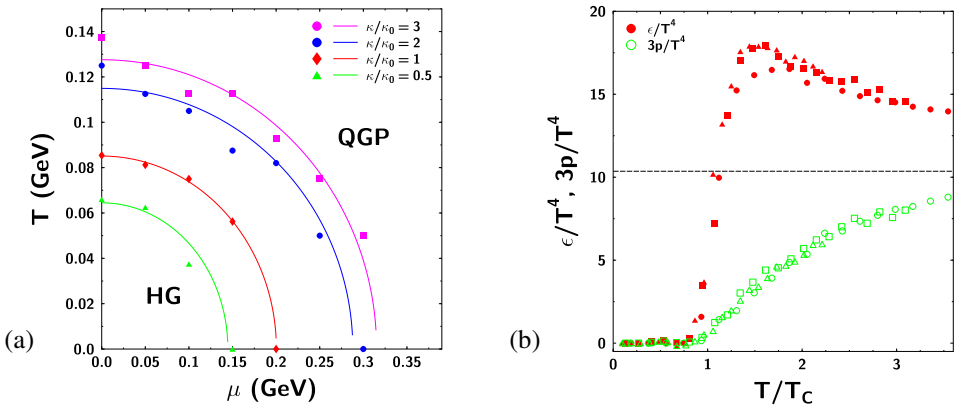

Abbildung 3
Thermische Eigenschaften der qMD: Bei tiefen Temperaturen und geringen Dichten bilden Farbladungen unter dem Einfluß des den Farbeinschluß erzwingenden Potentials farbneutrale Cluster, während bei hohen Temperaturen und/oder Dichten frei bewegliche Farbladungen auftreten. Teilbild a) zeigt die Phasengrenze für verschiedene Werte des Saitenspannungsparameters κ. An der Phasengrenze steigen Energiedichte und Druck der frei beweglichen Farbladungen als Funktion der Temperatur an (Teilbild b) und gehen näherungsweise zu den Stefan-Boltzmann-Werten über (Abbildungen 5.2 und 5.3, S. 81 und 82).

Erhaltung des Viererimpulses und unter Auswertung der Quantenzahlen der beteiligten Farbladungen ein Hadron oder eine hadronische Resonanz zugeordnet werden (Abschnitt 4.2). Der Zerfall solcher Resonanzen zu den Hadronen des Endzustandes wird von qMD behandelt, nicht aber weitere elastische oder inelastische Streuung der so gebildeten Hadronen.

Das qMD-Modell hat einige offensichtliche Schwachpunkte, die am Ende von Kapitel 4 diskutiert werden: Es enthält keine direkten Streuungen zwischen Quarks, die alleine durch das Paarpotential wechselwirken. Harte Gluonen werden als Freiheitsgrade vernachlässigt, und in der benutzten abelschen Näherung für das Farbfeld kommen keine Farbrotationen der Farbladungen zustande. Eine Konsequenz dieser Unzulänglichkeiten ist das Versagen des qMD-Modells in der Anwendung auf Proton-Proton-Streuung bei höchsten Energien. Die Potentialwechselwirkung ist instantan und bricht die allgemeine Poincaré-Kovarianz. Sie liefert ferner keine realistische Beschreibung der Verteilung des farbelektrischen Flusses, der die Farbladungen vernetzt. Einwände bezüglich einer möglichen Abnahme der Entropie während der Hadronisierung sind naheliegend, aber nicht stichhaltig, wie später in Abschnitt 7.4 gezeigt wird. Schließlich enthält die qMD keinerlei Quantenmechanik: Sie liefert ein kontinuierliches Spektrum an Clustermassen und kann aufgrund des fehlenden Pauli-Prinzips nicht auf kühle, dichte Quarkmaterie angewendet werden.

Alle diese Punkte lassen sich im Prinzip nachbessern. Zunächst ist aber wichtig festzuhalten, daß uns die qMD in ihrer in dieser Arbeit beschriebenen Form ein ideales, einfach zu handhabendes Modell an die Hand gibt, um den Übergang von einem System frei beweglicher Farbladungen zu einem Gas farbneutraler Hadronen vollständig dynamisch zu studieren. Entscheidend dabei ist das linear mit dem Abstand skalierende Potential, das den Farbeinschluß erzwingt und zur Ausbildung farbneutraler Cluster führt.

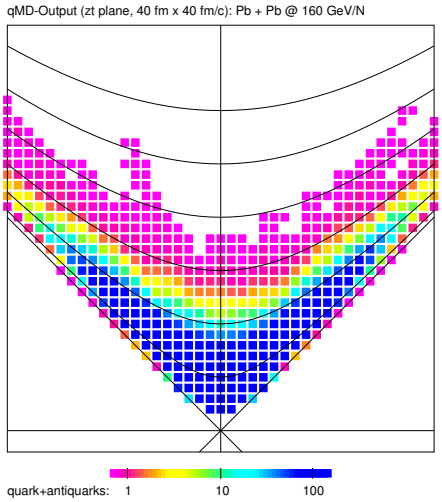

Abbildung 4
Raumzeitliche Entwicklung der Zahl der Quarks und Antiquarks in einer Pb+Pb-Kollision am CERN-SPS mit einer Strahlenergie von $E = 160\,\mathrm{GeV}/N$ in der Simulation mit qMD. Das Raumzeitgebiet der Abbildung erstreckt sich über $40\,\mathrm{fm}$ entlang der Strahlachse und umfaßt eine Zeitspanne von $40\,\mathrm{fm}/c$ im Schwerpunktsystem der Kollision. Linien konstanter Eigenzeit sind in Schritten von $\Delta\tau = 5\,\mathrm{fm}/c$ schwarz eingetragen. Nach einer Eigenzeit von $\approx 15\,\mathrm{fm}/c$ sind nahezu keine freien Quarks oder Antiquarks mehr übrig (Abbildung 6.7, S. 110).

Die thermischen Eigenschaften des qMD-Modells werden in Kapitel 5 mit Hilfe des Metropolis-Algorithmus im Monte-Carlo-Verfahren studiert. Dabei zeigt sich ein Übergang zwischen einer Phase mit Clusterbildung und Farbeinschluß bei tiefen Temperaturen und einer Phase frei beweglicher Quarks bei hohen Temperaturen und/oder Dichten, wie er von stark wechselwirkender Materie erwartet wird. An diesem Übergang steigen Energiedichte und Druck der frei beweglichen Farbladungen an und nähern sich bei hohen Temperaturen dem Stefan-Boltzmann-Grenzwert eines idealen Gases. Darüber hinaus wird am Übergang die Zustandsgleichung weich (Abbildung 5.4 auf S. 83). Zur Ordnung des Übergangs lassen sich aufgrund der *Finite-Size*-Aufweichungen (Abschnitt 5.2) noch keine Aussagen treffen. Es kann aber deutlich verfolgt werden, wie das Auftreten frei beweglicher Farbladungen zu einer Abschirmung des linearen Potentials zwischen Testladungen führt (Abschnitt 5.3). Die Auswirkungen dieser dynamischen Abschirmung auf das "Schmelzen" des J/Ψ in thermischer Umgebung werden ebenfalls in diesem Abschnitt vorgestellt.

Kapitel 6 wendet sich schließlich der Anwendung des qMD-Modells auf die Beschreibung ultra-relativistischer Schwerionenkollisionen am CERN-SPS zu. Der Anfangszustand für die Quarkdynamik wird hierbei durch das hadronische Transportmodell UrQMD bereitgestellt (Abschnitt 6.1), indem dessen hadronischer Inhalt in seine Valenzquarks zerlegt und in das qMD-Modell eingespeist wird. Das so initialisierte Gas von Farbladungen expandiert und bildet farbneutrale Cluster, die auf Hadronen abgebildet werden (Abbildung 4). Es zeigt sich, daß die dabei ablaufenden dynamischen Prozesse im allgemeinen nicht dem thermischen Gleichgewicht folgen (Abschnitt 6.2). Dies kommt zum Beispiel in unterschiedlichen Werten der aus Transversalimpulsspektren abgeleiteten Temperaturen der Quarks und Antiquarks und der aus Teilchenzahlverhältnissen gewonnenen Temperaturen der Hadronen zum Ausdruck. Ferner wird das Verfahren der Abbildung der farbneutralen Cluster auf hadronische Resonanzen diskutiert und dessen Einfluß auf die Zeitskala der Hadronisierung am Beispiel der Vektormesonen untersucht

Ein Vergleich von Resultaten der qMD-Simulationen mit Meßdaten für Schwefel-Gold-Kollisionen belegt schließlich, daß das qMD-Modell Phasenraumvertei-

lungen der Hadronen im Endzustand der Kollision sehr gut wiedergibt (Abschnitt 6.3). Er macht aber auch deutlich, daß die in qMD fehlenden Streuprozesse in der hadronischen Spätphase der Kollision zu falschen Ergebnissen mancher Teilchenzahlverhältnisse führt, insbesondere für Teilchen mit Seltsamkeit.

Die wirkliche Stärke des qMD-Modells liegt in dem Zugriff auf die Dynamik der Quark- und Antiquarkfreiheitsgrade, den es ermöglicht. Es eignet sich daher hervorragend zur Untersuchung von Fluktuationen in der Quarkphase und deren Schicksal während der Hadronisierung sowie zur dynamischen Beschreibung der Bildung farbneutraler Cluster, einschließlich sogenannter exotischer hadronischer Cluster mit mehr als drei Farbladungen. Diese Themen sind Gegenstand von Teil III dieser Arbeit.

Ergebnisse zweier Modellstudien: Fluktuationen und Exotica

Als erste Anwendung der qMD wird in Kapitel 7 die Verwendung von Fluktuationen der elektrischen Ladung als Nachweiskriterium für das Quark-Gluon-Plasma behandelt. Da in einem Quark-Gluon-Plasma die elektrische Ladung in kleineren Einheiten über eine größere Anzahl von Ladungsträgern verteilt ist als in einem Hadronengas, erwartet man, mit Hilfe geeignet normierter Maße der ereignisweisen Fluktuationen der elektrischen Ladung in Schwerionenkollisionen ein Kriterium zu

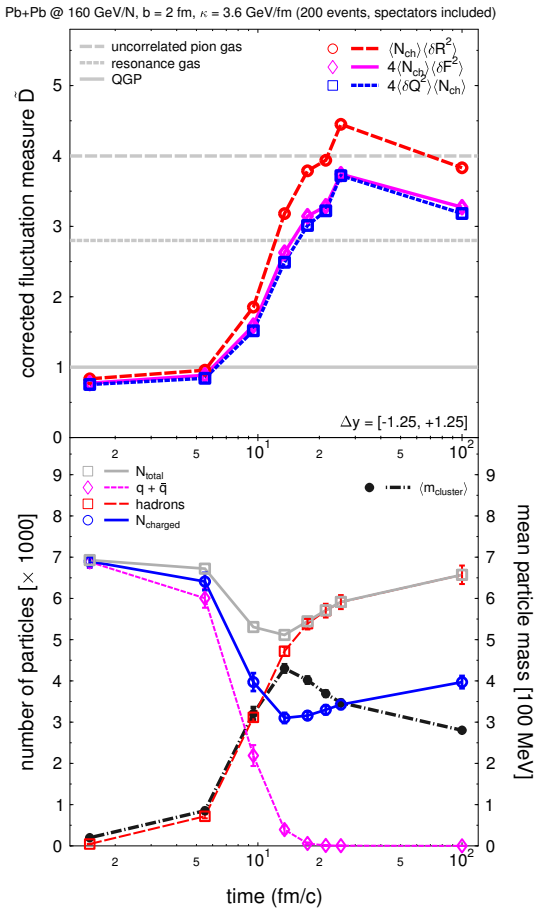

Abbildung 5
Ergebnisse der qMD-Analyse von Fluktuationen der elektrischen Ladung als Funktion der Zeit in nahezu zentralen Blei-Blei-Kollisionen bei einer Energie von 160 GeV/N ($\sqrt{s}_{NN} = 17.3$ GeV). Das obere Feld der Abbildung zeigt die Zeitentwicklung dreier verwandter Fluktuationsmaße, die in Gleichung (7.1) auf Seite 132 definiert sind. Die horizontalen Linien markieren die Werte, die für diese Maße in den drei unterschiedlichen physikalischen Situationen eines Quark-Gluon-Plasmas, eines Pionengases und eines Hadronengases nach dem Zerfall von Resonanzen zu erwarten wären. Das untere Feld der Abbildung zeigt parallel dazu die zeitliche Entwicklung der Anzahl frei beweglicher Quarks und Antiquarks (♢), der Zahl der Hadronen (□, gestrichelte Linie) und geladener Teilchen (○) und der mittleren Masse aller Teilchen (Quarks, farbneutrale Cluster und Hadronen im Endzustand) im System (●). Die ausgezogene graue Linie (□) gibt die Gesamtzahl aller Teilchen im System an (Abbildung 7.4, S. 143).

finden, das zwischen beiden Systemen unterscheiden kann. Dabei soll das kleinere Fluktuationssignal des Quark-Gluon-Plasmas aufgrund der Ladungserhaltung unverändert auf das hadronische System übergehen und somit experimentell zugänglich sein. Tatsächlich wurden in Experimenten aber immer nur die Fluktuationsmaße gemessen, die für ein Hadronengas erwartet werden, und zwar selbst bei RHIC-Kollisionsenergien, die keinen Zweifel daran lassen, daß vorübergehend ein Quark-Gluon-Plasma vorgelegen hat.

Die qMD-Modellrechnung zeigt, daß die Hadronisierung über Clusterbildung alle Fluktuationssignale des Quark-Gluon-Plasmas auslöschen kann: In der Simulation steigen die Fluktuationsmaße als Funktion der Zeit vom Wert für das Quark-Gluon-Plasma auf den des Pionengases, um dann mit dem Zerfall aller Resonanzen wieder leicht abzunehmen. Dieses Verhalten geht Hand in Hand mit der Expansion des Systems und der Zusammenballung der frei beweglichen Quarks und Antiquarks zu farbneutralen Clustern, die dann auf hadronische Resonanzen abgebildet werden (Abbildung 5). Ladungsfluktuationsmaße müssen im allgemeinen auf die Zahl der geladenen Teilchen in einem System normiert werden, damit sinnvolle Aussagen möglich sind. Die ursprüngliche Argumentation für das Überleben der geringen Werte der Fluktuationsmaße während der Hadronisierung beruht auf einer Abschätzung der Anzahl geladener Quarks und Antiquarks aus der Anzahl der geladenen Pionen im Endzustand. Hierzu wird die Erhaltung der Entropie verwendet, wobei die Quarks und Gluonen im Plasma als ideale Quantengase angesehen werden. Man könnte denken, daß der Anstieg der Fluktuationsmaße in den qMD-Simulationen ein Artefakt der Clusterbildung und außerdem nicht mit der Erhaltung der Entropie verträglich ist. Wir sehen jedoch, daß das einfache Abzählargument zur Abschätzung der Entropie zu kurz greift, da die Cluster sehr massiv und außerdem kurzlebig sind. Deshalb bedeutet die Bildung von Clustern nicht automatisch eine Verringerung der Entropie. Im Endzustand wiederum ist die Zahl der Teilchen in etwa so hoch wie die der anfänglichen Quarks und Antiquarks, bei höherer mittlerer Masse. So kann die Erhaltung der Entropie während der gesamten zeitlichen Entwicklung des Systems gewährleistet werden.

In Kapitel 8 wird als zweites Anwendungsbeispiel die Erzeugung von farbneutralen Clustern untersucht, die mit mehr als drei Valenzquarks und/oder -antiquarks über die bekannten Mesonen und Baryonen hinausgehen. Diese Möglichkeit der Existenz sogenannter exotischer Hadronen hat durch die kürzliche, umstrittene Entdeckung des Pentaquarkzustandes Θ^+ erneutes Interesse erfahren. Ausgehend von der Idee, daß die Hadronisierung eines Quark-Gluon-Plasmas durch die Bildung von farbneutralen Clustern ein günstiges Umfeld für die Entstehung höherer Multiplettzustände sein könnte, wird die Bildung von farbneutralen Clustern aus bis zu sechs Quarks oder Antiquarks untersucht.

Die Ausdehnung der Kriterien für die Isolierung farbneutraler Cluster und deren Abbildung in hadronische Zustände auf exotische Cluster führt zu erstaunlich hohen relativen Anzahlen dieser Exotica. Aufgrund der Größe der entsprechenden Hadronen-Multipletts bedeutet dies aber nicht, daß spezifische exotische Zustände tatsächlich in hoher Zahl bevölkert werden können. Dies zeigt sich zum Beispiel bei Deuteronen, deren direkte Produktion durch Clusterbildung in qMD mit den experimentellen Daten verglichen werden kann. Hier liefert qMD um einen Faktor ≈ 5 zu geringe Werte, was durch die Vernachlässigung des wichtigen Produktions-

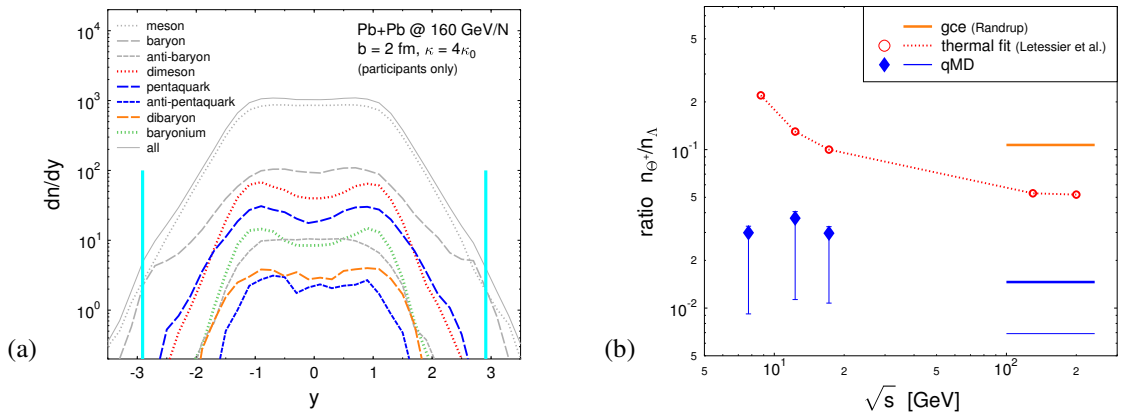

Abbildung 6
Produktion exotischer Hadronen in qMD: Während die Rapiditätsverteilungen von Dimesonen, Pentaquarks, Dibaryonen und Baryonia (Teilbild a) zu implizieren scheinen, daß Exotica in hoher Zahl produziert werden, darf man nicht vergessen, daß allenfalls einige wenige Zustände der riesigen exotischen Multiplettstrukturen möglicherweise stabil sind. Im Fall des Pentaquarkzustandes Θ^+ reduziert sich dadurch die auf Λ^0 bezogene Anzahl (Teilbild b) je nach verwendetem Kopplungsschema für Spin und Flavour auf Werte deutlich unterhalb der Abschätzungen aus thermischen Modellen (Abbildungen 8.4 und 8.28, siehe S. 163 und 196).

kanals für Deuteronen in hadronischer Koaleszenz verstanden werden kann. Mit entsprechender Vorsicht sind die qMD-Resultate für H-Dibaryon und Y-Baryonium sowie auch die Daten für Pentaquarks zu behandeln.

Die Untersuchung von Rapiditäts- und Transversalimpulsspektren der exotischen Cluster weist darauf hin, daß die besten Aussichten für die experimentelle Identifizierung exotischer Hadronen an den Flanken der zentralen Plateaus der Rapiditätsverteilung zu finden sind. Für Pentaquarkzustände wird das kontinuierliche Massenspektrum analysiert und mit dem Ergebnis einer Faltung von Meson- und Baryonmassenspektren verglichen. Dabei zeigt sich, daß Pentaquarkzustände im Mittel um etwa $200 - 300\,\mathrm{MeV}$ mehr Masse haben als aufgrund naiver Koaleszenz zu erwarten wäre. Es folgt eine detaillierte Analyse der Verteilung der Pentaquarkzustände über die Seltsamkeit sowie über Spin und Isospin, die in einer Abschätzung für das Verhältnis Θ^+/Λ^0 mündet. Dabei werden die Vorhersagen thermischer Modelle für dieses Verhältnis deutlich unterschritten. Dies ist ein typisches Merkmal der Hadronisierung durch Rekombination, bei der in einem vorgegebenen Massenintervall exotische Zustände aufgrund der Kombinatorik der beitragenden Farbladungen deutlich seltener bevölkert werden als herkömmliche Hadronen. In thermischen Modellen kann hier lediglich ein viel geringerer Unterschied aufgrund von Spin- und Isospinmultiplizitäten bestehen.

Bei der Analyse der Daten exotischer Cluster aus den qMD-Simulationen hinsichtlich ihrer Verteilung über Seltsamkeit, Spin und Isospin wird ein Unterschied deutlich zwischen thermisch initialisierten Systemen und solchen, deren Anfangsbedingungen mit UrQMD gewonnen wurden: Nur die thermisch initialisierten Systeme weisen eine gleichförmige Verteilung der Cluster über alle diese Größen auf. Bei den mit UrQMD initialisierten Daten stellen sich Abweichungen ein, die durch Korrelationen erklärt werden können, die auf die Zerlegung des hadronischen In-

halts von UrQMD zurückgehen. Dies ist natürlich eine spezielle Eigenschaft der gekoppelten UrQMD-qMD-Simulation. Sie deutet aber darauf hin, daß die Untersuchung solcher Verteilungen ein gutes Maß für die Thermalisierung und Dekorrelierung des in einer Schwerionenkollision gebildeten Quarksystems liefern könnte.

Schlußfolgerungen

Die vorliegende Arbeit zeigt, daß die Quark-Molekulardynamik qMD ein tragfähiges und ausbaubares Werkzeug zur Verfügung stellt, um die Hadronisierung eines heißen, dichten Quark-Gluon-Plasmas durch Rekombination dynamisch zu untersuchen. Im letzten Teil der Arbeit wird in Kapitel 9 diskutiert, auf welche weiteren Fragestellungen die qMD angewandt und wie sie erweitert werden kann.

Die am Ende von Kapitel 5 beschriebene Untersuchung zum Schmelzen des J/Ψ in thermischer Umgebung könnte ohne weiteres auf die dynamischen Bedingungen von Ereignissen am SPS ausgedehnt werden und im Hinblick auf RHIC und LHC auch Bottom-Freiheitsgrade einschließen. Die in Kapitel 5 vorgestellte Analyse von SPS-Ereignissen könnte generell systematisch erweitert werden, sowohl im Hinblick auf Untersuchungen von Teilchenmultiplizitäten und Phasenraumverteilungen als auch im Hinblick auf kollektive Phänomene wie gerichteten und elliptischen Fluß, die in dieser Arbeit leider gar nicht erwähnt werden konnten. Die Fluktuationsanalyse aus Kapitel 6 könnte auch Fluktuationen von transversaler Energiedeposition und transversalem Impuls einschließen. Die Suche nach exotischen Clustern ließe sich auf die vermuteten D_{sJ}-Zustände ausdehnen.

Alle diese Analysen können für den Energiebereich des SPS und speziell auch im Hinblick auf das CBM-Programm (Compressed Baryonic Matter) des geplanten Ausbaus der Anlagen der GSI zu FAIR (Facility for Antiproton and Ion Research) ausgeführt werden.

Von eher grundsätzlichem Interesse wäre eine vertiefende Untersuchung der Nichtgleichgewichtsvorgänge sowie der in den dynamischen Rechnungen im Vergleich zu den thermischen Analysen auftretenden Unterschiede in der Temperatur des Hadronisierungsübergangs. Hier spielen sowohl Effekte der endlichen räumlichen Ausdehnung als auch der kurzen Lebensdauer des rasch expandierenden Systems freibeweglicher Farbladungen eine Rolle, die Abweichungen von den Gleichgewichtseigenschaften erwarten lassen.

Schließlich werden mögliche Änderungen des Modells selbst diskutiert: Es wäre interessant zu sehen, welche Auswirkungen die Verwendung von Konstituentenmassen der Quarks haben würde. Bei der Anwendung auf Energien von RHIC und darüber hinaus könnte es erforderlich werden, neben anderen Anfangsbedingungen aus Partonkaskaden oder Rechnungen zur Teilchenproduktion in klassischen Yang-Mills-Feldern auch Quarkstreuungen, eventuell mit Farbaustausch, sowie harte Gluonen als dynamische Freiheitsgrade in Betracht zu ziehen. Zuletzt könnte man darüber nachdenken, den Ansatz der Potentialwechselwirkung zu verbessern, etwa durch Einbeziehung weiterer Terme, oder aber durch eine vollständige Umstellung auf Netze von Farbflußröhren, wie sie im Rahmen des Friedberg-Lee-Modells dynamisch berechnet werden können.

Table of Contents

List of Figures

Part I

Quantum chromodynamics and the quark-gluon plasma – issues and models

omnis ut est igitur per se natura duabus
constitit in rebus; nam corpora sunt et inane

— Titus Lucretius Carus

This thesis presents a model for the dynamical description of deconfined quark matter created in ultra-relativistic heavy ion collisions, using classical point particles subject to a colour potential interaction.

Before immerging into all the technical details of a work covering a very small, restricted spot of scientific research that is a thesis, we will start with a brief sketch of the vast background against which it is set. A semi-historical outline in chapter 1 provides a general overview of the issues and problems that have led to today's understanding of elementary matter. More specifically, we will be lead to the open questions involving the search and characterization of the quark-gluon plasma (QGP), using ultra-relativistic heavy ion collisions as an experimental tool. It is obvious that this overview is far from comprehensive.

Nowadays experiments in high energy physics are very complex. The interpretation of data often requires models which allow to formulate expectations for experimental results on the basis of well-established underlying physical theories. Only then, interesting, new features and phenomena can be isolated. This is all the more important in the field of quark-gluon plasma physics, where the underlying theory, quantum chromodynamics (QCD), is solvable only at very high energies.

QCD itself, and some more simplified theories derived from it, will be discussed briefly in chapter 2. Then, some of the models used to describe partonic degrees of freedom as encountered in ultra-relativistic heavy ion collisions at the highest energies will be described in chapter 3. This discussion will allow a better appraisal of the model presented in this thesis, quark molecular dynamics (qMD).

The qMD model describes quarks as classical point particles which carry are colour charge and are subject to a confining potential interaction. This allows the dynamical description of quarks degrees of freedom in heavy ion collisions, including a recombination scheme for hadronization.

The qMD model itself, its thermal properties and its application to heavy ion collision will be described in part II. Two model studies concerning charge fluctuations as a probe of deconfinement, and the creation of exotic hadrons in heavy ion collisions, are the subject of part III.

Chapter 1

From atoms to the QGP – an overview

1.1 The standard model of elementary particle physics

2005 was singled out as the world year of physics in order to commemorate Albert Einstein's *annus mirabilis* of one hundred years ago.[1] Most people know that this year marks the birth of special relativity. With some more interest in physics, they may be aware also of the formulation of the quantum hypothesis of light, which earned Einstein the Nobel price in 1921. In contrast, his papers on Brownian motion may appear less spectacular, and are not so well known today, probably for this reason. Indeed, when looking back from a modern point of view, it is hard to imagine that Einstein's analysis of Brownian motion was substantial to proof "by inspection" the existence of atoms—still contested at that time by such established scientists as Mach and Ostwald. That atoms exist, and, ironically, are not the indivisible constituents of matter the Greek natural philosophers Demokritus and Leukipp and their many followers throughout the ages had in mind, became a matter of fact within this first decade of the last century.

Einstein, when formulating the equivalence of inertial mass and energy as a consequence of special relativity in his last paper of the *annus mirabilis*, rightly speculated that this might explain the large amounts of energy set free from the probes of radium, the new element that Marie Curie had managed to isolate a short time before. It was in fact the study of radioactivity that helped to establish the substructure of atoms: While Einstein was revolutionising the theoretical underpinnings of physics from his desk at the patent office in Bern, Rutherford in Montreal, and later in Manchester, embarked on a series of experiments that eventually revealed what this substructure was. Together with Soddy, he showed that α particles, this first flavour of radioactive rays discovered by Becquerel, were in fact

[1] For Einstein's achievements of 1905, see e. g. [1]. A general account of the development of physics in the 20th century can be found in [2]. The evolution of high energy physics and the understanding of the structure of matter is treated in more detail in [3], and for the emergence of the standard model of elementary particle physics, [4] is a comprehensive source. For a specific history of the quark model and QCD, see [5], and the recent, more popular account [6]. This section does not contain any references to the primary literature. They can be found in the texts mentioned before, especially in [3, 4, 5].

some part of the atoms of helium. Furthermore, they could establish that radioactivity, in fact, can transmute elements, those building blocks of matter chemists had come to accept as unchangeable when emancipating from alchemistic ways of thinking. But the most important experiment, both methodological and because of its physical significance, lay still ahead in 1905.

It were the scattering experiments conducted by Rutherford's assistants Geiger and Marsden in 1909 that could only be understood if the atom was accepted as something essentially empty, with very light, negatively charged electrons rushing around a very small and dense central nucleus with positive charge. How such a strange and ethereal compound object, naively imagined as some miniature planetary system, could be responsible for the solid appearance of matter was a riddle that could not be solved before the constitution of quantum mechanics. But with the Pauli exclusion principle and the wave equations of Schrödinger and Dirac at hand, there was a vague feeling among physicists around 1928 that the end of physics may be in close reach, with all matter understood as consisting of atoms, built from electrons and protons and bound together by electromagnetic fields.[2]

Of course, like so often before and after 1928, the proclamation of the end of physics proved to be premature. Dirac's equation had solutions with negative energy which could be interpreted as antimatter—and in 1932, Anderson discovered in fact the positron, the antimatter partner of the electron. However, concerning the structure and binding of matter, two different developments of that time may be considered as even more important: Chadwick's discovery in 1932 of the neutron, the uncharged partner of the proton as a building block of the atomic nucleus, was the first important step to understand the structure of matter. Evidently, there had to be a strong, short range interaction, independent of electrical charge, which binds together neutrons and protons in the nucleus, and whose properties could explain the observed binding energies of different nuclei with the Bethe-Weizsäcker formula. The differences between neutrons and protons were described by Heisenberg using different orientations of a vector in an abstract isospin space. In this theory of isospin, the neutron and the proton are different manifestations of one strongly interacting particle, the nucleon. Furthermore, it became clear in the early 1930s that β decay, the second flavour of radioactivity characterized by the emission of an electron from the nucleus, must involve an interaction that is not electromagnetic. Pauli had postulated the uncharged neutrino in order to safe the conservation of energy and momentum in β decay. This particle, which could be definitely reconstructed in experiment only more than 20 years later, turned out to be an important building block in Fermi's theory of this so-called weak interaction, which successfully described β decay as a transmutation of a neutron into a proton, an electron, and an antineutrino. Thus, there was a new particle, the neutron, and two new interactions, the strong one and the weak one. The concept of the structure of matter emerging from this knowledge is shown schematically in figure 1.1.

On the theoretical side, electromagnetism was formulated as a quantized gauge field theory in th 1940s, which was to set a model for both the understanding of the

[2]Max Born is sometimes said to have proclaimed, after learning about the Dirac equation, that "physics, as we know it, will be over in six months". This quote is apocryphal and not substantiated by the historical sources. In any case, it conveys the general first excitement created by the Dirac equation and its predictive power.

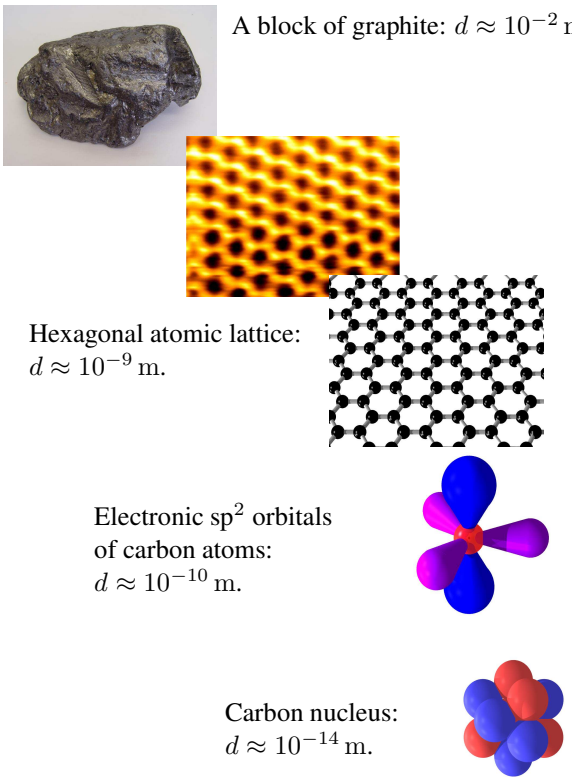

Figure 1.1
The structure of matter: The physical properties of a chunk of graphite can be understood from its atomic structure, as graphite consists of layers of atoms in a hexagonal ordering. This atomic structure is a consequence of the sp^2 hybridization of the electronic orbitals. The electrons, again, are bound together by the strong electric field of the positively charged atomic nucleus. The nucleus is built up of six protons and six neutrons, hold together by the strong force. But even the tiny nucleons, with diameters $\approx 10^{-15}\,\mathrm{m}$, are not elementary yet. While the structure of matter as shown in this figure is known since the 1930s, methods to make it directly visible are more recent: The hexagonal plane of carbon atoms in graphite has been imaged using an atomic force microscope [7], and electronic orbitals of molecules and atoms can be sampled with femtosecond laser techniques [8].

weak and the strong interactions. For the electromagnetic and weak interactions, the discovery of the muon, and much later the tauon, had to be incorporated in the theory. Most important, however, Fermi's theory could be replaced by a gauge theory, constructed along similar lines as electromagnetism, but substituting the local phase invariance U(1) of electromagnetism by the larger, non-abelian gauge group SU(2)×U(1). A non-abelian gauge theory was first constructed by Yang and Mills in 1954, when they tried to establish a local version of Heisenberg's isospin symmetry between proton and neutron. The theory of Yang and Mills was not successful for the description of the strong interaction, but adapted to the weak interactions, it allowed for an unification of electromagnetism and the weak interaction in the non-abelian theory of Weinberg, Glashow, and Salam. This unified theory predicted the so-called weak currents, and the W and Z vector bosons, which transmit the weak interaction in the same way as the photon mediates the electromagnetic interaction. Weak currents and the vector bosons were detected at CERN in 1973 and 1983, respectively.

Since the electroweak interaction is very short range, the gauge bosons have to be massive, and in order to allow for massive gauge bosons, gauge symmetry must be spontaneously broken, in a way analogous to the breaking of rotational symmetry in a ferromagnet by spontaneous magnetization. This could be built into the theory by the so-called Higgs mechanism. The Higgs mechanism not only gives mass to the gauge bosons and all the massive fermions. As a further consequence, it predicts the existence of the so far undetected Higgs particle. Neutrinos are the sole fermions to remain massless in the standard version of electroweak theory, so

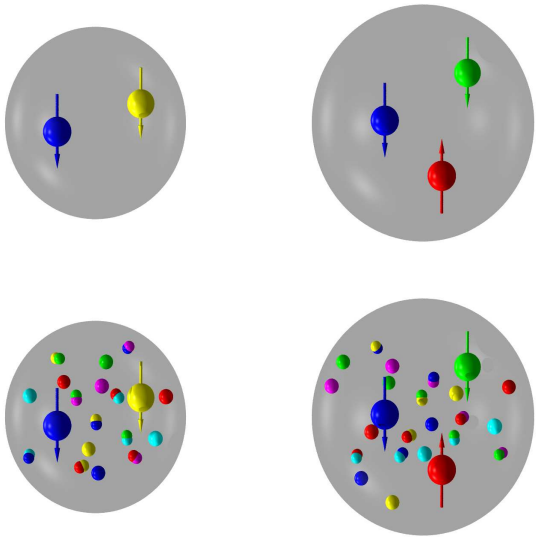

Figure 1.2
Hadrons have a substructure: In the naive constituent quark model, a meson is built up from a quark and an antiquark carrying colour and anticolour (upper left panel), and a baryon from three quarks with three different colours (upper right panel). The arrows indicate up and down quarks ($\uparrow = \mathrm{u}$, $\downarrow = \mathrm{d}$) and antiquarks ($\downarrow = \bar{\mathrm{u}}$, $\uparrow = \bar{\mathrm{d}}$). Hence, the figure shows a π^- and a neutron. However, the physical content of the hadrons is much bigger, including sea quarks and antiquarks (small spheres) and gluons (small double spheres—lower panels), as described by so-called structure functions.

understanding the experimentally observed small neutrino mass and the detection of the Higgs boson are the most imminent open issues of the electroweak model.

In parallel to the development of the electroweak model, strong interaction physics has taken a much more involved path, and left much more questions open until today. It was argued by Yukawa in 1935 that the strong interaction between nucleons should be mediated by massive particles, which were in fact found as the pions in the 1940s. However, the number of strongly interacting particles went on to increase, as more and more particles were discovered: strange particles such as the kaons and hyperons, an many states of very short lifetime, called resonance particles. The zoo of strongly interacting particles—bosons, as the pions and the kaons, known as mesons, and fermions, as the nucleons and the hyperons, known as baryons—seemed quite mysterious, when Gell-Mann and Ne'eman in 1961 came up with the $\mathrm{SU}(3)$-flavour scheme, thus providing in a kind of periodic system for hadrons. This scheme, which was called the "eightfold way", classifies all known hadrons in particle multiplets which are identified with irreducible representations of the flavour group $\mathrm{SU}(3)$.[3] One of its immediate successes was the prediction of the Ω^-, a baryon with strangeness $S = -3$ and spin $s = 3/2$. A natural explanation for the structure of the "eightfold way" could be given by Gell-Mann and Zweig in 1964 with the quark model. In this model, all baryons are composed of three subnucleonic particles, the quarks, while mesons are made up of a quark-antiquark pair. These quarks have fractional electric charges, and, technically speaking, they correspond to fundamental representations of the $\mathrm{SU}(3)$ flavour group. Curiously, baryons made up of three quarks revealed themselves to be totally symmetric with respect to the combined quantum numbers of spin and flavour. Since quarks are fermions, the Pauli principle requires a further quantum

[3] The application of the theory of groups and their representation to the classification of elementary particles is explained in some detail in appendix B. The multiplets of mesons and baryons that follow from the representation theory of the extended flavour group $\mathrm{SU}(4)$, which includes charm, are shown in appendix A.

number, in which the quarks wave function of a baryon has to be completely antisymmetric. Such quantum numbers were proposed by Greenberg, and Han and Nambu, still in the same year as the quark model, and are now known as colour. The colour model implies that each quark occurs in one of three different colours, which correspond to the fundamental representation of a further SU(3), the colour group. Hadronic wave functions built up of quarks are completely antisymmetric singlets. This means that in a mesons, the quark and the antiquark carry colour and anticolour, respectively, while in baryon, the three quarks carry three different colours. The upper part of figure 1.2 shows the substructure of the negative pion and the neutron emerging from this so-called naive constituent quark model.

The naive quark model of the 1960s had, despite its successes, a serious problem: there was no direct experimental evidence for quarks, and no dynamical theory of their interaction. Nambu has suggested in 1965 that the interaction between quarks with colour may be mediated by eight vector particles, which were later identified as gluons, but there was no hint at the existence of such particles. In the very tradition of Rutherford's experiments at the beginning of the century, scattering experiments of Hofstadter in 1956 had revealed that the proton is not a point particle. However, there were no signs of a point-like substructure either, and for this reason, the most serious contenders to explain hadronic structure remained the so-called dual models. These models, which are at the origin of nowadays string theory, tried to explain the huge number of hadronic resonances as excitations of a tiny, vibrating string. In particular, they could predict the experimentally observed Regge slope, the linear relation $J = \alpha\, m^2 + \alpha_0$ between angular momentum J and mass squared m^2 of hadrons and hadronic resonances.

The situation changed in favour of the quark model in 1969, when the experiments of Friedman, Kendall, and Taylor with deep inelastic scattering of electrons on protons at SLAC did find, indeed, point-like scattering centres with spin $s = 1/2$ within the proton. These point-like centres were dubbed partons and identified with the quarks and the tentative exchange particles of Nambu. In 1973 Gross, Wilczek, and Politzer realized that non-abelian gauge theories have the property of "asymptotic freedom": at very short distances, or at very high momentum exchange, the particles in such a theory have small coupling and behave as if free. This was exactly the behaviour found for the partons in deep inelastic scattering. Thus, it was perfectly reasonable to write down a dynamical theory of quarks, based on the non-abelian colour group SU(3) as the gauge group responsible for the interaction. Gell-Mann, together with Fritzsch and Leutwyler, assembled the pieces and called the theory quantum chromodynamics (QCD). It was argued that the non-abelian nature of the gauge field is responsible for the fact that no free colour charges can be observed, a conjecture that is called "colour confinement". We will say more about it in the following section. The lower part of figure 1.2 shows the modern picture of the hadron, as it follows from QCD: the valence quarks of the naive quark model are embedded in a sea of gluons and virtual quark-antiquark pairs, called sea quarks.

With the formulation of QCD, the essential parts of the modern standard model of elementary particle physics and the structure of matter were on the table—new particles to be found later could be integrated easily into the scheme and were even predicted for reasons of consistency of the model. When working on the integra-

Table 1.1
The building blocks of matter in the standard model: Matter is built up of fermions, which come in three families of equal electric charges, but different masses. To each particle in the table, there is a corresponding antiparticle.

	particle		charge
e	μ	τ	-1
ν_{e}	ν_μ	ν_τ	0
u	c	t	$+2/3$
d	s	b	$-1/3$
$\longrightarrow$	mass	$\longrightarrow$	

Table 1.2
The gauge bosons of the standard model which mediate the different interactions.

electroweak	strong	gravitational
γ, Z^0, $\mathrm{W}^\pm$	g	graviton
A_μ, Z_μ, W_μ	T^a_μ	$h_{\mu\nu}$

tion of quarks into the electroweak theory, for example, Glashow, Iliopoulos, and Maiani had proposed in 1970 that the strange quark should have a massive partner in order to complete a doublet of weak isospin. This new quark flavour, the charm quark, was indeed found in 1974, when two experimental groups discovered a narrow meson with a mass of $3.1\,\mathrm{GeV}$. This particle, the J/Ψ, was interpreted as a bound state of a charm-anticharm pair. That a third family of quarks beyond the doublets up, down and strange, charm should exist was proposed in 1973 by Kobayashi and Maskawa in order to account for the CP violation which is observed in the decay of kaons and which is necessary to explain the asymmetry of matter and antimatter in the early universe. Again, the discovery of the Υ meson in 1977 vindicated this proposal, since the Υ could be understood as a bound bottom-antibottom state, as the fifth quark flavour was called. The discovery of its partner in weak isospin, the top quark with the extreme mass of $174\,\mathrm{GeV}$, had to wait until 1995, when the Tevatron at Fermilab could produce enough energy for its creation. The lepton of the third family, the τ meson was known since 1975.

With the discovery of the top quark, the particle table of the standard model as listed in table 1.1 was complete. All matter is built up of these fermions, which come in three families of equal charges, but different masses. The decay width of the Z boson as measured at LEP shows that there are only three low-mass or even massless neutrinos, which strongly suggests that there is no fourth family of fermions. The gauge bosons of the standard model are listed in table 1.2. This table also includes the graviton, which is thought to mediate gravity. It may seem odd that gravity, the first theory constructed from a gauge principle, has so far defied all attempts to a formulation as a fully quantized theory. However, one should not forget that for gravity, it is the metric tensor and not the connection derived from it which is the dynamical degree of freedom.

Whereas the standard model is complete and essentially unchanged since more than 30 years, there are many open questions left which it does not answer: What are the reasons for the parameters of the model? How can the different mass scales of the three different families be understood? Is there some simpler scheme behind? Does the Higgs boson exist, and what is its mass? How is the small mass

of the neutrinos created, which can not be caused by the left-right mixing scalar Higgs? And what is the cause of the hierarchy problem, the huge gap between the electroweak and the gravitational coupling? To the last question, and some of the former, the concepts of supersymmetry and large extra dimensions (LXD) may give some answers. And there are high expectations that the Large Hadron Collider (LHC) will provide experimental support for some of these ideas once it starts operating in 2008. But this is not our primary concern in this thesis: We come back now to QCD and the quark-gluon plasma.

1.2 Difficult QCD, manifold QCD

That quantum chromodynamics offers a theory describing the fundamental building blocks of nuclear matter, quarks and gluons, and their interaction, does not imply that all problems concerning elementary matter are solved. On the contrary: Due to the non-abelian nature of the gauge group $\mathrm{SU}(3)$, gluons are self-interacting, which generates such peculiarities of QCD as colour confinement and asymptotic freedom. We will discuss these aspects of QCD in some more detail in chapter 2. Here, we provide a short, qualitative description of these features.

1.2.1 Some peculiarities of QCD: Asymptotic freedom, colour confinement, and the string picture

Asymptotic freedom, the general feature of non-abelian gauge theories that the coupling constant becomes small at high momentum exchange, means that high energy scattering processes between quarks and gluons can be calculated to a high precision using the tools of perturbation theory. Thus, perturbative QCD (pQCD) allows predictions that can be checked in experiment and that provide essential tests for the correctness of QCD. For example, the number of colours and the fractional charges of quarks enter the ratio of the cross sections for hadron production to muon-antimuon production in electron-positron annihilation, and data show complete agreement with the predictions of QCD. Gluon bremsstrahlung is responsible for three-jet events, which were discovered at DESY in 1979. The self-interaction of gluons, the triple-gluon-vertex, contributes to the decay width of the Z boson and was confirmed in the high-precision measurements of the Z boson at LEP.[4]

However, no free colour charges, neither quarks nor gluons, could ever be found in experiments. This is colour confinement. Perturbative QCD copes with it through the introduction of fragmentation functions, which describe how to replace a high-energy parton by a bunch of hadrons. But the main problem is the low-energy regime, where the coupling is large and no exact analytic tools are available. As a consequence, the ground state of quarks and gluons at low energy, the hadrons, can be described only by numerical methods using lattice QCD, or by approximations to full QCD. Such model approximations to QCD at low energies are for example the bag models, potential models, or models involving classical solutions of the gauge field, such as monopoles or instantons. Some of them will be discussed in more detail in the following chapter. Besides providing means to

[4] Detailed explanations and references can be found, e. g., in the textbooks [9, 10].

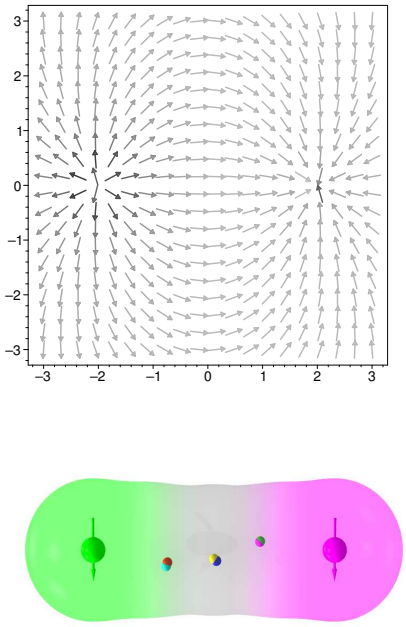

Figure 1.3
Field configurations created by two charges for the electromagnetic and the strong interaction: While the electric field of a dipole is spread over the whole space (upper figure), the field of the strong force is confined to a flux tube connecting the two charges (lower figure). Since the flux density in the flux tube is independent of the distance, the same holds for the energy density of the colour field, giving rise to a constant string tension κ.

describe hadrons, these models can help to develop a qualitative understanding of QCD at low energy.

One of these qualitative pictures emerging from models of low energy QCD is the string picture (figure 1.3): While the electrostatic field of two electric charges is spread over the whole space, the analogous colourelectric field of two colour charges is confined to a so-called flux tube connecting both sources. This formation of a flux tube is a consequence of the self-interaction of the gluon field. Because of the confinement of the colourelectric field, its flux density is roughly constant along the flux tube, and independent of the distance of the two charges. The same holds for the energy density of the colourelectric field. Thus, the formation of a flux tube gives rise to an increase of the interaction energy of the colour charges which is linear in distance and can be described by a constant string tension κ. The string picture is essential to many models that are used to study QCD: It provides a connection to the pre-quark dual string models and Regge trajectories [11, 12]. It relates modern multi-dimensional string theory and four-dimensional gauge theories [13]. It emerges from simulations of QCD on the lattice [14]. It is used as a leading term of the interaction energy at large separations in the Cornell potential and in other potential models, which are used to describe the spectrum of mesonic states [15, 16, 17, 18]. All these different models agree on a value of $\kappa \approx 0.9\,\mathrm{GeV/fm} = 0.46\,\mathrm{GeV}^2$ for the string constant. A potential interaction that increases linearly with separation is the central ingredient of the qMD model (see chapter 4) which is the subject of this thesis.

Most important, the string picture provides a very appealing explanation for colour confinement: In order to separate the quark-antiquark pair in a meson, it would be necessary to rip them apart. But any attempt to do so results in the formation of a colourelectric flux tube, and requires an amount of energy that increases linearly with the separation distance. Eventually, the energy of the constant

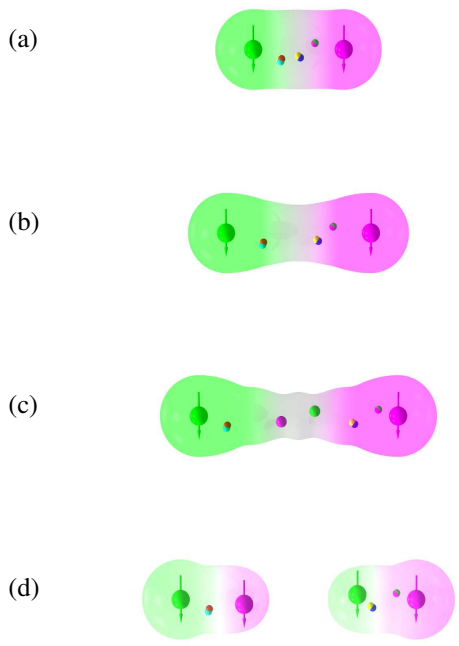

Figure 1.4
When two colour charges in a meson are separated (a), the energy contained in the flux tube of the field of the strong force increases linearly with distance (b). The energy of the constant field in the flux tube allows the tunnelling of a quark-antiquark pair from the vacuum: a virtual pair is promoted to a real pair (c). This process breaks the flux tube, leading to the formation of two mesons (d). This mechanisms prevents the separation of free colour charges and ensures colour confinement.

colourelectric field is sufficient to allow the tunnelling of a virtual quark-antiquark pair from the vacuum in the flux tube to become a real pair. Thus, this process breaks the flux tube, and the final state contains two mesons instead of one (figure 1.4). Analogous arguments hold for any attempt to separate a colour charge from a colour neutral object. This shows the impossibility of creating free, single colour charges, either quarks or gluons: All colour charges are concealed in colour neutral objects, which are the hadrons.

It should be noted, however, that there is still no rigorous, analytic proof of confinement starting from the Lagrangean of QCD.

1.2.2 Recent surprises: Are there pentaquarks out there?

Hadrons are made of quarks, in configurations that are colour neutral singlet states: a baryon contains three valence quarks with three different colours, and a meson is made up of a quark-antiquark pair with colour and anticolour. It is obvious that both colour neutrality and confinement can be fulfilled also for bigger clusters of quarks and/or antiquarks. Thus, the possibility of hadronic objects different from standard mesons and baryons, which were dubbed exotica, was imagined since the early times of QCD [19, 20], and studied for example in the framework of the MIT bag model [21]. However, experiments did not find any convincing signals for the existence of exotica [22]. In 2003, a Japanese group reported the identification of a so-called pentaquark Θ^+, a state made up of four light quarks and an antistrange quark [23]. This spurred a lot of activity, but it is still doubtful whether the Θ^+ actually exists. Chapter 8 reviews the situation and gives a detailed discussion of the creation of exotic hadrons by quark recombination in heavy ion collisions, as seen in the qMD model used in this thesis.

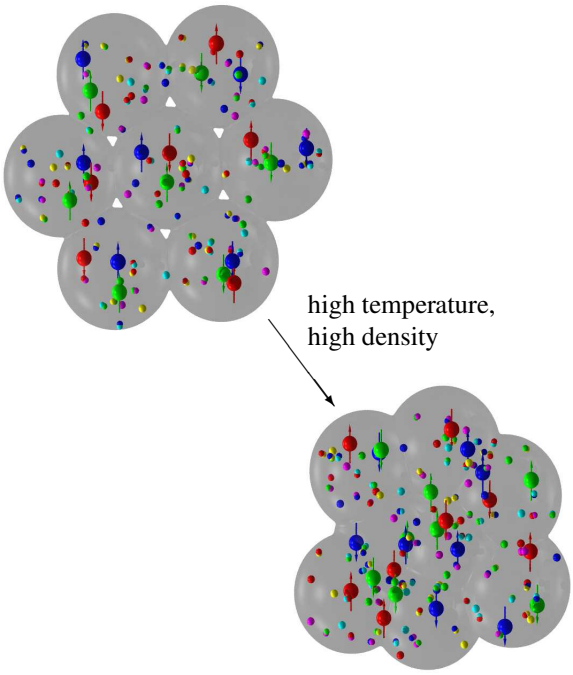

Figure 1.5
Transition from hadronic nuclear matter (top) to a QGP (bottom): Under high density or at high temperature, nucleons strongly overlap. This overlap creates an extended region of deconfined quark-gluon matter, where quarks and gluons are free to propagate without bounds. Such a situation can occur in the core of a neutron star, or it may be created for a fleeting moment of some $10^{-23}\,\mathrm{s}$ in a heavy ion collision.

1.2.3 The phase diagram of QCD and the quark-gluon plasma

In standard nuclear matter at its ground state, with a density of $\rho_0 \approx 0.16\,\mathrm{n/fm^3} \approx 150\,\mathrm{MeV/fm^3}$, quarks and gluons are contained within well-defined nucleons. The interaction of the nucleons, as described by the various nuclear forces, can be understood as a van der Waals type remainder of the fundamental, strong interaction of the quarks and gluons. It was the insight of Collins and Perry [24] that under extreme density and pressure, as found for example in neutron stars, this situation can change: The ground state of strongly interacting matter then is formed by an extensive bag of deconfined quarks and gluons, with no hadronic correlations left (figure 1.5). Since nucleons, and quarks, are fermions, compression at $T \approx 0\,\mathrm{MeV}$ (as for ground state nuclear matter) goes hand in hand with an increase of the Fermi energy, or the chemical potential μ.

It turns out that high chemical potential at low temperature is not the only means to create deconfined quarks and gluons out of hadronic matter: high temperature at low chemical potential works as well. Information about strongly interacting matter at finite temperature and moderate chemical potential stem mainly from simulations of QCD on the lattice [25, 26].

Plotting the relevant degrees of freedom of strongly interacting matter as a function of temperature and chemical potential yields the phase diagram of QCD, which is shown schematically in figure 1.6: Nuclear matter in its ground state is has a temperature $T \approx 0\,\mathrm{MeV}$ and a quark chemical potential $\mu_0 = 308\,\mathrm{MeV}$. With moderately higher chemical potential, this is also the matter found in neutron stars. For $\mu \lesssim \mu_0$ and $T \lesssim 150\,\mathrm{MeV}$, strongly interacting matter forms a hadron gas, or a dense hadronic system. At sufficiently high temperature or chemical potential, the deconfinement transition from hadrons to the quark-gluon plasma

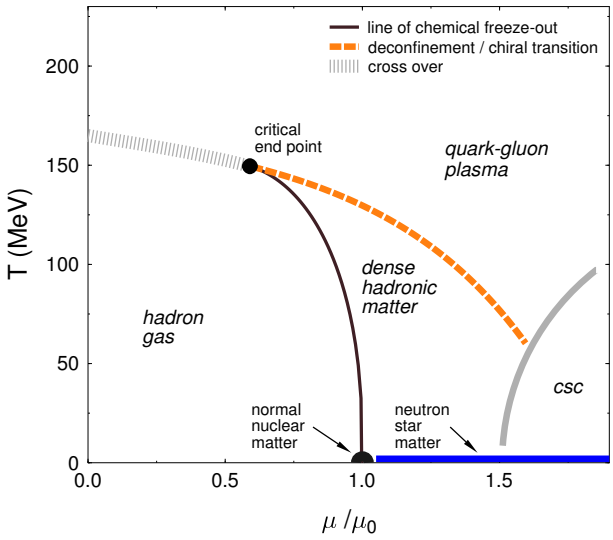

Figure 1.6
A schematic representation of the phase diagram of QCD matter in the (T, μ) plane: Shown are the lines delineating the chemical freeze-out (solid) and the chiral/deconfinement transition (dashed), ending at the critical point, which is linked to the $\mu = 0$ axis by a line of cross-over at $T \approx 170\,\mathrm{MeV}$. At high chemical potential and low temperature, colour superconductivity (csc) sets in. Nuclear matter at the ground state is at $T = 0$ and $\mu = \mu_0$.

occurs. This transition is thought to be of first order for high chemical potential, and ending in a critical point, where it is of second order. It is a cross-over, i. e. a smooth transition between a hadron gas and a quark-gluon plasma, in the region of the phase diagram between the critical end point and the T axis, which is hit at $T \approx 170\,\mathrm{MeV}$. Finally, at high chemical potential and low temperature, cool and dense quark matter is supposed to undergo at least one further phase transition, and becomes a colour superconductor [27]. The nature of the quark-gluon plasma at high temperature is not completely clear so far: It is known for quite some time that it is most probably not an ideal gas of non-interacting quarks and gluons [28]. Recent data from RHIC indicate that it is a strongly coupled plasma, dubbed the sQGP [29], and are interpreted as signs of an ideal fluid [30].

The deconfinement transition goes hand in hand with the restauration of chiral symmetry, i. e. the vanishing of the mass of the quarks. While quarks bound in nucleons can be described as so-called constituent quarks, whose large effective mass of $m \approx m_{\mathrm{nucleon}}/3$ is caused mainly by the interaction with the gluons, deconfined quarks are nearly massless. Beyond the deconfinement, or chiral, transition, they have small, so-called current masses of $m_{\mathrm{u,d}} \approx 10\,\mathrm{MeV}$. This implies that only $\approx 3\%$ of the mass of the nucleon stems from the Higgs mechanism—the main contribution comes from the strong interaction, as described by the breaking of chiral symmetry. It can be helpful to represent the phase diagram of QCD as a function of density instead of chemical potential. Assuming strongly interacting matter as a Fermi gas of nucleons, the density can be calculated from the temperature and the chemical potential using the grand canonical ensemble. The resulting phase diagram, which exhibits the coexistence regions related to the first order phase transition, is shown in figure 1.7. The liquid-gas transition of diluted nuclear matter and its critical point are also included [31].

Exact data about the phase diagram of QCD is still missing. Its exploration, including the verification of the first order transition and the location of the critical point, and the characterization of dense baryonic matter and the quark-gluon plasma are primary goals of current research.

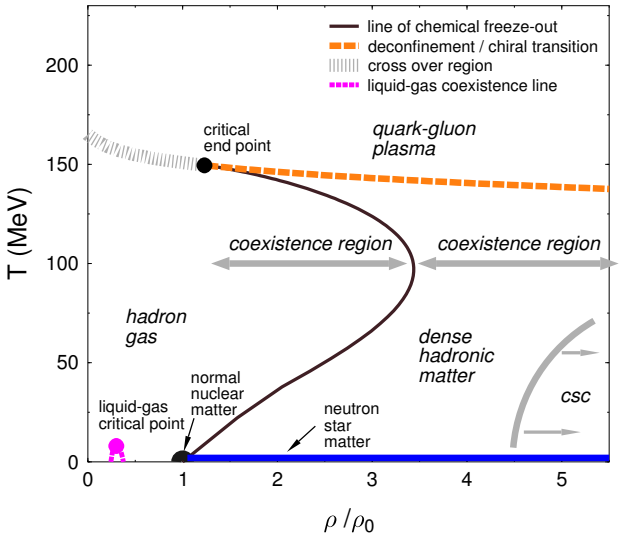

Figure 1.7
The phase diagram of figure 1.6, mapped to the (T, ρ) plane using the ideal Fermi gas model for the description of the hadron gas. The figure shows the coexistence regions related to the first order phase transition. Moreover, it includes the liquid-gas transition in diluted nuclear matter, together with its critical point.

Unfortunately, strongly interacting matter away from ground state nuclear matter only occurs in nature under extreme conditions: A quark-gluon plasma at high temperature $T \gtrsim 200\,\mathrm{MeV}$ and zero chemical potential $\mu \approx 0\,\mathrm{MeV}$ did exist, according to current knowledge, only within the first 10 microseconds of the history of the universe [32]. Dense and cool quark matter at temperatures $T \lesssim 10\,\mathrm{MeV}$ and chemical potential $\mu \gtrsim 1.2 - 2\,\mu_0$ can occur in the interior of neutron stars [33]. The only method at hand to study the phase diagram of QCD in experiment are collisions of the nuclei of heavy atoms at ultra-relativistic energies, which are discussed now.

1.3 The experimental search for the QGP: Ultra-relativistic heavy ion collisions

If two atomic nuclei collide with centre of momentum frame energies exceeding $\sqrt{s}_{NN} \approx 8\,\mathrm{GeV}$, nuclear matter is compressed to a degree that confinement of colour charges in the hadrons of the nucleus can be overruled. At much higher energies, partons within the colliding nucleons scatter, thereby producing large numbers of new partons. In both cases, for a very short time $\Delta t \lesssim 10\,\mathrm{fm}/c \approx 3 \cdot 10^{-23}\,\mathrm{s}$, a deconfined quark-gluon plasma is created, and chiral symmetry is temporarily restored. Such collisions occur, for example, when iron nuclei of the cosmic radiation with energies up to $E \approx 10^6\,\mathrm{GeV}/N$ hit on argon nuclei of the upper atmosphere. In a controlled way, they are produced in experiments at heavy ion accelerators, such as SIS at GSI in Darmstadt, SPS at CERN in Geneva, or AGS and RHIC at BNL in Brookhaven.

At the SPS, lead nuclei are brought to collision with energies of $20-160\,\mathrm{GeV}/N$ in target mode ($\sqrt{s}_{NN} = 6.4 - 17.4\,\mathrm{GeV}$), while at RHIC, gold-gold collisions are studied in the collider mode with energies in the range $\sqrt{s}_{NN} = 62 - 200\,\mathrm{GeV}$. Experiments at all these machines aim to explore the phase diagram of QCD. Collisions at RHIC, for example, create a hot quark-gluon plasma with $\mu \approx 0\,\mathrm{MeV}$, while studies at the SPS probe regions with lower temperatures and finite $\mu \approx$

$50 - 100\,\mathrm{MeV}$. The analysis of collective observables such as flow suggest that the transition to the quark-gluon plasma happens already below the lowest SPS collision energies [34, 35]. The planned FAIR (Facility for Antiproton and Ion Research) at GSI will provide collision energies in the range $\sqrt{s}_{NN} \approx 5 - 10\,\mathrm{GeV}$, which is thought to be ideally suited to study highly compressed baryonic matter, the deconfinement/chiral transition, and perhaps even the critical point. The heavy ion program at the LHC will study conditions very close to the first microseconds of the big bang: With $T \gtrsim\approx 400\,\mathrm{MeV}$ and $\mu \approx 0\,\mathrm{MeV}$, LHC should find the transition of the strongly coupled sQGP to the free, non-interacting perturbative plasma.

1.3.1 What happens in an ultra-relativistic heavy ion collision?

Figure 1.8 shows snapshots of an ultra-relativistic collision of two lead nuclei at the SPS with a beam energy of $E = 80\,\mathrm{GeV}/N$, or $\sqrt{s}_{NN} = 12.4\,\mathrm{GeV}$, and an impact parameter of $b = 4\,\mathrm{fm}$. The figures have been calculated using the simulation codes UrQMD for the initial stage, and qMD for the expansion and recombination of the deconfined system, as will be described in detail in chapter 6.

The impinging nuclei collide, thereby creating a zone of hot, compressed matter, where deconfinement is overcome and colour charges are set free. As mentioned before, the detailed dynamics of the early phase and the transition of baryonic matter to deconfined quarks and gluons depends on the energy of the collision, with either compression or multiple partonic scatterings playing the dominant role. How this early phase of the collision, the formation of an pre-equilibrated partonic system, happens in detail is not completely clear yet.

Once a quark-gluon plasma is formed, it will expand, and cool down during expansion. When the temperature falls below the line of the deconfinement transition, hadrons are formed, which will interact further. Hadronic interactions can be both inelastic and elastic, until so-called chemical freeze-out is reached and hadronic collisions become purely elastic. Finally, the expanding system is so diluted that there are no more interactions—this is the so-called kinetic freeze-out. The final state hadrons, which may undergo weak decays, can reach the detector.

In qMD simulations, such as shown in figure 1.8, only the expansion and recombination of coloured quarks is treated, as well as the decays of hadrons and hadronic resonances formed at recombination. Gluons are handled in an effective way through the use of a colour potential interaction, as will be discussed in detail in chapter 4. No further hadronic rescattering is included in the model.

The quark-gluon plasma created in an ultra-relativistic heavy ion collision exists only in a very small region of space, in the order of some $V_{\mathrm{QGP}} \approx (10\,\mathrm{fm})^3$, and for a very short time span in the order of $\Delta t \lesssim 10\,\mathrm{fm}/c \approx 3 \cdot 10^{-23}\,\mathrm{s}$. All information about this fleeting state has to be reconstructed from final state hadrons which are measured in the detector. It is not clear, a priori, that any clear evidence for the phase transition and the properties of the plasma can be measured at all under these conditions: From solid state physics, it is well known that sharp signatures of phase transitions are smeared out by finite size effects, and take time to build up due to critical slowing down [36, 37]. Thus, it is extremely important to identify robust signals that allow safe conclusions about the hot and dense intermediate phase

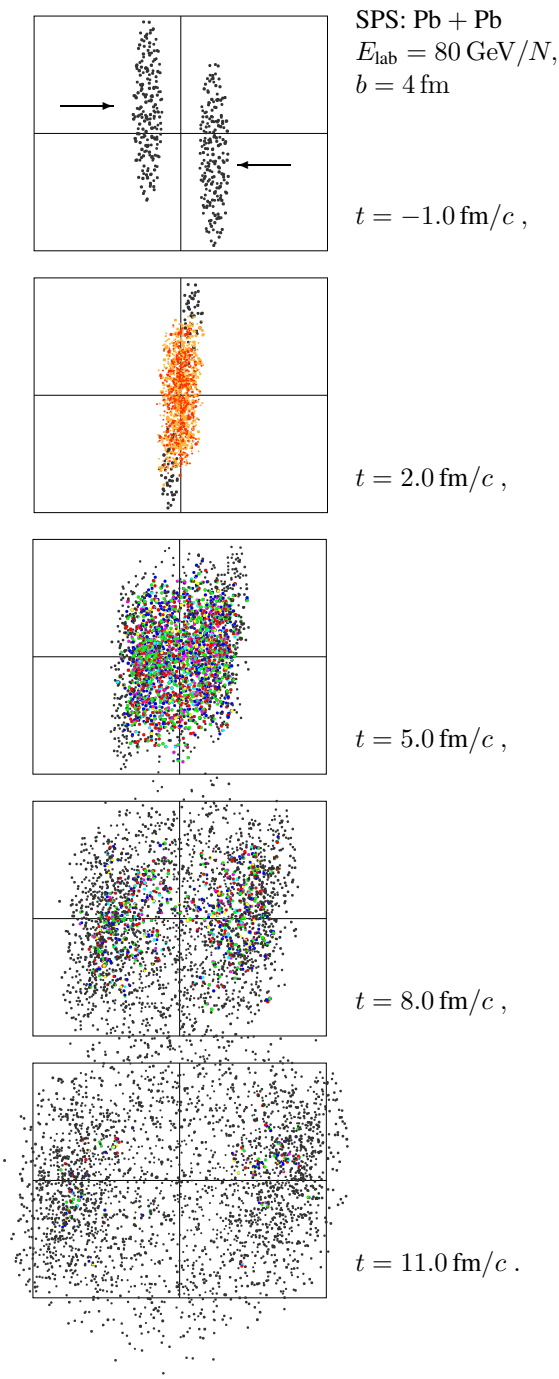

Figure 1.8
Snapshots of an ultra-relativistic heavy ion collision at the SPS with a beam energy of $E = 80\,\text{GeV}/N$, corresponding to $\sqrt{s}_{NN} = 12.4\,\text{GeV}$, and an impact parameter $b = 4\,\text{fm}$: The upper panel shows the incoming nuclei before impact. In the collision, a hot and dense zone of colliding particles is created (shown in orange and red), where the quarks and gluons of the reacting hadrons can be set free. As the hot fireball expands, it cools down, and finally, all coloured matter is confined again in hadrons, which can reach the detector. These snapshots have been calculated using the simulation codes UrQMD and qMD, as will be discussed in detail in chapter 6. The unit of time is $1\,\text{fm}/c = 0.33\,10^{-23}\,\text{s}$. The actual size of the snapshots is $20\,\text{fm} \times 16\,\text{fm}$.

of a heavy ion collision from the measurable hadrons, and other particles such as photons and leptons. Ideally, unique criteria should be established to distinguish a plasma of quarks and gluons form a hot and dense hadron gas.

1.3.2 How to recognize a quark-gluon plasma?

Many different observables have been proposed as signals to recognize a quark-gluon plasma created in an ultra-relativistic heavy ion collision. Here, we will

briefly mention some of them, which are either relevant to this thesis project, or of high interest in current research. Comprehensive reviews with detailed references to the vast literature can be found in [38, 39, 40, 41].

Fluctuation and correlation signals

Measuring fluctuations in conserved charges, energy, or transverse momentum of final state hadrons can provide signals of the QGP since fluctuations are sensitive to the underlying degrees of freedom [42]. Moreover, the theory of phase transitions suggests that strong fluctuations in all these observables should occur in the vicinity of the critical point. Likewise, correlations between final state hadrons can indicate the deconfined stage [43]. Chapter 7 addresses fluctuations of electric charge as signals of the QGP. Unfortunately, as it comes out, these signals are washed out by the hadronization dynamics.

Particle ratios: Strangeness and charm

Strangeness is a good indicator of a QGP, since its costs much less energy to produce a strange quark-antiquark pair in a deconfined environment than a kaon-antikaon pair in a hadron gas [44]. Moreover, the dynamics of hadronization will enrich strange quarks in the deconfined phase [45, 46]. As a result, if a QGP has been created in a collision, multistrange baryons are more abundant than expected from a purely hadronic system, as can be seen in SPS data. Similar arguments hold for charm. The qMD model does not handle properly the creation of strange-antistrange quark pairs in the QGP. Strangeness distillation, however, can be observed in the model, as will be discussed in section 8.4 in connection with pentaquarks.

QGP at the SPS and the "horn"

Among the strangeness signals, the ratio of positive kaons to positive pions as a function of the collision energy shows a horn like behaviour at lower SPS energy. This signature, which is not observed in proton-proton data and can not be reproduced by hadronic models, is interpreted as a signal for the onset of deconfinement at lower SPS energy [47]. It would be a tempting project to study this signal using the qMD model. However, this is not done here. It would require either the use of different initial conditions than those provided by UrQMD (the use of these initial conditions is discussed in chapter 6), or the modelling of processes such as gluon fusion in order to meet the strangeness chemistry of the deconfined phase.

What can be learned form the J/Ψ?

It was suggested that in a deconfined environment, the interaction between charm-anticharm pairs should be screened by unbound colour charges. As a result, the J/Ψ particle was expected to melt in a QGP [48]. There are reports of an observed "anomalous suppression of the J/Ψ" in central Pb+Pb collisions at the SPS, i. e. of fewer J/Ψ particles measured than expected from production and absorption processes involving only hadronic matter. However, this signature is murkier than originally thought. Moreover, there is evidence from lattice calculations that correlated quark-antiquark states such as the J/Ψ may survive at temperatures well

beyond the phase transition [49, 50]. Screening and the melting of the J/Ψ in a thermal, deconfined environment can be observed in the qMD model, as will be shown in section 5.3. However, there are qualitative and quantitative differences to the behaviour of a real QGP, as we will see.

Photons and dileptons as messengers from the early stage

Photons and dileptons, i. e. lepton-antilepton pairs created by the decay of virtual photons, or by vector mesons with the quantum numbers of a photon, are sensitive probes to the central zone of the collision, since they do have no strong interaction with the nuclear medium, whether it is deconfined or hadronic. Thus, thermal photons may serve as a thermometer, while dileptons allow to reconstruct the spectral density of vector mesons like the ρ [51]. This last signal is of interest in connection with the restauration of chiral symmetry. Photons and dileptons are not treated in this thesis, but the mass of the ρ is discussed in some more detail in section 6.2 in connection with the mass distribution of hadronic clusters formed in qMD.

Jet quenching at RHIC and Mach cones in quark matter

When two nuclei collide at RHIC energies, the scattering of partons can produce pairs of jets with high transverse momentum. If the production of such a jet pair occurs in a deconfined medium, one or both jets can loose energy to the medium through strong interaction processes, such as gluon bremsstrahlung. The observation of single jets with high momentum, without a partner in the opposite direction, can be understood as the creation of a jet pair at the edge of a zone of deconfined matter, where one jet can escape, while the other jet looses its energy to the medium. Thus, single jets signal the presence of a QGP. Indeed, such single jet events have been observed at RHIC. Even more interesting, the away-side partner jet does not simply disappear, but instead, a broad structure can be observed in angular momentum distributions. This has been interpreted as the signature of a Mach cone, created by the supersonic partner jet as it transverses the deconfined medium [52]. It would be interesting to study this phenomenon with the qMD model. Unfortunately, in the current version this can not be done, since the interaction of the fast jet with the coloured medium is described insufficiently. This may be an option for further studies with an improved model.

Signals of quark recombination at RHIC

RHIC measurements have provided data that very strongly suggest that hadronization of the expanding plasma of quarks and gluons occurs via the recombination of constituent quarks to hadrons. There are several experimental observations which can be explained easily within this picture. Examples are the unexpected high ratio of proton to pion yield as a function of transverse momentum for transverse momenta of $p_\perp \approx 3 - 4\,\mathrm{GeV}/c$ [53, 54, 55, 56, 57, 58], and the universal scaling of the elliptic flow as a function of transverse momentum for different particle species with constituent quark content [59, 60]. These findings have strongly intensified the interest in quark recombination models for the description of hadronization.

The qMD model accomplished a fully dynamical description of hadronization via the recombination of quarks, albeit current quarks instead of constituent quarks.

How this works in detail will be discussed in part II of this thesis. Unfortunately, the requirements of statistics forbid the direct application of the qMD model to the study of elliptic flow. The calculation of transverse momentum spectra for collisions at RHIC energies may be feasible, for example by some suitable restrictions in rapidity. However, here, we will discuss the complete, dynamical evolution of collisions using qMD only at SPS energies.

The importance of model building

Experiments with ultra-relativistic heavy ion collisions are extremely involved, and their interpretation requires the extraction of interesting, revealing information from all the data collected about the several hundreds to thousands of particles that reach the detector in each event. The interpretation of these data is only possible with the help of models that allow to formulate expectations for experimental results on the basis of well-established physical ideas. Only then, interesting, new features and phenomena can be isolated. Thus, for example, signatures for the quark-gluon plasma can be considered as relevant only if they can not be reproduced by any model using hadronic degrees of freedom only.

Some of the models that are used to study heavy ion collisions will be discussed in chapter 3. This allows a better assessment of the specific features of the qMD model used in this thesis. As we will explain in part II, the qMD model tries to implement some features of QCD, most important a confining interaction, into a classical molecular dynamics. This model is then used to study the hadronization of quarks in the expanding fireball of a ultra-relativistic heavy ion collision. But before, we will delve into some more details concerning QCD.

Chapter 2

QCD and some of its models

In this chapter, we will discuss some features of QCD which are of relevance to the qMD model. For example, results obtained from one-gluon exchange will be used later to describe the colour dependence of the relative interaction between quarks. Moreover, approximation schemes are discussed which allow the construction of models that incorporate characteristic properties of QCD. Thus, the Nambu-Jona-Lasinio model shows the spontanoeus breaking of chiral symmetry, and the Friedberg-Lee model describes the built-up of colourelectric flux tubes which enforce colour confinement. The qMD model tries to embrace elements of these approaces in a very simplified way.

2.1 QCD as the theory of strong interactions

Quantum chromodynamics (QCD) is the quantum field theory that describes the interaction of quarks by a non-abelian gauge field, the gluon field. The gluon field is a generalization of the photon field of quantum electrodynamics, with the essential difference that it is self-interacting. The local symmetry of QCD, a generalization of the phase invariance $\mathrm{U}(1)$ of the electromagnetic interaction, is the non-abelian group $\mathrm{SU}(3)$, which acts on the so-called colour degree of freedom of quarks.

2.1.1 Remembering QED

The free Dirac that describes fermions is characterized by the Lagrangean

$$\mathcal{L}_{\text{Dirac}} = \bar{\psi}\left(\mathrm{i}\gamma^{\mu}\partial_{\mu} - m\right)\psi \ . \tag{2.1}$$

In quantum mechanics, the absolute phase of a wave function is not observable. This fact is reflected by the invariance of the Dirac Lagrangean under global phase transformations $\psi \to \psi' = \mathrm{e}^{\mathrm{i}q\theta}\psi$. Such a transformation is called a $\mathrm{U}(1)$ transformation, since the phase factor is an element of the continuous group $\mathrm{U}(1)$ of transformations of complex numbers, $\mathrm{U}(1) = \{A : \mathbb{C} \to \mathbb{C}, AA^{\dagger} = \mathbb{I},\ \det A = 1\}$. This is just the unit circle S^1, parametrized by the angle θ. If, following the ideas of Weyl and Fock, this phase transformation is stipulated to be local,

$$\psi \longrightarrow \psi' = \mathrm{e}^{\mathrm{i}q\theta(x)}\psi \ , \tag{2.2}$$

the Lagrangean (2.1) picks up an extra term $\bar{\psi}\mathrm{i}\gamma^\mu \mathrm{i}q\partial_\mu\theta(x)\psi = -q\bar{\psi}\gamma^\mu\psi\partial_\mu\theta(x)$ and is no longer invariant. Invariance can be restored by adding an extra term $-q\bar{\psi}\gamma^\mu A_\mu\psi$ to (2.1), where under the local phase transformation (2.2), A_μ changes to $A'_\mu = A_\mu - \partial_\mu\theta(x)$. This is exactly the change of the electromagnetic four-potential under a gauge transformation,[1] hence A_μ is identified with the electromagnetic four-potential, and q with the electric charge of the particle. Thus, the Lagrangean for a charged fermion coupled to the electromagnetic field reads

$$\mathcal{L}_{\text{Dirac}} = \bar{\psi}\left(\mathrm{i}\gamma^\mu(\partial_\mu + \mathrm{i}qA_\mu) - m\right)\psi - \frac{1}{4}F_{\mu\nu}F^{\mu\nu} \,, \tag{2.3}$$

where the Lagrangean of the free electromagnetic field, $\mathcal{L}_{\text{EM}} = -\frac{1}{4}F_{\mu\nu}F^{\mu\nu}$, has been added. $F_{\mu\nu}$ are the components of the completely antisymmetric tensor of the electromagnetic field strength, which is obtained as the exterior derivative of the four-potential A, $F = \mathrm{d}A$, or in components

$$F_{\mu\nu} = \partial_\mu A_\nu - \partial_\nu A_\mu \,. \tag{2.4}$$

In short, one obtains the Lagrangean that describes fermions which interact with the electromagnetic field through the so-called minimal coupling prescription, which means a replacement of the partial derivative ∂_μ in the original, non-interacting Lagrangean (2.1) by the covariant derivative D_μ,

$$\partial_\mu \longrightarrow D_\mu = \partial_\mu + \mathrm{i}qA_\mu \,. \tag{2.5}$$

Keep in mind that also in the definition of $F_{\mu\nu}$ in (2.4), the covariant derivative (2.5) has to be used, but that in the case of the abelian $\mathrm{U}(1)$ symmetry, the term $\mathrm{i}q(A_\mu A_\nu - A_\nu A_\mu)$ is zero.

Generalising this procedure to the colour degree of freedom yields the Lagrangean of QCD.

2.1.2 From colour to QCD

As mentioned in chapter 1, the Pauli principle applied to the three valence quarks in a baryon requires an extra degree of freedom for quarks, which is called colour. Introducing colour means to replace the Dirac spinor of a quark by a triplet of Dirac spinors. There are three different colours, conveniently called red, green, and blue,[2] corresponding to three unit vectors in colour space:

$$|R\rangle = \begin{pmatrix}1\\0\\0\end{pmatrix} \,, \quad |G\rangle = \begin{pmatrix}0\\1\\0\end{pmatrix} \,, \quad |B\rangle = \begin{pmatrix}0\\0\\1\end{pmatrix} \,. \tag{2.6}$$

[1] Keep in mind that with $A^\mu = (\phi, \vec{A})$, where ϕ is the scalar potential and $\vec{A}$ the vector potential, and with $\partial^\mu = (1/c\,\partial/\partial t, -\vec{\nabla})$, the transformed field $A^{\mu\prime} = A^\mu - \partial^\mu\theta(x)$ has the zero component $\phi - (1/c)\partial\theta(x)/\partial t$ and the three-component $\vec{A} + \vec{\nabla}\theta(x)$, reproducing the well-known rules for gauge transformations in electrodynamics.

[2] This labelling of colours is nowadays well known from the RGB colour model of computer graphics. It is less known that it was introduced by Maxwell in one of his first scientific papers in 1855, extending ideas of Thomas Young [61].

A general quark state in colour space can thus be written as

$$|\psi\rangle = r|R\rangle + g|G\rangle + b|B\rangle = \begin{pmatrix} r \\ g \\ b \end{pmatrix} , \tag{2.7}$$

where r, g, and b are Dirac spinors. Generalizing the phase transformation (2.2) to such a colour three-vector means to replace the group of symmetry transformations from abelian $\mathrm{U}(1)$ to non-abelian $\mathrm{SU}(3) = \{A : \mathbb{C}^3 \to \mathbb{C}^3, AA^\dagger = \mathbb{I},\ \det A = 1\}$. A more extended discussion of the group $\mathrm{SU}(3)$, and more generally $\mathrm{SU}(N)$, and its use in elementary particle and nuclear physics can be found in appendix B. As shown there, any transformation of the group $\mathrm{SU}(N)$ can be characterized by $N^2 - 1$ parameters. Thus, the transformation replacing (2.2) then reads

$$|\psi\rangle \longrightarrow |\psi'\rangle = \mathrm{e}^{\mathrm{i}\, g_\mathrm{s} \mathrm{T}_a \theta^a(x)} |\psi\rangle \ , \tag{2.8}$$

where $\mathrm{T}_a, a = 1, \ldots, 8$ are the eight generators of $\mathrm{SU}(3)$, and the parameters $\theta^a(x)$, which are just numbers, are eight rotation angles. Again, in the case of a local gauge symmetry we are considering, the parameters $\theta^a(x)$ depend on the space-time coordinate. The electric charge q is replaced by g_s, the coupling constant of QCD. Technically speaking, coloured quarks correspond to the fundamental representation of the $\mathrm{SU}(3)$ colour gauge group, which is just characterized by the transformation law (2.8).

The generators T_a of $\mathrm{SU}(3)$ are usually expressed with the help of the so-called Gell-Mann matrices [62] λ_a, where $\mathrm{T}_a = \lambda_a/2$ and

$$\lambda_1 = \begin{pmatrix} 0 & 1 & 0 \\ 1 & 0 & 0 \\ 0 & 0 & 0 \end{pmatrix} , \quad \lambda_4 = \begin{pmatrix} 0 & 0 & 1 \\ 0 & 0 & 0 \\ 1 & 0 & 0 \end{pmatrix} , \quad \lambda_6 = \begin{pmatrix} 0 & 0 & 0 \\ 0 & 0 & 1 \\ 0 & 1 & 0 \end{pmatrix} ,$$
$$\lambda_2 = \begin{pmatrix} 0 & -\mathrm{i} & 0 \\ \mathrm{i} & 0 & 0 \\ 0 & 0 & 0 \end{pmatrix} , \quad \lambda_5 = \begin{pmatrix} 0 & 0 & -\mathrm{i} \\ 0 & 0 & 0 \\ \mathrm{i} & 0 & 0 \end{pmatrix} , \quad \lambda_7 = \begin{pmatrix} 0 & 0 & 0 \\ 0 & 0 & -\mathrm{i} \\ 0 & \mathrm{i} & 0 \end{pmatrix} ,$$
$$\lambda_3 = \begin{pmatrix} 1 & 0 & 0 \\ 0 & -1 & 0 \\ 0 & 0 & 0 \end{pmatrix} , \quad \lambda_8 = \frac{1}{\sqrt{3}} \begin{pmatrix} 1 & 0 & 0 \\ 0 & 1 & 0 \\ 0 & 0 & -2 \end{pmatrix} . \tag{2.9}$$

Quarks and the weight diagram of SU(3)

Before constructing the interaction of quarks and the colour fields from the gauge principle, we note that the diagonal generators from (2.9), T_3 and T_8, can be used to represent colour charges in a two-dimensional diagram, the so-called weight diagram. Since the colour states (2.6) are eigenvectors of both T_3 and T_8, the corresponding eigenvalues can be used as coordinates in a two-dimensional plane. For the state $|G\rangle$, for example, one finds

$$\mathrm{T}_3|G\rangle = \frac{1}{2} \begin{pmatrix} 1 & 0 & 0 \\ 0 & -1 & 0 \\ 0 & 0 & 0 \end{pmatrix} \begin{pmatrix} 0 \\ 1 \\ 0 \end{pmatrix} = -\frac{1}{2}|G\rangle = \frac{(\lambda_3)_{22}}{2}|G\rangle \tag{2.10}$$

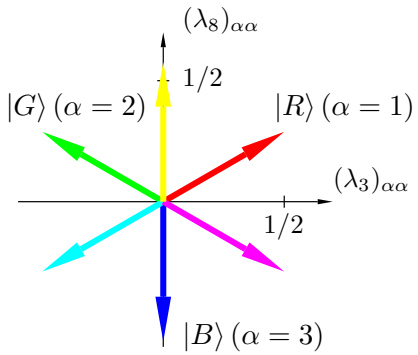

Figure 2.1
The weight diagram of single colour charges and anticharges.

and

$$\mathrm{T}_8|G\rangle = \frac{1}{2\sqrt{3}}\begin{pmatrix}1&0&0\\0&1&0\\0&0&-2\end{pmatrix}\begin{pmatrix}0\\1\\0\end{pmatrix} = \frac{1}{2\sqrt{3}}|G\rangle = \frac{(\lambda_8)_{22}}{2}|G\rangle\ . \tag{2.11}$$

Similar, one has

$$\begin{aligned}\mathrm{T}_3|R\rangle &= \frac{1}{2}|R\rangle = \frac{(\lambda_3)_{11}}{2}|R\rangle\ , \quad \mathrm{T}_8|R\rangle = \frac{1}{2\sqrt{3}}|R\rangle = \frac{(\lambda_8)_{11}}{2}|R\rangle\ ,\\ \mathrm{T}_3|B\rangle &= 0|B\rangle = \frac{(\lambda_3)_{33}}{2}|B\rangle\ , \quad \mathrm{T}_8|B\rangle = -\frac{1}{\sqrt{3}}|B\rangle = \frac{(\lambda_8)_{33}}{2}|B\rangle\ .\end{aligned} \tag{2.12}$$

These eigenvalues define the so-called weight vectors $\vec{w}_\alpha$ of the three colours, given by

$$\vec{w}_\alpha = \frac{1}{2}\begin{pmatrix}(\lambda_3)_{\alpha\alpha}\\(\lambda_8)_{\alpha\alpha}\end{pmatrix}, \quad \alpha = 1,2,3\ (= R,G,B)\ . \tag{2.13}$$

Written explicitly, they read

$$\begin{aligned}\vec{w}_G = \begin{pmatrix}-\frac{1}{2}\\ \frac{1}{2\sqrt{3}}\end{pmatrix} = \frac{1}{\sqrt{3}}\begin{pmatrix}\cos\,150^\circ\\ \sin\,150^\circ\end{pmatrix}, \quad \vec{w}_R = \begin{pmatrix}\frac{1}{2}\\ \frac{1}{2\sqrt{3}}\end{pmatrix} = \frac{1}{\sqrt{3}}\begin{pmatrix}\cos\,30^\circ\\ \sin\,30^\circ\end{pmatrix},\\ \vec{w}_B = \begin{pmatrix}0\\ -\frac{1}{\sqrt{3}}\end{pmatrix} = \frac{1}{\sqrt{3}}\begin{pmatrix}\cos\,270^\circ\\ \sin\,270^\circ\end{pmatrix}.\end{aligned} \tag{2.14}$$

Figure 2.1 shows the weight diagram of the three charges R, G, and B, together with the corresponding anticharges $\bar{R}$, $\bar{G}$, and $\bar{B}$, which are cyan, magenta, and yellow. When combining colour charges to build colour neutral hadrons, the condition of colour neutrality can be expressed formally by the requirement that the weight vectors of all colour charges involved sum up to zero.

Antiquarks

When describing the antiparticle state that corresponds to the quark state (2.7), the spinorial part of the antiquark wave function follows from the standard charge

conjugation operator for Dirac spinors, with the charge conjugated spinor obtained as

$$\psi_{\mathcal{C}} = \mathcal{C}\,\bar{\psi}^T\ , \quad \bar{\psi} = \psi^\dagger\gamma_0\ , \quad \mathcal{C} = \begin{pmatrix} & & & 1 \\ & & -1 & \\ & -1 & & \\ 1 & & & \end{pmatrix}\ . \tag{2.15}$$

Here, ψ stands for the three spinors r, g, and b in (2.7), and $\mathcal{C}$ is the charge conjugation matrix, defined as usual by the relation $\mathcal{C}\gamma_\mu\mathcal{C}^{-1} = -\gamma_\mu^{\mathsf{T}}$. The charge conjugated colour part is obtained from the following reasoning: Instead of using the complex vector $|\psi\rangle$ as in (2.7), transforming under the fundamental representation of SU(3) according to (2.8), we start by considering the conjugated vector $\langle\psi| = |\psi\rangle^\dagger$ and the action of the conjugated transformation matrix from the right, hence

$$\langle\psi| = |\psi\rangle^\dagger \ \longrightarrow\ \langle\psi|' = |\psi'\rangle^\dagger = \left(\mathrm{e}^{\mathrm{i}\,g_s\mathrm{T}_a\theta^a(x)}|\psi\rangle\right)^\dagger = \langle\psi|\mathrm{e}^{-\mathrm{i}\,g_s\mathrm{T}_a^\dagger\theta^a(x)}\ . \tag{2.16}$$

Written in components and using the explicit realization of the generators T_a by the Gell-Mann matrices (2.9), this reads

$$(r^*, g^*, b^*) \longrightarrow (r^*, g^*, b^*)' = (r^*, g^*, b^*)\,\mathrm{e}^{-\mathrm{i}\frac{g_s}{2}(\lambda_a^\dagger)_{cd}\theta^a(x)} \tag{2.17}$$

where $*$ stands for complex conjugation. Taking into account that $(\lambda_a^\dagger)_{cd} = (\lambda_a^*)_{dc}$, the transformation (2.17) can be written using column vectors as

$$\begin{pmatrix} r^* \\ g^* \\ b^* \end{pmatrix} \longrightarrow \begin{pmatrix} r^* \\ g^* \\ b^* \end{pmatrix}' = \mathrm{e}^{\,\mathrm{i}\frac{g_s}{2}(-\lambda_a^*)_{dc}\theta^a(x)} \begin{pmatrix} r^* \\ g^* \\ b^* \end{pmatrix}\ . \tag{2.18}$$

Thus, the colour vector of the antiquark is given by

$$|\psi\rangle_{\mathcal{C}} = \begin{pmatrix} r^* \\ g^* \\ b^* \end{pmatrix}\ , \tag{2.19}$$

or, written explicitly and using the names cyan (antired), magenta (antigreen), and yellow (antiblue),

$$\vec{q}_{\bar{R}} = \vec{q}_C = \begin{pmatrix} 1 \\ 0 \\ 0 \end{pmatrix}\ , \quad \vec{q}_{\bar{G}} = \vec{q}_M = \begin{pmatrix} 0 \\ 1 \\ 0 \end{pmatrix}\ , \quad \vec{q}_{\bar{B}} = \vec{q}_Y = \begin{pmatrix} 0 \\ 0 \\ 1 \end{pmatrix}\ . \tag{2.20}$$

The difference between anticolour and colour is that the anticolour vectors (2.20) transform under the so-called conjugated representation of SU(3). This representation, characterized by the transformation rule (2.18), is different from the fundamental representation (2.8). Its generators can be read off from (2.18) to be

$$\mathrm{T}_{\mathcal{C},a} = -\frac{1}{2}\,\lambda_a^*\ . \tag{2.21}$$

The unit vectors (2.20) are still eigenvectors of the diagonal generators $\mathrm{T}_{\mathcal{C},3}$ and $\mathrm{T}_{\mathcal{C},8}$, but due to the minus sign in (2.21), the eigenvalues have opposite sign. As a consequence, in the weight diagram shown in figure 2.1, the anticolours are localized at positions that are point symmetric to the origin with respect to the corresponding colours.

Gauging rotations in colour space

In order to formulate a Dirac Lagrangean invariant under the symmetry transformation (2.8) along the same line as done for electromagnetism, the minimal coupling prescription is invoked once more. The contributions created by taking partial derivatives of the exponential in (2.8) will contain terms from all eight parameters $\theta^a(x)$, which have to be balanced by the gauge field. Hence, the covariant derivative must read

$$\partial_\mu \longrightarrow D_\mu = \partial_\mu + \mathrm{i}\, g_\mathrm{s} \mathrm{A}_\mu = \partial_\mu + \mathrm{i}\, g_\mathrm{s} A^a_\mu \mathrm{T}_a = \partial_\mu + \mathrm{i}\, \frac{g_\mathrm{s}}{2} A^a_\mu \lambda_a \ , \tag{2.22}$$

where a summation over all eight generators T_a is implied and the notation $\mathrm{A}_\mu = A^a_\mu \mathrm{T}_a$ has been used. Thus, there are eight gauge fields A^a_μ, which will be identified with the gluons.

Applying the minimal coupling prescription to the Dirac Lagrangean is straight forward. However, the Lagrangean of the gauge fields requires special care: Using the covariant derivative (2.22) yields

$$\begin{aligned} \mathrm{F}_{\mu\nu} &= D_\mu \mathrm{A}_\nu - D_\nu \mathrm{A}_\mu = \partial_\mu \mathrm{A}_\nu + \mathrm{i} g_\mathrm{s} \mathrm{A}_\mu \mathrm{A}_\nu - \partial_\nu \mathrm{A}_\mu - \mathrm{i} g_\mathrm{s} \mathrm{A}_\nu \mathrm{A}_\mu \\ &= \partial_\mu \mathrm{A}_\nu - \partial_\nu \mathrm{A}_\mu + \mathrm{i} g_\mathrm{s} [\mathrm{A}_\mu, \mathrm{A}_\nu] \ , \end{aligned} \tag{2.23}$$

where the commutator term $[\mathrm{A}_\mu, \mathrm{A}_\nu]$ does not vanish due to the non-abelian character of SU(3). In fact, using the so-called structure constants f^c_{ab} of SU(3) which are defined through the commutator relation of the generators T_a,

$$[\mathrm{T}_a, \mathrm{T}_b] = \mathrm{i}\, f_{ab}{}^c \, \mathrm{T}_c \ , \tag{2.24}$$

one obtains

$$[\mathrm{A}_\mu, \mathrm{A}_\nu] = [A^a_\mu \mathrm{T}_a, A^b_\nu \mathrm{T}_b] = A^a_\mu A^b_\nu [\mathrm{T}_a, \mathrm{T}_b] = \mathrm{i} A^a_\mu A^b_\nu \, f_{ab}{}^c \, \mathrm{T}_c \ , \tag{2.25}$$

The Lagrangean of the gauge field is then obtained as

$$\begin{aligned} \mathcal{L}_\text{gauge} &= -\frac{1}{2} \, \mathrm{Tr}\, \mathrm{F}_{\mu\nu} \mathrm{F}^{\mu\nu} \\ &= -\frac{1}{2} \, \mathrm{Tr}\, (\partial_\mu A^a_\nu \mathrm{T}_a - \partial_\nu A^a_\mu \mathrm{T}_a - g_\mathrm{s} A^m_\mu A^n_\nu \, f_{mn}{}^a \, \mathrm{T}_a) \\ &\qquad \cdot (\partial^\mu A^{\nu b} \mathrm{T}_b - \partial^\nu A^{\mu b} \mathrm{T}_b - g_\mathrm{s} A^{\mu k} A^{\nu l} \, f_{kl}{}^b \, \mathrm{T}_b) \ . \end{aligned} \tag{2.26}$$

Using the relation $\mathrm{Tr}(\mathrm{T}_a \mathrm{T}_b) = \frac{1}{2} \, \delta_{ab}$, this reads

$$\mathcal{L}_\text{gauge} = -\frac{1}{4} \sum_a F^a_{\mu\nu} F^{\mu\nu\, a} \ , \tag{2.27}$$

with

$$F^a_{\mu\nu} = \partial_\mu A^a_\nu - \partial_\nu A^a_\mu - g_\mathrm{s} A^k_\mu A^l_\nu \, f_{kl}{}^a \ . \tag{2.28}$$

The last term in (2.28) introduces a self-coupling of the gauge fields A^a_ν—this self-coupling of the gluons, due to the non-abelian character of SU(3), is one essential difference between QCD and QED. The other big difference is the absolute value

of the coupling constant g_s at low energies, which is much bigger than in QED. These two facts are at the origin of all the peculiarities of QCD.

Now, all the ingredients to write down the Lagrangean of QCD are together: There are six flavours of quarks, (u, d, s, c, b, t), each one coming in all three colours, so

$$\mathcal{L}_\mathrm{QCD} = \sum_i \bar{q}_i \left(\mathrm{i}\gamma^\mu(\partial_\mu + \mathrm{i}g_\mathrm{s}\textstyle\sum_a A^a_\mu \mathrm{T}_a) - m_i\right) q_i - \frac{1}{4}\sum_a F^a_{\mu\nu}F^{\mu\nu\,a} \ , \quad (2.29)$$

where the sum over i runs over all flavours and the sum over a over all eight generators of $\mathrm{SU}(3)$. Keep in mind that q_i is a spinor with colour, but that spinor and colour indices are not shown.

2.1.3 One-gluon exchange: Quarks and gluons at tree level

The interaction of quarks subject to the strong interaction is described by the exchange of gluons. Hence, it is natural to consider the simplest of the corresponding processes, the one-gluon exchange. Everything works as in QED, but there is one point one has to take into account: the coupling constant is not small at low momentum exchange. As a consequence, results obtained from tree-level diagrams have no quantitative value at low energies.

As we will explain in more detail at the end of this section, this situation changes at high momentum exchange, where due to asymptotic freedom the coupling constant gets small, setting the ground for perturbative QCD (pQCD).

The interaction part of the QCD Lagrangean (2.29) reads

$$\mathcal{L}_\mathrm{int} = -g_\mathrm{s}\sum_a \bar{q}_i\,\gamma^\mu A^a_\mu \mathrm{T}_a\, q_i \ . \quad (2.30)$$

To get a better physical understanding of the interaction of quarks and gluons, we now rewrite the colour part of the interaction term, using linear combinations of the six non-diagonal generators from (2.9), which we will recognize as generalizations of the well known $\mathrm{SU}(2)$ ladder operators. We choose

$$\begin{aligned}
\mathrm{E}_1^+ &= \mathrm{T}_1 + \mathrm{i}\mathrm{T}_2 = \begin{pmatrix}0&1&0\\0&0&0\\0&0&0\end{pmatrix}, \qquad \mathrm{E}_1^- = \mathrm{T}_1 - \mathrm{i}\mathrm{T}_2 = \begin{pmatrix}0&0&0\\1&0&0\\0&0&0\end{pmatrix}, \\
\mathrm{E}_2^+ &= \mathrm{T}_4 - \mathrm{i}\mathrm{T}_5 = \begin{pmatrix}0&0&0\\0&0&0\\1&0&0\end{pmatrix}, \qquad \mathrm{E}_2^- = \mathrm{T}_4 + \mathrm{i}\mathrm{T}_5 = \begin{pmatrix}0&0&1\\0&0&0\\0&0&0\end{pmatrix}, \\
\mathrm{E}_3^+ &= \mathrm{T}_6 + \mathrm{i}\mathrm{T}_7 = \begin{pmatrix}0&0&0\\0&0&1\\0&0&0\end{pmatrix}, \qquad \mathrm{E}_3^- = \mathrm{T}_6 - \mathrm{i}\mathrm{T}_7 = \begin{pmatrix}0&0&0\\0&0&0\\0&1&0\end{pmatrix}.
\end{aligned} \quad (2.31)$$

Acting on a green quark, represented by $|G\rangle$ as defined in (2.6), E_1^+ yields a red quark, E_3^- yields a blue quark, while all other operators $\mathrm{E}_i^\pm$ annihilate $|G\rangle$, and so on:

$$\mathrm{E}_1^+|G\rangle = \begin{pmatrix}0&1&0\\0&0&0\\0&0&0\end{pmatrix}\begin{pmatrix}0\\1\\0\end{pmatrix} = \begin{pmatrix}1\\0\\0\end{pmatrix} = |R\rangle \ , \quad (2.32)$$

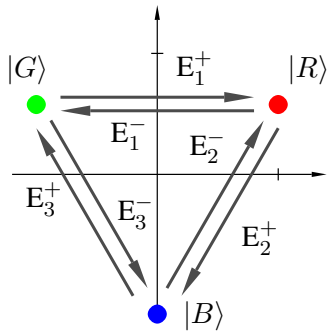

Figure 2.2
The ladder operators $\mathrm{E}_i^+, i = 1, 2, 3$ shift the colour state of the quarks in the clockwise direction. The action of the operators $\mathrm{E}_i^-, i = 1, 2, 3$, is in the opposite direction.

$$\mathrm{E}_3^-|G\rangle = \begin{pmatrix} 0 & 0 & 0 \\ 0 & 0 & 0 \\ 0 & 1 & 0 \end{pmatrix} \begin{pmatrix} 0 \\ 1 \\ 0 \end{pmatrix} = \begin{pmatrix} 0 \\ 0 \\ 1 \end{pmatrix} = |B\rangle \ , \tag{2.33}$$

$$\mathrm{E}_2^+|G\rangle = \begin{pmatrix} 0 & 0 & 0 \\ 0 & 0 & 1 \\ 0 & 0 & 0 \end{pmatrix} \begin{pmatrix} 0 \\ 1 \\ 0 \end{pmatrix} = \begin{pmatrix} 0 \\ 0 \\ 0 \end{pmatrix} = |0\rangle \ . \tag{2.34}$$

Thus, the operators $\mathrm{E}_{\pm i}$, with $i = 1, 2, 3$, act as ladder operators—they shift colour. This can be represented schematically as shown in figure 2.2. Note that the sign convention chosen for $\mathrm{E}_2^\pm$ in the definitions (2.31) differs from the convention used for $\mathrm{E}_1^\pm$ and $\mathrm{E}_3^\pm$. This implies that the action of all three operators E_i^+ is to shift the states in the diagram in clockwise direction.
Solving equations (2.31) for the T_i, the interaction term (2.30) of the QCD Lagrangean reads

$$\begin{aligned} \mathcal{L}_{\text{int}} = -g_\text{s} \sum_a \bar{q}_i \, \gamma^\mu A_\mu^a \mathrm{T}_a \, q_i = -g_\text{s} \bar{q}_i \gamma^\mu \Big(& A_\mu^{(3)} \mathrm{T}_3 + A_\mu^{(8)} \mathrm{T}_8 \\ & + \frac{1}{2}(A_\mu^{(1)} - \mathrm{i} A_\mu^{(2)}) \mathrm{E}_1^+ + \frac{1}{2}(A_\mu^{(1)} + \mathrm{i} A_\mu^{(2)}) \mathrm{E}_1^- \\ & + \frac{1}{2}(A_\mu^{(4)} + \mathrm{i} A_\mu^{(5)}) \mathrm{E}_2^+ + \frac{1}{2}(A_\mu^{(4)} - \mathrm{i} A_\mu^{(5)}) \mathrm{E}_2^- \\ & + \frac{1}{2}(A_\mu^{(6)} - \mathrm{i} A_\mu^{(7)}) \mathrm{E}_3^+ + \frac{1}{2}(A_\mu^{(6)} + \mathrm{i} A_\mu^{(7)}) \mathrm{E}_3^- \Big) q_i \\ = -g_\text{s} \bar{q}_i \gamma^\mu \Big(& A_\mu^{(3)} \mathrm{T}_3 + A_\mu^{(8)} \mathrm{T}_8 + \frac{(R\bar{G})_\mu}{\sqrt{2}} \mathrm{E}_1^+ + \frac{(G\bar{R})_\mu}{\sqrt{2}} \mathrm{E}_1^- \\ & + \frac{(B\bar{R})_\mu}{\sqrt{2}} \mathrm{E}_2^+ + \frac{(R\bar{B})_\mu}{\sqrt{2}} \mathrm{E}_2^- + \frac{(G\bar{B})_\mu}{\sqrt{2}} \mathrm{E}_3^+ + \frac{(B\bar{G})_\mu}{\sqrt{2}} \mathrm{E}_3^- \Big) q_i \ , \end{aligned} \tag{2.35}$$

where we have used the abbreviations

$$\begin{aligned} (R\bar{G})_\mu &= \frac{1}{\sqrt{2}}(A_\mu^{(1)} - \mathrm{i} A_\mu^{(2)}) \ , \quad (G\bar{R})_\mu = \frac{1}{\sqrt{2}}(A_\mu^{(1)} + \mathrm{i} A_\mu^{(2)}) \ , \\ (B\bar{R})_\mu &= \frac{1}{\sqrt{2}}(A_\mu^{(4)} + \mathrm{i} A_\mu^{(5)}) \ , \quad (R\bar{B})_\mu = \frac{1}{\sqrt{2}}(A_\mu^{(4)} - \mathrm{i} A_\mu^{(5)}) \ , \\ (G\bar{B})_\mu &= \frac{1}{\sqrt{2}}(A_\mu^{(6)} - \mathrm{i} A_\mu^{(7)}) \ , \quad (B\bar{G})_\mu = \frac{1}{\sqrt{2}}(A_\mu^{(6)} + \mathrm{i} A_\mu^{(7)}) \ . \end{aligned} \tag{2.36}$$

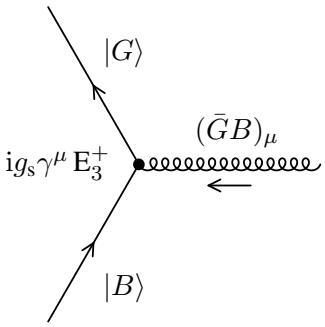

Figure 2.3
The incoming blue quark interacts with the gluon field, which carries the colour anti-green and blue, thus changing the colour of the quark to green.

Equation (2.35) yields a transparent decomposition of the interaction according to the colours of the quarks involved. For example, the interaction with the gluon field can transform a blue quark b into a red quark r; according to the definition of the ladder operators (2.31), only the term involving E_2^- will contribute, yielding

$$\mathcal{L}_{\mathrm{int},B\to R} = -g_\mathrm{s}\bar{r}\gamma^\mu(B\bar{R})_\mu\,\mathrm{E}_2^-\,b = -g_\mathrm{s}\bar{r}\gamma^\mu(B\bar{R})_\mu\,r\ . \tag{2.37}$$

This motivates the notation $(R\bar{B})^\mu$ for the corresponding combination of gluon fields $(A_\mu^{(4)} - \mathrm{i}A_\mu^{(5)})$. This interaction is show schematically in the Feynman diagram 2.3. Note that it is important to discern between incoming and outgoing gluons – as they carry colour charge, colour and anticolour will interchange when changing the direction of 4-momentum of the gluon. For the uncharged photon, this discrimination was not necessary.
There is a direct correspondence between the combination of gluon fields A_μ^a to the fields $(C\bar{C}')^\mu$ in (2.36) and the ladder operators $\mathrm{E}_i^\pm$ by the identification of the row with the colour and the line with the anticolour of the gluon:

$$\begin{aligned}(G\bar{R})^\mu \longleftrightarrow \mathrm{E}_1^- &= \begin{pmatrix}0&0&0\\1&0&0\\0&0&0\end{pmatrix} = \begin{pmatrix}0\\1\\0\end{pmatrix}\otimes(1,0,0)\\ &= |G\rangle\otimes|R\rangle^\dagger = |G\rangle\otimes\langle R|\end{aligned} \tag{2.38}$$

This allows to use the abbreviations

$$\begin{aligned}\mathrm{T}_3 &= \frac{1}{2}\begin{pmatrix}1&0&0\\0&-1&0\\0&0&0\end{pmatrix}\\ &\longleftrightarrow A_\mu^{(3)}\mathrm{T}_3 = \frac{1}{\sqrt{2}}\left(\frac{1}{\sqrt{2}}\left((R\bar{R})_\mu - (G\bar{G})_\mu\right)\right)\mathrm{T}_3\end{aligned} \tag{2.39}$$

and

$$\begin{aligned}\mathrm{T}_8 &= \frac{1}{2\sqrt{3}}\begin{pmatrix}1&0&0\\0&1&0\\0&0&-2\end{pmatrix}\\ &\longleftrightarrow A_\mu^{(8)}\mathrm{T}_8 = \frac{1}{\sqrt{2}}\left(\frac{1}{\sqrt{6}}\left((R\bar{R})_\mu + (G\bar{G})_\mu - 2(B\bar{B})_\mu\right)\right)\mathrm{T}_8\end{aligned} \tag{2.40}$$

for the diagonal gluons. We now see that the eight gluon fields

$$\begin{aligned}&(R\bar{G})_\mu\ ,\ \ (R\bar{B})_\mu\ ,\ \ (G\bar{R})_\mu\ ,\ \ (G\bar{B})_\mu\ ,\ \ (B\bar{R})_\mu\ ,\ \ (B\bar{G})_\mu\ ,\\ &\frac{1}{\sqrt{2}}\left((R\bar{R})-(G\bar{G})\right)_\mu\ ,\ \ \frac{1}{\sqrt{6}}\left((R\bar{R})+(G\bar{G})-2(B\bar{B})\right)_\mu\end{aligned} \tag{2.41}$$

are just the octet of the decomposition of the product representation

$$3\otimes\bar{3}=8\oplus 1 \tag{2.42}$$

of SU(3) in an octet and a singlet. The colour singlet

$$\frac{1}{\sqrt{3}}\left((R\bar{R})+(G\bar{G})+(B\bar{B})\right)_\mu \tag{2.43}$$

is not a gluon—the reason is that the gluon as a gauge particle comes in the adjoint representation which is 8-dimensional, or, physically speaking, the colour singlet would couple to matter in colour singlet states, thus establishing colour forces between colourless matter which is not observed!

The use of the ladder operators $\mathrm{E}_i^\pm, i=1,2,3$ together with the diagonal operators T_3 and T_8 instead of the original generators $\mathrm{T}_i, i=1,\ldots,8$ of the group SU(3) is usually referred to as the Cartan decomposition. It can be derived in a systematic manner applicable to a large class of Lie groups (the so-called semisimple ones), not just for SU(3). To construct the Cartan decomposition, one first determines the maximal number of diagonal operators H_i (in our case just two, $\mathrm{H}_1=\mathrm{T}_3$ and $\mathrm{H}_2=\mathrm{T}_8$), the so-called Cartan subalgebra. In a second step one calculates linear combinations E_α of the remaining matrices which solve the eigenvalue equations $[\mathrm{H}_i,\mathrm{E}_\alpha]=\alpha_i\mathrm{E}_\alpha$. In the case of SU(3), this procedure gives just the ladder operators $\mathrm{E}_j^\pm, j=1,2,3$ as in (2.31). The eigenvalues α_i (for $i=3$ and $i=8$) of $\mathrm{E}_j^\pm$, for example

$$\left.\begin{aligned}[\mathrm{H}_1,\mathrm{E}_1^-]&=-1\,\mathrm{E}_1^-\\ [\mathrm{H}_2,\mathrm{E}_1^-]&=\ \ 0\,\mathrm{E}_1^-\end{aligned}\right\}\ \Rightarrow\ \alpha_3=-1\ ,\alpha_8=0 \tag{2.44}$$

and

$$\left.\begin{aligned}[\mathrm{H}_1,\mathrm{E}_3^+]&=-\frac{1}{2}\,\mathrm{E}_3^+\\ [\mathrm{H}_2,\mathrm{E}_3^+]&=+\frac{\sqrt{3}}{2}\,\mathrm{E}_3^+\end{aligned}\right\}\ \Rightarrow\ \alpha_3=-\frac{1}{2}\ ,\quad \alpha_8=\frac{\sqrt{3}}{2}\ , \tag{2.45}$$

can, again, be used to map the ladder operators $\mathrm{E}_i^\pm, i=1,2,3$ in the weight diagram. This mapping yields exactly the hexagonal diagram corresponding to the octet. That here, the eigenvalue problem is solved with the commutator acting as the operator that is diagonalized expresses the fact that the gluon field is in the adjoint representation of SU(3).

In the qMD model, we will use the so-called abelian approximation and restrict the gluon exchange to the diagonal gluons (2.39) and (2.40), hence colour charges of the gluons will be fixed. The dependence of the interaction on the colours of the will be motivated by the one-gluon exchange, which we will discuss now.

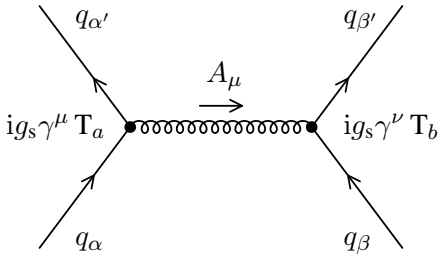

Figure 2.4
One-gluon exchange between quarks with colours α and β, and α' and β'.

One-gluon exchange

Figure 2.4 shows the Feynman diagram for the exchange of one gluon between two quarks coming in with colours α and β, and going out with colours α' and β', as derived for the interaction term (2.30) in the Lagrangean of QCD.

The amplitude of this scattering process looks very similar to the corresponding expression in QED,

$$\mathcal{M}_{\alpha\alpha'\beta\beta'} \;=\; -g_\mathrm{s}^2\;\bar{q}_\alpha\gamma^\mu\mathrm{T}_a\,q_{\alpha'}\,\mathcal{D}^{ab}_{\mu\nu}(p)\,\bar{q}_\beta\gamma^\nu\mathrm{T}_b\,q_{\beta'} \tag{2.46}$$

where $\mathcal{D}^{ab}_{\mu\nu}(q) = D_{\mu\nu}(p)\delta^{ab}$ is the gluon propagator. Taking into account that a quark in a definite colour state $|\alpha\rangle$ is described by a product state $q_\alpha = \psi_\alpha \otimes \vec{q}_\alpha$, where ψ is a Dirac spinor and $\vec{q}_\alpha$ a vector in $\mathbb{C}^3$, the three-dimensional vector space of the fundamental representation of SU(3), the amplitude factorizes in the colour part and the Dirac part,

$$\mathcal{M}_{\alpha\alpha'\beta\beta'} \;=\; -g_\mathrm{s}^2\;\underbrace{\bar{\psi}_1\gamma_\mu\psi_1 D^{\mu\nu}(q)\bar{\psi}_2\gamma_\nu\psi_2}_{\text{Dirac part}}\;\underbrace{\vec{q}^{\,\dagger}_{\alpha'}(\mathrm{T}_a)\vec{q}_\alpha\delta^{ab}\vec{q}^{\,\dagger}_{\beta'}(\mathrm{T}_b)\vec{q}_\beta}_{\text{colour part}}\;. \tag{2.47}$$

The Dirac part is identical to QED and yields the known $1/p^2$ behaviour in momentum space, which would translate into the static potential

$$V(r) = C^\mathrm{c}_{\alpha\alpha'\beta\beta'}\cdot\frac{g_\mathrm{s}^2}{4\pi}\frac{1}{r^2} = C^\mathrm{c}_{\alpha\alpha'\beta\beta'}\cdot\frac{\alpha_\mathrm{s}}{r^2}\;, \tag{2.48}$$

where α_s is the coupling of QCD, corresponding to the Sommerfeld fine structure constant, and $C^\mathrm{c}_{\alpha\alpha'\beta\beta'}$ follows from the colour part of (2.47),

$$C^\mathrm{c}_{\alpha\alpha'\beta\beta'} = \sum_{a=1}^{8}\vec{q}^{\,\dagger}_{\alpha'}\mathrm{T}_a\vec{q}_\alpha\,\vec{q}^{\,\dagger}_{\beta'}\mathrm{T}_a\vec{q}_\beta = \frac{1}{4}\sum_{a=1}^{8}(\lambda^a)_{\alpha\alpha'}\,(\lambda^a)_{\beta\beta'}\;. \tag{2.49}$$

In discussions of the one-gluon exchange between quarks, one usually decomposes the colour part of the wave function of the two quarks involved in the antitriplet and the sextet, according to $\mathbf{3}\otimes\mathbf{3} = \overline{\mathbf{3}}\oplus\mathbf{6}$. Then, the interaction is calculated for both representations, by summing the matrix elements (2.46) with the corresponding colour factors (2.49) over all the contributing combinations of quark colours. This shows thatthe sextet is repulsive, while the antitriplet is attractive—that last result is important and often used in colour superconductivity.

Here, with the application in the qMD model in mind, we follow a different strategy. In the qMD model, we will consider colour as a fixed charge of a classical, distinguishable particle. To be consistent, we then have to restrict ourselves to interactions which do not exchange colour charges, so $\alpha = \alpha'$ and $\beta = \beta'$. In the so-called "abelian approximation" of QCD, which we will explain in the following section, we find a justification to do so. Thus, the sum (2.49) runs only over the diagonal Gell-Mann matrices λ_3 and λ_8. and we are left with the colour factors

$$C^{\mathrm{c}}_{\alpha\beta} = \frac{1}{4} \sum_{a=3,8} (\lambda^a)_{\alpha\alpha} (\lambda^a)_{\beta\beta} = \vec{w}_\alpha \cdot \vec{w}_\beta \; . \tag{2.50}$$

In the last step we have made use of the weight vectors (2.13) of the fundamental colour charges. Expression (2.50) gives the sign and relative strength of the interaction between two colour charges that we will use in the qMD model.

2.1.4 Limits of the one-gluon exchange

In QED, calculations involving the exchange of one photon yield already very reliable results. The reason is the smallness of the fine structure constant, which is $\alpha_{\mathrm{em}} = 1/137$ in the limit of small momentum exchange. This situation is different for the colour interaction: Here, the strong coupling constant is in the order of 1 in the limit of small momentum exchange, hence one-gluon exchange yields no useful results, and perturbation theory is not applicable. This is at the heart of the problem to find the exact ground state and the excitation spectrum of QCD at low energies, a task that has not been solved yet.

However, when going beyond the tree level, it is known from QED that the coupling constant increases according to

$$\alpha_{\mathrm{em}}(Q^2) = \frac{\alpha_{\mathrm{em}}(\mu^2)}{1 - \dfrac{\alpha_{\mathrm{em}}(\mu^2)}{3\pi} \log \dfrac{Q^2}{\mu^2}} \; , \tag{2.51}$$

where $Q^2 = -q^2 > \mu^2$ is the momentum exchange and μ fixes a mass scale. This running means that α_{em} grows from $\alpha_{\mathrm{em}} = 1/137.036\ldots$ at low relative momentum to $\alpha_{\mathrm{em}} = 1/128.9$ at relative momenta corresponding to the energy of the Z mass, $Q = 91\,\mathrm{GeV}$. The running of the coupling constant is due to loop corrections to the photon propagator.

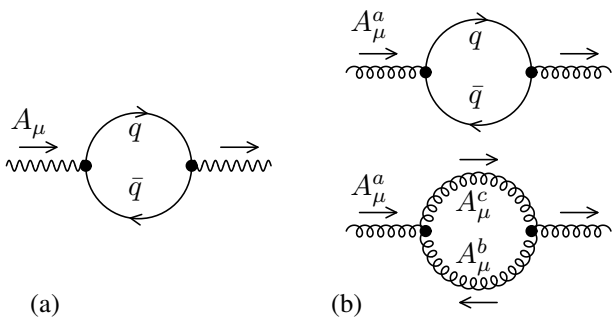

Figure 2.5
Loop corrections to the photon and gluon propagators: While the photon propagator is dressed at one-loop level only by the vacuum polarization (a), the gluon propagator is also affected by gluon loops (b).

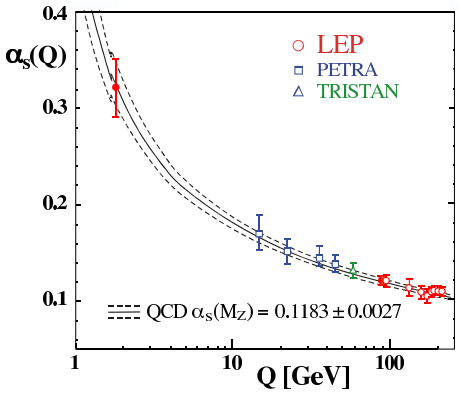

Figure 2.6
The running coupling constant of QCD, as measured at different momentum exchange at HERA. One sees the decrease in α_s with increasing momentum exchange. From [63].

In QCD, the situation is different due to the contribution of gluons in the loop corrections. As shown in figure 2.5, because of the gluon-gluon coupling, the free gluon propagator gets corrections not only from quark-antiquark loops, corresponding to the vacuum polarization, but also from gluon loops, which do not occur in QED. As a consequence, the running of the coupling constant of QCD is modified to

$$\alpha_s(Q^2) = \frac{\alpha_s(\mu^2)}{1 - \frac{\alpha_s(\mu^2)}{3\pi}\frac{2N_f - 11N_c}{4}\log\frac{Q^2}{\mu^2}} \,. \tag{2.52}$$

Here, N_f is the number of flavours, and N_c is the number of colours. The term $-11N_c$ contains the contributions from the gluon loop shown in the lower part of figure 2.5(b). For the physical number of six flavours and three colours, the sign of the log term is different than in QED, hence the coupling constant decreases as $1/(1 + c \log x)$ with increasing momentum exchange. This is asymptotic freedom. It means that at high momentum exchange, the colour interaction between quarks gets weaker, and perturbative methods can be applied. Figure 2.6 shows current experimental data for the momentum dependence of the coupling constant α_s.

2.2 Working with QCD

In QCD, the standard tools of perturbation theory work only at large momentum exchange, where the coupling constant α_s is small. Therefore, some new, different methods are necessary if one wants to study the low-energy regime of the theory. Unfortunately, there are no exact, analytic solutions at hand. For this reason, some approximation scheme is necessary. In general, there are two different strategies that are used. On the one hand, approximative or numerical solutions to full QCD can be applied. On the other hand, QCD can be replaced by some simpler theory, described by a Lagrangean that is inspired by the full Lagrangean of QCD, and which retains some characteristic properties of QCD such as symmetries. Here, we will give two examples of the first approach which are used to motivate the ansatz that yields the qMD model. The second approach is discussed in section 2.3, since it comprehends to models that are alternatives to the qMD model.

2.2.1 Approximation schemes for the gluon field

Since most peculiarities of QCD stem from the self-interaction of the gluons, it seems natural to look for exact solutions of the classical equations of motion of the gluon field and to study their properties. This is especially interesting since these equations allow for solutions with topological quantum numbers, which exhibit a particle-like behaviour.

One class of such classical solutions to the Euclidean equations of motion are the so-called instantons [64, 65], which, in Minkowski space, correspond to tunnelling events between degenerate classical vacua. The interaction of instantons with quarks generates the constituent mass of the quarks and breaks the chiral symmetry. With increasing temperature, instantons and antiinstantons form closely bound molecules. The interaction of these molecules with quarks does not generate a quark mass anymore. Thus, chiral symmetry is restored through the binding of instantons and antiinstantons to molecules. There is an analogy with a much simpler system in condensed matter physics, the XY model in two dimensions. This systems exhibits a phase transition, the Berezinsky-Kosterlitz-Kosterlitz (BKT) transition [66, 67, 68], which is understood as the unbinding at high temperatures of pairs of topological, particle-like objects, so-called vortices and antivortices. Like instantons, vortices are characterized by topological winding numbers. Unlike the instanton liquid, however, vortices and antivortices are bound to pairs below the transition temperature.

Another class of topologically non-trivial solutions to the classical equations of motion of the gluon field are the hedgehog-like monopole solutions [69, 70]. These monopoles play an essential role in a scenario for the description of colour confinement that is similar to type-2 superconductivity in condensed matter physics [71, 72, 73]. In the picture of "abelian dominance", a partial gauge fixing for the gluon field is introduced which leaves only abelian degrees of freedom. In this gauge, monopoles appear, which have an attractive interaction and condense into pairs that act like Cooper pairs in a superconductor in condensed matter physics.

In a standard type-2 superconductor, superconductivity driven by the condensation of Cooper pairs goes hand in hand with a confinement of the magnetic field into quantized flux tubes as a consequence of the Meissner effect. Here, Cooper pairs formed from monopoles create a dual Meissner effect and yield a confinement of the abelian, chromoelectric field into flux tubes. The effect is called dual because the electric field is forced into flux tubes, as opposed to the magnetic field in standard solid-state superconductivity. As soon as the colourelectric flux is confined to tubes, we are left with the common string picture described in section 1.2, which results in the confinement of colour charges. Thus, the scenario of the dual superconductor emerging from the condensation of monopoles provides a qualitative explanation for the creation of colourelectric flux tubes and of colour confinement [74]. It has other attractive features which will be discussed in the following paragraph.

2.2.2 QCD on the lattice

The second approach to full QCD is to discretize the Lagrangean and to put everything on a finite space-time lattice. Then, with the help of state of the art computers,

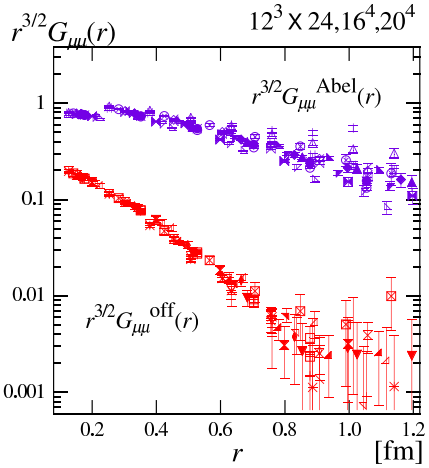

Figure 2.7
Mass of off-diagonal gluons as found in pure gauge lattice QCD [77]: The logarithmic plot for the scalar correlation $r^{3/2}G_{\mu\mu}(r)$ shows a Yukawa-type decrease with distance for the off-diagonal gluon propagator, indicating a mass for the off-diagonal gluons.

suitable correlation functions of quarks and gluons can be calculated. This ansatz, called lattice gauge theory (LGT) [75, 76], exploits the fact that the Euclidean action can be interpreted as the Hamiltonian of a four-dimensional statistical system. Then, numerical methods of statistical mechanics like the Metropolis algorithm can be applied. Moreover, attributing quarks to lattice points and the gluons of the gauge field to the bonds linking lattice points corresponds very closely to the geometry of gauge theories.

Of the ample range of results and insights gained from QCD on the lattice, we mention here only two: First, in recent years clever algorithms have allowed to calculate properties of QCD at both finite T and finite μ. Calculations at finite μ were thought impossible for a long time, and this breakthrough was essential for the establishment of the phase diagram of QCD shown in figure 1.6 [26]. Second, calculating QCD on the lattice has helped to provide a numerical check of the scenario of "abelian dominance" and the condensation of monopoles as the mechanism providing colour confinement.

Using the so-called maximally abelian gauge for the gluon field [78], the off-diagonal gluons behave like vector bosons with a mass $m_{\text{eff}} \approx 1.2\,\text{GeV}$ (see figure 2.7), corresponding to an effective interaction length of $r \lesssim 0.2\,\text{fm}$ [77, 79]. Thus, over longer distances, only the abelian gluons can mediate interactions. This provides a justification for the scenario of abelian dominance in the infrared and the corresponding picture of colour confinement. Moreover, the effective mass and short range of the off-diagonal gluons has as a further consequence that colour changing interactions between quarks require close encounters of the order of $r \approx 0.2\,\text{fm}$.

From all these results, the following, effective picture for the interaction of quarks and gluons can be inferred: quarks carry a colour charge that is fixed and can be exchanged between two quarks only over very short distances, as mediated through the exchange of a massive off-diagonal gluon. The diagonal sector of the gluon field arranges itself in a network of flux tubes connecting the quarks and mediating the confining interaction over longer distances. This scheme can be made more qualitative and quantitative using the Friedberg-Lee model to be discussed in the following section. Moreover, it is used as a motivation for the construction of the qMD model, which will be described in detail in chapter 4.

2.3 Models of QCD

An alternative to the search for approximation schemes to full QCD is the replacement of the Lagrangean of full QCD by a simpler Lagrangean, which retains symmetries and essential features of QCD, but is more tractable. As an example for an approach based on symmetry considerations, we present the Nambu-Jona-Lasinio (NJL) model [80, 81, 82]. An example of a Lagrangean which models essential features of the gluon field and the formation of flux tubes is given by the Friedberg-Lee model [83, 84]. Both approaches model quark degrees of freedom, and both have been applied to the description of heavy ion collisions [85, 86, 87]. They both are complementary to the qMD model used in this thesis. Finally, we briefly mention potential models, which are very successful in the description of mesons and baryons, thus for the treatment of the low-energy ground state of QCD.

2.3.1 The NJL model

If all quark masses are equal, QCD has an exact symmetry group which mixes quark flavours. Taking into account only up, down, and strange quarks (the heavy quark flavours are too different in mass), this is the original $\mathrm{SU}(3)_{\text{flavour}}$ symmetry of Gell-Mann,

$$\psi = \begin{pmatrix} u \\ d \\ s \end{pmatrix} \quad , \quad \psi \longrightarrow \psi' = \mathrm{e}^{\mathrm{i}\,\mathrm{T}_a\theta^a}\psi \; . \tag{2.53}$$

It transforms $\bar{\psi} = \psi^\dagger\gamma^0$ to $\bar{\psi}' = \psi^\dagger \mathrm{e}^{-\mathrm{i}\,\mathrm{T}_a\theta^a}\gamma^0 = \bar{\psi}\,\mathrm{e}^{-\mathrm{i}\,\mathrm{T}_a\theta^a}$ (keeping in mind that $\mathrm{T}_a^\dagger = \mathrm{T}_a$), and leaves invariant terms such as $\bar{\psi}\psi$, $\bar{\psi}\gamma^\mu\partial_\mu\psi$, hence the Lagrangean (2.29) for $m_\mathrm{u} = m_\mathrm{d} = m_\mathrm{s}$. Note that this symmetry is a global symmetry which is not gauged. Now, if we furthermore suppose that all quarks are even massless, $m_\mathrm{u} = m_\mathrm{d} = m_\mathrm{s} = 0$, there is one more symmetry operation, involving a γ_5 matrix,

$$\psi \longrightarrow \psi' = \mathrm{e}^{\mathrm{i}\,\gamma_5\mathrm{T}_a\theta^a}\psi \; . \tag{2.54}$$

This symmetry is the so-called chiral symmetry. Since $\gamma_5^\dagger = \gamma_5$, it acts on the conjugated spinor as

$$\bar{\psi} = \psi^\dagger\gamma^0 \longrightarrow \bar{\psi}' = \psi^\dagger \mathrm{e}^{-\mathrm{i}\,\gamma_5\mathrm{T}_a\theta^a}\gamma^0 \tag{2.55}$$

Now, $\gamma_5\gamma^0 = -\gamma^0\gamma_5$, hence $(\gamma_5)^n\gamma^0 = (-1)^n\gamma^0(\gamma_5)^n$, and, using the series expansion of the exponential, one has

$$\bar{\psi}' = \psi^\dagger \mathrm{e}^{-\mathrm{i}\,\gamma_5\mathrm{T}_a\theta^a}\gamma^0 = \psi^\dagger\gamma^0 \mathrm{e}^{+\mathrm{i}\,\gamma_5\mathrm{T}_a\theta^a} = \bar{\psi}\,\mathrm{e}^{+\mathrm{i}\,\gamma_5\mathrm{T}_a\theta^a} \; . \tag{2.56}$$

Thus, a mass term like $m\bar{\psi}\psi$ is not invariant under the transformation (2.54)! But terms involving further gamma matrices, such as $\bar{\psi}\gamma^\mu\partial_\mu\psi$ and $\bar{\psi}\gamma^\mu\psi$, are invariant: Since the anticommutation relation $\gamma_5\gamma^\mu = -\gamma^\mu\gamma_5$ brings in an additional minus sign, we have $(\gamma_5)^n\gamma^0\gamma^\mu = \gamma^0\gamma^\mu(\gamma_5)^n$, and the term $\bar{\psi}\gamma^\mu$ transforms to

$$\begin{aligned} \bar{\psi}\gamma^\mu &= \psi^\dagger\gamma^0\gamma^\mu \\ &\longrightarrow \psi^\dagger \mathrm{e}^{-\mathrm{i}\,\gamma_5\mathrm{T}_a\theta^a}\gamma^0\gamma^\mu = \gamma^0\gamma^\mu\psi^\dagger \mathrm{e}^{-\mathrm{i}\,\gamma_5\mathrm{T}_a\theta^a} = \bar{\psi}\gamma^\mu \mathrm{e}^{-\mathrm{i}\,\gamma_5\mathrm{T}_a\theta^a} \; . \end{aligned} \tag{2.57}$$

So, in combination with (2.56), the invariance of $\bar{\psi}\gamma^\mu\partial_\mu\psi$ and $\bar{\psi}\gamma^\mu\psi$ is established.

The idea leading to the NJL Lagrangean is to consider massless QCD with its chiral symmetry and to replace the interaction mediated by the gluon field by some point coupling, as is done in the Fermi theory of weak interactions. This may seem to be a bold step since gluons have no bare mass, contrary to the vector bosons, but in fact, due to their self-interaction, they are dressed and require a strong effective mass, which justifies this approach. In this approach, one is left with terms that are chirally invariant, and the Lagrangean in its simplest form reads

$$\mathcal{L}_{\text{NJL}} = \bar{\psi}\mathrm{i}\gamma^\mu\partial_\mu\psi + G\sum_{a=1}^{8}\left((\bar{\psi}\lambda_a\psi)^2 + (\bar{\psi}\mathrm{i}\gamma_5\lambda_a\psi)^2\right) . \tag{2.58}$$

More chirally invariant interaction terms can, in principle, be taken into account [82]. But the essential feature of the NJL model is already contained in the Lagrangean (2.58): This is the spontaneous breaking of the chiral symmetry. In other words, due to the interaction terms $\sim \psi^4$, quarks acquire a mass at low temperatures. This is similar to the emergence of spontaneous magnetization in a ferromagnet at low temperatures. Although the Heisenberg Hamiltonian (or some similar model ansatz) which describes the interacting spins is rotational invariant, the magnetized ground state is not. In the NJL model, it is the chiral symmetry which is spontaneously broken.

However, there is an important difference to full QCD: The emergence of mass in the NJL model is not accompanied by colour confinement. Thus, nothing forbids the existence of single, coloured quarks in the NJL model. Very recently, there have been attempts to cure this problem by coupling quarks simultaneously to the chiral condensate and to a background temporal gauge field representing Polyakov loop dynamics [88]. This so-called PNJL model thus includes features of both chiral symmetry restoration and deconfinement. Implementations into dynamical simulations are not done yet, so for the time being, mesons and baryons in NJL models have to be understood as quark-antiquark and three-quark correlations [86, 89], and hadronization has to be enforced by hand for quarks that have gained mass through the breaking of symmetry [85].

2.3.2 The Friedberg-Lee model

In contrast to the NJL model, the Friedberg-Lee model [83, 84], which also has quarks as degrees of freedom, offers a dynamical description of the confining interaction mediated by the gluons. The central idea of the Friedberg-Lee model is to treat the gluon field as abelian and to model the effect of its self-interaction with the help of a colour-dielectric constant. Thus, the formation of flux tubes, and networks of abelian, colourelectric flux between quarks, can be studied dynamically. The Lagrangean used in the Friedberg-Lee model reads

$$\begin{aligned}\mathcal{L}_{\text{FL}} = \sum_i \bar{q}_i\Big(\mathrm{i}\gamma^\mu(\partial_\mu + \mathrm{i}g_{\text{s}}\textstyle\sum_a A^a_\mu \mathrm{T}_a) + g_0\sigma - m_i\Big)q_i \\ - \frac{1}{4}\,\kappa(\sigma)\,\sum_a F^a_{\mu\nu}F^{\mu\nu\,a} + \mathcal{L}_\sigma\ .\end{aligned} \tag{2.59}$$

In contrast to full QCD, the gluon field strength is taken to be abelian,

$$F^a_{\mu\nu} = \partial_\mu A^a_\nu - \partial_\nu A^a_\mu\ . \tag{2.60}$$

Moreover, a new, auxiliary scalar field σ is introduced which models the effects of colour confinement. The dynamics of the field σ follows from the Lagrangean

$$\mathcal{L}_\sigma = \frac{1}{2}\partial_\mu\sigma\partial^\mu\sigma - U(\sigma) \ , \quad U(\sigma) = \frac{a}{2!}\sigma^2 + \frac{b}{3!}\sigma^3 + \frac{c}{4!}\sigma^4 + B \ . \tag{2.61}$$

In the Friedberg-Lee model, the introduction of the colour-dielectric constant $\kappa(\sigma)$ in the Lagrangean of the gluon field in (2.59) forces the colour field into flux tubes and prevents its spreading over the whole space, although there is no self-interaction of the gluon field. Thus, due to the dynamical colour-dielectric constant, the model behaves different from a simple copy of abelian electrodynamics. The formation of flux tubes enforced by the dynamical colour-dielectric constant then leads to the confinement of colour charges. A network of colourelectric flux calculated with the Friedberg-Lee model for a given distribution of colour charges is shown in figure 4.2(b) on page 54. The Friedberg-Lee model has been applied to the description of the chromoelectric fields of mesons and baryons, where long standing questions concerning the distribution of chromoelectric flux could be answered [90, 91]. However, its application to the dynamical description of heavy ion collisions is hampered by the enormous numerical needs involved in the calculation of flux configurations.

2.3.3 Potential models

When the J/Ψ meson and its cousins, the excited states of charm-anticharm pairs, were discovered, it became clear soon that the spectrum of these states, the so-called charmonium spectrum, could be reproduced very well using the Schrödinger equation and a suitably chosen potential. One of these potentials used to describe the two-body interaction between the quark and the antiquark is the so-called Cornell potential [15, 16] (see figure 4.1 on page 52),

$$V(r) = -\frac{3}{4}\frac{\alpha_s}{r} + \kappa r \ . \tag{2.62}$$

The first term corresponds to the Coulomb interaction, while the linear increase of the second term ensures confinement. The slope parameter κ of the Cornell potential can be identified with the string constant of the colourelectric string connecting the quark and the antiquark. Alternative ansätze to model the interaction are described in [92]. The big success of the Cornell potential in the application to charmonium spectrum relies on the high current mass $m_\mathrm{c} \approx 1500\,\mathrm{MeV}$ of the charm quark,which justifies the description of charmonium as a nonrelativistic, two-particle bound state.

However, this does not mean that potential models can not be used to describe other mesons as well. Taking into account relativistic corrections, such as Breit-Fermi terms describing the colour hyperfine interaction, colourmagnetic spin-orbit coupling, and Thomas precession, potential models have been used successfully to describe mesons properties from the π to the Υ [17, 18], as well as baryon properties [93]. In this ansatz, constituent masses of $m_{\mathrm{u,\,d}} = 220\,\mathrm{MeV}$ and $m_\mathrm{s} = 419\,\mathrm{MeV}$ for the up, down, and strange quarks are used.

A model incorporating the Cornell potential between constituent quarks has been used to describe the dynamics of deconfined, primordial quark-gluon matter

in the early universe [94]. There, the motivation was to study the built-up of density fluctuations during the hadronization transition, which may have served as seeds for the growth of structure in the early universe. This model is very similar to the qMD model used here.

In the construction of the qMD model described in chapter 4, we are bold enough to use the non-relativistic Cornell potential (2.62) to describe the interaction of nearly massless current quarks. It is clear that this crude approximation can not yield a realistic hadron spectrum. However, it is used there as a first step to obtain a fully dynamical description of deconfined quarks and their hadronization through the formation of colour neutral clusters and recombination. Moreover, the successful Godfrey-Capstick-Isgur potential model shows a clear option of how this first ansatz could be improved.

Chapter 3

Model building to study heavy ion collisions

As discussed before, simulation codes are essential in order to make sense of experimental data measured in ultra-relativistic heavy ion collisions. Here, we briefly present some typical models which are used for the simulation of the various physical processes and phenomena occurring in such complex reactions.

The first class of simulation codes are hadronic transport models. In these models, the complete dynamics of the collision is described using hadronic degrees of freedom, augmented by the production and decay of hadronic strings. No explicit colour charges are involved. Hadronic models offer a natural benchmark against which robust signals providing evidence for the creation of a QGP have be to established. Examples of such models are the Frankfurt code UrQMD ("ultra-relativistic quantum molecular dynamics", [95, 96]) and the Gießen code HSD ("hadron string dynamics", [97]). UrQMD is of special interest to us, since it will provide initial conditions for the qMD model applied to the simulation of ultra-relativistic heavy ion collisions, as will be discussed in chapter 6.

Partonic, coloured degrees of freedom are modelled using so-called parton cascades. For the treatment of a thermalized quark-gluon system, a hydrodynamical description can be useful. Finally, there are several ansätze to model quark degrees of freedom, which can be compared with the qMD model.

3.1 Hadronic transport models: UrQMD, for example

Hadronic transport codes follow the evolution dynamics of the hadrons within the colliding nuclei. The description of particles takes into account the quantum nature of matter, in the case of UrQMD by modelling particles as Gaussian wave packets. Among the hadrons included in the simulation are not only nucleons and pions, but, depending of the sophistication of the model, ever more multiplet states and resonances. UrQMD includes more than 50 baryon species and five meson nonets. A detailed discussion can be found in the reviews [95, 96].

During the time evolution of the system, the hadrons will interact, either by elastic scattering, by inelastic scattering, or, at higher energies, by the formation and decay of string excitations (see figures 3.1–3.3). Moreover, inelastic scattering

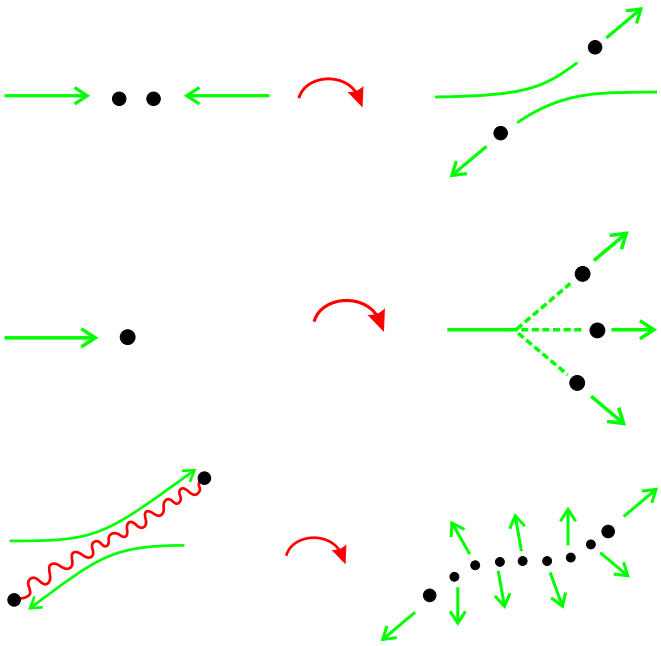

Figure 3.1
Elastic scattering of two hadrons is the most elementary process taken into account in hadronic transport models such as UrQMD. These processes are important for thermal equilibration of the hadronic system.

Figure 3.2
Inelastic collisions can produce heavy resonances whose decay into final state particles contributes to the chemical equilibration of the system. The corresponding back reactions are equally important for equilibration.

Figure 3.3
The string picture of particle production: Strongly interacting hadrons span a string of high energy density, which fragments and spits out new hadrons.

can produce resonances, which will subsequently decay. In the UrQMD model, these interactions are implemented using known vacuum cross sections or, where data are not available, extrapolations from known vacuum cross sections and estimates based on the additive quark model. The inelastic excitation of hadronic strings and their subsequent fragmentation is the dominant interaction between hadrons at centre of momentum energies $\sqrt{s} \gtrsim 5\,\mathrm{GeV}$. The conversion of the excited string back into hadrons is obtained according to the string fragmentation scenario. In the UrQMD model, a version of the LUND string fragmentation mechanism [98, 99] is used. The excitation and fragmentation of strings dominates the production of new particles in the UrQMD model.

One more technical aspect of the UrQMD model will be important to us in chapter 6, where the coupling of UrQMD to qMD will be discussed: At any time of the simulation, the UrQMD code propagates only particles, not strings. For this reason, all hadrons which are to be formed by the string break-up mechanism in the aftermath of an inelastic collision with a string excitation are determined at the very instant of the collision, but propagated for a certain amount of time without interaction with the remainder of the hadronic system. This by-passed time, where, physically speaking, all hadrons stemming from the fragmentation of the string do not yet exist, is the so-called formation time. Hadrons from string fragmentation within their formation time are called preformed hadrons.

With the implementation of the string mechanism, hadronic models such as UrQMD incorporate an essential feature of QCD and the substructure of hadrons. High-energy collisions of hadrons can result in the exchange of colour charge between partons in the colliding hadrons, and as a consequence, a flux tube of the colourelectric field is created. The string represents this flux tube, and its de-

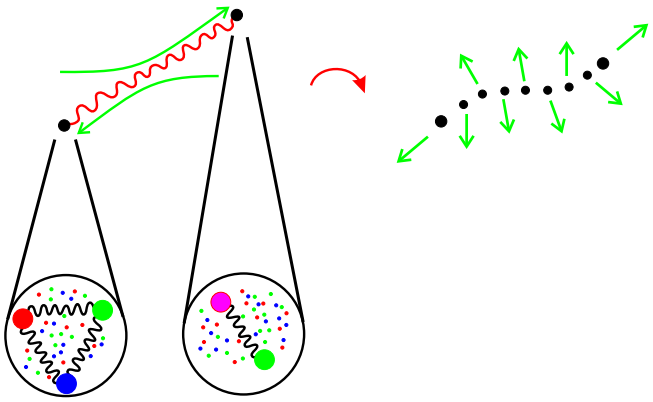

Figure 3.4
A closer look at hadrons, e. g. at higher collision energies with momenta corresponding to shorter wavelengths, reveals the partonic substructure of hadrons. Besides the valence quarks, all hadrons contain sea quarks and gluons, as described by structure functions. This substructure must be taken into account when analysing hadron collision of the highest energies, where the simple string picture (upper part of the figure) becomes insufficient.

cay corresponds to the creation of quark-antiquark and diquark-antidiquark pairs out of the vacuum by the Schwinger mechanism and the subsequent formation of hadrons. The time scale of these processes is the formation time, which is in the order of $\tau \approx 1 - 2\,\mathrm{fm}/c$.

The hadronic transport model UrQMD, including the creation and fragmentation of strings, yields a good description of many data measured at the CERN-SPS, with some notable exemptions such as strangeness production [100]. However, it is clear that at even higher energies, the partonic structure of the hadrons will become more and more important. A complementary picture of the processes in an ultra-relativistic heavy ion collision, starting from the highly energetic and asymptotically free partons, is provided by parton cascade models.

3.2 Partonic transport codes

When two nuclei collide at RHIC energies with $\sqrt{s}_{NN} \approx 60 - 200\,\mathrm{GeV}$ or higher, the partons in the nucleons—valence quarks, sea quarks, and gluons—suffer multiple hard scatterings, which generate a dense, highly excited zone of real partons. More parton scatterings during this initial, so-called pre-equilibrated phase, will eventually lead to a thermalized quark-gluon plasma [101].

Parton cascade models follow the evolution of these partonic degrees of freedom. Initial parton distributions are obtained by the resolution of the nucleons in the colliding nuclei into their parton substructure according to the measured nucleon structure functions. Then, parton interactions, as described by perturbative QCD, are used to model the evolution of the ensemble of partons during the course of the collision. Parton cascades can take into account parton subdivisions necessary to preserve covariance [102], and include inelastic processes such as multiple gluon scatterings $gg \leftrightarrow ggg$, which are important for the establishment of kinetic equilibrium on a time scale $\tau_{\mathrm{eq}} \approx 1\,\mathrm{fm}/c$ [103]. In typical cascade models, partons are propagated along straight lines between scattering events, and non-perturbative, collective field effects are neglected. However, it is possible, at least in principle, to taken into account potential interactions between partons in a fully Poincaré invariant way [104].

Since free partons are not observed due to colour confinement, parton cascades have to be supplemented by some means of hadronization. One option is to use the space-time distribution of the energy-momentum of equilibrated partons as an input for a hydrodynamical calculation, and to relegate hadronization to the hydrodynamical model. But in most cases, partons are either recombined, or converted into hadrons using so-called fragmentation functions. Recombination will be discussed in more detail in section 3.4. In fragmentation, the invariant cross section for the production of a hadron h with momentum p is given in the factorized form

$$E\,\frac{\mathrm{d}\sigma_h}{\mathrm{d}^3p} = \sum_a \int_0^1 \frac{\mathrm{d}z}{z^2} D_{a\to h}(z)\, E_a\, \frac{\mathrm{d}\sigma_a}{\mathrm{d}^3p_a}\ , \tag{3.1}$$

where σ_a is the cross section for the production of parton a with momentum $p_a = p/z$, and the sum runs over all parton species a. Thus, the parton production cross section is convoluted with the probability that parton a fragments into hadron h. The corresponding probabilities $D_{a\to h}(z)$ are the fragmentation functions.

3.3 Hydrodynamical models

For completeness, we briefly mention hydrodynamical models, where the quark-gluon system is modelled as a fluid. Here, the assumption of local thermal equilibration is constitutive. The dynamical evolution follows from the conservation of the energy-momentum tensor and the entropy current of the fluid, describing the expansion and cooling of the fireball. Initial conditions are obtained either from parton cascades, or from plausible assumptions about the phase space distribution of the hot and dense matter created in the collision. The fluid is not by necessity a quark-gluon plasma, it can be also a dense hadronic fluid, and a phase transition can be included in the model. In fact, all essential physics enters by the choice of a equation of state for the fluid, which can describe both a quark-gluon plasma and a hot and dense hadronic fluid. However, the conversion to dilute ground-state hadrons is achieved at the so-called freeze-out hypersurface, usually characterized by some freeze-out temperature, where the energy-momentum tensor of the fluid is mapped to the energy-momentum tensor of a hadron gas using the Cooper-Frye formula.

Hydrodynamical models are especially suited for the study of collective motion of hot and dense matter, such as longitudinal, transverse, or elliptic flow. For example, one-fluid hydrodynamical simulations in 3+1 space-time dimensions reveal a local minimum in the excitation function of transverse directed flow around AGS energies as a result of the transition to the quark-gluon plasma in equation of state the nuclear matter [105]. However, using three-fluid hydrodynamics [106, 107], it has been found that the results of these investigations are strongly influenced by the freeze-out definition and the non-equilibrium features encountered in heavy ion reactions.

The relativistic fluid of quarks can also be coupled to the non-equilibrium dynamics of a chiral field. This allows a study of the dynamical evolution of fluctuations and correlations caused by the chiral transition [108, 109]. Another aspect of

hydrodynamics applied to the description of heavy ion collisions that has recently risen interest concerns the question of viscosity. While it is argued that the partonic state created in RHIC collisions is a most ideal fluid [30], the inclusion of viscosity into hydrodynamical models can provide an improved description of the lifetime of the expanding system [110, 111].

3.4 ... and what about quarks and soft interactions?

The models mentioned so far that propagate particles deal either with hadrons, or with partons, whose interaction is well described by the hard processes of perturbative QCD. However, attempts to simulate the dynamics of the hot and dense region created in SPS and RHIC collisions within the VNI parton cascade model [112] show that in these systems, problems arise from non-perturbative quark-quark interactions. This should not come as a surprise—as has been pointed out by Müller and Harris, for example, the QGP is, at momentum transfer below the scale of chiral symmetry breaking $q^2 \lesssim q^2_{\mathrm{CSB}} \approx 1\,\mathrm{GeV}^2$, a gas of strongly interacting quarks and gluons [38]. Even at RHIC energies, leading order, and next-to leading order perturbative QCD seems to be inapplicable to understand the heated and compressed system, as was shown in [113, 114]. So, there is an obvious need to get a handle of the so-called soft regime, where quarks and gluons are strongly coupled and cannot be handled by perturbative QCD. A natural way to tackle this problem is to look for a description based on quarks, with a strong interaction that subsumes all gluonic degrees of freedom.

In the previous chapter, we have already mentioned two such approaches, based on the NJL and on the Friedberg-Lee models. In [132, 133], a simulation based on the Nambu-Jona-Lasinio model has been presented, where quarks are propagated on classical trajectories while their effective masses are calculated self-consistently according to the NJL equations of motion. Hadron production is driven by two-quark and three-quark collisions. Unfortunately, this approach does not provide confinement. In the Friedberg-Lee approach, the colour field is treated as a dynamical background field whose source are the quarks [87], which carry fixed colour charges. This scheme provides quite a realistic description of the colourelectric field which mediates the interaction between quarks, including colour confinement at low energy. Unfortunately, the numerics required to treat systems of the size of the fireball created in a heavy ion collision is still too time consuming to obtain results with useful statistics.

Taking into account these circumstances, it is natural that other approaches have been explored which treat quark degrees of freedom and their interaction. Here, we will present four of them: The quark coalescence model ALCOR, the recombination scheme used for the explanation of RHIC data, a Vlasov approach, and a molecular dynamics approach.

3.4.1 The coalescence model ALCOR and its descendents

The ALgebraic COalescence Rehadronization model ALCOR calculates hadron multiplicities by the redistribution of quarks into hadrons [115]. For example,

the total number $N_m(i,j)$ of mesons built up of a quark with the flavour i and an antiquark with flavour j is calculated as

$$N_m(i,j) = g_m\, C_m(i,j)\, a_i\, \bar{a}_j\, N_q(i) N_{\bar{q}}(j)\ , \tag{3.2}$$

where $N_q(i)$ is the number of quarks of flavour i, $g_m = 2s_m + 1$ is a spin degeneracy factor, the numbers a_i and $\bar{a}_j$ are normalization constants which are fixed by the total particle content of the system. All dynamics enters via the coalescence factor $C_m(i,j)$, which is approximated as

$$C_m(i,j) = \langle \sigma v \rangle\, \tau / V\ . \tag{3.3}$$

Here, V is the volume of the deconfined quark system, τ its lifetime, v the relative velocity of the coalescing quark and antiquark, and σ a cross section for coalescence. The factor $\langle \sigma v \rangle$ can be analyzed for realistic models of the expansion dynamics, and corresponding final state hadron numbers are obtained. The model has been extended to embrace rate equations and a confining equation of state [116]. However, even then it does not provide phase space distributions of the produced hadrons, but is restricted to particle numbers and ratios [117]. Calculations of momentum space distributions of hadrons obtained from the coalescence of massive quarks have been performed [118], but are not included yet in the ALCOR scheme.

3.4.2 The recombination model at RHIC

Recombination models similar in spirit to ALCOR, but including momentum space distributions, have been exploited to explain peculiarities observed in RHIC data. As mentioned before, the scenario of hadronization via the recombination of constituent quarks has been essential to make sense of several measurements at RHIC.

Thus, for example, the transverse momentum spectra $\mathrm{d}n\,/\mathrm{d}p_\perp$ of protons and pions reveal roughly equal numbers of particles for transverse momenta in the range $p_\perp \approx 3 - 5\,\mathrm{GeV}/c$. This is hard to understand if hadrons are produced merely by the fragmentation of hard partons: A parton fragmenting in a proton with some transverse momentum $p_{\perp,0}$ must have a higher the transverse momentum than a parton fragmenting in a pion with the same transverse momentum $p_{\perp,0}$. If, on the other hand, hadrons are produced by the recombination of partons, a proton with some transverse momentum $p_{\perp,0}$ can be obtained from three partons with transverse momenta $p_{\perp,0}/3$, while a pion with the some transverse momentum requires two partons with transverse momenta $p_{\perp,0}/2$. Thus, the production of protons requires less partonic transverse momentum [53, 54, 55, 56, 57, 58].

A second example for the success of the recombination model is provided by the explanation for the observed universality of scaled elliptic flow as a function of transverse momentum [59, 60]. Data from RHIC show that approximately

$$v_{2,m}(p_\perp) \approx 2v_{2,q}\left(\frac{p_\perp}{2}\right)\ , \quad v_{2,b}(p_\perp) \approx 3v_{2,q}\left(\frac{p_\perp}{3}\right)\ , \tag{3.4}$$

where $v_{2,m}$ is the coefficient of elliptic flow for mesons, and $v_{2,b}(p_\perp)$ the coefficient for baryons. A more sophisticated analysis is possible, including different flow for different quark flavours and hadron species [119]. Again, the pattern (3.4) can be

understood naturally in the framework of the recombination of constituent quarks, whose transverse momentum adds up to the transverse momentum of the hadron.

The starting point of the simplest coalescence model used to understand these features is the stipulation that the invariant spectrum of hadrons produced in coalescence is proportional to the product of the invariant spectra of the constituent partons. This means, for example, that the hadron spectra at mid-rapidity are obtained by those of the recombining partons by

$$\begin{aligned}\frac{\mathrm{d}^2N_{\,B}}{\mathrm{d}p_\perp^2}(\vec{p}_\perp) &= C_B(p_\perp)\left(\frac{\mathrm{d}N_{\,q}}{\mathrm{d}p_{\perp\,2}}(\vec{p}_\perp/3)\right)^3 ,\\ \frac{\mathrm{d}^2N_{\,M}}{\mathrm{d}p_\perp^2}(\vec{p}_\perp) &= C_M(p_\perp)\left(\frac{\mathrm{d}N_{\,q}}{\mathrm{d}p_{\perp\,2}}(\vec{p}_\perp/2)\right]^2 ,\end{aligned} \tag{3.5}$$

where the coefficients C_M and C_B are the probabilities for meson and baryon coalescence. It is assumed that the quark and antiquark distributions are the same [60]. In a more elaborate approach [55], the momentum distribution of pions, for example, is obtained by a folding procedure as

$$\begin{aligned}\frac{\mathrm{d}N_{\,\pi}}{\mathrm{d}^3\vec{p}_{\,\pi}} = g_\pi \int \mathrm{d}^3\vec{x}_1\,\mathrm{d}^3\vec{x}_2\,\mathrm{d}^3\vec{p}_1\,\mathrm{d}^3\vec{p}_2\, f_q(\vec{x}_1,\vec{p}_1) f_{\bar{q}}(\vec{x}_2,\vec{p}_2) \\ \times\,\delta^3(\vec{p}_\pi-\vec{p}_1-\vec{p}_2) f_\pi(\vec{x}_1-\vec{x}_2,\vec{p}_1-\vec{p}_2)\ ,\end{aligned} \tag{3.6}$$

where $f_q(\vec{x},\vec{p})$ and $f_{\bar{q}}(\vec{x},\vec{p})$ are the Wigner distribution functions for quarks and antiquarks, and the Wigner function for the pions is denoted by $f_\pi(\vec{x},\vec{p})$. The factor g_π takes into account the probability of forming a colour neutral spin zero pion from coloured quarks. Assuming that quarks and antiquarks are uniformly distributed in the fireball of volume V, the quark and antiquark Wigner functions are simply related to the corresponding momentum distributions as $f_{q,\bar{q}}(\vec{x},\vec{p}) = 1/V\mathrm{d}N_{q,\bar{q}}/\mathrm{d}^3\vec{p}$. The Wigner function for the pion depends on the spatial and momentum distributions of its constituent quark and antiquark. For simplicity, a uniform distribution over some restricted volume of phase space is used,

$$f_\pi(\vec{x},\vec{p}) \;=\; \frac{9\pi}{2\Delta_x^3\Delta_p^3}\,\Theta(\Delta_x-|\vec{x}|)\,\Theta(\Delta_p-|\vec{p}\,|)\ , \tag{3.7}$$

with cutoffs Δ_x and Δ_p in the phase space of the relative motion of the quark-antiquark pair. The uncertainty relation then requires $\Delta_x\Delta_p \geq \hbar$.

While all these recombination models for RHIC assume constituent masses for the recombining quarks, the consequences of the recombination of nearly massless current quarks on transverse momentum spectra has also been studied. Present data do not allow to distinguish between both scenarios [120].

Over all the successes of the recombination schemes applied to data obtained in RHIC events, it should be kept in mind that the current models do not include any colour degrees of freedom, and that the recombination dynamics is not driven by confining interactions. However, remembering the discussion of the Friedberg-Lee model and the numerically cumbersome attempts to use it for the description of heavy ion collisions, it is obvious that colour interactions are handled most practically in some effective way. Such a possibility is offered by the use of a confining potential interaction.

3.4.3 The Vlasov approach

This idea is realized in an approach [121] where the phase space evolution of interacting, coloured quark matter is analysed using the Vlasov equation for the one-particle distribution function $f_1(\vec{r},\vec{p},t) = \bar{f}_1(\vec{r},\vec{p},t) + \delta f_1(\vec{r},\vec{p},t)$,

$$\frac{\partial \bar{f}_1}{\partial t} + \frac{\vec{p}}{E}\,\vec{\nabla}_r \bar{f}_1 - \vec{\nabla}_r \bar{U} \cdot \vec{\nabla}_p \bar{f}_1 \;=\; \left\langle \vec{\nabla}_r \delta U \cdot \vec{\nabla}_p \delta f_1 \right\rangle \;. \tag{3.8}$$

Here, the potential $U = \bar{U} + \delta U$ of the interacting quarks is the confining Richardson potential, applied to each quark pair with relative strength obtained from the colour factor (2.49). Thus, the motivation and realization of this approach is very similar to the rationale behind the qMD model. However, the model is restricted to quarks—there are no antiquarks included. But then, if the Vlasov dynamics is amended by a frictional molecular dynamics, it shows a clustering transition for cool and dense quark matter, which helps the system to relax into minima of potential energy.

The model has been expanded to include antiquarks and applied to the description of Ne+Ne collisions at the SPS with a beam energy of $E = 100\,\mathrm{GeV}/N$ [122]. However, there is a caveat: The numerics used to solve the Vlasov equation is, once more, too greedy to allow useful event statistics.

3.4.4 The colour dynamics model

Since the colour of quarks is a gauge charge subject to changes with the exchange of non-diagonal gluons, it should, in principle, not be fixed, as it is done in the Friedberg-Lee model, the Vlasov approach presented before, or in the qMD model. A fully gauge symmetric treatment of the colour degree of freedom of quarks is possible and has been studied [123, 124]. In this approach, colour is treated as a dynamical vector that will rotate according to Hamiltonian equations of motion. Thus, the wave function of a quark with momentum $\vec{P}$ located at the point $\vec{R}$ is written as Gaussian wave packet,

$$\Psi(\vec{r}) = N\,\exp\left(-(\vec{r}-\vec{R}_i)^2/2L^2 - \mathrm{i}\vec{P}_i\cdot\vec{r}\right)\cdot\begin{pmatrix}\cos\alpha_i\;\mathrm{e}^{-i\beta_i}\;\cos\theta_i\\ \sin\alpha_i\;\mathrm{e}^{+i\beta_i}\;\cos\theta_i\\ \sin\theta_i\;\mathrm{e}^{i\varphi_i}\end{pmatrix}\;, \tag{3.9}$$

where the SU(3) colour state vector is parametrized by the four angles $\alpha_i, \beta_i, \theta_i$ and φ_i. The interaction of quarks depends on the orientation of the colour vectors involved and is described by a Cornell potential. However, this model has the drawback that it is very difficult to regain colourless hadrons out of the quark system, since the combined colour vectors of different quarks in general do not add up to zero. Thus, in this approach, some useful criterion for hadronization is missing.

The model has been amended to study the stability of quark matter at finite baryon density at zero temperature. To this end, colour rotations are frozen, and with the colour dependent potential interactions and the molecular dynamics method, this modified approach is very similar in spirit to the qMD model. The antisymmetrization of the wave function is neglected, but Fermi statistics is treated phenomenologically by introducing a Pauli potential which acts as a repulsive force

between quarks of the same colour, flavour and spin orientation. Minimum energy configurations of the system are searched for using cooling equations of motion with friction terms, akin to the Vlasov approach. However, without a dynamical criterion for hadronization, hadronic matter is modelled as quark matter where quark triplets are kept together by hand. This allows a comparison between quark and hadronic matter within the same model [125, 126]. While this approach is very promising, numerical requirements inhibit the application to the full dynamics of a heavy ion collision even more than for the Friedberg-Lee and Vlasov approaches.

3.4.5 The potential of qMD

As we have seen, there is a clear need of models that can handle quarks degrees of freedom for the description of the hadronization dynamics in ultra-relativistic heavy ion collisions. Moreover, there are many different approaches to meet this need, but all have some caveats:

Coalescence models are successful at RHIC, but they miss the detailed dynamics of hadronization and ignore colour as the driving force of recombination. NJL-type models describe the breaking of chiral symmetry, but include, so far, no confinement. Models derived from the Friedberg-Lee Lagrangean are very promising, since they can provide a good, dynamical description of the colourelectric interaction, but they are to demanding with respect to numerics. One may think that this need can be reduced if the colour interaction is modelled by a simple, confining pair potential interaction between colour charges. However, the problem of numerics still afflicts models that implement such a potential ansatz in a Vlasov approach. Finally, molecular dynamics models using potentials are impractical for the description of hadronization if colour is treated as the continuous degree of freedom it is in reality, since colour neutrality is difficult to obtain, and models with fixed colour have to be supplemented by hadronization criteria.

Thus, there is a solid raison d'être for a simple, numerically tractable model that describes quarks with a confining potential interaction and offers some sensible criteria for the handling of hadronization, i.e., the mapping of colour neutral configurations of quarks and/or antiquarks to hadrons.

A model with just these properties is the quark Molecular Dynamics model qMD [129, 130]. In this model, quarks and antiquarks are handled as classical point particles which are subject to a confining Cornell pair potential. The interplay between attractive and repulsive interactions results in the formation of well-defined, colour neutral clusters of quarks and/or antiquarks. These clusters are then mapped to hadrons and hadronic resonances, taking into account the conservation of four-momentum and the quantum numbers of spin, isospin, and strangeness. All this will be explained in detail in the following chapter. Thermal properties of the model are discussed in chapter 5, and the details of its adoption to heavy ion collisions can be found in chapter 6.

We mention again that a model very similar to qMD has been used before to study the generation of spontaneous density perturbations in the early universe, which were thought to be triggered by the hadronization of the primordial quark-gluon plasma [94]. However, it is the only model of this kind that is applied to the description of the hadronization in ultra-relativistic heavy ion collisions.

3.5 Coupling of models

Before going on with the discussion of the qMD model, we want to stress the importance of the coupling of different model approaches if one is interested in the full time evolution of an ultra-relativistic heavy ion collision.

Since all the models discussed in this chapter usually cover only partial aspects of the complex and intricate physics involved in all the different stages of the collision, some combination of these models is required. For example, the hydrodynamical evolution stops at the so-called freeze-out, where the fluid is mapped to a hadron gas. This hadron gas may still be very dense, so that effects of rescattering should be accounted for. To this end, on can feed the outcome into a hadronic transport model. This has been done for example with the UrQMD model [128].

Similar, as we will see in more detail in the next chapter, the qMD model is not well suited for the description of the initial stage of a collision, when particle production takes place. This stage has to be described by a different model. In this thesis, we will use the UrQMD model and its mechanism for the production of initial particles by string excitations. Other options are possible, such as parton cascades. Finally, the present version of qMD does not handle final state hadronic rescattering. Here, a coupling back to UrQMD may be an option.

As we will see, qMD provides a useful means to handle the full expansion dynamics of a hot end dense system of colour charges, and its conversion to a hadron gas by recombination.

Part II

The qMD model: Description and characterization

Calling a quark a quark makes no difference to the quark.

— Ian Hacking

In this part, we will present the qMD model in detail. We will describe how it is motivated, and discuss its basic features in chapter 4. We will see that the model in its present form is not suited to model proton-proton collisions, which should not come as a surprise. However, its thermal properties, which are presented in chapter 5, are very satisfying. The model shows a transition from a confining phase to a deconfined phase with rising temperature, going hand in hand with a softest point in the equation of state. Moreover, the potential interaction is screened in the deconfined phase.

In chapter 6, the qMD model is coupled to UrQMD as a generator for its initial conditions. In this way, a fully dynamical description of the expansion and hadronization of the fireball created in heavy ion collisions can be achieved. Non-equilibrium aspects of the expansion dynamics and hadronization by recombination of quarks and antiquarks are discussed in detail, and a comparison with experimental data of collisions at the CERN-SPS is presented.

The chapters of this part will reiterate results of Markus Hofmann's thesis [134], which have been presented in the publications [129, 127]. However, they also contain many new data and findings, such as the discussion of finite size scaling and Debye screening of the potential in chapter 5, and the detailed look at the dynamics of Pb+Pb collisions at the SPS in chapter 6.

Chapter 4

What is the quark molecular dynamics model qMD?

The quark molecular dynamics (qMD) model was developed [134] with the intention to accomplish a dynamical description of deconfined quark matter. It should cope with the strong interaction among quarks and antiquarks, characteristical for the so-called soft physics of QCD, and responsible for the hadronization transition from quarks to hadrons. This aim was attained by the construction of a molecular dynamics model where quarks are treated as classical point particles with a colour charge, which are subject to a potential interaction.

In this chapter, we will discuss the definition of the model, some of its characteristics, its motivation and drawbacks. As Markus Hofmann has shown in his thesis [134], the model has very satisfying thermal properties: it exhibits, for example, a transition between a clustering phase and a deconfined phase with increasing temperature or chemical potential. These properties will be presented in the following chapter 5. But not only thermal properties of quark matter are well described by the qMD model: its application to the fully dynamical description of heavy ion collisions at SPS energies yields results in close agreement with experimental data, as will be shown in chapter 6.

4.1 The Hamiltonian of the quark molecular dynamics

The Hamiltonian used in the qMD model reads [129, 130, 127]

$$\mathcal{H} = \sum_{i=1}^{N} \sqrt{\vec{p}_i^{\,2} + m_i^2} + \frac{1}{2} {\sum_{i,j}}' C_{ij}^{\mathrm{c}} V\left(|\vec{r}_i - \vec{r}_j|\right) \tag{4.1}$$

with

$$V\left(|\vec{r}_i - \vec{r}_j|\right) = -\frac{3}{4}\frac{\alpha_s}{|\vec{r}_i - \vec{r}_j|} + \kappa\,|\vec{r}_i - \vec{r}_j| \ , \tag{4.2}$$

where the Cornell potential (2.62) is used to describe the quark interaction (see figure 4.1). Here, $\vec{r}_i$ and $\vec{p}_i$ are the coordinate and three-momentum vectors of the quark (or antiquark) i in the centre of mass frame of the total system. In the sum, all

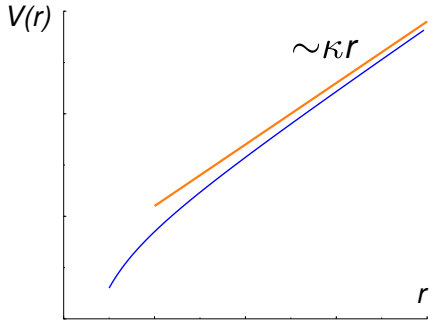

Figure 4.1
A schematic view of the Cornell potential between quarks. This non-relativistic potential, which is very successful for the description of heavy quark systems such as charmonia, is used in qMD also to model the interaction of light quarks. The diagram shows the interaction potential of a colour charge with its anticharge, which is attractive.

terms with $i = j$ are omitted, as is indicated by the prime at the summation symbol. Quarks and antiquarks carry a fixed colour charge—red, green, blue, and antired, antigreen, and antiblue, respectively. Four quark flavours (up, down, strange, and charm) with current masses $m_{\mathrm{u}} = m_{\mathrm{d}} = 10\,\mathrm{MeV}$, $m_{\mathrm{s}} = 150\,\mathrm{MeV}$, and $m_{\mathrm{c}} = 1500\,\mathrm{MeV}$ are taken into account. To allow a later mapping of quark clusters to hadronic states, all particles carry spin quantum numbers. The distinction between up and down quarks is drawn using isospin quantum numbers.

Sign and relative strength of the interaction are described by the colour factor C_{ij}^{c}, depending on the colour combination of each pair. As shown in (2.50), this factor is given by the scalar product,

$$C_{ij}^{\mathrm{c}} \;=\; -\vec{w}_i \vec{w}_j \;, \tag{4.3}$$

where we have identified the colour charge of each quark with its weight vector in the weight diagram. Weight vectors of anticolours are obtained by multiplication with factors -1, as was discussed in connection with equation (2.21). The weight vectors for the colour charges R, G, B, and $\bar{R}, \bar{G}, \bar{B}$ have been shown in figure 2.1.

The choice of the relative contribution (4.2) yields both attraction and repulsion among quarks. Fixing for example one colour as R, the relative strengths of the interaction with all other colours are

$$\text{attractive:} \quad C_{R\bar{R}} = \frac{1}{3}\,, \qquad C_{RG} = C_{RB} = \frac{1}{6}\,, \tag{4.4}$$

$$\text{repulsive:} \quad C_{RR} = -\frac{1}{3}\,, \quad C_{R\bar{G}} = C_{R\bar{B}} = -\frac{1}{6}\,. \tag{4.5}$$

4.1.1 The main features of qMD in brief

There are no explicit gluons in the qMD model. This does not mean, however, that all effects of gluons are completely neglected. At least the impact of so-called soft gluons is taken into account through the choice of the potential, which is excellent in rendering the interaction of heavy quarks by the strong force.

The linear increase at large distances of the potential $V(r)$ in (4.1) ensures the confining properties of the model: Single colour charges separated by a large distance from the rest of the system will have an energy which increases linearly with distance R, thus will be drawn back if the total colour charge is zero. Systems with

net colour charge would, in principle, be unstable, since equal colours repel each other. Thus, qMD can be applied only to quark systems which, on the whole, are colour neutral. This is, of course, no substantial restriction, since all systems occurring in nature to which the model may be applied are colour neutral. All particle reactions we want to study start from colour neutral hadrons. Since colour charge is conserved, colour neutrality will be maintained during the whole evolution of such systems.

We will see in an instant that whereas single colour charges have interaction energies proportional to distance R, this is not the case for colour neutral clusters. Between colour neutral clusters, the large contributions from all quark pairs cancel to a large extend, leaving only a residual interaction which drops faster than $1/R$ with distance. This is similar to electrodynamics, where between electrical neutral atoms, the small van der Waals interaction energy is the only residual effect of the Coulomb energy between the charges. The van der Waals interaction drops with distance as $1/R^6$ instead of the $1/R$ behaviour of the Coulomb interaction.

Both the dynamics of the system described by the Hamiltonian (4.1) and its thermal properties at low temperatures lead in fact to the formation of such colour neutral, only weakly interacting clusters. This is used to map the system to hadrons, as will be discussed later in this chapter.

In full QCD, the separation of colour charges results in the break-up of flux tubes of the colour electric field. This is the so-called Schwinger mechanism, which describes the production of particle-antiparticle pairs from the vacuum. A similar mechanism is implemented in qMD. However, although the potential interaction contains the string tension κ as a parameter, and the interaction energy for each pair of colour charges is calculated as if there were a colour string spanned in-between the charges, this construction should not to be understood as a physical picture of colour electric flux corresponding to the gluon field.

In fact, the Schwinger mechanism implemented in the model works between a given colour charge and the centre of charge of the rest of the system, which has the opposite charge for colour neutral systems. This implementation yields a satisfying modelling for single, energetic colour charges escaping from a large gas of colour charges, but is does not work well for systems which are small, or have high relative momenta. It is not tuned to describe the fragmentation of jets, and it fails, for example, in proton-proton collisions and in the description of particle production by string fragmentation.

As mentioned, the potential pair interaction is not meant to give a true physical description of the distribution of energy density of the gluon field, which would look more similar to a network of flux tubes linking only neighbouring colour charges, as shown in 4.2. Instead, the potential essentially ensures confinement between colour charges, with physically meaningful relative strengths for different charges. Hence, the slope parameter κ of the potential is considered as a free parameter of the model. As was shown be Hofmann, the choice of the slope parameter determines the transition temperature between a confined and deconfined phase in thermal systems [129]. We will discuss this point in more detail in the following chapter. In fact, in order to reach a realistic range of the transition temperature of around $160\,\mathrm{MeV}$, a rather high value of $\kappa = 4\kappa_0 = 3.6\,\mathrm{GeV/fm}$ should be chosen. Here, $\kappa_0 = 0.9\,\mathrm{GeV/fm} = 0.46\,\mathrm{GeV}^2$ is the string constant of the Cor-

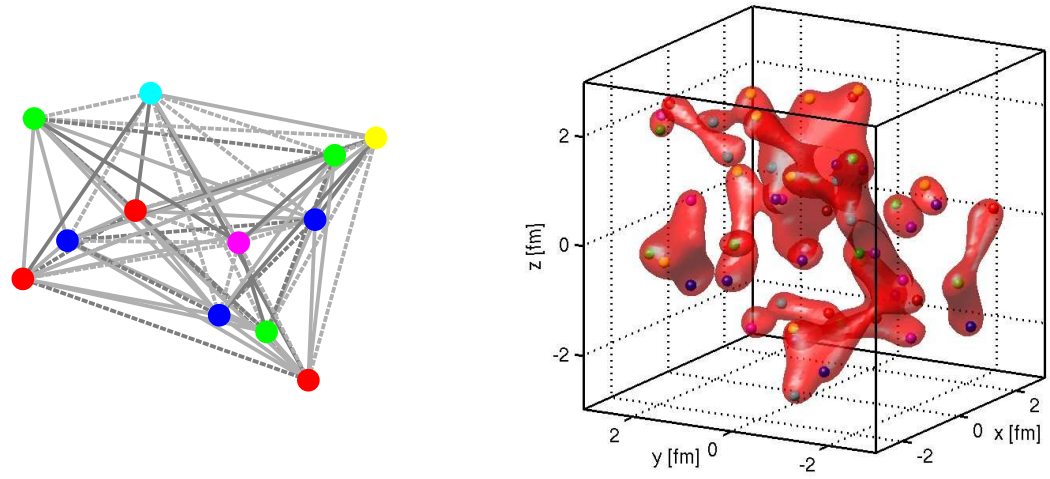

Figure 4.2
In qMD, potential interactions among all quark pairs are taken into account (a), which can be both attractive (solid lines) and repulsive (dotted lines) with two different absolute values (dark grey and light grey), depending on the colours of the quarks in the pair. These potential interactions can not easily be interpreted as colour flux tubes connecting colour charges. A more realistic distribution of the chromoelectric flux originating from a distribution of charges can be obtained with the help of the Friedberg-Lee model. Figure (b), by courtesy of Gunnar Martens, shows that even if two charges are connected by colour flux, this connection does not necessarily follow the shortest possible path: Real flux distributions are similar to patterns of link percolation.

nell potential for heavy quarks, which has been extracted from quarkonia states, the Regge slope, and lattice gauge theory.

The Hamiltonian (4.1) contains a mixture of the relativistically invariant kinetic energy and the potential interaction, which clearly breaks Lorentz invariance. The potential energy is understood to be evaluated always in the centre of momentum frame, which is the centre of mass frame of a heavy ion collision. We do not use relativistic corrections to the potential. As we have discussed, this could be done in principle. However, we should keep in mind that there is a further, conceptual difference to the potential models used in the detailed description of mesons and baryons: In qMD, the low current masses are used, whereas typical non-relativistic potential models use dressed constituent quarks, which have a much higher mass. Using current masses in qMD does not mean that the colour neutral clusters have low mass—as we will see, they can be quite heavy, gaining large parts of their mass from the high energy density of the potential.

A relativistic invariant treatment of our model could be achieved along the lines of Poincaré invariant dynamics as described in [104] for a parton cascade model.

As we will see in more detail later in this section, the time evolution of a system of quarks subject to the Hamiltonian (4.1) yields colour neutral quark clusters which are mapped to hadrons. Applied to heavy ion collisions, the model provides a dynamical description of hadronization via the recombination of quarks Its success when applied to SPS events [127] will be presented in chapter 6.

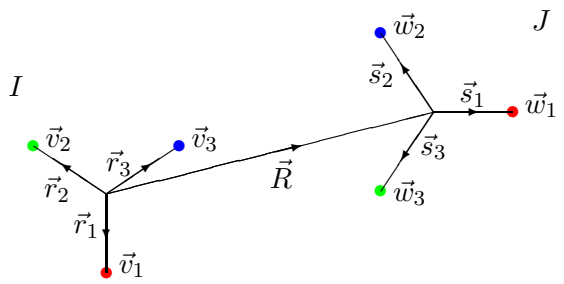

Figure 4.3
Configuration used in the calculation of the interaction of two colour neutral clusters I (with three colour charges, $N = 3$) and J (also three colour charges, $M = 3$).

4.1.2 Interaction of colour neutral clusters in qMD

We now calculate the interaction energy of two colour neutral clusters I and J with N and M colour charges, whose respective centres of colour charge are separated by the distance $\vec{R}$. Although the pair potential energy (4.2) describing the interaction of two colour charges increases without bound with distance, the contributions of both positive and negative interaction energies between colour charges cancel out to a large extent when considering the interaction energy of two colour neutral clusters. As we will see, this results in a dependence of the energy on the separation R of the clusters of less than $O(1/R^2)$.

Let us consider a static configuration where the colour charges q_i of cluster I (with $i = 1, \ldots, N$) are located at $\vec{r}_i$ and are described by their weight vectors $\vec{v}_i$, and where the colour charges q_j of cluster J ($j = 1, \ldots, M$) have weight vectors $\vec{w}_j$ and are at locations $\vec{R}+\vec{s}_j$. Such a configuration is shown in 4.3 for two clusters I and J with three different colour charges each.

Colour neutrality requires

$$\sum_{i=1}^{N} \vec{v}_i = 0 \,, \quad \sum_{j=1}^{M} \vec{w}_j = 0 \,, \tag{4.6}$$

and the definition of the centre of colour charge implies

$$\sum_{i=1}^{N} \vec{r}_i = 0 \,, \quad \sum_{j=1}^{M} \vec{s}_j = 0 \,. \tag{4.7}$$

We keep in mind that in (4.6) and (4.7), $\vec{v}_i$ and $\vec{w}_j$ are vectors in weight space, while $\vec{r}_i$ and $\vec{s}_j$ are vectors in real space.

The interaction energy of the two clusters I and J is

$$E_{IJ} = \sum_{i=1}^{N} \sum_{j=1}^{M} -\vec{v}_i \cdot \vec{w}_j \, V(|\vec{R} + \vec{r}_i - \vec{s}_j|) \,, \tag{4.8}$$

where the space-dependent part is given by the potential (4.2). For well-separated clusters with $|\vec{r}_i|, |\vec{s}_i| \leq |\vec{R}| = R$, we can expand the distance, using the abbrevia-

tions $\vec{r}_{ij} = \vec{r}_i - \vec{s}_j$, and $r_{ij} = |\vec{r}_i - \vec{s}_j|$,

$$\begin{aligned} |\vec{R} + \vec{r}_{ij}| &= (\vec{R} + \vec{r}_{ij})(\vec{R} + \vec{r}_{ij})^{1/2} = \Big(\vec{R}\cdot\vec{R} + 2\,\vec{r}_{ij}\cdot\vec{R} + \vec{r}_{ij}\cdot\vec{r}_{ij}\Big)^{1/2} \\ &= R\left(1 + 2\,\vec{r}_{ij}\cdot\frac{\vec{R}}{R^2} + \frac{\vec{r}_{ij}^{\,2}}{R^2}\right)^{1/2} \\ &= R\left(1 + \frac{\vec{r}_{ij}\cdot\vec{R}}{R^2} + \frac{1}{2}\left(\frac{\vec{r}_{ij}^{\,2}}{R^2} - \frac{(\vec{r}_{ij}\cdot\vec{R})^2}{R^4}\right) + O\Big((r_{ij}/R)^3\Big)\right) \end{aligned} \tag{4.9}$$

which yields for the potential the first term of the Taylor expansion

$$\begin{aligned} &V(|\vec{R} + \vec{r}_i - \vec{s}_j|) \\ &\qquad = V(R) + \left(\frac{\vec{r}_{ij}\cdot\vec{R}}{R} + \frac{1}{2}\left(\frac{\vec{r}_{ij}^{\,2}}{R} - \frac{(\vec{r}_{ij}\cdot\vec{R})^2}{R^3}\right)\right)\left.\frac{\partial V}{\partial r}\right|_R , \end{aligned} \tag{4.10}$$

where

$$\left.\frac{\partial V}{\partial r}\right|_R = \kappa + O(1/R^2)\,. \tag{4.11}$$

Inserting this expansion into expression (4.8) for the energy, we see that the first term vanishes, since

$$E^0_{IJ} = \sum_{i=1}^{N}\sum_{j=1}^{M} -\vec{v}_i\cdot\vec{w}_j\,V(R) = -V(R)\left(\sum_{i=1}^{N}\vec{v}_i\right)\left(\sum_{j=1}^{M}\vec{w}_j\right) = 0 \tag{4.12}$$

due to the charge neutrality conditions (4.6). In the limit where all colour charges of one colour neutral cluster are concentrated on one spot, hence $\vec{r}_i, \vec{s}_j \to 0$, this is the only term contributing to the energy (4.8).

The contribution from the second term of the expansion (4.10) can be written as

$$\begin{aligned} &\left(\sum_{i=1}^{N}\sum_{j=1}^{M} -\vec{v}_i\cdot\vec{w}_j\,(\vec{r}_i - \vec{s}_j)\right)\frac{\vec{R}}{R}\left.\frac{\partial V}{\partial r}\right|_R \\ &= -\left(\Big(\sum_{i=1}^{N}\vec{v}_i\otimes\vec{r}_i\Big)\Big(\sum_{j=1}^{M}\vec{w}_j\Big) - \Big(\sum_{i=1}^{N}\vec{v}_i\Big)\Big(\sum_{j=1}^{M}\vec{w}_j\otimes\vec{s}_j\Big)\right)\frac{\vec{R}}{R}\left.\frac{\partial V}{\partial r}\right|_R , \end{aligned} \tag{4.13}$$

and hence, due to conditions (4.6), it vanishes also. In the third term from (4.10),

$$\sum_{i,j} -\vec{v}_i\cdot\vec{w}_j\,\frac{1}{2}\,\frac{\vec{r}_{ij}^{\,2}}{R}\left.\frac{\partial V}{\partial r}\right|_R = \sum_{i,j} -\vec{v}_i\cdot\vec{w}_j\,\frac{\vec{r}_i^{\,2} - 2\vec{r}_i\cdot\vec{s}_j + \vec{s}_j^{\,2}}{2R}\left.\frac{\partial V}{\partial r}\right|_R . \tag{4.14}$$

the parts containing $\vec{r}_i^{\,2}$ and $\vec{s}_j^{\,2}$ do not contribute for the same reasoning that applies to (4.13). The mixed term reads

$$\begin{aligned} &\frac{1}{R}\left.\frac{\partial V}{\partial r}\right|_R\Big(\sum_{i,j}\vec{v}_i\cdot\vec{w}_j\,\vec{r}_i\cdot\vec{s}_j\Big) \\ &\qquad = \frac{1}{R}\left.\frac{\partial V}{\partial r}\right|_R\left(\Big(\sum_i\vec{v}_i\otimes\vec{r}_i\Big)\Big(\sum_j\vec{w}_j\otimes\vec{s}_j\Big)\right) = \frac{1}{R}\left.\frac{\partial V}{\partial r}\right|_R \mathrm{p}_I\cdot\mathrm{p}_J\,, \end{aligned} \tag{4.15}$$

where

$$\mathrm{p}_I = \sum_{i=1}^{N} \vec{v}_i \otimes \vec{r}_i \ , \qquad \mathrm{p}_J = \sum_{j=1}^{M} \vec{w}_j \otimes \vec{s}_j \tag{4.16}$$

denote the first moments of the colour charge distribution of clusters I and J. The moments p_I and p_J are generalizations of the dipole moments known from electrostatics to colour charge. Similarly, in the second part of the last term in (4.10),

$$(\vec{r}_{ij}\cdot\vec{R})^2 = (\vec{r}_i\cdot\vec{R} - \vec{s}_j\cdot\vec{R})^2 = (\vec{r}_i\cdot\vec{R})^2 - 2(\vec{r}_i\cdot\vec{R})(\vec{s}_j\cdot\vec{R}) + (\vec{s}_j\cdot\vec{R})^2 \ , \tag{4.17}$$

only the mixed term requires closer inspection, since the other terms do not contribute, again for the same reasons as in (4.13). The mixed term yields

$$\begin{aligned} &-\frac{1}{R^3}\frac{\partial V}{\partial r}\Big|_R \Big(\sum_{i,j} \vec{v}_i\cdot\vec{w}_j\,(\vec{r}_i\cdot\vec{R})(\vec{s}_j\cdot\vec{R})\Big) \\ &\qquad = -\frac{1}{R^3}\frac{\partial V}{\partial r}\Big|_R \left(\Big(\sum_i \vec{v}_i\otimes\vec{r}_i\Big)\cdot\vec{R}\,\Big(\sum_j \vec{w}_j\otimes\vec{s}_j\Big)\cdot\vec{R}\right) \\ &\qquad = -\frac{1}{R^3}\frac{\partial V}{\partial r}\Big|_R \Big((\mathrm{p}_I\cdot\vec{R})(\mathrm{p}_J\cdot\vec{R})\Big) \ . \end{aligned} \tag{4.18}$$

Thus, the interaction energy (4.8) is expressed as a series in powers of $1/R$,

$$E_{IJ} = \frac{1}{R}\frac{\partial V}{\partial r}\Big|_R \left(\mathrm{p}_I\cdot\mathrm{p}_J - \left(\mathrm{p}_I\cdot\frac{\vec{R}}{R}\right)\left(\mathrm{p}_J\cdot\frac{\vec{R}}{R}\right)\right) + O(1/R^2) \ . \tag{4.19}$$

In general, we do not expect to find static dipole moments in colour neutral clusters, where all colour charges are free to move. For this reason, the moments p_I and p_J are zero on the average. Hence, we have established that among colour neutral clusters at a distance R, there is no interaction of the order $O(1/R)$, although the pair potentials involved yield very strong contributions of the order $O(R)$ from each colour charge pair.

It is instructive to compare the situation in qMD with standard electrostatics, as shown in table 4.1. In electrostatics, the interaction potential between charges scales with distance R as $1/R$. Interactions between permanent dipoles are reduced by factor $1/R^2$ compared to charge interactions, yielding a distance dependence

	monopole -monopole	dipole -dipole	induced dipole-dipole
electrostatics	$\sim 1/R$	$\sim 1/R^3$	$\sim 1/R^6$
qMD	$\sim R$	$\sim 1/R$	$\sim 1/R^2$

Table 4.1
Distance dependence of interaction energies in standard electrostatics and in qMD. Charge neutral clusters without permanent dipole moments interact only via induced dipole-dipole (van der Waals) interactions, which scale like $1/R^6$ and $1/R^2$, respectively.

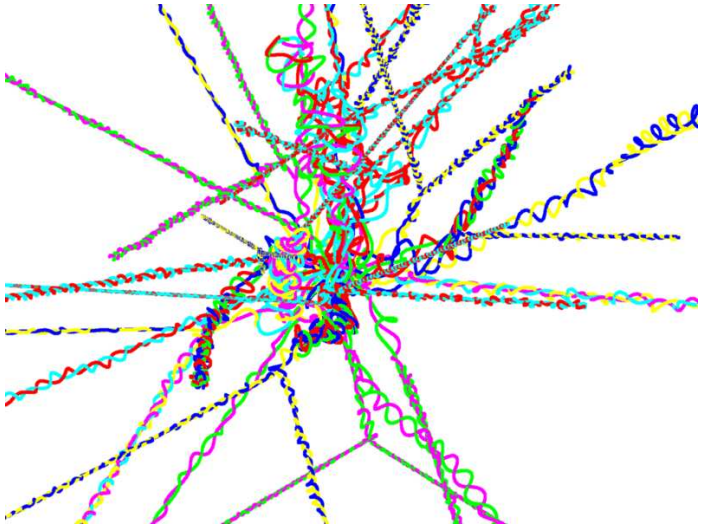

Figure 4.4
Free expansion of a systems of quarks and antiquarks, initialized at a temperature of $T_0 = 200\,\mathrm{MeV}$ in a spherical volume of $V_0 = 50\,\mathrm{fm}^3$. During expansion, the particles form colour neutral clusters of two or three colour charges. Dynamics of quark-antiquark pairs is described very well by the "yoyo" motion. The "splitting" of the intertwined trajectories corresponds to the creation of quark-antiquark pairs from the vacuum by the Schwinger mechanism.

$\sim 1/R^3$. As we have seen in (4.19), the same happens in qMD, where the distance dependence of the interaction among dipoles is reduced from $\sim R$ to $\sim 1/R$. In electrostatics, there are forces between charge neutral configurations even without permanent dipole moments. They are caused by fluctuations of the charge distributions and are called dispersive or London forces [135]. This interaction, which is one of the sources of the van der Waals interaction between neutral atoms and molecules, scales with distance like the square of the permanent dipole interaction, hence as $1/R^6$. A factor $1/R^3$ stems from the electric field created by the transient dipole moment of one charge neutral cluster at the location of the second cluster at distance R. This electric field creates a dipole moment in the second cluster by polarization. As a consequence of the interaction between the two dipoles, a second factor $1/R^3$ enters the distance law for the interaction energy of the charge neutral clusters. Analogous van der Waals interactions will occur in qMD, scaling with distance as $1/R^2$.

4.1.3 The "yoyo" motion of a quark antiquark pair

So far, we have not discussed in detail the motion of colour charges within a colour neutral cluster. We have only argued that on average, this motion cancels out any dipole moment. For a massless quark and antiquark pair, there is in fact a simple, exact solution to the equations of motion derived from the Hamiltonian (4.1): In the centre of momentum frame of the pair, both charges move on straight lines until a maximal separation d is reached, where the energy of the system is completely contained in the potential [136]. Here, the direction of motion of the quarks is reversed. The result of this dynamics is a so-called yoyo motion. Keep in mind that since the quarks have no mass, they always propagate with the speed of light.

4.1.4 Free expansion of a quark gas and the formation of clusters

The reduction of the interaction energy between colour neutral clusters compared to the energy of random distributions of colour charges will make it energetically

favourable for a system of colour charges to arrange itself in such clusters. The smallest colour neutral configurations are, of course, pairs of colour and anticolour, and triplets of three different colours.

We will discuss the results of Monte Carlo studies of configurations of colour charges and their thermal properties in chapter 5. Here, we have a qualitative look at the time evolution of a system of quarks and antiquarks, subject to the Hamiltonian (4.1). Figure 4.4 shows the trajectories of quarks and antiquarks in the free expansion of a gas, initialized at a temperature of $T_0 = 200\,\mathrm{MeV}$ in a spherical volume of $V_0 = 50\,\mathrm{fm}^3$. Details of the initialization procedure and the numerical integration of the equations of motion derived from the Hamiltonian (4.1) will be discussed later. What matters here is that, indeed, the initially homogeneous system, while expanding, rearranges itself in clusters of two or three quarks and antiquarks, carrying colour and anticolour or three different colours, respectively. Moreover, we can see the yoyo motion of quark-antiquark pairs, as expected from the analytic solution of the equations of motion.

It is this clustering which will allow us to map the system of quarks and antiquarks to a system of hadrons: quark antiquark pairs will be mapped to mesons, and triplets of quarks or antiquarks will be mapped to baryons or antibaryons, respectively. The details of this mapping will be explained in the following section.

Since our discussion of the interaction among colour neutral clusters is not restricted to clusters of two or three colour charges, the formation of larger colour neutral clusters is, of course, by no means forbidden. We will come back to this point in chapter 8, where we will discuss in detail the formation of colour neutral clusters with up to six colour charges, corresponding to so-called QCD exotica such as tetraquark, pentaquark and hexaquark states.

4.2 Hadronization in qMD

As we have seen, the dynamical evolution of a system of colour charges in qMD yields a segregation into colour neutral clusters, which interact among each other only via residual van der Waals forces. These clusters will be mapped into hadrons in a three step procedure: first, we have to identify colour neutral groups of quarks and antiquarks. Second, we have to establish that the interaction of the colour neutral cluster with the remaining system is indeed small. This amounts to checking the separation in space and calculating the net force on the cluster. Third, we have to identify the hadronic properties corresponding to the cluster, such as its four-momentum and its quantum numbers.

4.2.1 Identification of colour neutral clusters

In order to establish if a given colour charge i with momentum $\vec{p}_i$ at the location $\vec{x}_i$ in the centre of mass frame of the system is part of a colour neutral cluster, we start with a search for its N next neighbours. Here, $N = 2$ if we are interested only in standard hadrons of up to three quarks or antiquarks, while $N = 5$ when searching for larger, exotic clusters.

When calculating the distance between colour charge i and its neighbour j, located at $\vec{x}_j$ in the centre of mass frame of the system and with momentum $\vec{p}_j$, we

have to keep in mind that since both charges may be moving with relativistic velocities, their distance may be Lorentz contracted. In the following description of this well-known procedure to calculate the distance, we will denote the centre of mass frame of the whole system of colour charges as the laboratory frame, reserving the notion of centre of mass frame to the centre of momentum of the particles i and j.

The distance d_{cms} of particles i and j in their centre of mass frame fulfils

$$d_{\text{cms}}^2 = d_{\perp,\,\text{cms}}^2 + d_{\parallel,\,\text{cms}}^2 = d_{\perp,\,\text{lab}}^2 + \gamma^2 d_{\parallel,\,\text{lab}}^2 \;, \tag{4.20}$$

where we have decomposed the distance vector in its components parallel and perpendicular to the direction of motion of the centre of mass of the pair in the laboratory frame. In the second equation, we make use of the fact that the component perpendicular to the direction of motion is invariant when changing from the centre of mass frame to the laboratory frame, whereas the component parallel to the direction of motion is Lorentz contracted,

$$d_{\parallel,\,\text{lab}} = d_{\parallel,\,\text{cms}}/\gamma \;. \tag{4.21}$$

The γ factor is given by $\gamma = E/M$, where E and M are the energy and mass of the particle pair in the laboratory frame. In the laboratory frame, the two particles i and j have four-momenta

$$(E_i, \vec{p}_i) = \left(\sqrt{m_i^2 + \vec{p}_i^{\,2}}, \vec{p}_i\right) \;, \quad (E_j, \vec{p}_j) = \left(\sqrt{m_j^2 + \vec{p}_j^{\,2}}, \vec{p}_j\right) \;, \tag{4.22}$$

hence the total four-momentum of the pair is

$$(E, \vec{P}) = (E_i + E_j, \vec{p}_i + \vec{p}_j) = \left(\sqrt{M^2 + \vec{P}^2}, \vec{P}\right) \;, \tag{4.23}$$

where $\vec{P}$ is the total three-momentum of the pair in the laboratory frame,

$$\vec{P} = \vec{p}_i + \vec{p}_j \;, \tag{4.24}$$

and the total mass M is given by $\sqrt{M^2 + \vec{P}^{\,2}} = E_i + E_j$, hence

$$M^2 = (E_i + E_j)^2 - \vec{P}^{\,2} = E^2 - \vec{P}^{\,2} \;. \tag{4.25}$$

Thus, for the γ factor in (4.20), we have

$$\gamma^2 = \frac{E^2}{M^2} = \frac{E^2 - M^2}{M^2} + 1 = \frac{\vec{P}^{\,2}}{M^2} + 1 \;, \tag{4.26}$$

and, combining with equation (4.21), we find

$$\begin{aligned} d_{\text{cms}}^2 &= d_{\perp,\,\text{lab}}^2 + d_{\parallel,\,\text{lab}}^2 \left(1 + \frac{\vec{P}^{\,2}}{M^{\,2}}\right) = d_{\text{lab}}^2 + \frac{d_{\parallel,\,\text{lab}}^2 \vec{P}^{\,2}}{M^{\,2}} \\ &= \vec{d}_{\text{lab}}^{\,2} + \frac{(\vec{d}_{\text{lab}} \cdot \vec{P})^{\,2}}{M^{\,2}} \;, \end{aligned} \tag{4.27}$$

where

$$\vec{d}_{\text{lab}} = \vec{r}_i - \vec{r}_j \tag{4.28}$$

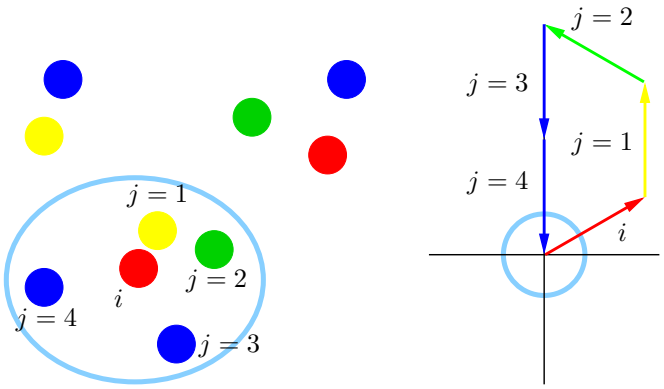

Figure 4.5
Search for colour neutral clusters in qMD: for each particle i, neighbouring particles are identified (left, counting neighbours with j) and their weight vectors summed up (right). If this sum reaches zero at some point, a colour singlet state can be constructed.

is the difference of the position vectors of the colour charges i and j in the laboratory frame.

Once we have established the list of neighbouring particles, we can check whether we have found a cluster of colour neutral particles, i. e. whether the sum of weight vectors of particle i and its neighbours j vanishes,

$$\vec{w}_i + \sum_{j=1}^{N} \vec{w}_j = \vec{0}\,. \tag{4.29}$$

This equation has the graphic interpretation that the sum of all weight vectors involved must end up at the origin of the weight diagram. If this is not the case, the cluster can not be a colour singlet representation. The whole procedure for searching colour neutral clusters is shown in figure 4.5.

4.2.2 Dissection of colour neutral clusters

Once we have identified a colour neutral cluster made up of colour charge i and its neighbours $j = 1, \ldots, N$, we have to check whether its interaction with the rest of the system is small and whether it is well separated from the remaining system. If both conditions are fulfilled, the cluster will be mapped to a hadronic state.

In order to estimate the interaction with the rest of the system, we calculate an average force exerted by all other colour charges on the $N_\mathrm{c} = N + 1$ particles in the cluster. If we denote the set of particles in the cluster with J, the average force is given by

$$\left|\left\langle \vec{F}_\mathrm{cluster} \right\rangle\right| = \frac{1}{N_\mathrm{c}} \left| \sum_{k \in J} \vec{F}_k \right| \tag{4.30}$$

where

$$\vec{F}_k = \sum_{l \notin J} \vec{F}_{kl} = \sum_{l \notin J} \vec{w}_k \cdot \vec{w}_l \, \vec{\nabla}_k V(|\vec{r}_k - \vec{r}_l|) \tag{4.31}$$

is the force exerted on colour charge k in the cluster by all other colour charges l not in the cluster.

As discussed before, we can expect the force $\langle \vec{F}_{\text{cluster}} \rangle$ to be small. As a criterion for smallness, we can compare it with the string constant κ in the potential (4.2), since κ has the dimension of a force. Thus, if

$$\left| \left\langle \vec{F}_{\text{cluster}} \right\rangle \right| < \kappa_{\text{cut}} = F_{\text{cut}} \kappa \ , \tag{4.32}$$

the interaction condition is considered as being fulfilled. Here, F_{cut} is a dimensionless constant which is a free parameter of the qMD model. It is chosen in the range of $F_{\text{cut}} = 0.005 - 0.01$.

Furthermore, the cluster is mapped to a hadron only if it is well separated from the remaining system. Two criteria account for the local separation condition: The ratio of the distances of the most distant charge within the cluster around charge i (the farthest neighbour) to the first particle not in the cluster should fulfil

$$\frac{d_{\text{min}}(\text{outside cluster})}{d_{\text{max}}(\text{inside cluster})} > \rho \ , \quad \text{where} \quad \rho = 2.5 \ , \tag{4.33}$$

and the absolute value of the distance of the first neighbouring particle not in the cluster should be larger than a separation distance r_0,

$$d_{\text{min}}(\text{outside cluster}) > r_0 \ , \quad \text{where} \quad r_0 = 0.8\,\text{fm} \ . \tag{4.34}$$

Both criteria help to avoid the mapping to hadrons in environments where nearby free colour charges still abound. This is important because in the present realization of the qMD model, the inverse process to hadronization, i. e., the dissolution of hadrons into their valence quark content, is not implemented into the evolution dynamics. Such a dissolution can be used for the initialization of the model, when hadrons and preformed hadrons from UrQMD will be mapped to quarks and antiquarks (see the following chapter 6), but there is no "melting" of hadrons which enter a space-time region of hot and dense quarks implemented in the model. Thus, the mapping to hadrons is irreversible and, therefore, it should occur only if this artificial irreversibility can not induce large errors. This is the case if for an expanding system, the mapping is performed only in environments where the colour charge density is already sufficiently dilute, as measured by the distance criteria (4.33) and (4.34).

If both the interaction and the separation condition are fulfilled according to the criteria (4.32), (4.33), and (4.34), the cluster is mapped to a hadronic state. Note that there is no condition on the relative momenta of the charges in the cluster. This is in marked difference to standard coalescence or recombination schemes as defined in (3.6)–(3.7), where proximity in momentum space is a prerequisite for combining particles, often disregarding their separation in real space. In qMD, high relative momenta of particles mapped to a hadron are possible. As we will see in the next section, this contributes to the mass of the hadronic state.

4.2.3 Mapping of colour neutral clusters to hadronic resonances

In the mapping of a colour neutral cluster to a hadronic state, correspondence in all quantum numbers and in four-momentum is required. Additive quantum numbers

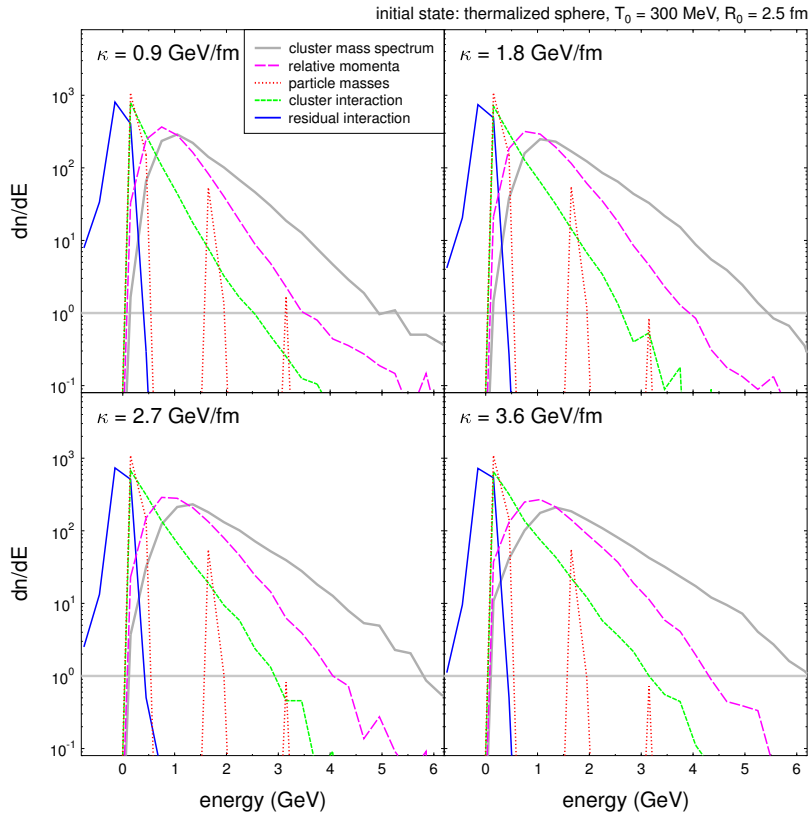

Figure 4.6
The mass of clusters produced in qMD has contributions from different energies according to (4.37). The plots show, for clusters formed in freely expanding systems of quarks and antiquarks initialized as a gas in a spherical volume of radius $r = 2.5\,\mathrm{fm}$ at a temperature of $T_0 = 300\,\mathrm{MeV}$, the energy spectra $\mathrm{d}n/\mathrm{d}E$ of these contributions for four different choices of the string constant κ. The different contributions are: the residual interaction δE (blue solid line), which can be negative, the potential interaction energy (green dashed line), the masses of the clustering quarks (red dotted line), and the contribution from the kinetic energy of the quarks (violet dotted line). The resulting total mass spectrum is very wide. It is represented by the solid grey line.

Q_{hadron} of the hadronic state are given by the sum of the corresponding quantum numbers Q_i of the colour charges in the cluster J,

$$Q_{\mathrm{hadron}} = \sum_{i \in J} Q_i \ . \tag{4.35}$$

Here, Q can be the z component of spin and isospin. As for the total spin of the hadronic state, it is chosen at random among the possible total spins allowed by the addition of the spins of the colour charges in the cluster, with relative weights calculated from the corresponding Clebsch-Gordan coefficients. Parity is not taken into account as a quantum number. For this reason, no distinction between Lorentz scalar and pseudoscalar, or Lorentz vector and pseudovector hadrons can be made.

The total three-momentum of the hadronic state in the centre of mass frame of the collision, $\vec{P}_{\mathrm{hadron}}$, is also obtained by summing the three-momenta $\vec{p}_i$ of the

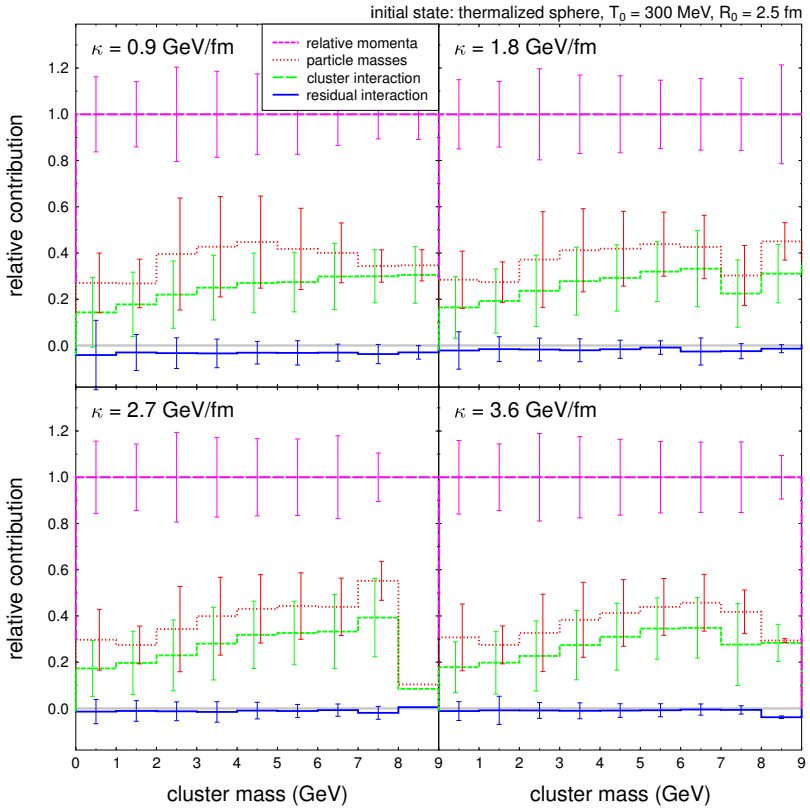

Figure 4.7
The relative contributions of the four energies to the total mass of clusters for the same system as in figure 4.6 as a function of the cluster mass. Shown are the (possibly negative) residual interaction δE (blue solid line), the potential interaction energy (green dashed line), the masses of the clustering quarks (red dotted line), and the contribution from the kinetic energy of the quarks (violet dotted line). Error bars indicate statistical fluctuations. Their considerable size reflects the widths of the $\mathrm{d}n/\mathrm{d}E$ distributions of the contributing energies. For each of the four values of the string constant κ, the contribution of the interaction energy to the cluster mass increases from $\sim 20\,\%$ at low mass to $\sim 35\,\%$ at high mass, mostly at the expense of the contribution from the kinetic energy.

colour charges,

$$\vec{P}_{\text{hadron}} = \sum_{i \in J} \vec{p}_i \ . \tag{4.36}$$

Contributing to the energy of the hadronic state are both the kinetic energies of the particles in the cluster, their interaction energy, and the interaction energy with the remainder of the system. Thus,

$$E_{\text{hadron}} = \sum_{i \in J} \left(E_i + \frac{1}{2} \sum_{j \in J, j \neq i} C_{ij}^{\text{c}} V(|\vec{r}_i - \vec{r}_j|) \right) + \delta E \ , \tag{4.37}$$

where $E_i = \sqrt{m_i^2 + \vec{p}_i^{\,2}}$, and δE represents the energy which is set free due to the field cut-off in the hadronization procedure. It contains the interaction of the colour charges in the cluster with all other colour charges in the system and is of

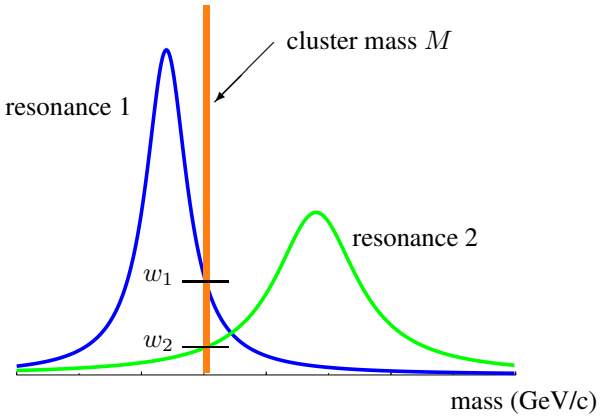

Figure 4.8
Mapping clusters to hadronic resonances in qMD: clusters of mass M are identified with resonances of the same quantum numbers as the cluster. If quantum numbers correspond to more than one resonance, one of them is chosen at random with a probability corresponding to the relative weights w_1 and w_2 at the cluster mass M (vertical bar).

the order $\delta E/E \lesssim 10^{-2}$ due to our choice of the cut-off parameter F_{cut} in (4.32). This energy δE is accounted for in the hadron mass in order to ensure energy conservation. From the energy and three-momentum of the hadronic state, its mass is inferred as

$$M_{\text{hadron}} = \sqrt{E^2_{\text{hadron}} - \vec{P}^{\,2}_{\text{hadron}}} \,. \tag{4.38}$$

As we will see, only a small contribution to the mass of a cluster calculated according to (4.38) will originate in the mass of the colour charges, i. e. the quarks and antiquarks. The main share of the mass originates from the potential interaction of the colour charges within the cluster, and from the relative three-momenta of the particles in the cluster. This is, again, in contrast to standard coalescence models where quarks carry large constituent masses and recombination criteria check proximity in momentum space, thus choosing quarks with small relative three-momenta for coalescence.

The clustering routine of qMD yields a wide distribution of cluster masses. This unphysical situation is, of course, due to the complete absence of quantum mechanics in the model. Hence, the clusters will preferably be mapped to resonances with a broad mass distribution, described by the Breit-Wigner formula

$$f(M) \sim \frac{\Gamma^2}{(M - m_0)^2 + (\Gamma/2)^2} \,, \tag{4.39}$$

where the peak masses m_0 and decay widths Γ are taken from the listings of the Particle Data Book [137]. Resonances are chosen according to the quantum numbers of spin, isospin, and strangeness and will subsequently decay into final state mesons and baryons. Since the masses of the clusters are in general far off the peak masses of resonances, these strong decays of hadronic clusters are very fast processes. They are part of the qMD model. All hadronic states taken into account in qMD are listed in appendix A.

In the case that the quantum numbers of the cluster allow a mapping to more than one resonance, the choice is done at random, with a selection probability corresponding to the relative strength of the possible resonances at the cluster mass M_{hadron} according to (4.38), as shown schematically in figure 4.8. A possible alternative to this clustering scheme will be presented briefly in section 6.2.

4.3 Opportunities for improvement: Approximations and problems with the qMD approach

As we will see in chapters 5 and 6, the qMD approach to the study of deconfined quark matter and its transition to hadrons yields sensible and promising results.

However, it is obvious that the quark molecular dynamics model has several insufficiencies, which we document here, along with some suggestions how the model could be improved. Such further improvements, however, will not be covered in the present thesis project.

4.3.1 Potential interaction: no hard scattering between quarks

Interaction between colour charges in qMD is mediated only via the interaction potential. This means that differential scattering cross sections follow qualitatively a Rutherford-like scattering behaviour with a very strong dependence on the scattering angle. In most other transport models, particle scattering includes important contributions from scatterings at hard repulsive cores, which result in a much more isotropic differential cross section.

As a consequence of the missing hard core repulsion effects in qMD, and the neglect of colour changing interactions to be discussed below in section 4.3.3, colliding streams of colour charges are nearly transparent for each other. One consequence of this behaviour, is a much too low particle production rate of qMD when applied to proton-proton collisions, as we will see below.

This restricts the applicability of the qMD model to the dynamics of expansion and cluster formation for quark systems in heavy ion collisions. Initial collisions and initial particle production is handled better by other models.

In principle, it would be possible to assign a finite cross section for elastic hard core scattering to every colour charge in qMD by hand. This would reduce the transparency in head-on collisions and improve the performance of the model in proton-proton collisions and the initial stage of nucleus-nucleus collisions.

4.3.2 No explicit gluons in qMD

The Hamiltonian (4.1) of qMD does not treat gluons as explicit degrees of freedom. As mentioned before, the model is motivated by the same reasoning which is used in the maximal abelian gauge approach to QCD and the dual superconductor scheme for colour confinement. Within this framework, non-diagonal gluons acquire masses of approximately $700\,\mathrm{MeV}$, corresponding to an interaction range of $\sim 0.3\,\mathrm{fm}$, and the condensation of monopoles in the gluon field compels the chromoelectric field to the formation of flux tubes (see section 2.2.1).

In these model pictures, there is no immediate need for an explicit treatment of gluons, since the gluon sector is handled in an effective way: all effects of gluons are subsumed in the potential interaction. It is clear, on the other hand, that the model pictures deal efficiently only with the soft gluon sector, where momentum exchange is low.

Hence, hard gluons, which grow ever more important with increasing temperature, or collision energy, are neglected. It is assumed that in heavy ion collisions at

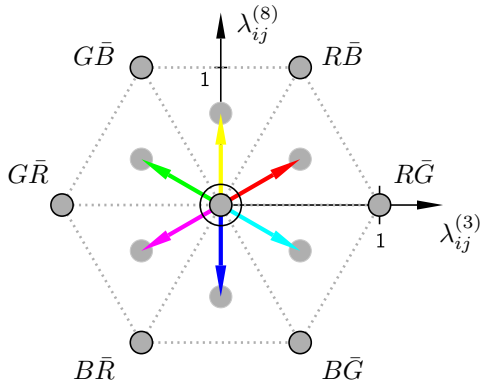

Figure 4.9
Extension of the colour charges to the octet: Starting from the charges of the triplet and the antitriplet, the colour charges of the octet are obtained by combinations of the weight vectors of the triplet and antitriplet. Besides the six states with differing colour and anticolour, there are two colour neutral combinations, located in the centre of the diagram.

RHIC energies, hard gluons make up the largest contribution to the particle content of the deconfined system [138]. The missing handling of these particles is a severe shortcoming of the qMD model if applied to RHIC energies.

A possible improvement would be the extension of the particle content of qMD from triplet and antitriplet charges in the weight diagram 2.1 to octet charges, which are the gluons. The extended weight diagram is shown in figure 4.9. The relative interaction could be obtained in a straight-forward application of the colour factors (4.3) to the octet charges.

However, it is not so clear how cope with these hard gluons at hadronization. Considered as constituent parts of colour neutral clusters, the hadronic states would correspond to hybrid states, containing quarks and valence gluons, or glueballs, containing only gluons. Since the experimental status of such states is far from clear, it is not obvious what to do with them. They could be treated simply as some kind of heavy resonances, which decay in well-known hadrons, albeit there is not much known about decay widths and lifetimes of these states.

There is, however, also a conceptual problem with including hard gluons in the clustering of colour neutral states, since at clustering, they may not be hard any more. Hard gluons could become soft ones, thus they could disappear from the system, transferring their colour charges to other particles. It is not clear a priori how this could be incorporated into the model in a consistent way.

4.3.3 Abelian approximation: no colour rotations

In the approximation which is used in qMD, colour is fixed quantum number for colour charges: Since interactions are mediated only by the diagonal gluons, a red quark will stay a red quark forever. This seems to be at odds with the gauge invariance of QCD, but, as we have seen, it can be motivated by the maximal abelian gauge picture of QCD. In this picture, however, off-diagonal gluons do not disappear, but they just acquire a considerable mass. Thus, to neglect them completely introduces errors as far as short range interactions between quarks with high momentum transfer are concerned: In such interactions, colour could be exchanged.

A naive implementation of colour exchange mediated by off-diagonal gluon could assign a certain probability for swapping colours to every pair of colour charges with a spatial distance of less than about $\sim 0.3\,\mathrm{fm}$ and high relative three-

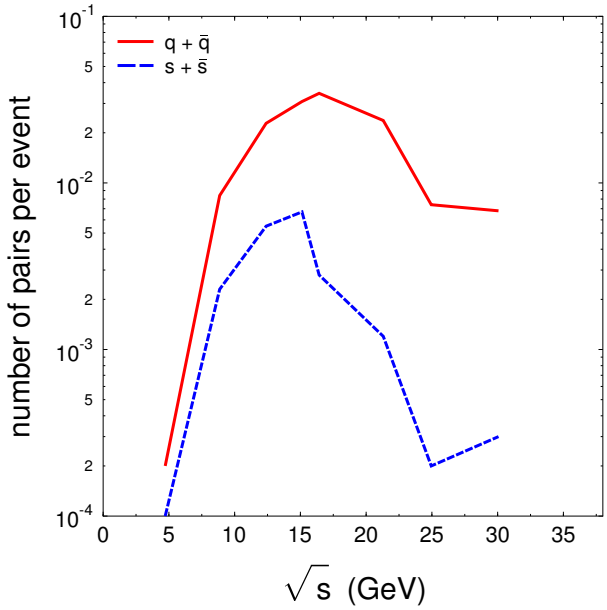

Figure 4.10
Production rate of quark-antiquark pairs in proton-proton collisions as a function of the collision energy. Transparency in qMD is responsible for the decrease of the number of produced pairs beyond an energy which corresponds roughly to upper SPS energy.

momentum. In the current version of qMD, this is not yet done. One could expect, for example, that such a colour exchange at short distance will improve the unsatisfactory performance of qMD in proton-proton collisions.

Much more sophisticated approaches could try to take into account the full machinery of colour transport, which follows from the classical Wong equation and has been analysed in detail by Elze and Heinz [139]. This, however, would involve an enormous amount of recoding of the present qMD implementation. Moreover, there is a further difficulty that arises with the treatment of colour as a dynamical, continuous degree of freedom: In such a model, it is difficult to define colour neutral clusters of quarks. The implementation of dynamical colour in [123], for example, shows that in practice, it is nearly impossible to obtain completely colour states in such a model.

4.3.4 Transparency of QMD in proton-proton collisions

This missing colour exchange, together with the absence of elastic hard core scattering, has serious consequences for the performance of the qMD model when applied to proton-proton collisions: Since the initial protons are colour neutral and the potential interaction is the only interaction at work between them, the colliding protons appear transparent to each other. Particle production is strongly suppressed, since the main mechanism for particle production, pair production in the strong colour field of flux tubes, can not contribute, simply because no strong colour fields are created. The formation of such strong fields would require either hard backward-scattering of colour charges, or exchange of colour charge between colour charges of high relative momenta. The first option is rare in the Rutherford-like potential scattering of qMD, the second option is not implemented.

The consequences of this approximations are very clearly visible in the excitation function for the production of quark-antiquark pairs in proton-proton collisions, as shown in figure 4.10. In this simulation, the protons have been modelled

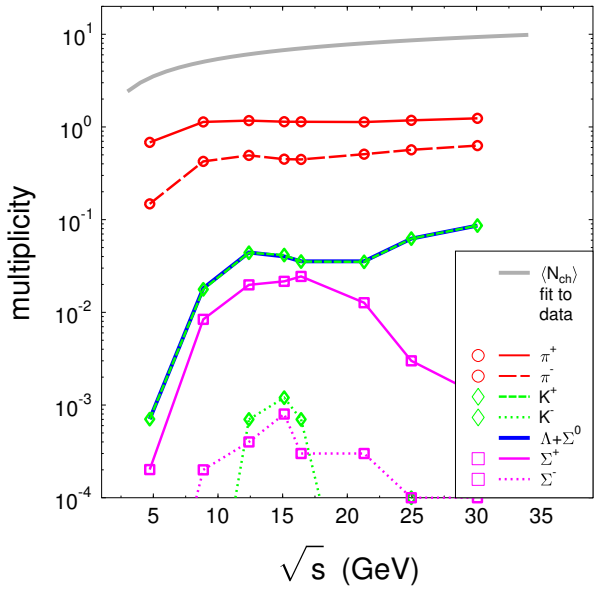

Figure 4.11
Inclusive charged particle production in proton-proton collisions as a function of the collision energy as obtained from qMD simulations. The overall particle production is much too low compared to experimental data. Furthermore, due to transparency in qMD, the inclusive particle production saturates with increasing energy.

as clusters of three quarks, with relative initial momenta and positions chosen in order to yield a cluster mass of the proton mass. These clusters where initialized head on, with relative cluster momenta corresponding to the energy $\sqrt{s}$ of the collision. Then, the Hamiltonian equations of motion of qMD were integrated numerically, with the cluster search switched off for $\Delta t = 10\,\mathrm{fm/c}$ in the centre of momentum frame of the collision in order to avoid premature clustering. During this time, quark-antiquark pairs could be produced. Finally, clustering was switched on, forming colour neutral hadronic resonances, which were allowed to decay into final state hadrons.

The most prominent feature of figure 4.10 is the maximum in the number of produced quark-antiquark pairs at approximately upper SPS energies. Particle production by pair creation should increase with energy—this is a lesson from experimental data, which is modelled very well in the LUND string picture. The failure of qMD in reproducing this behaviour can be understood from the transparency of qMD as described above: The two clusters corresponding to the protons pass through each other, with only the potential interaction at work. The higher the energy, the faster they are separated again, and the shorter the time the potential can act. In the end, colour neutral clusters have met, passed through each other, and separated again, with hardly any interaction at all and no particle production.

As a consequence of the deficient pair production, inclusive charged particle production is also low. This is shown in figure 4.11 for the same proton-proton collisions as before. Here, all final state hadrons are taken into account, and multiplicities are normalized to only those collisions with more than two particles in the final state, corresponding to inclusive measurements. Contributions to the final state particle yields stem from pair creation in the string break-up, and from the decay of heavy clusters. This means, for example, that due to the potential interaction of the colour charges, potential energy may be stored in one or both clusters. Hence, instead of clustering as a proton, the quarks will form a N^* resonance, for example, which on decay will produce new pions.

To compare to experimental data, figure 4.11 shows the parametrization of Thomé et al. [140] for the average multiplicity of charged particles produced in proton-proton collisions. It is given by

$$\left\langle N_{\text{charged}} \right\rangle = 0.88 + 0.44 \log s + 0.118 (\log s)^2 \,, \tag{4.40}$$

where s is in units of GeV^2. Particle multiplicities are dominated by pions, and in order to infer total particle multiplicities from charged particle multiplicities, one has to multiply the charged particle multiplicity (4.40) by $3/2$. It is obvious from figure 4.11 that the overall production of particles is much too low compared to experimental data. The saturation of the inclusive particle production with increasing energy for pions is caused mainly by the final state decays of clusters. This can be seen from the decrease of the production rate of Σ^+ particles with energy: positive hyperons can be produced only by the decay of very heavy clusters in the process $X \to \Sigma^+ K^0$, where X must have the quark content of the proton, or by the production of $s\bar{s}$ pairs. The second process is increasingly suppressed with energy, as shown in figure 4.10.

Without digging into further details, it is clear from the gross features of the particle production in proton-proton collisions using qMD that this model is not well suited to handle these processes. Similarly, we conclude that also the initial state of nucleus-nucleus collisions can not be treated properly using qMD. In chapter 6, we will see that we can use the hadronic model UrQMD to provide us with an initial state of quarks and antiquarks.

4.3.5 Colour strings or potential interaction between pairs of charges?

It is clear from the foregoing discussion that one of the sources for the failure of qMD in proton-proton collisions lies in the use of the potential interaction instead of a proper treatment of colour strings. The use of the linear potential is, on the one hand, motivated with the colour string picture in mind. On the other hand, as we have seen in discussing figure 4.2, it is not possible to attribute a physical meaning in the sense of flux tubes to the lines connecting colour charges, which correspond to the potential interactions.

Thus, it is not clear how to handle particle production via the Schwinger mechanism in a consistent way. Since qMD does not provide a proper, physical description of regions of high flux density, corresponding to high energy density of the chromoelectric field, particle production is not described correctly.

A real improvement of this situation can be achieved if the potential interaction is replaced by field configurations calculated dynamically. To do this, the Friedberg-Lee model of the Frankfurt-Gießen group [90, 91] would be a natural choice. The current implementations of this model calculate field configurations for static configurations of colour charges. This means that in each time step for the numerical integration of the equations of motions of the charges, this procedure must be repeated [87], which amounts to an enormous computational task. But it is obvious that the Friedberg-Lee model can provide much more realistic data about the field configurations and forces on colour charges than the naive potential ansatz, and it offers a much more natural framework to implement particle production by string break-up.

In this sense, the Friedberg-Lee and qMD approaches are complimentary, the Friedberg-Lee model providing more realistic configurations of the chromoelectric field, the qMD model handling the complete charge dynamics and the clustering of charges to colour neutral configurations. However, even then, chromomagnetic effects are not yet treated.

As an intermediate step, one could try to extract a set of heuristic rules from the patterns of field configurations obtained in the Friedberg-Lee model, which would be used to establish the colour fields created by a given configuration of colour charges. This could possibly allow the development of fast, realistic codes to handle the interaction between colour charges.

4.3.6 Worried about instantaneous interaction?

The present implementation of the potential interaction in the qMD model has some more obvious shortcomings. It uses an instantaneous interaction at a distance, with no retardation effects included, and as such manifestly breaks Lorentz invariance.

This is not, however, an insurmountable problem, since also here, remedies can be found: Retardation effects could be included in the potential, starting with the inclusion of the Breit term. Furthermore, chromomagnetic terms could be taken into account, in a way similar to the Lorentz force in electrodynamics. The result could be a potential interaction as complex as in the Capstick-Isgur-Godfrey ansatz [93, 18], which turned out to be very successful in the description of mesons and baryons. Moreover, it was shown in [104] that for parton cascade models, the use of potentials is not necessarily incompatible with the requirements of a fully Poincaré invariant dynamics.

So, we see that the deficiencies of instantaneous interaction in qMD could be cured by the use of better potential terms and an implementation of the invariant dynamics, which is, however, quite involved to bring to practice. A more convenient option would probably be to dismiss the potential interaction altogether and replace it with the field configurations calculated from the Friedberg-Lee model.

4.3.7 No quantum effects: no mass spectrum, no Pauli exclusion

As we have seen in figure 4.6, the masses of colour neutral clusters obtained in qMD follow a very wide distribution. There is no discrete mass spectrum, as it is known from the physical hadron states listed in the tables of the particle data group. This should, however, not be a surprise to anyone, since there is no quantum mechanics whatsoever included in qMD.

Even if quantum mechanics was taken into account, obtaining the mass spectrum of hadrons starting from valence quarks would be equal to solve the low energy sector of QCD, which is a formidable task. The before-mentioned potential ansätze come close to this for mesons and baryons. There are models which use properly antisymmetrized molecular dynamics of quarks [141], but they are limited to moderately small systems, as for example pentaquark clusters. Hence, applying these methods to the many-particle states of heavy ion collisions is extremely involved, and implementations in codes are very demanding.

Solving these problems is beyond the scope of a single thesis project, unless one comes up with some ingenious insight, which would be rewarded not only with a title, but probably also with a ticket to Stockholm.

But more down to earth, the neglect of the Pauli principle obviously forbids any reasonable application of the qMD model to regimes of high density and low temperature, where Fermi statistics are extremely important. Thus, for example, trying to apply qMD to study cool quark matter as it may occur in the core of neutron stars, or in regimes where colour-superconductivity may set in, is completely out of reach without any handling of the Pauli exclusion principle.

To cure this problem, and considering that antisymmetrized dynamics is out of scope for systems with more than of the order of ~ 10 colour charges, the best possibility is the use of some phenomenological Pauli potential, which is repulsive in both real and momentum space and thus suppresses the occupation of the same location in phase space by more than one colour charge. Such Pauli potentials have been applied with much success in quantum molecular dynamics descriptions of nuclei [142, 143] and are a natural part of hadronic models such as UrQMD in order to yield stable ground state nuclei.

Hence, the inclusion of a Pauli potential in qMD, which would be a comparably easy task, would extend appreciably the applicability of the model to cool and dense deconfined systems.

4.3.8 Cluster hadronization and entropy

While all objections mentioned so far concern the use of the specific Hamiltonian (4.1) and the approximations and omissions this implies, there is one important point one has to keep in mind concerning the clustering method used in the mapping of deconfined colour charges to hadrons. This point concerns the conservation of entropy. Thinking in a direct and naive way, entropy conservation seems to be grossly violated in the clustering procedure—and even worse, entropy seems to be decreasing, since the number of particles is decreasing by a factor between 2 and 3 at cluster formation, depending on the baryon content of the system.

Similar reasoning is routinely used when estimating the number of initial quarks and gluons in a heavy ion collision from counting pions. Since entropy in a heavy ion collision essentially measures the number of (massless) particles, one concludes from the number of final state pions that the number of quarks and gluons in the initial state should be at least the same.

It is, however, not straight-forward to transfer this reasoning to the situation encountered in qMD. First of all, gluons are incorporated in an effective way in the potential, thus their contribution to entropy is difficult to evaluate. Second, estimating entropy by counting particles works well for massless, weakly interacting particles without inner structure. In qMD, however, initial state colour charges interact strongly via the potential term. Furthermore, most of the colour neutral clusters are very massive, highly excited resonance states, which in fact will decay in most cases in two or more final state hadrons. Thus, for quarks both before clustering and at clustering, the sole number is an insufficient measure of entropy. We will come back to this point in more detail when considering charge fluctuations as a probe of deconfinement in chapter 7.

Concerning numbers, as a rule of thumb, the final state in a qMD simulation after the strong decay of all resonances contains roughly as many particles as there have been quarks in the initial state. Thus, the entropy argument is not as severe as it may appear at the first guess.

4.3.9 Where is the positive message?

Pondering all the shortcomings of the qMD approach listed in the previous sections, one may be pushed to the conclusion that this model is over-simplified and not adequate to describe any real physical situation before much improvement is applied.

However, before falling into depression, we should not forget that in the first place, the quark molecular dynamics in its present form offers a tractable model which is able to treat dynamically the recombination process for hadronization that occurs during the expansion of a hot and dense system of deconfined colour charges. Furthermore, the linear potential ensures "quark confinement" in an effective way. This makes qMD a unique model, worth of study despite all deficiencies.

It is to these achievements of the model that we will turn to now, starting with the thermal properties of qMD, before applying it to the dynamical description of heavy ion collisions.

Chapter 5

Thermal properties of the qMD model

Gaining insight in the thermal properties of the qMD model is a natural issue to tackle before embarking on further applications the of the model: What is its ground state? How many colour charges will typically arrange themselves to form colour neutral clusters at a given temperature and chemical potential? What can be said about the equation of state?

These are questions which, for systems described by a given Hamiltonian, are treated typically by Monte Carlo techniques. In these methods, a random sequence of phase space configurations is generated, which mimics different microstates corresponding to one macrostate in thermodynamical equilibrium. From this sequence of microstates, all kinds of macroscopic variables can be deduced.

The following section 5.1 states essential facts obtained from Monte Carlo simulations concerning the phase diagram of qMD and its equation of state. The model exhibits a transition from a clustering to a deconfined phase. These results have been presented in [134].

It is well-known from statistical mechanics that in small, finite systems, any signature of a transition between different phases is smeared out. Moreover, the transition temperature is shifted away from its exact value in the thermodynamic limit of infinite volume, usually to smaller, size-dependent values. This effect is known as finite-size scaling. A first, coarse look at finite-size scaling in qMD is presented in section 5.2. This work is by far non-exhaustive and could be extended.

Finally, as a consequence of the collective behaviour of the system, one expects that the fundamental, long-range potential interaction between colour charges is screened in the presence of a background of other, free colour charges. This is Debye screening, which is well-known from Coulomb systems of freely moving electric charges. Section 5.3 discusses Debye screening of the interaction between heavy colour charges ($c\bar{c}$ pairs) in qMD. One finds a strong dependence of screening on temperature, which dictates the correlations of background colour charges responsible for screening. As a direct consequence, we obtain a qualitative description of the "melting" of charmonium clusters in qMD.

5.1 The phase diagram and the equation of state of qMD

Before embarking on a full Monte Carlo study of the thermal properties of the qMD model, it is very instructive to use general thermodynamic arguments, which can give insight into the behaviour of the model at different temperatures.

As we have seen in chapter 4, the large potential energy of the interacting colour charges can be considerably lowered if the charges arrange themselves in clusters which are colour neutral. Hence, as the internal energy U_{qMD} is concerned, the formation of clusters is energetically favourable. However, the formation of clusters also lowers the entropy S of the system. Thus, it is not clear a priori if, at a given temperature T, the free energy

$$F_{\text{qMD}} = U_{\text{qMD}} - TS_{\text{qMD}} \tag{5.1}$$

is lowered by the formation of clusters and therefore, the system in thermal equilibrium at temperature T will condense into clusters. Nevertheless, it is evident from (5.1) that there should be some critical temperature T_{c} below which the free energy F_{qMD} is indeed lowered by clustering. Then, the corresponding lowering of the internal energy U_{qMD} overweights the rise of the entropic contribution $-TS_{\text{qMD}}$. Hence, we expect the system to form colour neutral clusters at sufficiently low temperatures.

We further expect from this thermodynamic reasoning that the colour neutral clusters should be as small as possible, since smaller clusters are more abundant in number and, consequently, contribute more to entropy S_{qMD} than bigger clusters. For this reason, thy lower the free energy F_{qMD} at a given temperature further than bigger clusters. Thus, we expect that in thermal equilibrium at low temperatures, most colour charges are grouped in clusters of two or three colour charges: "mesons", with colour and anticolour, and "baryons" and "antibaryons" with three different colours or anticolours, respectively.

We will come back on the entropy argument later in chapter 7, when discussing fluctuation signals for the QGP in the framework of the qMD model, and on the "small cluster argument" in chapter 8 in relation with our study of the formation of clusters made up of up to six colour charges Here, we will explore the thermal properties of qMD.

5.1.1 The partition function of qMD

When studying the thermal properties of a system defined by some specific Hamiltonian $\mathcal{H}$, the most important problem to solve is the calculation of the partition function Z of the system. From the partition function, the free energy is obtained, and all kinds of thermodynamical variables can be computed from the free energy. Unfortunately, exact calculations of partition functions are extremely rare.

In the case of qMD, the partition function $Z_{\text{qMD}}(\{\vec{v}_i\})$ for an ensemble $\{\vec{v}_i\}$ of N colour charges $\vec{v}_i, i = 1, \ldots, N$ in the centre of momentum frame is given by

$$Z_{\text{qMD}}(\{\vec{v}_i\}) = \frac{1}{N!\, h^{3N}} \prod_{i=1,\ldots,n} \int \mathrm{d}\vec{x}_i \int \mathrm{d}\vec{p}_i \, \mathrm{e}^{-\beta \mathcal{H}_{\text{qMD}}(\vec{x}_j, \vec{p}_j)} \; . \tag{5.2}$$

Here, $\beta = 1/T$ (with $k_{\text{Boltzmann}} = 1$) is the inverse temperature, and $\vec{x}_i$ and $\vec{p}_i$ are the three-coordinates and three-momentum of colour charge i in the system. Keep in mind that $\vec{v}_i$ is the weight vector of colour charge i, and that the total system has to be colour neutral, hence $\sum_{i=1}^{N} \vec{v}_i = 0$—see (4.6).

Colour is, in principle, a dynamical degree of freedom. Thus, one could expect it to be summed over in the partition function (5.2) as well, along with other internal degrees of freedom. However, as we have discussed in chapter 4, since the qMD model takes into account only diagonal gluons, colour becomes fixed for every colour charge, and is not subject to change during the evolution of the system. The same argument holds for the spin degree of freedom, which is not treated dynamically either. Hence, real space three-coordinates $\vec{x}_i$ and three-momenta $\vec{p}_i$ of the N colour charges in the system completely parametrize the phase space to be summed over in the partition function (5.2).

The factor $1/N!$ in (5.2) corresponds to the prescription of "correct Boltzmann counting" for classical particles subject to Boltzmann statistics [144]: as we have discussed in chapter 4, we treat all colour charges as distinguishable particles, disregarding Fermi statistics and the Pauli principle.

Using the explicit form (4.1) of the qMD Hamiltonian, we see that the integration over the three-momenta factorises from the rest of the partition function. It is known since long [145] how to solve the corresponding momentum integrals analytically. The resulting expression for $Z_{\text{qMD}}(\{\vec{v}_i\})$ reads

$$Z_{\text{qMD}}(\{\vec{v}_i\}) = \frac{1}{N!} \prod_{i=1,\dots,N} \frac{4\pi m_i^2}{\beta h^3} K_2(\beta m_i) \times \prod_{i=1,\dots,N} \int \mathrm{d}\vec{x}_i \exp\left(-\frac{\beta}{2} {\sum_{i,j}}' -\vec{v}_i \vec{v}_j V(|\vec{r}_i - \vec{r}_j|) \right) , \tag{5.3}$$

where m_i is the mass of colour charge i and $K_2(\xi)$ is a modified Bessel function. It is clear that the real space part of the partition function is much harder to treat analytically. One could be tempted to transform the integration over the three-coordinates $\vec{x}_i$ into some integral over the potential pair interaction $V_{ij} = V(|\vec{r}_i - \vec{r}_j|)$. Then, formally, one could write

$$Z_{\text{qMD, space}}(\{\vec{v}_i\}) = \int \mathcal{D}V_{ij} \frac{1}{\left| \frac{\partial V_a}{\partial x_b} \right|} \exp\left(-\frac{\beta}{2} {\sum_{i,j}}' \vec{v}_i \vec{v}_j V_{ij} \right) . \tag{5.4}$$

Now, keeping in mind that

$$\vec{v}_i = \begin{pmatrix} \sin \frac{1}{6}\left(n_i + \frac{1}{2}\right) 2\pi \\ \cos \frac{1}{6}\left(n_i + \frac{1}{2}\right) 2\pi \end{pmatrix} , \quad n_i = 0, 1, \dots, 5 \in \mathbb{Z}_6 = \mathbb{Z}/_{6\mathbb{Z}} , \tag{5.5}$$

equation (5.4) looks like the partition function of a six-state clock model (or $\mathbb{Z}_6$ model) spin glass [146].

The $\mathbb{Z}_6$ model, and more generally $\mathbb{Z}_N$ models, have been analysed in relation with the phase structures of gauge theories [147], and the occurrence of confinement in abelian QED at large coupling [148]. In the latter work, the deconfinement

transition in a four-dimensional $\mathrm{U}(1)$ gauge theory was shown to be equivalent to the vortex condensation of the well-known Berezinskii-Kosterlitz-Thouless (BKT) transition [66, 67, 68] in the two-dimensional XY model, where at high temperatures, free vortices appear. While the XY model is the limit of the $\mathbb{Z}_N$ model for $N \to \infty$, the BKT transition occurs already for $N = 6$ [149].

Spin glasses are characterized by exchange interaction strengths J_{ij} among coupled spins which are not fixed, as in standard models for magnetic systems with ferromagnetic or antiferromagnetic exchange, but follow some distribution law. In the partition function, this distribution is usually summed over. In the case (5.4) derived from qMD, due to the from of the potential, the couplings V_{ij} can take any real value. However, since they originate from the positions of colour charges in space, they are not independent, which forbids any straight-forward application of spin glass methods.

For this reason, we will not follow any further the search for some analytic treatment of the partition function of qMD, but resort to numerical methods instead.

5.1.2 The Metropolis algorithm applied to qMD

As we have seen, the system of interacting colour charges in complete thermal equilibrium is far from an ideal gas, but rather a strongly coupled fluid. This is encoded in the space part of the partition function (5.3), for which we did not find any analytic solution. Instead, we will now apply numerical techniques to analyse the properties of the system.

The thermal expectation value of a variable O in a system defined by the Hamiltonian $\mathcal{H}$ at the temperature $T = 1/\beta$ is given by

$$\langle O \rangle = \frac{1}{Z} \sum_{C(\vec{x}_j, \vec{p}_j)} O(\vec{x}_j, \vec{p}_j)\, \mathrm{e}^{-\beta \mathcal{H}(\vec{x}_j, \vec{p}_j)} \ , \tag{5.6}$$

where Z is the partition function and, again, the sum runs over all configurations $C(\vec{x}_j, \vec{p}_j)$ of the system—it is, in fact, an integral over the complete phase space. As we have argued before, colour and spin degrees of freedom are not dynamical in qMD. Hence, real space three-coordinates $\vec{x}_j$ and three-momenta $\vec{p}_j$ of the N colour charges in the system, with $k = 1, \ldots, N$, completely parametrize the phase space to be summed over in (5.6).

Since for qMD, the integral (5.6) can not be solved analytically, some approximation scheme is required. The method of choice in such a case is the adoption of the Metropolis algorithm [150, 151, 152], which generates an arbitrary series of N_{metro} N-particle phase space configurations $C_i, i = 1, \ldots, N_{\text{metro}}$. These configurations are microstates which each represent the equilibrium state of the system. From the phase space configurations C_i, the ensemble average of any variable O can be read off as the sum

$$\langle O \rangle = \frac{1}{N_{\text{metro}}} \sum_{i=1}^{N_{\text{metro}}} O(C_i) \ = \ \frac{1}{N_{\text{metro}}} \sum_{i=1}^{N_{\text{metro}}} O(\vec{x}_j^{(i)}, \vec{p}_j^{(i)}) \ , \quad j = 1, \ldots, N \ , \tag{5.7}$$

where the configuration C_i is completely defined through the phase space coordinates $(\vec{x}_k{}^{(i)}, \vec{p}_k{}^{(i)})$ of the N particles of the system. Note that in (5.7), the Boltzmann factor $\mathrm{e}^{-\beta\mathcal{H}}$ does not occur anymore in the sum. Instead, the phase space

configurations C_i are chosen not from a uniform distribution over phase space, but with relative weights corresponding to their Boltzmann factors. This choice of the configurations C_i is called "Importance Sampling" [152]. It is realized in the Metropolis algorithm by starting from some initial N-particle phase space configuration $C_i = (\vec{x}_k{}^{(i)}, \vec{p}_k{}^{(i)}, k = 1, \ldots, N)$ and then repeatedly creating new phase space test configurations $C_{i+1} = (\vec{x}_k{}^{(i+1)}, \vec{p}_k{}^{(i+1)}, k = 1, \ldots, N)$ by shaking all coordinates and momenta,

$$\begin{aligned} \vec{x}_k{}^{(i)} &\rightarrow \vec{x}_k{}^{(i+1)} = \vec{x}_k{}^{(i)} + \delta\vec{x}_k{}^{(i)} \ , \\ \vec{p}_k{}^{(i)} &\rightarrow \vec{p}_k{}^{(i+1)} = \vec{p}_k{}^{(i)} + \delta\vec{p}_k{}^{(i)} \ . \end{aligned} \tag{5.8}$$

In each iteration, the displacement $(\delta\vec{x}_k{}^{(i)}, \delta\vec{p}_k{}^{(i)})$ in phase space causes a change in the total energy of the system

$$\Delta E = E^{(i+1)} - E^{(i)} \ . \tag{5.9}$$

If $\Delta E < 0$, the test configuration C_{i+1} is energetically favourable compared to the old one, and, in the standard Metropolis scheme, it will be accepted as a new configuration. If, on the other hand, ΔE is positive, the test configuration C_{i+1} will be accepted as a new configuration only with a probability $\exp(-\Delta E/T)$, where T is the temperature of the system. This allows for a statistical increase of the free energy of the system, driven by the temperature T.

Starting from an arbitrary initial N-particle phase space configuration C_0, a sufficient number of iterations will transfer the system towards a stationary state, where further iteration will account for a thermal motion of the sample around the equilibrium state at temperature T. Then, all configurations C_i can be identified as representations of the thermalized state, and the calculation of thermodynamical observables according to (5.7) is possible.

With this method, we can calculate the energy density

$$\epsilon = \frac{1}{V} \langle \mathcal{H} \rangle \tag{5.10}$$

and—by using the virial theorem—the pressure of the interacting system,

$$p = \frac{1}{3V} \left\langle \sum_k \vec{p}_k \vec{v}_k + \sum_k \vec{r}_k \vec{\nabla}_k V \right\rangle \ , \tag{5.11}$$

where $\vec{v}_k = \vec{p}_k / E_k$ is the velocity of particle k, and the sum runs over all N colour charges in the system. From energy-density and pressure, we can then deduce the equation of state of qMD.

Furthermore, in every Metropolis step i, we can check which colour charges will cluster and would form hadrons according to our hadronization criterion. While not really forming hadrons and dissecting the colour charges from the system, but retaining the particles in the system for the next Metropolis step, we can calculate the ratio of free colour charges to hadronic clusters in each step. Moreover, by restricting the calculation of energy and pressure to those colour charges which are not part of these clusters, we can extract the partial pressure of the free colour

charges and, by taking the difference to the total pressure, the partial pressure of the hadronic clusters.

In practice, for our study of the thermal properties of the qMD model, we will initialize a thermal ideal gas of non-interacting colour charges at temperature T and chemical potential μ within a sphere of radius $R = 4\,\mathrm{fm}$. The walls of the sphere are supposed to be impenetrable and ideally reflecting for impinging colour charges. The total colour charge is chosen to be zero, hence the system is colour neutral. The real space distribution of the colour charges in the non-interacting system is homogeneous, and the momentum distribution is obtained at random from the well-known one-particle momentum distribution of an ideal relativistic gas with temperature T and chemical potential μ. Of course, once the interaction is taken into account, an ideal gas configuration will most probably not correspond to a configuration of the interacting system in equilibrium. Hence, the Metropolis algorithm is used to transfer the interacting gas to the equilibrium state, and then, to create a series of configurations to evaluate the expectation values (5.7).

When going from one N-particle phase space configuration C_i to the next, instead of changing the phase space coordinates of all particles, we will chose one particle at random and only change coordinates and momentum of this particle. This simplifies the calculation of the change of energy of the system, since only N interaction pairs have to be taken into account instead of all $N(N-1)$ pairs. However, since with this procedure, subsequent configurations C_i and C_{i+1} are highly correlated, one has to create a number N_{step} of configurations which are all discarded from the calculation of expectation values. Hence, the sum (5.7) takes into account the configurations $C_i, C_{i+N_{\text{step}}}, C_{i+2N_{\text{step}}}, \ldots$, where N_{step} is at least in the order of N, the number of particles in the system. A spherical system with a radius of $4\,\mathrm{fm}$ contains about 400 colour charges a temperature of $150\,\mathrm{MeV}$. In practice, we will choose $N_{\text{step}} = 10000$.

Furthermore, since the ideal gas initial state has to relax into an equilibrium state of the interacting system, we must skip the first Metropolis configurations generated from the ideal gas initial condition in the evaluation of (5.7). Concretely, we will skip the first $10 \times N_{\text{step}}$ configurations.

5.1.3 Thermal properties of qMD from the Metropolis algorithm

From the series of system configurations obtained in this way, we first study the ratio $\xi = N_{\text{c}}/(N_{\text{c}}+N_{\text{f}})$ of the number N_{c} of colour charges which will be mapped to colour neutral clusters according to our hadronization recipe to the total number of colour charges, which is the sum of N_{c} and N_{f}, the number of free colour charges. As mentioned above, this mapping is not performed, and the corresponding colour charges are not removed from the system. The ratio ξ is shown in figure 5.1 for different choices of the potential slope κ and the cut-off parameter F_{cut}. We find that at low temperatures, all colour charges are assigned to clusters ($\xi = 1$), while at high temperatures, colour charges are free ($\xi = 0$). A quite sharp transition between the two regimes occurs at some transition temperature T_{c}, with a width of the transition region of $\Delta T \approx 0.2 T_{\text{c}}$.

While the exact value of the transition temperature T_{c} depends on the choice of the model parameters κ and F_{cut}, such a T_{c} can be identified for each parameter

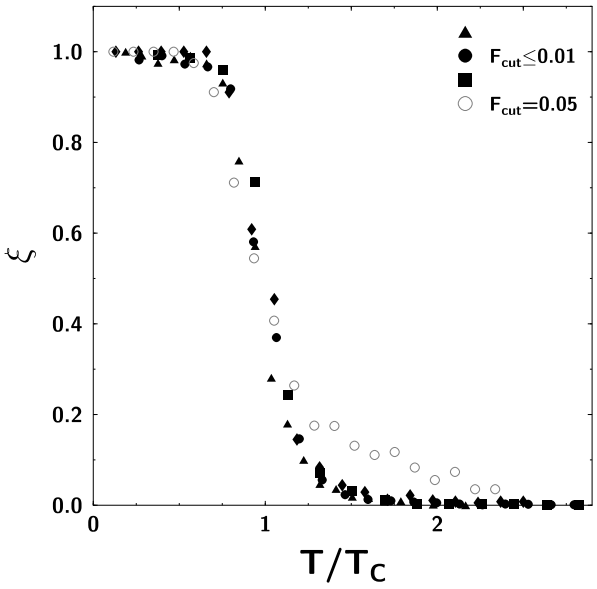

Figure 5.1
The transition from a clustering phase to a phase of free colour charges: the ratio ξ indicates the fraction of colour charges assigned to colour neutral clusters in thermal equilibrium by the clustering routine. At low temperatures, all colour charges are mapped to clusters ($\xi = 1$), while at high temperatures, colour charges are free ($\xi = 0$). The transition temperature depends on the choice of the model parameters, in particular of the string constant κ and the force cut-off parameter F_{cut} in (4.32). In this plot, this transition temperature is scaled to one for different parameter sets. (Figure taken from [134, 129].)

set. This is done either by choosing the temperature of the steepest slope, or—as in section 5.2—by fitting the function $\xi(T)$ with an $\operatorname{arctanh}$ whose inflexion point is chosen as the transition temperature. In figure 5.1, the ratio ξ is plotted for the parameters $\kappa = 0.9\,\text{GeV/fm}, 1.8\,\text{GeV/fm}$, and $F_{\text{cut}} = 0.05, 0.01, 0.005$ [134, 129]. The temperature T is scaled to the transition temperature T_{c} of the corresponding parameter set. One finds a clear-cut universal scaling behaviour for $F_{\text{cut}} \leq 0.01$. The actual value of the transition temperature is found to depend on κ and F_{cut} roughly as

$$T_{\text{c}} \sim \sqrt{\kappa \cdot F_{\text{cut}}}\,. \tag{5.12}$$

This relation can be made plausible from the hadronization mechanism implemented in qMD [129]: Since colour neutral clusters have a strongly suppressed residual interaction compared to free colour charges, we can consider them as bags of deconfined matter surrounded by a perfect colour dielectric medium, as in the MIT bag model. In this model, a cylindrical stretching of the bag, corresponding to the build-up of a flux tube, results in a string constant κ which is connected to the bag constant B according to $\kappa \sim \sqrt{B}$ [12]. On the other hand, the bag pressure for an ideal quark-gluon gas is known to rise as $B \sim T_{\text{c}}^4$. Thus, one is left with $T_{\text{c}} \sim \sqrt{\kappa}$. In the qMD model, the colour neutral cluster is declared a hadron if the remaining force drops below the cut-off $\kappa \cdot F_{\text{cut}}$, as described in (4.32). This is the string constant to use in the expression derived form the MIT bag model analogy. Putting everything together, one ends up with relation (5.12).

From its definition, we know that the smaller F_{cut}, the sharper the criterion for the dissection of a colour neutral cluster. Reaching a scaling limit means that the actual ratio of clustering colour charges does not depend any more on the actual value of F_{cut}, which is desirable since it removes some of the arbitrariness in the choice of F_{cut}. In fact, (5.12) shows that $F_{\text{cut}} \leq 0.01$ simply "renormalizes" the transition temperature T_{c}.

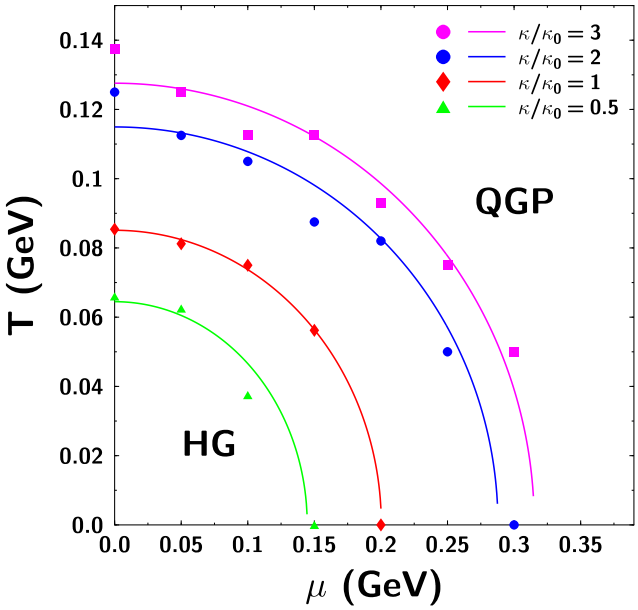

Figure 5.2
The phase diagram of qMD in the $T - \mu$ plane: The figure shows the transition temperature at different quark chemical potential for four different choices of the string constant κ, where $\kappa_0 = 0.9\,\mathrm{GeV/fm}$. The curves are fits to the transition points derived from the simulation data. (Figure taken from [129].)

All data shown in figure 5.1 were obtained at vanishing chemical potential, i. e. for equal numbers of colour charges and anticharges. It is of course of big interest to extend the analysis to systems with $\mu \neq 0$. This can be done in a straightforward manner in this Monte Carlo simulation, if one approximation is applied: The chemical composition is determined for the non-interacting system, where it can be calculated analytically, and it is not changed when the interaction potential is switched on. Of course, turning on the potential might make it thermodynamically favourable at $\mu > 0$ to add three colour charges to the system. Keep in mind that we have to respect total charge neutrality, so the smallest possible changes in the number of colour charges imply the addition or removal of either a charge-anticharge pair—which does not influence the relaxation to chemical equilibrium for $\mu > 0$—or of three different charges or anticharges. However, in systems which do not show large local fluctuations of colour charge, we can assume that neglecting such changes in the number of colour charges induces no big errors.

Results for the transition temperature obtained with different choices of κ at finite chemical potential are represented as the phase diagram of qMD in figure 5.2. It is very interesting to see that increasing the chemical potential lowers the transition temperature, similar to the behaviour of the real phase diagram of QCD shown in figure 1.6. Moreover, using large values of κ, even the transition temperature at $\mu = 0$ and the transition chemical potential close to $T = 0$ can be brought into the range of realistic values.

The most realistic curve of phase separation in figure 5.2 is obtained for the choice $\kappa = 3\kappa_0$, i. e. $\kappa = 2.7\,\mathrm{GeV/fm}$. Using the heuristic rule (5.12), we see that we can improve on this by increasing both κ and F_{cut}. However, F_{cut} should not excess the scaling limit 0.01. Hence, for realistic simulations, we will use $F_{\mathrm{cut}} = 0.01$ and $\kappa = 4\kappa_0 = 3.6\,\mathrm{GeV/fm}$. The transition temperatures found for $\mu = 0$ with these choices of parameters will be discussed in the next section, including system size dependence.

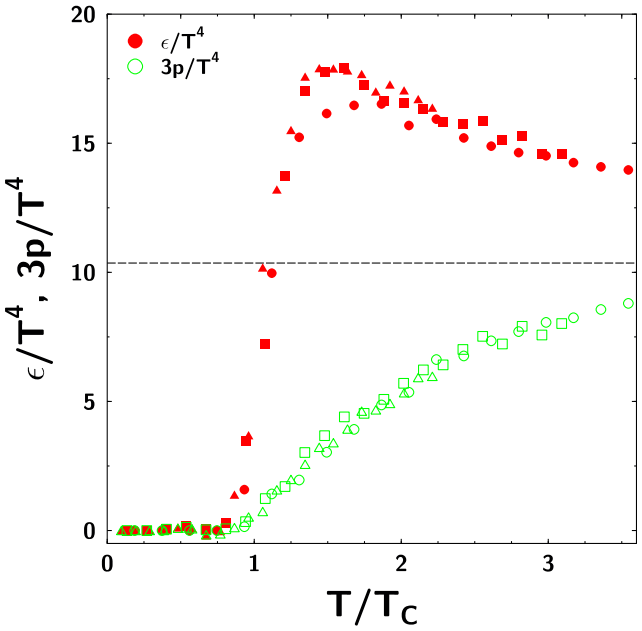

Figure 5.3
Energy density (lower curve, green open symbols) and pressure (upper curve, red full symbols) of unbound colour charges in qMD as a function of temperature, scaled by the T^4 behaviour of the free relativistic gas. Below the transition temperature T_c, both energy and pressure are zero, since all colour charges are bound to clusters. Above T_c, energy and pressure approach the Stefan-Boltzmann limit $\epsilon/T^4 = 3p/T^4 = (21/20)\pi^2 = 10.36$. (Figure taken from [134, 129].)

A continuous transition can also be observed in the energy and pressure dependence of the phase of free colour charges, which is shown in figure 5.3. The energy density ϵ and the pressure p are calculated according to (5.10) and (5.11) for those colour charges which are not mapped to clusters. As in figure 5.2, temperature is scaled to the transition temperature T_c, and the data points represent the results obtained for various values of $\kappa = 0.9\,\mathrm{GeV/fm}, 1.8\,\mathrm{GeV/fm}$, and $F_{\mathrm{cut}} = 0.01, 0.005$.

In the figure, both ϵ and p are scaled by T^4, and the pressure is multiplied by a further factor of 3. This scaling allows to compare our results to the Stefan-Boltzmann limit for non-interacting, massless particles. Neglecting the heavy charm quark, in the limit of high temperatures, energy-density, and pressure should behave as $\epsilon/T^4 = 3p/T^4 = (21/20)\pi^2 = 10.36$. This Stefan-Boltzmann behaviour is represented by the dashed line in figure 5.3. It is not yet reached at $T = 3.5T_c$, but it clearly lies in a range compatible with the qMD data.

Lattice calculations reveal a very similar transition, with a strong increase of energy density and pressure at the critical temperature [153]. However, the qMD finite-size simulation exhibits a much broader transition region. Note furthermore that the absolute values of lattice calculations for very high temperatures may not be compared to the qMD results as we neglect the contributions of hard gluons acting as particles. Nevertheless, it is exciting to see that the simple microscopic ansatz of the qMD model yields qualitative results comparable to full scale lattice simulations, which in other studies usually must be assumed as an input for model building [154].

Once pressure and energy density as a function of temperature are known, it is easy to derive the corresponding equation of state of the free colour charges, which is shown in figure 5.4. The steep rise of energy density at the transition temperature, compared with the slower increase of the pressure, results in a minimum of the equation of state in the transition region. Depending on the choice of the string

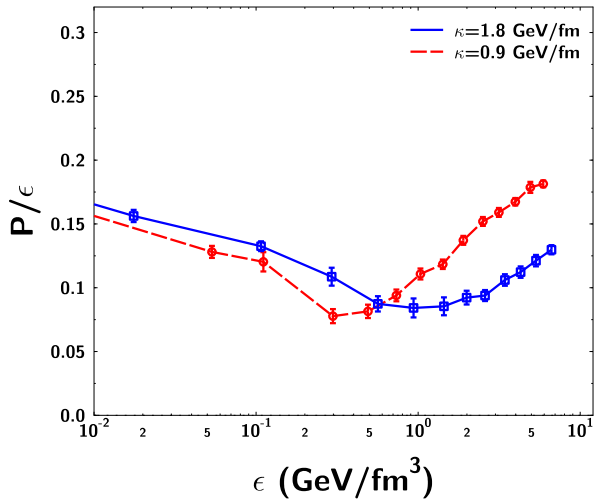

Figure 5.4
Equation of state for a gas of colour charges confined within a spherical container. The equilibrium pressure is extracted from the Monte Carlo evolution of the system using the Virial theorem. There is a "softest point" in the equation of state at energy densities of $\sim 0.3\,\mathrm{GeV/fm}^3$ and $\sim 1.0\,\mathrm{GeV/fm}^3$, respectively, depending on the choice of the string constant ($\kappa = 0.9\,\mathrm{GeV/fm}$ for the dashed, red curve, and $\kappa = 1.8\,\mathrm{GeV/fm}$ for the solid, blue curve). (Figure taken from [134, 129].)

constant, this yields a "softest point" in the equation of state at energy densities of $\epsilon_0 \sim 0.3\,\mathrm{GeV/fm}^3$ (for $\kappa = 0.9\,\mathrm{GeV/fm}$) and $\epsilon_0 \sim 1.0\,\mathrm{GeV/fm}^3$ (for $\kappa = 1.8\,\mathrm{GeV/fm}$), respectively.

5.1.4 Forces on colour charges in qMD from the Metropolis algorithm

The Metropolis algorithm yields a series of configurations of the system of interacting colour charges in thermal equilibrium. There are, of course, always fluctuations which involve deviations from a completely homogeneous distribution of charges. As a result, when going from one Monte Carlo configuration to the next, one finds fluctuations in the force acting on colour charges.

This effect is shown in figure 5.5, where the average radial force

$$F_{\mathrm{rad}}(r) = \left\langle \sum_i \vec{F}_i \hat{\vec{r}}_i \right\rangle \tag{5.13}$$

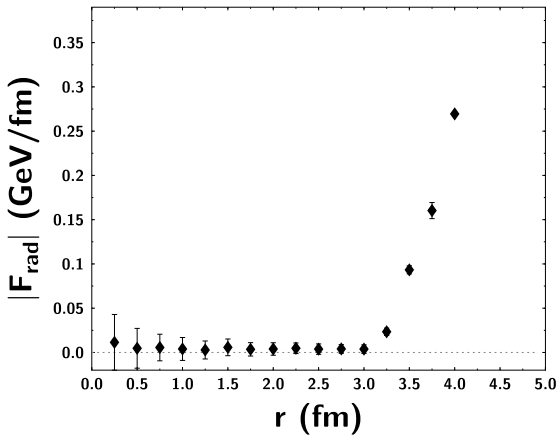

Figure 5.5
The average radial force on a colour charge in a gas confined within a spherical container depends on the distance of the charge from the centre of the system. In the bulk, the force averages to zero, but close to the edge of the gas, strong attractive forces build up, which would prevent the colour charge from leaving the system even if it was not confined within a spherical container. (Figure taken from [134, 129].)

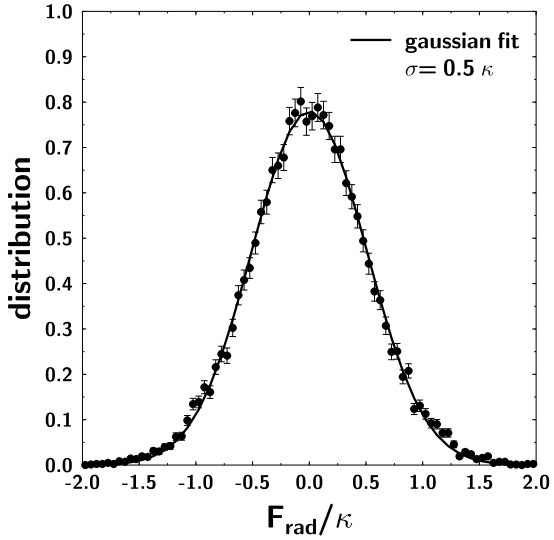

Figure 5.6
Even so the radial force on a colour charge close to the centre of the system confined within a spherical container is zero on average, there are large fluctuations within one Monte Carlo configuration. Radial forces on colour charges with a radial distance of $r < 1\,\mathrm{fm}$ can be both attractive and repulsive, acting towards or away from the centre of the sphere. The figure shows the distribution of these fluctuating radial forces. It is fitted very well by a Gaussian. On average, the force on a colour charge is zero. (Figure taken from [134, 129].)

acting on a colour charge at a distance r from the origin of a spherical, thermalized system ($R = 4\,\mathrm{fm}$, $T = 200\,\mathrm{MeV}$, $\mu = 100\,\mathrm{MeV}$) is plotted. On average, colour charges in the centre of the system do not feel any net interaction: colour is screened effectively in the central region. Close to the edge of the gas, on the other hand, strong attractive forces build up, which would prevent the colour charge from leaving the system even if it was not confined within a spherical container.

While taking the ensemble average of the radial force on a colour charge close to the centre of the spherical gas yields a vanishing force, as shown in figure 5.6, there are, however, large fluctuations of the radial force for colour charges within one Monte Carlo configuration. This is pointed out in figure 5.6, where the distribution of the radial colour forces $\vec{F}_i\,\hat{\vec{r}}_i$ for colour charges within a sphere of radius $r = 1\,\mathrm{fm}$ around the centre of the system and within the same Monte Carlo configuration is shown. One finds an almost perfect Gaussian distribution with a standard deviation $\sigma = 0.5\kappa$, indicating considerable fluctuations.

This means that even for equilibrated, homogeneous and globally and locally colour neutral configurations, there may occur quite strong inhomogeneities on a small scale. Hence, due to the colour interactions, we do not expect that the system of colour charges behaves completely hydrodynamically. For example, an expanding system, such as those studied in part III, will most probably not reduce smoothly temperature and density at expansion. Instead, the wide distribution shown in figure 5.6 indicate that during the expansion, the phase of free charges will rupture, and hadrons will condense both from its surface as well as from its interior.

5.1.5 Remarks on the order of the clustering transition and the properties of bulk matter in qMD

Note that from the data shown in figures 5.1 and 5.2, it is not possible to draw any conclusion about the order of the transition between the clustering and deconfined regimes of the qMD model. The smoothness of the transition may suggest that the

transition is of second order, or even a cross-over. However, we have to keep in mind that the results are obtained from Monte Carlo simulations of a spherical system with a radius of $R = 4\,\mathrm{fm}$, containing ≈ 1070 colour charges at $T = 200\,\mathrm{MeV}$ and $\mu = 100\,\mathrm{MeV}$. It is well-known that in any finite system, signatures of phase transitions are smoothed out by finite-size effects [37, 152, 36]. Finite system can not exhibit any discontinuities in the partition function, and in all the derived thermodynamical properties. This means that even a first-order phase transition between the clustering and deconfined regimes of qMD would not result in a sharp, pronounced step in the ratio $\xi(T)$, for example. A more elaborate analysis should therefore involve comparisons of the behaviour of systems of different size. First steps in this direction are presented in the following section 5.2.

Nevertheless, the gradual increase of energy density and pressure as a function of temperature close to the clustering transition suggests that it is most probably a smooth cross-over. This would also be in line with the ionization transition in hot atomic gases, where the creation of a Coulomb plasma does not involve a second or even first order phase transition.

Of course, it would be desirable to gain a better understanding of the nature and properties of the clustering transition for bulk colour charged matter in qMD. The usual method which is used to reduce the influence of finite-size effects on bulk properties is the application of periodic boundary conditions. While not allowing for non-analyticities in the partition function, periodic boundary conditions at least reduce the influences of surface and border effects, since then, all particles have the same number of neighbours and share the same local environment.

However, there are big obstacles against the naive application of periodic boundary conditions in systems with long-range interactions. This is well-known for the electrostatic Coulomb interaction, where, for example, the calculation of the energy of a periodic ionic crystal is only possible using the Ewald summation technique [155, 135]. In qMD, with its peculiar potential interaction which increases with distance, the situation is even worse than for electrostatic systems.

Several methods have been developed for the molecular dynamics simulation of systems with Coulomb interactions which extend the Ewald technique [156, 157, 158, 159]. But even then, one often does not use completely periodic boundary conditions, but instead is content with replicating the actual cell one tries to simulate once or several times in every direction. Besides in sold state physics, long-range Coulomb interactions are of growing importance for the understanding of biomolecules [160].

There is, of course, one more important long-range interaction, which is gravity. Here, further complications arise since the interaction is always attractive and no shielding or screening can occur. Although gravity is much weaker than the Coulomb interaction, the dynamical evolution of masses under the influence of gravity is of utmost importance if one wants to understand the evolution and structure formation of the universe. Here, extremely elaborate codes have been developed which allow to follow the dynamics of 10^{10} particles (each representing clumps of dark matter of $\approx 10^9 M_\odot$) over the whole history of the universe [161].

It is clear that the analysis of the properties of qMD could profit from the adaption of one or some of the highly developed techniques for the simulation of long-range interaction in solid state physics, biophysics, or astrophysics. However, we

will not follow these options in this thesis. Instead, we will simply use finite systems, which are either confined to a fixed region, as in the Monte Carlo simulations presented in this section, or which are allowed to expand freely. This will induce errors in the study of bulk properties of colour charge matter, for example for the transition temperature. However, when using the qMD model to study the expansion of a hot fireball of deconfined quark matter, this approach comes very close to the real situation.

5.2 Finite size effects on the transition temperature

As we have mentioned before, the finite size of the system used in our Monte Carlo simulations is expected to have several influences on the results obtained for the transition between clustering and deconfined phase, and for thermodynamical variables as pressure, energy density, and the equation of state.

One well-known effect of the finite size is the rounding of sharp signals of phase transitions expected for bulk matter. Thus, the transition to the clustering phase may be more prominent in the bulk. Similarly, the bulk behaviour of pressure and energy may result in a much more pronounced minimum in the equation of state than is visible in figure 5.4. Another effect of finite size is the shifting of the transition temperature as a function of the system size. This shift will be studied in this section.

In general, if a system exhibiting a phase transition is studied with restriction to a finite length scale L, characterising the finite size of the sample at hand, the transition temperature $T_{\mathrm{c}}(L)$ depends on L and is shifted away from the bulk transition temperature $T_\infty = T_{\mathrm{c}}(L \to \infty)$ according to the power law

$$\frac{T_{\mathrm{c}}(L) - T_\infty}{T_\infty} \sim \left(\frac{1}{L}\right)^{\lambda} , \tag{5.14}$$

where λ is a critical exponent which is related to the exponent which describes the divergence of the correlation length ξ at the transition. The direction of the shift depends on the boundary conditions of the finite sample: periodic boundary conditions in general increase the transition temperature compared to the bulk temperature [37], $T_{\mathrm{c}}(L) > T_\infty$, while open boundary conditions tend to decrease the transition temperature.

In statistical mechanics, finite-size analysis usually involves the comparison of systems of different size L. For non-relativistic systems, once a system size is chosen, the number of particles in the system stays constant if the temperature is varied. This situation is different for a relativistic system as described by qMD: here, if temperature increases, the total number of particles $\langle N_{\mathrm{total}} \rangle = \langle N \rangle + \langle \bar{N} \rangle$ is far from constant even if the volume is kept fixed, since with raising temperature, new particle-antiparticle pairs are created. Figure 5.7 shows the relation between temperature T and radius R of a sphere, containing on average $\langle N_{\mathrm{total}} \rangle = 100, 500, 1000$ and 5000 colour charges for qMD.

Thus, before starting a finite-size analysis, one has to decide whether one keeps fixed the volume or the average number of particles $\langle N_{\mathrm{total}} \rangle$. In solid state physics and statistical mechanics, this decision is not necessary. Here, we will keep the

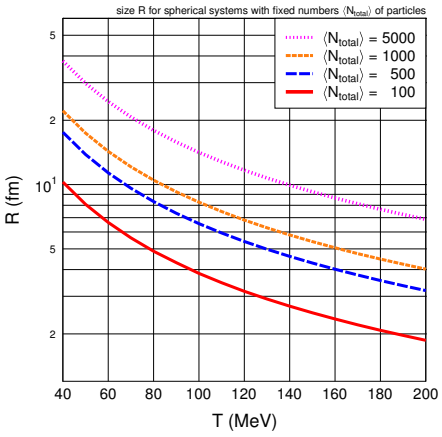

Figure 5.7
System size for different numbers of particles in th qMD relativistic gas at thermal equilibrium: With increasing temperature, the same number of colour charges is contained within a smaller volume.

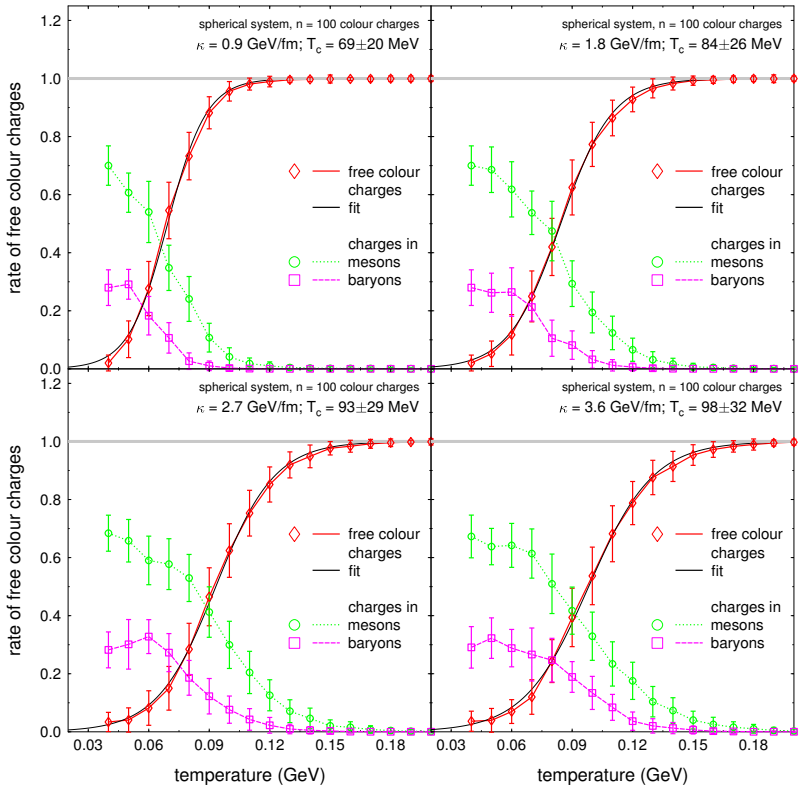

Figure 5.8
Transition from clusters to free colour charges in a system of 100 particles for four different values of the string constant κ and $F_{\text{cut}} = 0.01$. Since the number of particles depends on temperature, the system size is different for each temperature. The system is chosen as a sphere with radius R depending on temperature. The red curve shows the ratio of free colour charges $\bar{\xi}$, which increases at the transition. The ratios of colour charges in baryonic and mesonic clusters, ξ_{b} and ξ_{m}, are shown separately in the magenta (lower) and green (upper) curves. Transition temperatures are obtained by fitting an $\arctanh$ to $\bar{\xi}$. The "error" bar in the transition temperature indicates the width of the transition region.

average number of particles fixed, hence at different temperatures, we will compare systems of different length scales. There are two reasons to motivate this decision: First, the clustering transition is expected to be influenced more by the total number of colour charges then by the total volume of the system. Hence, it seems to be more reasonable to study this transition as a function of temperature in systems where the total number of particles is constant. Second, when applying the qMD model to the expansion and hadronization of a hot gas of quarks and antiquarks, the volume changes due to the expansion, while the number of quarks and antiquarks remains fairly constant, once the initial stage of particle production is over.

Figures 5.8 and 5.9 show the results for the clustering/deconfining transition as a function of temperature T in systems of $\langle N_{\text{total}} \rangle = 100$ and $\langle N_{\text{total}} \rangle = 1000$ colour charges, respectively. The chemical potential is set to zero, $\mu = 0$. The curves is the plots represent the ratios

$$\bar{\xi} = \frac{N_{\text{f}}}{N_{\text{c}} + N_{\text{f}}} , \quad \xi_{\text{b}} = \frac{N_{\text{b}}}{N_{\text{c}} + N_{\text{f}}} , \quad \text{and} \quad \xi_{\text{m}} = \frac{N_{\text{m}}}{N_{\text{c}} + N_{\text{f}}} , \tag{5.15}$$

where N_{f} is the number of free colour charges, N_{b} and N_{m} the number of charges mapped to baryonic and mesonic clusters, respectively, and $N_{\text{c}} = N_{\text{b}} + N_{\text{m}}$ the total number of charges going into clusters. Thus, $N_{\text{c}} + N_{\text{f}} = N_{\text{b}} + N_{\text{m}} + N_{\text{f}} =$

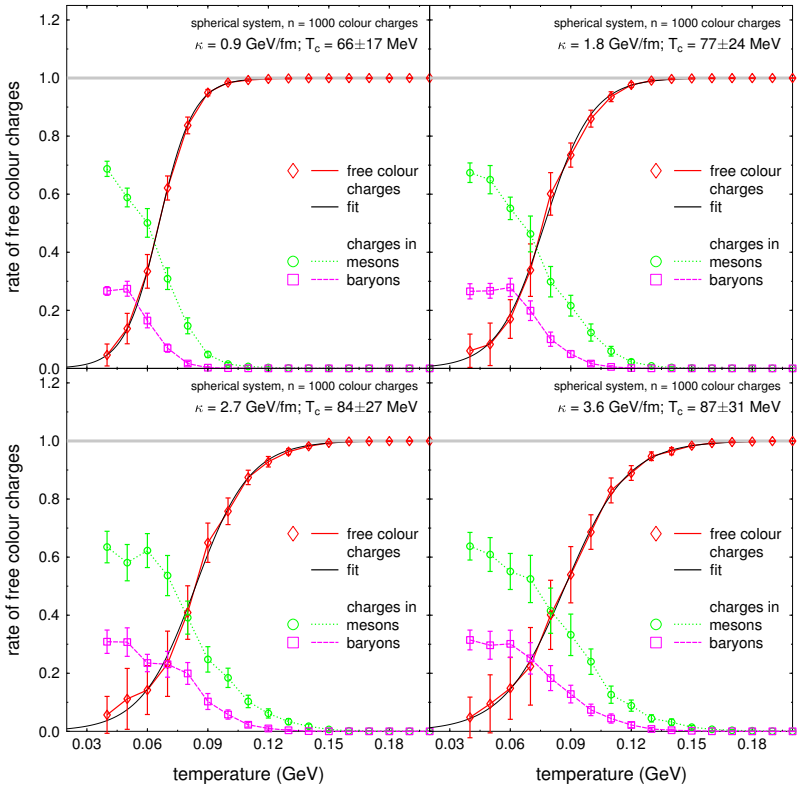

Figure 5.9
Transition from clusters to free colour charges in a system of 1000 particles for four different values of the string constant κ and $F_{\text{cut}} = 0.01$. As in figure 5.8, the system is chosen as a sphere with radius R depending on temperature such that it contains 1000 colour charges.

$\langle N_{\text{total}} \rangle$. The transition is studied for four different values of the string constant ($\kappa = 0.9\,\text{GeV/fm}$, $1.8\,\text{GeV/fm}$, $2.7\,\text{GeV/fm}$, $3.6\,\text{GeV/fm}$), and $F_{\text{cut}} = 0.01$. Note that there is no marked difference in the disappearance of baryonic and mesonic clusters with raising temperature.

The transition from the clustering to the deconfined phase becomes manifest as the increase of $\bar{\xi}$ with temperature. In order to extract the transition temperature T_{c} and to get a measure for the width ΔT of the transition region, we will fit $\bar{\xi}(T)$ by an $\operatorname{arctanh}$,

$$\bar{\xi}(T) = \frac{1}{2}\left(1 + \operatorname{arctanh}\frac{T - T_{\text{c}}}{\Delta T}\right) . \tag{5.16}$$

The results of these fits are shown as black curves in 5.8 and 5.9.

The transition temperatures and the widths of the transition region as derived from the fitting with (5.16) to the data for $\bar{\xi}(T)$ are shown in figure 5.10 as a function of the string constant κ used in the calculation. Note that the transition temperature is shifted towards lower temperatures for the larger system. There is also a small decrease in the width of the transition region in the larger system, at least for the lowest choice of the string constant, $\kappa = 0.9\,\text{GeV/fm}$, but this effect is much less pronounced – the width of the transition region can be considered as roughly independent from the system size.

We conclude that the transition from clustering to deconfined colour charges occurs in bulk matter at even lower temperatures than indicated by the lower curve in figure 5.10, valid for systems of $\langle N_{\text{total}} \rangle = 1000$ particles. Furthermore, finite-size effects shift the transition temperature upwards, but have no marked effect on the width of the transition region. This suggests that the transition from clustering to deconfinement in qMD is in fact a smooth cross-over.

It is clear that this analysis is just the beginning of a full-scale study of the finite-size scaling of qMD. Interesting as this may be, we will not investigate this any further. However, we will use figure 5.10 as a gauge for the equilibrium tran-

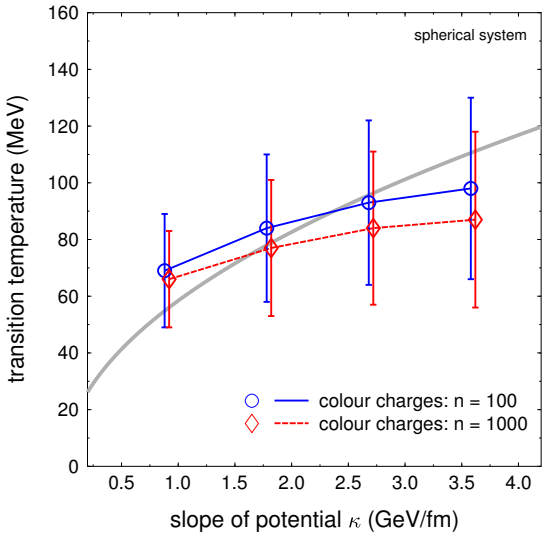

Figure 5.10
Transition temperatures as obtained from the fits of $\xi(T)$ to $\operatorname{arctanh}(T - T_{\text{c}})/\Delta T$ for different values of the string constant κ. The error bars indicate the widths ΔT of the transition region, as read off from the $\operatorname{arctanh}$. Smaller systems show higher transition temperatures, while the width of the transition region is nearly independent of the system size. The grey line indicates the scaling $\sim \sqrt{\kappa}$ as expected from (5.12)

sition temperatures of qMD. In all further simulations, we will use the same value of $F_{\text{cut}} = 0.01$ and the same values of κ that were used in the calculations of T_{c} shown in figure 5.10.

Finally, we note that a direct quantitative comparison of the transition temperatures found here and represented in the phase diagram in figure 5.2 is not straightforward since in the calculation of the phase diagram, a constant volume was used.

5.3 Debye screening of the potential

In QCD at the deconfinement transition, two effects are expected to happen: When crossing the deconfinement temperature from below, the string constant of the linear potential goes to zero, and the remaining Coulomb-like interaction potential gets screened. Technically speaking, the Meissner mass (which describes the penetration length of the colour electric field into the dielectric vacuum) vanishes, while the Debye mass becomes non-zero. This has, of course, immediate effects on bound states in the pair potential, the most prominent being the charmonia and bottomonia states. It was suggested that with the crossing of the deconfinement transition, the J/Ψ should melt [48]. This suppression of the J/Ψ was proposed as a signal for the formation of a quark-gluon plasma.

However, while the general picture about screening remains valid, there remain many open questions. For example, recent results from lattice calculations and spectral density analysis show that bound charmonia states can exist well above the deconfinement transition [49, 50, 162]. The "melting" of charmonia is a much more complex phenomenon than first suggested.

In the qMD model, the string constant κ is a fixed parameter of the model, not dependent on temperature. One could argue that in order to make the model more realistic, this string constant should be made temperature-dependent, or in some other way dependent on the local environment of the charges involved. This idea may be very interesting to follow on. However, it would make the model and the code much more involved and complicated. Anyway, in this thesis we will not follow this proposal any further.

A second point one might think of in order to improve the manageability of the qMD model is whether, motivated by Debye screening, one should either cut the potential interaction at some distance, or use a screened potential right from the beginning. Screening is an effect which is expected if there are many unbound colour charges, which effectively shield the interaction between two test charges at long distance. Here, we will see that in fact, screening is of test charges at long distance is included in qMD as an emergent effect. Thus, it would be inconsistent to use a screened potential as the fundamental potential. This is analogous to the situation in solid-state physics, where the fundamental pair potential between charges is always the $1/r$ Coulomb potential. Nevertheless, Debye-Hückel theory explains [163] how in an interacting many-body system, a screened Yukawa type potential arises to describe the effective interaction between two charges.

A manifestation of the screening of the potential is the melting of J/Ψ particles. How this happens in a thermalized, expanding environment of colour charges is shown in the last part of this section.

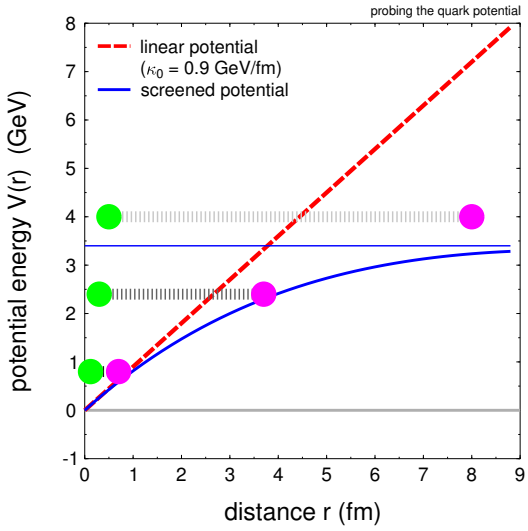

Figure 5.11
Schematic view of the effects of screening: In the screened potential, a pair of colour charges can become unbound if the energy of the pair exceeds the saturation energy of the screened potential.

5.3.1 Probing the effective potential between colour charges

The fundamental interaction potential between a colour charge and its anticharge used in the qMD model shows an unbounded linear increase, or a decrease, respectively, if two equal charges are considered. However, the effective pair-potential between two charges is expected to be screened at high temperatures due to the background of all other freely moving charges in the system. This is the well-known effect of Debye-Hückel screening. In the screened effective potential, pairs of charge and anticharge become unbound at energies exceeding the saturation energy of the potential. This effect is shown schematically in figure 5.11.

Here, we want to study how screening occurs in qMD as a function of temperature, hence as a function of the properties of the background. We expect that at temperatures below the transition temperature T_c, there is no screening, and the linear increase of the potential does not stop with distance. On the other hand, once the temperature reaches the transition region, free colour charges abound, moving freely in between test charges, thus screening their interaction.

In order to measure this screening effect, we use two heavy colour charges, a charm quark-antiquark pair, to probe the potential. The idea is straightforward and corresponds to the situation shown in figure 5.11: First, we create an equilibrated background gas of colour charges at a given temperature T with zero chemical potential. For concreteness, we confine this gas to a sphere with radius $R = 6fm$ and impenetrable, reflecting boundaries, as in the Metropolis studies presented in section 5.1. Into the centre of this background, we insert a charm quark and an anticharm quark at the same location, with three-momenta in opposite directions and initial kinetic energy $E_{\mathrm{kin},\,0}$. In the calculation of the interactions between colour charges, the Coulomb part is suppressed. Hence, the charm quark/antiquark pair is (as all other colour charges) subject to a potential which changes linearly with distance.

If there are no other charges, the quark and the antiquark will follow the typical yoyo motion described in chapter 4: The separation will increase until some

maximal distance r_{max} is reached. Then, the direction of the momenta changes, the particles will approach, pass by each other, separate again, and so on. At the maximal distance r_{max}, all the initial kinetic energy of the particles is transferred to potential energy, hence

$$E_{\text{kin, 0}} = 2\left(\sqrt{m_{\text{c}}^2 + \vec{p}_{\text{c}}^{\,2}} - m_{\text{c}}^2\right) = V(r_{\text{max}}) \,. \tag{5.17}$$

By varying the initial kinetic energy $E_{\text{kin, 0}}$ and monitoring the corresponding maximal distance r_{max}, it is thus possible to probe the shape $V(r)$ of the potential.

If other colour charges are present in the system, they will also interact with the charm-anticharm test particle pair. However, since the charm quarks have much more inertia than the other background charges, their main influence on the charm-anticharm pair is via the screening of the potential interaction. This effect can be measured by the same method explained before: We insert the charm/anticharm pair with different initial energies and monitor the maximal distance of the two particles over the time evolution of the system.

Thus, we first have to prepare the equilibrated background, using our Monte Carlo method. Then, we insert the charm quark/antiquark pair. Now, we follow the dynamical evolution of the total system, by numerical integration of the equations

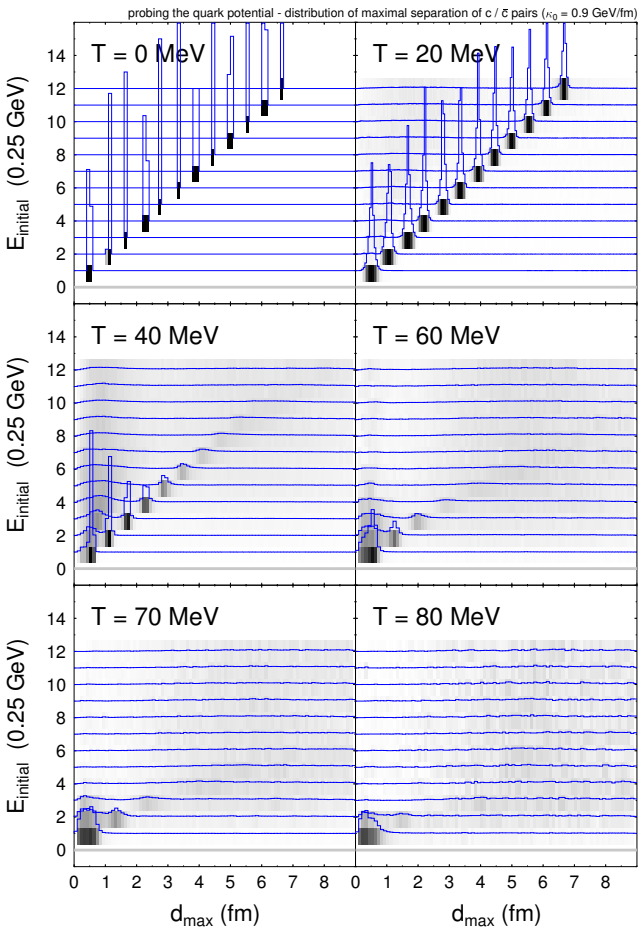

Figure 5.12
The distribution of the maximal separations $\mathrm{d}n/\mathrm{d}r_{\text{max}}$ of the charm/anticharm pair, initialized with different energies E, can be used to probe the shape of the effective colour potential. The blue curves represent the distribution $\mathrm{d}n/\mathrm{d}r_{\text{max}}$, the horizontal offset is proportional to the initial kinetic energy $E_{\text{kin, 0}}$ of the pair. While at low temperatures, the turning points follow exactly the shape of the linear potential, starting at a temperature of $T = 40\,\text{MeV}$, there are no more clear-cut turning points at high energies. This marks th onset of screening of the upper end of the potential. At a temperature of $T = 70\,\text{MeV}$, only very closely bound pairs can still survive.

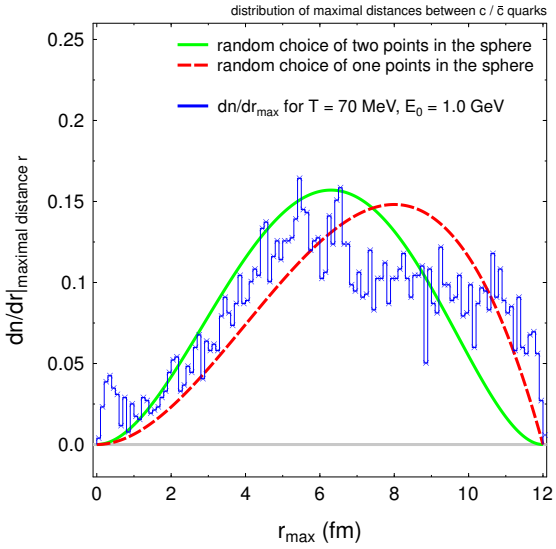

Figure 5.13
A detail of figure 5.12: The distribution of the maximal distances between the charm quark and antiquark for $E_{\mathrm{kin},\,0} = 1.0\,\mathrm{GeV}$ and $T = 70\,\mathrm{MeV}$ (blue histogram) shows that the particles are completely uncorrelated: The green solid curve shows the distribution of the distances of two points picked at random within the sphere, while the red dashed curve shows the distribution of the distances between one fixed point at the edge of the sphere and a second point chosen at random in the sphere [164].

of motion of all colour charges, background and test particles, using a Runge-Kutta method. We watch the system for a time interval of $\Delta t = 200\,\mathrm{fm}/c$, monitoring the distance between the test particles and noting all maximal separations. We use a low value of $\kappa = 0.9\,\mathrm{GeV/fm}$ for the string constant in order to reach the clustering transition at a low temperature. This has the advantage that there are not too many particles in the system, and that the simulation is numerically manageable. As we can see from figure 5.10 in the previous section, the transition temperature to be expected for this choice of κ is $T_\mathrm{c} \approx 70\,\mathrm{MeV}$.

The distribution of the maximal separations, $\mathrm{d}n/\mathrm{d}r_{\mathrm{max}}$, for different initial energies $E_{\mathrm{kin},\,0}$ of the charm quark/antiquark pair and for different temperatures of the thermal background, is shown in figure 5.11. At low temperatures, the extremely sharp distribution of the distances at the turning points exactly traces the shape of the linear potential. However, starting at a temperature of $T \approx 40\,\mathrm{MeV}$, this distribution becomes more and more blurred, beginning at the highest initial energies $E_{\mathrm{kin},\,0}$. This marks the onset of screening of the upper end of the potential. At a temperature of $T = 70\,\mathrm{MeV}$, only very closely bound pairs with small $E_{\mathrm{kin},\,0}$ can survive. Note that this is exactly at the transition temperature of the clustering transition. For higher energies, the distribution of distances at the turning points gets completely random, implying that the pair is not correlated any more. In fact, the distribution shown in figure 5.13 for $E_{\mathrm{kin},\,0} = 1.0\,\mathrm{GeV}$ and $T = 70\,\mathrm{MeV}$ suggests that the turning points are mainly caused by the reflexion of one of the charm or anticharm particles at the wall of the spherical container [164].

From the position and the widths of the maxima of the distributions $\mathrm{d}n/\mathrm{d}r_{\mathrm{max}}$ shown in figure 5.12, we can now reconstruct the shape of the effective potential between the charm-anticharm pair. This reconstruction is shown in figure 5.14. The screening of the potential becomes clearly visible. The grey lines correspond to effective potentials

$$V_{\mathrm{eff}}(r) = \kappa r\, \mathrm{e}^{-r/r_\mathrm{D}}\,, \tag{5.18}$$

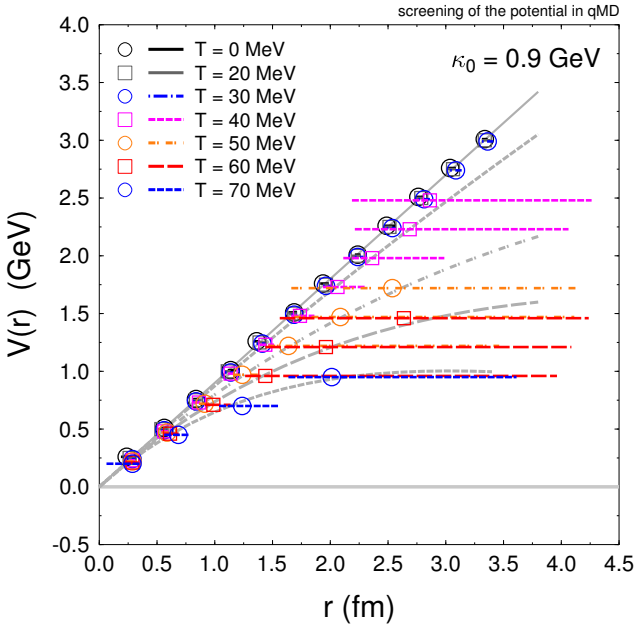

Figure 5.14
The screened pair potential, as extracted from the maxima and widths of the distribution of maximal separations shown in figure 5.12. The grey curves show fits with the ansatz (5.18) for the potentials. With the actual values of system parameters used in the simulation, $T = 70\,\mathrm{MeV}$ corresponds to the transition temperature for clustering.

which have been fitted to the data extracted from figure figure 5.12 by variation of the screening length r_D. The correct form of the effective potential is different from (5.18), since it should saturate at some fixed value $V_0 = V_\mathrm{eff}(r \to \infty) > 0$. However, for the distances probed by the charm-anticharm pairs in the qMD simulation, the ansatz (5.18) work perfectly well, since all data points are located at distances r smaller than the local maximum of the potential (5.18). The Debye length r_D in the screened potentials is $r_\mathrm{D} = 3\,\mathrm{fm}$ at $T = 70\,\mathrm{MeV}$, $r_\mathrm{D} = 5\,\mathrm{fm}$ at $T = 60\,\mathrm{MeV}$, $r_\mathrm{D} = 8.3\,\mathrm{fm}$ at $T = 50\,\mathrm{MeV}$, and $r_\mathrm{D} = 33\,\mathrm{fm}$ at $T = 40\,\mathrm{MeV}$.

Note that these results for the screening lengths are much larger than those obtained from perturbative QCD or lattice calculations, which are of the order $r_\mathrm{D} = 0.2-0.4\,\mathrm{fm}$ [165, 166], depending on temperature. Moreover, we should not forget that there is also a qualitative difference to the situation in real QCD. As mentioned before, in the quark-gluon plasma above deconfinement, Debye screening acts on the Coulomb part of the potential, while the linear part vanishes anyhow.

However, we have reached the important result that in the qMD model, the long range potential is indeed screened by freely moving colour charges. This has, of course, consequences for the survival of J/Ψ states. We will turn to this now.

5.3.2 Melting and recombination of the J/Ψ in the hot medium

Charm quarks with their current mass of $m_\mathrm{c} \approx 1500\,\mathrm{MeV}$ are to massive to be produced thermally in a substantial number in heavy ion collisions. They are created as charm-anticharm pairs in the initial collisions of highly energetic partons. In the naive picture of J/Ψ suppression in a hot, deconfined medium, Debye screening prevents this pair to emerge as a meson from the system, and instead of a J/Ψ, two D mesons are produced. If more than one charm-anticharm pair is created by initial hard processes, it is possible that J/Ψ mesons can be formed by the recombina-

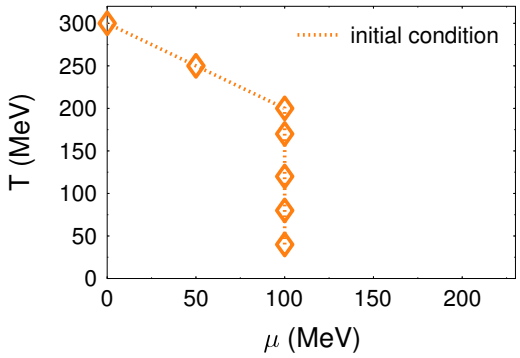

Figure 5.15
Initial conditions for temperature and chemical potential used in the qMD analysis of the melting of the J/Ψ. The string constant is chosen as $\kappa = 2.7\,\mathrm{GeV/fm}$.

tion of partners originating from different production processes. This option was proposed and discussed as relevant contribution to the total J/Ψ yield for heavy ion collisions at RHIC [167, 168]. Here, we can use the qMD model to obtain a qualitative check of this idea.

We initialize a system in a thermalized cylinder, with a Bjorken velocity profile in longitudinal direction. The values of temperature and chemical potential used for the initial conditions are shown in figure 5.15. The size of the system is chosen such that it contains 800 colour charges. The string constant is fixed at $\kappa = 2.7\,\mathrm{GeV/fm}$.

In this system, we insert 40 charm-anticharm pairs within a small distance Δr chosen at random and a relative momentum such that the total energy of the pair in the vacuum, as obtained from the rest masses of the quarks, their kinetic energies, and the potential energy of the colour field in between them, will correspond to the mass of the J/Ψ. We use a mass of $m_\mathrm{c} = 1500\,\mathrm{MeV}$ for the charm quark. Thus, there is a small residual energy of $E = 97\,\mathrm{MeV}$ to be accounted for by the potential interaction and the relative motion.

With these initial conditions—40 charm-anticharm pairs in a thermal background of 400 light quarks—, qMD starts running and produces hadrons with charm. The relative distribution of the 40 charm and anticharm quarks over the

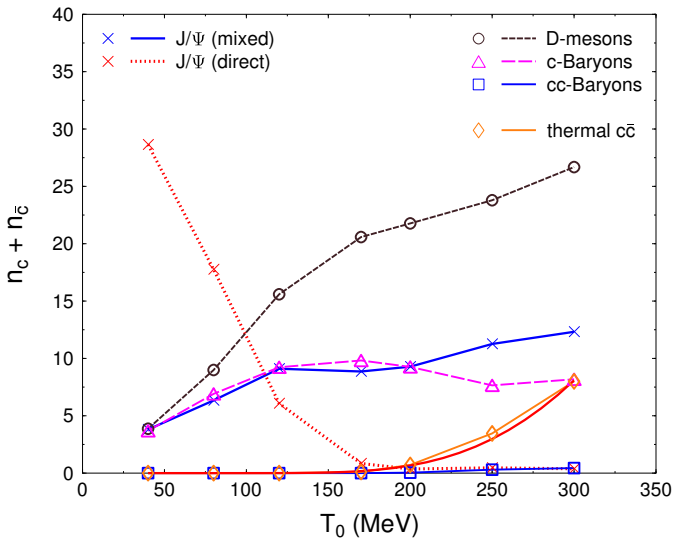

Figure 5.16
The melting of the J/Ψ: "direct J/Ψs" are suppressed with raising temperature, while "mixed J/Ψs" become more abundant. In general, at higher temperatures, charm quarks end up mostly in D mesons.

different species of charmed hadrons in the final state is shown in figure 5.16. Numbers for J/Ψs are shown separately for the two different classes of J/Ψs formed of quarks from the same initial charm-anticharm pair ("direct J/Ψs", red dotted line) and from different initial charm-anticharm pairs ("mixed J/Ψs", blue solid line). Mixed J/Ψs correspond to particles from the incoherent production mechanism of Thews [167].

The results show clearly how the number of direct J/Ψs drops fast with raising temperature, while the number of mixed J/Ψs increases slowly. This is the incoherent J/Ψ-enhancement in a plasma at high temperatures at work. Parallel to the increase of the mixed J/Ψs, the number of D mesons is growing. The plot sums up under D mesons both D and $\bar{D}$ mesons. Similar, the slowly increasing numbers of charmed baryons include charmed hyperons plus charmed anti-hyperons, and analogous for doubly charmed baryons. The slight decrease in the number of charmed baryons above $T = 200\,\mathrm{MeV}$ is caused by the different choice of zero chemical potential of the initial conditions at higher temperatures. Note that for temperatures above $T = 200\,\mathrm{MeV}$, there is also a small contribution of thermal charm and anticharm quarks to the total charm budget.

It is clear that this analysis could be extended to cover more realistic situations, as encountered in heavy ion collisions. For example, instead of a thermal background, a dynamically created system of deconfined colour charges could be used. Such an approach, where the initial condition for the gas of quarks and antiquarks is obtained from a UrQMD simulation of the first collisions of nuclei in a heavy ion collision, will be described in the following chapter. It would be interesting to look for signals of J/Ψ suppression as a function of collision energy, and impact parameter, for both SPS and RHIC energies. At SPS energies, one could hope to find signs of the onset of suppression, whereas at RHIC energies, the contribution of the enhancement from incoherent recombination can be studied.

Finally, there is no reason to stop with charm, when the third generation of quarks can be studied. While the top quark is too massive and too short-lived to be considered as a relevant degree of freedom in ultra-relativistic heavy ion collisions, the bottom quark is a promising object of investigations at RHIC, and even more so in the heavy-ion program at the LHC. The production mechanism of bottom quarks in high energy partonic collisions is similar to that of charm quarks. There are estimates for the production of bottom using perturbative QCD for both RHIC and the LHC [169, 170]. Bound states of bottom and antibottom quarks, the Υ mesons, and mesons and baryons with open bottom, can serve as a sensitive probes of the quark-gluon plasma [171].

In its current version, the qMD model does not include bottom degrees of freedom. But there are no obstacles to take bottom into account: The list of particles handled by qMD has to be augmented by the bottom quark and at least some of the mesons and baryons containing bottom. This is an unproblematic extension of the qMD code. It can be the starting point for interesting projects and future investigations into bottom with the help of qMD.

5.4 What next?

We have seen in this chapter that the simple, classical qMD model has thermal properties which make it well-suited to study aspects of a deconfined quark-gluon plasma and its transition to a hadron gas: The model exhibits a clustering phase at low temperatures and low chemical potential, with a phase boundary at least in qualitative agreement with the known facts of the phase diagram of QCD. The hadronization transition is accompanied by a softening of the equation of state. Effects of finite system size can be studied in detail. Finally, at high temperatures, the pair potential is screened dynamically by the influence of background charges, with consequences for the stability and abundances of bound quark-antiquark states.

It is a natural next step to apply this model to the fully dynamical situation encountered in ultra-relativistic heavy-ion collisions. This will be done in the following chapters.

Starting from a given initial phase space distribution of colour charges, the equations of motion derived from the qMD Hamiltonian (4.1) will be integrated numerically. The centre of momentum frame of the whole system will be used as the reference frame in which the potential interaction is evaluated. A Runge-Kutta method is used to solve the equations of motion. At time intervals of $\Delta t = 0.5\,\mathrm{fm}/c$, a search is performed for colour neutral clusters according to the criteria stated in section 4.2. Clusters fitting these criteria are mapped to hadrons, until no unclustered colour charges are left. Clusters are allowed to decay into final state hadrons, but there is no further interaction among them.

Using this scheme, we will follow the complete dynamics of the expanding and recombining system of quarks and antiquarks, and study the final results. The initial state will be either a thermalized gas, or it will be provided by the hadronic transport model UrQMD, as we will explain in detail in the following chapter.

Chapter 6

qMD in heavy ion collisions: Coupling to UrQMD

In this chapter, we will use the quark molecular dynamics model qMD to study the microscopical dynamics of the coloured, deconfined phase, and the subsequent hadron formation in ultra-relativistic heavy ion collisions.

The central idea is to use the hadronic transport model UrQMD to propagate the colliding nuclei until full overlap, and then to break down the hadronic particle content of UrQMD into the corresponding valence quarks. These quarks are used as an initial condition for the qMD simulation. Within qMD, we will follow the complete space-time evolution of the deconfined colour charges. To this end, we use a numerical integration of the equations of motion derived from the Hamiltonian (4.1), and check for colour neutral clusters according to the criteria stated in section 4.2. In the qMD model, quark recombination sets in right from the beginning, as we will see, and eventually brings back the deconfined system to a gas of hadrons. Besides hadronic spectra and particle ratios, the non-equilibrium dynamics of cluster hadronization and the loss of correlation among colour charges can be studied.

We will present some results for the complete time evolution in phase space for Pb+Pb events at the CERN-SPS. For S+Au collisions at the SPS, a detailed analysis of particle spectra and hadron ratios, including comparisons to both data and the results of hadronic transport calculations, was discussed in [127]. Here, we will summarize the main points of this publication.

6.1 Initial conditions for qMD from UrQMD

When two large nuclei collide with energies exceeding $\sqrt{s}_{NN} \approx 7\,\mathrm{GeV}$ per nucleon pair, hadronic matter can dissolve and, for a short time of $\approx 1 - 10\,\mathrm{fm}/c$, form a plasma of deconfined quarks and gluons. How this transition happens depends on the collision energy. However, there are still many open questions. If we want to describe the expansion and hadronization of the transient quark gas, we have to specify in the first place how to find a reasonable initial condition for the quarks dynamics. Note that in the spirit of qMD, we suppose that all effects of gluons are subsumed in the quark interaction potential.

beam energy E (GeV/N)	$\sqrt{s}_{NN}$ (GeV)	y	γ	d_0/γ (fm)	$t_\mathrm{x} = d_0/\gamma\beta$ (fm/c)
30.0	7.73	2.09	4.12	3.40	3.50
40.0	8.86	2.23	4.72	2.96	3.03
80.0	12.39	2.58	6.61	2.12	2.14
160.0	17.43	2.92	9.29	1.51	1.52

Table 6.1
Projectile and target rapidities in the centre of momentum frame, Lorentz γ factors, and times of complete crossing t_x after first contact for central Pb+Pb collisions at different SPS energies. The time t_x is obtained from the diameter $d \approx 14\,\mathrm{fm}$ of the lead nucleus through division by the γ factor and the corresponding $\beta = \sqrt{1 - 1/\gamma^2}$.

In heavy ion collisions at very high collision energies, the first scatterings involve partons from the colliding nuclei. These processes can be described very well by parton cascade models such as VNI. The results of parton cascade calculations could be fed into qMD. Then, however, one has to deal with the large numbers of hard gluons created in such cascades, for example by fragmentation of gluons into quark-antiquark pairs. Such an approach would be useful when studying collisions at RHIC energies, for example.

Here, we will proceed differently. We want to apply the qMD model to collisions at SPS energies, where hard processes are less dominant. In such collisions, stopping is important in creating densely compressed nuclear matter. In this hot and dense matter, deconfinement can set in. For collisions at SPS energies, the hadronic transport model UrQMD is known to yield reliable results [95]. As we have seen in chapter 3, it handles hadronic and string degrees of freedom, and thus includes important inelastic channels for particle production.

We will propagate the initial nuclei within the UrQMD model until the critical energy density for the onset of deconfinement is reached. We assume the dissolution of the hadronic degrees of freedom at an energy density of $\approx 1\,\mathrm{GeV/fm^3}$ in line with lattice calculations [172]. This energy density is reached approximately at full overlap, and decreases only slightly until the colliding nuclei have passed through each other [173]. At this later time t_x, all hadrons propagated in UrQMD which have undergone at least one scattering, i. e. all such mesons and baryons, but also all preformed particles contained in hadronic strings, are dissolved according to their valence quark content. The omission of unscattered hadrons from the decomposition takes care of spectator nuclei, which are not imported into qMD. Note, however, that in the S+Au data presented later, all hadrons are decomposed, including spectators. All quarks and antiquarks created by decomposition are used as an input and initial condition for the qMD model. Table 6.1 lists the times of complete crossing after first contact of two lead nuclei in central collisions for different SPS energies. In practice, this dissolution procedure is just the opposite of the clustering method described in chapter 4. Here, the quarks and antiquarks created by the decomposition of hadrons are set up at the very location of the hadron, with momenta and quantum numbers chosen such that all conservation laws are fulfilled. We will come back to this point in more detail after the following short discussion of gluons in qMD.

We have argued that the contribution of hard gluons is negligible at SPS energies, and that soft gluons are treated in an effective manner by means of the colour potential. But it is also justified to omit the explicit dynamics and fragmentation of soft, thermal gluons due to their small number. The number N of gluons in the interaction region of volume V and temperature T can be estimated using

$$N = Vg \int \frac{\mathrm{d}^3 p}{(2\pi)^3} \frac{1}{\exp(p/T) - 1} = V \frac{g}{\pi^2} \zeta(3) T^3 \,, \tag{6.1}$$

where the degeneracy is $g = 16$. For a central collision of lead nuclei at upper SPS energies, the volume of the overlap region is $V = 4\pi/3(d/2)^3/\gamma$, where $d \approx 14\,\mathrm{fm}$ is the diameter of the lead nucleus and $\gamma = 9.3$ is the Lorentz contraction factor for a beam energy of $E = 160\,\mathrm{GeV}/N$. Assuming a temperature of $T_0 = 200\,\mathrm{MeV} \approx 1\,\mathrm{fm}^{-1}$, this yields $\approx$ 300 thermal gluons, which is to be compared to (as we will see) ≈ 7000 quarks and antiquarks from decomposition. Thus, thermal gluons carry approximately 5% of the entropy of the system. Since the system is cooling at expansion, this estimate provides an upper bound on the number of thermal gluons. Thus, the additional fragmentation of these gluons is not expected to change the calculated yields and ratios significantly. As we see, the neglect of thermal gluons in the qMD simulations is well founded.

6.1.1 Decomposition of hadrons from UrQMD

The hadronic system propagated in UrQMD up to the time t_x of complete crossing can be characterized by the detailed distributions in phase space of the different hadronic species, the mesons, hadrons, resonances, and preformed hadrons contained in hadronic strings. At decomposition, every hadron is replaced by a quark-antiquark pair or by three quarks (or antiquarks), according to the valence quark content of the hadron. These colour charges are located at the same space-time point as the original hadron. Thus, the space-time distribution of the initial quarks in qMD will be the same as that of the hadrons from UrQMD.

The four-momenta of the colour charge, as well as the additive quantum numbers of spin, isospin, and colour, are distributed at random, but subject to the constraints arising from the conservation laws. Momentum distributions are described as functions of transverse momentum $p_\perp$ and rapidity y, where

$$p_\perp = \sqrt{p_x^2 + p_y^2} \,, \quad y = \operatorname{arctanh} \frac{p_z}{E} = \frac{1}{2} \log \frac{E + p_z}{E - p_z} \,. \tag{6.2}$$

Here, the z axis is oriented along the beam axis, and $p_\perp$ and y describe the dynamics of the collision away from and along the direction of the beam axis. Hadrons from UrQMD at decomposition come with transverse momentum and rapidity distributions $\mathrm{d}n^{(\mathrm{h})}/\mathrm{d}p_\perp$ and $\mathrm{d}n^{(\mathrm{h})}/\mathrm{d}y$. Other than for the space-time distributions, the momentum distributions $\mathrm{d}n^{(\mathrm{q})}/\mathrm{d}p_\perp$ and $\mathrm{d}n^{(\mathrm{q})}/\mathrm{d}y$ of quarks and antiquarks after decomposition will differ from the hadronic distributions. However, through the conservation of four-momentum in the decomposition procedure, they are related to the hadronic distributions, as we will discuss now in detail for the case of mesons. At hadronization via cluster formation, the inverse effect happens:

transverse momentum and rapidity distributions of the quarks and antiquarks are transferred back onto the corresponding distributions of the hadronic clusters.

Since mesons are two-particle clusters, conservation of four-momentum at decomposition and cluster formation enforces a strict relation between both sets of distributions. In the rest frame of the meson, the momenta of the quark and antiquark created at the decomposition are fixed by momentum conservation, and the direction of the axis of the momenta can take any orientation with equal probability. Then, the transverse momentum distribution $\mathrm{d}n^{(\mathrm{q})}/\mathrm{d}q_\perp$ of quarks and antiquarks is obtained from the distribution $\mathrm{d}^2n^{(\mathrm{q})}/\mathrm{d}q_\perp\,\mathrm{d}p_\perp$ of transverse momenta $q_\perp$ of colour charges created in the decomposition of mesons with a fixed transverse momentum $p_\perp$, followed by a summation over all meson transverse momenta:

$$\frac{\mathrm{d}n^{(q)}}{\mathrm{d}q_\perp}(q_\perp) = \int \mathrm{d}p_\perp \, \frac{\mathrm{d}^2n^{(\mathrm{q})}}{\mathrm{d}q_\perp\,\mathrm{d}p_\perp}(q_\perp, p_\perp) \; . \tag{6.3}$$

The same holds for the rapidity distribution. The distribution $\mathrm{d}^2n^{(\mathrm{q})}/\mathrm{d}q_\perp\,\mathrm{d}p_\perp$ is easy to obtain in the rest frame of the meson, where it is isotropic, and has to be boosted to the centre of collision frame, where the meson has transverse momentum p_{perp} and rapidity y. We will explain now how this works for both pions and kaons, where the masses of the quark and antiquark involved are equal and different, respectively.

Decomposition of mesons in their rest frame

When decomposing a meson in a quark and an antiquark, conservation of the four-momentum h of the meson in its rest frame means that

$$\mathsf{h} = \begin{pmatrix} m \\ 0 \end{pmatrix} = \mathsf{q}+\bar{\mathsf{q}} = \begin{pmatrix} E_q \\ \vec{p}_q \end{pmatrix} + \begin{pmatrix} E_{\bar{q}} \\ -\vec{p}_{\bar{q}} \end{pmatrix} = \begin{pmatrix} \gamma_q m_q \\ \gamma_q \vec{\beta}_q m_q \end{pmatrix} + \begin{pmatrix} \gamma_{\bar{q}} m_{\bar{q}} \\ -\gamma_{\bar{q}} \vec{\beta}_{\bar{q}} m_{\bar{q}} \end{pmatrix} \; . \tag{6.4}$$

Here, q and $\bar{\mathsf{q}}$ are the four-momenta of the quark and the antiquark, and $\vec{\beta}_q$ and $\vec{\beta}_{\bar{q}}$ are the three-vectors of their velocities, which are oriented in opposite directions.

Equal masses: Decomposition of pions

In the case of equal masses of the quark and the antiquark, $m_{\bar{q}} = m_q$, considering the zero-components of (6.4) yields

$$(\gamma_q + \gamma_{\bar{q}}) m_q = m \; , \tag{6.5}$$

and the equality of the components of the three-components means that

$$\gamma_q \vec{\beta}_q = \gamma_{\bar{q}} \vec{\beta}_{\bar{q}} \quad \text{or} \quad \vec{\beta}_q = \vec{\beta}_{\bar{q}} \sqrt{\frac{1-\beta_q^2}{1-\beta_{\bar{q}}^2}} \; , \quad \beta_q = \left|\vec{\beta}_q\right| \; , \quad \beta_{\bar{q}} = \left|\vec{\beta}_{\bar{q}}\right| \; . \tag{6.6}$$

The second equation in (6.6) implies $\beta_q = \beta_{\bar{q}}$ and thus $\gamma_q = \gamma_{\bar{q}}$: If $\beta_q < \beta_{\bar{q}}$, then $(1-\beta_q^2)/(1-\beta_{\bar{q}}^2) > 0$ and vice versa, resulting in a contradiction. Thus, the quark

and antiquark with equal masses move apart with the same velocity in opposite directions, as expected from non-relativistic reasoning. Hence,

$$\gamma_q = \frac{m}{2m_q} \,, \quad \beta_q = \sqrt{1 - \frac{1}{\gamma_q^2}} = \sqrt{1 - \frac{4m_q^2}{m^2}} \,, \tag{6.7}$$

and using the angles ϑ_q and φ_q to parametrize the orientation of the axis of the three-momenta of the quark and antiquark, we obtain for their four-momenta in the rest frame of the pion the expression

$$\mathsf{q} = \begin{pmatrix} \gamma_q m_q \\ \gamma_q \beta_q m_q \sin\vartheta_q \cos\varphi_q \\ \gamma_q \beta_q m_q \sin\vartheta_q \sin\varphi_q \\ \gamma_q \beta_q m_q \cos\vartheta_q \end{pmatrix} \,, \quad \bar{\mathsf{q}} = \begin{pmatrix} \gamma_q m_q \\ -\gamma_q \beta_q m_q \sin\vartheta_q \cos\varphi_q \\ -\gamma_q \beta_q m_q \sin\vartheta_q \sin\varphi_q \\ -\gamma_q \beta_q m_q \cos\vartheta_q \end{pmatrix} \,. \tag{6.8}$$

Different masses: Decomposition of kaons

Here we consider the combination $q\bar{s}$ with one up/down quark and one antistrange quark, and will omit the bar in the notation of the antistrange quark for simplicity. Masses and three-velocities are denoted with m_q and $\vec{\beta}_q$, and m_s and $\vec{\beta}_s$, respectively. Equality of the zero-components of the four-momenta (6.4) implies

$$\gamma_q m_q + \gamma_s m_s = m \quad \text{or} \quad \gamma_s = \frac{1}{m_s}(m - \gamma_q m_q) \,. \tag{6.9}$$

In the condition to be fulfilled by the three-momenta,

$$\gamma_q m_q \vec{\beta}_q = \gamma_s m_s \vec{\beta}_s \quad \text{or} \quad \gamma_q^2 m_q^2 \beta_q^2 = \gamma_s^2 m_s^2 \beta_s^2 \tag{6.10}$$

we can use $\beta^2 = 1 - 1/\gamma^2$ and (6.9) and solve for γ_q to obtain

$$\gamma_q^2 m_q^2 \beta_q^2 = m_q^2(\gamma_q^2 - 1) = m_s^2(\gamma_s^2 - 1) = m^2 + \gamma_q^2 m_q^2 - 2\gamma_q m_q m - m_s^2$$

or

$$2\gamma_q m_q^2 m = m^2 + m_q^2 - m_s^2 \,. \tag{6.11}$$

Thus,

$$\gamma_q = \frac{m^2 + m_q^2 - m_s^2}{2m_q m} \quad \text{and} \quad \gamma_s = \frac{m^2 + m_s^2 - m_q^2}{2m_s m} \,, \tag{6.12}$$

as well as

$$\beta_q = \sqrt{1 - \frac{4m_q^2 m^2}{(m^2 + m_q^2 - m_s^2)^2}} \quad \text{and} \quad \beta_s = \sqrt{1 - \frac{4m_s^2 m^2}{(m^2 + m_s^2 - m_q^2)^2}} \,. \tag{6.13}$$

The ratio of the absolute values of the three-velocities reads

$$\frac{\beta_q}{\beta_s} = \frac{m^2 + m_s^2 - m_q^2}{m^2 + m_q^2 - m_s^2} \,, \tag{6.14}$$

and finally, we are left with the four-velocities of the quark and the antistrange quark

$$\mathsf{q} = \begin{pmatrix} \gamma_q m_q \\ \gamma_q \beta_q m_q \sin\vartheta_q \cos\varphi_q \\ \gamma_q \beta_q m_q \sin\vartheta_q \sin\varphi_q \\ \gamma_q \beta_q m_q \cos\vartheta_q \end{pmatrix} , \quad \mathsf{s} = \begin{pmatrix} \gamma_s m_s \\ -\gamma_s \beta_s m_s \sin\vartheta_q \cos\varphi_q \\ -\gamma_s \beta_s m_s \sin\vartheta_q \sin\varphi_q \\ -\gamma_s \beta_s m_s \cos\vartheta_q \end{pmatrix} . \quad (6.15)$$

Transformation to the moving frame of the meson

So far, we have described the decomposition of the meson in a quark and an antiquark in the rest frame M of the meson, where its four-momentum is given by $\mathsf{h} = (m, \vec{0})$. In order to obtain number distributions of quarks and antiquarks in the centre of momentum frame C of the full collision out of the corresponding meson distributions, we have to boost the quark four-momenta q and $\bar{\mathsf{q}}$, and q and $\bar{\mathsf{s}}$, respectively, with the active Lorentz-Transformation A from the frame C to the rest frame M of the meson. This Lorentz transformation is given by

$$\mathsf{h} = \begin{pmatrix} m \\ 0 \\ 0 \\ 0 \end{pmatrix} \mapsto \mathsf{A}\mathsf{h} = \begin{pmatrix} E \\ p_x \\ p_y \\ p_z \end{pmatrix} = \begin{pmatrix} \gamma m \\ \gamma\beta_x m \\ \gamma\beta_y m \\ \gamma\beta_z m \end{pmatrix} = \begin{pmatrix} \cosh y \sqrt{p_\perp^2 + m^2} \\ p_\perp \sin\varphi_p \\ p_\perp \cos\varphi_p \\ \sinh y \sqrt{p_\perp^2 + m^2} \end{pmatrix} , \quad (6.16)$$

where $\vec{\beta} = (\beta_x, \beta_y, \beta_z)$ is the velocity of the meson in the collision frame C and acts as the boost parameter of the Lorentz transformation A. Thus, A can be written in the standard form (indices i and j label space coordinates x, y, z)

$$\mathsf{A} = \begin{pmatrix} \gamma & \gamma\beta_x & \gamma\beta_y & \gamma\beta_z \\ \gamma\beta_x & & & \\ \gamma\beta_y & & \delta_{ij} + \dfrac{\gamma - 1}{\beta^2}\beta_i\beta_j & \\ \gamma\beta_z & & & \end{pmatrix} , \quad \beta = \left|\vec{\beta}^2\right| , \quad \gamma = \frac{1}{\sqrt{1-\beta^2}} . \quad (6.17)$$

In the expressions (6.16) and (6.17), $p_\perp$, φ_p, and y denote transverse momentum, azimuthal angle of the transverse momentum, and rapidity of the meson in the collision frame C. From these meson quantities, the boost parameters β_i which define the Lorentz transformation A according to (6.17) can be determined as

$$\beta_x = \frac{p_\perp \sin\varphi_p}{\cosh y \sqrt{p_\perp^2 + m^2}} , \quad \beta_y = \frac{p_\perp \cos\varphi_p}{\cosh y \sqrt{p_\perp^2 + m^2}} , \quad \beta_z = \tanh y , \quad (6.18)$$

and

$$\gamma = \frac{1}{m} \cosh y \sqrt{p_\perp^2 + m^2} . \quad (6.19)$$

This provides us with all expressions necessary to calculate the distributions in rapidity and transverse momentum of quarks created in the decomposition of mesons.

Transverse momentum and rapidity spectra of quarks and antiquarks

The number density of quarks and antiquarks with transverse momentum $q_\perp$ originating from the decomposition of mesons with transverse momentum $p_\perp$ is given by

$$\frac{\mathrm{d}^2 n}{\mathrm{d}p_\perp \mathrm{d}q_\perp}(q_\perp, p_\perp) = \int \mathrm{d}^3\tilde{p} \int \frac{\mathrm{d}\Omega_q}{4\pi} \frac{\mathrm{d}^3 n_\mathrm{m}}{\mathrm{d}\vec{p}^{\,3}}(\tilde{\vec{p}})\ \delta(\tilde{p}_\perp - p_\perp) \times \Big(\delta\big((\mathsf{Aq})_\perp - q_\perp\big) + \delta\big((\mathsf{A\bar{q}})_\perp - q_\perp\big)\Big)\,, \tag{6.20}$$

where $(\mathsf{Aq})_\perp$ and $(\mathsf{A\bar{q}})_\perp$ denote the transverse momenta of the quark and antiquark created in the decomposition of the meson in the collision frame C. The solid angle Ω_q parametrizes the axis of decomposition in the rest frame M of the meson, and the momentum distribution of the meson is given by $\mathrm{d}^3 n_\mathrm{m}/\mathrm{d}\vec{p}^{\,3}$. The integral in (6.20) sums up all possible decompositions of mesons with transverse momentum $p_\perp$ and projects onto quarks with transverse momentum $q_\perp$. The corresponding expression for the rapidity distribution of quarks and antiquarks generated by the decomposition of mesons with rapidity y_m reads

$$\frac{\mathrm{d}^2 n}{\mathrm{d}y_\mathrm{m} \mathrm{d}y_\mathrm{q}}(y_\mathrm{m}, y_\mathrm{q}) = \int \mathrm{d}^3\tilde{p} \int \frac{\mathrm{d}\Omega_q}{4\pi} \frac{\mathrm{d}^3 n_\mathrm{m}}{\mathrm{d}\vec{p}^{\,3}}(\tilde{\vec{p}})\, \delta(\tilde{y} - y_\mathrm{m}) \times \Big(\delta\big(y(\mathsf{Aq}) - y_\mathrm{q}\big) + \delta\big(y(\mathsf{A\bar{q}}) - y_\mathrm{q}\big)\Big)\,, \tag{6.21}$$

where $y(\mathsf{Aq})$ and $y(\mathsf{A\bar{q}})$ denote the rapidities of the quark and antiquark created in the decomposition of the meson. Any further evaluation of the distributions (6.20) and (6.21) requires knowledge of the momentum distribution $\mathrm{d}^3 n_\mathrm{m}/\mathrm{d}\vec{p}^{\,3}$ of the mesons.

Decomposition of thermal mesons

To be specific, let us assume a thermal distribution of the meson momenta. It is clear that the momentum distribution of mesons (and preformed mesons) at complete overlap of the colliding nuclei is not thermal, but as a first guess, this assumption is not completely off the mark. Hence, starting with

$$\frac{\mathrm{d}^3 n_\mathrm{m}}{\mathrm{d}\vec{p}^{\,3}}(\tilde{\vec{p}}) = N \exp(-E/kT) = N \exp\left(-\cosh\tilde{y}\,\sqrt{\tilde{p}_\perp^2 + m^2}\Big/kT\right)\,, \tag{6.22}$$

and expressing the volume element in momentum space with the help of rapidity y, transverse momentum $p_\perp$, and azimuthal angle φ_p,

$$\mathrm{d}^3\tilde{p} = \mathrm{d}\tilde{p}_\perp \mathrm{d}\tilde{y}\, \mathrm{d}\varphi_{\tilde{p}}\, \cosh\tilde{y}\, \tilde{p}_\perp \sqrt{\tilde{p}_\perp^2 + m^2}\,, \tag{6.23}$$

the distribution (6.20) of the transverse momentum of the quarks and antiquarks reads

$$\begin{aligned}\frac{\mathrm{d}^2 n}{\mathrm{d}p_\perp \mathrm{d}q_\perp}(q_\perp, p_\perp) \;=\; N \int \mathrm{d}\tilde{p}_\perp\, \mathrm{d}\tilde{y}\ \mathrm{d}\varphi_{\tilde{p}} \int \frac{\mathrm{d}\Omega_q}{4\pi}\, \cosh\tilde{y}\, \tilde{p}_\perp \sqrt{\tilde{p}_\perp^2 + m^2} \\ \times\, \delta(\tilde{p}_\perp - p_\perp) \exp\Big(-\cosh\tilde{y}\,\sqrt{\tilde{p}_\perp^2 + m^2}\Big/kT\Big) \\ \times\, \Big(\delta(\mathsf{Aq}_\perp - q_\perp) + \delta(\mathsf{A\bar{q}}_\perp - q_\perp)\Big)\,.\end{aligned} \tag{6.24}$$

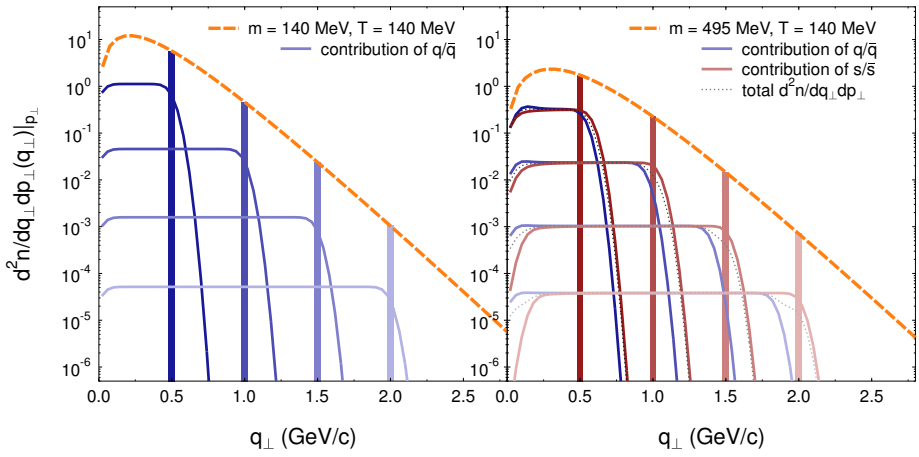

Figure 6.1
Transverse momentum distributions of thermal pions (left) and kaons (right) at a temperature of $T = 140\,\mathrm{MeV}$ (dotted, orange lines), and the corresponding transverse momentum distributions of quarks and antiquarks (solid lines) created by decomposing mesons with fixed transverse momenta $p_\perp = 0.5\,\mathrm{GeV}/c$, $1.0\,\mathrm{GeV}/c$,$1.5\,\mathrm{GeV}/c$, and $2.0\,\mathrm{GeV}/c$, as indicated by the vertical bars. In the asymmetric case of the decomposition of kaons, the distributions of the heavy strange (anti)quark are shown in violet, while the light quark distributions are plotted in blue. Note that the distributions shown cover all rapidities.

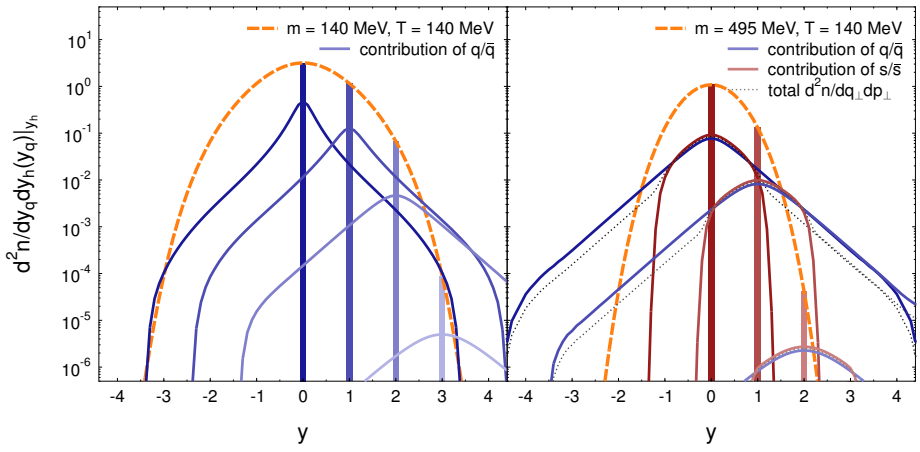

Figure 6.2
Rapidity distributions of thermal pions (left) and kaons (right) at a temperature of $T = 140\,\mathrm{MeV}$ (dotted, orange lines), and the corresponding rapidity distributions of quarks and antiquarks (solid lines) created by decomposing mesons with fixed rapidities $y_\mathrm{h} = 0, 1, 2$ and 3, as indicated by the vertical bars. Colour codes are the same as in figure 6.1.

The integral over $\tilde{p}_\perp$ just amounts to a replacement of $\tilde{p}_\perp$ by $p_\perp$ due to the first δ function. Expressing the four-momenta q and $\bar{\mathsf{q}}$ as a function of Ω_q using (6.8), and the Lorentz transformation A as a function of $\tilde{p}_\perp$, $\tilde{y}$, and $\varphi_{\tilde{p}}$ according to (6.17)

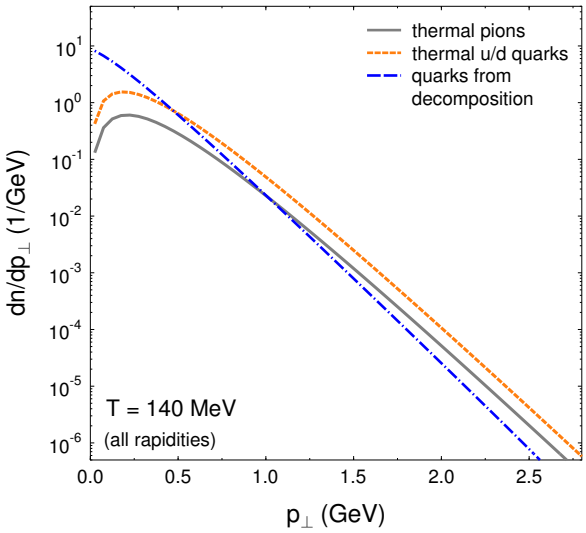

Figure 6.3
Transverse momentum spectra of quarks and antiquarks from the decomposition of hadrons are not thermal: The distribution obtained from (6.25) using (6.3) (blue dashed line) is markedly different from a thermal distribution of up/down quarks at a temperature of $T = 140\,\mathrm{MeV}$ (orange dotted line).

and (6.18), we are left with

$$\frac{\mathrm{d}^2 n}{\mathrm{d}p_\perp\,\mathrm{d}q_\perp}(q_\perp, p_\perp) = N \int \mathrm{d}\tilde{y}\,\mathrm{d}\varphi_{\tilde{p}} \int \frac{\mathrm{d}\Omega_q}{4\pi} \cosh\tilde{y}\, p_\perp \sqrt{p_\perp^2 + m^2} \times \exp\Big(-\cosh\tilde{y}\,\sqrt{p_\perp^2+m^2}\Big/kT\Big)\Big(\delta\Big(\big(\mathsf{A}(p_\perp,\tilde{y},\varphi_{\tilde{p}})\mathsf{q}(\Omega_q)\big)_\perp - q_\perp\Big) + \delta\Big(\big(\mathsf{A}(p_\perp,\tilde{y},\varphi_{\tilde{p}})\bar{\mathsf{q}}(\Omega_q)\big)_\perp - q_\perp\Big)\Big)\,. \quad (6.25)$$

A further analytic treatment of the problem could make use of the explicit expressions for q, $\bar{\mathsf{q}}$, and A given in (6.8) and (6.18). However, these calculations are extremely cumbersome and not very illuminating. Instead, figure 6.1 presents the result of a numerical solution of the integral (6.25) for a thermal meson distribution with $T = 140\,\mathrm{MeV}$. The figure shows the distributions $\mathrm{d}^2 n^{(\mathrm{q})}/\mathrm{d}q_\perp\,\mathrm{d}p_\perp$ of quarks and antiquarks created by the decomposition of thermal mesons with transverse momenta $p_\perp = 0.5\,\mathrm{GeV}/c, 1.0\,\mathrm{GeV}/c, 1.5\,\mathrm{GeV}/c$, and $2.0\,\mathrm{GeV}/c$. Note that all transverse momentum distributions are integrated over the full rapidity range of the systems at hand.

The quark rapidity distributions (6.21) can be treated in a completely analogous way. The results of the numerical evaluation of the corresponding integrals for the decomposition of thermal mesons are shown in figure 6.2.

It is important to note that the quark and antiquark distributions which follow from the decompositions of mesons according to equations (6.3) and (6.20) are in general not thermal, even if the meson distributions are thermal. This is highlighted in figure 6.3, which shows the transverse momentum distributions for thermal mesons at $T = 140\,\mathrm{MeV}$, for quarks and antiquarks obtained from decomposition, and for thermal light quarks at $T = 140\,\mathrm{MeV}$. Both quark distributions are markedly different. If one tries to extract a temperature out of the decomposition distribution, its steeper slope will mimic a temperature which is lower than that of the original meson gas.

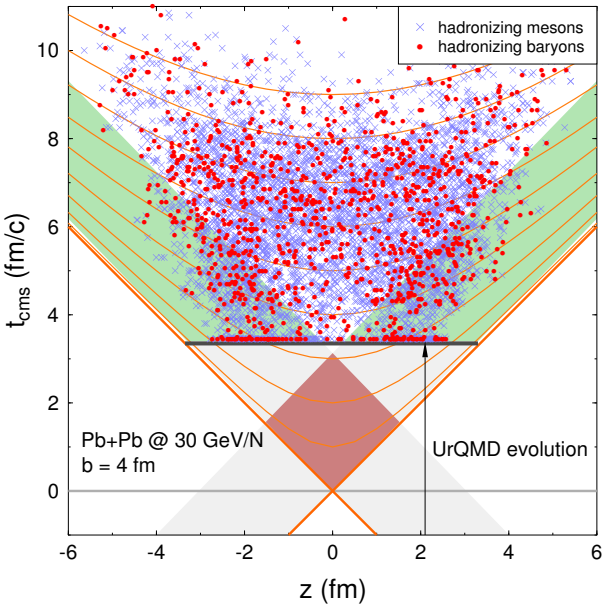

Figure 6.4
Space-time evolution of a Pb+Pb collision at the SPS with a beam energy of $E = 30\,\mathrm{GeV}/N$, as seen with UrQMD for the first $3.5\,\mathrm{fm}/c$ after initial contact, and qMD for the expansion of the hot and dense system. Grey bands mark the path of the initial nuclei, and the spectator nucleons. Dots and crosses tag the space-time points where mesonic and baryonic clusters are formed. Final clusters decays are not included in the figure.

After these preliminaries, we are now ready to study the expansion dynamics of quark systems created from UrQMD initial conditions. Thus, we obtain a complete picture of the expansion and hadronization of the fireball created in an ultra-relativistic heavy ion collision.

6.2 Expansion dynamics of a heavy-ion collision in qMD

This complete dynamics, from the initial interactions of the colliding nuclei through the formation of deconfined colour charges and the subsequent hadronization during the expansion of the hot and dense system, is illustrated in the snapshots of figure 1.8 in chapter 1. The event shown in these figures describes a collision of lead nuclei at the SPS with a beam energy of $E = 80\,\mathrm{GeV}/N$ and an impact parameter of $b = 3\,\mathrm{fm}$. The colliding nuclei are propagated in UrQMD until complete crossing at $t_\mathrm{x} = 2.1\,\mathrm{fm}/c$. Here and in the remainder of this work, $t = 0\,\mathrm{fm}/c$ corresponds to the instant of first contact of the colliding nuclei, and time is measured in the centre of momentum frame of the collision, unless stated otherwise. At time t_x, all hadrons from UrQMD, excluding spectators, are decomposed into quarks. The calculation of the subsequent dynamics of the system is assigned to qMD, where the expansion of the colour charges, their clustering, and the decay of clusters to final state hadrons is handled.

More instructive than the snapshots of the collision in figure 1.8 is a space-time diagram representing the expansion along the beam axis z, as shown in figure 6.4. The origin of the light cone in this plot at $t = 0\,\mathrm{fm}/c$, $z = 0\,\mathrm{fm}$ corresponds to the very first interaction between particles from the colliding nuclei. The system at hand is a Pb+Pb collision at the SPS with a beam energy of $E = 30\,\mathrm{GeV}/N$, and a corresponding crossing time $t_\mathrm{x} = 3.5\,\mathrm{fm}/c$ (see table 6.1). This time, where the switching from UrQMD to qMD dynamics takes place, is marked by the black horizontal bar. The grey bands trace the paths of the initial nuclei in UrQMD, and

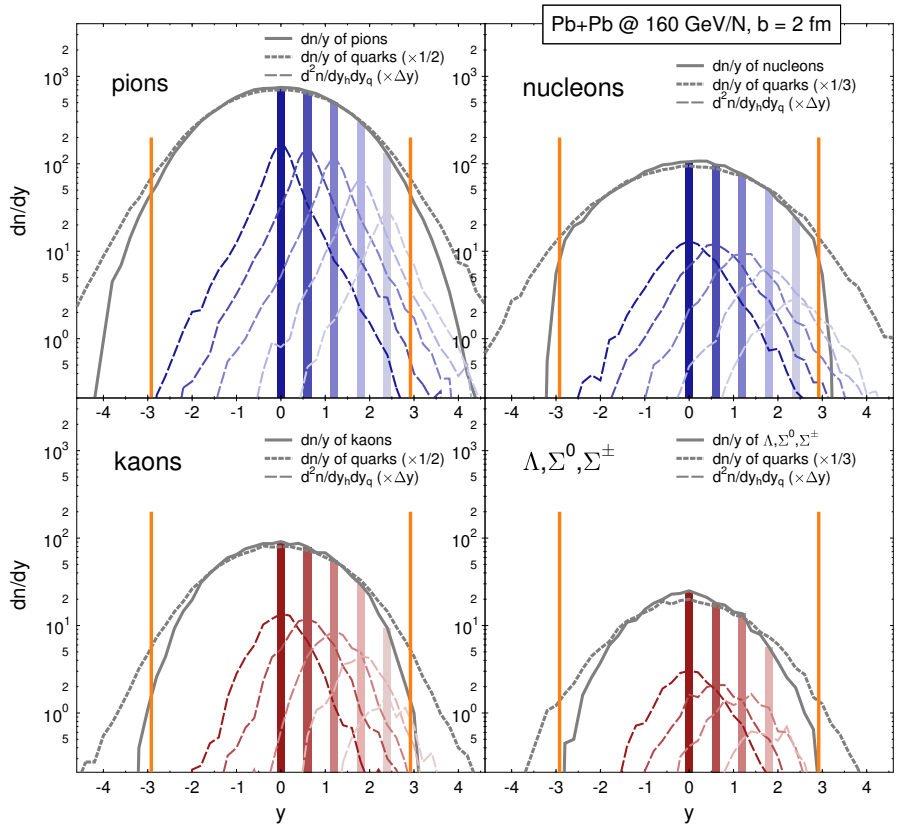

Figure 6.5
Decomposition of hadrons in qMD simulations of Pb+Pb collisions at the SPS with a beam energy of $E = 160\,\mathrm{GeV}/N$, propagated in UrQMD until complete crossing at $t_\mathrm{x} = 1.5\,\mathrm{fm}/c$: Rapidity distributions of hadrons are shown as grey solid lines, and of quarks and antiquarks after decomposition as dashed grey lines. The differential distributions follow qualitatively the distributions shown in figure 6.1. Vertical bars mark the rapidity of the initial projectile and target nuclei.

follow them through the region of the first interactions in the red, shaded area. Note that with $\beta = \sqrt{1 - 1/\gamma^2} = 0.97$, the deviation of the path of the nuclei from the light cone is barely visible in this figure. The green bands mark the path of spectator hadrons in qMD. Finally, the blue crosses and red dots mark the space-time coordinates (t, z) of the formation of mesonic and baryonic clusters from recombining quarks and antiquarks, respectively. Note that the figure contains no direct information about the transverse expansion of the system; clustering times only yield upper bounds for the radial distance of clustering from the beam axis. We will come back to clustering times and clustering radii again in section 8.3.

There is one important point to note in space-time evolution of clustering as shown in figure 6.4: Hadronization via the recombination of quark and antiquarks to clusters occurs at any stage and at any point during the expansion of the system. In our model, there is no such thing as a clear-cut hypersurface marking the transition from deconfined matter to hadrons. Instead, we have a completely dynamical description of the gas of deconfined colour charges and its coalescence to colour neutral clusters.

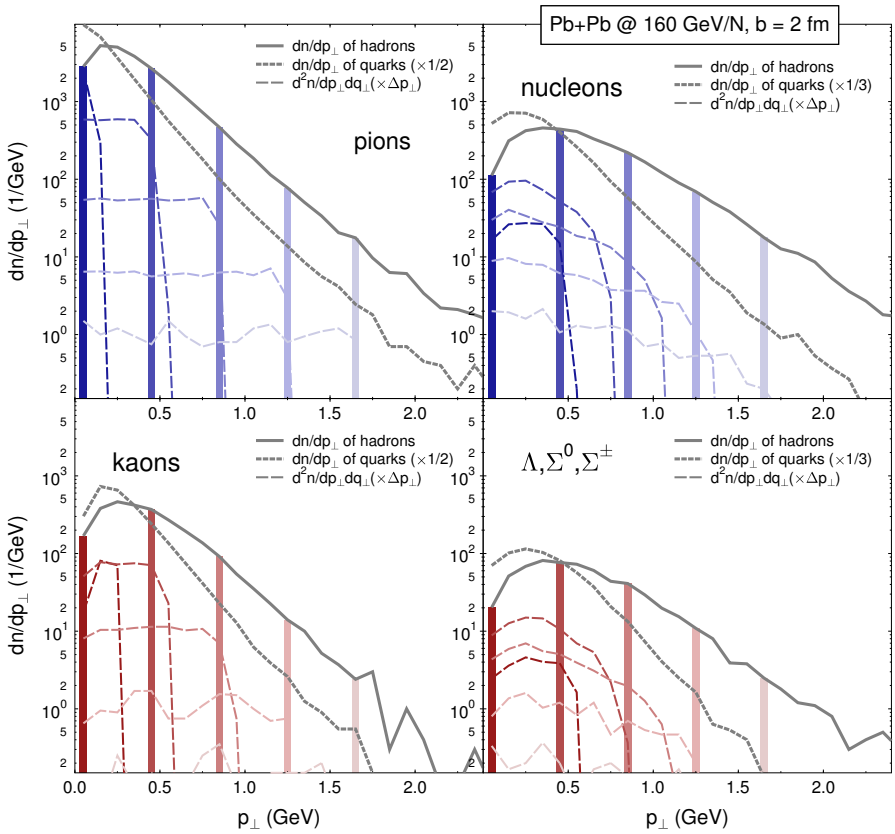

Figure 6.6
Decomposition of hadrons in qMD simulations of the same collisions as in figure 6.5, here for transverse momentum spectra. Transverse momentum distributions of hadrons are shown as grey solid lines, and of quarks and antiquarks after decomposition as dashed grey lines. The differential distributions follow qualitatively the distributions shown in figure 6.2. Note the marked change in slope between hadron and quark spectra in the decomposition of baryons.

6.2.1 A detailed look at Pb+Pb collisions at upper SPS energies

To study this time evolution in more detail, we will now turn to central Pb+Pb collisions ($b = 2\,\mathrm{fm}$) at the SPS with a beam energy of $E = 160\,\mathrm{GeV}/N$. Here, the crossing time when switching from UrQMD to qMD takes place is $t_\mathrm{x} = 1.5\,\mathrm{fm}/c$.

Figures 6.5 and 6.6 show the rapidity and transverse momentum distributions of both the hadrons propagated in UrQMD, excluding spectator nuclei, and of the quarks and antiquarks obtained from decomposition. All spectra are plotted for the moment of switching dynamics from UrQMD to qMD at $t_\mathrm{x} = 1.5\,\mathrm{fm}/c$. Remember that the hadron content of UrQMD used here includes many preformed hadrons, which are still within their formation time, but, nevertheless, are decomposed into quarks and antiquarks and imported to qMD.

The spectra in figures 6.5 and 6.6, including the differential distributions, are similar to the distributions calculated for thermal pion and kaon gases in figures 6.1 and 6.2, but not identical. The biggest difference can be seen in the rapidity distributions, which, in the UrQMD simulation data of the hadrons, are broader

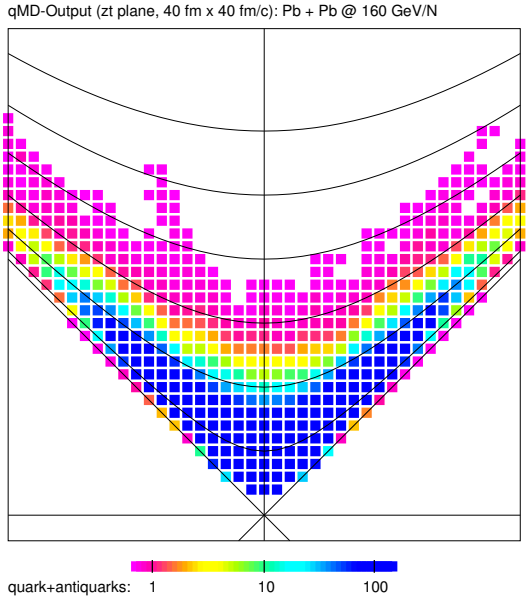

Figure 6.7
Space-time evolution of the numbers of quarks and antiquarks in a Pb+Pb collision at the SPS with a beam energy of $E = 160\,\mathrm{GeV}/N$, as seen in qMD. The space-time region shown in the plot extends over $40\,\mathrm{fm}$ along the z axis and $40\,\mathrm{fm}/c$ in the centre of momentum frame of the collision. Black curves are lines of equal eigen time in steps of $\Delta\tau = 5\,\mathrm{fm}/c$. After eigen times of $\approx 15\,\mathrm{fm}/c$, almost no unclustered quarks or antiquarks are left.

and flatter than for the thermal gas. This is due to the longitudinal expansion of the system, which, in the rapidity interval between projectile and target rapidities, is closer to the boost invariant Bjorken scenario than to the Landau scenario of the expanding fireball. The decomposition procedure spreads the rapidity distributions, and allocates many quarks and antiquarks in the region outside the range of the initial projectile and target rapidities.

Another marked feature in the transverse momentum distributions shown in figure 6.6 is the difference in slopes between the hadronic and quark distributions. As we have seen in figure 6.2, slopes of quarks from decomposition are steeper than the initial hadronic slopes. This effect is especially pronounced for baryons. We will come back to this point later.

The quarks and antiquarks from decomposition, with rapidity and transverse momentum spectra as described in figures 6.5 and 6.6, provide the initial condition of the qMD dynamics. Figure 6.7 shows the time evolution of the density of quarks and antiquarks in the system with these initial conditions in the light cone of the first interaction. It is, in a sense, complementary to the space-time diagram in figure 6.4, where only hadronic degrees of freedom are plotted. Black curves are lines of equal eigen time $\tau = \sqrt{t^2 - z^2}$ in steps of $\Delta\tau = 5\,\mathrm{fm}/c$. The density of quarks and antiquarks decreases with eigen time τ, with $n(\tau)$ independent of z over a wide range along the beam axis. After eigen times of $\approx 15\,\mathrm{fm}/c$, almost no unclustered quarks or antiquarks are left.

The approximate invariance in the decrease of the density of unclustered quarks and antiquarks along the z axis is seen best by switching from the centre of momentum frame coordinates t, z to eigen time τ and space-time rapidity ζ, given by

$$\zeta = \operatorname{arctanh} \frac{z}{t} \,, \qquad z = \tau \sinh \zeta \,, \tag{6.26}$$

$$\tau = \sqrt{t^2 - z^2} \,, \qquad t = \tau \cosh \zeta \,. \tag{6.27}$$

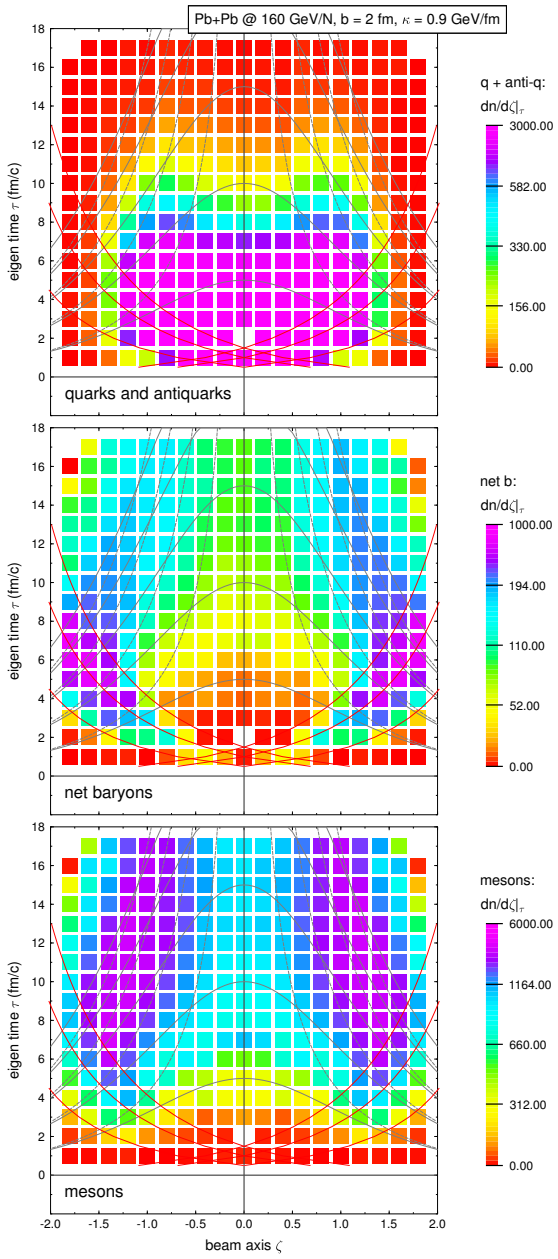

Figure 6.8
Space-time evolution in coordinates (τ, ζ) of particle densities in a Pb+Pb collision at the SPS with a beam energy of $E = 160\,\mathrm{GeV}/N$, as seen by the qMD model in steps of $\Delta\tau = 1\,\mathrm{fm}/c$. The figures show, from top to bottom, the densities $\mathrm{d}n/\mathrm{d}\zeta$ for quarks and antiquarks, for net baryons, and for mesons. Grey lines indicate lines of equal time t, and grey dotted lines are lines of constant z coordinate. The red lines trace the trajectories of freely streaming particles at different positions along the beam axis in the original nuclei, as explained in the text. For high eigen times τ, the distributions in space-time rapidity $\mathrm{d}n/\mathrm{d}\zeta$ is identical to the rapidity distribution $\mathrm{d}n/\mathrm{d}y$. Note that the decrease in the density of quarks and antiquarks is nearly independent of ζ over three units of ζ, and that the region of central ζ has only $\approx 60 - 70$ net baryons per unit of ζ. Thus, for $|\zeta| \lessapprox 1.5$, the system is quite close to the Bjorken scenario.

In these coordinates, a particle moving along the z axis with constant velocity β_z that passes through the origin of the coordinate system (t, z) at $t = 0\,\mathrm{fm}/c$ has the constant coordinate $\zeta = \operatorname{arctanh} z/t = \operatorname{arctanh} \beta_z$. Moreover, since $\beta_z = \tanh y$, as noted in (6.18), in this case the space-time rapidity ζ is identical to the kinematical rapidity y defined in (6.2).

The uppermost plot in figure 6.8 shows the number density $\mathrm{d}n\,/\mathrm{d}\zeta$ for quarks and antiquarks in the (τ, ζ) coordinates, for $|\zeta| < 2.0$, and $\tau < 18\,\mathrm{fm}/c$. This chart corresponds to figure 6.7. For a better comparability, lines of constant time t and constant coordinate z are included as grey lines, and grey dotted lines, respectively. Furthermore, the interpretation of the figure requires knowledge of the kinematics

of the colliding nuclei in the (τ, ζ) coordinates. Since the nuclei have a finite, albeit Lorentz-contacted, extension along the beam axis z, different particles in a cut through the nuclei along the beam axis would follow trajectories

$$z(t) = \pm(\beta_z t - \alpha d_0/\gamma) \,, \quad \text{with } 0 \leq \alpha \leq 1, \text{ and } \gamma = \frac{1}{\sqrt{1-\beta_z^2}} \tag{6.28}$$

if they were freely streaming through each other without interactions. Here, the different signs stand for particles in the projectile and target nucleus, α parameterizes the cut through the nuclei along the beam axis, $\gamma = 9.29$ for this collision, and $d_0 \approx 14\,\mathrm{fm}$ is the diameter of the lead nucleus in its rest frame. The trajectories (6.28) do not follow the simple transformation $\zeta = \operatorname{arctanh} z/t = \operatorname{arctanh} \beta_z$ since they do not pass the origin of the light cone. They are shown in the figures 6.8 as red lines for $\alpha = 1/3, 2/3$, and 1. However, for high eigen times $\tau \to \infty$, the offset $\alpha d_0/\gamma$ becomes negligible, and the trajectories (6.28) approach the lines of constant $\zeta = y = \pm 2.92$. Moreover, for large eigen times τ, the distributions in space-time rapidity $\mathrm{d}n/\mathrm{d}\zeta$ become identical to the rapidity distributions $\mathrm{d}n/\mathrm{d}y$.

Looking at the density of quarks and antiquarks in the upper plot in figure 6.8, one can see that its decrease with eigen time τ is nearly independent of ζ over three units of ζ around $\zeta = 0$. At the eigen time $\tau \approx 15\,\mathrm{fm}/c$ after the first collisions, almost no deconfined colour charges are left, as was already visible in figure 6.7.

Concurrent with the decrease in the density of quarks and antiquarks, the number densities of net baryons and mesons increase. This is shown in the middle plot in figure 6.8 for net baryons, and in the lower plot for mesons. There is a high density of net baryons along the path of the initial nuclei at $\tau \approx 5\,\mathrm{fm}/c$, $\zeta \approx \pm 1.6$. The region of central ζ has only $\approx 60 - 70$ net baryons per unit of ζ. Note that the blue spikes of net baryon density moving inwards in ζ correspond to baryonic matter moving outwards in z coordinates, as can be seen by comparison to the grey, dotted lines representing lines of constant z. The same holds for the violet regions of high meson densities in the lower plot, which correspond to mesons actually moving outward in z coordinates. Mesons populate the region of central ζ much more than net baryons, and at later times τ, not shown any more in the plot, reach a quite homogeneous distribution in ζ for the central region $|\zeta| \lessapprox 1.5$. Together with the low net baryon density in this same region of ζ, we can conclude that the system is quite close to the Bjorken scenario for $|\zeta| \lessapprox 1.5$.

The rapidity distributions of the hadronic clusters formed during the expansion are shown once more in figure 6.9, but this time for the kinematic rapidity y. The plots in figure 6.9 indicate the rapidity distributions of both hadronic clusters (solid lines) at formation, and of the recombining quarks and antiquarks contributing to the clusters (dashed grey lines). The distributions are roughly flat over two units of rapidity around $y = 0$. The plots on the right show results for baryons, not for net baryons as in figure 6.8. Furthermore, the differential distributions $\mathrm{d}^2 n/\mathrm{d}y_\mathrm{h}\,\mathrm{d}y_\mathrm{q}$ show that hadrons clustering at rapidity y_h can recombine quarks and antiquarks spread over several units of rapidity. Note that the hadronic clusters populating the distributions in figure 6.9 do not correspond to the final state particles, since most of them are resonances that will decay quickly. In this spirit, the label "pion" does not mean final state pions, but mesonic clusters with the quantum numbers of the pion. These include pion resonances of higher multiplets such as the $\pi(1300)$, but

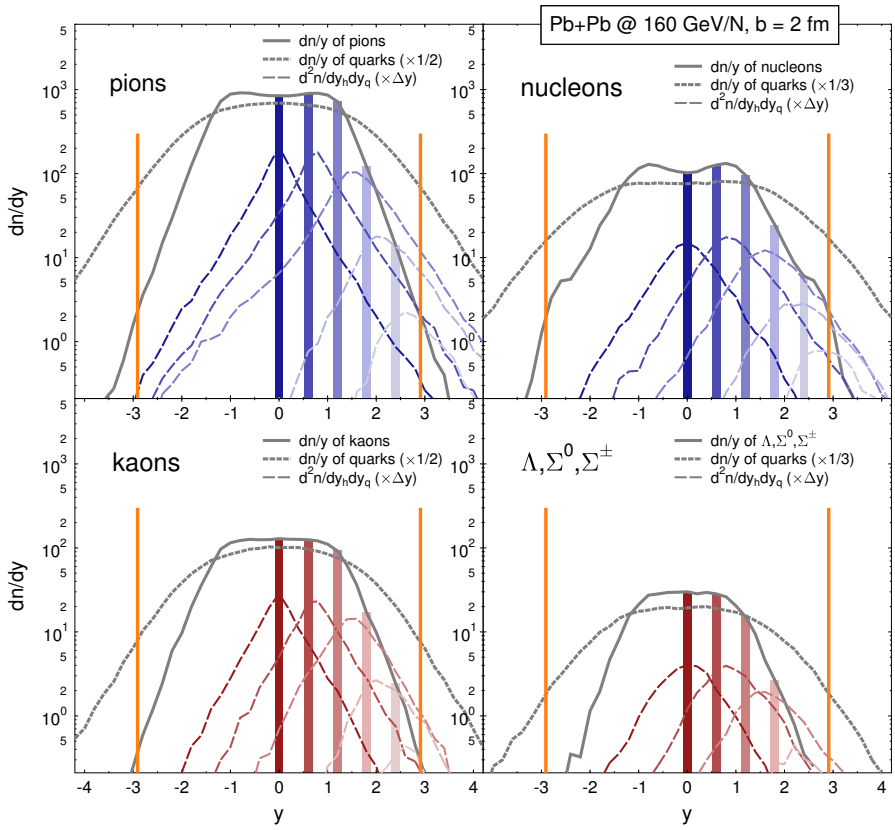

Figure 6.9
Rapidity distributions $\mathrm{d}n/\mathrm{d}y$ of hadronic clusters formed in qMD (solid grey lines) by the recombination of quarks. The rapidity distributions of the recombining quarks are shown as dashed grey lines, and the differential distributions $\mathrm{d}^2n/\mathrm{d}y_\mathrm{h}\,\mathrm{d}y_\mathrm{q}$ of quarks and antiquarks forming a hadronic cluster with rapidity y_h (solid vertical bars) are represented by the coloured dashed lines. Clustering in qMD recombines quarks which can be spread over several units of rapidity. Note that "pion" etc. denotes clusters with quantum numbers of the pion, including particles from higher multiplets.

also the scalar mesons $a_0(980)$ and $a_0(1450)$, since the clustering routine of qMD can not distinguish between Lorentz pseudoscalar and Lorentz scalar particles.

Figure 6.10 shows the transverse momentum distributions of hadronic clusters at formation, in the same way as the rapidity distributions in figure 6.9. The differential distributions $\mathrm{d}^2n/\mathrm{d}p_\perp\,\mathrm{d}q_\perp$ of quarks and antiquarks forming a hadronic cluster with transverse momentum $p_\perp$ are more washed out than at decomposition, which were shown in figure 6.6, but are qualitatively identical to these. The most prominent feature in the transverse momentum distributions in figure 6.10 are the differences in the slopes between the spectra of hadronic clusters and quarks. It is especially dramatic for the baryonic clusters. While at decomposition, the hadron spectra are steepened to yield the quark and antiquark spectra, the inverse process takes place here. While the spectra of colour charges recombining to mesons or baryons show roughly the same slope, the transverse momentum distribution of baryons after recombination is much flatter than the distribution of mesons. This is recombination at work: It is exactly the mechanism which is invoked to explain

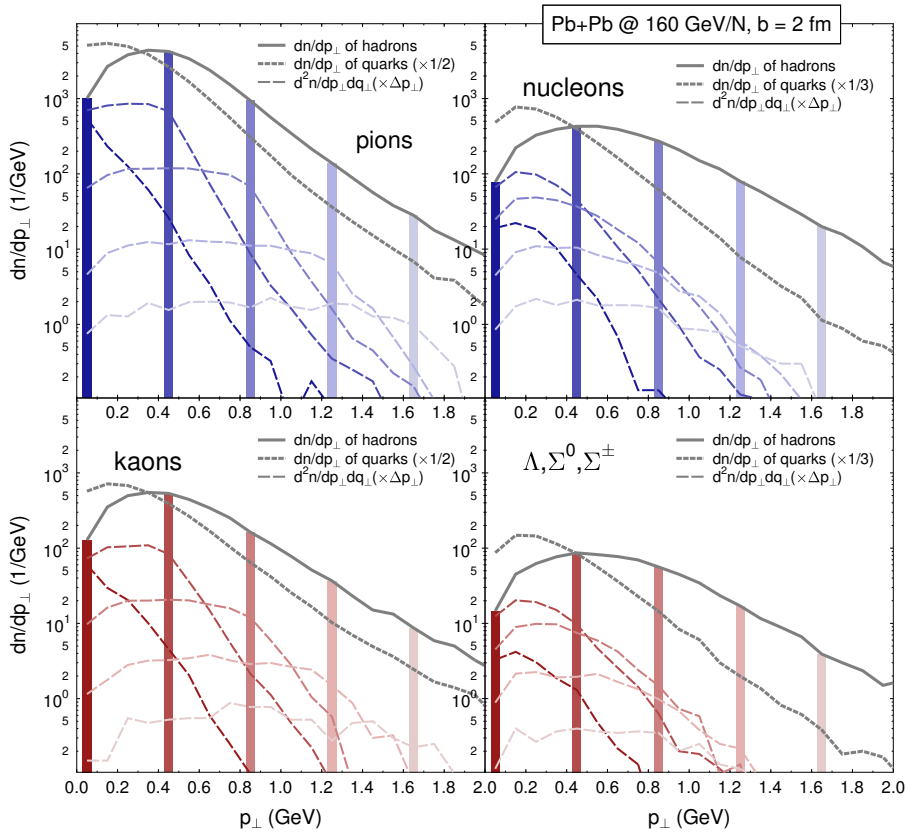

Figure 6.10
Transverse momentum distributions $\mathrm{d}n/\mathrm{d}p_\perp$ of hadronic clusters formed in qMD (solid grey lines) by the recombination of quarks. The transverse momentum distributions of the recombining quarks are, again, shown as dashed grey lines, and the differential distributions $\mathrm{d}^2n/\mathrm{d}p_\perp\,\mathrm{d}q_\perp$ of quarks and antiquarks forming a hadronic cluster with transverse momentum $p_\perp$ are represented by the coloured dashed lines. Note that transverse momentum distributions of baryons are much flatter than those of the quarks: This is quark recombination at work.

the high ratio of the proton to pion transverse momentum spectra at RHIC energies below the fragmentation region, thus for $p_\perp \approx 2-5\,\mathrm{GeV/fm}$ [53]. For the SPS system studied here, the overall transverse momenta are smaller, of course.

6.2.2 Thermal expansion or non-equilibrium dynamics?

We have shown in the previous section 6.2 that the phase space distribution of quarks and antiquarks obtained from the decomposition of hadrons is not thermal, even if the initial hadrons are fully thermalized. Here, we will study the issue of non-equilibrium effects and thermalization in Pb+Pb collisions at the SPS with a beam energy of $160\,\mathrm{GeV}/N$ in more detail. We will see that the expansion dynamics of qMD is, indeed, not a process in thermal equilibrium.

Even for non-thermal systems, we can try to fit the transverse mass spectra of quarks and antiquarks at mid-rapidity to a thermal distribution and extract an

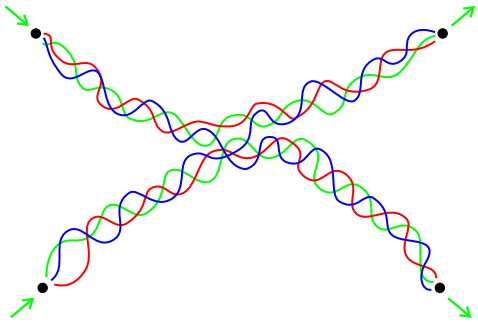

Figure 6.11
In the classical qMD model, the space-time trajectory of each colour charge can be followed from its creation in the decomposition of some hadron until its merger in a colour neutral cluster. This allows the distinction between mixed and direct hadrons. If colour charges are exchanged, as the blue quark in the figure, the resulting hadrons are mixed.

effective temperature from its slope. Transverse mass

$$m_\perp = \sqrt{m^2 + p_\perp^2} \tag{6.29}$$

is for the light current quarks propagated in qMD nearly the same as transverse momentum. Thermal transverse mass spectra at mid-rapidity for particles of mass m at a temperature T and a chemical potential μ are are described by

$$\left.\frac{1}{m_\perp^2}\frac{\mathrm{d}^2 n}{\mathrm{d}m_\perp\,\mathrm{d}y}\right|_{y\cong 0} = \frac{gV\mathrm{e}^{\mu/T}}{(2\pi)^2}\,\mathrm{e}^{-m_\perp/T}\,, \tag{6.30}$$

thus, a logarithmic plot shows a linear decrease with $m_\perp$, where the slope is the inverse temperature. A thermalized gas of quarks and antiquarks will cool down at expansion, and we would expect the same behaviour for the inverse slope of the transverse mass distributions obtained by fitting to the distribution (6.30).

Figure 6.12 shows the transverse mass distributions of quarks and antiquarks in the initial state from decomposition in the plot on the left, and at recombination in the plot on the right. One further distinction is made in the figure: In the qMD simulation, the space-time trajectory of each colour charge can be followed from its origin at the decomposition of some hadron until its end in a colour neutral cluster. Thus, it is possible to discern whether the same quarks and antiquarks created from the decomposition of one hadron recombine together again, or whether the formation of a cluster merges colour charges originating from different hadrons. We will speak of direct and mixed hadrons, and direct and mixed quarks, to distinguish both cases. It is clear that we should expect no big changes in the phase space distributions of direct quarks over the time evolution in qMD. In such a case, for example, a quark-antiquark pair is created from a meson, both colour charges are propagated over some distance, and then recombine again to a mesonic cluster. The situation for direct quarks from baryons is analogous.

This is indeed what can be seen in figure 6.12. While the distributions of direct and mixed quarks and antiquarks in the initial state are nearly identical, there is a big difference between both distributions at clustering. Fitting the slopes with the thermal distribution (6.30) yields effective temperatures of $T_{\mathrm{i,\,m}} = 127\,\mathrm{MeV}$ and $T_{\mathrm{i,\,d}} = 115\,\mathrm{MeV}$ for the mixed respectively direct quarks and antiquarks in the initial state. This small difference can be understood from the bias brought into

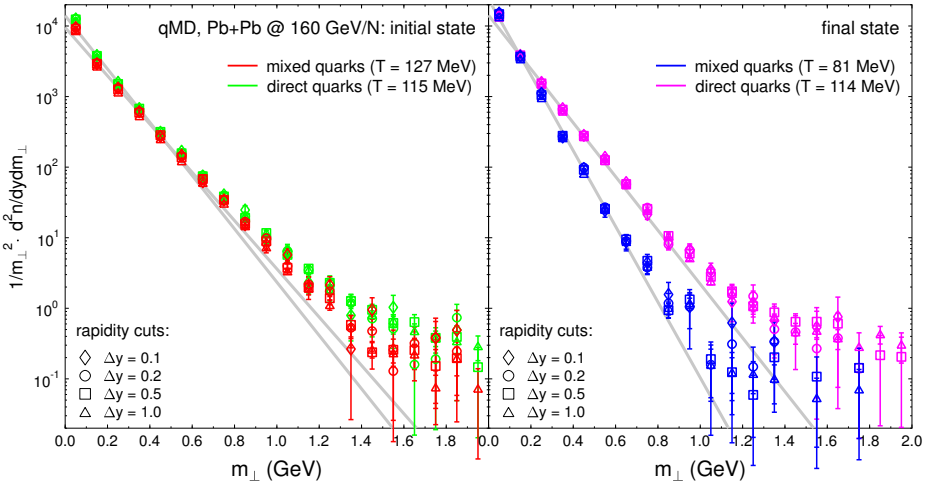

Figure 6.12
Transverse mass distribution of initial (left) and clustering (right) quarks and antiquarks in a qMD model calculation for Pb+Pb collisions at the SPS with a beam energy of $E = 160\,\mathrm{GeV}/N$. Slopes are lower for colour charges at hadronization than in the initial state, consistent with a cooling at the expansion. The difference is more pronounced for mixed quarks and antiquarks than for direct particles.

the initial quarks and antiquarks according to their fate at hadronization: One expects that mixing is more probable in a population of colour charges with higher relative momenta, or a higher temperature. Not much speculation is necessary to interpret the slopes in the distributions of quarks and antiquarks at clustering. Here, the distribution of direct quarks is nearly unchanged and fitted with $T_{\mathrm{f,\,d}} = 114\,\mathrm{MeV}$, while the effective temperature of the mixed quarks has dropped to $T_{\mathrm{f,\,m}} = 81\,\mathrm{MeV}$. Mixed quarks show the behaviour expected for a thermalized, expanding system. This is reasonable, since they have undergone interactions with colour charges from other hadrons. In the qMD simulations of SPS systems discussed in this section, only about $30\,\%$ of all quarks and antiquarks are mixed.

We have argued that it is not clear a priori that the inverse slope parameter $T_{\mathrm{f,\,m}}$ is indeed a temperature of the mixed quarks at clustering, since the quark gas is not necessarily thermalized. This point is emphazised further if we compare the inverse slope parameter $T_{\mathrm{f,\,m}}$ to the temperature of the transition from the deconfined to the clustering phase in a thermal system, as discussed in the previous chapter. The data shown in 6.12 were obtained from a qMD run with a slope parameter for the potential interaction of $\kappa = 0.9\,\mathrm{GeV/fm}$. There are ≈ 2000 mixed quarks and antiquarks in the central Pb+Pb collision under consideration. Thus, from the results of the thermal studies presented in the previous chapter in figure 5.9, we expect a transition temperature of $T_{\mathrm{c}} = 66 \pm 17\,\mathrm{MeV}$. This is lower than the inverse slope parameter $T_{\mathrm{f,\,m}} = 81\,\mathrm{MeV}$ of the recombining quarks and antiquarks. We can interpret these findings in two different ways: On the one hand, the phase space distribution of colour charges at recombination may be not thermal. On the other hand, if it is thermal, then the transition to hadrons in the dynamical expansion of the hot, cooling gas of quarks and antiquarks sets in at higher temperatures than in an equilibrated situation. Note that one might expect a lower transition temperature due to supercooling, but this is evidently not the case. In both interpretations, we

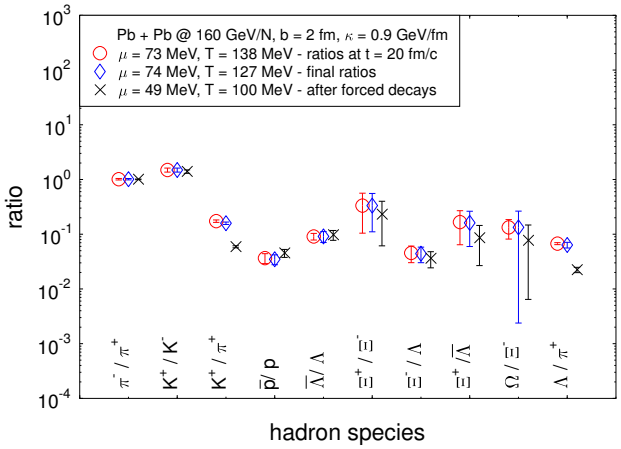

Figure 6.13
Hadron ratios from the hadronic yields of qMD, at $t = 30\,\mathrm{fm/c}$, at $t = 20\,\mathrm{fm/c}$, and after the forced decay of all resonances. Temperatures from hadron ratios are higher than the inverse slope parameters from quark transverse masses, in line with the recombination picture.

come to the conclusion that the dynamical expansion of the deconfined system in qMD is a non-equilibrium process.

Figure 6.10 has shown that the slopes in transverse momentum of the hadronic clusters at recombination are flatter than those of the quark and antiquark distributions. If we interpret the slopes as inverse effective temperatures, this means that we expect increased temperatures for the hadronic system after clustering compared to the deconfined quark gas. There is a second way to extract a temperature from the hadronic yield of a relativistic heavy ion collision, which uses a fit of the ratios of the different hadron species to the ratios of a thermalized hadron gas.

Such a fit is done for the data shown in figure 6.13, using ratios of hadronic clusters and hadrons for the SPS system at hand at $t_1 = 20\,\mathrm{fm/c}$, at $t_2 = 100\,\mathrm{fm/c}$, and after the forced decay of all resonances. The final decay essentially increases the number of pions in the system, and hence shifts all ratios involving pions. The fitting to a thermal hadron gas is done with the code used in [174] for hadrons with vacuum masses. As a result, temperatures of $T_1 = 138\,\mathrm{MeV}$, $T_2 = 127\,\mathrm{MeV}$, and $T_\mathrm{f} = 100\,\mathrm{MeV}$ are obtained for the three different time steps, and baryon chemical potentials of $\mu_1 = 73\,\mathrm{MeV}$, $\mu_2 = 74\,\mathrm{MeV}$, and $\mu_\mathrm{f} = 49\,\mathrm{MeV}$. The temperature T_1, which is closest to the situation at clustering, is indeed higher than the inverse slope parameters of both mixed and direct quarks at clustering.

All these data can be merged into the following sketch of heavy-ion collisions at the SPS, as described by qMD coupled to UrQMD: The initial phase space distribution of quarks and antiquarks created by the decomposition of hadrons from UrQMD is not thermal. Inverse slope parameters of transverse mass spectra are much lower for the colour charges than for the initial hadrons. During the expansion dynamics, which is Bjorken-like around mid-rapidity, part of the quarks and antiquarks recombine to hadrons in the very same configuration as they have been created. There is essentially no change in the momentum space configuration of these direct quarks and antiquarks. The second population of deconfined colour charges mixes constituents of different initial hadrons at recombination. These mixed quarks and antiquarks are characterized by markedly lower inverse slope parameters of transverse mass spectra at clustering than in the initial state, which can be interpreted as signs of cooling. However, even for this population of colour

charges, there is no complete thermalization, as can be seen from the discrepancy between the inverse slope parameter of recombining quarks and antiquarks and the transition temperature for hadronization in equilibrium. Clustering generates hadronic states with inverse slope parameters higher than those of the quarks and antiquarks. Most of these hadronic states are resonances far off their peak masses, which will decay on a timescale of $\approx 10\,\mathrm{fm}/c$ into the final state hadronic yields.

It is difficult to disentangle which of these effects reflect some real physical phenomena, and what are artifacts of the qMD model. However, if hadronization via the recombination of quarks and antiquarks is taken serious, it is clear that the momentum space distributions of clustering colour charges and of emerging clusters can not be simultaneously thermal. Also, the increase of inverse slope parameters when changing from quarks to hadrons will then correspond to some real physical process.

Of course, the properties of the deconfined phase are not directly accessible in experiment. Thus, a more detailed analysis of the final hadronic particles and their phase space distribution is necessary. We will present the results of such an analysis for S+Au collisions at the SPS with a beam energy of $E = 200\,\mathrm{GeV}/N$ in the following section 6.3.

Considering the wealth of data collected by the NA49 collaboration in the Pb+Pb program at the SPS, it is clear that this analysis should be extended to cover all these systems. Collisions over the energy range of the SPS, with beam energies $E = 20\,\mathrm{GeV}/N - 160\,\mathrm{GeV}/N$, are ideal objects for studies using qMD coupled to UrQMD. Here, a detailed analysis could include rapidity and transverse momentum spectra, collective flow of quarks and hadronic clusters, particle ratios at clustering and in the final state, and fluctuations, both event-by-event and within single events. It should invoke comparisons of all these observables between both pure UrQMD and coupled UrQMD/qMD studies, and experimental data. As a result, robust signals for the creation of a quark-gluon plasma and hadronization via recombination at the SPS could be identified.

First steps in this direction are taken in chapters 7 and 8: In chapter 7 we will see that, unfortunately, fluctuation signals characteristic of deconfined colour charges are washed out at hadronization through recombination. The results in chapter 8 show, among other things, that the recombination model predicts lower yields of large exotic clusters than thermal models.

6.2.3 Improving the cluster mass spectrum?

So far, we have been using the standard clustering routing of qMD, which creates a broad, continuous distribution of cluster masses. Clusters are determined according to the colour neutrality and cut-off criteria described in section 4.2, and identified with hadrons according to their quantum numbers, independent of mass. Thus, most clusters correspond to resonances far off their pole masses, as mentioned before. As an example, the orange, dashed curve in figure 6.14 shows the mass distribution of clusters which are identified as vector mesons in the hadronization of central Pb+Pb events at a beam energy of $E = 160\,\mathrm{GeV}/N$. Vector mesons in qMD include the ρ, with a mass $m_\rho = 770\,\mathrm{MeV}$ and a width $\Gamma_\rho = 150\,\mathrm{MeV}$, the a_1, with a mass $m_a = 1230\,\mathrm{MeV}$ and a width $\Gamma_a = 400\,\mathrm{MeV}$, and also the b_1,

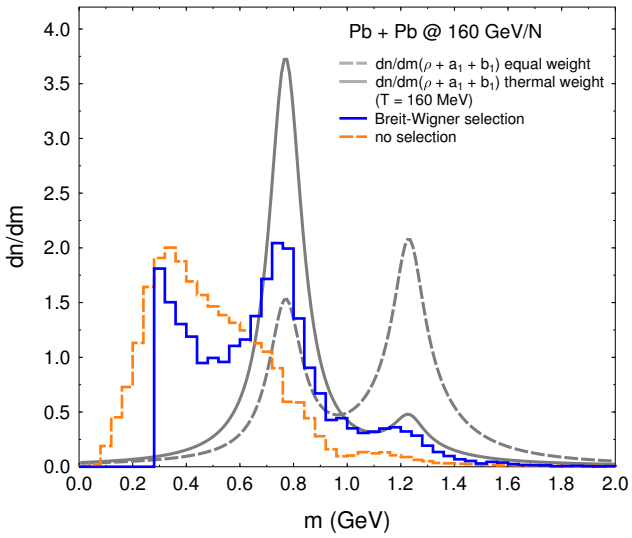

Figure 6.14
The mass spectrum of vector mesons created by clustering of quark-antiquark pairs with spin $s = 1$ and isospin $T = 1$ in qMD: The orange, dashed histogram shows the distribution obtained from standard clustering, the blue histogram the distribution from cluster acceptance according to the Breit-Wigner distribution of vector meson masses (dashed grey line). It can be compared to the weighted sum of Breit-Wigner distributions for the temperature $T = 160\,\mathrm{MeV}$ (solid grey line).

with a mass $m_b = 1230\,\mathrm{MeV}$ and a width $\Gamma_b = 140\,\mathrm{MeV}$. Note that qMD does not distinguish parity, hence a quark-antiquark pair with spin $s = 1$ and isospin $T = 1$ can be identified as both the Lorentz vector particles ρ and a_1, and the pseudovector particle b_1.

One can argue that this standard mapping procedure is quite unrealistic, since it is at odds with the physical mass distribution of hadronic resonances, which is described using the well-known Breit-Wigner distribution

$$\frac{\mathrm{d}n}{\mathrm{d}m} = \frac{N}{2\pi} \frac{\Gamma}{(m - m_0)^2 + \Gamma^2/4} \,. \tag{6.31}$$

Thus, a more realistic alternative to the standard mapping of quarks to hadronic clusters may be obtained by the introduction of an additional criterion for cluster formation: A colour neutral group of quarks with mass m and the quantum numbers of a specific hadronic resonance will be accepted as a hadronic cluster only with a probability $p(m)$, where p is proportional to the Breit-Wigner distribution (6.31) for the mass m. In this case, rejected clusters will not be considered as hadrons. Instead, the quarks and antiquarks in the cluster candidate will simply be propagated further as colour charges, until finally, they will end up in some cluster.

In practice, this extended clustering procedure has been implemented for the vector mesons ρ, a_1, and b_1. The mass distribution of these mesons obtained in this way is shown as the blue histogram in figure 6.14. The selection of clusters has been biased with the equally weighted sum of the Breit-Wigner distributions of the three vector mesons. Thus, the probability of cluster acceptance is given by

$$p(m) = a \frac{N}{2\pi} \sum_{i=\rho,a_1,b_1} \frac{1}{3} \frac{\Gamma_i}{(m - m_i)^2 + \Gamma_i^2/4} \,, \tag{6.32}$$

where a is a scaling factor. This probability is proportional to the Breit-Wigner distribution shown as the grey, dashed curve in figure 6.14. Moreover, in this calculation, all clusters with masses below two pion masses have been rejected since they cannot decay into final state pions. This explains the sudden onset in the mass

distribution at the $2m_\pi$ threshold. There is a remaining enhancement of vector mesons for masses below $\approx 500\,\mathrm{MeV}$, which can not be completely suppressed. However, the two-peak structure of the mass distribution becomes clearly visible.

Note that in a thermalized resonance gas, the mass spectrum of vector mesons does not follow a distribution proportional to the probability (6.32). This is because in a thermal environment, the contribution of the higher mass states to the total distribution is smaller than for the equal weight distribution (6.32). In fact, assuming for simplicity Boltzmann statistics, the relative weights w_ρ and $w_{a,b}$ for the contributions of the ρ and the a_1 and b_1 are given by

$$w_\rho : w_{a,b} \;=\; \sqrt{m_\rho}\,\mathrm{e}^{-m_\rho/T} : \sqrt{m_{a,b}}\,\mathrm{e}^{-m_{a,b}/T}\;. \tag{6.33}$$

For a temperature of $T = 160\,\mathrm{MeV}$, this yields relative contributions of $w_\rho : w_{a,b} = 1 : 0.0713$, or $w_\rho : w_a : w_b = 0.8752 : 0.0624 : 0.0624$. The resulting mass spectrum

$$\frac{\mathrm{d}n}{\mathrm{d}m} \;=\; \frac{N}{2\pi} \sum_{i=\rho,a_1,b_1} w_i\,\frac{\Gamma_i}{(m-m_i)^2+\Gamma_i^2/4} \tag{6.34}$$

is shown as the solid grey curve in figure 6.14. There is at least some qualitative agreement between this curve and the Breit-Wigner biased cluster mass distribution. The total yield in the peaks cannot be matched because of the high number of low-mass vector mesons in qMD. However, there is one interesting, systematic difference between both distributions: The peaks in the cluster mass distribution are lower than the peaks of the mass spectrum (6.34).

There has been a very long discussion about the properties of vector mesons in a hot and dense nuclear medium. It was argued that as sign of the onset of the restauration of chiral symmetry [175], the width of the vector mesons should broaden, and the pole mass may be lowered compared to the values of these quantities in the vacuum [176, 177]. In heavy ion collisions, such an effect can be studied by the analysis of dileptons from the decay of vector mesons [51].

In our dynamical, Breit-Wigner biased cluster recombination model for hadronization, we observe a small downward shift in the peak masses of vector mesons, which is largest for the heavy a_1 and b_1 mesons. This shift is due to the thermal distribution of clusters masses, which are more abundant in the low-energy wing of the Breit-Wigner distribution than on the high-energy side. Thus, naive recombination suggests a lowering of peak masses of resonances in ultra-relativistic heavy-ion collisions due to the inhomogeneous population of the Breit-Wigner distributions of the resonances. However, this idea is probably an oversimplification. We note that recent data of the NA60 collaboration for indium-indium collision at the SPS suggest that there is a broadening of the ρ meson in the hot and dense environment, but no mass shift [178].

Implementing the Breit-Wigner bias in the clustering routine of qMD has, of course, consequences for the time scale of the hadronization transition in the expansion of the hot gas of colour charges. Since the possible rejection of cluster candidates introduces one more criterion which has to be met in the clustering procedure, the whole process will be slowed down. This is clearly visible in figure 6.15, which shows the clustering rates of all mesons and of vector mesons, with

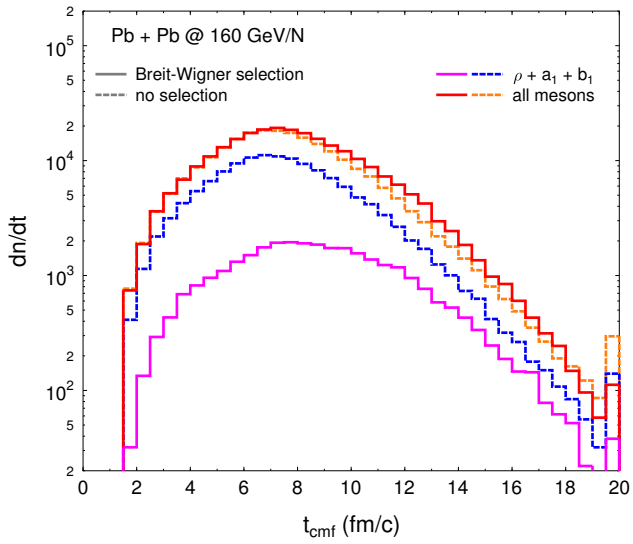

Figure 6.15
Introducing the Breit-Wigner bias in the clustering routine of qMD slows down the clustering process: Here, clustering has been modified for vector mesons. The resulting clustering rate (pink solid line) peaks later than the standard clustering rate (blue dashed line). The total meson clustering rates are also higher at later times with Breit-Wigner bias (red solid line) than without (orange dashed line).

and without the Breit-Wigner clustering bias for the vector mesons. With the extra criterion, clustering rates for vector mesons peak at later times, and clustering of all mesons is lightly higher at later times. There is one obvious problem if the clustering bias is introduced only for the vector mesons: Besides the shift in the time of peak clustering, the total rates are lower by nearly one order of magnitude for $t \approx 3-10\,\mathrm{fm}/c$. This is easy to understand: rejected quark-antiquark clusters with spin $s = 1$ have a high chance to recombine again at later times with spin $s = 0$. Thus, they can populate states of scalar mesons where there is no Breit-Wigner clustering bias.

Introducing the Breit-Wigner bias for all hadronic resonances could be an interesting study. It would most probably delay the hadronization time, and it may have interesting consequences for particle yields, and maybe also for spectra. Here, however, we cannot do it. Instead, we continue with a presentation of the results for hadronic yields obtained from collisions between S and Au nuclei at the SPS at a beam energy of $200\,\mathrm{GeV}/N$.

6.3 Application to heavy ion collisions at the SPS

Figure 6.16 shows the evolution of the rapidity densities of net baryons (dotted red lines), mesons (dashed grey lines), and quarks and antiquarks (full black lines) in collisions between S and Au nuclei at the SPS at a beam energy of $200\,\mathrm{GeV}/N$ [127]. As before, the initial state for the qMD calculation was calculated using UrQMD, and after crossing at $t_\mathrm{x} = 1.5\,\mathrm{fm}/c$, the hadronic content of UrQMD is decomposed into quarks and antiquarks and propagated further with qMD. In the simulation shown in figure 6.16, all hadrons from UrQMD are decomposed, including spectators. However, these remnants of the gold nucleus rehadronize immediately. The quarks and antiquarks at central rapidities start to form mesons. After $t \approx 20\,\mathrm{fm}/c$, all quarks and antiquarks have recombined to hadrons and the collision ceases.

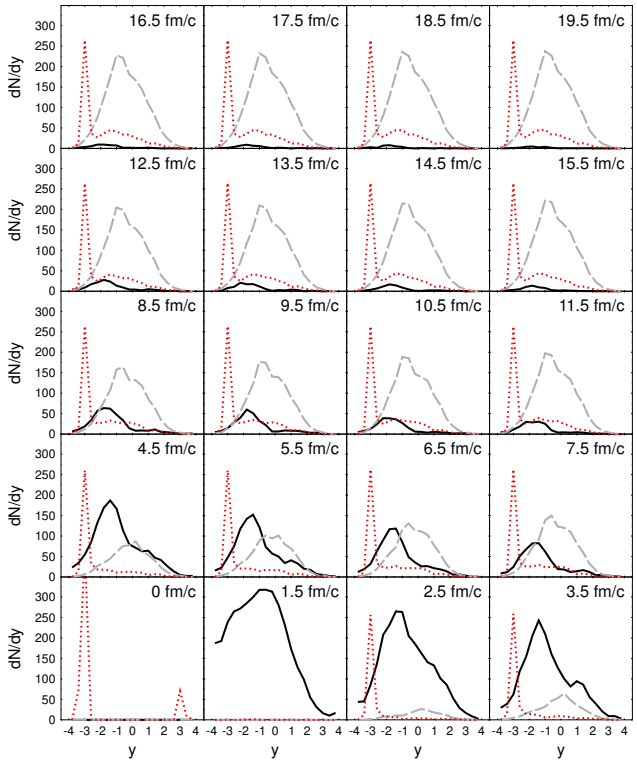

Figure 6.16
Time evolution of the rapidity distributions of net baryons (dotted red lines), mesons (dashed grey lines), and quarks and antiquarks (full black lines) in collisions between S and Au nuclei at the SPS at a beam energy of $200\,\mathrm{GeV}/N$. In this coupled UrQMD/qMD simulation, all hadrons from UrQMD are decomposed, including spectators. The remnants of the gold nucleus rehadronize immediately, while the quarks and antiquarks at central rapidities start to form mesons.

The time evolution of the particle multiplicities in figure 6.17 shows again that the production of hadronic clusters starts immediately after the beginning of the collision. The very steep start of both curves for the time interval $t \approx 1.5{-}2.5\,\mathrm{fm}/c$ is due to the rehadronization of the spectator nuclei. The further time evolution is characterized by the rapid expansion of the initial hot and dense system, with a nearly exponential decay of the quark multiplicity. At later times, the multiplicity curves saturate. The slight, ongoing increase in the hadron multiplicity after $t \approx 20\,\mathrm{fm}/c$, when essentially all unclustered quarks and antiquarks are gone, is due to the decay of hadronic resonances.

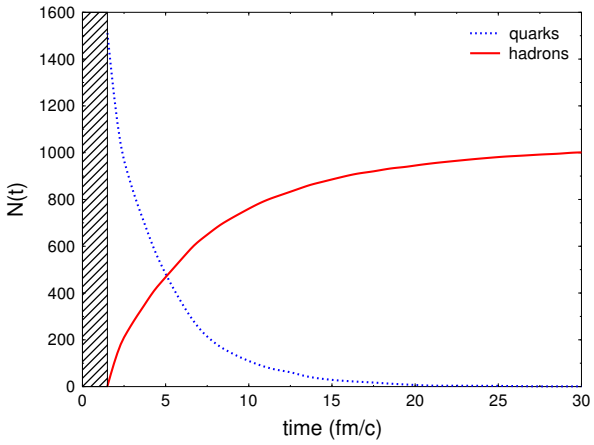

Figure 6.17
Time evolution of the total number of quarks and antiquarks, and hadrons in the system. After a steep, initial drop of the quark and antiquark multiplicity due to rehadronization of spectator, it follows roughly an exponential decay. The slight increase in the hadron multiplicity at later times is due to the decay of resonances.

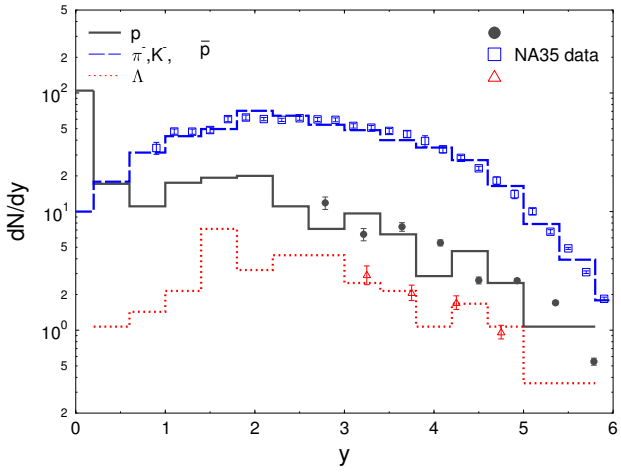

Figure 6.18
Rapidity distributions of protons, Λs, and negatively charged hadrons h^- in central S+Au collisions at SPS (200 GeV/N) from qMD compared to NA35 data [179].

Decay of hadronic resonances is also responsible for the observation that the number of final hadrons is larger than the number of 2- and 3-clusters which can be formed out of the quarks and antiquarks in the initial state. As mentioned before, qMD includes the possible dynamical production of $q\bar{q}$ pairs in overcritical colour fields. However, in the present model, hadronization at SPS is basically driven by quark rearrangement: On average, only 0.1 quark-antiquark pairs per event are produced by string breakup in a S+Au collision! The reason is that by dissolving the hadronic content of UrQMD one starts with a configuration which is colour neutral on long scales. Thus, colour fluctuations large enough to yield strong colour fields which could drag quark-antiquark pairs out of the vacuum are never reached. Moreover, strong fields are dynamically screened by the moving quarks.

Let us now confront the qMD results to experimental data. Figure 6.18 compares the rapidity densities for protons (full gray line), Λs (dotted red line), and negatively charged hadrons h^- from qMD to NA35 data (see [179] and references therein). A surprisingly good description of the experimental data (symbols) by the non-equilibrium quark dynamics is found over all rapidities.

Figure 6.19 explores the transverse expansion of the hadronizing quark system. The transverse momentum spectrum of negatively charged particles is compared to NA35 data. An overall good agreement is found.

Finally we want to investigate the hadro-chemical evolution and the behaviour of hadron ratios in the qMD model. Figure 6.20 displays the time development of several hadron ratios in the course of the hadronization (shaded areas denote the measured ratios from NA 35). The particle ratios stay nearly constant during the colour charge-hadron conversion. This may explain the success of statistical model analysis [180]. However, baryons seem to be produced in the later stage of the hadronization. The discrepancies between the ratios of p/π^+ and $(\Lambda_0 + \Sigma_0)/\mathrm{p}$ obtained from the qMD approach and the measured data can be understood from the missing hadronic rescattering in our approach. This can be seen by comparing the measured hadron ratios in figure 6.21 not only with the qMD calculation (diamonds) but also to ratios obtained with full UrQMD simulations (open circles).

While the proton to antiproton ratio remains unaltered as compared to the UrQMD calculation alone (and nearly one order of magnitude lower than the exper-

imental value), ratios involving protons or antiprotons alone or the net proton number are by factors 2–5 higher in qMD than UrQMD, yielding a better fit to data for the $\bar{\mathrm{p}}/\pi^-$ ratio, but an increasing overestimation for the p/π^+ and the $(\mathrm{p}-\bar{\mathrm{p}})/\mathrm{h}^-$ ratio. Simultaneously, the ratio of $\Lambda/(\mathrm{p}-\bar{\mathrm{p}})$ drops against the value from UrQMD. Both trends can be understood as consequences of hadronic rescattering in the UrQMD model. Hadronic rescattering lowers the number of antiprotons in the final state, and, by inelastic baryon-baryon and antikaon-baryon collisions, yields a systematic population of hyperons at the expense of protons. These channels are not implemented in the present version of our qMD model. In qMD, Δ resonances for example (which are abundant around the first $10\,\mathrm{fm}/c$ of the collision) cannot create hyperons and kaons by inelastic collisions, but eventually always yield nucleons and pions. As this simplification of the combined UrQMD+qMD approach with respect to a full UrQMD treatment shifts the calculated ratios away from the known experimental values, this can be seen as a clear sign for the importance of hadronic rescattering.

Since the hadron ratios in the combined approach show differences due to missing rescattering, and the transverse mass spectra and rapidity distribution of figures 6.19 and 6.18 can also be reproduced by the UrQMD model [95, 181], we can ask to which extent this combination of models may be useful or necessary.

But as we have seen before, the qMD approach can provide us with detailed information about the dynamics of the system of deconfined colour charges and their transition to hadrons through recombination. Whenever a new hadron is formed, the correlation between the quarks clustering to build this hadron can be studied. The mean value of the path length these quarks have travelled within the quark phase from their points of origin until the clustering point and the distance in space between the origins of the involved quarks can be studied.

Figure 6.22 shows the combined distribution of the mean path length travelled by the quarks and the original distance between the quarks forming a new hadron in S+Au collisions at SPS energies of $200\,\mathrm{GeV}/N$. Quarks stemming from the same initial hadron correlation, propagating coherently and reclustering again to form the same hadron, build up a large background at zero initial distance. These are the

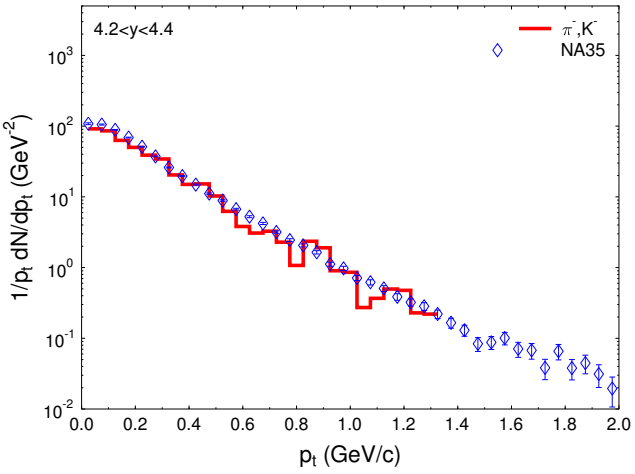

Figure 6.19
Transverse mass spectrum of negative charged hadrons in central S+Au collisions at SPS ($200\,\mathrm{GeV}/N$) from qMD compared to NA35 data [179].

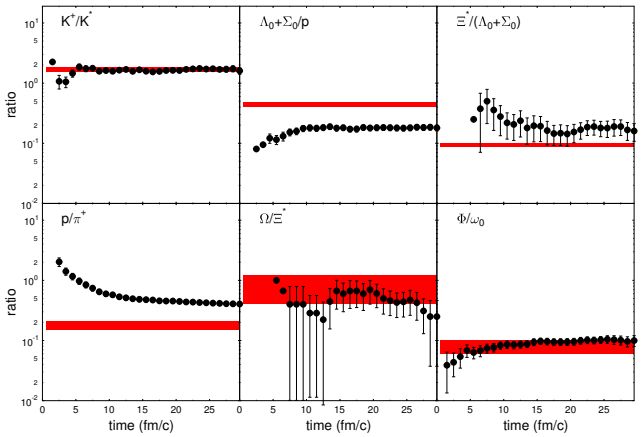

Figure 6.20
Time evolution of the particle ratios in central S+Au collisions at SPS ($200\,\mathrm{GeV}/N$). The shaded areas indicate data taken from [179].

direct quarks mentioned before. The essence of this distribution is shown again in figure 6.23, which indicates the number distribution for the mean path travelled by direct quarks (solid line) and mixed quarks (dotted line).

It can be seen that the reclustering of direct quarks is quite fast: in this case, a hadron is decomposed into two or three quarks, these quarks propagate a short distance of about $2.2\,\mathrm{fm}$ (this diffusion length is marked by the grey bar) and re-hadronize again. The hadron formation follows an exponential decay of the quark cluster to hadrons with a decay length equal to the diffusion length of $2.2\,\mathrm{fm}$.

On the other hand, the rearrangement of mixed quarks to form new, different hadrons happens on a length scale of about $3\,\mathrm{fm}$. Following this rearrangement, the clusters decay exponentially with a decay length of $4.8\,\mathrm{fm}$.

A measure of the relative mixing within the quark system—and also for thermalization which means homogenization of the population of phase space and complete loss of correlations—are the relative numbers of direct and mixed hadrons. The ratio r of mixed hadrons to the total number of hadrons formed from the quark system is $r = 0.574 \pm 0.008$ for the S+Au collision at $200\,\mathrm{GeV}/N$, with an error from statistics. A value of $r = 1$ would indicate complete rearrangement of

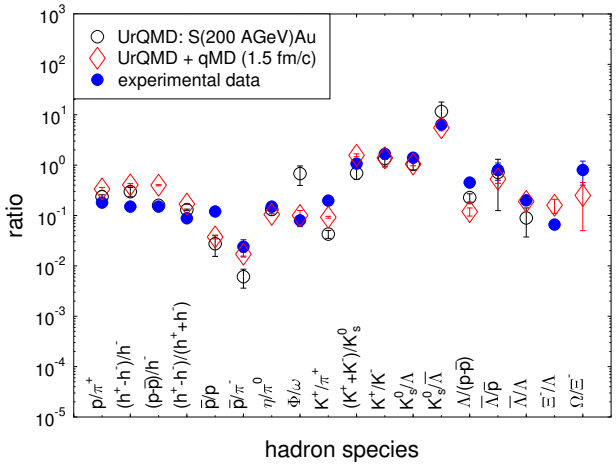

Figure 6.21
Particle ratios in central S+Au collisions at SPS ($200\,\mathrm{GeV}/N$). Experimental data are taken from [179].

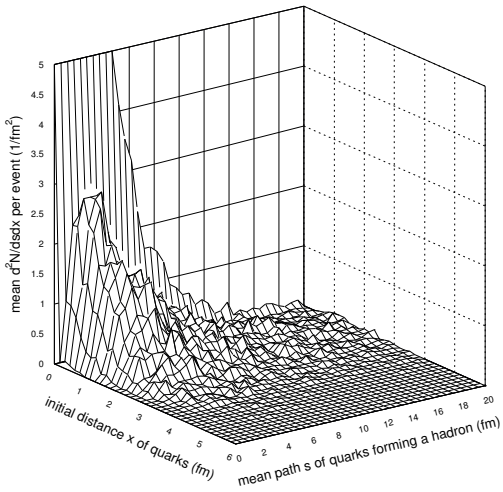

Figure 6.22
Hadronization in S+Au collisions at SPS ($200\,\mathrm{GeV}/N$): Number density distribution of mean diffusion path and initial distance of quarks forming a hadron within qMD.

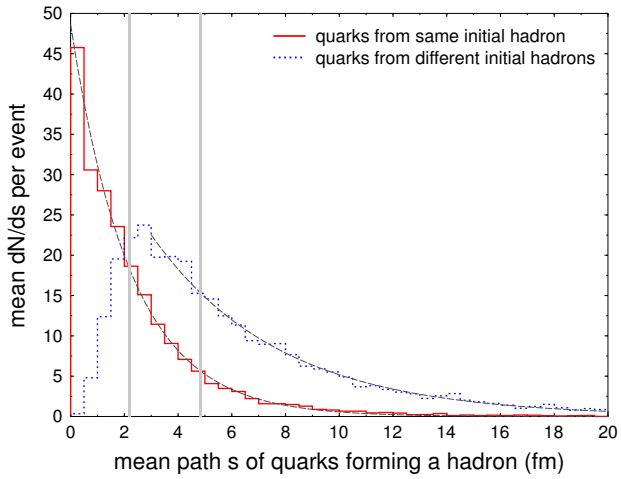

Figure 6.23
Hadronization in S+Au collisions at SPS ($200\,\mathrm{GeV}/N$): Number density distribution of mean diffusion path of quarks forming a hadron from the same initial hadron (solid line) and from different initial hadrons (dashed line) within qMD. Fitting the decay profiles yields diffusion lengths of $2.2\,\mathrm{fm}$ and $4.8\,\mathrm{fm}$, respectively.

quarks and thus complete loss of correlations in the quark system. Considering the presumed transition to the quark-gluon plasma in Pb+Pb collisions at $160\,\mathrm{GeV}/N$, one would expect a much larger value of r. However, as we have mentioned before, the ratio of mixed hadrons in these Pb+Pb collisions is only $r \approx 0.3$. This is an interesting observation which should be studied in more detail, and with more statistics for the Pb+Pb events.

6.4 Conclusion: options for qMD in heavy ion collisions

As we have seen, coupling the qMD model to UrQMD yields a very interesting glimpse at the non-equilibrium quark dynamics for heavy-ion collisions at SPS energies. Good agreement with experimental S+Au data at $200\,\mathrm{GeV}/N$ is found. This includes rapidity spectra, transverse momentum spectra and hadron ratios of mesons. An analogous, follow-up study could analyse the wealth of data available from the Pb+Pb program of the NA 49 collaboration.

While the missing rescattering in the qMD distorts the relative numbers of final state baryons and antibaryons, the coupled approach allows a detailed look at the dynamics of the system if quarks and antiquarks and the hadronization through recombination of colour charges. In the qMD approach, the hadronization transition is mainly driven by the rearrangement of quarks and antiquarks, while the production of quark-antiquark pairs does not contribute to the dynamics.

With the access to quark degrees of freedom, the coupled UrQMD/qMD approach opens options not available to hadronic models. The dynamical rearrangement and diffusion of quarks and antiquarks, for example, can be observed with the help of balance functions [43]. The qMD model could provide dynamical calculations of these observables. However, such an analysis requires very large statistics, which is, unfortunately, not available at present. Another possibility is the study of event-by-event fluctuations and the effects of the deconfined phase on fluctuation signals. Again, not all such observables can be analyzed due to high demands in statistics in order to obtain reliable results. However, fluctuations in electric charge can be studied using relatively moderate sample sizes, and, hence, are ideally suited for an analysis with the qMD model. Thus, we can exploit the full dynamics of quarks and antiquarks in our model and observe the consequences of their fractional electric charges for the time evolution of charge fluctuations. This is presented in the following chapter 7.

It is well known that QCD does not preclude the existence of colour neutral, hadronic states made up of more than a quark-antiquark pair, or three quarks. Such states are called exotic hadrons, and interest in them has been resuscitated by recent experimental findings about pentaquarks. Hadronization via quark recombination should apply to exotic hadrons in the same way it works for standard hadrons, and the qMD model provides a tool to study dynamically the formation of possible exotic hadronic clusters. This idea is pursued further in chapter 8.

Finally, more possible applications of the qMD model will be discussed in the conclusions in chapter 9.

Part III

The qMD model: Two applications to heavy ion collisions

Die Wahrheit ist nicht zu scheiden von dem Wahn, daß aus den Figuren des Scheins einmal doch, scheinlos, die Rettung hervortrete.

— Theodor Wiesengrund Adorno

In this part, we will present the results of two model studies which apply the qMD model to two specific problems encountered in ultra-relativistic heavy ion collisions. Initial conditions for the quark dynamics are obtained from UrQMD, as described in detail in the previous chapter 6.

Chapter 7 is a study of event-by-event fluctuations in electric charge. Such fluctuations have been proposed as a clear criterion to distinguish a deconfined system from a hadrons gas. However, experimental data show hadron gas fluctuation measures even at RHIC, where deconfinement is taken for granted. We will see how the dynamics of quark recombination washes out the quark-gluon plasma signal in the fluctuation criterion. Moreover, we will discuss briefly the problem of entropy at recombination.

In the second application in chapter 8, we study the formation of exotic hadronic clusters, larger than usual mesons and baryons. We see that such clusters could provide new measures for the thermalization and homogenization of a deconfined gas of colour charges. Moreover, number estimates for exotic clusters from recombination are considerably lower than corresponding predictions from thermal models, providing a clear difference between statistical hadronization and hadronization via quark recombination. A detailed analysis is provided for pentaquark candidates such as the Θ^+.

The main results of chapter 7 have been the content of a poster presentation for the conference Quark Matter 2005 in Budapest. The estimates for the yields of pentaquarks and the Θ^+ have been presented in a talk the conference SQM 2004 (Strange Quark Matter) in Cape Town and are published in [182].

Chapter 7

Charge fluctuations as a signal for the QGP

Event-by-event fluctuations of electric charge have been proposed as a clear signal for the formation of a quark-gluon plasma in ultra-relativistic heavy ion collisions. In the deconfined phase, electric charge is distributed in smaller quanta over more carrier particles than in a hadron gas. Thus, fluctuation measures derived from the so-called D measure, $D \sim \left\langle \delta Q^2 \right\rangle / \left\langle N_{\text{charge}} \right\rangle$ are expected to differ by a factor of 3–4 between a quark-gluon plasma and a hadron gas. This estimate is based on the local conservation of electric charge and the conservation of entropy at the transition from a QGP (with gluons contributing to entropy) to a gas of nearly massless pions. Experimental data, however, consistently yield the hadron gas values for these fluctuation measures, even at RHIC energies where the formation of a deconfined, partonic phase can not be doubted. It has been argued that these experimental findings can be explained naturally if hadronization is understood as the coalescence of constituent quarks.

Here, we will apply the quark molecular dynamics model, which provides a fully dynamical description of the transition from a gas of interacting quarks to hadrons via the formation of colour neutral clusters. We can study the time dependence of the fluctuation measure D in detail. We find an increase of D from the QGP value to the hadron gas value, going hand in hand with the transformation of quarks and antiquarks into hadrons. At upper SPS energies, this model picture includes entropy conservation. Thus, we can conclude that the non-observation of the naive quark-gluon plasma D measure in experiment provides strong evidence for quark recombination as the mechanism for hadronization.

This chapter is organized as follows: The next section 7.1 describes in a short overview how charge fluctuation measures can be used in principle to establish a deconfined phase of fractional electric charges. Then, in section 7.1, we look in detail at the fluctuation measure D. We discuss how the relevant estimates are obtained, and what are the differences to the original reasoning we expect for our quark coalescence model. In section 7.3, we present our results. Since entropy is an essential quantity in all these considerations, we will discuss its behaviour at recombination in section 7.4. Conclusions are drawn in section 7.5.

7.1 What charge fluctuations can teach us

Event-by-event fluctuations of observables of different kind have been proposed and investigated by experiment as signals for the formation of a deconfined, partonic phase in ultra-relativistic heavy ion collisions [42]. Besides fluctuations in transverse energy and momentum, fluctuations of conserved charges are among the most promising signals, since they can be measured easily in experiment. In order to separate fluctuations due to possible phase transitions from merely geometrical fluctuations due to different impact parameters, one has to consider measures of normalized charge fluctuations. Thus, it was proposed [183, 184] that the fluctuation measure for electric charge,

$$D = \langle N_{\text{ch}} \rangle \left\langle \delta R^2 \right\rangle \approx 4 \langle N_{\text{ch}} \rangle \left\langle \delta F^2 \right\rangle \approx 4 \, \frac{\left\langle \delta Q^2 \right\rangle}{\langle N_{\text{ch}} \rangle} \tag{7.1}$$

where Q is the electric charge, N_{ch} is the number of charged particles, $F = Q/N_{\text{ch}}$, and $R = (1 + F)/(1 - F)$, could provide a clear signal for the formation of a deconfined partonic phase. It was argued that, depending on the nature of the system of charged particles,

$$D = \begin{cases} 1 & \text{for a quark-gluon plasma} \\ 2.8 & \text{for a resonance gas} \\ 4 & \text{for an uncorrelated pion gas.} \end{cases} \tag{7.2}$$

A quark-gluon plasma should show a lower fluctuation measure than a hadron gas, mainly since in the deconfined plasma, electric charge is distributed in smaller quanta over more carrier particles than in the hadron gas.

As electric charge is conserved locally, fluctuations in $\left\langle \delta Q^2 \right\rangle$ are expected to survive hadronization, and, consequently, be observable in the hadronic final state. Thus, the main problem consists in obtaining an estimate for the number of charged particles in the partonic phase from the experimentally accessible number of charged hadrons in the final state. The QGP value of D in (7.2) follows from the assumption of the conservation of entropy at the transition from a QGP to a gas of nearly massless pions, with gluons contributing to entropy. The contribution of gluons is important at this point, since this marks a difference to the quark recombination scenario.

To make sure that fluctuations of electric charge yield reliable measures for the physical state of the charged system, two further points have to be taken into account: First, since the total electric charge in a heavy ion collision is completely fixed by the atomic numbers of the colliding nuclei, fluctuations can be observed only if the phase space is restrained, e. g. by restricting the analysis to a fixed rapidity interval. As discussed in [185], this implies that two correction factors C_μ and C_y must be included in (7.1). Hence, D is replaced by

$$\begin{aligned} \tilde{D} &= \frac{1}{C_\mu \, C_y} \, \langle N_{\text{ch}} \rangle_{\Delta y} \left\langle \delta R^2 \right\rangle_{\Delta y} \\ &\approx \frac{4}{C_\mu \, C_y} \, \langle N_{\text{ch}} \rangle \left\langle \delta F^2 \right\rangle \approx \frac{4}{C_\mu \, C_y} \, \frac{\left\langle \delta Q^2 \right\rangle}{\langle N_{\text{ch}} \rangle} \, , \end{aligned} \tag{7.3}$$

where

$$C_\mu = \frac{\langle N_+ \rangle^2_{\Delta y}}{\langle N_- \rangle^2_{\text{total}}} \,, \qquad C_y = 1 - \frac{\langle N_{\text{ch}} \rangle_{\Delta y}}{\langle N_{\text{ch}} \rangle_{\text{total}}} \,. \tag{7.4}$$

Here, $\langle \ldots \rangle_{\Delta y}$ denotes the event-by-event average over the rapidity interval Δy around mid-rapidity, and N_+ and N_- are given by $N_\pm = (N_{\text{ch}} \pm Q)/2$. Note that N_+ and N_- are equal to the number of positively and negatively charged particles, respectively, exactly if all charges are unit charges, as in a pion gas. With the correction factors C_μ and C_y applied, the corrected fluctuation measure $\tilde{D}$ is, again, exacted to yield the values given in (7.1) for the uncorrected measure D.

Second, one has to make sure that fluctuation signals are not completely washed out by charge diffusion during the time evolution into the final hadronic state as measured in the detector. Results of these investigations [186] show that it is possible to choose rapidity intervals such that fluctuation signals will in fact survive.

Experimental measurements of D and $\tilde{D}$ have been obtained by both the STAR [187, 188, 189] and PHENIX [190, 191] collaborations at RHIC. Experimental studies of SPS data by NA49 [192] and CERES [193] have focused on a sightly different fluctuation measure [194, 195]. All these data, however, consistently yield values for these fluctuation measures close to the hadron gas, even at RHIC energies where the formation of a deconfined, partonic phase can not be doubted. This situation has been dubbed the "D paradox" [196].

It has been argued that the experimental results can be explained naturally if hadronization is understood as the coalescence of constituent quarks [197, 196], where gluons contribute to the mass of valence quarks. In this picture, fluctuations in the quark phase are caused by fluctuations in the number of constituent quarks, and gluons do not contribute explicitly to the entropy balance. This means that the estimates yielding to (7.2) can not be applied. As mentioned before in chapter 3, the scenario of hadronization via the recombination of constituent quarks has been applied successfully to the description of peculiarities in the intermediate transverse momentum spectra at RHIC of baryons and mesons [53, 54, 55, 56, 57, 58]. Furthermore, it offers an explanation for the observed universality of scaled elliptic flow as function of transverse momentum for different hadron species [59, 60]. Thus, it is natural to invoke it also in order to understand the behaviour of the D measure at the transition from deconfined colour charges to hadrons.

Here, we will use our qMD model, which describes dynamically this transition from a gas of interacting quarks to hadrons via the formation of colour neutral clusters. This allows us study in detail the time dependence of the fluctuations in electric charge. We can further follow the time dependence of the numbers of charged particles and the mean mass of the particles and clusters in the system, thus monitoring entropy. From charge fluctuation and numbers of charged particles, we can, of course, follow the time dependence of the fluctuation measure $\tilde{D}$. We will apply the model to Pb+Pb collisions at the SPS with beam energies $E = 30\,\text{GeV}/N, 80\,\text{GeV}/N$, and $160\,\text{GeV}/N$ in the coupled UrQMD/qMD approach as described in the previous chapter 6. Expanding this study to RHIC energies is desirable, however, numerically too involved at present.

In our study, we find an increase of $\tilde{D}$ from the QGP values in the initial quark phase to the hadron gas value, going hand in hand with the transformation of quarks

into hadrons. At upper SPS energies, this model picture includes entropy conservation. Thus, we can conclude that the experimentally observed fluctuation measures favour the scenario of coalescence of constituent quarks for the description of hadronization.

Before presenting the results of our qMD simulations in section 7.3, we will, in the following section, discuss in more detail the rationale behind the estimates for the D measure in different systems of fluctuating electric charges.

7.2 Charge fluctuations in different systems

Prior to a more detailed discussion of the estimates for the fluctuation measure D in different systems, we stress that the approximate equivalence between the three fluctuation measures in (7.1) derived from $\langle \delta R^2 \rangle$, $\langle \delta F^2 \rangle$, and $\langle \delta Q^2 \rangle$ has to be taken with care. While results derived from $\langle \delta F^2 \rangle$ or $\langle \delta Q^2 \rangle$ are generally not very different, for $R = (1+F)/(1-F)$, the general expression for fluctuations of a ratio,

$$\left\langle \left(\delta \frac{A}{B} \right)^2 \right\rangle = \frac{\langle A \rangle^2}{\langle B \rangle^2} \left\langle \left(\frac{\delta A}{\langle A \rangle} - \frac{\delta B}{\langle B \rangle} \right)^2 \right\rangle , \tag{7.5}$$

should be used to calculate the fluctuations of R. Using $A = 1 + F$, $B = 1 - F$, with $\langle 1 \pm F \rangle = 1 \pm \langle F \rangle$ and $\delta(1 \pm F) = \pm \delta F$, one obtains for the square to be averaged over in (7.5)

$$\left(\frac{\delta A}{\langle A \rangle} - \frac{\delta B}{\langle B \rangle} \right)^2 = \frac{4\,(\delta F)^2}{(1+\langle F \rangle)^2 (1-\langle F \rangle)^2} . \tag{7.6}$$

This means that

$$\langle R^2 \rangle = \frac{4\,\langle \delta F^2 \rangle}{(1-\langle F \rangle)^4} . \tag{7.7}$$

Note that already for $\langle F \rangle = \langle Q/N_{\rm ch} \rangle = 0.1$, the fourth order changes the proportionality constant in (7.1) from 4 to 6.09. At lower SPS energies, $\langle F \rangle$ is usually even larger then 0.1, causing big differences between the measures derived from $\langle \delta R^2 \rangle$ and $\langle \delta F^2 \rangle$, respectively.

Now, coming to the fluctuation measure D, we will evaluate the expression (7.1) for four different systems: (1) for a pion gas, (2) for a hadronizing quark-gluon plasma, (3) for the quark phase of qMD, and (4) for the hadronic clusters from qMD.

7.2.1 Pion Gas

In the pion gas, the number of charged particles equals the number of charged pions, $N_{\rm ch} = N_{\pi^+} + N_{\pi^-}$, and the total charge Q is given by $Q = N_{\pi^+} - N_{\pi^-}$. Fluctuations in Q are given by $\delta Q = \delta N_{\pi^+} - \delta N_{\pi^-}$, with square $\delta Q^2 = \delta N_{\pi^+}^2 + \delta N_{\pi^-}^2 - 2\delta N_{\pi^+} \delta N_{\pi^-}$, yielding for the expectation value

$$\langle \delta Q^2 \rangle = \langle \delta N_{\pi^+}^2 \rangle + \langle \delta N_{\pi^-}^2 \rangle - 2\,\langle \delta N_{\pi^+} \delta N_{\pi^-} \rangle . \tag{7.8}$$

Neglecting the correlation term and assuming nearly poissonian fluctuations of the numbers of positive and negative pions,

$$\left\langle \delta N_{\pi^+}^2 \right\rangle = w_\pi \left\langle N_{\pi^+} \right\rangle \ , \quad \left\langle \delta N_{\pi^-}^2 \right\rangle = w_\pi \left\langle N_{\pi^-} \right\rangle \ , \tag{7.9}$$

where w_π is slightly larger then 1 due to Bose statistics, one obtains

$$\left\langle \delta Q^2 \right\rangle = w_\pi (\langle N_{\pi^+} \rangle + \langle N_{\pi^-} \rangle) = w_\pi \left\langle N_{\mathrm{ch}} \right\rangle \ . \tag{7.10}$$

Thus, for the pion gas one expects the fluctuation measure

$$D\big|_{\text{pion gas}} \approx 4 \ . \tag{7.11}$$

In a realistic hadronic system, one has to take into account resonance decays which introduce correlations into the system. It is clear form (7.8) that correlations reduce the fluctuations of Q and hence yield a value of D smaller than 4. This effect is of the order of 30 % [198].

7.2.2 Quark Gluon Plasma

Considering for simplicity an isospin symmetric system consisting only of up and down quarks and antiquarks, the number of charged particles is $N_{\mathrm{ch}} = N_{\mathrm{u}} + N_{\bar{\mathrm{u}}} + N_{\mathrm{d}} + N_{\bar{\mathrm{d}}}$, and the charge is $Q = Q_{\mathrm{u}} (N_{\mathrm{u}} - N_{\bar{\mathrm{u}}}) + Q_{\mathrm{d}} (N_{\mathrm{d}} - N_{\bar{\mathrm{d}}})$ with $Q_{\mathrm{u}} = +2/3$, $Q_{\mathrm{d}} = -1/3$. This implies for the charge fluctuations

$$\delta Q = Q_{\mathrm{u}} (\delta N_{\mathrm{u}} - \delta N_{\bar{\mathrm{u}}}) + Q_{\mathrm{d}} (\delta N_{\mathrm{d}} - \delta N_{\bar{\mathrm{d}}}) \tag{7.12}$$

with squares

$$\begin{aligned} \delta Q^2 = {} & Q_{\mathrm{u}}^2 \left(\delta N_{\mathrm{u}}^2 + \delta N_{\bar{\mathrm{u}}}^2 \right) + Q_{\mathrm{d}}^2 \left(\delta N_{\mathrm{d}}^2 + \delta N_{\bar{\mathrm{d}}}^2 \right) \\ & + \text{correlation terms} \ , \end{aligned} \tag{7.13}$$

where the correlation terms include all combinations $Q_i Q_j \, \delta N_i \delta N_j$ with $i, j = \mathrm{u}, \mathrm{d}$. Again, fluctuations in the numbers of quarks can be estimated by

$$\left\langle \delta N_{\mathrm{u}}^2 \right\rangle = w_{\mathrm{u}} \left\langle N_{\mathrm{u}} \right\rangle \ , \quad \left\langle \delta N_{\mathrm{d}}^2 \right\rangle = w_{\mathrm{d}} \left\langle N_{\mathrm{d}} \right\rangle \ , \tag{7.14}$$

which are slightly sub-poissonian with $w_{\mathrm{u}}, w_{\mathrm{d}} \lesssim 1$ due to Fermi statistics. Fluctuations in the numbers of antiquarks behave in an analogous way, so

$$\begin{aligned} \left\langle \delta Q^2 \right\rangle &= Q_{\mathrm{u}}^2 \, w_{\mathrm{u}} (\langle N_{\mathrm{u}} \rangle + \langle N_{\bar{\mathrm{u}}} \rangle) + Q_{\mathrm{d}}^2 \, w_{\mathrm{d}} (\langle N_{\mathrm{d}} \rangle + \langle N_{\bar{\mathrm{d}}} \rangle) \\ &= Q_{\mathrm{u}}^2 \, w_{\mathrm{u}} \left\langle N_{\mathrm{u}+\bar{\mathrm{u}}} \right\rangle + Q_{\mathrm{d}}^2 \, w_{\mathrm{d}} \left\langle N_{\mathrm{d}+\bar{\mathrm{d}}} \right\rangle \end{aligned} \tag{7.15}$$

where $N_{\mathrm{u}+\bar{\mathrm{u}}}$ is the number of up quarks and antiquarks, and similar for down quarks.

The expectation value of the number of charged particles in the quark-gluon system is $\langle N_{\mathrm{ch}} \rangle = \langle N_{\mathrm{u}} \rangle + \langle N_{\bar{\mathrm{u}}} \rangle + \langle N_{\mathrm{d}} \rangle + \langle N_{\bar{\mathrm{d}}} \rangle = \langle N_{\mathrm{u}+\bar{\mathrm{u}}} \rangle + \left\langle N_{\mathrm{d}+\bar{\mathrm{d}}} \right\rangle = \langle N_{\mathrm{q}+\bar{\mathrm{q}}} \rangle$. So, for an isospin symmetric quark-gluon system with $\langle N_{\mathrm{u}+\bar{\mathrm{u}}} \rangle = \left\langle N_{\mathrm{d}+\bar{\mathrm{d}}} \right\rangle = \langle N_{\mathrm{q}+\bar{\mathrm{q}}} \rangle / 2$, one would expect

$$\left\langle \delta Q^2 \right\rangle = \left(\frac{4}{9} \cdot \frac{1}{2} \, w_{\mathrm{u}} + \frac{1}{9} \cdot \frac{1}{2} \, w_{\mathrm{d}} \right) \langle N_{\mathrm{q}+\bar{\mathrm{q}}} \rangle \approx \frac{1}{4} \left\langle N_{\mathrm{q}+\bar{\mathrm{q}}} \right\rangle \ , \tag{7.16}$$

which yields the estimate for the fluctuation measure

$$D\big|_{\text{quarks in QGP}} \approx 1 \ . \tag{7.17}$$

At this point, one has to keep in mind that this quark fluctuation measure is, of course, not accessible in experiments where only hadrons can be detected. Hence, one has to relate this result to purely hadronic observables.

Fluctuations in electric charge will be the same after hadronization of the quark-gluon system, due to the strict local conservation of electric charge. However, the number of charged particles after hadronization is of course different from the number of charged quarks $\langle N_{\mathrm{q}+\bar{\mathrm{q}}} \rangle$ which has entailed the result (7.17). It is at this point that different model scenarios about hadronization come into play, since they yield different estimates for the number of charged quarks and antiquarks from the experimentally observed number of charged final state hadrons.

A first estimate for the relation between the numbers of charged particles before and after hadronization was derived using entropy conservation [183]. It is assumed that the time evolution is isentropic, and that all particles involved are massless, in thermal equilibrium, and non-interacting. This means that the initial state is considered as a gas of massless quarks and gluons, while the final hadronic state is regarded as a gas of massless pions. This assumption for the final state is justified since the pion mass is comparable to temperature and pions carry most of the electric charge. It has to be reconsidered, however, in baryon rich systems, e. g. at lower SPS energies.

Using the well know relations between entropy density σ and number density n for ideal, massless Bose and Fermi gases,

$$\sigma_{\text{Bose}} = 3.6\, n_{\text{Bose}} \ , \quad \sigma_{\text{Fermi}} = 4.2\, n_{\text{Fermi}} \tag{7.18}$$

on is lead to an estimate for the entropy of the (non-interacting) quark-gluon system with Volume V_{qgs},

$$S_{\text{qgs}} = V_{\text{qgs}} \cdot \sigma_{\text{qgs}} = 3.6 \left\langle N_{\mathrm{g}} \right\rangle + 4.2 \left(\langle N_{\mathrm{q}+\bar{\mathrm{q}}} \rangle \right) \tag{7.19}$$

where $\left\langle N_{\mathrm{g}} \right\rangle$ is the expectation value for the number of gluons and $\langle N_{\mathrm{q}+\bar{\mathrm{q}}} \rangle$ the expectation value for number of charged quarks and antiquarks, which was used in deriving (7.17).

Supposing now that hadronization converts all quarks and gluons into pions, conservation of entropy implies that the entropy of the final state pion gas is the same as the entropy of the quark-gluon system. Since pions are Bose particles, relation (7.18) means that

$$S_\pi = 3.6 \langle N_\pi \rangle = S_{\text{qgs}} = 3.6 \left\langle N_{\mathrm{g}} \right\rangle + 4.2 \ \langle N_{\mathrm{q}+\bar{\mathrm{q}}} \rangle \ . \tag{7.20}$$

Isospin symmetry implies that 2/3 of all pions are charged, hence

$$\langle N_{\text{ch, hadrons}} \rangle = \frac{2}{3} \langle N_\pi \rangle = \frac{2}{3} \left(\left\langle N_{\mathrm{g}} \right\rangle + \frac{7}{6} \langle N_{\mathrm{q}+\bar{\mathrm{q}}} \rangle \right) \ . \tag{7.21}$$

Here, to emphasize this again, $\langle N_{\text{ch, hadrons}} \rangle$ is the expectation value for the number of charged hadrons emerging from the quark-gluon system *after* hadronization,

while $\langle N_{\mathrm{q}+\bar{\mathrm{q}}} \rangle$ is the expectation value for the number of charged partons (quarks) in the quark-gluon system *before* hadronization.

Assuming that there are roughly as many gluons in the system as quarks and antiquarks, $\langle N_{\mathrm{g}} \rangle = \langle N_{\mathrm{q}+\bar{\mathrm{q}}} \rangle$, (7.21) implies

$$\langle N_{\text{ch, hadrons}} \rangle \approx \frac{4}{3} \langle N_{\mathrm{q}+\bar{\mathrm{q}}} \rangle \ , \tag{7.22}$$

hence from (7.16) follows

$$D\big|_{\text{pions from QGP}} \approx \frac{3}{4} \ . \tag{7.23}$$

This means that the fluctuation measure D in (7.23) for pions from a quark-gluon plasma – which have inherited their fluctuations in electric charge from the quarks – should be much lower than the corresponding measure (7.11) for a purely hadronic pion gas.

It should be noted that D in (7.23) can be obtained from purely hadronic observables by counting pions, hence $D = \langle N_{\text{ch, hadrons}} \rangle \left\langle \delta R^2 \right\rangle$ with $R = N_+/N_- = N_{\pi^+}/N_{\pi^-}$ and $\langle N_{\text{ch, hadrons}} \rangle = \langle N_{\pi^+} + N_{\pi^-} \rangle$.

A second, quite different estimate is obtained in the hadronization scenario via coalescence of quarks and antiquarks [197]. Here, it is assumed that gluons do not contribute to entropy, but, instead, dress the valence quarks, thus establishing constituent quarks. A rough estimate in this scenario yields for the number of hadrons an expectation value which is half the expectation value of the number of quarks and antiquarks,

$$\langle N_{\text{hadrons}} \rangle = \frac{1}{2} \langle N_{\mathrm{q}+\bar{\mathrm{q}}} \rangle \ . \tag{7.24}$$

Assuming all hadrons being pions and 2/3 of them being charged due to isospin symmetry, the number of charged hadrons is expected to be

$$\langle N_{\text{ch, hadrons}} \rangle = \frac{2}{3} \langle N_{\text{hadrons}} \rangle = \frac{1}{3} \langle N_{\mathrm{q}+\bar{\mathrm{q}}} \rangle \ . \tag{7.25}$$

There is a difference by a factor of 4 compared to the isentropic QGP estimate in (7.22), and in the resulting fluctuation measure,

$$D\big|_{\text{pions from QGP by quark coalescence}} \approx 3 \ , \tag{7.26}$$

all traces of the deconfined phase are almost lost.

There is of course a problem concerning entropy within this scenario, since the number of particles is halved by coalescence. Furthermore, the formation of light pions through coalescence of dressed, heavy constituent quarks is problematic. However, both difficulties can be overcome if coalescence results mainly in heavy resonances, which decay into final state hadrons, thus increasing again the total number of particles and producing pions to a large extent as decay products. At the same time, resonance decay decreases the fluctuation measure. This decrease by a factor of roughly 30%, however, is not big enough to reduce D to the QGP value.

This extended coalescence scenario – going through an intermediate stage of resonances – is exactly what happens in the qMD model, which we will discuss next.

7.2.3 Quark phase of qMD

In the quark phase of qMD, charge fluctuations are the same as those calculated for the quark-gluon system in (7.16), hence $\langle \delta Q^2 \rangle = \langle N_{\mathrm{q}+\bar{\mathrm{q}}} \rangle / 4$. Furthermore, the number of charged particles also equals the number of quarks, $\langle N_{\mathrm{ch}} \rangle = \langle N_{\mathrm{q}+\bar{\mathrm{q}}} \rangle$. This means that

$$D\big|_{\text{quarks in qMD}} \approx 1 \ , \tag{7.27}$$

as for the quark-gluon system. Note that charm and strange quarks which are covered by the qMD model are neglected in this analysis, since their relative number is small and charge fluctuations are dominated by those of the light quarks.

7.2.4 Hadronic clusters from qMD

All quarks propagated in the qMD model finally end up in hadronic clusters, which subsequently decay into the final state hadrons. In order to establish an estimate for the fluctuation measure D of the charged clusters emerging from the recombination of quarks, we can use arguments similar to those yielding the estimate (7.26) for D of pions from a quark-gluon system by quark coalescence.

Again, the expectation value of fluctuations in electric charge will be the same for the recombined clusters after hadronization as for the quark system, hence $\langle \delta Q^2 \rangle = \langle N_{\mathrm{q}+\bar{\mathrm{q}}} \rangle / 4$ as before.

However, the number of charged clusters from recombination in qMD differs drastically from the estimate (7.21) for the number of charged pions derived from the conservation of entropy and is more similar to the quark coalescence estimate (7.25). In the recombination method used in qMD, all quarks end up in baryonic or mesonic clusters containing three and two quarks and/or antiquarks, respectively, so

$$\langle N_{\mathrm{q}+\bar{\mathrm{q}}} \rangle = 3 \left\langle N_{\mathrm{b}+\bar{\mathrm{b}}} \right\rangle + 2 \langle N_{\mathrm{m}} \rangle \ . \tag{7.28}$$

Here, $\left\langle N_{\mathrm{b}+\bar{\mathrm{b}}} \right\rangle$ and $\langle N_{\mathrm{m}} \rangle$ are the expectation values for the numbers of baryonic and mesonic clusters, respectively. These clusters populate all isospin multiplets, hence $\mathbf{2} \otimes \mathbf{2} \otimes \mathbf{2} = \mathbf{4} \oplus \mathbf{4} \oplus \mathbf{2}$ for the baryonic and $\mathbf{2} \otimes \mathbf{2} = \mathbf{3} \oplus \mathbf{1}$ for the mesonic clusters. Of all these states, 5 of the 8 baryonic (corresponding to the proton, the charged Δ and the N^{*+} resonances) and 2 of the 4 mesonic states (corresponding to the charged pions) are electrically charged, so

$$\begin{aligned} \langle N_{\mathrm{q}+\bar{\mathrm{q}}} \rangle &= 3 \cdot \frac{8}{5} \left\langle N_{\text{ch, b}+\bar{\mathrm{b}}} \right\rangle + 2 \cdot \frac{2}{1} \langle N_{\text{ch, m}} \rangle \\ &= 4 \left(\langle N_{\text{ch, m}} \rangle + \frac{6}{5} \left\langle N_{\text{ch, b}+\bar{\mathrm{b}}} \right\rangle \right) \\ &\approx 4 \langle N_{\text{ch, clusters}} \rangle \ , \end{aligned} \tag{7.29}$$

where $\left\langle N_{\text{ch, b}+\bar{\mathrm{b}}} \right\rangle$ and $\langle N_{\text{ch, m}} \rangle$ are the expectation values for the numbers of *charged* of baryonic and mesonic clusters, respectively. In the last equation in (7.29), the contributions of charged baryonic and mesonic clusters are summed up to the total number of charged clusters $\langle N_{\text{ch, hadrons}} \rangle$, taking into account that $\left\langle N_{\text{ch, b}+\bar{\mathrm{b}}} \right\rangle / 5$

is small compared to $\langle N_{\text{ch, hadrons}} \rangle$. This estimate is even more extreme than the coalescence estimate in (7.25). It follows that after recombination, $\langle \delta Q^2 \rangle \approx \langle N_{\text{ch, hadrons}} \rangle$, hence

$$D\big|_{\text{clusters from qMD}} \approx 4 \; . \tag{7.30}$$

This means that the simple recombination scheme implemented in qMD completely destroys the fluctuation measure expected from the smaller charge fluctuations in the quark phase. The reason for this, of course, is due to the transient decrease of entropy in qMD related to the coalescence of quarks into clusters.

Since most of the clusters formed by recombination immediately decay into stable hadrons, entropy is roughly conserved in the overall time evolution of the system in qMD. However, as discussed before, this means that the fluctuation measure D for the final state hadrons is affected in a way similar to the modifications caused to the pion gas value due to decays of resonances, decreasing $D \approx 4$ by a factor of about 0.3 [198]. Thus, one would expect for the fluctuation measure of final state hadrons coming from qMD

$$D\big|_{\text{final state from qMD}} \approx 3 \; . \tag{7.31}$$

The estimates (7.30) and (7.31) can easily be checked with qMD data. We will now turn to the discussion of the results of our simulations.

7.3 Results for fluctuations from the qMD model

We have investigated the time development of the fluctuation measure D for nearly central Pb+Pb collisions at SPS energies of 30, 80, and $160\,\text{GeV}/N$ ($\sqrt{s}_{NN} = 7.7, 12.4$, and $17.4\,\text{GeV}$) with fixed impact parameter $b = 2\,\text{fm}$ over the whole evolution of the system, from an initial hot fireball of deconfined quarks to the final hadronic state. To this end, the colliding nuclei are propagated with the hadronic transport code UrQMD until complete crossing, as described in the previous chapter 6. Times t_{x} of complete crossing after the first contact of the nuclei in the centre of momentum frame are listed in table 6.1. At these instants, all particles of the UrQMD simulation run which have undergone at least one elastic or inelastic collision—hadrons, resonances, and preformed hadrons from string decays within their formation time—are decomposed into quarks and antiquarks according to their quantum numbers, and taking into account local conservation of four-momentum. This decomposition procedure, which has been discussed in detail in chapter 6, provides the initial condition for the further time evolution within the qMD model.

Hadronization is described dynamically by qMD via the formation of colour neutral clusters. This allows access to the numbers of quarks, hadronic clusters and hadrons, and their electric charges, at any instant of the evolution of the system. The sample of events used for the fluctuation analysis includes 200 events.

Comparing figures 7.1 and 7.2, which show the corrected fluctuation measure D as derived from the three different fluctuating variables given in (7.3) for different widths of the rapidity window, we see that both the initial and finite state quarks,

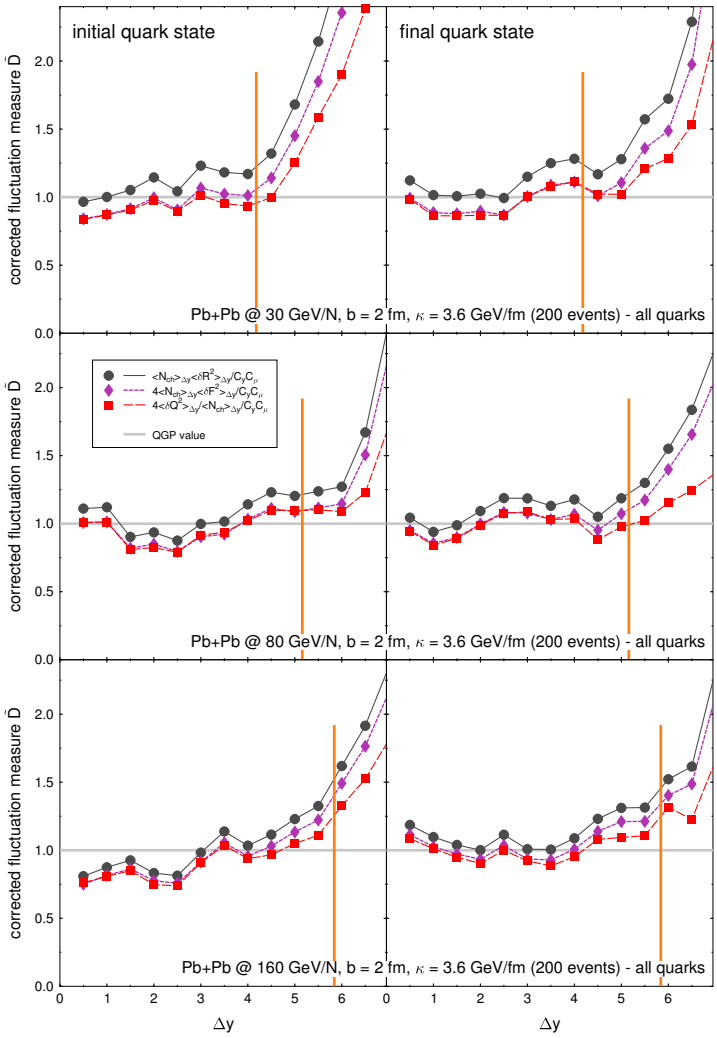

Figure 7.1
Fluctuation measures for quarks and antiquarks in qMD for Pb+Pb collision at different SPS energies, for different widths Δy of the rapidity interval used in the analysis. Distance in rapidity between projectile and target in the different systems is indicated by the vertical bar. Fluctuations for initial state quarks and antiquarks are shown in the left panel, fluctuations at hadronization in the right panel. In all systems, all three different fluctuation measures correspond very well to the expected value of $D \approx 1$. Note that during the evolution of the system, the rapidity window in which $D \approx 1$ is valid widens for the lowest collision energy, but is virtually unchanged for the other systems.

and the clustering and final state hadrons, show exactly the fluctuation measures expected for quarks, and for hadrons, respectively. This is a puzzle, since there has to be some continuous evolution of the fluctuation measure.

The reason for this is found in the coalescence used in the clustering routine. To see this, consider figure 7.3, which shows the fluctuation measure D for Pb+Pb collisions at the SPS with a beam energy of $E = 30\,\mathrm{GeV}/N$ at three different times $t = 0, 20$, and 40 fm/c after the initial collisions. In this calculation, cluster dissection is switched off, hence we are dealing with quarks and antiquarks all the

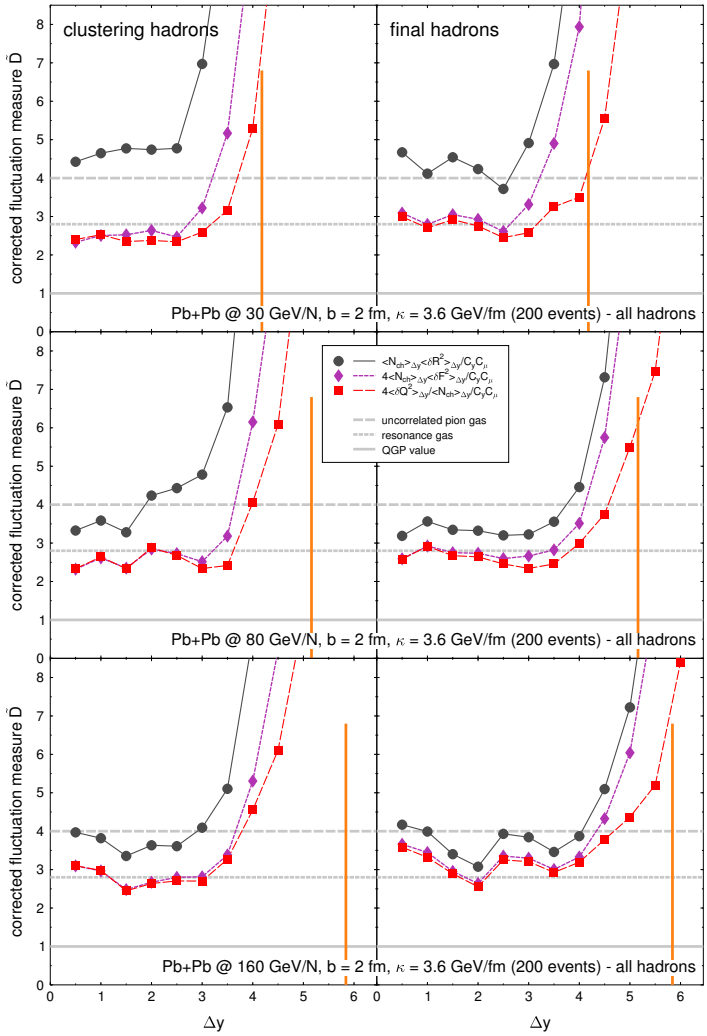

Figure 7.2
Fluctuation measures for hadronic clusters and final state hadrons obtained in qMD for Pb+Pb collision at different SPS energies. Clustering hadrons are shown in the left panel, final state hadrons after the decay of resonances are shown on the right panel. Here, one has to take care that not all fluctuation measures yield equal results. However, the overall result corresponds to the value expected of D for an uncorrelated pion gas, or a resonance system.

time. However, we can now observe how the colour charges arrange themselves in hadronic clusters. Nevertheless, the fluctuation measure still shows the behaviour expected for quarks.

In order to see better how the D measure evolves in time, we now focus on our sample of nearly central Pb+Pb events at upper SPS energies of $160\,\mathrm{GeV}/N$ ($\sqrt{s}_{NN} = 17.3\,\mathrm{GeV}$). The rapidity window for the fluctuation analysis is chosen with a fixed width of $\Delta y = 2.5$ centred around mid-rapidity.

We follow in detail the time evolution of the numbers of quarks, hadrons, charged and total particles, and the mean mass of all particles, as well as the charge fluctuations, over the whole strongly interacting history of the system. Monitoring

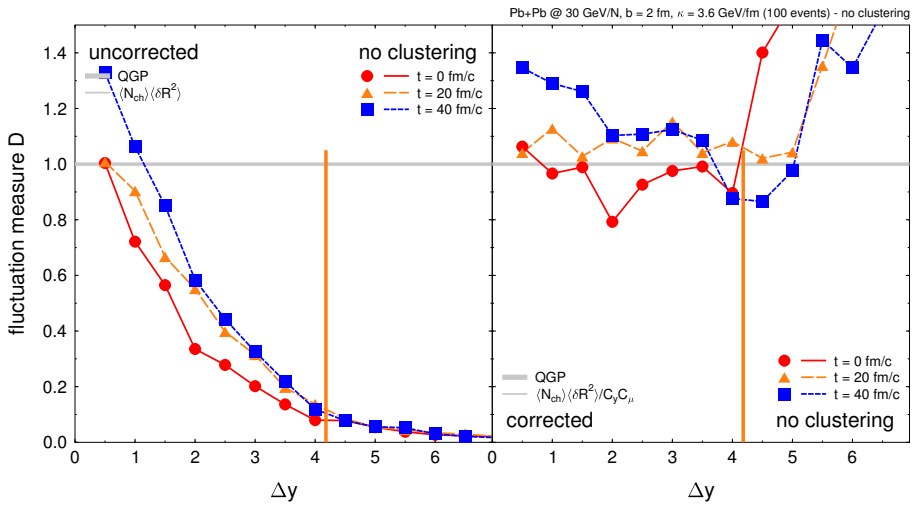

Figure 7.3
Fluctuation measures of quarks and antiquarks with (right) and without (left) corrections for the width of the rapidity window in Pb+Pb collisions at the SPS with a beam energy of $E = 30\,\mathrm{GeV}/N$ at different times. Here, the dissection of hadronic clusters has been switched off, and the fluctuation measure shows the behaviour expected for quarks and antiquarks over the whole evolution of the system. Even at $t = 40\,\mathrm{fm/c}$, where all quarks have arranged themselves in hadronic clusters, the fluctuation measure is not that of hadrons.

the total number of particles and their mean mass allows to follow qualitatively the evolution of entropy of the system. Charge fluctuation measures D, corrected according to (7.3), are calculated as a function of time from fluctuations in all three quantities, $\langle \delta R^2 \rangle$, $\langle \delta F^2 \rangle$, and $\langle \delta Q^2 \rangle$ following the definition (7.1). The results of this analysis are shown in figure 7.4.

The lower panel of figure 7.4 shows the time evolution of numbers of particles and the mean particle mass. The conversion of quarks into hadronic clusters and final state hadrons is clearly visible. At $t \approx 10 - 15\,\mathrm{fm}/c$, nearly all quarks have gone into clusters. This situation corresponds to the minimum in the total number of particles and the maximum of the mean particle mass: as discussed before, the formation of mesonic and baryonic clusters alone reduces the total number of particles by a factor somewhat larger than 2, depending of the baryon and antibaryon content of the system. At the same time, the mean mass increases drastically, since the cluster masses follow a broad and wide mass spectrum. However, these hadronic clusters are not stable, and at later times they will decay, as is visible in the further increase in the total number of particles at times $t \geq 20\,\mathrm{fm}/c$, where the mean particle mass decreases again.

The upper panel of figure 7.4 shows the time evolution of the three different fluctuation measures defined in (7.1). Measures derived from $\langle \delta F^2 \rangle$ and $\langle \delta R^2 \rangle$ are nearly identical, while there is a small difference building up between these two and the measures derived from $\langle \delta R^2 \rangle$. As discussed in (7.7), this is due to the finite value of $\langle \delta F \rangle = \langle Q/N_{\mathrm{ch}} \rangle$, which increases with time as the number of charged particles drops roughly by a factor of 2 (see lower panel) between initial and final state.

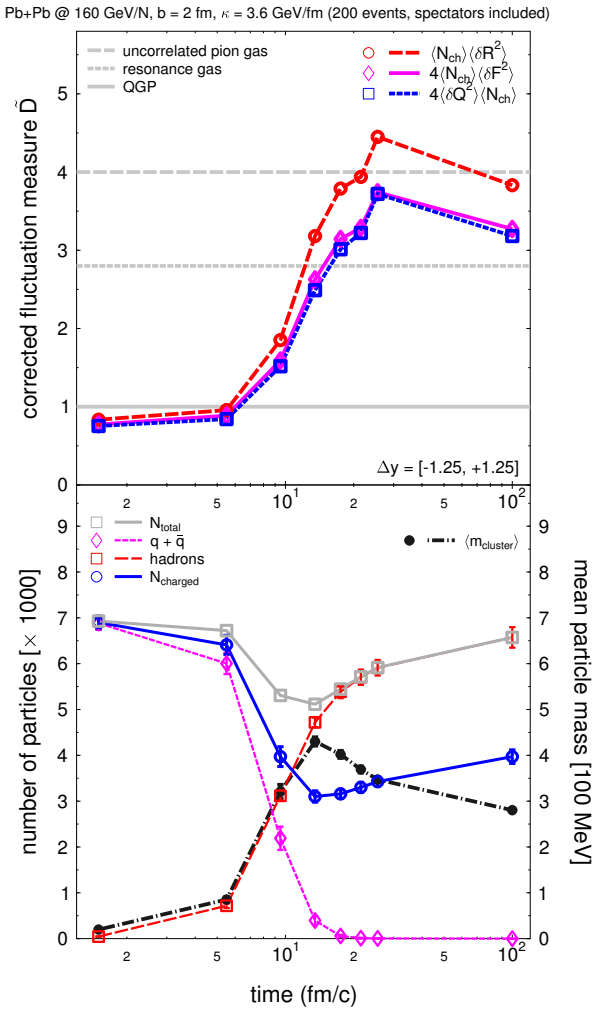

Figure 7.4
Results of the fluctuation analysis for nearly central Pb+Pb collision at 160 GeV/N ($\sqrt{s}_{NN} = 17.3$ GeV) as function of time. The upper panel shows the time evolution of the three different fluctuation measures defined in (7.1). Horizontal lines indicate the fluctuation measures expected for different physical situations. The lower panel shows the time evolution of the numbers of quarks and antiquarks (♢), hadrons (□, dashed line), and charged particles (○), as well as the mean mass of the particles (quarks, colour neutral clusters, and final state hadrons) in the system (●). The upper solid, grey line indicates the total number of particles in the system (□, solid grey line).

The main point of the plot, however, is the smooth increase of all three measures from the QGP value $D \approx 1$ to the pion gas value $D \approx 4$ in the time interval between $t = 5 - 25$ fm/c, with a small decrease to $D \approx 3.5$ for the final hadronic state (plotted at t = 100 fm/c), when all hadronic clusters have decayed. Comparison with the lower panel shows how the time evolution of D goes neatly hand in hand with the conversation of quarks into hadronic clusters and final state hadrons. It should be kept in mind that the transition from quarks to hadrons in the qMD model is not instantaneous, but smooth over time, depending on the local conditions of colour interactions according to the dynamical criteria for cluster formation.

7.4 Entropy in the recombining system

Focusing on entropy, we see that the total number of particles in the initial and final state is roughly the same, with the final state particles being more massive. Since the simple entropy estimate by counting particle numbers is surely an oversim-

plification for the interacting initial quark gas and the massive, final state hadron gas, entropy non-decrease is not violated. This is valid also at intermediate times, where in the entropy budget, the low number of particles is compensated by the high mean particle masses.

To clarify this point, we note that for a non-interacting, relativistic gas of N point particles with mass m at the temperature T in a volume V, and subject to classical Boltzmann statistics, entropy can be calculated analytically [199]. The total Hamiltonian is the sum of single-particle Hamiltonians

$$\mathcal{H} = \sum \sqrt{(mc^2)^2 + (c\vec{p}_i\,)^2}\,, \tag{7.32}$$

and the N-particle partition function

$$Z(T,V,N) = \frac{1}{N!} Z_1(T,V)^N \tag{7.33}$$

factorizes in a product of one-particle partition functions, yielding

$$Z_1(T,V) = \frac{1}{h^3} \int \mathrm{d}^3q\ \mathrm{d}^3p\ \mathrm{e}^{-\mathcal{H}/k_\mathrm{B}T}\,. \tag{7.34}$$

This integral can be solved analytically using the modified Bessel function $K_2(x)$. In units $\hbar = c = k_\mathrm{B} = 1$ and with the dimensionless variable $u = \beta m = m/T$, the resulting partition function reads

$$Z(T,V,N) = \frac{1}{N!} \left(4\pi V \left(\frac{T}{2\pi}\right)^3 u^2\, K_2(u) \right)^N\,. \tag{7.35}$$

From the Helmholtz free energy, $F(T,V,N) = -T \log Z(N,V,T)$, entropy follows according to the standard relation, $S(T,V,N) = -\partial F/\partial T|_{V,N}$. One obtains

$$S(T,V,N) = N \left[4 + \log\left(4\pi\, \frac{V}{N} \left(\frac{T}{2\pi}\right)^3 u^2\, K_2(u) \right) + u\, \frac{K_1(u)}{K_2(u)} \right]\,. \tag{7.36}$$

For small u, this can be expanded as

$$S(T,V,N) = N \left[4 + \log\left(8\pi\, \frac{V}{N} \left(\frac{T}{2\pi}\right)^3 \right) + \frac{1}{4}\frac{m^2}{T^2} + O\left(\frac{m^4}{T^4}\right) \right]\,. \tag{7.37}$$

We see that the simple scaling of entropy with the number of particles is augmented by the logarithm term and the expansion in m^2/T^2, which, for the masses and temperatures at hand, has obvious importance.

Figure 7.5 shows the entropy (7.36) for a spherical system with radius $R = 6\,\mathrm{fm}$ at the temperature $T = 200\,\mathrm{MeV}$ as a function of the number of particles and the scaled particle mass $u = m/T$. Using $1 = \hbar c = 197.327\,\mathrm{MeV}\cdot\mathrm{fm}$, or $1\,\mathrm{MeV}\cdot\mathrm{fm} = 0.00507$, the argument of the logarithm reads

$$\frac{V}{N} \left(\frac{T}{2\pi}\right)^3 = \frac{4\pi}{3N} \left(\frac{RT}{2\pi}\right)^3 = \frac{4\pi}{3N} \left(\frac{6.08}{2\pi}\right)^3\,. \tag{7.38}$$

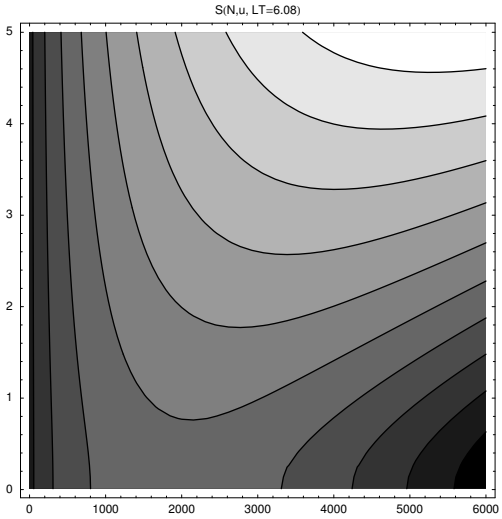

Figure 7.5
Entropy (7.36) of a relativistic gas in the canonical ensemble as a function of the number of particles N and the scaled mass $u = m/T$. A spherical system with radius $R = 6\,\mathrm{fm}$ at the temperature $T = 200\,\mathrm{MeV}$ is assumed. Even with a decreasing number of particles, entropy can stay constant or increase if the particle mass increases.

Note that in the usual picture of the time evolution of the hot and dense system created in a heavy ion collision, the product VT^3, or RT, stays approximately constant. This describes the cooling of the expanding system. In fact, the expansion dynamics $V \sim 1/T^3$ is derived for an isentropic time evolution.

Thus, as we can see from figure 7.5, a decrease in the number of particles during the expansion does not necessitate a decrease of entropy. In fact, entropy can stay constant, or even increase, if the mass of the particles increases. Such a change most probably drives the system away from a local maximum of entropy, but this may correspond to the observations made in the time evolution of the qMD model: Here, cluster recombination reduces the number of particles. Instead, very massive clusters are created, and. this mass increase allows for a non-decrease of entropy. However, most clusters are unstable, i. e., not in equilibrium, and decay very rapidly to lighter, final state hadrons.

It is clear that the canonical ensemble with a fixed number of particles is not the best description for the dynamical, expanding system in a heavy ion collision, where particles can be created and the grand-canonical ensemble is more appropriate. However, the qMD model fits well in the canonical picture, since the number of quark and antiquarks in the deconfined phase is nearly constant, with very small contributions from colour string decays. Moreover, it is important to note that a detailed analysis of entropy involves much more than a mere counting of particles in the system, disregarding of particle masses.

7.5 Discussion and conclusion

As we have seen, our model study achieves a fully dynamical description of the transition from a strongly interacting quark gas to a final state hadronic system. The analysis of the fluctuation measure D vindicates neatly the expectations deduced from the properties of the model: At the initial state, the system is a gas of quarks, and fluctuations in charge at early times clearly yield the value $D \approx 1$ expected for a quark gas. As the system expands and cools with time, quarks are

subsequently collected in clusters, causing a steep increase of D towards the value $D = 4$ expected from the cluster coalescence analysis in (7.29) and (7.30). The small decrease of D at later times can be understood as the consequence of cluster decay, decreasing D in a similar way as for a resonance gas compared to a pion gas.

In combination with the experimental findings, our results speak strongly in favour of the scenario of quark coalescence for the transition from the quark-gluon plasma to a hadron gas. In this scenario, gluons do not contribute much to entropy, but dress up the valence quarks instead, causing their large constituent masses. In our model, gluons are completely subsumed into the potential interaction between quarks, and the dressing of quarks finds its correspondence in the high mass of the colour neutral clusters, which is due to a large part to the interaction energy of the quarks in the cluster, thus the gluons.

We conclude that the D puzzle is a paradox only when describing the transition from QGP to a hadron gas as the transition from a gas of massless, non-interacting quarks and gluons to a gas of massless pions. The paradox disappears if hadronization is understood in the scenario of quark coalescence.

Finally, we mention that besides the fluctuations in electric charge discussed in this chapter, other signals of the QGP involving charge fluctuations have been proposed recently, such as charge transfer fluctuations [200] and baryon-strangeness correlations [201]. Especially the last signal does not rely on estimates of the total number of particles involved and requires knowledge only of strangeness and baryon number. It will be quite straightforward to adopt the qMD analysis presented in this chapter to these signals.

Chapter 8

Exotic hadronic clusters and pentaquarks

As we have seen in chapter 2, the theory of QCD describes quarks as fundamental representations of its gauge group, the colour group $\mathrm{SU}(3)_\mathrm{c}$. Due to confinement, the low energy regime of QCD allows only colour singlets, so only certain combinations of quarks and antiquarks are possible. This constraint is fulfilled by the common mesons and baryons, made up of a quark and an antiquark with colour and anticolour, or of three quarks with three different colours, respectively.

However, mesons and baryons are not the end of the story: Colour neutrality can be fulfilled whenever the difference between the number of quarks n_q, and the number of antiquarks, $n_{\bar{q}}$, is a multiple of three,

$$n_q - n_{\bar{q}} \equiv 0 \mod 3 \,. \tag{8.1}$$

This triality condition opens the possibility of the existence of so-called exotic hadronic states, such as the tetraquark ($n_q = 2$, $n_{\bar{q}} = 2$, "dimeson"), the pentaquark ($n_q = 4$, $n_{\bar{q}} = 1$), the hexaquark ($n_q = 6$, $n_{\bar{q}} = 0$, "dibaryon", or $n_q = 3$, $n_{\bar{q}} = 3$, "baryonium"), and so on. The possible states for up to six quarks and antiquarks are listed in table 8.1. Note that colour neutral states could also contain contributions of gluons, or even be purely gluonic. Such states are called hybrids or glueballs, respectively. However, we will not discuss any of these in this thesis.

Speculations about exotic states are as old as the quark model, and serious estimates about their properties and spectroscopy began with the bag models of the 1970s [19, 20, 21]. However, in spite of experimental search programs, no substantial evidence for the existence of exotic hadrons could be found for a long time.

state	quark content
meson	$q\bar{q}$
baryon	qqq
tetraquark ("dimeson")	$qq\bar{q}\bar{q}$
pentaquark	$qqqq\bar{q}$
hexaquark ("baryonium")	$qqq\bar{q}\bar{q}\bar{q}$
hexaquark ("dibaryon")	$qqqqqq$

Table 8.1
Colour singlet states built up from up to six quarks and antiquarks. The charge conjugated states of the antibaryon, antipentaquark, and antidibaryon are not listed.

Concerning pentaquark states, then referred to as Z^* resonances, a contemporary review concludes that "the evidence indicates that Z^* resonances do not exist." [22, on p. 191].

This situation changed in 2003, when indications for the existence of the so-called Θ^+ pentaquark, made up of four light quarks and an antistrange quark, were found in several different experiments, such as in photoproduction on nuclei [23, 202], protons [203], and deuterons [204, 205]. Furthermore, the identification of the Ξ^{--} pentaquark (made up of two strange quarks, two light quarks, and a light antiquark, and belonging to the same multiplet as the Θ^+) was reported for proton-proton collisions at the CERN-SPS [206], and the HERMES experiment at DESY claimed the identification of a charmed pentaquark state, built from four light quarks and an anticharm quark [207]. Finally, there are very recent data for deuteron-gold collisions at STAR [208] that are interpreted as signals of a Θ^{++} pentaquark, which would be an isospin partner of the Θ^+.

Despite these assertions of discovery, however, the final experimental verdict on the existence of these pentaquark states is still out. Besides several experiments confirming at least the Θ^+, there is a growing number of experiments whose data strongly contest the existence of pentaquark states. Pentaquarks are by far not the first example of signals with a confidence interval of several σ that eventually turn out to be spurious [209]. Negative results are reported, in general, from high-energy experiments where pentaquark states would be created by fragmentation.

While the controversy about the factual existence is still going on, it is legitimate to discuss whether these or other pentaquark states could be found in the aftermath of an ultra-relativistic heavy ion collision. The hadronization of the transient quark-gluon plasma created in such events could render possible the formation of colour neutral states involving more than the one quark and one antiquark, or more than three quarks, thus transcending the mundane world of mesons and baryons. As we have discussed repeatedly before, there are strong reasons to support the view that hadronization from ultra-relativistic heavy ion collision occurs through quark recombination. Thus, the non-observation of pentaquarks in high-energy fragmentation experiments is not an objection to the possible formation of these states in ultra-relativistic heavy ion collisions.

Hence, it is reasonable to assume that any exotic hadronic state, if formed by quark recombination out of an expanding, cooling quark-gluon plasma, will emerge from some colour neutral cluster of colour charges. Thus, if the Θ^+ pentaquark in fact exists and is created during the hadronization stage of a quark-gluon plasma along with all other types of hadrons and hadronic resonances, it should emerge from a colour neutral cluster of two up quarks, two down quarks, and one strange antiquark. Searching for such clusters can hence yield upper estimates for the numbers of Θ^+ pentaquarks out of quark recombination from a deconfined, strongly interacting system.

Soon after the first reports on the discovery of the pentaquark Θ^+, abundances of pentaquark states created in ultra-relativistic heavy ion collision were estimated from the standard statistical model picture, using the grand canonical ensemble [210]. This analysis has been refined by taking into account strangeness chemistry [211]. Thus, the Θ^+ pentaquark and the corresponding members of its multiplet with higher strangeness have been recognized as possibly important probes of the

deconfinement transition in heavy ion collisions, following the lines of the well-known strangeness enhancement argument. Furthermore, dynamical studies of the creation of pentaquarks in collisions at RHIC energies have been done [212] using hydrodynamical calculations.

Here, we apply the qMD model to study the formation of colour neutral exotic multi-quark clusters at the hadronization stage of an ultra-relativistic heavy ion collision. We search for colour neutral clusters made up of up to six colour charges, respectively. We thus obtain estimates for the numbers and phase space distributions of exotic hadronic states produced by clustering in heavy ion collisions, including the members of the pentaquark multiplets. We find pentaquark states with masses which are higher than the mesonic and baryonic clusters produced, in agreement with the experimental data about the pentaquark states. Pentaquark states are surprisingly abundant in our model, contributing to more than 5 % of the $\mathrm{d}n/\mathrm{d}y$ distribution halfway between mid-rapidity and projectile rapidity. Restriction to the quantum numbers of the Θ^+, however, yields results below thermal model estimates. Within the limitations of our model, we conclude that both at the SPS and the future CBM experiment at GSI, pentaquark states could be found.

This chapter is organized as follows: We begin with a discussion of exotic hadrons and the known facts and open questions about pentaquark states in section 8.1. After a short description of the application of the qMD model to the search for exotic clusters in section 8.2, we present our results for the production of exotic hadrons in ultra-relativistic heavy ion collision at SPS and RHIC energies in section 8.3, discussing yields and rapidity distributions of tetra-, penta-, and hexaquarks. We analyse the mass distribution of clusters, present transverse momentum spectra, and the space-time dynamics of hadronization in the qMD model. We then focus on pentaquark states in section 8.4. We analyse yields differentiating first by strangeness, then by isospin and spin in section 8.5, thus arriving at estimates for the production of Θ^+ in section 8.6. We conclude with a discussion of our results in section 8.7. All group theoretical calculations are presented in detail in the appendices B and C.

8.1 Exotic clusters in the quark model and pentaquarks

Pentaquarks belong to a class of hadronic objects transcending the usual mesons and baryons – they are built up of four quarks and one antiquark. Within the quark model and QCD as a dynamical theory of quarks, the existence of such states in the colourless hadronic world is not forbidden: The necessary condition for colour neutral states involving more than three quarks and/or antiquarks is the requirement of at least one colour singlet $\mathbf{1}$ occurring in the decomposition of the product state of the quarks and/or antiquarks into a direct sum. Formally, quarks are described by fundamental triplets $\mathbf{3}$ of $\mathrm{SU}(3)_{\mathrm{colour}}$, and antiquarks by conjugated triplets $\overline{\mathbf{3}}$. Then, a state involving q quarks and p antiquarks can be colour neutral if

$$\underbrace{\mathbf{3}\otimes\cdots\otimes\mathbf{3}}_{q\text{ times}}\otimes\underbrace{\overline{\mathbf{3}}\otimes\cdots\otimes\overline{\mathbf{3}}}_{p\text{ times}} \stackrel{!}{=} \mathbf{1}\oplus\text{higher representations}\,. \tag{8.2}$$

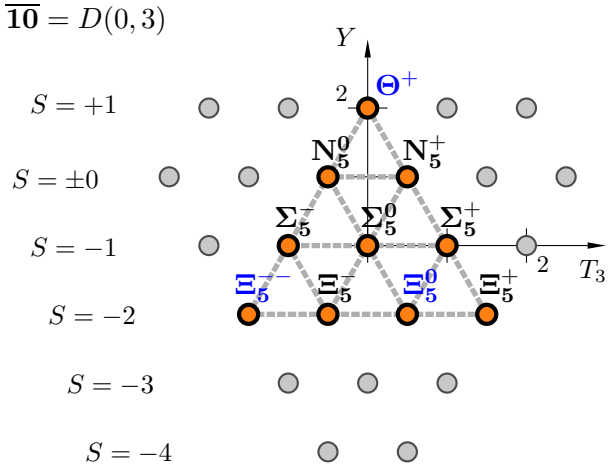

Figure 8.1
An antidecuplet of possible pentaquark states (orange disks) was predicted by the SU(3) Skyrme model. In the quark scheme, this multiplet is part of the much larger multiplet structure (8.3), whose states in the T_3-Y-plane are shown as grey disks. Hypercharge Y and strangeness S are related via $Y = S + B$, where $B = 1$ is the baryon number of the pentaquark states. States with experimental evidence are shown in blue.

This condition is fulfilled for mesons and baryons, due to the well known decompositions $\mathbf{3} \otimes \overline{\mathbf{3}} = \mathbf{1} \oplus \mathbf{8}$ (see (B.34) in appendix B.6) and $\mathbf{3} \otimes \mathbf{3} \otimes \mathbf{3} = \mathbf{1} \oplus 2 \cdot \mathbf{8} \oplus \mathbf{10}$ (B.36). It is fulfilled furthermore for states of two quarks and two antiquarks (B.41), four quarks and one antiquark (B.42), three quarks and three antiquarks (B.46), six quarks (B.45), and so on. All group theoretical arguments are explained in detail in appendix B.6. The possible combinations for up to six quarks and antiquarks are listed in table 8.1. Colour neutral quark combinations other than mesons and baryons are usually called *exotic states*. Exotic states which according to their quantum numbers can not be confused with mesons and baryons are often called *manifestly exotic*. It is clear that only manifestly exotic states can easily and unambiguously be identified as exotic.

8.1.1 Pentaquarks: Classification and experimental data

For pentaquark states, constructed from four quarks and one antiquark, the decomposition (8.2) is calculated in (B.42). It reads

$$\mathbf{3} \otimes \mathbf{3} \otimes \mathbf{3} \otimes \mathbf{3} \otimes \overline{\mathbf{3}} \;=\; 3 \cdot \mathbf{1} \oplus 8 \cdot \mathbf{8} \oplus 4 \cdot \mathbf{10} \oplus 2 \cdot \overline{\mathbf{10}} \oplus 3 \cdot \mathbf{27} \oplus \mathbf{35} \;, \quad (8.3)$$

and contains the singlet $\mathbf{1}$, meaning that pentaquark states can be colour neutral, indeed. The classification of pentaquark states constructed from up, down, and strange quarks can be read off the very same decomposition (8.3), now understood in terms of the group $\mathrm{SU}(3)_{\text{flavour}}$. This means that the fundamental triplet $\mathbf{3}$ and the conjugated triplet $\overline{\mathbf{3}}$ describe the three flavours of quarks and antiquarks, respectively. The decomposition (8.3) thus specifies the assignment of pentaquark states to several different multiplets. We will come back to this classification at the end of this section.

As mentioned before, while the existence of exotic hadrons has been recognized as a theoretical possibility since the early days of the quark model [19, 20, 21], experimental search programs at that time did not find any results confirming this hypothesis. Interest in pentaquark states was revived when a nonlinear chiral model, the SU(3) Skyrme model [213], could be used to predict the existence of

state	quark content	mass (MeV)	width (MeV)	reference
Θ^+	$udud\bar{s}$	1539 ± 2	≤ 1	[23]; [137, 217]
Ξ_5^{--}	$ddss\bar{u}$	1862 ± 2	< 18	[206]
Ξ_5^0	$ddss\bar{u}$	1862 ± 2	< 18	[206]
Θ^{++}	$uuud\bar{s}$	1528 ± 7	< 15	[208]
Θ_c^+	$udud\bar{c}$	3099 ± 8	≈ 12	[207]

Table 8.2
Experimental claims for pentaquark states. The status of the Θ^+ is not completely clear yet. Both states of the Ξ_5 and the charmed partner of the Θ^+, the Θ_c^+, have been found in only one experiment each, and are not confirmed by any other data. The Θ^{++} reported from STAR also needs confirmation.

an antidecuplet $\overline{\mathbf{10}}$ of hadronic states [214]. For the lightest member of the antidecuplet, the Θ^+, the model yields a mass of $1530\,\mathrm{MeV}$ with a small width of only $15\,\mathrm{MeV}$. In Skyrme-type models, hadrons are described as topologically nontrivial configurations of a chiral field. Nevertheless, a connection to the quark model can be established. Thus, the valence quark content of the Θ^+ is $uudd\bar{s}$—it is a pentaquark. The states of this antidecuplet in the plane of isospin projection T_3 and hypercharge Y are shown in the weight diagram 8.1. At the top of the multiplet, with strangeness $S = +1$ and baryon number $B = +1$, the pentaquark Θ^+ is manifestly exotic: It carries one antistrange quark, and with the positive baryon number, it can not be explained as an antihyperon.

This prediction has motivated a search for the Θ^+ in photon-nucleus collisions at the Laser-Electron Photon facility (LEPS) at SPring-8 in Japan. Indeed, in photoproduction on ^{12}C nuclei, a signal was found [23] corresponding to the reaction

$$\gamma + \mathrm{n} \longrightarrow \Theta^+ + \mathrm{K}^- \longrightarrow \mathrm{n} + \mathrm{K}^+ + \mathrm{K}^- \,, \tag{8.4}$$

where the final state kaons are measured and the neutron and the intermediate Θ^+ are reconstructed. The mass of the Θ^+ is found to be $1540 \pm 10\,\mathrm{MeV}$, with a small width of $15\,\mathrm{MeV}$. The result from LEPS were soon confirmed in experiments with photoproduction on nuclei [202], protons [203], and deuterons [204, 205]. Negative results of searches for isospin partners [215, 216] support the view that the Θ^+ is an isosinglet, and that its classification at the tip of the antidecuplet is indeed correct. The spin of the Θ^+ is not known experimentally. It is usually assumed to be $s = 1/2$, in accordance with the Skyrme model prediction. Furthermore, the parity of the Θ^+ is not known either. According to the Skyrme model, again, it is supposed to be positive. We will come back to these points at the end of this section.

The NA 49 collaboration at the CERN-SPS [206] has reported the identification of two states of the Ξ_5 isoquartet with strangeness $S = -2$ in proton-proton collisions. At a mass of $1862 \pm 2\,\mathrm{MeV}$ and width of $18\,\mathrm{MeV}$, the states Ξ_5^{--} and Ξ_5^0 were reconstructed from their decays into $\Xi^-\pi^-$ and $\Xi^-\pi^+$, respectively. The Ξ_5^{--}, located at the lower left of the antidecuplet in figure 8.1 with $S = -2$, is manifestly exotic, since the electric charge $Q = -2$ can not be reached by adding only one third quark to the two strange quarks. These experimental results are compiled in table 8.2, along with further data that will be discussed below.

However, experimental evidence for the existence of these pentaquark states is far from safe. Reviews of the experimental situation can be found, e. g. in

[217, 218, 219]. For the Ξ_5, there is criticism that the result is at odds with earlier data of the same experiment [220]. Moreover, a compilation in [218] lists nine experiments whose search for the Ξ_5 was negative, against no confirming data. One can conclude that the Ξ_5 states most probably do not exist. The situation for the Θ^+ is better: [217] lists ten experiments with positive signals, against eleven negative results. There is a general tendency that high-energy experiments, where the Θ^+ is expected to be produced through fragmentation, yield negative results. For example, all data from e^+e^- collisions show no signal of the Θ^+. If the positive results for the Θ^+ will survive further scrutiny, the production mechanism may yield valuable insights [221].

Suppression of the Θ^+ production in fragmentation may not exclude its production in ultra-relativistic heavy-ion collisions, where quark recombination seems to play an even more important role in hadronization at lower transverse momentum. With the STAR detector at RHIC, the identification of Θ^+ pentaquarks is possible in principle [222, 223]. However, preliminary results are ambiguous [224]. Very recently, data from deuteron-gold collisions are reported [208] that can be interpreted as signals of a Θ^{++} pentaquark, with a mass of $1530 \pm 7\,\mathrm{MeV}$. Note that if this result is confirmed, and if the Θ^{++} is indeed an isopartner of the Θ^+, then the classification of the Θ^+ as part of the antidecuplet is no longer possible. In this case, both particles belong to the isotriplet with $S = +1$ of the **27** representation of SU(3), and there is a not yet detected neutral partner Θ^0.

This reminds us that the antidecuplet is only one piece in the much larger multiplet structure of pentaquark states. Focussing temporary on flavour only and neglecting spin, we have seen that this multiplet structure is described by the decomposition (8.3). Taken all together, it contains $3^5 = 243$ states. The complete

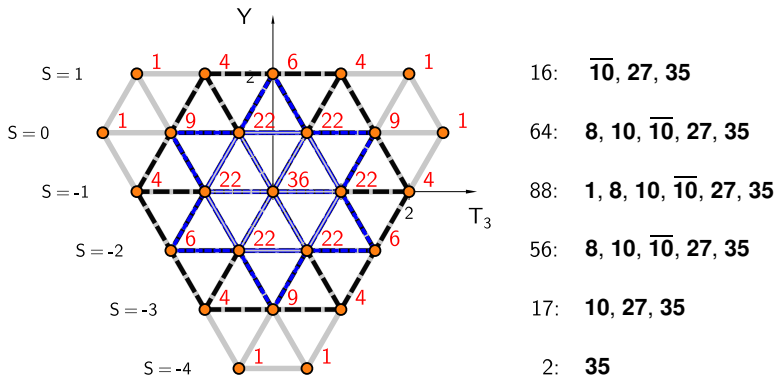

Figure 8.2
Pentaquark states of the simple quark model in the isospin-hypercharge plane, ignoring spin. The following multiplets of $\mathrm{SU}(3)_{\mathrm{flavour}}$ are shown in the figure: the **35** is indicated by grey lines, embracing the complete range in hypercharge Y and isospin projection T_3 of the possible states; the **27** is the symmetric multiplet shown with dotted lines; the **10** and $\overline{\mathbf{10}}$ are the blue triangles with tip down (**10**) and up ($\overline{\mathbf{10}}$), respectively; and the **8** is the central multiplet marked by the thin grey line. The singlet **1** is in the centre; it is not marked explicitly. Strangeness S and hypercharge Y are related by $Y = S + B$, where $B = 1$ is the baryon number. Electric charge follows according to the Gell-Mann–Nishijima relation $Q = T_3 + Y/2$. The list on the right specifies the multiplicity for a given strangeness, together with the contributing SU(3) multiplets.

scheme of these states in the isospin-hypercharge plane is shown in figure 8.2. The construction of the corresponding multiplets, both algebraically using Young tables and with a graphical method, is described in detail in the appendices B.6 and B.7. All irreducible multiplets occurring in the decomposition (8.3) are plotted separately in figure B.4. Accounting for spin is possible by a more elaborate analysis based on SU(6) for the combined degrees of freedom of flavour and spin. This scheme increases the overall number of states to 1260 (see appendix C.3, and the discussion in section 8.5), but yields a unique isosinglet with strangeness $S = +1$ and spin $s = 1/2$, which may be identified with the Θ^+.

The huge multiplet structure notwithstanding, most experimental facts and claims about pentaquarks can be accounted for with the antidecuplet $\overline{\mathbf{10}}$ alone. Only if the STAR data about the Θ^{++} are confirmed, the larger $\mathbf{27}$ would be needed to accommodate the isotriplet with strangeness $S = +1$. Other STAR data hint at a state that may be a N_5 or a Ξ_5^0 [224]. Even if confirmed, the classification of such a state is ambiguous, since it is not manifestly exotic: it may belong to the $\overline{\mathbf{10}}$, but it could be part of an octet $\mathbf{8}$ as well, or be some mixture of different representations. A discussion of possible strange and non-strange partners of the Θ^+ can be found in [225], and an overview over theoretical models of the multiplet structure of the $\overline{\mathbf{10}}$ is given in [226].

The plethora of states shown in figure 8.2 is most probably not realized in nature. However, we will use it when applying the qMD model to the formation of pentaquark states, because clusters formed in qMD will populate all multiplets. We will assume that those clusters mapped to states which do not exist in nature will decay immediately into a baryon and a meson.

Up to now, our discussion of pentaquark states was restricted to the three flavours up, down, and strange. The HERMES experiment at DESY has claimed the identification of a charmed pentaquark state [207], which is built from four light quarks and an anticharm quark. This state is the charmed partner of the Θ^+, where the antistrange quark is replaced by the anticharm quark, and is called the Θ_c^+. Its properties are listed in table 8.2. However, as for the NA 49's claim of the Ξ_5, the Θ_c^+ could not be found in any other experiment so far.

8.1.2 Pentaquarks: Model building

So far, we have not discussed any models of the internal structure of pentaquark states. Here, we will cover briefly some of the current ideas about the structure of the Θ^+ in the quark model. Much more details can be found in the reviews [227, 228], and in the "ideosyncratic overview" [229].

The first notion that may come to ones mind when considering the structure of the Θ^+ is a bound state of a neutron and a positive kaon. Then, however, the Θ^+ is above threshold, with

$$\delta m = m_{\Theta^+} - m_\mathrm{n} - m_{\mathrm{K}^+} \approx 105\,\mathrm{MeV}\ . \tag{8.5}$$

Furthermore, using (6.12), the γ factor of the radial motion of the kaon in the centre of momentum frame is

$$\gamma_{\mathrm{K}^+} = \frac{m_{\Theta^+}^2 + m_{\mathrm{K}^+}^2 - m_\mathrm{n}^2}{2 m_\mathrm{n} m_{\mathrm{K}^+}} = 1.13 \tag{8.6}$$

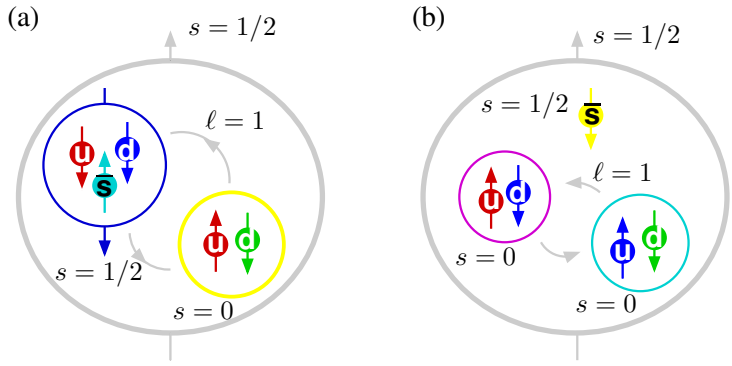

Figure 8.3
Models of coupling two up quarks, two down quarks, and one antistrange quark to a pentaquark with spin $s = 1/2$ and isospin $T = 0$: The Karliner-Lipkin model (a) couples an up-down diquark with a triquark. Both components are spatially separated due to the relative angular momentum $\ell = 1$. The total spin is $s = 1/2$, parity is $P = +1$. The Jaffe-Wilzcek model (b) couples the antistrange quark with two up-down isosinglet spin singlet diquarks. The diquarks are in relative p waves, so parity is also $P = +1$.

resulting in a kaon momentum in the centre of momentum frame of $p = 267\,\mathrm{MeV}$. Such a nK^+ molecule or resonance would be unstable and decay very quickly, causing a much bigger width than observed in experiments.

Thus, most models use an older idea [230, 231] that the quarks and the antiquark in the Θ^+ should arrange in groups which, different from the uud and $d\bar{s}$ in the nK^+ molecular model, carry colour charges and are bound together by strong colour electric forces. Two main models have been proposed along these line: the triquark-diquark model of Karliner and Lipkin [232], and the diquark model of Jaffe and Wilczek [233].

In the Karliner-Lipkin model, one up quark and one down quark couple to a diquark, which is a spin singlet and a $\overline{\mathbf{3}}$ of the decomposition $\mathbf{3} \otimes \mathbf{3} = \mathbf{6} \oplus \overline{\mathbf{3}}$ in both flavour and colour. The remaining two quarks and the antiquark form a triquark with spin $s = 1/2$. Concerning colour and flavour, the triquark is a $\mathbf{3}$ in colour and a $\overline{\mathbf{6}}$ in flavour of the decomposition (B.38), $\mathbf{3} \otimes \mathbf{3} \otimes \overline{\mathbf{3}} = \mathbf{15} \oplus \overline{\mathbf{6}} \oplus 2 \cdot \mathbf{3}$. Hence in colour, the triquark and the diquark can couple like a quark and an antiquark in a meson. In flavour, the $\overline{\mathbf{6}}$ combines with the $\overline{\mathbf{3}}$ to the $\overline{\mathbf{10}}$ of $\overline{\mathbf{6}} \otimes \overline{\mathbf{3}} = \mathbf{8} \oplus \overline{\mathbf{10}}$. In order to keep the two pairs of up and down quarks apart, the diquark and the triquark are in a relative p wave state, thus have orbital angular momentum $\ell = 1$. The configuration of the Karliner-Lipkin model is shown schematically in figure 8.3 (a).

In the Jaffe-Wilczek model, the four quarks are coupled to two diquarks of one up and one down quark each. As for the diquark in the Karliner-Lipkin model, both diquarks are supposed to be spin singlets and antitriplets $\overline{\mathbf{3}}$ in both flavour and colour. As colour is concerned, the two diquarks couple with the antiquark to a colour neutral state exactly as the three antiquarks in an antibaryon. Similarly, in flavour space, the coupling of two diquarks and the antiquark is analogous to the coupling of three antistrange quarks in the $\overline{\Omega}$. Again, mixing of the two pairs of up and down quarks is avoided by a relative orbital angular momentum $\ell = 1$ of the two diquarks. Even more so, it is required by the Pauli principle: The state of

the four quarks is $\mathbf{3}$ in colour, $\overline{\mathbf{6}}$ in flavour, and $\mathbf{1}$ in spin. In the completely antisymmetric spin-flavour-colour state of four quarks, the $\mathbf{3}$ for colour occurs together with $\mathbf{210}$ for spin-flavour, see (C.15). However, the spin-flavour $\mathbf{210}$ does not contain a contribution of a spin singlet combined with a $\overline{\mathbf{6}}$ in flavour, as can be seen e. g. from the tables in [234]. Thus, the state of two diquarks in the Jaffe-Wilczek model can be completely antisymmetric only if orbital excitation is involved. The Jaffe-Wilczek model is shown in figure 8.3 (b).

Due to the relative orbital angular momentum, both models predict a positive parity for the pentaquark states of the $\overline{\mathbf{10}}$,

$$P\left(q^4\bar{q}^1\right) \;=\; (1)^4(-1)^1(-1)^{(\ell=1)} \;=\; +1\;, \tag{8.7}$$

as does the SU(3) Skyrme model. Remember that parity, as well as spin, is not known experimentally. On the other hand, so-called uncorrelated quark models of the pentaquark, where all particles are in relative s waves [235], predict a negative parity, since the last factor in (8.7) is 1 for $\ell = 0$. When using qMD to search for pentaquark clusters in the hadronization stage of heavy ion collisions, we will assume for simplicity the uncorrelated quark model.

8.1.3 Other exotic states: Theory and experimental status in brief

So far we have not mentioned tetraquark and hexaquark states, the other exotic combinations of quarks and antiquarks listed in 8.1. Our qMD study will not include them in detail, although there are no principle obstacles, and an extension of the pentaquark analysis is straight-forward. However, for those states, the physical status, both experimental and theoretical, is not so clear-cut.

Concerning dimesons ($qq\bar{q}\bar{q}$ states), there are hints that some Lorentz-scalar mesons are in fact tetraquarks states. Candidates include the isoscalars $f_0(600)$ (the σ), $f_0(980)$, and the isovector $a_0(980)$. The $f_0(980)$ and $a_0(980)$ might be in fact some $K\overline{K}$ molecular states, just around threshold. However, studies of the decay of ϕ mesons favour a tetraquark structure for both $f_0(980)$ and $a_0(980)$ [236, 237]. In this case, they would be non-strange members of an octet built up from a spin-singlet diquark which is an antitriplet in colour and flavour, and a spin-singlet antidiquark which is a triplet in colour and flavour [19]. The recently discovered charmed-strange mesons $D^{\pm}_{sJ}(2317)$ and $D^{\pm}_{sJ}(2460)$ [238, 239, 240] are further interesting possible tetraquark states. If these states were simple $c\bar{s}$ mesons, they should have a higher mass and broader width. Again, there is the possibility that they are molecules of D-mesons with kaons, DK and DK^*, respectively [241]. However, the interpretation as a $cq\bar{q}\bar{q}$ tetraquark [242], where q stands for an up, down, or strange quark, is generally preferred. A topical review of all these issues can be found in [243] and [137, section "non-$q\bar{q}$ mesons" on p. 848 ff].

For baryonia ($qqq\bar{q}\bar{q}\bar{q}$ states), the situation is even more ambigous. The situation up to 1999 is reviewed in [244]. A chinese experiment reports the discovery of a narrow $p\bar{p}$ resonance just below threshold [245], which does not correspond to any known particle and could be a baryonium state of up and down quarks and antiquarks with spin $s = 0$ and isospin $T = 0$, a protonium. Furthermore, there is a prediction of a $uds\bar{u}\bar{d}\bar{s}$ state, also with $s = 0$ and $T = 0$, and a mass of only

$1210\,\mathrm{MeV}$ [246]. This so-called Y-baryonium may be produced from the baryon-free quark-gluon plasma created in ultra-relativistic heavy-ion collisions.

Finally, for dibaryons, there is no experimental clue so far that they exist at all. Of course, the deuteron d, with quark content $qqqqqq$, spin $s = 1$, and isospin $T = 0$, can be considered as a hexaquark configuration [247]. However, it is clearly a bound state of a well-defined neutron and proton, with a binding energy of 0.00239 proton masses. The most prominent other dibaryon is the isoscalar H-dibaryon ($qqsqqs$, with $s = 0, T = 0$, a $\Lambda\Lambda$ state), which has been predicted nearly 30 years ago [248], but has never shown up in experiment. Other states include the d'-dibaryon ($qqqqqq$, with $s = 0, T = 0$, a NN state [249]) the $d^\star$-dibaryon ($qqqqqq$, with $s = 3, T = 0$, a $\Delta\Delta$ state [250]), and the di-Ω-dibaryon ($ssssss$, with $s = 0, T = 0$ [251]). Besides of missing empirical evidence, these last three states suffer from ambiguitites also on the side of theory, for example concerning masses, widths, or structure. However, there are estimates that the d' may be detectable in heavy-ion collisions [252], and chances are even better for the dibaryons with strangeness [253], such as the H-dibaryon [254] and the di-Ω [255]. In our qMD study, we give only overall yields for these hexaquark states without further, detailed analysis.

Before presenting these results, the following section describes how the qMD model is modified in order to study the formation of exotic hadronic states, and gives a short discussion of the capabilities and limit of our approach.

8.2 The qMD model adopted to the study of exotica

In chapter 6, we have described how we use the qMD model in order to simulate heavy-ion collisions for systems at CERN-SPS energies: The hadronic transport code UrQMD provides a distribution of hadrons, hadronic resonances, and preformed hadrons at maximal overlap of the colliding nuclei. The decomposition of all these particles into their valence quark content is then used as the initial condition for the further time evolution of the system within the qMD model according to the Hamiltonian (4.1). The dynamics of qMD results in the formation of colour neutral quark clusters. In the model studies of chapter 6 and chapter 7, quark-antiquark clusters and clusters of three quarks or three antiquarks have been mapped to hadrons and hadronic resonances as listed in the Particle Data Book, taking into account the quantum numbers of spin, isospin, and strangeness. The subsequent decay of the resonances has yielded the final state hadron distributions.

In this chapter, we extend the search for colour neutral clusters to include all possible combinations of up to six quarks and/or antiquarks, as listed in table 8.1. All other criteria to recognize a colour neutral cluster are exactly the same as described in section 4.2. The search for colour neutral pentaquark states has been shown in figure 4.5. Note that the implementation of the cluster search disfavours the identification of exotic clusters which could be easily split in two standard hadrons: In such a case, the cluster search would identify a group of two or three colour charges as colour neutral, and stop there. Thus, standard mesons or baryons would be found. This corresponds to the idea mentioned before that exotic hadrons should contain correlations of three quarks or a quark-antiquark pair only if these

are not colour singlets. Other than in chapter 6 and chapter 7, we do not handle the mapping of identified colour neutral clusters to hadronic states: We will just consider all such clusters as non-interacting with the rest of the system. This restriction releases us from the task of taking care of the essentially unknown mass spectrum of exotic states. However, we will gain information about mass distribution of clusters. Thus, we can study gross properties of the clusters, such as mass, four-momentum, space-time coordinates of the centre of mass of the emerging cluster. Furthermore, we obtain rapidity distributions, transverse momentum spectra, and times and radii of cluster formation. Most important, quantum numbers of the cluster such as strangeness and isospin can be calculated from coupling the corresponding quantum numbers of the quarks and antiquarks making up the cluster. This allow its identification as a candidate for the formation of specific exotic hadrons. Focussing eventually on pentaquark clusters, we will study the distribution of strangeness over these clusters.

Of course, we can not predict masses or widths of multi-quark clusters. This is not possible with a Hamiltonian as simplistic as ours, and without quantum mechanics. Also, we can not say whether a multi-quark cluster is stable, i. e. corresponding to some exotic state, or will never form in a more realistic simulation. What our model can describe, however, is the dynamical formation of colour neutral clusters which are the precondition for the formation of hadrons. Thus, the rationale is the following: Exotic clusters produced in qMD may not correspond to physically stable states — in fact, most will not, since qMD will populate the full multiplet structure, which is not realized in nature. But, on the other hand, every exotic hadron should stem from a colour neutral quark cluster as described by qMD. This is, in a nutshell, the idea of hadronization via the recombination of quarks. We suppose that all colour neutral clusters without correspondence to real hadronic states are spurious and will be artifacts of our simplified model. Physically speaking, we can imagine that these colour neutral groups of quarks would arrange themselves in a way to form existing hadronic and exotic states.

Thus, in order to make concrete predictions about numbers, the big unknown factor is which multiplets are realized in nature. For the pentaquark states, for example, the issue is whether other pentaquark multiplets besides the antidecuplet may contain stable particles. When deriving estimates for the possible number of Θ^+ created at hadronization, we will suppose that, according to current knowledge, the Θ^+ is an isosinglet with spin $s = 1/2$, which makes it unique in the spin-flavour $\mathrm{SU}(6)$ coupling scheme (see appendix C.3), and allows for 2 out of 243 states in the flavour $\mathrm{SU}(3)$ scheme.

We will run the qMD code with the search for exotic clusters for full SPS events and for hadronization from a cylindrical slice, initialized with a thermal distribution of quarks and antiquarks with $T = 250\,\mathrm{MeV}$ and $\mu = 0\,\mathrm{MeV}$. The radius of the slice is $R = 8\,\mathrm{fm}$, and the width is $d = 1\,\mathrm{fm}$, resulting in a volume of $V_0 \approx 200\,\mathrm{fm}^3$. There is no velocity profile superimposed to the thermal motion of the quarks and antiquarks in the initial state. The thermal initial condition is chosen in order to fit the situation at RHIC where a full simulation of all quarks involved exceeds the available computing power when trying to get enough statistics. SPS collisions of Pb+Pb are studied at $30\,\mathrm{GeV}/N$ ($\sqrt{s}_{NN} = 7.8\,\mathrm{GeV}$), $80\,\mathrm{GeV}/N$ ($\sqrt{s}_{NN} = 12.3\,\mathrm{GeV}$), and $160\,\mathrm{GeV}/N$ ($\sqrt{s}_{NN} = 17.3\,\mathrm{GeV}$), thus spanning the

energy range of the experiment from the lowest energy where talking about deconfined quarks may be sensible to the upper energy limit of the machine. The impact parameter is fixed at $b = 2\,\mathrm{fm}$ for all simulations, corresponding to the class of 5 % most central collisions.

8.3 qMD results for the formation of exotic clusters

Table 8.3 shows the abundances of clusters with up to six quarks and/or antiquarks produced using the four different initial conditions for full SPS and thermal systems. Numbers in brackets indicate percentages of the total hadronic yield. Keep in mind that here and in the following, hadronic yield means colour neutral clusters, without mapping to specific hadronic states or resonances, and without final decay

hadronic state		SPS: Pb + Pb, $b = 2\,\mathrm{fm}$ 30 GeV/N		80 GeV/N		160 GeV/N		thermal events: $T_0 = 250\,\mathrm{MeV}$, $\mu_0 = 0\,\mathrm{MeV}$	
mesons:	$N_{\mathrm{m}}^{(6)}$	1160.0	(72.7 %)	1900.0	(77.8 %)	2460.0	(80.1 %)	235.0	(77.3 %)
baryons:	$N_{\mathrm{b}}^{(6)}$	273.0	(17.2 %)	296.0	(12.2 %)	302.0	(9.8 %)	15.6	(5.0 %)
antibaryons:	$\overline{N}_{\bar{\mathrm{b}}}^{(6)}$	4.1	(0.25 %)	15.0	(0.60 %)	25.8	(0.9 %)	15.6	(5.2 %)
dimesons:	$N_{\mathrm{d}}^{(6)}$	67.3	(4.2 %)	119.0	(4.9 %)	156.0	(5.1 %)	17.2	(5.7 %)
pentaquarks:	$N_{\mathrm{p}}^{(6)}$	64.4	(4.1 %)	72.2	(3.0 %)	78.2	(2.5 %)	6.5	(2.2 %)
antipentaquarks:	$\overline{N}_{\bar{\mathrm{p}}}^{(6)}$	0.8	(0.05 %)	3.33	(0.10 %)	6.3	(0.2 %)	6.5	(2.2 %)
dibaryons:	$N_{\mathrm{bb}}^{(6)}$	10.0	(0.6 %)	10.5	(0.40 %)	10.3	(0.3 %)	0.7	(0.2 %)
antidibaryons:	$\overline{N}_{\mathrm{bb}}^{(6)}$	0.0	(0.0 %)	0.01	(0.0 %)	0.06	(0.0 %)	0.6	(0.2 %)
baryonia:	$\overline{N}_{\mathrm{b\bar{b}}}^{(6)}$	13.6	(0.9 %)	24.2	(1.0 %)	32.2	(1.1 %)	6.0	(2.0 %)

Table 8.3
Abundances per event of clusters corresponding to hadronic states with up to six quarks and/or antiquarks for different conditions. The initial volume of the thermal system is $V_0 = 100\,\mathrm{fm}^3$. Note that the mapping to specific hadrons or resonances and final state decays of resonances are not included. Furthermore, the numbers given for SPS events do not include spectators.

hadronic state		SPS: Pb + Pb, $b = 2\,\mathrm{fm}$ 30 GeV/N		80 GeV/N		160 GeV/N		thermal events: $T_0 = 250\,\mathrm{MeV}$, $\mu_0 = 0\,\mathrm{MeV}$	
mesons:	$N_{\mathrm{m}}^{(3)}$	1400.0	(79.4 %)	2280.0	(84.8 %)	2960.0	(87.1 %)	300.0	(86.4 %)
baryons:	$N_{\mathrm{b}}^{(3)}$	358.0	(20.3 %)	390.0	(14.5 %)	402.0	(11.9 %)	23.6	(6.8 %)
antibaryons:	$\overline{N}_{\mathrm{b}}^{(3)}$	5.2	(0.3 %)	18.9	(0.7 %)	33.4	(1.0 %)	23.6	(6.8 %)

Table 8.4
Reference abundances per event of non-exotic hadronic states of up to three quarks and/or antiquarks for the same initial conditions as listed in table 8.3. Again, mapping to specific hadrons and resonance decay as are not taken into account.

of resonances. We have analysed data from 300 simulation events at $30\,\mathrm{GeV}/N$, 200 events each at $80\,\mathrm{GeV}/N$ and $160\,\mathrm{GeV}/N$, and 2000 thermal events. For later reference, table 8.3 shows the numbers of standard mesons, baryons, and antibaryons for the same initial conditions, but obtained with a search for clusters of up to three quarks and/or antiquarks only. This is indicated by the notation ${N_i}^{(3)}$ for the different particle classes, as opposed to the notation ${N_i}^{(6)}$ in the extended search. The total number of quarks and antiquarks is the same for both simulations, but the distribution over the different types of clusters is different.

The first remarkable fact about table 8.3 is the large number of exotic states produced, with tetraquarks and pentaquarks outnumbering the antibaryons at SPS energies. The thermal events are initialized with zero chemical potential, hence there are equal numbers of baryons and antibaryons, pentaquarks and antipentaquarks, and so on. Most interestingly, the number of dimeson states is larger than the number of baryon states, and 2 % of the clusters correspond to baryonia! However, one has to keep in mind that these clusters populate the huge multiplet structures of exotic hadrons, whereas only some of these states really exist in nature. For pentaquark states, we will discuss this point in detail in the following section 8.4. Here, we will briefly comment on the dibaryon and baryonia results. When proceeding from the overall yield of these hexaquark clusters to specific states, the reduction in number is by more than two orders of magnitude.

Table 8.5 lists in detail the total yields for dibaryon clusters with quantum numbers of the deuteron d, the d' dibaryon, the $d^\star$ dibaryon, and the H dibaryon. Remember that cluster quantum numbers are calculated by coupling the quantum numbers of the recombining quarks and antiquarks. The dibaryon yields drop with increasing energy, which is to be expected since the chemical potential is going down, and the systems under consideration become more end more baryon-free. At SPS energies, the ratio of deuterons to all dibaryons is remarkably high, accounting for roughly 4 % of the total dibaryon yield. It drops with increasing energy, and is only 2 ‰ for the thermal system. This high share of deuterons in the qMD data for dibaryons at SPS energies can be interpreted as a remaining quark correlation, stemming from the protons and neutrons of the UrQMD input. The decomposition of baryons with isospin $T = 1/2$ into quarks induces an antiferromagnetic corre-

hadronic state		SPS: Pb + Pb, $b = 2$ fm						thermal events: $T_0 = 250\,\mathrm{MeV}$, $\mu_0 = 0\,\mathrm{MeV}$	
		30 GeV/N		80 GeV/N		160 GeV/N			
dibaryons:	$N_{\mathrm{bb}}^{(6)}$	10.0	(0.6 %)	10.5	(0.40 %)	10.3	(0.3 %)	0.7	(0.2 %)
deuterons:	$N_{d}^{(6)}$	0.40	(0.25 ‰)	0.41	(0.17 ‰)	0.35	(0.11 ‰)	0.0015	(0.005 ‰)
d' dibaryons:	$N_{d'}^{(6)}$	0.07	(0.04 ‰)	0.13	(0.05 ‰)	0.09	(0.03 ‰)	0.0005	(0.002 ‰)
$d^\star$ dibaryons:	$N_{d^\star}^{(6)}$	0.07	(0.04 ‰)	0.04	(0.01 ‰)	0.05	(0.02 ‰)	0.0000	(0.000 ‰)
H dibaryons:	$N_{\mathrm{H}}^{(6)}$	0.003	(0.002 ‰)	0.01	(0.004 ‰)	0.02	(0.005 ‰)	0.002	(0.008 ‰)

Table 8.5
Abundances per event of dibaryon clusters corresponding to the deuteron, the $d'-$ and $d^\star$-dibaryon, and the H-dibaryon. Statistics is poor, especially for the thermal events.

lation among the isospin projection T_z of these quarks. This correlation favours a lower isospin of clusters formed by quark recombination than would be expected in an uncorrelated situation. A similar phenomenon will be studied with better statistics in the strangeness distribution of pentaquarks in the next section 8.4. For spin and isospin, it is observed again in the distribution of pentaquark states from clustering over these quantum numbers, as we will see in section 8.5.

Deuteron yields have been measured at both the SPS and at RHIC. For central Pb+Pb collisions at beam energies of $160\,\mathrm{GeV}/N$ and $80\,\mathrm{GeV}/N$, the NA49 collaboration has measured the number density per rapidity of deuterons [256, 257] as $\mathrm{d}n_d/\mathrm{d}y \approx 0.3$ and $\mathrm{d}n_d/\mathrm{d}y \approx 0.6$, respectively. Lowering the collision energy increases this number further, which is consistent with AGS data. Note that this trend is also visible in the qMD data. However, the absolute ratios of deuterons to all hadrons differ markedly: In central collisions with the energy $160\,\mathrm{GeV}/N$, the number density of negatively charged hadrons is $\mathrm{d}n_{\mathrm{h}^-}/\mathrm{d}y \approx 200$ [258], corresponding to a total yield for all hadrons of roughly $\mathrm{d}n_{\mathrm{h}}/\mathrm{d}y \approx 600$. Hence, deuterons make up about $0.5\,‰$ of all hadrons at mid-rapidity in central collisions with $E = 160\,\mathrm{GeV}/N$, which is higher than the relative number of $0.11\,‰$ found in the qMD simulation. Since the qMD calculation does not yet include final resonance decays in the total number of hadrons, this value should even be lowered further. Note that here, we compare mid-rapidity ratios at the SPS with total ratios from qMD. However, for the rough estimate used here, this difference can be neglected. In Au+Au collisions at $\sqrt{s}_{NN} = 200\,\mathrm{GeV}$, the PHENIX collaboration [259] has found $\mathrm{d}n_d/\mathrm{d}y \approx 0.07$ for deuterons in the $20\,\%$ most central collisions. The number density of charged particles in this centrality is roughly $\mathrm{d}n_{\mathrm{ch}}/\mathrm{d}y \approx 650$ [260]. Estimating the total number density of particles as $\mathrm{d}n/\mathrm{d}y \approx 1000$, this amounts to a relative yield of deuterons compared to all hadrons of $\approx 0.07‰$. In comparison, the relative number of deuterons is $\approx 0.005‰$ only in the thermal qMD simulation. Again, this number has to be lowered further when resonance decays are taken into account.

Taken all together, the qMD estimate for the deuteron yield from clustering is about one order of magnitude below the measured value at the SPS, and even more so at RHIC. However, one has to keep in mind that all deuteron data are explained very well by coalescence of protons and neutrons after hadronization. This is sensible, since the deuteron is only weakly bound compared to the H-dibaryon, for example. Thus, the qMD result is not refuted by the deuteron data. But it makes clear that our qMD clustering results for exotica have to be taken with a grain of salt: rescattering effects may play an important role, both destroying these particles, and creating them through hadronic coalescence. However, these processes are completely neglected in our study, which focusses solely on "primordial" exotic clusters, which are created by quark recombination.

Compared to the deuteron, the d' and the $d^\star$ dibaryons are suppressed by a factor which changes from ≈ 6 at lower SPS to ≈ 3 for the thermal system. Note that from the uncorrelated coupling of 6 spin doublets, $\mathbf{2} \otimes \mathbf{2} \otimes \mathbf{2} \otimes \mathbf{2} \otimes \mathbf{2} \otimes \mathbf{2} = \mathbf{7} \oplus 5 \cdot \mathbf{5} \oplus 9 \cdot \mathbf{3} \oplus 5 \cdot \mathbf{1}$, the abundance of the spin singlet d' states should be 5/9 of the abundance of the spin triplet deuteron. The difference of the d'/d ratio from qMD data to uncorrelated coupling may again be a hint at remaining quark correlations surviving in qMD from the UrQMD input.

hadronic state		SPS: Pb + Pb, $b = 2\,\mathrm{fm}$						thermal events: $T_0 = 250\,\mathrm{MeV}$, $\mu_0 = 0\,\mathrm{MeV}$	
		30 GeV/N		80 GeV/N		160 GeV/N			
baryonia:	$N^{(6)}_{\mathrm{b\bar{b}}}$	13.6	(0.86 %)	24.2	(1.0 %)	32.2	(1.1 %)	6.0	(2.0 %)
protonium:	$N^{(6)}_{p\bar{p}}$	0.2	(0.1 ‰)	0.2	(0.1 ‰)	0.3	(0.1 ‰)	0.005	(0.02 ‰)
Y-baryonium:	$N^{(6)}_{\mathrm{Y}}$	0.02	(0.01 ‰)	0.02	(0.01 ‰)	0.08	(0.03 ‰)	0.010	(0.04 ‰)

Table 8.6
Abundances per event of baryonium clusters corresponding to the protonium and the Y-baryonium. Statistics is poor, especially for the thermal events. However, the relative abundance of baryonia clearly shows the increase in the thermal system with $\mu = 0$ over the SPS systems.

The yield for the H-dibaryon is even smaller than for the d' and the $d^\star$ at SPS energies. On the order of $2 \cdot 10^{-6}$ of all hadronic clusters, it increases with energy. This increase is plausible since the strangeness content of the quark system increases with energy. In the thermal system, the contribution of the H-dibaryon to all hadrons is comparable to the thermal deuteron yield. However, conclusions about the detectability at RHIC are difficult to draw. As discussed before, deuterons are special because of their low binding energy and high production rate through hadronic coalescence. Besides, the H-dibaryon has to be reconstructed from its decay products. A detailed discussion can be found in [261]. Nevertheless, the qMD estimate supports the view that H-dibaryons stemming from quark recombination may be detected at RHIC, if they exist.

Table 8.6 indicates the numbers for the baryonium clusters corresponding to the Y-baryonium and the protonium. Baryonia are more abundant than dibaryons by a factor of 2–3 at SPS energies. In the thermal system, they occur 10 times more often than dibaryons, contributing $2\,\%$ of all hadrons. This, again, is a consequence of the vanishing chemical potential in the thermal system, since baryonia have baryon number $B = 0$. At SPS energies, protonium states make up roughly $1\,\%$ of all baryonia. This share is only $1\,‰$ in the thermal system. In contrast, the Y-baryonium, which is about one order of magnitude more rare than the protonium at SPS energy, is more abundant than the protonium in the thermal system. Here, it accounts for $0.04\,‰$ of all hadronic clusters and $2\,‰$ of all baryonia. The total abundance per event of the Y-baryonium can be read off immediately from table 8.6 for SPS energies, growing from 0.02 to 0.08. For RHIC, we can obtain an estimate using the relative contribution of $0.04\,‰$ of all hadrons from qMD and the total number of produced particles of about 7000 in central Au+Au collisions at $\sqrt{s}_{NN} = 200\,\mathrm{GeV}$, yielding ≈ 0.15 Y-baryonia per event. These numbers can be compared with the result of the thermal model estimates in [246]: The general trend is the same, but the thermal model numbers are consistently higher by about one order of magnitude than the qMD quark recombination data. This is a marked difference between the thermal model and quark recombination.

More detailed qMD studies of dibaryon and baryonium states would provide us with interesting information. Yields and distributions in rapidity and momentum could serve as indications for possible experimental search programs. Furthermore, the results could shed more light on the relations between the thermal model

and quark recombination. However, a much higher statistics of qMD data will be needed to obtain reliable, quantitative results. For this reason, we will not discuss hexaquark states in more detail here.

Concerning tetraquarks, the abundances listed in table 8.3 are very high, reaching $\approx 5\,\%$ of the total hadron yield. We have to keep in mind that most of these states do not correspond to real particles. This reduces the dimeson yield drastically. Here, we do not study dimeson states at all. The light scalar meson tetraquark candidates are mostly too wide to be studied in heavy-ion experiments. So far, there is only an analysis of the $f_0(980)$ [262]. However, the strange-charmed states $D_{sJ}^{\pm}(2317)$ and $D_{sJ}^{\pm}(2460)$ may be more interesting objects of further investigation: With their quark content, one might expect them to be produced much more copiously through quark recombination from a deconfined medium than in lepton or hadron collider experiments. If these particles are in fact tetraquarks, production by recombination should be more efficient than through fragmentation, and leave observable traces in the transverse momentum distribution. Such a study is possible in qMD in principle and will be interesting for the future, but here, no analysis of D_{sJ} states has been done yet.

Turning finally to pentaquarks, the overall numbers listed in table 8.3 are, again, very high. They suggest that the chances to observe such states are best at lower SPS energies, where $\approx\ 4\,\%$ of all hadronic clusters in qMD are pentaquarks. Here, the percentage of these exotic states is highest, and moreover, the total number of particles produced is smaller, enhancing the chances to reconstruct pentaquarks from their decay products. But also for the thermal system, $\approx 2\,\%$ of all clusters still are pentaquarks.

To avoid wrong conclusions from the abundance of pentaquark clusters given in table 8.3, we recall once more that most of these clusters which are produced in qMD simulations do not correspond to possibly stable pentaquark states in nature. As mentioned before, in a more realistic treatment, these spurious clusters should be dissolved again, with the quarks involved clustering later in other combinations. For specific pentaquark states such as the Θ^+, this results in a reduction which can be estimated roughly by the size of complete pentaquark flavour multiplet structure, which contains $3^5 = 243$ states. Of course, a detailed analysis of the quantum numbers of the pentaquark clusters is necessary before conclusions about abundances for specific states are possible. Such an analysis for the Θ^+ will be presented in detail in the following sections 8.4–8.6.

In order to identify exotic states in experiment, besides the overall abundances, the distribution over rapidity is important, since it may offer hints which kinematic region of the collision events offer the best chances to find the needle in the haystack of all hadronic tracks. We will turn to this point now and present qMD results of the detailed dynamics of the expansion of the quark system and the formation of colour neutral clusters, including exotica.

8.3.1 Rapidity distribution of exotic clusters

Figure 8.4 shows the rapidity distribution of all clusters with up to six quarks and/or antiquarks for SPS initial conditions with beam energies of $30\,\mathrm{GeV}/N$ (top) and $160\,\mathrm{GeV}/N$ (bottom). The vertical bars indicate the rapidities of projectile and

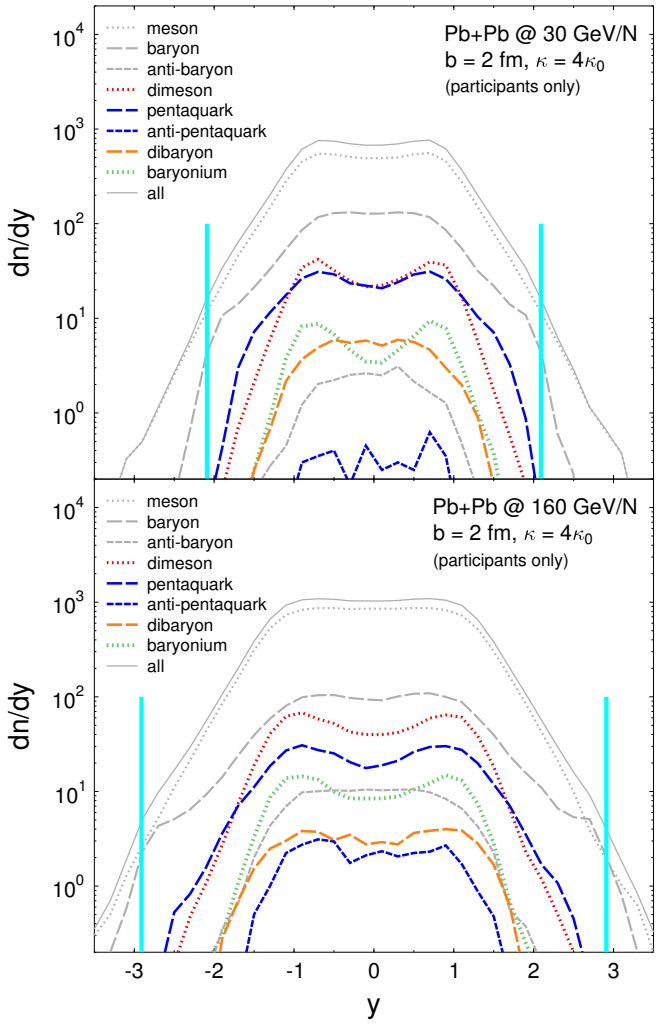

Figure 8.4
Rapidity distribution of clusters with different quark content for SPS initial conditions with beam energies of 30 GeV/N (top) and 160 GeV/N (bottom). Spectators are not included. The rapidities of projectile and target are marked by vertical bars.

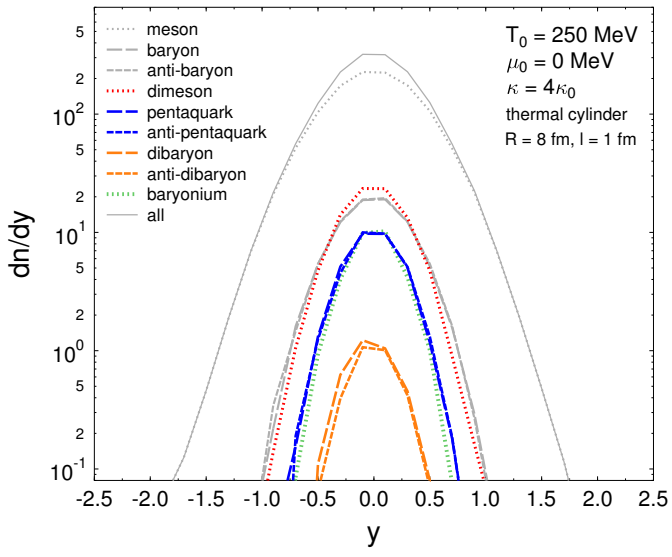

Figure 8.5
Rapidity distribution of clusters of different quark content from thermal initial conditions. The initial quark system fills a cylindrical space with a volume of $V_0 \approx 200\,\mathrm{fm}^3$ and has temperature $T = 250\,\mathrm{MeV}$ and chemical potential $\mu = 0\,\mathrm{MeV}$.

target in the centre of momentum frame. Spectators are not included. The most interesting feature in the plots are the high shoulders of the dimeson, pentaquark and baryonia distributions. They are more prominent at $30\,\mathrm{GeV}/N$ than at $160\,\mathrm{GeV}/N$ and located away from mid-rapidity about $\Delta y \approx \pm 0.8$ and $\Delta y \approx \pm 1.2$, respectively. They roughly coincide with the edges of the central plateau in the total cluster distribution.

The qMD results for rapidity distributions obtained with thermal initial conditions simulating the central region of a collision at RHIC are shown in figure 8.5. They are qualitatively different from the SPS results: Here, the distributions of larger clusters scale roughly with the distributions of mesons and baryons. Note that no realistic shapes of the rapidity distributions can be obtained because of the special choice of the thermal initial conditions. However, properly scaled multiplicities at mid-rapidity and total abundances can be compared with RHIC data.

Leaving all information contained in these plots about tetraquark and hexaquark states for other studies, we want to focus now on the pentaquark data. The enhancement of pentaquarks compared to mesons and baryons at the edges of the central plateau of the total hadron distributions becomes more obvious when it is related to the distributions expected from naive coalescence. In a simple coalescence picture in rapidity space, we would expect that the rapidity distribution of pentaquarks when searching for clusters of up to six quarks and antiquarks, $\mathrm{d}N_{\mathrm{p}}{}^{(6)}/\mathrm{d}y$, follows roughly the product of the distributions of mesons and baryons when searching only for clusters of three colour charges, $\mathrm{d}N_{\mathrm{m}}{}^{(3)}/\mathrm{d}y$ and $\mathrm{d}N_{\mathrm{b}}{}^{(3)}/\mathrm{d}y$. As a consequence of simple chemical reaction dynamics for the production of pentaquarks, we would thus expect

$$\frac{\mathrm{d}N_{\mathrm{p}}^{(\mathrm{naive})}}{\mathrm{d}y} \approx C \cdot \frac{\mathrm{d}N_{\mathrm{m}}^{(3)}}{\mathrm{d}y} \cdot \frac{\mathrm{d}N_{\mathrm{b}}^{(3)}}{\mathrm{d}y}\,, \tag{8.8}$$

where C is a normalization constant making sure that the total cluster content in the product distribution equals the total number of pentaquark clusters. Figures 8.6 and 8.7 show the comparison between the distributions $\mathrm{d}N_{\mathrm{p}}{}^{(6)}/\mathrm{d}y$ and $\mathrm{d}N_{\mathrm{p}}{}^{(\mathrm{naive})}/\mathrm{d}y$ for the SPS and thermal events,respectively. The distributions for pentaquarks are the same as in figures 8.4 and 8.5. Both figures also show the distributions of mesons and baryons in the reference data sets, which have been scaled down from $\mathrm{d}N_{\mathrm{m}}{}^{(3)}/\mathrm{d}y$ and $\mathrm{d}N_{\mathrm{b}}{}^{(3)}/\mathrm{d}y$ by constant factors α_{m} and α_{b} such that the integrals over rapidity equal the number of pentaquark clusters, i. e. with $\alpha_{\mathrm{m}} = N_{\mathrm{m}}{}^{(3)}/N_{\mathrm{p}}{}^{(6)}$ and $\alpha_{\mathrm{b}} = N_{\mathrm{b}}{}^{(3)}/N_{\mathrm{p}}{}^{(6)}$.

In the SPS data in figure 8.6, the pentaquark distribution $\mathrm{d}N_{\mathrm{p}}{}^{(6)}/dy$ is lower than the scaled product distribution (8.8) from naive coalescence in the rapidity region of the central plateau. Consequently, it is markedly higher in the rapidity range between the plateau and projectile and target rapidities. At the upper SPS energy, the pentaquark distribution follows quite well the scaled distribution of mesons, $\alpha_{\mathrm{m}}\mathrm{d}N_{\mathrm{m}}{}^{(3)}/\mathrm{d}y$. In contrast, the thermal data for the rapidity distribution in figure 8.7 show a nearly perfect agreement between the pentaquark distribution and the expectation from the naive coalescence.

The difference between the full SPS events and the thermal initial condition indicates that the details of the initial state and full dynamics of the expanding system play an important role for the rapidity distribution of pentaquark clusters.

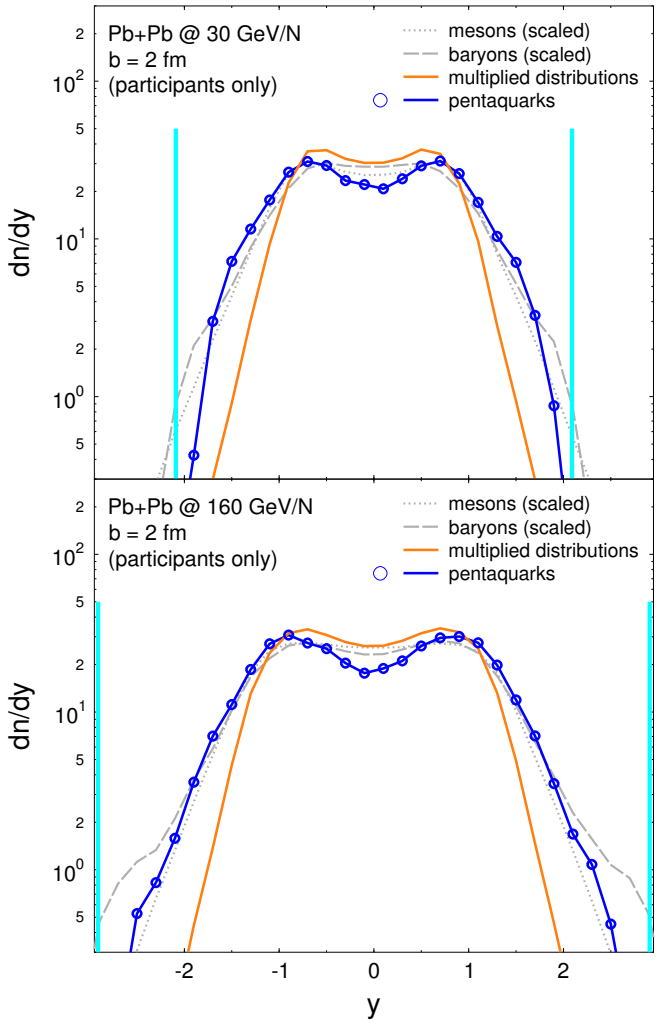

Figure 8.6
Rapidity distributions of pentaquarks compared to the distributions expected from naive coalescence for SPS initial conditions with beam energies of 30 GeV/N (top) and 160 GeV/N (bottom). Pentaquarks are suppressed compared to the coalescence distribution in the region of the central plateau, and exceed the expectation from coalescence between the plateau and projectile and target rapidities. For the beam energy of 160 GeV/N, the pentaquark distribution follows quite well the scaled meson distribution in this later region in rapidity space.

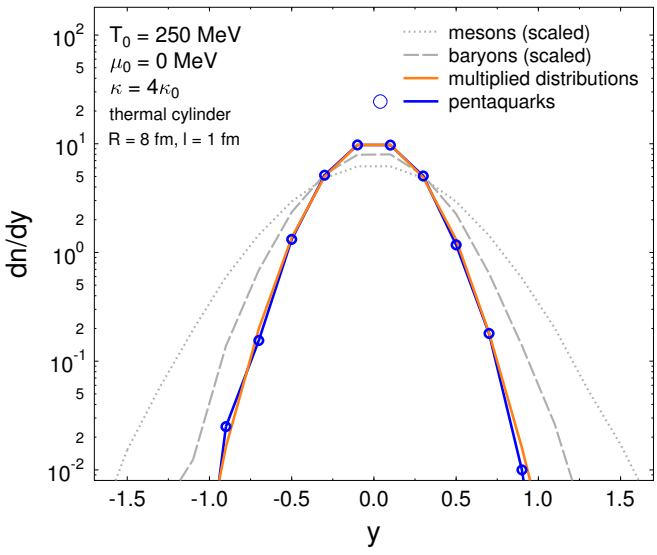

Figure 8.7
The rapidity distributions of pentaquarks for thermal initial conditions shows a nearly perfect agreement with the distribution expected from naive coalescence.

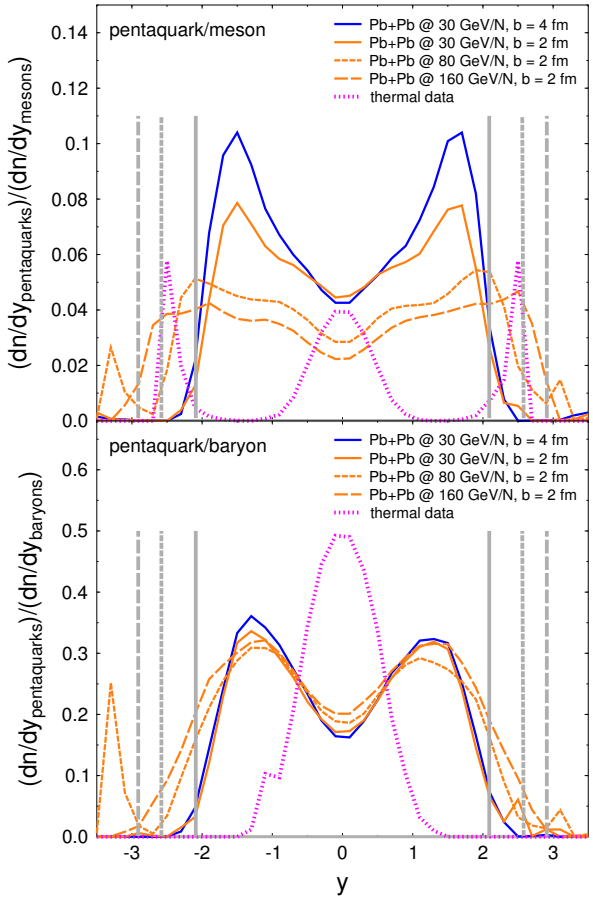

Figure 8.8
Rapidity distributions of pentaquark clusters scaled to the distribution of mesons (upper figure) and baryons (lower figure) for the different systems under consideration. The most prominent feature is the high ratio of pentaquarks to baryons at all SPS energies at $\approx \Delta y = \pm 1.5$ from mid-rapidity. Note that the thermal system does not include the dynamics of a full collision event.

The reason may be found in flow effects, but to find a definitive answer will require a more detailed study than is done here. However, we conclude that our qMD simulation suggests that the best option to find pentaquarks in heavy ion collision experiments may be found in the kinematic regions between projectile and target rapidity and the central plateau in rapidity space.

This is highlighted again in figure 8.8. Here, the rapidity distributions of pentaquark clusters for the different systems are scaled to the distribution of mesons and baryons, respectively. The upper part of the figure shows the ratio $(\mathrm{d}N_{\mathrm{p}}{}^{(6)}/dy)/(\mathrm{d}N_{\mathrm{m}}{}^{(6)}/dy)$ as a function of rapidity, the lower part the ratio $(\mathrm{d}N_{\mathrm{p}}{}^{(6)}/dy)/(\mathrm{d}N_{\mathrm{b}}{}^{(6)}/dy)$. The scaling to mesons is nearly constant for SPS beam energies of $80\,\mathrm{GeV}/N$ and $160\,\mathrm{GeV}/N$, but has a strong enhancement at $\approx \Delta y = \pm 1.5$ from mid-rapidity for the lowest SPS energy. Furthermore, this enhancement is larger for less central collisions, as shown by the data with impact parameter $b = 4\,\mathrm{fm}$. In the scaling to baryons, the remarkable enhancement around $\approx \Delta y = \pm 1.5$ is roughly the same for all SPS data. This feature is especially interesting for the experimental identification of pentaquarks, since they have to be reconstructed from the baryon and meson to which they decay. The reconstruction can be achieved best in a kinematical region where the background of other baryons and mesons is as low as possible, hence where the ratios plotted in figure 8.8 are highest. Note

that the ratio for the thermal system are difficult to interpret in a similar manner since the simulations do not include the full three-dimensional dynamics of an expanding quark system created at RHIC.

As mentioned before, the high relative abundance of pentaquark clusters shown in figure 8.8 should not lead to premature conclusions about the relative number of specific pentaquark states such as the Θ^+. The reduction by a factor of ≈ 243 means that even the most optimistic estimates in the kinematical region $\Delta y \approx \pm 1.5$ around mid-rapidity will be of the order of 1 pentaquark cluster per 1000 baryons.

Pentaquark clusters thus do not follow a simple chemical coalescence picture. This can also be seen in the mass distribution of clusters, where correlations between quarks in dimeson and pentaquark clusters going beyond simple coalescence are manifest in the extra mass of the clusters, as we will see now.

8.3.2 Mass distribution of exotic clusters

As discussed before, colour neutral clusters produced by the purely classical qMD model have masses which follow a wide, continuous distribution. The mass distributions for clusters of up to six quarks and/or antiquarks are shown in figure 8.9 for the SPS systems, and in figure 8.10 for the thermal initial condition. Note that both figures use different mass scales. At the higher SPS energy, pentaquark clusters dominate the distribution for masses beyond $\approx 2.5\,\mathrm{GeV}$. For the lower energy, pentaquark clusters dominate between $\approx 1.8\,\mathrm{GeV}$ and $\approx 2.8\,\mathrm{GeV}$. Above that, dibaryon clusters become the most important contributors. In the thermal system, the mass distribution is dominated by mesons, dimesons, and baryonia clusters, all of which have baryon number $B = 0$.

There is no major dependence of the mass distribution on the value of the string constant κ, which is used in the qMD model as the slope parameter of the linear potential. Tuning the string constant changes the temperature of the transition to clusters, as discussed in section 5.1, but has nearly no influence on the mass distribution of the clusters. This can be seen in figure 8.11, where mass distributions obtained from thermal initial conditions are plotted. In both figures, a cylindrical system with radius $R = 4\,\mathrm{fm}$ and length $l = 1\,\mathrm{fm}$ was initialized with a temperature of $T = 180\,\mathrm{MeV}$ and a chemical potential of $\mu = 100\,\mathrm{MeV}$. The string constant was chosen as $\kappa = 1.8\,\mathrm{GeV/fm}$ in the upper figure, and $\kappa = 3.6\,\mathrm{GeV/fm}$ in the lower figure. Both sets of mass distributions for the different types of colour neutral clusters are nearly identical.

The mass distributions are, however, strongly influenced by the available energy, either from different beam energies of the colliding nuclei or from different initial temperatures. This can been seen by comparing the upper and lower part of figure 8.9 for different SPS energies, or by comparing figure 8.10 with the lower part of figure 8.11 for different initial temperatures of thermal systems. The higher the energy, the more massive clusters are possible. This is of course in agreement with the requirements from classical statistical mechanics, where a mass distribution $\sim \mathrm{e}^{-m/k_\mathrm{B}T}$ is expected.

This dependence of the mass distributions on the available energy and the slope parameter of the potential can be understood by considering that clustering depends on the interplay of both attractive and repulsive interactions in the system. This

balance is not changed when attraction and repulsion are changed on the same footing by tuning the linear slope of the potential. Higher energies, on the other hand, mean that parts of the system can expand further before forming clusters, thus creating more massive clusters. Furthermore, the energy of the relative motion of the particles forming the cluster will be higher.

8.3.3 Binding energy of clusters from folded mass distributions

We can deduce a mean value for the extra mass of exotic clusters compared to a naive coalescence of mesons and baryons from an analysis of the mass distributions $\mathrm{d}N_\mathrm{i}{}^{(6)}/\mathrm{d}m$ of these clusters. Here, we will discuss pentaquark clusters only.

If we suppose that exotic clusters are formed simply by sticking together meson and baryon clusters, we can obtain the resulting distribution of cluster masses by a simple folding procedure. To this end, we start with the mass distributions $\mathrm{d}N_\mathrm{m}{}^{(3)}/\mathrm{d}m$ and $\mathrm{d}N_\mathrm{b}{}^{(3)}/\mathrm{d}m$ of mesons and baryons which are obtained if we allow only for the formation of clusters with two or three quarks and/or antiquarks.

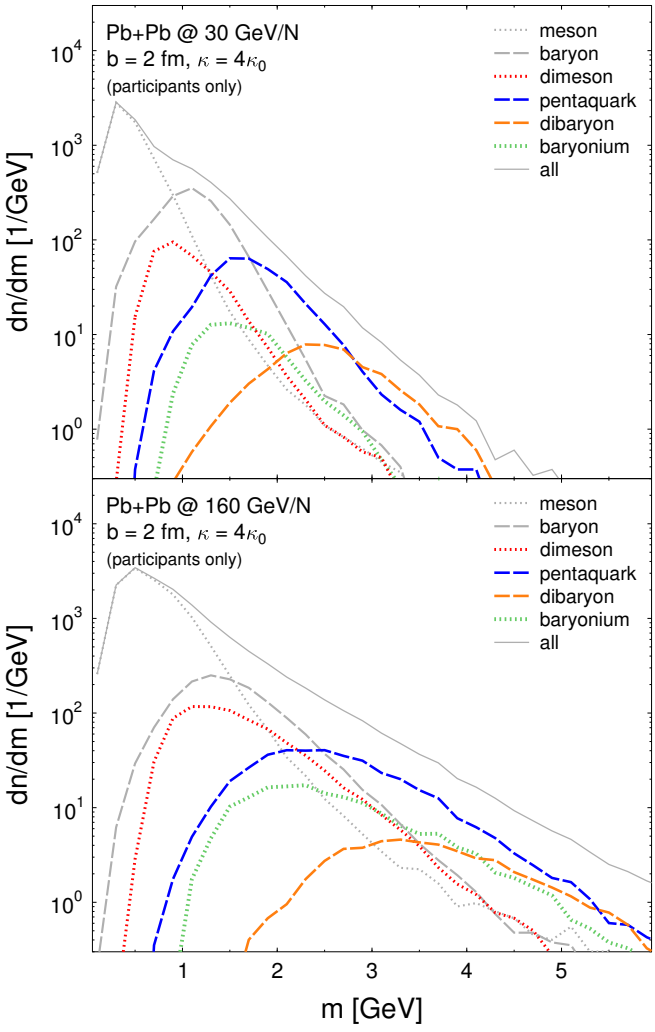

Figure 8.9
Mass distribution of clusters of up to six quarks and/or antiquarks for SPS initial conditions with beam energies of 30 GeV/N (top) and 160 GeV/N (bottom). Distributions of antibaryons and antipentaquarks are not shown, but contribute to the total cluster mass distribution (thin grey line).

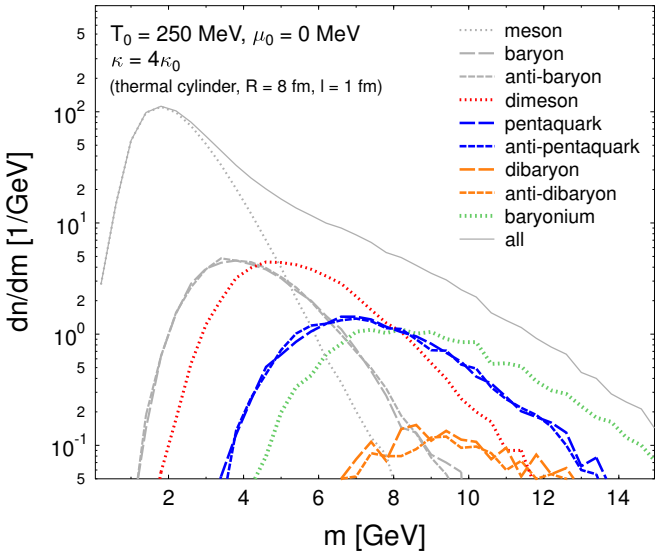

Figure 8.10
Mass distribution of clusters of up to six quarks and/or antiquarks from thermal initial conditions ($T_0 = valunit250MeV$, $\mu = 0\,\mathrm{MeV}$). Antiparticles are equal in weight to particles.

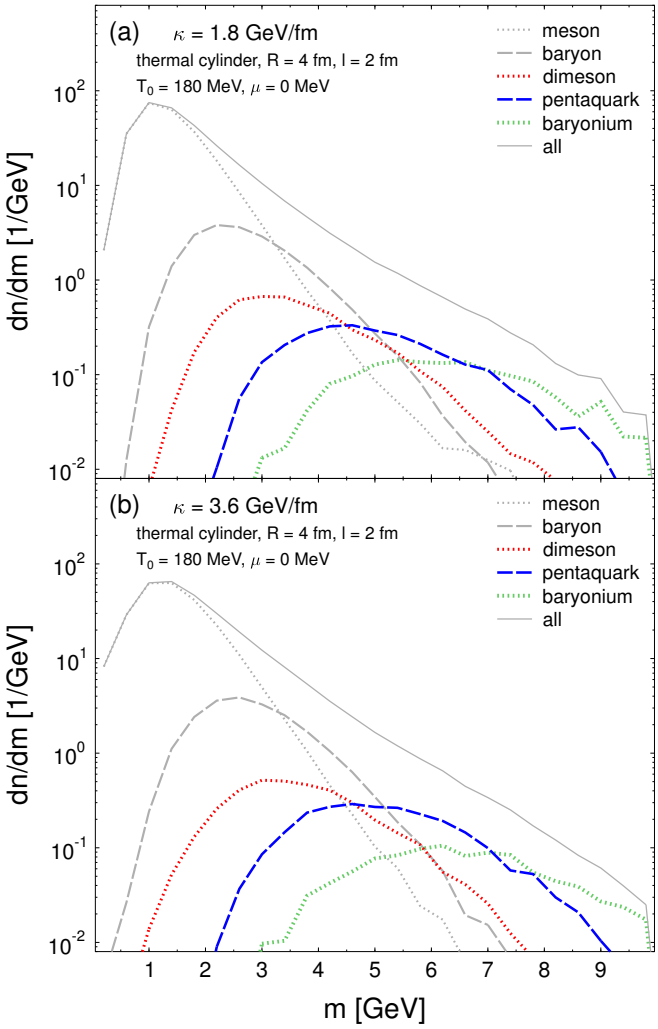

Figure 8.11
Mass distribution of clusters of up to six quarks and/or antiquarks from thermal initial conditions with $T_0 = 180\,\mathrm{MeV}$ and $\mu = 100\,\mathrm{MeV}$. Data in both figures differ in the values used for the slope parameter, with $\kappa = 1.8\,\mathrm{GeV/fm}$ in the upper figure (a), and $\kappa = 3.6\,\mathrm{GeV/fm}$ in the lower figure (b). Antibaryons and antipentaquarks are not shown, but contribute to the total cluster yield (thin grey lines). There are no big differences in the mass distributions of both data sets. However, the mass distributions are peaked at lower energies than in the thermal distributions for $T_0 = 250\,\mathrm{MeV}$ shown in figure 8.10. Note that the mass scale is different in both figures.

The mass distribution of pentaquark clusters obtained from a naive coalescence of these mesons and baryons then reads

$$\begin{aligned}\left.\frac{\mathrm{d}N_{\mathrm{p}}^{(\mathrm{naive})}}{\mathrm{d}m}\right|_{m_0} &= N\int \mathrm{d}m_1 \int \mathrm{d}m_2 \left.\frac{\mathrm{d}N_{\mathrm{m}}^{(3)}}{\mathrm{d}m}\right|_{m_1} \left.\frac{\mathrm{d}N_{\mathrm{b}}^{(3)}}{\mathrm{d}m}\right|_{m_2} \delta\left(m_1+m_2-m_0\right) \\ &= N\int \mathrm{d}\tilde{m}\, \frac{\mathrm{d}N_{\mathrm{m}}^{(3)}}{\mathrm{d}m}(\tilde{m}) \frac{\mathrm{d}N_{\mathrm{b}}^{(3)}}{\mathrm{d}m}(m_0-\tilde{m})\ ,\end{aligned} \tag{8.9}$$

where N is a normalization factor which ensures that the integral of the distribution equals the total number of pentaquark clusters ${N_{\mathrm{p}}}^{(6)}$. A mass distribution of dimesons can be obtained in an analogous fashion by replacing $\mathrm{d}{N_{\mathrm{b}}}^{(3)}/\mathrm{d}m$ with $\mathrm{d}{N_{\mathrm{m}}}^{(3)}/\mathrm{d}m$ in (8.9), and a replacement of $\mathrm{d}{N_{\mathrm{m}}}^{(3)}/\mathrm{d}m$ by $\mathrm{d}{N_{\mathrm{b}}}^{(3)}/\mathrm{d}m$ or $\mathrm{d}{N_{\bar{\mathrm{b}}}}^{(3)}/\mathrm{d}m$ would provide us with an estimate for dibaryon and baryonium cluster distributions.

Figure 8.12 shows all distributions involved for the analysis of pentaquark cluster masses at lower and upper SPS energies. For the thermal initial conditions with temperature $T = 250\,\mathrm{MeV}$ and chemical potential $\mu = 0\,\mathrm{MeV}$, the corresponding distributions are plotted in figure 8.13. The normalization of the meson and baryon mass distributions $\mathrm{d}{N_{\mathrm{m}}}^{(3)}/\mathrm{d}m$ and $\mathrm{d}{N_{\mathrm{b}}}^{(3)}/\mathrm{d}m$ is chosen such that integrated distributions equal the total abundances of pentaquark clusters in the systems under study, ${N_{\mathrm{p}}}^{(6)}$. The folded distributions are normalized in the same way.

It can be neatly seen that the folded distributions are similar to the full pentaquark distributions up to an overall shift in mass, and a slight stretching for the most massive clusters. The shift can be identified with the mean extra energy of a pentaquark cluster due to the extra bindings within the cluster. If the pentaquark cluster were composed simply of one colour neutral mesonic and another colour neutral baryonic cluster, there would be no extra mass. However, we have seen that the clustering routine works such that groups of three quarks or a quark-antiquark pair within a pentaquark cluster are not colour neutral. Thus, there is some extra colour electric interaction, which is responsible for the extra mass. Remembering that the more massive clusters are larger, it is plausible that the extra colour electric mass increases with the total mass.

The shift in the mass distributions can be quantified by minimising the sum of squared mass differences over mass bins,

$$\chi^2(i) = \sum_{\text{bins } j} \left(\left.\frac{\mathrm{d}N_{\mathrm{p}}^{(\mathrm{naive})}}{\mathrm{d}m}\right|_{\text{bin } j} - \left.\frac{\mathrm{d}N_{\mathrm{p}}^{(6)}}{\mathrm{d}m}\right|_{\text{bin}j+i} \right)^2 , \tag{8.10}$$

where $\mathrm{d}{N_{\mathrm{p}}}^{(\mathrm{naive})}/\mathrm{d}m\,|_{\text{bin } j}$ is the number of pentaquark clusters in the folded distribution of 2- and 3-clusters from (8.9), evaluated in bin j, and $\mathrm{d}{N}^{(6)}{}_{\mathrm{p}}/\mathrm{d}m\,|_{\text{bin}j+i}$ is the corresponding number in the distribution of pentaquark clusters, evaluated in the shifted bin j. Minimization is done over the shift i of bins.

Similar results can be obtained from the analysis of dimeson clusters. The resulting mean extra masses for both dimeson and pentaquark clusters in the different systems under consideration are listed in table 8.7. The errors for the mass shifts are the bin widths of the mass distributions used in the minimization procedure according to (8.10).

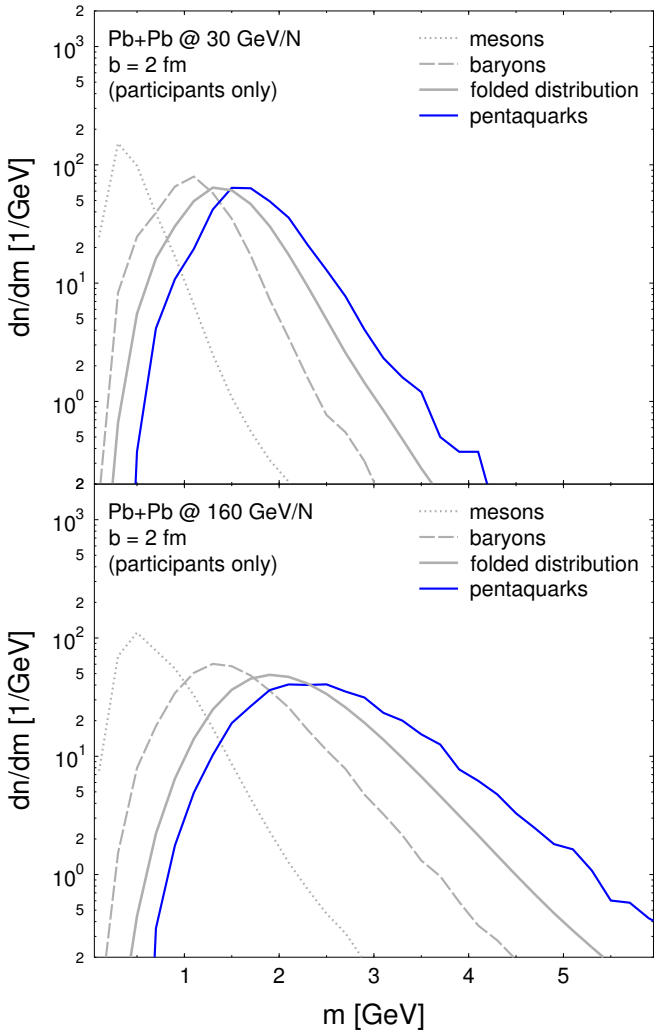

Figure 8.12
Folding the mass distribution of mesons (grey dotted lines) and baryons (grey dashed lines) obtained with SPS initial conditions yields a mass distribution (grey lines) which can be compared to the observed mass distribution of pentaquark clusters (blue lines). There is a relative shift between both distributions which can be used to estimate the mean additional mass of a pentaquark cluster in comparison to the naive coalescence model. All distributions have been normalized to the total abundance of pentaquark clusters.

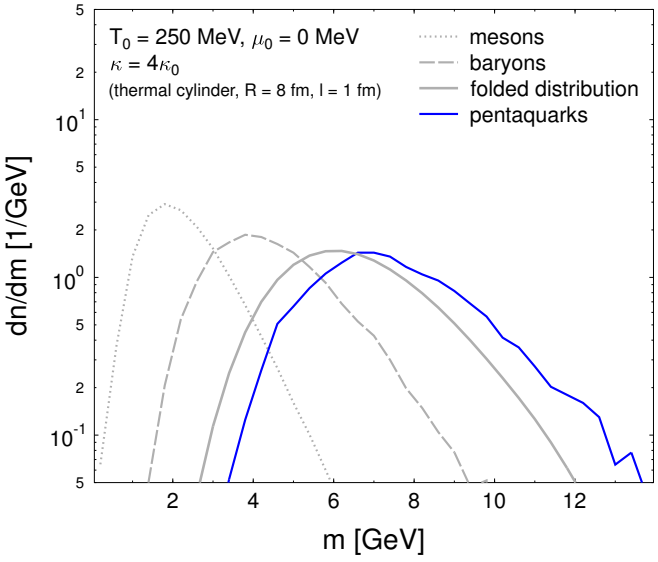

Figure 8.13
Folded mass distributions (grey line) of mesons (grey dotted line) and baryons (grey dashed line) and the mass distribution of pentaquarks (blue line) for thermal initial conditions.

Table 8.7
Mean extra masses of dimeson (δm_{d}) and pentaquark (δm_{p}) clusters relative to naive coalescence, obtained by shifting the folded mass distributions and minimising the quadratic differences to the full data according to equation (8.10).

system	δm_{d} (MeV)	δm_{p} (MeV)
Pb + Pb @ $30\,\mathrm{GeV}/N$	150 ± 50	200 ± 50
Pb + Pb @ $80\,\mathrm{GeV}/N$	100 ± 50	200 ± 50
Pb + Pb @ $160\,\mathrm{GeV}/N$	100 ± 50	300 ± 50
$T_0 = 180\,\mathrm{MeV}$, $\mu = 100\,\mathrm{MeV}$	600 ± 100	600 ± 100
$T_0 = 250\,\mathrm{MeV}$, $\mu = 0\,\mathrm{MeV}$, $\kappa = 4\kappa_0$	850 ± 50	700 ± 50

Considering pentaquark clusters, it is interesting to note that, at least for SPS systems, the extra mass of these clusters is comparable to the mass difference $\delta m = 105\,\mathrm{MeV}$ of the Θ^+ pentaquark to the neutron-kaon threshold. In these systems, the overall mass distributions of baryons and mesons are also found to lie within a realistic range. The thermal systems are different in this respect: Here, both the mass shift of exotic clusters above threshold and the overall mass distributions of baryons and mesons are very high. However, it has to be kept in mind that these high masses refer to colour neutral clusters which correspond mostly to resonances. After their decay to final state hadrons, a more mundane mass distribution will emerge.

8.3.4 Transverse momentum spectra of exotic clusters

The qMD code provides us with the full dynamics of the expanding quark system, including the formation of exotic clusters. Thus, we can complement the rapidity distributions of these clusters given in section 8.3.1 with information about transverse momentum. The corresponding spectra are shown in figure 8.14 for systems at the lowest and highest SPS energies, and in figure 8.15 for the net-baryon free thermal system with initial temperature $T_0 = 250\,\mathrm{MeV}$.

At transverse momenta of $p_\perp \gtrsim 1.5\,\mathrm{GeV}/c$, the contribution of pentaquark clusters to the total transverse momentum spectrum becomes comparable to the contributions of mesons and baryons in the SPS systems, while the high $p_\perp$ tails of the thermal distributions are, again, dominated by dimeson and baryonium clusters. Here, of course, the same restrictions apply that have been discussed in connection with the total cluster yields, since most exotic clusters are spurious.

Usually, transverse momentum spectra of particles in heavy ion collisions are used to fit inverse slope parameters, which are interpreted in the sense of temperature and collective transverse flow. Here, such an analysis could be done in principle. However, one has to take into account that the masses within one class of clusters are widely distributed. Thus, the effects of collective flow which usually scales with mass will be washed out. A flow analysis can be done either with the final state hadrons, or with clusters of maybe different quark content, but within certain mass bins. Here, we do not use the transverse momentum spectra for any further analysis.

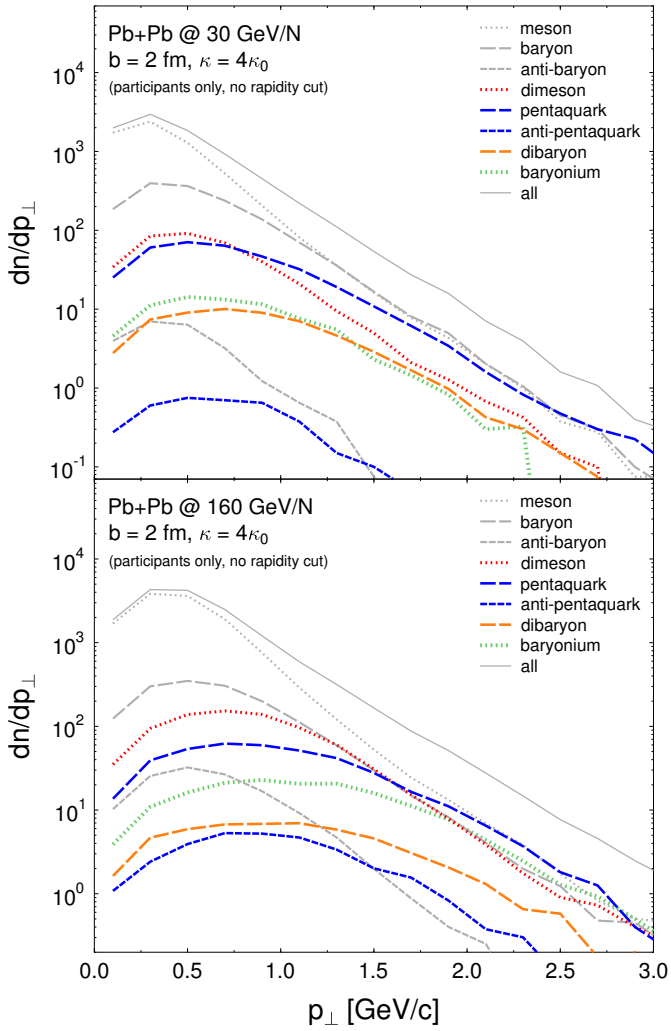

Figure 8.14
Transverse momentum spectra for clusters of up to six quarks and/or antiquarks in qMD with SPS initial conditions.

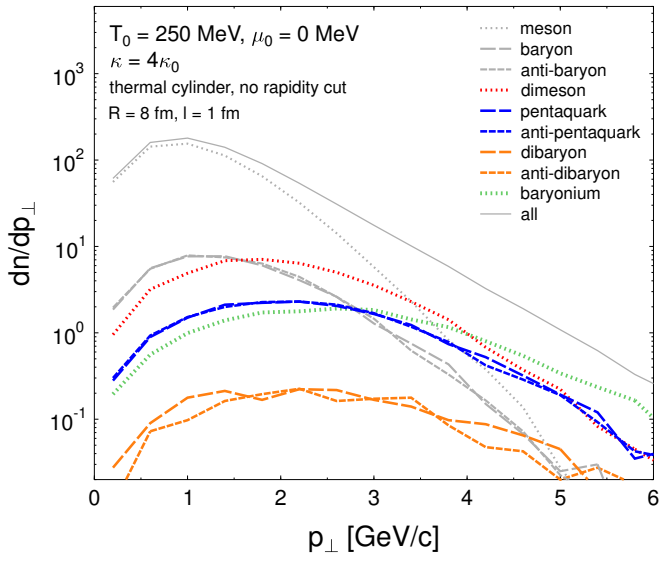

Figure 8.15
Transverse momentum spectra for clusters of up to six quarks and/or antiquarks in qMD with thermal initial conditions.

8.3.5 Hadronization dynamics

Besides information concerning rapidity and transverse momentum of all colour charges and clusters, qMD gives us full knowledge about the space-time dynamics of the expansion and recombination.

Figures 8.16 and 8.17 show the rates $\mathrm{d}n/\mathrm{d}\tau$ at which the different types of clusters are formed in the SPS and thermal events. Time in these figures is the eigen time τ corresponding to the space-time coordinates (t, x, y, z) of the formation of a cluster in the centre of momentum frame C of the collision. Here, space coordinates (x, y, z) are those of the centre of mass of the cluster in the frame C. As we have seen in time (6.27), eigen time τ is calculated from these coordinates as

$$\tau \,=\, \sqrt{t^2 - z^2} \,=\, t\sqrt{1 - z^2/t^2} \,=\, t\sqrt{1 - \bar{\beta}_z^2}\,, \tag{8.11}$$

where $\bar{\beta}_z = z/t$ acts as an estimate for the longitudinal velocity of the clustering colour charges. It is clear that τ as defined in (8.11) is the exact eigen time only in the case of non-interacting matter expanding from one single space-time point along one dimension. Here, it is used as a simple means to take into account the differing time dilatation factors of matter at different rapidities.

The vertical bars in figure 8.16 mark the crossing times t_{x} in the collision frame C where the switching from the UrQMD to the qMD dynamics takes place. These times depend on the energy of the collision. They are listed in table 6.1. Note that the time scales t and τ are identical only in the transverse plane, where $z = 0$. The switch from UrQMD to the qMD, as shown in figure 6.4, involves the decomposition of all hadrons into quarks and antiquarks at the same time t_0 in the frame C. This manifold of space-time events is not a hyperboloid of constant eigen time τ. At forward and backward rapidities, space-time hypersurfaces of constant t_0 correspond to a whole stack of hyperboloids of different constant eigen times $\tau < t_0$. If matter away from central rapidity forms clusters immediately after decomposition, it can recombine with $\tau < t_0$. This explains the apparent onset of clustering $\mathrm{d}n\,/\mathrm{d}\tau$ before decomposition.

Note again that in all data, recombination sets in right from the beginning of the time evolution. As we have seen in chapter 6, this is a typical feature of qMD, where the deconfined matter is not modelled as a homogeneous gas which cools down as it expands and undergoes a phase transition to hadrons at some time, but treated fully dynamically with local criteria for the formation of colour neutral clusters.

In the SPS events, cluster formation first increases during the expansion, then goes through a maximum and switches to an exponential decrease. For a collision energy of $30\,\mathrm{GeV}/N$, the initial increase is by a factor of 2–3, and the maximal rate is reached at $\Delta\tau \approx 4\,\mathrm{fm}/c$ after the switching to the qMD dynamics. The final exponential decrease of clustering is roughly about one order of magnitude every $\delta\tau = 2\,\mathrm{fm}/c$. The rates of meson, dimeson, and baryonium cluster formation have similar time evolutions and differ only by the absolute scale. Baryon, pentaquark, and dibaryon clustering rates peak at slightly increasing times, and decay with longer lifetimes. This means that at later times, more pentaquarks and dibaryons are formed than any other type of clusters. At a collision energy of $160\,\mathrm{GeV}/N$, the

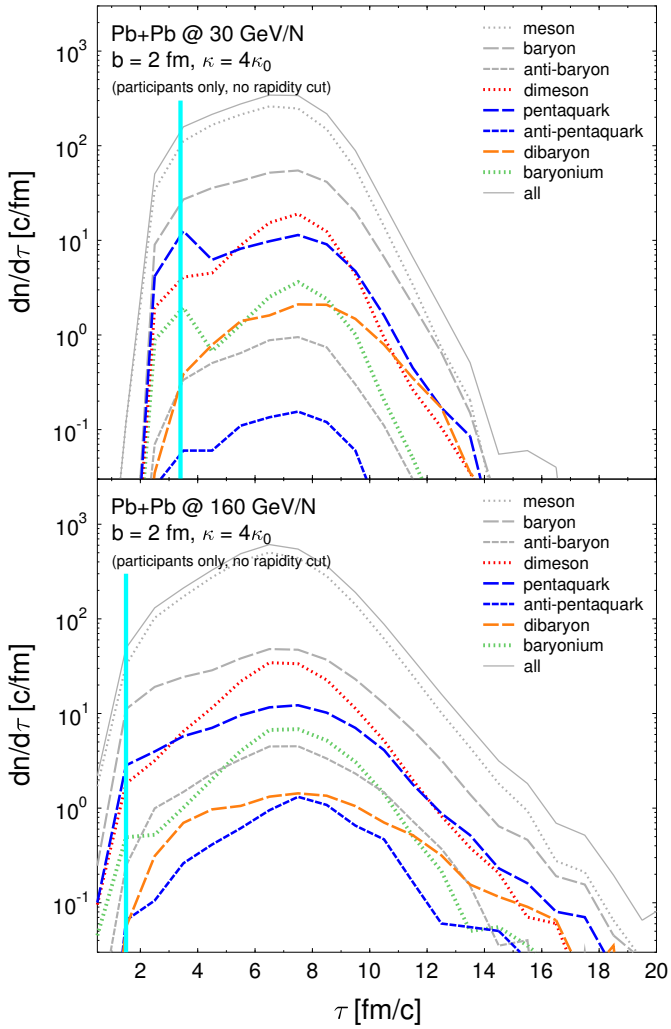

Figure 8.16
Time evolution of clustering rates for different types of clusters in qMD with SPS initial conditions. Rates are plotted as a function of eigen time of the cluster formation event. The vertical bars represent the switching from UrQMD to qMD dynamics in the centre of momentum frame of the collision. The apparently early onset of clustering is due to the use of eigen time, as explained in the text. Increasing the collision energy stretches the time evolution of the clustering rates.

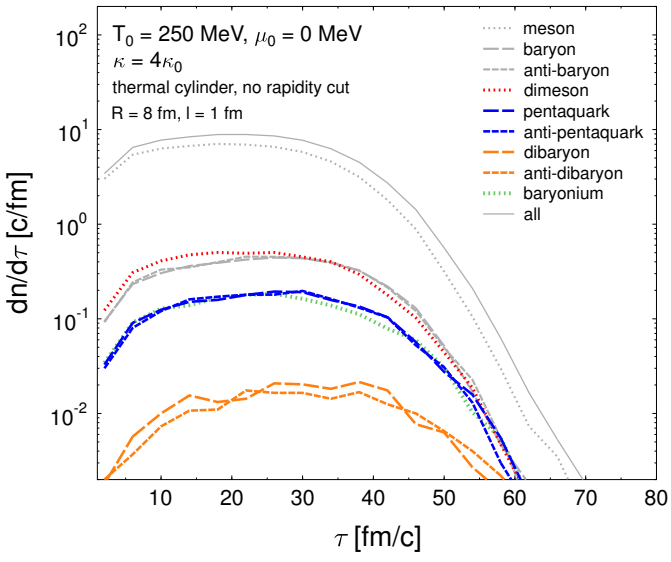

Figure 8.17
Clustering rates as a function of eigen time for different types of clusters as in 8.16, but for thermal initial conditions.

overall picture is similar, but more stretched in time. Moreover, the initial increase in the clustering rates is by a factor of 10. Maximal rates are reached at $\Delta\tau \approx 8\,\mathrm{fm}/c$ after switching to the qMD dynamics, and the final decay rates decrease every $\delta\tau = 3\,\mathrm{fm}/c$ by one order of magnitude. Again, the time dependence of rates is similar for meson, dimeson and baryonium clusters, and for pentaquark and dibaryon clusters. The final exponential decay becomes slower with increasing baryon number of the clusters. Since rates are plotted as functions of eigen time, the slowing down of the dynamics at the higher collision energies is not an artifact of higher time dilatation, but reflects a physically longer lifetime of the higher energetic fireball.

In the thermal system, clustering rates stay constant for a much longer time, and the final phase of cluster formation decreases roughly by a factor of 10 every $\Delta\tau = 10\,\mathrm{fm}/c$, much slower than in the SPS data. Here, the clustering rates of baryons, antibaryons, and dimesons follow the same time evolution, as do the the rates for pentaquarks, antipentaquarks, and baryonia, and those of dibaryons and antidibaryons. Again, clustering rates peak at later times with increasing cluster sizes, and final lifetimes are larger for bigger clusters. The long lifetime of the quark and antiquark system can be understood as an extension of the pattern of lifetimes increasing with energy observed for the SPS systems. It is due to the high temperature and the complete thermalization of the quarks and antiquarks in the initial state.

In addition to the time distribution of clustering rates, we can also look at the typical radial distances $r_\perp = \sqrt{x^2 + y^2}$ from the collision axis where cluster formation takes place. These radial distributions are shown in figures 8.18 for the SPS and 8.19 for the thermal events. The radii of the initial systems are marked by the vertical bars. For the SPS events with a constant impact parameter $b = 2\,\mathrm{fm}$ of the colliding lead nuclei, both the minimal and maximal radii of the overlap region are shown.

In the SPS collisions, the radial distribution of clustering is almost constant for radii smaller than the initial system size. Clustering rates fall very quickly with increasing radius outside the region filled by the initial system. Here, rates drop by more than one order of magnitude with each $\delta r_\perp = 1\,\mathrm{fm}$ for the smaller beam energy of $30\,\mathrm{GeV}$. The exponential decrease is slower for larger clusters. At the highest beam energy of $160\,\mathrm{GeV}$, rates drop outside the initial system at lower rates than at $30\,\mathrm{GeV}$, but still by one order of magnitude with each $\delta r_\perp = 1.5\,\mathrm{fm}$. This radial distribution of clustering rates means that there is not much radial expansion of the initial quark system. Instead, most clusters are formed during the longitudinal expansion. The situation is different for the thermal system shown in 8.19. Here, clustering rates increase with distance from the central axis of the system, and reach maxima at $\approx 1\,\mathrm{fm}$ outside the initial system radius, before decreasing exponentially with further distance. This shape of the radial clustering rates is a sign of the transverse expansion of the hot gas of quarks and antiquarks, which was initialized without any non-thermal, longitudinal velocity profile. Furthermore, the long lifetime of the thermal system, about four times as long as in the SPS events, fosters the build-up of radial flow.

So far, the analysis of the space-time distribution of cluster formation has dealt with data from the standard qMD clustering procedure: Once a cluster is formed,

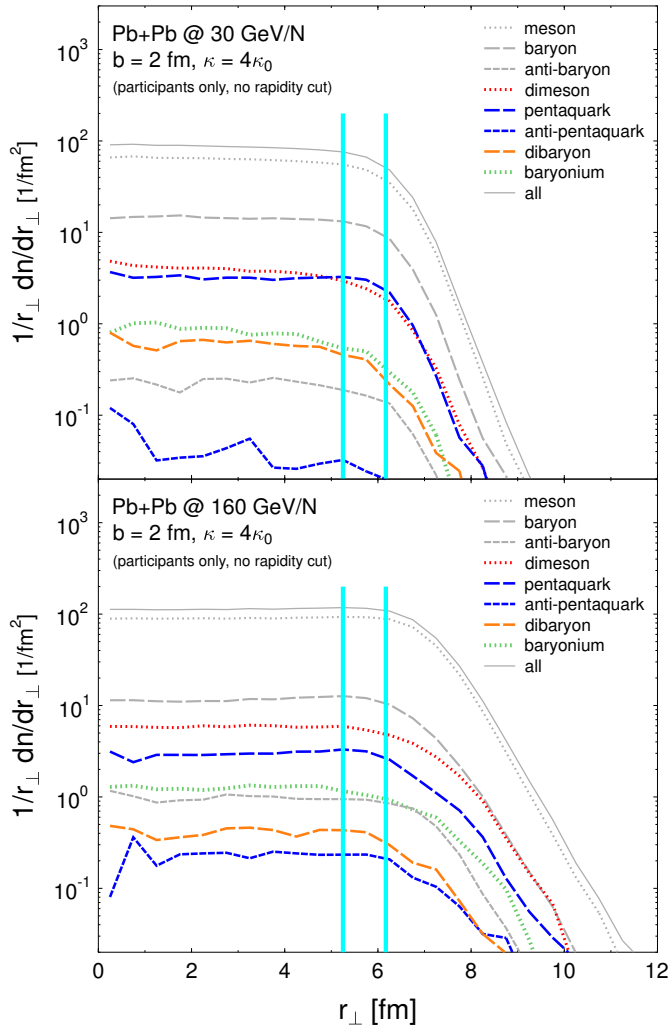

Figure 8.18
Clustering radii for different types of clusters in qMD for SPS initial conditions. The vertical bars mark the minimal and maximal radii of the overlap region of the two colliding nuclei at the impact parameter $b = 2\,\mathrm{fm}$ which has been used in the simulations. There is an increasing amount of clustering at larger radii with increasing collision energy.

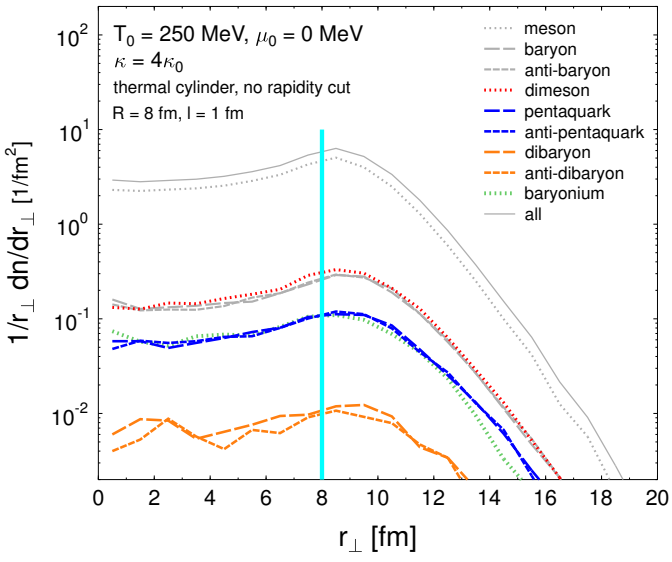

Figure 8.19
Clustering radii for different types of clusters in qMD as in 8.18, but for thermal initial conditions.

its quark and antiquark content is "frozen", it is considered as a hadron and does not interact any further with the remaining colour charges. We call this procedure "hadronization" in qMD. All results for exotic clusters presented so far have been obtained in this way. However, a closer look at the qMD dynamics of colour charges without hadronization, as shown for example in figure 4.4, reveals that in the long run, correlations of more than three colour charges are unstable and will decay into groups of three quarks or antiquarks, or in quark-antiquark pairs. Thus, without the standard qMD hadronization procedure, there would be no exotic clusters. This effect is studied in more detail in figures 8.20 and 8.21 for central SPS events with a collision energy of $30\,\mathrm{GeV}/N$.

Figure 8.20 shows the time evolution of clustering in the centre of momentum frame of the collision using the standard qMD hadronization procedure. The plots represent the relative numbers of quarks and antiquarks contained in the different types of clusters. Note that the relative yields of different clusters as given in table 8.3 are recovered after division by the cluster size and a new normalization. The figure on the left shows the time evolution when searching only for 2- and 3-clusters, corresponding to mesons, baryons, and antibaryons. In the figure on the right, the cluster search is extended to exotic clusters with up to six quarks and/or antiquarks. Since some colour charges end up in exotic clusters, the relative numbers of colour charges in standard hadronic clusters is reduced compared to the first case, whose final relative yields are indicated by the horizontal lines.

In comparison, the time evolution shown in figure 8.21 starts with the same initial conditions as in figure 8.20, but cluster hadronization is suppressed. Instead, the initial content of quarks and antiquarks is propagated through the entire time evolution of the system. The clustering routine just counts which types of clusters would hadronize at different times, and the corresponding fractions of quarks and antiquarks are shown in the figures. Again, search is done for 2- and 3-clusters only in the figure on the left, and extended to 4-, 5-, and 6-clusters in the figure on the right. Note that the figures 8.20 and 8.21 use different time scales. The build-up of clusters takes about twice as long if the actual hadronization procedure is suppressed. However, the final fractions of colour charges in standard hadrons are not affected.

The situation is different for tetraquark and pentaquark clusters. Here, such clusters in fact form, but their fraction reaches a maximum and then goes down again. In the end, all quarks and antiquarks end up in mesonic and baryonic clusters. This corresponds to the previous observation that larger, exotic quark clusters are unstable in the quark dynamics. Furthermore, even at the maximum, the relative number of colour charges in tetraquark and pentaquark clusters is one order of magnitude smaller than in the case when hadronization is accomplished.

Comparing figures 8.20 and 8.21 shows that there is a certain arbitrariness in the number of exotic clusters derived from the standard qMD hadronization procedure. While final numbers derived for mesons and baryons do not depend on this procedure, yields of exotic hadrons do. Considering only the classical quark dynamics of qMD, exotic states would be negligible in the final outcome. Here, we argue again that a colour neutral exotic cluster which is separated from the remaining system according to the qMD hadronization criteria and whose quantum numbers correspond to an existing hadronic state would, in fact, form such a state.

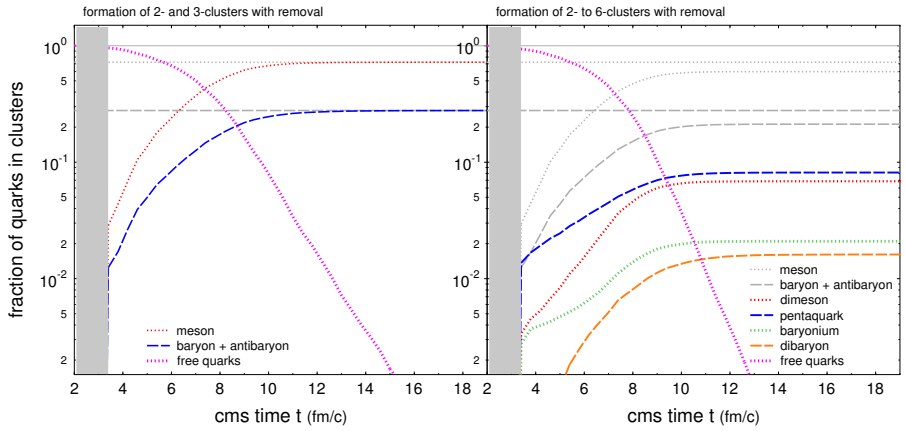

Figure 8.20
Dynamics of cluster formation for SPS events with a collision energy of $30\,\mathrm{GeV}/N$. Clusters do not interact with the rest of the system after hadronization. The curves represent the fraction of quarks and antiquarks frozen in clusters of different size. In the data set on the left, only 2- and 3-clusters are hadronized. Data on the right include the hadronization of larger clusters. As a consequence, relative numbers of colour charges ending up in 2- and 3-clusters are smaller than in the first case, whose final relative yields are indicated by the horizontal lines. Note that the relative fraction of colour charges in clusters of different size is not the same as the relative numbers of clusters.

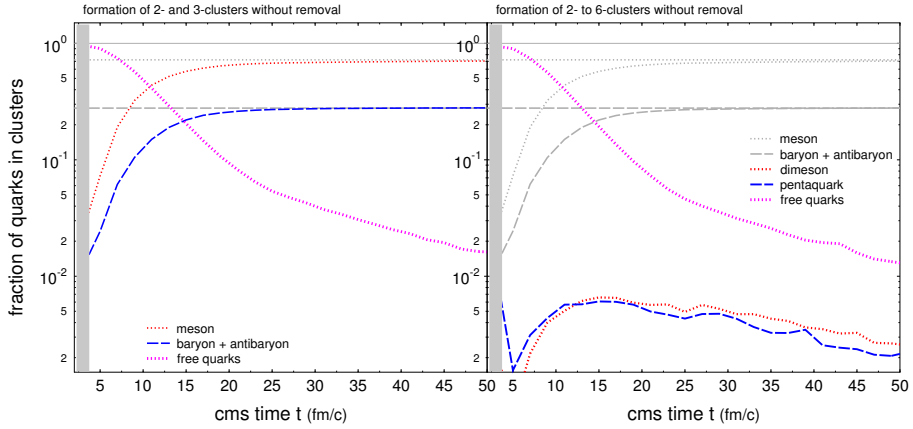

Figure 8.21
Dynamical evolution with the same initial conditions as in figure 8.20, without hadronization of clusters. The clustering routine only checks which clusters would hadronize at different times. On the left, search is done only for 2- and 3-clusters. On the right, 4-, 5-, and 6-clusters are included in the search. Dimeson and pentaquark correlations emerge over time, but eventually decay again. Note that the time scale is different from figure 8.20.

Since colour neutral, this state has no more interaction with the remaining colour charges. However, we have to keep in mind that the estimates from the qMD cluster hadronization procedure are best understood as upper limits for the yields of exotic hadrons.

8.4 Strangeness of pentaquarks in qMD

Finally, in this and the following section, we come back to a detailed analysis of pentaquark clusters produced in qMD using the standard hadronization procedure. We will study the distribution of pentaquark clusters over strangeness, before focussing on the isoscalar strangeness $S = +1$ state, the Θ^+, in section 8.5. The distribution of pentaquarks over strangeness, if it were accessible in heavy ion collisions, could yield a new and sensitive probe of thermalization.

8.4.1 Strangeness of pentaquarks as a probe of thermalization

Analysing pentaquark yields with different strangeness is of interest for both practical and theoretical reasons. The reconstruction of pentaquark states from experimental data is a formidable task for pentaquark states with $S = 0$. It is more feasible for the states with $S = -1$, and the manifest exotic states with $S = +1$, $S = -2$, $S = -3$, and $S = -4$. From the theoretical side, these states are of interest because they could be used as indicators of equilibration and signals for the formation of a quark-gluon plasma, as we will see.

The abundances of pentaquark clusters, differentiated along strangeness, are listed in table 8.8 for Pb+Pb collisions at the SPS with energies of 30, 80, and $160\,\mathrm{GeV}/N$, and for the thermal initial conditions with $T_0 = 250\,\mathrm{MeV}$ and $\mu = 0\,\mathrm{MeV}$. The same data are plotted in figure 8.22, where the relative numbers are further broken down according to whether the antiquark in the pentaquark cluster is an anti-up or anti-down ($\bar{q}$) quark (data points connected by dashed lines) or an antistrange $\bar{s}$ quark (points connected by solid lines).

Note that the antiquark in pentaquarks of a given SU(3) multiplet is not always a $\bar{q}$ quark (or a $\bar{s}$ quark) for all states of the multiplet. Thus, states from one multiplet can correspond to points on both lines in figure 8.22. For example, the Θ^+ from the antidecuplet contains one $\bar{s}$-quark and four q quarks, while the Ξ_5^{--}

	SPS: Pb + Pb, $b = 2\,\mathrm{fm}$						thermal events:	
Strangeness S	30 GeV/N		80 GeV/N		160 GeV/N		$T_0 = 250\,\mathrm{MeV}$, $\mu_0 = 0\,\mathrm{MeV}$	
pentaquarks $N_\mathrm{p}^{(6)}$	64.4	(4.1 %)	72.2	(3.0 %)	78.2	(2.5 %)	6.5	(2.2 %)
$S = +1$	2.44	(3.80 %)	4.25	(5.90 %)	4.92	(6.30 %)	0.43	(7.00 %)
$S = 0$	55.20	(85.80 %)	57.30	(79.40 %)	59.10	(75.60 %)	1.68	(27.10 %)
$S = -1$	6.47	(10.00 %)	9.99	(13.80 %)	13.00	(16.60 %)	2.25	(36.40 %)
$S = -2$	0.27	(0.40 %)	0.63	(0.90 %)	1.13	(1.45 %)	1.41	(22.70 %)
$S = -3$	0.00	(0.01 %)	0.03	(0.04 %)	0.04	(0.04 %)	0.37	(6.00 %)
$S = -4$	0.00	(0.00 %)	0.00	(0.00 %)	0.00	(0.00 %)	0.04	(0.70 %)

Table 8.8
Abundances of pentaquark clusters produced with standard cluster hadronization of qMD for different initial conditions. The first line gives the total yield of pentaquark clusters per event. This yield is broken down according to different strangeness S of the clusters in the following lines.

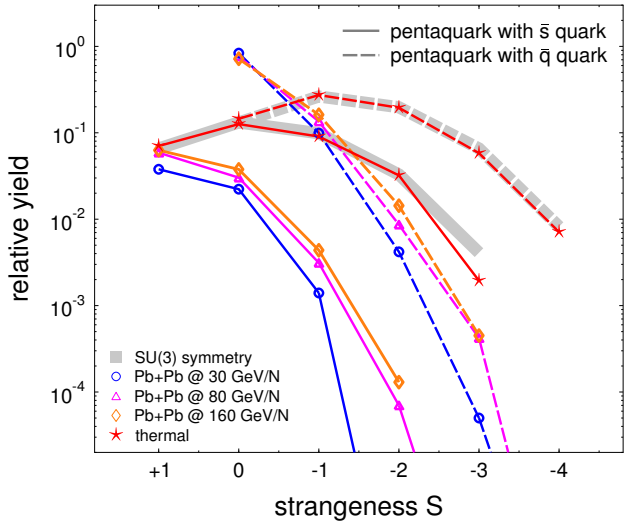

Figure 8.22
Relative numbers of pentaquark clusters with different strangeness from qMD simulations for different initial conditions. The thick gray line shows the relative numbers expected in a completely flavour SU(3) symmetric situation.

from the same multiplet contains one $\bar{q}$ quark together with two q quarks and two s quarks. This means that the Θ^+ contributes to the point for $S = +1$ on the solid line, while the Ξ^{--} contributes to the point for $S = -2$ on the dashed line. Keep in mind that the relative numbers for different strangeness shown in table 8.8 cannot be translated in relative numbers of Θ^+/Ξ^{--} without a detailed analysis of isospin multiplicities. We will discuss this point later in this section.

The thick grey lines in figure 8.22 show the relative numbers which are expected in a completely flavour SU(3) symmetric situation. They can either be counted from the SU(3) multiplets shown in figure 8.2, or, which is equivalent, calculated from the combinatorial abundance

$$p(q^n \bar{q}^{\overline{n}} s^m \bar{s}^{\overline{m}}) = c \cdot \frac{5!}{n!\overline{n}!m!\overline{m}!} p(q)^n p(\bar{q})^{\overline{n}} p(s)^m p(\bar{s})^{\overline{m}} \,, \tag{8.12}$$

where

$$n + \overline{n} + m + \overline{m} = 5 \,, \quad \text{and either} \quad \overline{m} = 0 \quad \text{or} \quad \overline{n} = 0 \,. \tag{8.13}$$

Moreover, the probabilities to find a quark of a given flavour in a cluster are given by $p(q) : p(\bar{q}) : p(s) : p(\bar{s}) = 2 : 2 : 1 : 1 = 1/3 : 1/3 : 1/6 : 1/6$ in the SU(3) symmetric case. The normalization constant c in equation (8.12) is obtained by summing up all combinations of the non-negative integers $n, m, \overline{n}, \overline{m}$ fulfilling the constraint (8.13).

The important observation visible in figure 8.22 is that the relative numbers follow very closely the expectation from SU(3) symmetry in the case of thermal initial conditions, while there are strong deviations visible in the SPS data. This can be made even more obvious by scaling the pentaquark cluster yields obtained in the qMD simulations to the distribution expected from SU(3) symmetry, as shown in figure 8.23. The overall discrepancies are bigger for the lower than for the higher SPS energy.

This should not come as a big surprise if we take into account that the quark systems from the SPS collisions can not be expected to be completely SU(3)-symmetric. The thermal system, however, with an initial temperature of $T_0 \sim$

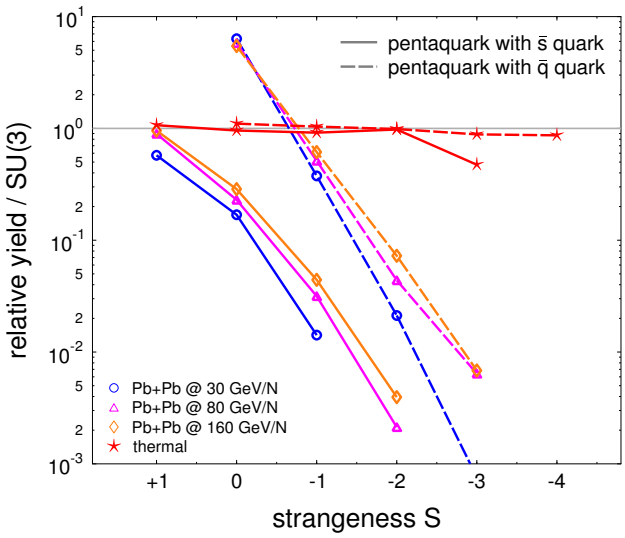

Figure 8.23
Relative numbers of pentaquark clusters as shown in figure 8.22, now scaled to the expected yields in a completely flavour SU(3) symmetric situation (grey lines in figure 8.22). There is good agreement for the thermal system, but huge deviations for the SPS systems.

$1.6\,m_{\mathrm{s}}$, is very close to this condition. This deviance from SU(3) symmetry in SPS events can be taken into account quite easily by comparing the relative numbers of pentaquark clusters to the numbers obtained from using equation (8.12) with realistic probabilities $p(q)$, $p(\bar{q})$, $p(s)$, and $p(\bar{s})$ for these systems, corresponding to the physical situation at hand. These probabilities can be obtained either from temperatures and chemical potentials (and the correct strangeness suppression factors), or, in our simulation, by a simple counting of the overall number of quarks and antiquarks of the different flavours in the simulation.

Thus, in the qMD simulations, we can determine the probabilities $p(q)$, $p(\bar{q})$, $p(s)$, and $p(\bar{s})$ by counting, and use these probabilities to calculate the probability to find a specific quark combination in a pentaquark cluster according to equation (8.12). Finally, we can compare the pentaquark yields obtained in this way with the actual pentaquark cluster abundances resulting from the full qMD dynamics and hadronization. The results of this scaling are shown in figure 8.24. As before, data from thermal initial conditions correspond very well to the combinatorial expectations. The agreement of the data from the SPS calculations with the combinatorial expectations is much better than it is with the distribution in the completely SU(3) symmetric case, which is shown in figure 8.23. However, there is still a remaining discrepancy by factors of up to 5 and 0.2, respectively, from what we expect from combinatorics! Note that, unfortunately, the curves containing the Θ^+ with strangeness $S = +1$ and the Ξ_5^{--} with $S = -2$ both lie below the combinatorial expectation for SPS data.[1]

The deviation from combinatorics in the qMD data for SPS events is a puzzling observation. It suggests that within our simulation, there is no complete thermalization and homogenization of the quark and antiquark system in these events. Instead, there are correlations among colour charges carried over into the quark system from the original hadrons.

[1] The Ξ_5^{--} has a $\bar{q}$ as the antiquark. The combination of a $\bar{s}$ quark with three s quarks and one q quark which also yields $S = -2$ has isospin $T = \frac{1}{2}$ and hence cannot mix with the Ξ^{--}. It does not belong to the antidecuplet.

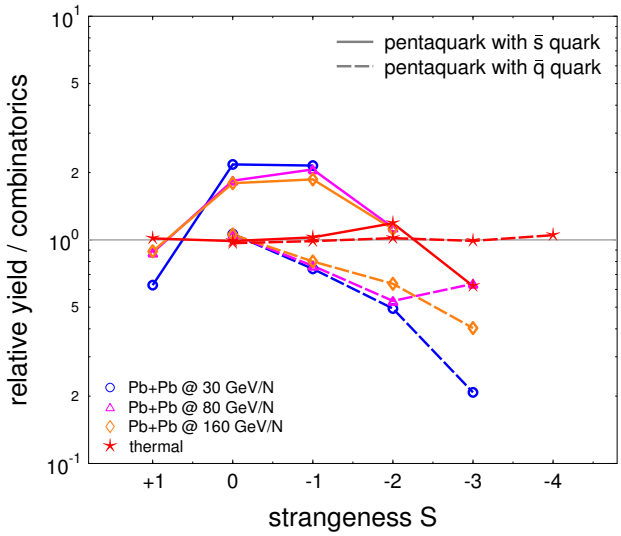

Figure 8.24
The relative numbers of pentaquarks with different strangeness, normalized to the combinatorial expectation values according to equation (8.12) with realistic quark flavour probabilities $p(q)$, $p(\bar{q})$, $p(s)$, and $p(\bar{s})$.

This phenomenon is, of course, in part due to the dynamics and the approximations of the qMD model. It does not necessarily imply that there is no thermalization in SPS events. However, it shows that the distribution of strangeness over different pentaquark states, if it could be measured in heavy ion collisions, could provide us with a good and sensitive probe for the actual thermalization of the intermediate, deconfined system. This is a new possible signal, which is due essentially to the larger combinatorial scope in recombining five quarks and antiquarks as compared to the common three quark states in baryons.

That homogenization of quarks and antiquarks and the loss of correlations from the initial hadronic state—or the absence of correlation loss—is indeed at the origin for the deviations from simple combinatorics in the distribution of strangeness over pentaquark clusters can be checked within the qMD data. If insufficient homogenization is to blame for these deviations, the effect should be much bigger for pentaquark clusters whose quarks and antiquark have their origin in only two hadrons rather than in three, four, or five hadrons. This is, of course, a purely classical concept which has no counterpart in reality, where particles with equal quantum numbers are indistinguishable. However, it can be checked easily in the qMD code, where the complete history of each colour charge is known.

Figure 8.25 shows the distribution of pentaquark clusters over strangeness for SPS data at $30\,\mathrm{GeV}/N$, scaled to the combinatorial expectation, and broken down according to the number of individual hadrons providing the quarks and antiquark in the cluster. In order to increase statistics, a smaller impact parameter of $b = 6\,\mathrm{fm}$ was chosen in the calculations. In the figure, no distinction is made as to whether the antiquark in the pentaquark cluster is a $\bar{q}$ or a $\bar{s}$ antiquark. For this reason, the distribution of all pentaquark clusters equals the distribution for clusters containing a $\bar{s}$ at $S = +1$. For all other values of strangeness, it follows very closely the distribution for clusters with a $\bar{q}$ since there are many more clusters with a $\bar{q}$ than with a $\bar{s}$ antiquark. No clusters with $S = -4$ have been found in the sample. The distribution of pentaquark clusters over strangeness clearly approaches the combinatorial expectation, represented by the constant line, when

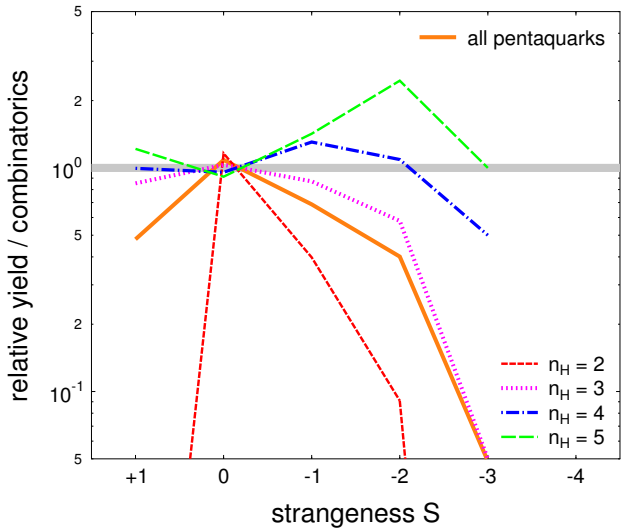

Figure 8.25
Relative numbers of pentaquark clusters with different strangeness, normalized to the combinatorial expectation values according to equation (8.12), for different numbers of initial hadrons contributing to the quark content of the cluster. No distinction of the flavour of the antiquark is made. Deviations from the combinatorial distribution are smaller for clustering involving less correlated quarks and antiquarks.

the number n_{H} of contributing hadrons increases from $n_{\mathrm{H}} = 2$ to $n_{\mathrm{H}} = 4$. In the extreme case of $n_{\mathrm{H}} = 5$, statistics is poor. Thus, we can conclude that the deviations from combinatorics visible in the qMD data of SPS events are, indeed, caused by the correlations of quarks and antiquarks remaining from their hadronic origin. We have encountered a similar effect earlier when studying the relative yield of different dibaryon clusters in section 8.3.

8.4.2 Rapidity distribution and clustering rates of pentaquarks

Before zooming in on yields for the Θ^+ pentaquark, we present the rapidity distributions of pentaquark clusters with different strangeness in the qMD calculations for SPS events, and have a short look at pentaquark clustering rates.

The rapidity distribution of pentaquark clusters with different strangeness in qMD is shown in figure 8.26 for SPS events with collision energies of $30\,\mathrm{GeV}/N$ and $160\,\mathrm{GeV}/N$. The Θ^+ pentaquark contributes to the $S = +1$ data with a $\bar{s}$ antiquark as shown in the blue, solid line marked with circles. The rapidity distribution of these states follows closely the total rapidity distribution of all pentaquark states, scaled down by a factor of 25 at the lower, and 15 at the higher collision energy. Furthermore, the distribution is a little flatter than the total rapidity distribution, especially at the higher energy. The Ξ_5^{--} and its isospin partners contribute to the $S = -2$ data with $\bar{q}$ antiquark, which are shown in the orange, short-dashed line below the $S = +1$, $\bar{s}$ data. In all datasets, there is not much information in the distribution of pentaquark clusters with different strangeness beyond total number scaling. This is even more the case for the rapidity spectra from our thermal events, which, therefore, are not shown here.

However, there is an interesting feature in the clustering rates of pentaquark clusters with different strangeness shown in figure 8.27. We can see that the time when clustering rates reach their maxima increases with strangeness. This can be observed best in the data for clusters with a $\bar{q}$ antiquark at the collision energy of $160\,\mathrm{GeV}/N$: Here, the peaking times increases from $t_{\mathrm{p}} \approx 7\,\mathrm{fm}/c$ for $S = 0$ clusters with a $\bar{q}$ antiquark to $t_{\mathrm{p}} \approx 9\,\mathrm{fm}/c$ for $S = 2$ clusters. A similar trend is visible

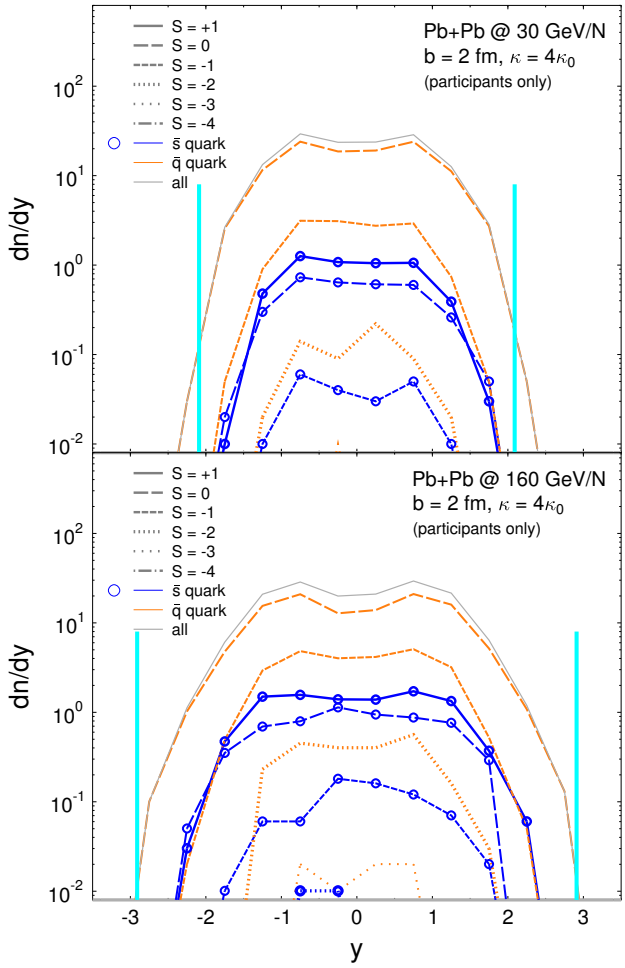

Figure 8.26
Rapidity distribution of pentaquark clusters in qMD data for SPS initial conditions, broken down according to the strangeness S of the pentaquark.

in the results for clusters with a $\bar{s}$ antiquark. This can be interpreted as a manifestation of strangeness distillation [45, 46, 263], which has been observed in qMD calculations before [134, 264]: A deconfined quark system with non-vanishing chemical potential contains more up and down quarks than antiquarks. On the other hand, the number of strange and antistrange quarks is exactly the same, due to strangeness conservation. At hadronization, the biggest part of strangeness (and antistrangeness) ends up in kaons. However, since there are more up and down quarks than up and down antiquarks, kaons withdraw antistrange quarks more efficiently from the deconfined matter than strange quarks. As a consequence, the shrinking deconfined quark system is enriched in strange quarks.

The idea of strangeness distillation was proposed originally as a scenario for the formation of strangelets and multistrange clusters in heavy ion collisions and as a clear signal for the formation of a quark-gluon plasma. Experimental search programs at the AGS, the SPS, and at RHIC did not find any strangelets so far [265, 266, 267]. However, it is invoked to understand the pattern of abundances of multistrange baryons in heavy ion collisions which can not be understood from hadronic models alone [100]. Here, it can be seen at work in a model which dynamically handles explicit quark degrees of freedom.

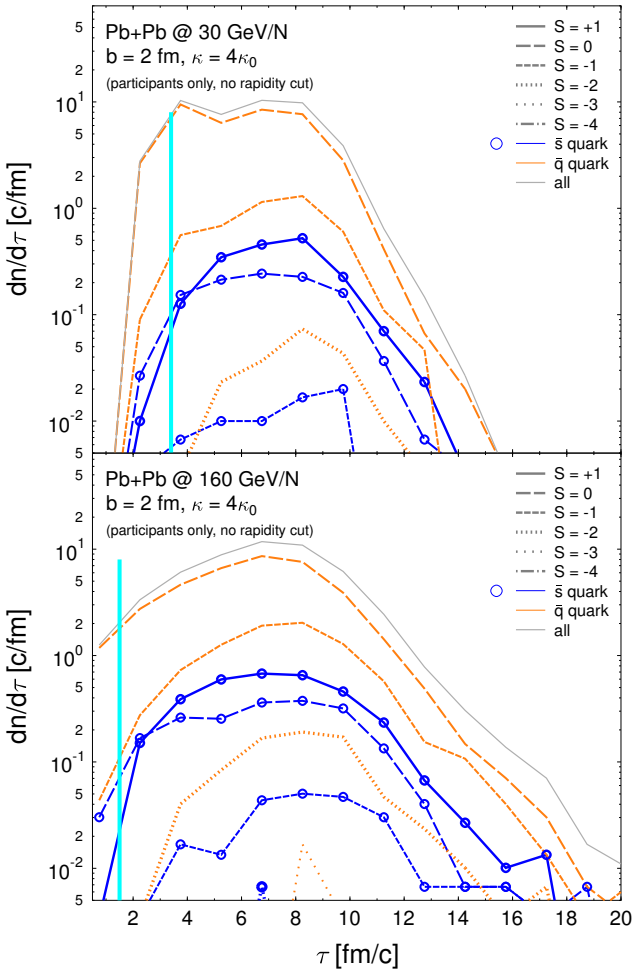

Figure 8.27
Clustering rates for pentaquark clusters in qMD for SPS initial conditions, broken down according to the strangeness S of the pentaquark. The tendency that clustering rates peak later with increasing pentaquark strangeness, best visible in the data for pentaquarks with a $\bar{q}$ antiquark at a beam energy of $160\,\mathrm{GeV}/N$, can be interpreted as a manifestation of strangeness distillation.

8.5 Isospin and spin of pentaquarks in qMD

In this section, we analyse in detail how the yields of pentaquark clusters produced in qMD with a given strangeness are distributed with respect to isospin, and spin. We will find correlations in the distribution of clusters over spin and isospin in the qMD results for SPS events, similar to those in the abundances with respect to strangeness encountered in the previous section.

The analysis of isospin and spin then allows predictions for the abundances of specific pentaquark states to be produced in the quark recombination scheme. In the following section 8.6, we will focus on the ratio of the Θ^+/Λ, which was obtained before only from thermal models [210, 211].

8.5.1 Coupling quarks to pentaquarks: Different schemes

Table 8.9(a) shows raw data and estimates we have already discussed: It lists qMD simulation yields of pentaquark clusters with different strangeness, produced in 200 events for Pb+Pb collisions at the SPS with impact parameter $b = 2\,\mathrm{fm}$ and a beam energy of $E = 160\,\mathrm{GeV}/N$. The row labelled “data” contains the numbers of

(a) numbers for:	$S=+1$	$S=0$	$S=-1$	$S=-2$	$S=-3$	$S=-4$	all
data	979.00	11768.00	2586.00	225.00	7.00	0.00	15565.00
SU(6)	1111.79	4200.08	5385.98	3458.89	1260.02	148.24	
SU(3)	1024.86	4099.42	5636.71	3587.00	1088.91	128.11	
combinatorics	1101.66	10910.63	3182.47	352.50	17.41	0.32	

(b) numbers for $S=1$:	$T=0$	$T=1$	$T=2$
data	130.00	611.00	238.00
SU(6)	74.12	667.07	370.60
SU(3)	128.11	576.48	320.27
$N(S=1)\cdot$ SU(6)	65.27	587.40	326.33
$N(S=1)\cdot$ SU(3)	122.38	550.69	305.94
$N(S=1)\cdot$ SU(2)	122.38	550.69	305.94
combinatorics $\cdot$ SU(6)	73.44	661.00	367.22
combinatorics $\cdot$ SU(3)	137.71	619.69	344.27
combinatorics $\cdot$ SU(2)	137.71	619.69	344.27

(f) probabilities of quark flavours	
$p(q)$	0.5369
$p(\bar{q})$	0.3833
$p(s)$	0.0399
$p(\bar{s})$	0.0399

(c) numbers for $S=1, T=0$:	$s=\frac{1}{2}$	$s=\frac{3}{2}$	$s=\frac{5}{2}$
data	58.00	57.00	15.00
SU(6)	24.71	49.41	—
SU(3) $\cdot$ SU(2)	40.03	64.05	24.02
$N(S=1)\cdot$ SU(6)	21.76	43.51	—
$N(S=1)\cdot$ SU(3) $\cdot$ SU(2)	38.24	61.19	22.95
$N(S=1)\cdot$ SU(2) $\cdot$ SU(2)	38.24	61.19	22.95
combinatorics $\cdot$ SU(6)	24.48	48.96	—
combinatorics $\cdot$ SU(3) $\cdot$ SU(2)	43.03	68.85	25.82
combinatorics $\cdot$ SU(2) $\cdot$ SU(2)	43.03	68.85	25.82
$N(S=1,T=0)\cdot$ SU(2)	40.63	65.00	24.38

(d) numbers for $S=-2$:	$T=\frac{1}{2}$	$T=\frac{3}{2}$	
data	115.00	110.00	
SU(6) $[\overline{\mathbf{10}};\mathbf{27}+\mathbf{35}]$	1976.51	296.48	1185.90
SU(3) $[\overline{\mathbf{10}};\mathbf{27}+\mathbf{35}]$	2049.71	512.43	1024.86
$N(S=-2)\cdot$ SU(6)	128.57	19.29	77.14
$N(S=-2)\cdot$ SU(3)	128.57	32.14	64.29
$N(S=-2)\cdot$ SU(2)	112.50	112.50	—
combinatorics $\cdot$ SU(6)	201.43	30.21	120.86
combinatorics $\cdot$ SU(3)	201.43	50.36	100.71
combinatorics $\cdot$ SU(2)	176.25	176.25	—

(e) numbers for $S=-2, T=\frac{3}{2}$:	$s=\frac{1}{2}$		$s=\frac{3}{2}$		$s=\frac{5}{2}$	
data	49.00		54.00		7.00	
SU(6) $[\overline{\mathbf{10}};\mathbf{27}+\mathbf{35}]$	98.83	296.48	197.65	592.95	—	296.48
SU(3) $[\overline{\mathbf{10}};\mathbf{27}+\mathbf{35}]\cdot$ SU(2)	160.13	320.27	256.21	512.43	96.08	192.16
$N(S=-2)\cdot$ SU(6)	6.43	19.29	12.86	38.57	—	19.29
$N(S=-2)\cdot$ SU(3) $\cdot$ SU(2)	10.04	20.09	16.07	32.14	6.03	12.05
$N(S=-2)\cdot$ SU(2) $\cdot$ SU(2)	35.15	—	56.25	—	21.10	—
combinatorics $\cdot$ SU(6)	10.07	30.21	20.14	60.43	—	30.21
combinatorics $\cdot$ SU(3) $\cdot$ SU(2)	15.74	31.47	25.18	50.36	9.44	18.88
combinatorics $\cdot$ SU(2) $\cdot$ SU(2)	55.08	—	88.12	—	33.05	—
$N(S=-2,T=3/2)\cdot$ SU(2)	34.38	—	55.00	—	20.63	—

Table 8.9
Total numbers of pentaquark clusters in qMD simulations of 200 events for Pb+Pb collisions with $b=2\,\mathrm{fm}$ at the SPS with a beam energy of $E=160\,\mathrm{GeV}/N$.

pentaquark clusters with different strangeness S produced in qMD. These numbers are compared to the numbers to be expected if the total number of 15 165 pentaquark clusters is distributed over strangeness (1) according to the combinatorial expectation (8.12) (in row "combinatorics"), (2) according to a complete flavour SU(3) symmetry (in row "SU(3)"), and (3) according to a complete spin-flavour SU(6) symmetry (in row "SU(6)"). The probabilities for a quark or antiquark having a given flavour, which are used in (8.12), are listed in table 8.9(f). They are obtained by simple quark counting in the qMD initial conditions. The relative numbers of pentaquark states with different strangeness in the case of complete SU(3) symmetry can be read off from the numbers of states with a given strangeness in the multiplet structure in figure 8.2. This yields

$$\begin{aligned} n_{S=+1} : n_{S=0} : n_{S=-1} : n_{S=-2} : n_{S=-3} : n_{S=-4} \\ = 16 : 64 : 88 : 56 : 17 : 2 \ . \end{aligned} \tag{8.14}$$

The analogous pentaquark multiplet structure for the spin-flavour SU(6) coupling scheme is shown in figure C.1 in appendix C.3, where a more detailed explanation of spin-flavour SU(6) can be found. The resulting ratios in a completely SU(6) symmetric situation are

$$\begin{aligned} n_{S=+1} : n_{S=0} : n_{S=-1} : n_{S=-2} : n_{S=-3} : n_{S=-4} \\ = 90 : 340 : 436 : 280 : 102 : 12 \ . \end{aligned} \tag{8.15}$$

Distributing the total yield of pentaquark clusters over strangeness according to the ratios (8.14) and (8.15) results in the numbers given in rows "SU(3)" and "SU(6)" in table 8.9(a). A comparison of the qMD data to the SU(3) expectation was shown in figure 8.23, and to the combinatorial expectation in figure 8.24. We have seen that the SPS results show no full SU(3) symmetry. Similarly, full SU(6) symmetry is badly violated. Instead, the combinatorial expectation gives a reasonable description of the distribution over strangeness.

Tables 8.9(b) and 8.9(c) focus on pentaquark clusters with strangeness $S = +1$, which include the Θ^+, whereas tables 8.9(d) and 8.9(e) look in detail on clusters with $S = -2$, where the Ξ_5^{--} is to be found.

While the clustering routine of qMD establishes the strangeness content of a pentaquark cluster by simple quark flavour counting, isospin and spin are determined according to the correct Clebsch-Gordan coupling of SU(2). Thus, the row "data" in table 8.9(b) shows how the 979 pentaquark clusters with strangeness $S = +1$ are distributed over isospin T, and in the row "data" of table 8.9(c), the yield of the 130 isoscalar $S = +1$ pentaquark clusters is broken down once more according to spin. Tables 8.9(d) and 8.9(e) do the same for $S = -2$ states. As a result, and assuming a spin $s = 1/2$ for both the Θ^+ and the Ξ_5^{--}, we obtain the following yields per event:

$$n_{\Theta^+} = 0.29 \ , \quad n_{\Xi_5^{--}} = 0.061 \ . \tag{8.16}$$

For the Ξ_5, we have assumed that the 49 clusters with $S = -2$, $T = 3/2$, and $s = 1/2$ are equally distributed over the four different isospin projection T_3. The yields given in (8.16) have statistical errors which are in the order of $1/\sqrt{200} = 7\%$.

Furthermore, they may suffer from systematic errors since the coupling of spin and flavour in the qMD clustering routine is done independently.

In order to assess these systematic effects, tables 8.9(b)–8.9(e) also give numbers of pentaquark cluster yields under the assumption of full spin-flavour SU(6) symmetry, and flavour SU(3) symmetry combined with a SU(2) symmetric spin coupling. Remember that the SU(6) scheme yields a complete classification in strangeness, isospin, and spin, which is shown in (C.17). Corresponding numbers are listed in the rows labelled "SU(6)". Numbers for flavour coupling are listed in tables 8.9(b) and 8.9(d) in the rows labelled "SU(3)", and with independent flavour and spin coupling under the label "SU(3) · SU(2)" in tables 8.9(c) and 8.9(e). Moreover, these coupling schemes can be restricted to pentaquark clusters with a given strangeness—in our case to clusters with $S = +1$ and $S = -2$. Among such clusters, besides the SU(6) and SU(3) coupling, simple isospin SU(2) coupling of the up and down quarks can be considered. These strangeness restricted couplings can be related to both the qMD yields for these values of S, as listed under "data" in table 8.9(a), and to the combinatorial expectation values, as listed under "combinatorics" in table 8.9(a). This then yields the numbers listed under "$N(S = S_0) \cdot \mathrm{SU}(M)$" and "combinatorics · SU(M)" (with $S_0 = +1, -2$ and $M = 2, 3, 6$) in tables 8.9(b)–8.9(e). We will now explain in more detail how these numbers are obtained.

8.5.2 SU(6) coupling of quarks to pentaquarks

In the SU(6) classification of pentaquark states given in (C.17), there are exactly two multiplets which are isoscalars for strangeness $S = +1$, the $\left(\overline{\mathbf{10}}; 1/2\right)$ and the $\left(\overline{\mathbf{10}}; 3/2\right)$. Through their spin multiplicities, they contribute 2 and 4 states to the $S = -1$, $T = 0$ pentaquark states. Remember that the SU(6) scheme contains in total 1260 states. Thus, $6/1260$ out of 15565 total pentaquark clusters would have these quantum numbers under perfect SU(6) symmetry, or 74.12. The $S = -1$, $T = 1$ states are populated by the $2 \times 3 \times 2 = 12$ states of the two $(\mathbf{27}; 1/2)$ multiplets, the 24 states of the two $(\mathbf{27}; 3/2)$ multiplets, and the 18 states of the $(\mathbf{27}; 5/2)$ multiplet, providing altogether 54/1260 out of 15565 or 667.07 states. Similar, the $S = -1$, $T = 2$ states come from the multiplets $(\mathbf{35}; 1/2)$ and $(\mathbf{35}; 3/2)$ with 10 and 20 states, respectively, providing $(30/1260) \cdot 15565 = 370.60$ states.

All these numbers can be understood best when splitting up the cut at $S = +1$ through the SU(6) multiplet structure C.1 according to the contributing SU(3) multiplets as follows:

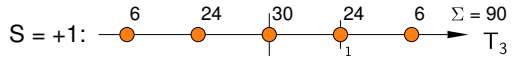

(8.17)

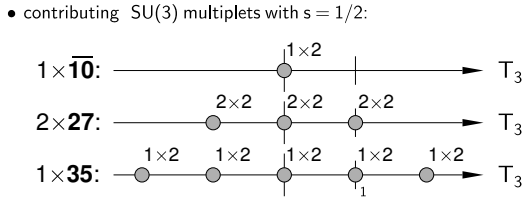

(8.18)

• contributing SU(3) multiplets with s = 3/2:

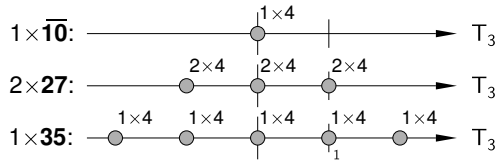

(8.19)

• contributing SU(3) multiplets with s = 5/2:

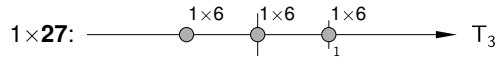

(8.20)

Here, the numbers indicate the multiplicities of the states, whose strangeness, isospin projection, and spin are all specified. Finally, we can read from this listing that among the $S = -1$, $T = 0$ states in (8.18) and (8.19), 2 out of 2+4 have spin $s = 1/2$, while the remaining ones have spin $s = 3/2$. There are no $s = 5/2$ states with $S = -1$ and $T = 0$ in SU(6). Thus, full SU(6) symmetry predicts a multiplicity of $(2/1260) \cdot 15565 = 24.71$ for Θ^+ pentaquarks in 200 events.

A similar argument applies to the $S = -2$ pentaquark states. Here, on has to bear in mind that the $\overline{\mathbf{10}}$ has isospin $T = 3/2$ for $S = -2$, but that the multiplets **27** and **35** contribute to $T = 3/2$, $S = -2$ as well. The following partitioning of the cut at $S = -2$ through the SU(6) multiplet structure C.1 according to the contributing SU(3) multiplets is useful:

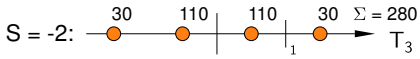

(8.21)

• contributing SU(3) multiplets with s = 1/2:

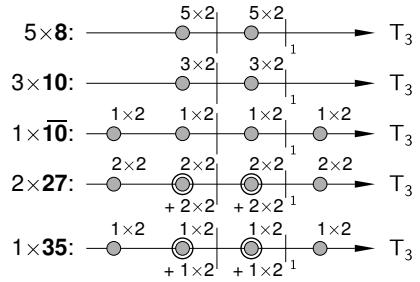

(8.22)

• contributing SU(3) multiplets with s = 3/2:

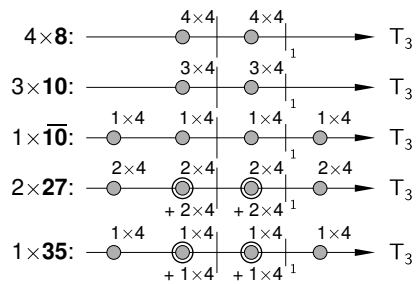

(8.23)

• contributing SU(3) multiplets with s = 5/2:

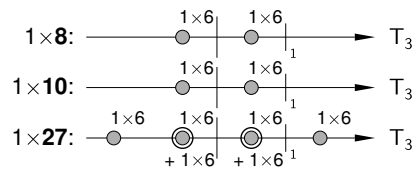

(8.24)

For example, there are $(160/1260) \cdot 15565 = 1976.51$ pentaquark states with $S = -2$ and $T = 1/2$ to be expected in the fully SU(6) symmetric case (none of those in a flavour $\overline{\mathbf{10}}$), whereas the estimate for $S = -2$ and $T = 3/2$ is $(120/1260) \cdot 15565 = 1482.38$ pentaquarks. Of these, however, only $(24/1260) \cdot 15565 = 296.48$ are flavour $\overline{\mathbf{10}}$ states, thus candidates for the Ξ_5. Zooming in onto the $S = -2$, $T = 3/2$, $s = 1/2$ states of the Ξ_5 isospin quadruplet, SU(6) symmetry predicts $(8/1260) \cdot 15565 = 98.83$ states, out of which one quarter, hence 24.71, are expected to be Ξ_5^{--} states. It should be no surprise that this number is the same as for the Θ^+, since we have considered both states as members of the same multiplet and assumed a full SU(6) symmetry.

8.5.3 SU(3) coupling of quarks to pentaquarks

The SU(3) classification is a little bit simpler: The decomposition (8.3) shows that there are two $\overline{\mathbf{10}}$ multiplets with $T = 0$ for $S = +1$. Since there are 243 SU(3) states altogether, this yields $2/243$ out of 15565 or 128.11 states for the Θ^+. Keep in mind that spin is not yet taken into account. Contributions to isospin $T = 1$ multiplets for $S = +1$ stem from the three **27** multiplets, providing $3 \cdot 3/243$ of all states, and to the $T = 2$ multiplets from the single **35** multiplet, contributing 5/243 of the states. All this can be seen best in the following cut through the multiplet structure in figure 8.2 for $S = +1$:

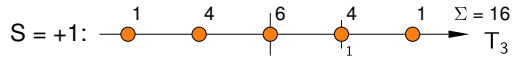

(8.25)

• contributing SU(3) multiplets:

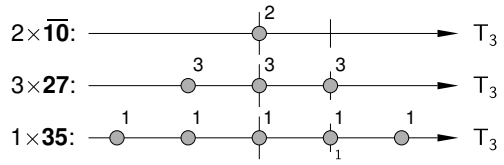

(8.26)

The analogous splitting for the $S = -2$ states reads:

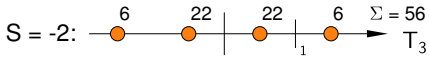

(8.27)

• contributing SU(3) multiplets:

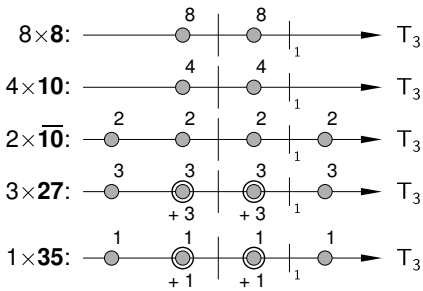

(8.28)

Thus, full SU(3) symmetry predicts $(32/243) \cdot 15565 = 2049.71$ pentaquark states with $S = -2$ and $T = 1/2$, and $(24/243) \cdot 15565 = 1537.28$ states with $S = -2$ and $T = 3/2$. Of these states, however, $(16/243) \cdot 15565 = 1024.86$ are members

of flavour **27** and **35** multiplets, leaving $(8/243) \cdot 15565 = 512.43$ clusters for the Ξ_5 isospin quadruplet. Again, one quarter of these are expected to be Ξ_5^{--} states, or 128.11 particles, as for the Θ^+.

Since the flavour SU(3) scheme does not couple spins, calculation of spin is done independently of flavour coupling. It amounts to a simple coupling of five SU(2) spins, which follows from the known decomposition of the product of five $s = 1/2$ doublets in irreducible multiplets:

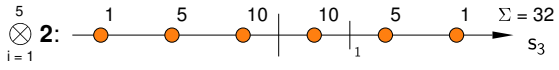

(8.29)

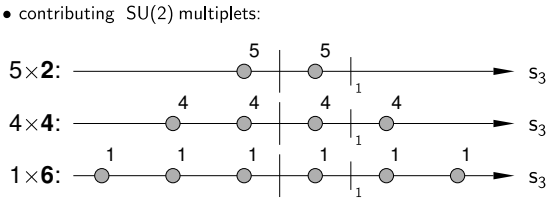

(8.30)

We see that only $10/32 = 5/16$ of all flavour SU(3) can be considered to be spin $s = 1/2$ states. Thus, complete flavour SU(3) symmetry with independent coupling of spin predicts 40.03 clusters for Θ^+ and Ξ_5^{--} in 200 events. These numbers are listed in tables 8.9(c) and 8.9(e) in the rows labelled with "SU(3) · SU(2)". Note that the independent coupling of flavour and spin predicts states with $S = +1$, $T = 0$, and $s = 5/2$, which are absent in the combined spin-flavour SU(6) scheme.

8.5.4 Restricting SU(6) and SU(3) couplings to fixed strangeness

As we have discussed before, full spin-flavour SU(6) and flavour SU(3) symmetric conditions are not achieved in the SPS events. This is clearly visible in the multiplicities of pentaquark states: The multiplicities for a given strangeness are slightly overestimated for $S = +1$, but grossly wrong for $S = -2$ in both coupling schemes. Focussing on specific states, the yields of Θ^+ are underestimated, while those of the Ξ_5 are overestimated. However, this does not mean that the detailed analysis of how pentaquarks with different strangeness are distributed over isospin and spin in the SU(6) and SU(3) coupling schemes is useless. We have seen that combinatorial yields for different strangeness according to (8.12) are in good agreement with the qMD data, with deviations which can be understood from correlations in the deconfined system.

Hence, we can distribute these combinatorial yields for $S = +1$ and $S = -2$ over spin and isospin according to the SU(6) and SU(3) decompositions (8.17), (8.21), (8.25), and (8.27). Furthermore, we can apply this distribution to the actual qMD yields of pentaquark clusters with $S = +1$ and $S = -2$.

For example, the decomposition of (8.17) shows that in the SU(6) coupling scheme for $S = +1$, the total number of 90 states splits up into 6 states in $T = 0$ isospin singlets, 54 states in $T = 1$ isospin triplets, and 30 states in $T = 2$ isospin quintets. Distributing the actual yield of 979 pentaquark clusters with $S = +1$, or the combinatorial expectation of 1101.66 clusters with $S = +1$, over isospin according to the ratios $6 : 54 : 30$ gives the numbers in the rows "$N(S = 1) \cdot$

SU(6)" and "combinatorics · SU(6)" in table 8.9(b). The same analysis can be repeated with ratios derived from the SU(3) coupling scheme—from (8.25), they are $2:9:5$—, and for pentaquark clusters with $S=-2$ as well. In the latter case, the SU(6) scheme (8.21) gives a distribution of clusters over states with $T=1/2$ and $T=3/2$ according to the ratio $160:120=4:3$, where only 24 out of 120 or 1/5 of the states with $T=3/2$ correspond to the flavour $\overline{\mathbf{10}}$ multiplet. For a SU(3) coupling according to (8.27), clusters with $T=1/2$ and $T=3/2$ are populated according to the same ratio $32:24=4:3$, but with 8 out of 24 or 1/3 of the states with $T=3/2$ corresponding to the flavour $\overline{\mathbf{10}}$ multiplet.

8.5.5 Isospin SU(2) coupling for fixed strangeness

Note that as flavour is concerned, the qMD model distinguishes strange quarks from the light isospin quark doublet, and only couples isospin. For pentaquark clusters with $S=+1$, this means that the isospins of the four quarks are added. We can compare the yields from the isospin coupling realized in qMD to the distribution of pentaquark clusters with $S=+1$ over isospin under the assumption of a full isospin symmetric coupling. The relative numbers of multiplets with a given isospin can be calculated using the Clebsch-Gordan coefficients for SU(2), or read off from the decomposition of the product of the four isospin doublets in irreducible isospin multiplets, as shown in the following scheme:

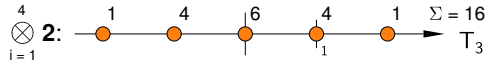

(8.31)

• contributing SU(2) multiplets:

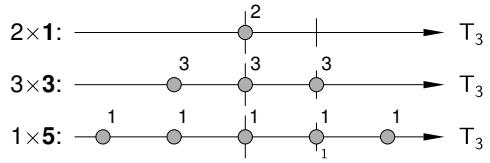

(8.32)

Thus, the distribution over isospin in the pure SU(2) coupling is $2:9:5$ for the ratios of $T=0$ to $T=1$ to $T=3$. Since the states with $S=+1$ lie at the border of the SU(3) multiplets, this result is the same as in the SU(3) scheme, but it is different from the SU(6) scheme. For pentaquark clusters with $S=-2$, the distribution over isospin can be obtained from the well known decomposition of the combination of two isospin doublets and one conjugated doublet,

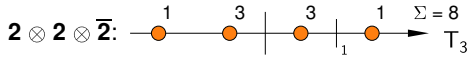

(8.33)

• contributing SU(2) multiplets:

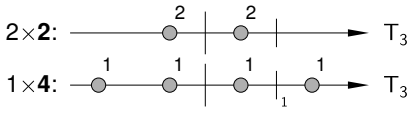

(8.34)

Here, equal weight is given to the states with $T=1/2$ and $T=3/2$.

Applying these ratios for the distribution over isospin in the SU(6), SU(3), and SU(2) coupling schemes to the numbers $N(S=+1)$ and $N(S=-2)$ of

pentaquark clusters with strangeness $S = +1$ and $S = -2$, and to the combinatorial yields of these clusters, yields all numbers produced in tables 8.9(b) and 8.9(d). Finally, in order to obtain the distributions of the $S = +1$, $T = 0$ and the $S = -2$, $T = 3/2$ states over spin which are listed in 8.9(c) and 8.9(e), we recall that these follow directly in the SU(6) coupling scheme, and from an independent spin SU(2) coupling in the flavour SU(3) and isospin SU(2) coupling scheme. This yields the numbers listed in the rows labelled "$N(S = S_0) \cdot \mathrm{SU}(M) \cdot \mathrm{SU}(N)$" and "combinatorics $\cdot \mathrm{SU}(M) \cdot \mathrm{SU}(N)$". If the spin coupling is applied to the actual qMD yield of all $S = +1$, $T = 0$ and $S = -2$, $T = 3/2$ pentaquark clusters, the numbers in the last rows in tables 8.9(c) and 8.9(e) are obtained. We will now discuss some aspects of the wealth of numbers contained in table 8.9.

8.5.6 Insights from the different coupling schemes

First of all, we could expect that the distribution of pentaquark clusters over isospin for $S = +1$ and $S = -2$ in table 8.9(b) and table 8.9(d), as given by the actual qMD data, is in close match with the numbers obtained from isospin coupling according to (8.31) and (8.33), which are listed as $N(S = +1) \cdot \mathrm{SU}(2)$ and $N(S = -2) \cdot \mathrm{SU}(2)$. However, although qMD uses isospin coupling, qMD data are higher than these numbers for low isospin and lower for high isospin for both $S = +1$ and $S = -2$ clusters.

A similar observation can be made when considering the distribution over spin of the pentaquark clusters with $S = +1$, $T = 0$ and $S = -2$, $T = 3/2$ in table 8.9(c) and table 8.9(e). Since qMD couples spin and isospin independently, one would presume that the actual data of abundances with different spins follow the numbers $N(S = S_0, T = T_0) \cdot \mathrm{SU}(2)$ obtained by spin coupling of the quarks in the corresponding clusters. The numbers $N(S = S_0) \cdot \mathrm{SU}(2) \cdot \mathrm{SU}(2)$ expected from isospin and spin coupling should be very close to the abundances $N(S = S_0, T = T_0) \cdot \mathrm{SU}(2)$, which is indeed the case. However, again, the actual data from qMD show an enhancement for states with low spin and a suppression for high spin compared to these numbers.

Since the deviations are especially large for states with the extreme couplings $T = 2$, and $s = 5/2$, we can suspect that they are caused by correlations in the quark system, in a similar manner as in the deviations in the distribution of pentaquark cluster numbers over strangeness from the combinatorial expectation. If the original hadrons contain predominantly low spin states, the projections of the spins of quarks and antiquarks after decomposition will be predominantly antiparallel. Out of spins with such an antiferromagnetic correlation, less high spin states are obtained when coupling back to hadrons than from an uncorrelated gas. The same applies for isospin.

We can check this conjecture with a look at the corresponding numbers for pentaquark clusters obtained from events with thermal initial conditions. The relevant abundances are shown in table 8.10. Here, we find a much better agreement of the actual qMD data with results obtained when applying isospin and spin coupling to the quarks in clusters with $S = +1$ and $S = -2$. Especially for the high spin states, the discrepancies are on the level of $10\,\%$, compared to $300\,\%$ in the SPS events. The deviation in the isospin distribution numbers for $S = -2$ can be

(a) numbers for:	$S=+1$	$S=0$	$S=-1$	$S=-2$	$S=-3$	$S=-4$	all
data	435.00	1679.00	2252.00	1405.00	372.00	44.00	6187.00

(b) numbers for $S=1$:	$T=0$	$T=1$	$T=2$
data	51.00	248.00	136.00
$N(S=1)\cdot$ SU(2)	54.38	244.69	135.94

(f) probabilities of quark flavours	
$p(q)$	0.3423
$p(\bar{q})$	0.3423
$p(s)$	0.1577
$p(\bar{s})$	0.1577

(c) numbers for $S=1, T=0$:	$s=\frac{1}{2}$	$s=\frac{3}{2}$	$s=\frac{5}{2}$
data	19.00	24.00	8.00
$N(S=1)\cdot$ SU(2) $\cdot$ SU(2)	16.99	27.19	10.20
$N(S=1,T=0)\cdot$ SU(2)	15.94	25.50	9.56

(d) numbers for $S=-2$:	$T=\frac{1}{2}$	$T=\frac{3}{2}$	
data	777.00	628.00	
$N(S=-2)\cdot$ SU(2)	702.50	702.50	—

(e) numbers for $S=-2, T=\frac{3}{2}$:	$s=\frac{1}{2}$		$s=\frac{3}{2}$		$s=\frac{5}{2}$	
data	200.00		316.00		112.00	
$N(S=-2)\cdot$ SU(2) $\cdot$ SU(2)	219.53	—	351.25	—	131.72	—
$N(S=-2,T=3/2)\cdot$ SU(2)	196.25	—	314.00	—	117.75	—

Table 8.10
Total numbers of pentaquark clusters in qMD simulations of 1000 events for thermal initial conditions with $T_0 = 250\,\mathrm{MeV}$ and $\mu = 0\,\mathrm{MeV}$.

understood by the contribution of $qssss\bar{s}$ clusters, which have $S=-2$, $T=1/2$, and contribute $\approx 14\,\%$ to all $S=-2$ clusters in the thermal events.

Thus, we have found in the distribution of spin and isospin of pentaquark clusters a similar pattern as in the distribution of strangeness: In the qMD data for SPS events, recombining quarks still bear correlations left form their hadronic origins. Again, this does not necessarily reflect some real, physical phenomenon in SPS collisions. However, it shows that such distributions may be used as signs of thermalization and homogenization of the deconfined phase.

Finally, we can come back to the abundance of clusters with quantum numbers of the Θ^+ and Ξ_5^{--}. The numbers provided in (8.16) come from actual qMD data. We have seen in detail how the use of different flavour and spin coupling schemes applied to clusters with strangeness $S=+1$ and $S=-2$ will change this result. Table 8.9(c) shows that the yield of Θ^+ can be lowered by a factor ≈ 2.5 if the spin-flavour SU(6) coupling scheme is used. This suppression is even bigger for the Ξ_5^{--}, with a factor 5–7 for SU(6). The reason for this large differences is to be found in the use of the isospin coupling scheme in qMD, which can not discriminate whether a $T=3/2$ quadruplet belongs to the flavour antidecuplet, or to the **27** or **35** multiplets. We conclude that the coupling scheme used in the qMD model may overestimate the numbers of produced Θ^+ and Ξ_5^{--} by factors of ≈ 2.5 and $\approx 5-7$, respectively.

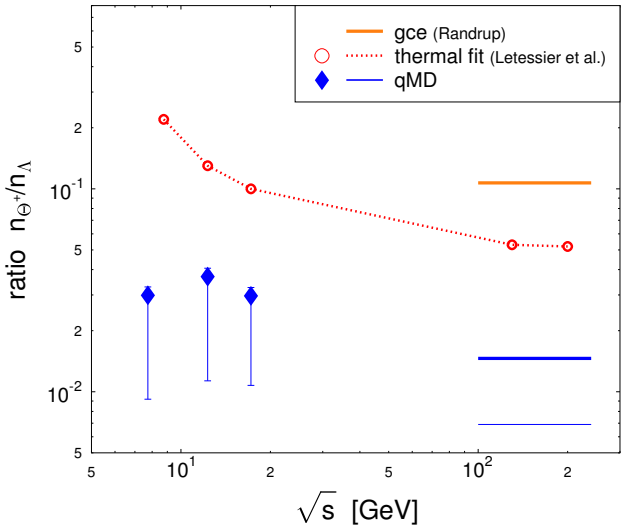

Figure 8.28
Excitation function of the ratio Θ^+/Λ from qMD calculations, compared to predictions of the grand-canonical ensemble and the statistical hadronization model, including appropriate strangeness suppression factors.

8.6 Yields of Θ^+ pentaquarks and the Θ^+/Λ_0 ratio

There remains one major problem in the interpretation of the pentaquark yields for SPS events given in (8.16), $n_{\Theta^+} = 0.3$ and $n_{\Xi_5^{--}} = 0.06$, which is not touched by the extended discussion of the role of spin and flavour coupling in the last section. So far, we have been talking about pentaquark *cluster* yields, and ignored the mapping to actual hadronic states. The main difference lies in the wide mass distribution of pentaquark clusters, as shown in figures 8.9 and 8.10, which are in marked contrast to the small widths of the actual hadrons, such as the Θ^+ and Ξ_5^{--}.

Here, we argue that we can overcome this problem by considering not absolute yields of pentaquark states, but ratios to other hadrons. Since the masses of standard hadronic clusters follow the same wide distribution as those of pentaquark clusters, we can assume that the effects of the neglected mapping to actual hadrons cancel out.

To be specific, we will consider the ratio of Θ^+ pentaquarks to strange Λ_0 baryons. Moreover, this ratio has been estimated for heavy ion collisions in the framework of thermal models. In [210], the grand canonical ensemble was used to obtain estimates for thermal systems with different sets of parameters for temperature and chemical potential, all suited to RHIC conditions. A more sophisticated thermal modelling includes proper strangeness suppression factors, and can then also be applied to the SPS regime [211]. These thermal model results, together with the ratio of Θ^+/Λ_0 obtained in the qMD simulations, are shown in 8.28 as a function of the energy available in the collision. The grand canonical estimate is applied to the RHIC regime, as are the data from the thermal events calculated in qMD. The error bars in the qMD data indicate the uncertainties from the proper spin-flavour coupling within the pentaquark clusters. As we have seen, they will most certainly lower the actual qMD yields, and thus also the Θ^+/Λ ratio.

The result of the qMD results for the Θ^+/Λ_0 ratio are nearly one order of magnitude below the predictions of the statistical hadronization model, which is already below the grand canonical ensemble. Remember that in section 8.3, we have found

a similar difference between qMD and thermal model predictions for the yield of the Y-baryonium. This suggests that thermal models may be too optimistic in their predictions of the abundances of exotic hadrons. At least, the dynamical quark recombination in the qMD model shows that abundances of exotic hadrons in heavy ion collisions may be a good probe to discern statistical hadronization from quark recombination scenarios.

There is, however, a drawback in the qMD simulation data. At the moment, they do not include the effects of rescattering in the hadronic phase. As can be seen in the data for deuterons, hadronic rescattering can be an important factor. The experimental abundance of deuterons at both SPS and RHIC energies is also about one order of magnitude higher than the clustering results for deuterons in qMD simulations. However, the experimental deuteron yield can be understood purely from coalescence in the late, hadronic phase of the collision. On the other hand, there may be feeding to the Θ^+ from the decay of other pentaquark states. In [221] it was suggested that the main production mechanism for the Θ^+ may be the decay of $N^\star$ pentaquarks, which are $qqqs\bar{s}$ states with orbital excitation.

Thus, it is possible that the qMD results should be adjusted upwards by both late stage coalescence of Θ^+, and feeding from $N^\star$. Unfortunately, both effects can not be treated satisfactorily in the current qMD model.

8.7 Discussion of the results

In this chapter, we have seen how the qMD model can be applied to the search for exotic hadrons, which may be created by quark recombination in the hadronization stage of an ultra-relativistic heavy-ion collision. The search comprises clusters of up to six quarks and/or antiquarks, and estimates for the abundances of deuterons, Y-baryonia, and Θ^+ and Ξ_5 pentaquarks are inferred from the qMD data.

Deuteron yields can be compared to experimental data, and estimates for other exotic hadrons can be contrasted with the predictions of thermal models and statistical hadronization.

The qMD prediction for deuteron abundances lies about one order of magnitude below the observed data. However, these data are understood best by hadronic coalescence in the late, hadronic rescattering stage of the collision.

For exotic hadrons in general, the quark recombination scheme of qMD gives numbers about one order of magnitude below the thermal model. This may be used to discriminate between statistical hadronization and quark recombination as the mechanism of hadronization.

Focussing on pentaquark clusters, a detailed analysis of the distribution of clusters over strangeness, and of clusters with specific strangeness over isospin and spin, has been carried out. All these distributions are found to be sensitive to the actual thermalization and homogenization of the deconfined system, and may be used as a probe for the degree of loss of hadronic correlations in a quark-gluon plasma. However, this is of course feasible only if some pentaquark states really exist and can be reconstructed in heavy-ion collisions.

Concerning this detectability of exotic hadrons, we note that the qMD model provides, besides gross number estimates, detailed distributions in rapidity and

transverse momentum. The rapidity distribution of pentaquarks suggests that these exotic states may be detectable best at the edges of the central plateaus in the rapidity distributions.

Part IV

The qMD model: Conclusions and Outlook

Die Eule der Minerva beginnt erst mit der einbrechenden Dämmerung ihren Flug.

— Georg Wilhelm Friedrich Hegel

In this last part, we summarize what has been achieved so far to promote our understanding of ultra-relativistic heavy ion collisions through the application of the qMD model. We recapitulate the main results, before moving on to a discussion of possible further applications and to roads to improve and expand the model.

Chapter 9

What have we learned?

9.1 What has been achieved?

The subject of this thesis is the quark molecular dynamics model qMD, which provides a description of the recombination dynamics of a system of colour charges which are subject to a confining potential interaction. We have studied the properties and characteristical features of this model, and we have applied it to problems of current interest in the field of ultra-relativistic heavy ion collisions.

The first part of this thesis has traced the background of this study: We have followed the development of our current understanding of the structure of matter, from atoms down to the scale of quarks and gluons. We have seen how these constituents interact, how these interactions are understood within the theoretical framework of QCD, and how the complexity of QCD is reflected in the phase diagram of elementary matter, which is the subject of current research. The only experimental means so far to study the phase diagram are heavy ion collisions at ultra-relativistic energies. The interpretation of data obtained in these experiments requires model studies and simulations, which allow to formulate expectations and predictions on the basis of well-established physical phenomena, and which provide a benchmark for the identification of signals of novel and interesting physics.

Models on the market for the simulation of ultra-relativistic heavy ion collisions are in most cases either hadronic or partonic transport codes. The treatment of effects of soft QCD and quark degrees of freedom based on model theories derived from QCD, such as NJL- and Friedberg-Lee models, is demanding in numerics and, unfortunately, not very practical for the study of ultra-relativistic heavy ion collisions. However, these soft degrees of freedom are essential if one wants to understand in the dynamics of hadronization. Hadronization driven by the recombination of quarks leaves a distinctive signature in several experimental observables at RHIC, so it is very important that it can be described in some dynamical model. RHIC data showing recombination are usually interpreted in terms of coalescence models, which miss the dynamics that drives recombination. More elaborate models include a potential interaction between quarks. The dynamical evolution is then be obtained by Vlasov methods, or by molecular dynamics.

In this thesis, we have used the quark molecular dynamics model qMD, where quark are described as a system of classical point particles which carry colour

charges are subject to a confining potential interaction. As it comes out, the dynamical evolution of such a system results in the formation of colour neutral clusters. In contrast to other potential interaction ansätze, the qMD model is supplemented with a dynamical criterion for the mapping of these colour neutral clusters of quarks and antiquarks to hadrons and hadronic resonances.

The characteristical features of the qMD model, its thermal properties and its application to the description of heavy ion collisions at the SPS have been presented in part II of this thesis.

Details of the models are discussed in chapter 4. The criteria for the identification of colour neutral clusters and the mapping to hadrons are described, and the weaker points of the model are identified, such as the missing of quantum mechanics and the Pauli principle, or the deficiencies in the description of proton-proton collisions due to the purely soft, potential interaction between particles. However, chapter 5 reveals the appealing thermal properties of the system: The transition from a deconfined to a clustering phase, and the corresponding softening of the equation of state. The phase diagram of the qMD model is presented, and the influence of the model parameters, as well of a finite system size, on the transition temperature are discussed. The model exhibits dynamical screening, which is studied with respect to the "melting" of the J/Ψ in a thermal environment. Finally, in chapter 6, the application of the qMD model to the description of heavy ion collisions at the SPS is presented. The hadronic model UrQMD is used to provide the initial conditions. We have seen how the phase space distributions of hadrons from UrQMD are converted into the corresponding distributions of quarks, how these quark distributions evolve in time and are mapped back again to hadronic distributions. The complete expansion dynamics can be studied. We see, moreover, that the time evolution is out of equilibrium, and that conventional measures for temperature derived from transverse momentum spectra or particle ratios yield very different results for temperature. There is an influence of the cluster formation criteria on the time scale of hadronization, which is examined at the example of vector mesons. Finally, an analysis of the full dynamics and the final state hadron yields of S+Au collisions at the CERN-SPS reveals that the overall description obtained from the qMD model is very reasonable, but that for a quantitative account of all particle species, a detailed treatment of rescattering should be supplemented.

The true strength of the qMD model is the access to the dynamics of the quark degrees of freedom. This has been exploited in part III of this thesis, where fluctuations of electric charge and the formation of exotic hadrons are studied.

Event-by-event fluctuations of electric charge have proposed as a signal that allows to distinguish between a quark-gluon plasma and a hadron gas. However, experimental data only show the hadron gas signal, even for collisions at RHIC, where the transient formation of a deconfined phase is undisputed. It has been proposed that this can be understood as a consequence of the hadronization via the recombination of quarks. Indeed, the qMD model offers a unique possibility to check this proposal in a simulation: In chapter 7, we follow the complete time evolution of the fluctuation measure and see how it changes smoothly from the value of the QGP to the value of a hadron gas, while quarks and antiquarks recombine to hadronic clusters. Thus, cluster hadronization does, indeed, destroy the fluctuation signal expected from a quark-gluon plasma. Since in the estimation of fluctua-

tions, entropy conservation is important, we have included a discussion of entropy in qMD. There, we argue that the temporary decrease in the number of particles caused by the formation of clusters is balanced by the high mass of the clusters, so that on the whole, entropy is conserved in the process of hadronization.

Finally, in chapter 8, we have studied the formation of exotic hadrons in the qMD model. This investigation was motivated by the recent excitement about the alleged discovery of pentaquark states, and we have started with a short review on exotic hadrons, before embarking on the study on the formation on exotic clusters made up of up to six colour charges. The qMD model provides us with detailed phase space distributions of exotic hadrons. There are high yields of exotic states, which, however, are due to the size of the corresponding multiplets: Only some of these states are proposed to be stable, and all others decay immediately into standard hadrons. For the deuteron, H dibaryons, and Y baryonium, number estimates are deduced. The comparison of the deuteron yield to experimental data shows the importance of final state rescattering, which, unfortunately, is not included in the qMD model. Then, we have focussed on pentaquark states. We obtain rapidity distributions, which may be helpful in experimental search programs. We find an extra mass of the pentaquark clusters compared to the simple coalescence which is in the order of the observed mass above threshold. The time evolution of the formation of pentaquarks with different strangeness shows signs of strangeness distillation. We have analysed the population of the complete multiplet structure over strangeness, isospin, and spin in order to obtain a number estimate for the $\Theta+$. This estimate is markedly below thermal model predictions. This emerges as a typical feature of cluster hadronization: number estimates are much lower than from thermal models. Moreover, the distribution of exotic states over strangeness, spin, and isospin turns out to be very sensitive to thermalization and correlations among quarks. In the qMD simulations of SPS events, there are correlations among quarks induced by their common origin in hadrons from UrQMD. This is, of course, in part an artifact of the model. However, if the signal itself, the distribution of states over some large multiplet structure, could be measured, this would provide very revealing insight in the nature of the deconfined matter.

9.2 What can be done next?

As an outlook, we give a short sketch of further studies and applications that are possible with the qMD model, and of options that are open to improve it and to make it more realistic.

9.2.1 Further applications of the qMD model

We have mentioned already several obvious further applications of the qMD model in its current version in the main text, which we outline once more here.

Thermodynamical and dynamical studies

This thesis contains already a study of the thermodynamical properties of the qMD model, including finite size effects. Since these last effects are expected to be important in the finite reaction volume encountered in a heavy ion collision, further

and more precise investigations can be rewarding. While finite size effects have been studied for fixed numbers of particles, looking at the effects at fixed volume could be complementary. Moreover, finite time effects could be examined, concerning for example the time scale on which screening is built up.

Finite time effects are important if the dynamical evolution of an expanding fireball is analyzed. In this respect, a more detailed analysis of the full phase space evolution of SPS events, including the different non-equilibrium effects and temperature scales encountered, could provide illuminating insights in the non-equilibrium expansion dynamics. Moreover, the detailed analysis presented for S+Au collisions at the SPS could be extended over the whole range of the Pb+PB program at the SPS, where copious data is available from the NA 49 collaboration.

Fluctuation and correlation signals

Th qMD model offers a unique access to the study of fluctuation and correlation signals that are driven by quark degrees of freedom. The fluctuation studies of electric charge can be extended to new fluctuation and correlation probes, such as the baryon-strangeness correlation and charge transfer fluctuation signals. These are very straightforward, rewarding projects. Moreover, examinations of fluctuations in transverse energy and momentum could be tried.

Heavy quark flavours

This thesis includes a discussion of the melting of the J/Ψ in an thermal environment. This study also demonstrates the importance of "mixed" J/Ψ, where the contributing charm quarks are not created in the same scattering process. This study could be expanded to dynamical environments, as they occur in heavy ion collisions. This might provide insight in the use of the J/Ψ and its suppression as a probe of deconfinement. First steps in this direction have already been done, but are not reported in this thesis. Moreover, with respect to RHIC physics, a quantitative evaluation of the role of "mixed" J/Ψs would be interesting. Finally, at RHIC, and even more so at the LHC, bottom quarks are expected to be created in heavy ion collisions. The present version of qMD does not include bottom, but an extension of the model in this dimension of flavour space is straightforward

Exotica

It may be interesting to extend the detailed study of pentaquark states to hexaquarks also, in order to obtain better data for dibaryon and baryonia predictions. Moreover, some tetraquark (or presumed tetraquark) states such as the D_{sJ} or the scalar mesons, if understood as tetraquarks, could be examined.

Recombination signals at RHIC

As has been discussed, RHIC data show several peculiarities that are explained best in the quark recombination scheme. The qMD model offers, in principle, everything that is needed to study this effects. There is only one drawback: For full RHIC events, the model hits the ceiling of forbidding numerical needs if more than single events are to be studied. Thus, studies of elliptic flow, but also of moderately high transverse momentum, are not possible with reasonable statistics. Charm elliptic flow at RHIC, for example, is an extremely interesting object of

investigation, but numerically forbidden. Here, a resort could be found in a clever preparation of suited initial conditions which mimic, for example, RHIC conditions after thermalization of the quark-gluon plasma at mid-rapidity.

9.2.2 Amendments of the model

From the comparison of the qMD model with other approaches that treat quark degrees of freedom in chapter 3, and from the discussion of the weaker points of the model in chapter 4, we could deduce several proposals how to improve qMD, which we summarize here.

Improving the potential interaction

The Cornell potential which is used in qMD is, quite obviously, not the best one could do. One could think about the inclusion of relativistic corrections, such as Breit-Fermi terms. Moreover, the inclusion of a Pauli potential to mimic Fermi statistics would be an important prerequisite to use qMD in the regime of low temperature and low density.

However, as has been discussed in chapter 4, using a potential interaction is not the most satisfying approach to model the colourelectric field. It would be worthwhile to replace the potential interaction by a Friedberg-Lee type network of local strings. Since this is not a workable option because of the computing requirements, the development of heuristic rules to describe the network of colourelectric flux could be helpful. It is not clear, however, how cut-off criteria for hadronization could be defined in such a scheme.

A dynamical string constant or a cut-off in the range of the interaction?

If one sticks to the potential interaction, one might think about an improvement of the qMD model if the fixed value of the string constant is replaced by a dynamically determined value. This could mimic the vanishing of the string constant above the deconfinement temperature in full QCD. However, one has to keep in mind that the potential interaction between quarks is nonlocal and extends over the whole volume of the system. Thus, a consistent modelling of a temperature dependent string constant works only if there is exactly one temperature for the whole system. Since the non-equilibrium character of qMD, which allows for different local temperatures in different parts of the system, is a big advantage, it may not be very helpful to insist on a single, global temperature as required by the consistent introduction of a temperature dependent string constant.

Similar, one might think of the introduction of a cut-off of the range of the potential in order to mimic screening. However, as we have seen, screening is implemented dynamically in qMD, thus, the introduction of a cut-off leads to double counting of degrees of freedom. Moreover, the introduction of a cut-off spoils the overall confining properties of a system of colour charges that is colour neutral on the whole.

Quark masses and gluons

Another, more feasible option to introduce local model parameters is the use of quark masses that are dynamically calculated. For example, masses could dependent on the local density as in NJL model in order to mimic the chiral transition.

Thus, the interplay between the chiral and the deconfinement transition could be studied. A more modest change of the model is obtained if the current quark masses are replaced by constituent masses, as used in most recombination and potential models. It would be interesting to investigate the influence of the constituent mass on hadron abundances and ratios, but also on hadron phase space distributions and the expansion dynamics of the system. Moreover, fluctuation signals will most probably be influenced, since the introduction of constituent masses reduces the correlation length of quarks recombining to hadrons in both rapidity and transverse momentum.

Finally, gluons are not treated as explicit particles in qMD. It is possible to introduce gluons as particles, as discussed in chapter 4. Then, however, on has to think about what to do with all the hybrid hadrons and glueballs that will be produced by the clustering routine.

However, there is one option that is most interesting: One could mimic the exchange of massive, non-diagonal gluons by the introduction of a colour exchange between quarks at very close encounters, with distances $d \lesssim 0.2\,\mathrm{fm}$. This could result in major improvements of the qMD model in the description of proton-proton collisions, where right now, the cross section is much to low at high energies.

Coupling to other models

As discussed in chapter 3, most models used in the description of heavy ion collisions do not cover the whole range of physical interactions involved in such events. Thus, the qMD model is well suited to the description of hadronization through the dynamical recombination of quarks. However, the initial state has to be provided from elsewhere, and final state hadronic rescattering is important for the quantitative understanding of particle multiplicities and ratios.

So far, the initial state used on qMD is either thermal, or provided by UrQMD. With regard to applications of qMD to RHIC physics, parton cascades or calculations of particle production in classical fields may be better suited in this respect. Final state interactions could be treated by feeding the hadronic content to UrQMD to handle rescattering. All this are options that could be checked with the present version of qMD, independent of all other optional changes, and promise interesting insights.

9.3 Looking ahead

As we have seen, there is a real need for models that can handle quark degrees of freedom to study in detail the different phenomena involved in the expansion and hadronization of hot, deconfined, strongly interacting matter. The qMD model provides such an approach, in a numerically tractable manner, with interesting and promising results so far.

Perhaps the most natural application of the model is the examination and analysis of fluctuations and correlations, which reveal imprints of the partonic degrees of freedom in the final state hadronic yields. This is an area of research of high current interest, and checks and inputs from model studies are welcome.

However, many more aspects of the fascinating subject of strongly interacting matter can be studied with this model.

Appendices

Appendix A lists all particles—quarks and non-exotic hadrons—which are propagated dynamically in the qMD model. The compilation of hadrons includes all states which can be produced either by the recombination of quarks and antiquarks, or in the decay of hadronic resonances.

The discussion of exotic hadrons and pentaquarks in chapter 8 has made extensive use of the classification of multi-quark states according to irreducible representations of the flavour and spin-flavour symmetry groups. Appendix B acts as a short, self-contained introduction to the role of the special unitary groups SU(N) and their representations in elementary particle physics. It is far from comprehensive, but includes the construction of irreducible multiplets using Young tables, and the graphical methods applicable to the construction and depiction of representations of SU(3). The calculation of the SU(3) multiplet structure for multiquark states of up to six quarks and/or antiquarks is presented in detail.

Finally, appendix C explains the motivation behind the use of the spin-flavour symmetry group SU(6) for the classification of hadrons. It shows how this symmetry can be applied to the cataloguing of all possible s-wave pentaquark states, including spin.

Appendix A

Quarks and hadrons in qMD

qMD is a molecular dynamics simulation of quarks and antiquarks which are treated as classical particles, characterized by four-coordinates, four-momenta, and colour charge, which describes the coupling to the potential interaction. Besides this, quarks and antiquarks carry spin, isospin, and the flavour quantum numbers of strangeness and charm. The spin quantum number is used for accounting purposes only and is evaluated in the mapping of colour neutral clusters onto hadrons. The isospin quantum number T allows to distinguish between u and d quarks.

The hadronization routine maps colour neutral clusters onto hadrons and hadronic resonances according to the quantum numbers and the four-momentum of the cluster. All hadronic data needed to this end are taken from the tables of the Particle Data Group (PDG, [137]).

The following tables list the properties of quarks, mesons, and baryons taken into account in the qMD model. Exotic hadronic states involving more then three quarks or antiquarks will be discussed in the appendices B and C.

A.1 Quarks in qMD

The qMD model as used in this thesis takes into account quarks of the 1st and 2nd generation and their antiparticles with the properties listed in table A.1.

The quarks u and d are considered as symmetric states of an isospin doublet q and distinguished by the 3-component of isospin:

$$\mathrm{u} = \mathrm{q}(T_3 = +1/2) \ , \qquad \mathrm{d} = \mathrm{q}(T_3 = -1/2) \ . \tag{A.1}$$

Note that this symmetry is explicitly broken in nature, and that PDG lists different masses for the u and d quark. Here, the masses of the q and s quarks are current masses, the mass of the c quark is derived from the analysis of the charmonium

particle	mass [MeV/]	width [MeV]	spin	B	T	S	C	colour charge
q	5	0.0	1/2	1/3	1/2	0	0	**3**
s	150	0.0	1/2	1/3	0	-1	0	**3**
c	1500	0.0	1/2	1/3	0	0	1	**3**

Table A.1
Quarks in qMD.

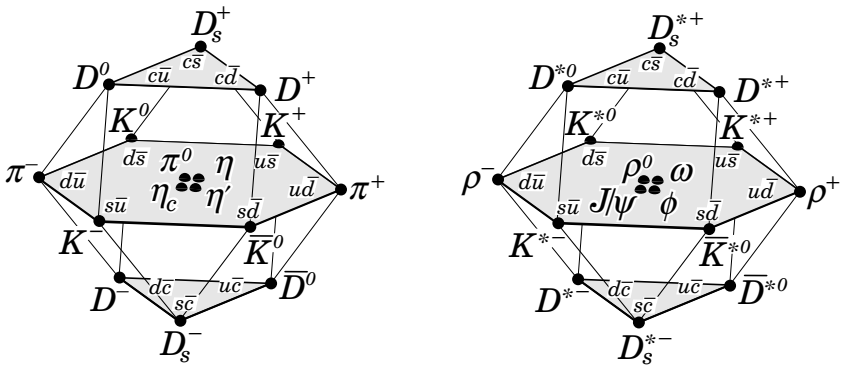

Figure A.1
The 16-plet of pseudoscalar (left) and vector (right) mesons made up of quarks and antiquarks from the 1st and 2nd generation (diagrams taken from [268]).

spectrum. B, S, and C denote the baryon number, strangeness, and charm quantum number, respectively. The fractional electric charge of the quarks can be calculated from the 3-component of isospin T_3, the hypercharge $Y = S + B$, and the charm quantum number C using the generalized Gell-Mann–Nishijima formula

$$Q = T_3 + \frac{Y}{2} + \frac{C}{2} = T_3 + \frac{1}{2}(B + S + C) \; . \tag{A.2}$$

Colour charges take values of R, G, B in the triplet $\mathbf{3}$, the fundamental representation of the colour group $\mathrm{SU}(3)_\mathrm{c}$.

Antiquarks are not listed. They carry the negative values of the quantum numbers B, T, S and C of the quarks stated in the table, and colour charges from the antitriplet $\bar{\mathbf{3}}$.

A.2 Mesons in qMD

Most mesons—colour neutral states of one quark and one antiquark—occur as either Lorentz pseudoscalars with spin $s = 0$ or Lorentz vectors with spin $s = 1$. Taking into quarks and antiquarks from the 1st and 2nd generation, the representation theory of SU(4) yields the pseudoscalar and the vector 16-plets shown in figure A.1. In qMD, all these states can in principle occur when clusters are mapped to hadrons, or in the decay of heavy hadrons and hadronic resonances.

A.2.1 Pseudoscalar mesons in qMD

Pseudoscalar mesons as implemented in qMD are listed in table A.2. Here and in the following table A.3, the net content of u and d quarks of a meson is denoted with U/D. This means that a meson with $U/D = -1$ contains one $\bar{\mathrm{u}}$ or $\bar{\mathrm{d}}$ antiquark. Note that by historical reasons, mesons with strangeness $S = +1$ contain one $\bar{\mathrm{s}}$ antiquark, while mesons with charm $C = +1$ contain one c quark. The colour charge of all mesons is $\mathbf{1}$, of course, since all hadrons are colour neutral $\mathrm{SU}(3)_\mathrm{c}$ singlets. The widths of kaons and charmed mesons are reduced by hand to $10^{-6}\,\mathrm{MeV}$ in qMD in order to suppress weak decays. This allows to compare the

particle	mass [MeV]	width [MeV]	T	U/D	S	C	spin	colour charge
π	138	0	1	0	0	0	0	**1**
η	549	$1.2 \cdot 10^{-6}$	0	0	0	0	0	**1**
K	495	10^{-6}	0.5	1	1	0	0	**1**
$\bar{K}$	495	10^{-6}	0.5	-1	-1	0	0	**1**
η_s	958	0.21	0	0	0	0	0	**1**
η_c	2979	10^{-6}	0	0	0	0	0	**1**
D	1865	10^{-6}	0.5	-1	0	1	0	**1**
D_s	1968	10^{-6}	0	0	1	1	0	**1**
$\bar{D}$	1865	10^{-6}	0.5	1	0	-1	0	**1**
$\bar{D}_s$	1968	10^{-6}	0	0	-1	-1	0	**1**

Table A.2 Pseudoscalar mesons in qMD.

results of the qMD simulations with experimental data, where these particles are reconstructed from their decay products.

The physical mesons η and η' are superpositions of the flavour states $1/\sqrt{2}(\mathrm{u\bar{u}}+\mathrm{d\bar{d}})$ – the symmetric isospin singlet – and $\mathrm{s\bar{s}}$. In qMD, for simplicity, this mixing is ignored. Thus, the coupling of a light q quark with a $\bar{\mathrm{q}}$ antiquark to an isospin singlet is considered as the η meson, while the combination $\mathrm{s\bar{s}}$ is considered as the η'. For this reason, the η' is denoted as η_s in table A.2. The same applies to the Lorentz vector mesons ω and ϕ.

A.2.2 Vector mesons in qMD

As in table A.3, the width of the J/Ψ is reduced by hand to $10^{-6}\,\mathrm{MeV}$ in qMD in order to suppress all decays, and the ϕ is the $\mathrm{s\bar{s}}$ state, with the contribution of the isosinglet $1/\sqrt{2}(\mathrm{u\bar{u}}+\mathrm{d\bar{d}})$ ignored.

A.2.3 Higher mesonic states

Besides the mesonic states of the pseudoscalar and vector $\mathrm{SU}(4)$-16-plets listed in tables A.2 and A.3, there are excited mesonic states of pseudoscalars and vectors, and states related to the scalar, Lorentz pseudovector and tensor multiplets.

particle	mass [MeV]	width [MeV]	T	U/D	S	C	spin	colour charge
ρ	770	149	1	0	0	0	1	**1**
ω	783	8.43	0	0	0	0	1	**1**
$K^\star(892)$	892	49.8	0.5	1	1	0	1	**1**
$\bar{K}^\star(892)$	892	49.8	0.5	-1	-1	0	1	**1**
ϕ	1020	4.41	0	0	0	0	1	**1**
J/Ψ	3097	10^{-6}	0	0	0	0	1	**1**
$D^\star(2007)$	2007	2.1	0.5	-1	0	1	1	**1**
$D_s^\star(2536)$	2536	2.3	0	0	1	1	1	**1**
$\bar{D}^\star(2007)$	2007	2.1	0.5	1	0	-1	1	**1**
$\bar{D}_s^\star(2536)$	2536	2.3	0	0	-1	-1	1	**1**

Table A.3 Vector mesons in qMD.

Table A.4
Higher mesonic states in qMD.

Excited pseudoscalar states

particle	mass [MeV]	width [MeV]	T	U/D	S	C	spin	colour charge
$\pi(1300)$	1300	400	1	0	0	0	0	**1**
$\eta(1295)$	1295	35	0	0	0	0	0	**1**

Scalar states

particle	mass [MeV]	width [MeV]	T	U/D	S	C	spin	colour charge
a_0	980	57	1	0	0	0	0	**1**
f_0	980	33.6	0	0	0	0	0	**1**

Pseudovector states

particle	mass [MeV]	width [MeV]	T	U/D	S	C	spin	colour charge
a_1	1235	400	1	0	0	0	1	**1**
b_1	1235	150	1	0	0	0	1	**1**
h_1	1170	311	0	0	0	0	1	**1**
f_1	1285	24	0	0	0	0	1	**1**
$\omega(1390)$	1390	110	0	0	0	0	1	**1**

Some of theses states are implemented in the qMD model. They are listed in table A.4. Note, however, that the clustering routine of qMD cannot distinguish between scalars and pseudoscalars, and between vectors and pseudovectors, since it does not account for parity. Thus, a quark-antiquark cluster with spin $s = 0$ may be mapped by the clustering routine to either a scalar or a pseudoscalar meson, and cluster with $s = 1$ to both a vector or a pseudovector meson.

With their high masses and broad widths, these higher mesonic states are important for qMD, since they facilitate the mapping of colour neutral quark-antiquark clusters to hadronic states. As we have seen, the mass spectrum of these clusters is very wide, and a mapping onto the two 16-plets would be too restrictive.

A.3 Baryons in qMD

Baryons are colour neutral states made up of three quarks with three different colours. Taking into account quarks of the 1st and 2nd generation, the lowest possible baryonic states can be classified into two multiplets with 20 states each: one 20-plet with spin $s = 1/2$, which contains the octet including the nucleons, and one 20-plet with spin $s = 3/2$, containing the decuplet with the Δ resonances. Both multiplets are shown in figure A.2. The present version of qMD includes all these baryons, with properties as listed in tables A.5 and A.6. As for the u and d quarks, isospin is considered as a perfect symmetry in qMD. Thus, different members of isospin multiplets, such as the proton and the neutron as states of the nucleon N, all have the same mass. For the same reason, they are not listed separately in tables A.5 and A.6.

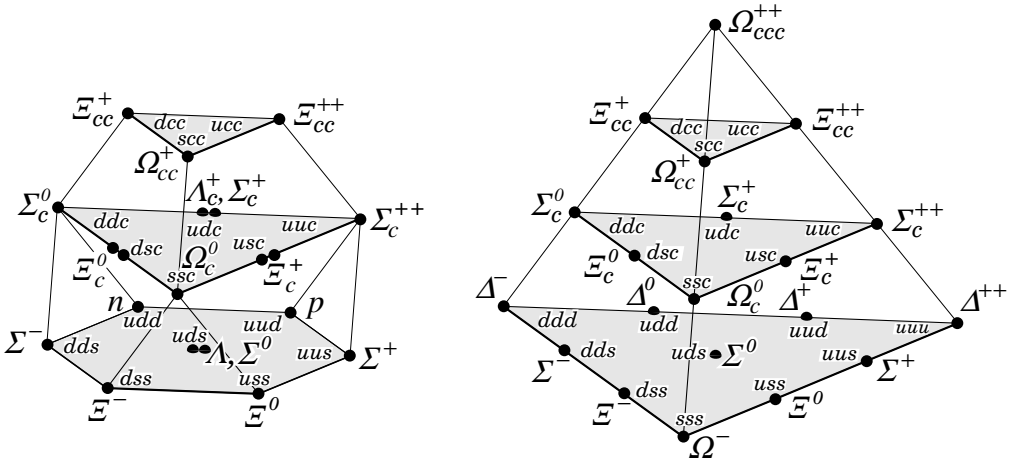

Figure A.2
The SU(4)-20-plets of baryons with spin $1/2$, containing the nucleon doublet (left), and with spin $3/2$, containing the quadruplet of the Δ resonances (right; both diagrams taken from [268]).

A.3.1 Baryon multiplet with spin $s = 1/2$.

particle	mass [MeV]	width [MeV]	T	U/D	S	C	spin	colour charge
N	938	10^{-6}	1/2	3	0	0	1/2	**1**
Σ	1190	$2.46 \cdot 10^{-3}$	1	2	-1	0	1/2	**1**
Λ	1116	$0.76 \cdot 10^{-3}$	0	2	-1	0	1/2	**1**
Ξ	1317	$0.68 \cdot 10^{-3}$	1/2	1	-2	0	1/2	**1**
Σ_c	2455	0.6	1	2	0	1	1/2	**1**
Λ_c	2285	0.6	0	2	0	1	1/2	**1**
Ξ_c	2470	1.4	1/2	1	-1	1	1/2	**1**
Ω_c	2700	2.6	0	0	-2	1	1/2	**1**
Ξ_{cc}	3200	20	1/2	1	0	2	1/2	**1**
Ω_{cc}	4000	1	0	0	-1	2	1/2	**1**

Table A.5
The baryon multiplet with spin $s = 1/2$ as included in qMD.

A.3.2 Baryon multiplet with spin $s = 3/2$

particle	mass [MeV]	width [MeV]	T	U/D	S	C	spin	colour charge
Δ	1232	115	3/2	3	0	0	3/2	**1**
$\Sigma(1385)$	1385	36	1	2	-1	0	3/2	**1**
$\Xi(1530)$	1530	10	1/2	1	-2	0	3/2	**1**
Ω	1673	1	0	0	-3	0	3/2	**1**
$\Sigma_c(2520)$	2520	1.5	1	2	0	1	3/2	**1**
$\Xi_c(2645)$	2645	2.0	1/2	1	-1	1	3/2	**1**
$\Omega_c(3000)$	3000	1	0	0	-2	1	3/2	**1**
$\Xi_{cc}(4000)$	4000	1	1/2	1	0	2	3/2	**1**
$\Omega_{cc}(4000)$	4000	1	0	0	-1	2	3/2	**1**
$\Omega_{ccc}(5000)$	5000	1	0	0	0	3	3/2	**1**

Table A.6
The baryon multiplet with spin $s = 3/2$ as included in qMD.

Note that tables A.5 and A.6 include charmed baryons with $C = 2$ and $C = 3$ which have not been observed in experiment yet. The masses of these states are based on assumptions from the constituent quark model.

A.3.3 Baryon resonances

Besides the ground state baryons of the two 20-plets shown in figure A.2, there are many more, excited baryonic states. These are resonances with higher main quantum numbers and the states with orbital angular momentum which populate the different Regge trajectories. qMD includes the higher baryonic resonances listed in table A.7. Again, these resonance states are important in qMD for the mapping of colour neutral clusters to hadrons.

Table A.7
Baryon resonances implemented in qMD.

particle	mass [MeV]	width [MeV]	T	U/D	S	C	spin	colour charge
N(1440)	1440	200	1/2	3	0	0	1/2	**1**
N(1520)	1520	125	1/2	3	0	0	3/2	**1**
N(1535)	1535	150	1/2	3	0	0	1/2	**1**
N(1650)	1650	150	1/2	3	0	0	1/2	**1**
N(1675)	1675	155	1/2	3	0	0	2.5	**1**
N(1680)	1680	125	1/2	3	0	0	2.5	**1**
N(1700)	1700	100	1/2	3	0	0	3/2	**1**
$\Delta(1620)$	1620	140	3/2	3	0	0	1/2	**1**
$\Delta(1700)$	1700	250	3/2	3	0	0	3/2	**1**
$\Delta(1900)$	1900	150	3/2	3	0	0	1/2	**1**
$\Delta(1905)$	1905	300	3/2	3	0	0	2.5	**1**
$\Delta(1910)$	1910	220	3/2	3	0	0	1/2	**1**
$\Delta(1920)$	1920	250	3/2	3	0	0	3/2	**1**
$\Delta(1930)$	1930	250	3/2	3	0	0	2.5	**1**
$\Delta(1950)$	1950	240	3/2	3	0	0	3.5	**1**
$\Lambda(1405)$	1405	55	0	2	-1	0	1/2	**1**
$\Lambda(1520)$	1520	15.6	0	2	-1	0	3/2	**1**
$\Lambda(1600)$	1600	150	0	2	-1	0	1/2	**1**
$\Lambda(1670)$	1670	35	0	2	-1	0	1/2	**1**
$\Lambda(1690)$	1690	60	0	2	-1	0	3/2	**1**
$\Sigma(1660)$	1660	100	1	2	-1	0	1/2	**1**
$\Sigma(1670)$	1670	60	1	2	-1	0	3/2	**1**
$\Sigma(1750)$	1750	90	1	2	-1	0	1/2	**1**
$\Xi(1820)$	1820	24	1/2	1	-2	0	3/2	**1**
$\Omega(2250)$	2250	55	0	0	-3	0	1/2	**1**
$\Lambda_c(2593)$	2593	0.8	0	2	0	1	1/2	**1**
$\Lambda_c(2625)$	2625	0.8	0	2	0	1	3/2	**1**
Ω_{ccc}	4600	30	0	0	0	3	1/2	**1**
$\Xi_c(3000)$	3000	1	1/2	1	-1	1	3/2	**1**

Appendix B

The groups SU(N) and their representations

In this appendix, we start by motivating the use of representations of the special unitary groups SU(N) in physics. We will describe the construction of irreducible representations out of products of representations using Young tables. This technique is then applied to the construction of the multiplet structure of states with up to six quarks or antiquarks in SU(3), including the pentaquark multiplets.[1]

B.1 Internal symmetries in quantum mechanics

In quantum mechanics, particles are described by vectors in a complex Hilbert space. A simple example of this formalism is the space representation, where a Hilbert space vector is just a complex function, $\psi(\vec{x},t)$, and the probability p of finding a particle at time t and position $\vec{x}$ is given by $|\psi(\vec{x},t)|\mathrm{d}x^{\,3}$. However, there may be properties of particles which cannot be accommodated by the spatial distribution of the probability p alone. These are properties such as spin, which are described by so-called internal quantum numbers. In the case of spin, Pauli proposed a formalism using a two-component complex function $\Psi(\vec{x},t)$,

$$\Psi(\vec{x},t) = \begin{pmatrix}\psi_\uparrow(\vec{x},t)\\ \psi_\downarrow(\vec{x},t)\end{pmatrix} = \psi_\uparrow(\vec{x},t)\begin{pmatrix}1\\0\end{pmatrix} + \psi_\downarrow(\vec{x},t)\begin{pmatrix}0\\1\end{pmatrix}\ . \tag{B.1}$$

Thus, a particle with spin is described at each point in space and time not by a complex number, but by a two-dimensional complex vector instead. Other internal quantum numbers are isospin, which is expanded to flavour to include strangeness and charm, combinations of spin and flavour, and colour. Particles are then described by complex N-vectors, where $N = 2, 3, 4$, or 6. Note that in the case of colour and flavour, each component of the function $\Psi(\vec{x},t)$ will in general be a

[1] Discussions of the groups SU(N), their representations, and the application of this theory to nucear and particle physics can be found, e. g., in the texts of Guidry [269] and, in much more detail and with many examples, of Greiner and Müller [270]. A concise account of the mathematical background, including the rules for handling Young tables, is given in the chapter on semisimple Lie groups in [271].

Dirac four-spinor. The Dirac structure usually factors out and is not mentioned any longer in this appendix.

Internal quantum numbers are important since they are associated with internal symmetries of the system. In symmetric situations, the Hamiltonian does not depend on the orientation of the complex N-vector $\Psi(\vec{x},t)$. Kinetic terms are symmetric in this sense. As we known from the example of spin, this symmetry can be broken by external fields, or by interactions among particles. But if the Hamiltonian of a system is symmetric, the physical situation is not changed if the N-vector $\Psi(\vec{x},t)$ describing a particle is replaced by the "rotated" N-vector

$$\Psi(\vec{x},t)' = A\Psi(\vec{x},t) \; . \tag{B.2}$$

Here, A is a complex $N \times N$-matrix and belongs to the group $\mathrm{SU}(N)$ of special unitary transformations of a complex N-dimensional vector space,

$$\mathrm{SU}(N) \; = \; \left\{ \, A : \mathbb{C}^N \to \mathbb{C}^N, \; AA^\dagger = \mathbb{I}, \; \det A = 1 \, \right\} \; . \tag{B.3}$$

It is clear that A has to be unitary in order to conserve probability, thus $A \in \mathrm{U}(N)$. The further restriction to unitary transformations with unit determinant, $A \in \mathrm{SU}(N)$, is possible since the difference is a global phase factor which is the same for all components of $\Psi(\vec{x},t)$. Since state vectors can always be multiplied by constant phases, this difference can be neglected. Formally, $\mathrm{U}(N)$ is isomorphic to $\mathrm{SU}(N) \otimes \mathrm{U}(1)/\mathbb{Z}_N$, where the factor $\mathrm{U}(1)/\mathbb{Z}_N$ contains the global phase.

The groups $\mathrm{SU}(N)$ are, of course, more general objects than the realizations as unitary $N \times N$-matrices with unit determinant. There are many more possibilities how to identify each element of $\mathrm{SU}(N)$ with some automorphism of a complex vector space V of dimension $M > N$ while maintaining the group structure. These possibilities are called representations of $\mathrm{SU}(N)$. However, the realization as unitary $N \times N$-matrices with unit determinant acting on a complex vector space of dimension N is special: it corresponds to the smallest possible representation of $\mathrm{SU}(N)$ containing the full structure of the group, and it can be used to define the properties of the group. For this reason, it is called the *defining representation* or the *fundamental representation*. Furthermore, the fundamental representation is the starting point for the construction of higher representation, as we will discuss in the sections B.4 and B.5.

B.2 The groups $\mathrm{SU}(N)$ and their generators

Before going on, we will discuss the important parametrization of the elements of the groups $\mathrm{SU}(N)$ as exponentials and the concept of the generators of the group and their algebra.

Any unitary matrix U of the unitary group $\mathrm{U}(N)$ can be written as an exponential of some hermitian matrix H,

$$U = \mathrm{e}^{\mathrm{i}H} \; , \quad U \in \mathrm{U}(N) \; , \quad H^\dagger = H \; . \tag{B.4}$$

The matrix H, again, can be expanded as a sum

$$H = \vartheta_0 \mathbb{I} + \sum_{l=1}^{N^2-1} \vartheta^l T_l \; , \tag{B.5}$$

where the N^2-1 linear independent matrices T_l are traceless. Thus, the matrices

$$A = \exp\left(\mathrm{i} \sum_{l=1}^{N^2-1} \vartheta^l T_l \right) \tag{B.6}$$

are unitary and have unit determinant, since $\det(\exp B) = \exp(\mathrm{Tr}\, B)$ for any matrix B and $\mathrm{Tr}\, T_l = 0$ for all T_l in (B.6). Note that the sum in the exponent of (B.6) does not include the multiple of the unit matrix, $\vartheta_0 \mathbb{I}$. But this just means that a global phase factor has been dropped. With the discussion following definition (B.3) in mind, we see that this corresponds to the transition from $\mathrm{U}(N)$ to $\mathrm{SU}(N)$. Thus, any element of the group $\mathrm{SU}(N)$ can be written in the form (B.6). The parametrization (B.6) of the elements of $\mathrm{SU}(N)$ makes it evident how the groups $\mathrm{SU}(N)$ are continuous groups connected to the unit transformation. Such groups are called *Lie groups*.

If the coefficients ϑ^l in (B.6) are small, the exponential can be expanded as

$$A = \mathbb{I} + \mathrm{i} \sum_{l=1}^{N^2-1} \vartheta^l T_l + \dots \ . \tag{B.7}$$

Any matrix $B \in \mathrm{SU}(N)$ can be obtained as a product of matrices (B.7). Thus, the N^2-1 linear independent traceless matrices T_l are called the *generators* of $\mathrm{SU}(N)$: they generate infinitesimal transformations of the group. In the fundamental representation of $\mathrm{SU}(2)$, the generators are traceless, hermitian 2×2 matrices which can be expressed using the Pauli matrices. We know from elementary quantum mechanics that they describe angular momentum operators, which generate rotations of the quantum state. For $\mathrm{SU}(3)$ in the fundamental representation, there are eight different traceless, hermitian 3×3 matrices, which can be expressed using the Gell-Mann matrices (2.9),

$$\text{fundamental representation of SU(3)}: \qquad T_i = \frac{1}{2}\,\lambda_i \ , \quad i = 1, \dots, 8 \ . \tag{B.8}$$

In the case that the $\mathrm{SU}(N)$ symmetry is a local gauge symmetry, the coefficients ϑ_l in (B.6) and (B.7) are functions of the space-time coordinates $(\vec{x}, t)$. As we have seen when discussing colour $\mathrm{SU}(3)$ in (2.22), one has $\vartheta^l = g_\mathrm{s} A^l_\mu(\vec{x}, t)$, where the $A^l_\mu(\vec{x}, t)$ are Lorentz vectors: they represent the gluon fields. Furthermore, we have seen in (2.31) how the generators of $\mathrm{SU}(3)$ can be used to construct generalized ladder operators. In the representation theory of $\mathrm{SU}(2)$, the ladder operators change the z component of spin by one unit, i. e., they switch between different states within one multiplet. In an analogous way, the generators of $\mathrm{SU}(N)$ meditate changes between states in multiplets corresponding to representations of these groups.

Since the generators of $\mathrm{SU}(N)$ are N^2-1 linear independent matrices, they span a vector space of dimension N^2-1. But there is an even richer mathematical structure: A product of two generators T_a and T_b can be defined by considering the commutator $[T_a, T_b] = T_a T_b - T_b T_a$. The commutator can be expressed as a sum of generators,

$$[T_a, T_b] = \sum_c \mathrm{i}\, f^c_{ab}\, T_c \ . \tag{B.9}$$

This product makes the vector space spanned by the generators T_a of the Lie group SU(N) a *Lie algebra*, which is denoted by su(N). The coefficients f^c_{ab} are called *structure constants*. The Lie algebra is completely defined through the specification of the structure constants. Since the complete group can be reconstructed from the generators through (B.6), this means that the structure constants define the Lie group. In the case of su(2), the structure constants are given by the completely antisymmetric symbol ϵ_{ijk}, $f^c_{ab} = \epsilon_{abc}$, and the algebra defined by (B.9) is just the algebra of angular momentum operators. From a mathematical point of view, the Lie algebras su(N) are important since it is easier to study representations of the algebra than of the group. On the other hand, representations of su(N) yield representations of SU(N) through the exponential mapping (B.6).

B.3 Representations of SU(N) applied to physics

This mathematical structure now offers a general scheme for the implementation of internal symmetries into quantum mechanics: First, chose some symmetry group SU(N), and then, identify the fundamental and the higher representations with multiplets of particles which have equal energy (or mass) as long as there are no symmetry breaking terms or interactions in the Hamiltonian. Generalized ladder operators derived from the generators of the group will mediate transitions within the multiplets. Thus,

- **SU**(2)

is used to describe spin, isospin, or weak isospin. In the case of spin, the two components in the two-dimensional fundamental representation describe the orientations of spin parallel and antiparallel to the quantization axis. In the case of isospin, they describe neutron and proton, or up and down quark. Applied to the weak interaction, weak isospin combines the left handed electron-neutrino ν_e with the left handed electron, and analogous for the left handed ν_μ and μ, and ν_τ and τ. Note that weak isospin is a gauged SU(2) symmetry, while isospin in the strong interactions is not.[2]

- **SU**(3)

is used to describe flavour or colour. In the case of flavour, the three dimensions in the fundamental representation correspond to the up, down, and strange quark. In the case of colour, they correspond to the colours R, G, and B, as we have seen in (2.6). In this sense, quarks are described by fundamental representations of $\mathrm{SU}(3)_\mathrm{colour}$. Note again that colour is a gauged symmetry, while flavour is not.

- **SU**(4)

is used when flavour symmetry is extended to include charm, and in the combined treatment of spin and isospin in Wigner's theory of supermultiplets, which is discussed in appendix C. The representation theory of $\mathrm{SU}(4)_\mathrm{flavour}$ yields the classification of baryon and meson multiplets shown in figures A.1 and A.2.

[2] When Yang and Mills formulated non-abelian SU(2) gauge theory, their motivation was to apply it to isospin. This approach was not successful, since there are no known bosons which can be understood as gauge particles coupling to strong isospin.

- **SU**(6)

is an extension of the SU(4) supermultiplet theory which yields a unified description of SU(3) flavour and spin. As we will see in appendix C, it explains while there is a baryon octet with spin $s = 1/2$ and a baryon decuplet with spin $s = 3/2$.

We have seen that we can identify single particles with fundamental representations of some symmetry group SU(N). We will extend this construction to multi-particle states, but before, we have to understand how to treat antiparticles. When discussing the colour charge of antiquarks in equations (2.19)–(2.21), it became clear that antiquarks, like quarks, are represented by three-dimensional complex vectors. However, transformations of SU(3) acting on antiquarks are not generated by the generators of the fundamental representation (B.8), but instead by the generators (see (2.21)) of the so-called

$$\text{conjugated representation of SU}(3): \qquad T_i = -\frac{1}{2}\,\lambda_i^* \,, \quad i = 1, \ldots, 8 \,. \tag{B.10}$$

Thus, the conjugated representation of SU(3) has the same dimension as the fundamental representation, but is different. This is a generic feature of representations of SU(N): Besides the N-dimensional fundamental representation, there is a second N-dimensional representation, which is called the *conjugated representation*, and which is different of the fundamental representation for $N > 2$. In the application to physics, single particles are indentified with the fundamental representation, while single antiparticles are indentified with the conjugated representation.

Now, we can address the issue of multi-particle states, containing both particles and antiparticles in the fundamental and conjugated representation of SU(N), respectivley. Do multi-particle states also correspond to representations of the same symmetry group, and to which representations do they belong? The answer should yield the multiplet structure and the internal quantum numbers of these states. It is given by the representation theory of SU(N) and the construction of sums of irreducible representations out of product representations.

B.4 Product representations and their decomposition

The general idea behind the decomposition of product representations is known from SU(2) and the combination of spin. As a starting point, we consider two fundamental representations F_1 and F_2, corresponding to two particles, which operate on two two-dimensional spaces spanned by the states

$$\Psi_{1,\uparrow} = \begin{pmatrix} 1 \\ 0 \end{pmatrix} \,, \quad \Psi_{1,\downarrow} = \begin{pmatrix} 0 \\ 1 \end{pmatrix} \,, \quad \Psi_{2,\uparrow} = \begin{pmatrix} 1 \\ 0 \end{pmatrix} \,, \quad \Psi_{2,\downarrow} = \begin{pmatrix} 0 \\ 1 \end{pmatrix} \,. \tag{B.11}$$

Then, one constructs the *product representation* $R = F_1 \otimes F_2$, which acts on the four-dimensional space V spanned by the states

$$\Psi_{1,\uparrow} \otimes \Psi_{2,\uparrow} = \begin{pmatrix} 1 \\ 0 \end{pmatrix} \otimes \begin{pmatrix} 1 \\ 0 \end{pmatrix} = \begin{pmatrix} 1 \\ 0 \\ 0 \\ 0 \end{pmatrix} , \quad \Psi_{1,\uparrow} \otimes \Psi_{2,\downarrow} = \begin{pmatrix} 1 \\ 0 \end{pmatrix} \otimes \begin{pmatrix} 0 \\ 1 \end{pmatrix} = \begin{pmatrix} 0 \\ 1 \\ 0 \\ 0 \end{pmatrix} ,$$

$$\Psi_{1,\downarrow} \otimes \Psi_{2,\uparrow} = \begin{pmatrix} 0 \\ 1 \end{pmatrix} \otimes \begin{pmatrix} 1 \\ 0 \end{pmatrix} = \begin{pmatrix} 0 \\ 0 \\ 1 \\ 0 \end{pmatrix}, \quad \Psi_{1,\downarrow} \otimes \Psi_{2,\downarrow} = \begin{pmatrix} 0 \\ 1 \end{pmatrix} \otimes \begin{pmatrix} 0 \\ 1 \end{pmatrix} = \begin{pmatrix} 0 \\ 0 \\ 0 \\ 1 \end{pmatrix}. \tag{B.12}$$

Now, this four-dimensional representation R is *reducible*, which means that by a suitable change of the base (B.12), all matrices representing group elements of SU(2) correspond to block matrices, with one block of size 3×3 and one block of size 1×1. Thus, the four-dimensional space V supporting the representation R decomposes into one three-dimensional subspace V_1 and one one-dimensional subspace V_2, where $V = V_1 \oplus V_2$ and each subspace V_1 and V_2 supports a representation of SU(2). The representations I_1 and I_2 acting on the subspaces V_1 and V_2 can not be further reduced by other base changes. For this reason, they are called *irreducible representations*. Here, the three-dimensional representation I_1 acts on V_1 spanned by the states

$$\begin{cases} \Psi_{\uparrow\uparrow} = \Psi_{1,\uparrow} \otimes \Psi_{2,\uparrow} \,, \\ \Psi^{\mathrm{s}}_{\uparrow\downarrow} = \frac{1}{\sqrt{2}} \left(\Psi_{1,\uparrow} \otimes \Psi_{2,\downarrow} + \Psi_{1,\downarrow} \otimes \Psi_{2,\uparrow} \right) \,, \\ \Psi_{\downarrow\downarrow} = \Psi_{1,\downarrow} \otimes \Psi_{2,\downarrow} \end{cases} \tag{B.13}$$

and describes a triplet of spin $s = 1$. The one-dimensional representation I_2 acts on V_2 spanned by the state

$$\Psi^{\mathrm{a}}_{\uparrow\downarrow} = \frac{1}{\sqrt{2}} \left(\Psi_{1,\uparrow} \otimes \Psi_{2,\downarrow} - \Psi_{1,\downarrow} \otimes \Psi_{2,\uparrow} \right) \,, \tag{B.14}$$

and describes a singlet of spin $s = 0$. The state $\Psi^{\mathrm{a}}_{\uparrow\downarrow}$ in (B.14) is completely antisymmetric under the exchange of the two particles, while the states (B.13) are completely symmetric. Thus, the product representation R of two fundamental representations F_1 and F_2 of SU(2) is decomposed into two the direct sum of two irreducible representations I_1 and I_2,

$$R = F_1 \otimes F_2 = I_1 \oplus I_2 \,, \tag{B.15}$$

where I_1 and I_2 have well-defined behaviour under the exchange of the two factors F_1 and F_2. In general, the dimension of the representation is used to denote it. Thus, one writes the decomposition (B.15) as

$$\mathbf{2} \otimes \mathbf{2} = \mathbf{1} \oplus \mathbf{3} \,, \tag{B.16}$$

where $\mathbf{2}$ is the fundamental representation, $\mathbf{1}$ denotes the completely antisymmetric singlet (B.14), and $\mathbf{3}$ stands for the completely symmetric triplet (B.13).

There are now several obvious questions to be asked: How can the decomposition (B.16) be extended to include more factors, corresponding to the construction of product states of more than two particles? Which irreducible representations occur in the decomposition, and what are their dimensions and symmetries? Furthermore, how can all this be extended to the symmetry groups SU(N) for $N > 2$? Formally, we construct a product representation R of m fundamental representations F and n conjugate representations C, corresponding to the combination of

m particles and n antiparticles. Remember that F and C are different for $N > 2$. Then, we seek for the decomposition of R as a direct sum over irreducible representations I_j:

$$R = \underbrace{F \otimes \cdots \otimes F}_{m \text{ times}} \otimes \underbrace{C \otimes \cdots \otimes C}_{n \text{ times}} = \sum_j \oplus I_j \ . \tag{B.17}$$

The sum on the right hand side of (B.17) is called the *Clebsch-Gordan series* of the product representation R. Note that R acts on a vector space of dimension $d = N^{m+n}$ (both fundamental and conjugate representations are N-dimensional), thus the irreducible representations I_j in (B.17) operate on vector spaces V_j where

$$\sum_j \dim(V_j) = N^{m+n} \ . \tag{B.18}$$

The calculation of Clebsch-Gordan series of product representations is a central result of the representation theory of SU(N). We will not go into more details of this theory, but merely quote its results. They are expressed through the calculus of so-called Young tables, which we will present in the following section.

B.5 How to construct and decompose product representations of SU(N) with the help of Young tables

The calculus of Young tables is an ingenious graphical scheme for the determination of Clebsch-Gordan series (B.17). The central idea is to depict each irreducible representation I of SU(N) by an arrangement of small boxes, a so-called *Young table*, which has to fulfil the following set of rules:

1. A Young table is a set of left-justified rows of boxes.
2. The number of boxes in a row never increases when going down from row to row.
3. A Young table depicting some irreducible representation of SU(N) has at most N rows.
4. Young tables which differ by left-aligned columns of N boxes depict the same irreducible representation.

Thus, among the arrangements of boxes

$Y_1 =$  , $Y_2 =$  , $Y_3 =$ 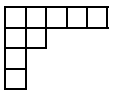 , $Y_4 =$  , (B.19)

Y_4 violates rule 2 and is not an admissible Young table, Y_3 is fine for depicting an irreducible representation for $N \geq 4$ (rule 3), and Y_1 and Y_2 depict irreducible representations for $N \geq 3$. In the case of $N = 3$, Y_1 and Y_2 depict the same irreducible representation (rule 4).

There are two algebraic notations in use to describe the Young tables corresponding to some irreducible representation of SU(N). The first notation just denotes the numbers of boxes in one row. It is written as $[\,\lambda_1,\ldots,\lambda_N\,]$, with N non-negative integers λ_i. To comply with rule 2, $\lambda_i \geq \lambda_j$ for each pair (i,j) with $1 \leq i,j \leq N$ and $i < j$. The second notation, $D(\delta_1,\ldots,\delta_{N-1})$, uses $N-1$ non-negative integers $\delta_1,\ldots,\delta_{N-1}$. They describe the difference in the number of boxes in the ith and $i+1$st row, thus $\delta_i = \lambda_i - \lambda_{i+1}, i = 1,\ldots,N-1$. Since the integers δ_i are non-negative, rule 2 is automatically fulfilled. Furthermore, rule 4 is already built into the notation $D(\delta_1,\ldots,\delta_{N-1})$: Young tables which differ by columns of N boxes on the left and depict the same irreducible representation of SU(N) are described by the same set of integers $\delta_1,\ldots,\delta_{N-1}$. Using these notations, the Young tables $Y_1 - Y_3$ in (B.19) can be written as:

$$\mathrm{SU}(4): \quad \begin{cases} Y_1 = [4,3,2,0] = D(1,1,2)\ , \\ Y_2 = [2,1,0,0] = D(1,1,0)\ , \\ Y_3 = [5,2,1,1] = D(3,1,0)\ . \end{cases} \tag{B.20}$$

$$\mathrm{SU}(3): \quad \begin{cases} Y_1 = [4,3,2] = D(1,1)\ , \\ Y_2 = [2,1,0] = D(1,1)\ . \end{cases} \tag{B.21}$$

The coincident notation $D(1,1)$ in (B.21) for both Young tables shows neatly that the corresponding representations of SU(3) are the same.

The notation $D(\delta_1,\ldots,\delta_{N-1})$ for Young tables depicting irreducible representations of SU(N) also yields the dimension of the representation. It can be calculated using the formula

$$\dim D(\delta_1,\ldots,\delta_{N-1}) \;=\; \prod_{j=0}^{N-2} \prod_{i=1}^{N-j-1} \frac{\sum_{k=0}^{j} \delta_{i+k} + j + 1}{j+1}\ . \tag{B.22}$$

In the special cases of $N = 2$ (only one row of boxes) and $N = 3$ (only two rows of boxes), this reduces to the expressions

$$\begin{aligned} N = 2: &\quad \dim D(\delta_1) \;=\; \delta_1 + 1\ , \\ N = 3: &\quad \dim D(\delta_1,\delta_2) \;=\; \frac{1}{2}(\delta_1+1)(\delta_2+1)(\delta_1+\delta_2+2)\ . \end{aligned} \tag{B.23}$$

The central idea of Young calculus can now be expressed in an algorithm which determines how to combine two Young tables Y_1 and Y_2 depicting two representations into a series of new Young tables. This series then just corresponds to the Clebsch-Gordan series (B.17), and depicts the contributing irreducible representations.

In order to calculate the product $Y_1 \otimes Y_2$ of two Young tables Y_1 and Y_2, one begins by noting in each box of table Y_2 the number of the row in which the box occurs. Then, one constructs all possible new Young tables Y_j which can be obtained by adding the boxes of table Y_2 to the boxes of table Y_1. The new tables Y_j must meet the following requirements:

1. Each new table Y_j has to fulfil the rules 1–4 of admissible Young tables.

2. In each new table Y_j, the numbers in the boxes that have been added from table Y_2 to table Y_1 do not decrease within one row when running along the row from left to right.

3. The numbers in the boxes that have been added from table Y_2 to table Y_1 are strictly increasing within one column when going down the column from top to bottom.

4. When running through the boxes of table Y_j along a path which checks each row from left to right and all rows from top to bottom, at any step in the path, the number of boxes stemming from table Y_2 which contain the number i is smaller or equals the number of boxes already encountered which contain the number $i-1$.

These rules are known as the *Littlewood-Richardson rules*. By the combination of Y_1 and Y_2 to all Young tables Y_j compliant with the Littlewood-Richardson rules, one obtains the decomposition

$$Y_1 \otimes Y_2 \;=\; \sum_j \oplus Y_j \;, \tag{B.24}$$

which corresponds to the sought-after decomposition (B.17) of a product representation into a direct sum of irreducible representations. The dimensions of the irreducible representations can be read off the Young tables Y_j using (B.22). The Littlewood-Richardson rules apply distributively, thus

$$Y_1 \otimes Y_2 \otimes Y_3 \;=\; \Big(\sum_j \oplus Y_j\Big) \otimes Y_3 \;=\; \sum_j \oplus (Y_j \otimes Y_3) \;=\; \sum_{j,k} \oplus Y_{j,k} \;. \tag{B.25}$$

As an example of the application of the Littlewood-Richardson rules, we calculate the product

$$\ydiagram{2} \otimes \ydiagram{1,1} \;=\; \ydiagram{2} \otimes \begin{array}{|c|}\hline 1 \\ \hline 2 \\ \hline \end{array} \;=\; \begin{array}{|c|c|c|}\hline \multicolumn{2}{c}{} & 1 \\ \hline 2 \\ \cline{1-1} \end{array} \;\oplus\; \begin{array}{|c|c|}\hline \multicolumn{2}{c}{} \\ \hline 1 \\ \hline 2 \\ \cline{1-1} \end{array} \;. \tag{B.26}$$

The combinations

$$\begin{aligned} Y_1 &= \begin{array}{|c|}\hline 1 \\ \hline \multicolumn{1}{c}{} \\ \cline{1-1} 2 \\ \cline{1-1} \end{array} \;, \quad Y_2 = \begin{array}{|c|c|c|c|}\hline \multicolumn{2}{c}{} & 2 & 1 \\ \hline \end{array} \;, \quad Y_3 = \begin{array}{|c|c|}\hline \multicolumn{2}{c}{} \\ \hline 2 \\ \hline 1 \\ \cline{1-1} \end{array} \;, \\ Y_4 &= \begin{array}{|c|c|c|c|}\hline \multicolumn{2}{c}{} & 1 & 2 \\ \hline \end{array} \;, \quad Y_5 = \begin{array}{|c|c|}\hline \multicolumn{2}{c}{} \\ \hline 1 & 2 \\ \hline \end{array} \;, \quad Y_6 = \begin{array}{|c|c|}\hline \multicolumn{2}{c}{} \\ \hline 2 & 1 \\ \hline \end{array} \;, \end{aligned} \tag{B.27}$$

are not allowed in the sum on the right-hand side of (B.26), since they violate the rules 1 (for Y_1), 2 (for Y_2 and Y_6), 3 (for Y_3), or 4 (for Y_3, Y_4, and Y_5).

Now, one piece is still missing before we can apply the calculus of Young tables to determine the irreducible decomposition of product states of particles and antiparticles: We have to know how to depict the fundamental and conjugate representations of SU(N) as Young tables. This rule is simple: The fundamental representation, corresponding to a single particle, is depicted as a single box,

$$|\Psi\rangle_{\mathrm{SU}(N)} \;=\; \ydiagram{1} \;=\; [\,1, \underbrace{0, \ldots, 0}_{N-1}\,] \;\cong\; D(1, \underbrace{0, \ldots, 0}_{N-2}) \;, \tag{B.28}$$

while the conjugate representation, corresponding to a single antiparticle, is depicted as a row of $N-1$ boxes,

$$|\overline{\Psi}\rangle_{\mathrm{SU}(N)} \;=\; \left.\begin{array}{c}\square\\ \vdots\\ \square\end{array}\right\}_{N-1 \text{ boxes}} \;=\; [\underbrace{1,\ldots,1}_{N-1},0\,] \;\cong\; D(\underbrace{0,\ldots,0}_{N-2},1\,)\;. \qquad \text{(B.29)}$$

The dimension of both the fundamental and the conjugate representation is N.

With the depiction of the fundamental and conjugate representation as Young tables at hand, we can now proceed to the calculation of the decomposition (B.17) of product states. This will be done in the following section for the case of $\mathrm{SU}(3)$ and $m+n \leq 6$.

B.6 Product representations of SU(3) and their decomposition into irreducible representations

As an application of the calculus of Young tables, we will now construct the product representations of $\mathrm{SU}(3)$ for multiparticle states made of up to six particles and/or antiparticles and their decomposition into irreducible representations. Specifically, we will consider the combination of quarks and antiquarks, which are identified with fundamental representations $\mathbf{3}$ and conjugated representations $\overline{\mathbf{3}}$ of $\mathrm{SU}(3)$, respectively. Following the rules (B.29) and (B.29) for $\mathrm{SU}(3)$, the Young table corresponding to the fundamental representation is just one box, while the Young table of the conjugated representation consists of two boxes in a column. Thus, we start with

$$|q\rangle_{\mathrm{SU}(3)} \;=\; \mathbf{3} \;=\; \square\,, \quad |\bar{q}\rangle_{\mathrm{SU}(3)} \;=\; \overline{\mathbf{3}} \;=\; \begin{array}{c}\square\\ \square\end{array}\,. \qquad \text{(B.30)}$$

and construct multiparticle states of m quarks and n antiquarks, given by

$$R \;=\; \underbrace{\mathbf{3}\otimes\cdots\otimes\mathbf{3}}_{m \text{ times}}\otimes\underbrace{\overline{\mathbf{3}}\otimes\cdots\otimes\overline{\mathbf{3}}}_{n \text{ times}} \;=\; \sum_j \oplus I_j\;. \qquad \text{(B.31)}$$

We will construct all these states for $m+n \leq 6$ and their decomposition into irreducible representations I_j using the technique of Young tables. In the following section B.7, we will present a graphical method which can do the same and, furthermore, yields the well-known graphical illustration of particle multiplets.

The decomposition (B.31) applied to states of quarks and antiquarks is important for both colour and flavour $\mathrm{SU}(3)$:

The physics of colour shows that only colour neutral states can be observed in nature—this is colour confinement. Formally, the colour neutral state corresponds to the trivial, completely antisymmetric $\mathbf{1}$ representation of $\mathrm{SU}(3)$. Colour neutrality thus requires the decomposition (B.31) to contain the $\mathbf{1}$ representation at least once. This restriction yields the allowed quark-antiquark combinations for colour neutral hadronic states which are listed in table 8.1.

Interpreting, on the other hand, $\mathrm{SU}(3)$ as the flavour group and considering the decomposition (B.31) for all combinations of quarks and antiquarks which are compatible with colour neutrality, we are led to the well-known flavour multiplets,

such as the octet for mesons ($m = n = 1$) and the octet and decuplet for baryons ($m = 3, n = 0$). For the choice of $m = 4, n = 1$, we obtain a classification of all pentaquark multiplets.

The non-negative integers δ_1 and δ_2 which are used to label representations of SU(3) are usually denoted as p and q. Young tables of SU(3) have at most three rows, where p denotes the difference of the numbers of boxes between the first and second row, and q is the difference of the numbers of boxes between the second an third row. According to (B.23), the dimension of the irreducible representation $D(p, q)$ is given by

$$\dim D(p,q) \;=\; \frac{1}{2}(p+1)(p+q+2)(q+1)\;. \tag{B.32}$$

Table B.1 lists all representations $D(p, q)$ of SU(3) for $p + q \leq 6$ along with their dimensions and Young tables. Note that different representations can have the same dimension. Thus, the representations $D(2, 1)$ and $D(4, 0)$ are both 15-dimensional. In such cases, the difference is manifest in the symmetry: while $D(4, 0)$ is completely symmetric, $D(2, 1)$ has a mixed symmetry.

We now calculate the decomposition (B.31) of multiquark states into irreducible representations for combinations with $m + n \leq 6$, thus for combinations of up to six quarks or antiquarks.

p	q	dimension	Young table	p	q	dimension	Young table
0	0	$\mathbf{1}$		5	0	$\mathbf{21}$	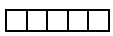
1	0	$\mathbf{3}$		0	5	$\overline{\mathbf{21}}$	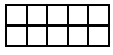
0	1	$\overline{\mathbf{3}}$		4	1	$\mathbf{35}$	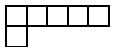
2	0	$\mathbf{6}$		1	4	$\overline{\mathbf{35}}$	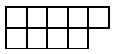
0	2	$\overline{\mathbf{6}}$		3	2	$\mathbf{42}$	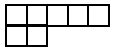
1	1	$\mathbf{8}$		2	3	$\overline{\mathbf{42}}$	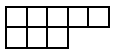
3	0	$\mathbf{10}$		6	0	$\mathbf{28}$	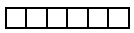
0	3	$\overline{\mathbf{10}}$		0	6	$\overline{\mathbf{28}}$	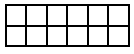
2	1	$\mathbf{15}$		5	1	$\mathbf{48}$	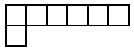
1	2	$\overline{\mathbf{15}}$		1	5	$\overline{\mathbf{48}}$	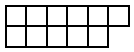
4	0	$\mathbf{15}_{\mathrm{s}}$		4	2	$\mathbf{60}$	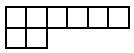
0	4	$\overline{\mathbf{15}}_{\mathrm{s}}$		2	4	$\overline{\mathbf{60}}$	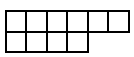
3	1	$\mathbf{24}$		3	3	$\mathbf{64}$	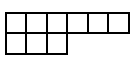
1	3	$\overline{\mathbf{24}}$					

Table B.1
All irreducible representations $D(p, q)$ of the group SU(3) for $p + q \leq 6$ with their dimensions and Young tables. The dimensions of the representations can be calculated according to equation (B.32). Representations whose Young tables consist of only one row of boxes are completely symmetric. Thus, the representation $\mathbf{15}_{\mathrm{s}}$ is completely symmetric, as indicated by the index. Representations whose Young tables consist of only one column of boxes are completely antisymmetric. All other representations have mixed symmetries.

Two quarks form diquark states. The decomposition reads

$$\begin{aligned}\mathbf{3}\otimes\mathbf{3} &= \square\otimes\square = \square\!\square\oplus\begin{smallmatrix}\square\\\square\end{smallmatrix}\\ &= D(2,0)\oplus D(0,1)\\ &= \mathbf{6}\oplus\overline{\mathbf{3}}\,.\end{aligned} \tag{B.33}$$

It does not contain the singlet representation $\mathbf{1}$. This corresponds to the experimental fact that diquarks carry colour charge and can not be observed as free particles. However, a quark and an antiquark can be combined to form a meson,

$$\begin{aligned}\mathbf{3}\otimes\overline{\mathbf{3}} &= \square\otimes\square\!\square = \square\!\square\!\square\oplus\begin{smallmatrix}\square\!\square\\\square\end{smallmatrix}\\ &= D(1,0)\oplus D(1,1)\\ &= \mathbf{1}\oplus\mathbf{8}\,,\end{aligned} \tag{B.34}$$

which can be in a colour neutral state. In flavour $\mathrm{SU}(3)$, the $\mathbf{8}$ is the meson octet. Two antiquarks form an anti-diquark state,

$$\begin{aligned}\overline{\mathbf{3}}\otimes\overline{\mathbf{3}} &= \begin{smallmatrix}\square\\\square\end{smallmatrix}\otimes\begin{smallmatrix}\square\\\square\end{smallmatrix} = \begin{smallmatrix}\square\!\square\\\square\!\square\end{smallmatrix}\oplus\square\\ &= D(0,2)\oplus D(1,0)\\ &= \overline{\mathbf{6}}\oplus\mathbf{3}\,,\end{aligned} \tag{B.35}$$

which decomposes into states conjugated to the states of the diquark and cannot be observed as a free particle. Three quarks form a baryon,

$$\begin{aligned}&\mathbf{3}\otimes\mathbf{3}\otimes\mathbf{3}\\ &\quad= \square\otimes\square\otimes\square = \left(\square\!\square\oplus\begin{smallmatrix}\square\\\square\end{smallmatrix}\right)\otimes\square = \square\!\square\!\square\oplus\begin{smallmatrix}\square\!\square\\\square\end{smallmatrix}\oplus\begin{smallmatrix}\square\!\square\\\square\end{smallmatrix}\oplus\begin{smallmatrix}\square\\\square\\\square\end{smallmatrix}\\ &\quad= D(3,0)\oplus D(1,1)\oplus D(1,1)\oplus D(0,0)\\ &\quad= \mathbf{10}\oplus 2\cdot\mathbf{8}\oplus\mathbf{1}\,,\end{aligned} \tag{B.36}$$

and three antiquarks from an antibaryon,

$$\begin{aligned}&\overline{\mathbf{3}}\otimes\overline{\mathbf{3}}\otimes\overline{\mathbf{3}}\\ &\quad= \begin{smallmatrix}\square\\\square\end{smallmatrix}\otimes\begin{smallmatrix}\square\\\square\end{smallmatrix}\otimes\begin{smallmatrix}\square\\\square\end{smallmatrix} = \left(\begin{smallmatrix}\square\!\square\\\square\!\square\end{smallmatrix}\oplus\square\right)\otimes\begin{smallmatrix}\square\\\square\end{smallmatrix} = \begin{smallmatrix}\square\!\square\!\square\\\square\!\square\!\square\end{smallmatrix}\oplus\begin{smallmatrix}\square\!\square\\\square\!\square\\\square\end{smallmatrix}\oplus\begin{smallmatrix}\square\!\square\\\square\!\square\\\square\end{smallmatrix}\oplus\begin{smallmatrix}\square\\\square\\\square\\\square\end{smallmatrix}\\ &\quad= D(0,3)\oplus 2\cdot D(1,1)\oplus D(0,0)\\ &\quad= \overline{\mathbf{10}}\oplus 2\cdot\mathbf{8}\oplus\mathbf{1}\,,\end{aligned} \tag{B.37}$$

since both decompositions contain the singlet $\mathbf{1}$. Interpreted as flavour, the decomposition (B.36) contains the baryon octet and decuplet, and the analogous, conjugated multiplets for antibaryons occur in the decomposition (B.37). The states

$$\begin{aligned}&\mathbf{3}\otimes\mathbf{3}\otimes\overline{\mathbf{3}}\\ &\quad= \square\otimes\square\otimes\begin{smallmatrix}\square\\\square\end{smallmatrix} = \left(\square\!\square\oplus\begin{smallmatrix}\square\\\square\end{smallmatrix}\right)\otimes\begin{smallmatrix}\square\\\square\end{smallmatrix} = \square\oplus\begin{smallmatrix}\square\!\square\\\square\end{smallmatrix}\oplus\begin{smallmatrix}\square\!\square\\\square\!\square\end{smallmatrix}\oplus\square\\ &\quad= D(1,0)\oplus D(2,1)\oplus D(0,2)\oplus D(1,0)\\ &\quad= \mathbf{15}\oplus\overline{\mathbf{6}}\oplus 2\cdot\mathbf{3}\,,\end{aligned} \tag{B.38}$$

$$
\begin{aligned}
&\mathbf{3}\otimes\mathbf{3}\otimes\mathbf{3}\otimes\mathbf{3}\\
&\quad=\square\otimes\square\otimes\square\otimes\square=\Big(\square\!\square\!\square\oplus 2\cdot\begin{array}{l}\square\!\square\\ \square\end{array}\oplus\begin{array}{l}\square\\ \square\\ \square\end{array}\Big)\otimes\square\\
&\quad=\square\!\square\!\square\!\square\oplus\begin{array}{l}\square\!\square\!\square\\ \square\end{array}\oplus 2\cdot\begin{array}{l}\square\!\square\!\square\\ \square\!\square\end{array}\oplus 2\cdot\begin{array}{l}\square\!\square\\ \square\!\square\end{array}\oplus 2\cdot\square\oplus\square\\
&\quad=D(4,0)\oplus 3\cdot D(2,1)\oplus 2\cdot D(0,2)\oplus 3\cdot D(1,0)\\
&\quad=\mathbf{15}_{\mathrm{s}}\oplus 3\cdot\mathbf{15}\oplus 2\cdot\overline{\mathbf{6}}\oplus 3\cdot\mathbf{3}\,,
\end{aligned}
\tag{B.39}
$$

and

$$
\begin{aligned}
&\mathbf{3}\otimes\mathbf{3}\otimes\mathbf{3}\otimes\overline{\mathbf{3}}\\
&\quad=\square\otimes\square\otimes\square\otimes\begin{array}{l}\square\\ \square\end{array}=\Big(\square\!\square\!\square\oplus 2\cdot\begin{array}{l}\square\!\square\\ \square\end{array}\oplus\begin{array}{l}\square\\ \square\\ \square\end{array}\Big)\otimes\begin{array}{l}\square\\ \square\end{array}\\
&\quad=\begin{array}{l}\square\!\square\!\square\\ \square\end{array}\oplus\square\!\square\oplus 2\cdot\begin{array}{l}\square\!\square\!\square\\ \square\!\square\end{array}\oplus 2\cdot\square\!\square\oplus 2\cdot\begin{array}{l}\square\\ \square\end{array}\oplus\begin{array}{l}\square\\ \square\end{array}\\
&\quad=D(3,1)\oplus 3\cdot D(2,0)\oplus 2\cdot D(1,2)\oplus 3\cdot D(0,1)\\
&\quad=\mathbf{24}\oplus 2\cdot\overline{\mathbf{15}}\oplus 3\cdot\mathbf{6}\oplus 3\cdot\overline{\mathbf{3}}
\end{aligned}
\tag{B.40}
$$

do not contain any $\mathbf{1}$ representations and are thus not allowed as free particle states. In the decomposition (B.39) of $\mathbf{3}\otimes\mathbf{3}\otimes\mathbf{3}\otimes\mathbf{3}$, one has to keep in mind that the completely symmetric representation $\mathbf{15}_{\mathrm{s}}=D(4,0)=\square\!\square\!\square\!\square$ and the representation $\mathbf{15}=D(2,1)=\begin{array}{l}\square\!\square\!\square\\ \square\end{array}$ with mixed symmetry are different, although both are 15-dimensional. The combination

$$
\begin{aligned}
&\mathbf{3}\otimes\mathbf{3}\otimes\overline{\mathbf{3}}\otimes\overline{\mathbf{3}}\\
&\quad=\square\otimes\square\otimes\begin{array}{l}\square\\ \square\end{array}\otimes\begin{array}{l}\square\\ \square\end{array}=\Big(\begin{array}{l}\square\!\square\!\square\\ \square\end{array}\oplus\begin{array}{l}\square\!\square\\ \square\!\square\end{array}\oplus 2\cdot\square\Big)\otimes\begin{array}{l}\square\\ \square\end{array}\\
&\quad=\begin{array}{l}\square\!\square\!\square\!\square\\ \square\!\square\end{array}\oplus\square\!\square\!\square\oplus\begin{array}{l}\square\!\square\!\square\\ \square\end{array}\oplus\begin{array}{l}\square\!\square\\ \square\!\square\!\square\end{array}\oplus\begin{array}{l}\square\!\square\!\square\\ \square\end{array}\oplus 2\cdot\begin{array}{l}\square\\ \square\\ \square\end{array}\oplus 2\cdot\begin{array}{l}\square\!\square\!\square\\ \square\end{array}\\
&\quad=D(2,2)\oplus D(3,0)\oplus D(1,1)\oplus D(0,3)\oplus D(1,1)\\
&\qquad\qquad\qquad\qquad\qquad\qquad\oplus 2\cdot D(0,0)\oplus 2\cdot D(1,1)\\
&\quad=\mathbf{27}\oplus\mathbf{10}\oplus\overline{\mathbf{10}}\oplus 4\cdot\mathbf{8}\oplus 2\cdot\mathbf{1}
\end{aligned}
\tag{B.41}
$$

contains the $\mathbf{1}$ representation and, therefore, is a possible combination in the colour neutral hadronic world. These are the dimeson states, which may embrace the $f_0(800)$ and $D_{\mathrm{s}}(2317)$ particles [239, 272].

In the same way, the combination of four quarks and one antiquark contains the $\mathbf{1}$ representation:

$$
\begin{aligned}
&\mathbf{3}\otimes\mathbf{3}\otimes\mathbf{3}\otimes\mathbf{3}\otimes\overline{\mathbf{3}}\\
&\quad=\square\otimes\square\otimes\square\otimes\square\otimes\begin{array}{l}\square\\ \square\end{array}\\
&\quad=\Big(\square\!\square\!\square\!\square\oplus 3\cdot\begin{array}{l}\square\!\square\!\square\\ \square\end{array}\oplus 2\cdot\begin{array}{l}\square\!\square\\ \square\!\square\end{array}\oplus 3\cdot\square\Big)\otimes\begin{array}{l}\square\\ \square\end{array}\\
&\quad=\begin{array}{l}\square\!\square\!\square\!\square\\ \square\end{array}\oplus\square\!\square\!\square\oplus 3\cdot\begin{array}{l}\square\!\square\!\square\!\square\\ \square\!\square\end{array}\oplus 3\cdot\square\!\square\!\square\oplus 3\cdot\begin{array}{l}\square\!\square\!\square\\ \square\end{array}\\
&\qquad\qquad\qquad\qquad\oplus 2\cdot\begin{array}{l}\square\!\square\\ \square\!\square\!\square\end{array}\oplus 2\cdot\begin{array}{l}\square\!\square\\ \square\end{array}\oplus 3\cdot\begin{array}{l}\square\!\square\\ \square\end{array}\oplus 3\cdot\begin{array}{l}\square\\ \square\\ \square\end{array}\\
&\quad=D(4,1)\oplus 4\cdot D(3,0)\oplus 3\cdot D(2,2)\oplus 8\cdot D(1,1)\\
&\qquad\qquad\qquad\qquad\qquad\qquad\oplus\,2\cdot D(0,3)\oplus 3\cdot D(0,0)\\
&\quad=\mathbf{35}\oplus 3\cdot\mathbf{27}\oplus 4\cdot\mathbf{10}\oplus 2\cdot\overline{\mathbf{10}}\oplus 8\cdot\mathbf{8}\oplus 3\cdot\mathbf{1}\,.
\end{aligned}
\tag{B.42}
$$

These are the pentaquark states. The $\Theta^+(1540)$, the first pentaquark states which has been observed in experiment [23], has strangeness $S = +1$ and belongs to the one of the two antidecuplets $\overline{\mathbf{10}}$. We will go into more detail about the pentaquark states in the following section B.6. The combinations

$$\begin{aligned}
\mathbf{3}\otimes\mathbf{3}\otimes\mathbf{3}\otimes\mathbf{3}\otimes\mathbf{3} &= \square\otimes\square\otimes\square\otimes\square\otimes\square \\
&= \Big(\square\!\square\!\square\!\square \oplus 3\cdot\begin{array}{l}\square\!\square\!\square\\ \square\end{array} \oplus 2\cdot\begin{array}{ll}\square & \square\\ \square & \square\end{array} \oplus 3\cdot\square\Big)\otimes\square \\
&= \square\!\square\!\square\!\square\!\square \oplus \begin{array}{l}\square\!\square\!\square\!\square\\ \square\end{array} \oplus 3\cdot\begin{array}{l}\square\!\square\!\square\!\square\\ \square\end{array} \oplus 3\cdot\begin{array}{ll}\square & \square\\ \square & \square\end{array} \oplus 3\cdot\square\!\square \\
&\qquad\qquad \oplus\, 2\cdot\begin{array}{ll}\square & \square\\ \square & \square\end{array}\square \oplus 2\cdot\begin{array}{l}\square\\ \square\end{array} \oplus 3\cdot\square\!\square \oplus 3\cdot\begin{array}{l}\square\\ \square\end{array} \\
&= D(5,0)\oplus 4\cdot D(3,1)\oplus 5\cdot D(1,2)\oplus 6\cdot D(2,0)\oplus 5\cdot D(0,1) \\
&= \mathbf{21}\oplus 4\cdot\mathbf{24}\oplus 5\cdot\overline{\mathbf{15}}\oplus 6\cdot\mathbf{6}\oplus 5\cdot\overline{\mathbf{3}}\,,
\end{aligned} \tag{B.43}$$

and

$$\begin{aligned}
\mathbf{3}\otimes\mathbf{3}\otimes\mathbf{3}\otimes\overline{\mathbf{3}}\otimes\overline{\mathbf{3}} &= \square\otimes\square\otimes\square\otimes\begin{array}{l}\square\\ \square\end{array}\otimes\begin{array}{l}\square\\ \square\end{array} \\
&= \Big(\begin{array}{l}\square\!\square\!\square\\ \square\end{array} \oplus 2\cdot\begin{array}{ll}\square & \square\\ \square & \square\end{array} \oplus 3\cdot\square\!\square \oplus 3\cdot\begin{array}{l}\square\\ \square\end{array}\Big)\otimes\begin{array}{l}\square\\ \square\end{array} \\
&= \begin{array}{ll}\square & \square\\ \square & \square\end{array}\square \oplus \square\!\square\!\square\!\square \oplus \begin{array}{l}\square\!\square\!\square\\ \square\end{array} \oplus 2\cdot\begin{array}{lll}\square & \square & \square\\ \square & \square & \square\end{array} \oplus 2\cdot\begin{array}{ll}\square & \square\\ \square & \square\end{array}\square \oplus 2\cdot\begin{array}{ll}\square & \square\\ \square & \square\end{array} \\
&\qquad\qquad \oplus 3\cdot\begin{array}{l}\square\!\square\!\square\\ \square\end{array} \oplus 3\cdot\square \oplus 3\cdot\begin{array}{ll}\square & \square\\ \square & \square\end{array} \oplus 3\cdot\square \\
&= D(3,2)\oplus D(4,0)\oplus 6\cdot D(2,1)\oplus 2\cdot D(1,3) \\
&\qquad\qquad \oplus 5\cdot D(0,2)\oplus 6\cdot D(1,0) \\
&= \mathbf{42}\oplus 2\cdot\overline{\mathbf{24}}\oplus\mathbf{15}_{\mathrm{s}}\oplus 6\cdot\mathbf{15}\oplus 5\cdot\overline{\mathbf{6}}\oplus 6\cdot\mathbf{3}
\end{aligned} \tag{B.44}$$

do not contain any $\mathbf{1}$ representations, but they are present in the dibaryon and baryonium states,

$$\begin{aligned}
\mathbf{3}\otimes\mathbf{3}\otimes\mathbf{3}\otimes\mathbf{3}\otimes\mathbf{3}\otimes\mathbf{3} &= \square\otimes\square\otimes\square\otimes\square\otimes\square\otimes\square \\
&= \Big(\square\!\square\!\square\!\square\!\square \oplus 4\cdot\begin{array}{l}\square\!\square\!\square\!\square\\ \square\end{array} \oplus 5\cdot\begin{array}{ll}\square & \square\\ \square & \square\end{array}\square \oplus 6\cdot\square\!\square \oplus 5\cdot\begin{array}{l}\square\\ \square\end{array}\Big)\otimes\square \\
&= \square\!\square\!\square\!\square\!\square\!\square \oplus \begin{array}{l}\square\!\square\!\square\!\square\!\square\\ \square\end{array} \oplus 4\cdot\begin{array}{l}\square\!\square\!\square\!\square\!\square\\ \square\end{array} \oplus 4\cdot\begin{array}{ll}\square & \square\\ \square & \square\end{array}\square\!\square \oplus 4\cdot\square\!\square\!\square \\
&\qquad \oplus 5\cdot\begin{array}{ll}\square & \square\\ \square & \square\end{array}\square\!\square \oplus 5\cdot\begin{array}{lll}\square & \square & \square\\ \square & \square & \square\end{array} \oplus 5\cdot\begin{array}{l}\square\!\square\\ \square\end{array} \\
&\qquad\qquad \oplus 6\cdot\square\!\square\!\square \oplus 6\cdot\begin{array}{l}\square\!\square\\ \square\end{array} \oplus 5\cdot\begin{array}{l}\square\!\square\\ \square\end{array} \oplus 5\cdot\begin{array}{l}\square\\ \square\end{array} \\
&= D(6,0)\oplus 5\cdot D(4,1)\oplus 9\cdot D(2,2)\oplus 5\cdot D(0,3) \\
&\qquad\qquad \oplus 16\cdot D(1,1)\oplus 10\cdot D(3,0)\oplus 5\cdot D(0,0) \\
&= 5\cdot\mathbf{35}\oplus\mathbf{28}\oplus 9\cdot\mathbf{27}\oplus 5\cdot\overline{\mathbf{10}}\oplus 16\cdot\mathbf{8}\oplus 10\cdot\mathbf{10}\oplus 5\cdot\mathbf{1}\,,
\end{aligned} \tag{B.45}$$

and

$$\begin{aligned}
\mathbf{3}\otimes\mathbf{3}\otimes\mathbf{3}\otimes\overline{\mathbf{3}}\otimes\overline{\mathbf{3}}\otimes\overline{\mathbf{3}} &= \square\otimes\square\otimes\square\otimes\begin{array}{l}\square\\ \square\end{array}\otimes\begin{array}{l}\square\\ \square\end{array}\otimes\begin{array}{l}\square\\ \square\end{array} \\
&= \Big(\begin{array}{ll}\square & \square\\ \square & \square\end{array}\square \oplus \square\!\square\!\square\!\square \oplus 6\cdot\begin{array}{l}\square\!\square\!\square\\ \square\end{array} \oplus 2\cdot\begin{array}{lll}\square & \square & \square\\ \square & \square & \square\end{array}\square \oplus 5\cdot\begin{array}{ll}\square & \square\\ \square & \square\end{array} \oplus 6\cdot\square\Big)\otimes\begin{array}{l}\square\\ \square\end{array} \\
&= \begin{array}{ll}\square & \square\\ \square & \square\end{array}\square\!\square \oplus \begin{array}{l}\square\!\square\!\square\!\square\!\square\\ \square\end{array} \oplus \begin{array}{ll}\square & \square\\ \square & \square\end{array}\square\!\square \oplus \begin{array}{l}\square\!\square\!\square\!\square\!\square\\ \square\end{array} \oplus \square\!\square\!\square \\
&\qquad \oplus 6\cdot\begin{array}{l}\square\!\square\!\square\\ \square\end{array}\square \oplus 6\cdot\square\!\square\!\square \oplus 6\cdot\begin{array}{l}\square\!\square\\ \square\end{array} \oplus 2\cdot\begin{array}{l}\square\!\square\!\square\!\square\\ \square\end{array} \\
&\qquad\qquad \oplus 2\cdot\begin{array}{l}\square\!\square\!\square\\ \square\end{array}\square \oplus 2\cdot\begin{array}{ll}\square & \square\\ \square & \square\end{array}\square \oplus 5\cdot\begin{array}{lll}\square & \square & \square\\ \square & \square & \square\end{array} \oplus 5\cdot\begin{array}{l}\square\!\square\\ \square\end{array} \oplus 6\cdot\begin{array}{l}\square\!\square\\ \square\end{array} \oplus 6\cdot\begin{array}{l}\square\\ \square\end{array}
\end{aligned}$$

$$
\begin{aligned}
&= D(3,3) \oplus 2 \cdot D(4,1) \oplus 7 \cdot D(3,0) \oplus 9 \cdot D(2,2) \\
&\qquad \oplus 2 \cdot D(1,4) \oplus 7 \cdot D(0,3) \oplus 17 \cdot D(1,1) \oplus 6 \cdot D(0,0) \qquad \text{(B.46)} \\
&= \mathbf{64} \oplus 2 \cdot \mathbf{35} \oplus 2 \cdot \overline{\mathbf{35}} \oplus 7 \cdot \mathbf{10} \oplus 7 \cdot \overline{\mathbf{10}} \oplus 9 \cdot \mathbf{27} \oplus 17 \cdot \mathbf{8} \oplus 6 \cdot \mathbf{1} \; .
\end{aligned}
$$

Baryonium and dibaryon states thus could be observable as free particles. However, as we have discussed in chapter 8, the experimental evidence for these states is sparse.

B.7 Graphical construction of irreducible representations of SU(3) and their multiplets

The technique of Young tables as discussed in section B.5 allows to calculate the decomposition of product representations, but the results tell us only the dimensions and information about the symmetries of the irreducible representations. However, more knowledge about the states in a multiplet corresponding to some irreducible representations may be welcome. In the case of flavour SU(3), for example, the electric charge and the strangeness of the particles in the multiplets are quantities we want to know. They can be read off easily from graphical representations of multiplets, as shown in figures A.1 and A.2. Here, we will discuss how these graphical representations of multiplets can be obtained for SU(3), and will apply this scheme to the pentaquark multiplets in SU(3). The inclusion of charm is a straightforward generalization, going from two-dimensional diagrams to the three-dimensional objects shown in figures A.1 and A.2. We will not discuss it, since we do not need it.

The starting point of the graphical representation of multiplets is the observation that some of the generators T_a of the Lie algebra (B.9) can be simultaneously diagonalized. The maximal set of these generators forms a Lie subalgebra, which is called the *Cartan subalgebra*. In general, the Cartan subalgebra of the Lie algebra su(N) is spanned by $N-1$ generators. Thus, in the case of SU(3), there are two generators in the Cartan subalgebra. Using the fundamental representation, these generators are found to be the diagonal matrices T_3 and T_8,

$$
T_3 = \frac{1}{2}\lambda_3 = \frac{1}{2}\begin{pmatrix} 1 & 0 & 0 \\ 0 & -1 & 0 \\ 0 & 0 & 0 \end{pmatrix}, \quad T_8 = \frac{1}{2}\lambda_8 = \frac{1}{2\sqrt{3}}\begin{pmatrix} 1 & 0 & 0 \\ 0 & 1 & 0 \\ 0 & 0 & -2 \end{pmatrix} . \qquad \text{(B.47)}
$$

Now, the unit vectors that span the fundamental representation are eigenvectors of both Cartan matrices. For example,

$$
\begin{aligned}
T_3 \begin{pmatrix} 1 \\ 0 \\ 0 \end{pmatrix} &= \frac{1}{2}\begin{pmatrix} 1 & 0 & 0 \\ 0 & -1 & 0 \\ 0 & 0 & 0 \end{pmatrix}\begin{pmatrix} 1 \\ 0 \\ 0 \end{pmatrix} = +\frac{1}{2}\begin{pmatrix} 1 \\ 0 \\ 0 \end{pmatrix} , \\
T_8 \begin{pmatrix} 1 \\ 0 \\ 0 \end{pmatrix} &= \frac{1}{2\sqrt{3}}\begin{pmatrix} 1 & 0 & 0 \\ 0 & 1 & 0 \\ 0 & 0 & -2 \end{pmatrix}\begin{pmatrix} 1 \\ 0 \\ 0 \end{pmatrix} = +\frac{1}{2\sqrt{3}}\begin{pmatrix} 1 \\ 0 \\ 0 \end{pmatrix} .
\end{aligned} \qquad \text{(B.48)}
$$

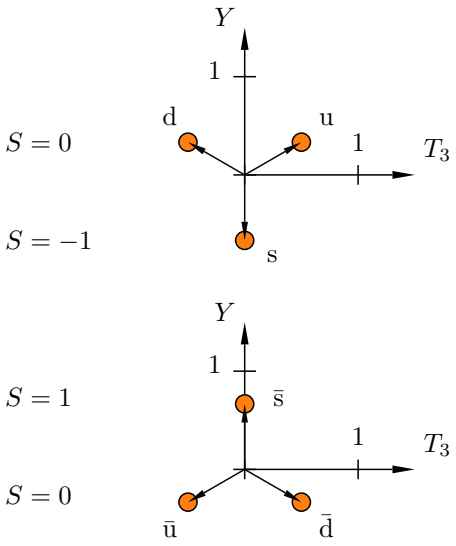

Figure B.1
Triplets of the fundamental representation $D(1,0)$ (top) and the conjugated representation $D(0,1)$ (bottom) of the group SU(3) in the weight diagram. In the case of flavour SU(3), the fundamental triplet contains the u, d, and s quark, while the conjugated triplet embraces the antiquarks $\bar{\mathrm{u}}$, $\bar{\mathrm{d}}$, and $\bar{\mathrm{s}}$. Strangeness S is related to the eigenvalues of hypercharge Y and isospin component T_3 through the relation $Y = S + \frac{1}{3}$ for the quark triplet ($B = 1/3$) and $Y = S - \frac{1}{3}$ for the antiquark triplet ($B = -1/3$).

Thus, each unit vector can be identified with its the pair of eigenvalues under the action of both T_3 and T_8,

$$\begin{pmatrix}1\\0\\0\end{pmatrix} \leftrightarrow \begin{pmatrix}+\frac{1}{2}\\+\frac{1}{2\sqrt{3}}\end{pmatrix}, \quad \begin{pmatrix}0\\1\\0\end{pmatrix} \leftrightarrow \begin{pmatrix}-\frac{1}{2}\\+\frac{1}{2\sqrt{3}}\end{pmatrix}, \quad \begin{pmatrix}0\\0\\1\end{pmatrix} \leftrightarrow \begin{pmatrix}0\\-\frac{1}{\sqrt{3}}\end{pmatrix}. \tag{B.49}$$

These pairs of eigenvalues are called *weight vectors*.[3] The assignment (B.49) is exactly what we have done in (2.13) and (2.14) for the case of colour SU(3). For flavour SU(3), the weight vector assignment (B.49) applied to the unit vectors of the fundamental representation, the up, down, and strange quark, reads

$$\mathrm{u} \longleftrightarrow \begin{pmatrix}+\frac{1}{2}\\+\frac{1}{2\sqrt{3}}\end{pmatrix}, \quad \mathrm{d} \longleftrightarrow \begin{pmatrix}-\frac{1}{2}\\+\frac{1}{2\sqrt{3}}\end{pmatrix}, \quad \mathrm{s} \longleftrightarrow \begin{pmatrix}0\\-\frac{1}{\sqrt{3}}\end{pmatrix}. \tag{B.50}$$

Using the explicit form (B.10) for the generators T_a in the conjugate representation, the same scheme yields the weight vector assignment

$$\bar{\mathrm{u}} \longleftrightarrow \begin{pmatrix}-\frac{1}{2}\\-\frac{1}{2\sqrt{3}}\end{pmatrix}, \quad \bar{\mathrm{d}} \longleftrightarrow \begin{pmatrix}+\frac{1}{2}\\-\frac{1}{2\sqrt{3}}\end{pmatrix}, \quad \bar{\mathrm{s}} \longleftrightarrow \begin{pmatrix}0\\+\frac{1}{\sqrt{3}}\end{pmatrix} \tag{B.51}$$

for antiquarks. Plotting the weight vectors of particles and antiparticles in two-dimensional diagram yields the so-called *weight diagram*. The weight diagram for quarks is shown in the upper part of figure B.1, the corresponding diagram for antiquarks in the lower part of figure B.1.

[3] If, instead of the fundamental representation as in (B.49), one uses the adjoint representation, the vector built out of the eigenvalues under the action of the generators from the Cartan subalgebra is called the *root vector*.

Note that the vertical axis of B.1 is not scaled to the eigenvalues under the action of T_8, but uses the operator

$$Y = \frac{2}{\sqrt{3}} T_8 \tag{B.52}$$

instead. This scaling is motivated by physics: While the z-component of the isospin is given as the eigenvalue under the action of T_3, hence the first component of the weight vector, the operator Y describes the *hypercharge*

$$Y = B + S \,, \tag{B.53}$$

where B is the baryon number and S is strangeness. Using the Gell-Mann–Nishijima formula (A.2), this yields the electrical charge of the particle,

$$Q = T_3 + \frac{Y}{2} = T_3 + \frac{1}{2}(B + S) \,. \tag{B.54}$$

A point in the weight diagram, characterized by the values of T_3 and Y, is called a *state*. A state may be degenerate, if its multiplicity is more then 1. Switching between neighbouring states in the weight diagram is possible through the so-called *generalized ladder operators*

$$T_\pm \,=\, T_1 \pm \mathrm{i}\, T_2 \,, \quad U_\pm \,=\, T_6 \pm \mathrm{i}\, T_7 \,, \quad V_\pm \,=\, T_4 \pm \mathrm{i}\, T_5 \,, \tag{B.55}$$

which, in the case of colour, had been called $\mathrm{E}_i^\pm$ – see (2.32). For example, acting on the state corresponding to the up quark, the ladder operator V_- yields

$$V_- \begin{pmatrix} 1 \\ 0 \\ 0 \end{pmatrix} \,=\, \begin{pmatrix} 0 & 0 & 0 \\ 0 & 0 & 0 \\ 1 & 0 & 0 \end{pmatrix} \begin{pmatrix} 1 \\ 0 \\ 0 \end{pmatrix} \,=\, \begin{pmatrix} 0 \\ 0 \\ 1 \end{pmatrix} \,, \tag{B.56}$$

which is the strange quark. Similarly, T_- shifts the up quark to the down quark, corresponding to a lowering of the z-component of the isospin by one unit, while all other operators annihilate the up quark.

The ladder operators (B.55) can be used to construct the weight diagrams for all irreducible representations $D(p, q)$ in a systematic manner. The idea is to start with one non-degenerate state, which is called the *state of highest weight*, $|\Psi_{\mathrm{hw}}\rangle_{p,q}$. It corresponds to the up quark in the fundamental representation $D(1, 0)$. The location of $|\Psi_{\mathrm{hw}}\rangle_{p,q}$ in the weight diagram can be obtained using the formulae

$$\begin{aligned} T_3 \, |\Psi_{\mathrm{hw}}\rangle_{p,q} &= \frac{1}{2}(p + q) \, |\Psi_{\mathrm{hw}}\rangle_{p,q} \,, \\ Y \, |\Psi_{\mathrm{hw}}\rangle_{p,q} &= \frac{1}{3}(p - q) \, |\Psi_{\mathrm{hw}}\rangle_{p,q} \,. \end{aligned} \tag{B.57}$$

The ladder operators (B.55) act on the state of highest weight according to

$$T_+ \, |\Psi_{\mathrm{hw}}\rangle_{p,q} \,=\, V_+ \, |\Psi_{\mathrm{hw}}\rangle_{p,q} \,=\, U_- \, |\Psi_{\mathrm{hw}}\rangle_{p,q} \stackrel{!}{=} 0 \tag{B.58}$$

and

$$(V_-)^{p+1} \, |\Psi_{\mathrm{hw}}\rangle_{p,q} \,=\, (U_+)^{q+1} \, |\Psi_{\mathrm{hw}}\rangle_{p,q} \stackrel{!}{=} 0 \,. \tag{B.59}$$

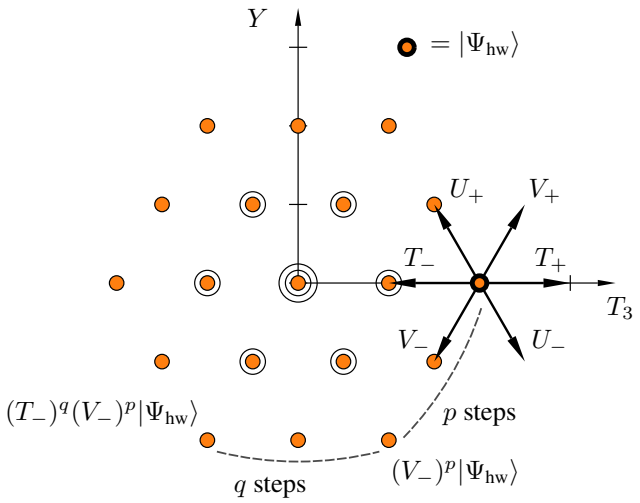

Figure B.2
The multiplet of the representation $D(2,2)$ of SU(3). Starting from the state of highest weight, $|\Psi_{\rm hw}\rangle$, the states on the boundary of the multiplet are obtained through p-fold application of the ladder operators V_-, followed by q-fold application of T_- and completion by symmetry. The multiplicity of the states is indicated by the circles. For example, there are 3 states in this multiplet with $(T_3, Y) = (0, 0)$.

Thus, the states of the multiplet corresponding to $D(p,q)$ form a regular pattern with a threefold symmetry in the weight diagram. The border of this diagram is obtained through p-fold application of V_- on $|\Psi_{\rm hw}\rangle_{p,q}$ (moving to the lower left in the $T_3 - Y$-plane by p steps), followed by a q-fold application of T_- (moving q steps to the left), and two rotations of the array of states thus created by $2\pi/3$ around the centre of the weight diagram. This is shown in figure B.2 for $D(2,2)$, along with the action of the ladder operators (B.55) on $|\Psi_{\rm hw}\rangle_{p,q}$. The state of highest weight, located at $(T_3, Y) = (2, 0)$ according to (B.57), is marked by the thick black circle.

The multiplicity of the states on the boundary of a multiplet created by these rules is 1. The shape of this outermost layer is described by the pair of integers (p, q). The multiplicity increases by 1 when going inward by one layer in the multiplet until a layer with a triangular shape is encountered. Going one layer inward, the shape is described by $(p', q') = (p - 1, q - 1)$. A triangular shape is obtained when either $p' = 0$ or $q' = 0$. In the multiplet of the representation $D(2,2)$, shown in figure B.2, this means that the innermost state in the weight diagram has multiplicity 3, as indicated by the circles. The multiplicity of a state in a multiplet equals the number of different combinations of particles which have the same quantum numbers T_3 and Y. Adding up all multiplicities yields the dimension of the representation shown in the diagram. The dimension of the representation $D(2,2)$ is obtained as $12 + 2 \times 6 + 3 \times 1 = 27$, in agreement with (B.32).

Irreducible representation of SU(3) are uniquely defined by the two parameters p and q. To each pair (p, q), a unique multiplet can be constructed, starting from the state of highest weight and following the rules just described. For this reason, the irreducible representations of SU(3), and more general of SU(N), are called *highest weight representations*.

So, we know how to construct multiplets of irreducible representations $D(p,q)$ of SU(3) in the $T_3 - Y$-plane. We will now describe how to construct multiplets of product representations in the weight diagram. The central idea is easy: In order to obtain the multiplet of a product representation $R = A \otimes B$, one starts with a plot the multiplet of representation A in the weight diagram. Then, all states

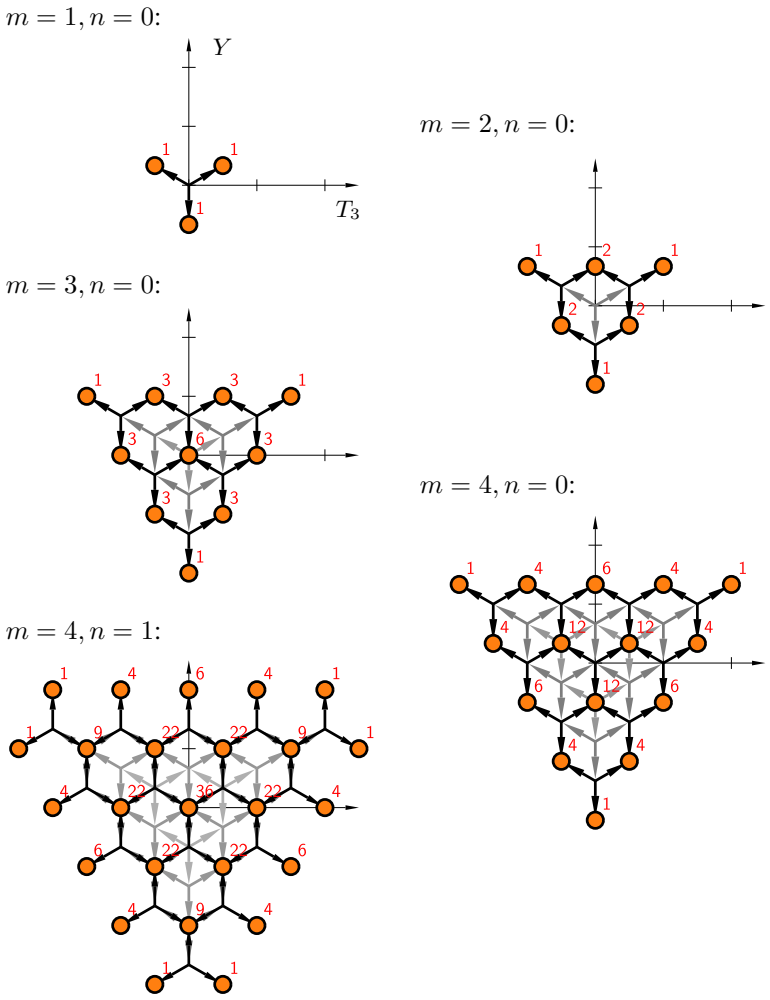

Figure B.3
Successive construction of all states of the product $\mathbf{3} \otimes \mathbf{3} \otimes \mathbf{3} \otimes \mathbf{3} \otimes \bar{\mathbf{3}}$ in the weight diagram. Numbers in red indicate the multiplicities of the states, i. e., the number of different combinations of quarks corresponding to the same values of (T_3, Y). The construction starts with the fundamental triplet (top left diagram of the figure). In the second step (top right diagram), one fundamental triplet is anchored at each state of the first triplet, yielding 9 states with 6 different values of (T_3, Y). The procedure is repeated two more times with the fundamental triplet, and in the last step (bottom left diagram), a conjugated triplet is added for the antiquarks.

of the product R are obtained by anchoring the multiplet B subsequently to all states a_i of the multiplet A, multiplying the multiplicity of all states of B by the multiplicity of the anchoring state a_i. This yields all states of the multiplet of the product representation R, along with their multiplicities.

This procedure is exemplified in figure B.3 for the stepwise construction of the multiplet of all pentaquark states, $\mathbf{3} \otimes \mathbf{3} \otimes \mathbf{3} \otimes \mathbf{3} \otimes \bar{\mathbf{3}}$. Here, $m = 4$ fundamental triplets corresponding to the representation $\mathbf{3}$ are combined with $n = 1$ conjugated triplet, corresponding to $\bar{\mathbf{3}}$. The multiplicity of each state in the weight diagram is indicated at every step. The multiplicities add up to $3^5 = 243$ in the last multiplet.

The multiplet M thus obtained is not reducible. However, the decomposition into irreducible multiplets can be deduced from its weight diagram. To this end, one simply has to subtract multiplets of irreducible representations $D(p, q)$ until no states are left in M. Using the known structure of multiplets corresponding to irreducible representations and subtracting always the largest possible $D(p, q)$, this is a straightforward procedure which results in the unique decomposition.

In the example of the pentaquark states, described by the final $m = 4, n = 1$ multiplet in figure B.3, the largest irreducible multiplet corresponds to $D(4, 1) =$

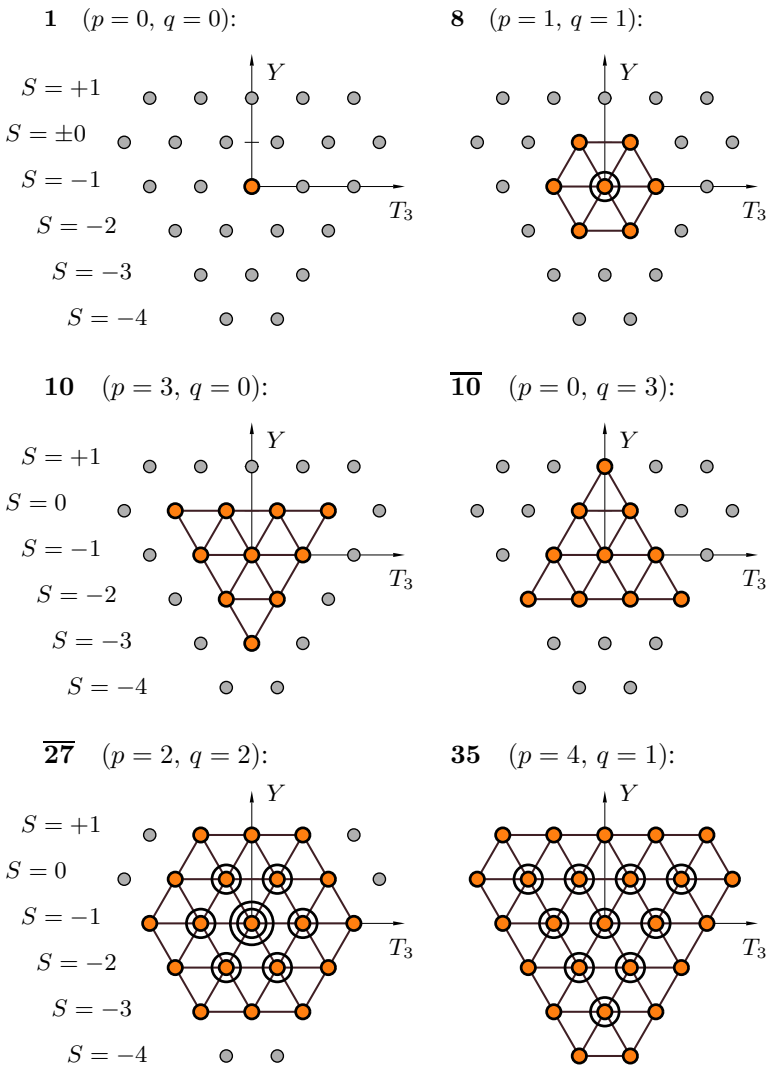

Figure B.4
Pentaquark states are described by the product representation $\mathbf{3} \otimes \mathbf{3} \otimes \mathbf{3} \otimes \mathbf{3} \otimes \bar{\mathbf{3}}$, which can be decomposed into a sum of irreducible representations. The figure shows the different irreducible representations which occur in this decomposition. Multiplicities are indicated by the circles around the states.

35, since its boundary is described by $p = 4$ and $q = 1$. The representation $D(4,1)$ occurs only once, due to the non-degenerate states at the boundary of the $m = 4, n = 1$ multiplet. Once the states of the $D(4,1)$ multiplet are removed, the outermost remaining states correspond to $D(4,1) = \mathbf{27}$, with threefold degeneracy. The next step shows that there are two $D(0,3) = \overline{\mathbf{10}}$ representations, and so on, until the complete decomposition (B.42) is recovered. The multiplets which occur in this decomposition are shown in figure B.4.

Thus, we see that the results obtained by the calculus of Young tables can be reproduced by the graphical method. The graphical method gives as a plus the complete multiplet structure of all states. However, it is very clumsy to use, so, if one is only interested in the irreducible decomposition of product states, the Young technique is superior. On the other hand, the rules of the graphical method can be implemented very easily in recursive computer codes which calculate multiplet structures and multiplicities. In fact, all data shown in figure B.3 and the diagrams themselves have been calculated by small programs, and not by hand.

Appendix C

Classification of pentaquark states using the combined spin-flavour SU(6)

When discussing the multiplet structure of pentaquark states, it can not be taken for granted that all multiplets which occur in the irreducible decomposition (B.42) of the product representation $\mathbf{3} \otimes \mathbf{3} \otimes \mathbf{3} \otimes \mathbf{3} \otimes \overline{\mathbf{3}}$ correspond to physical pentaquark multiplets. The irreducible decomposition (B.42) describes the flavour part of the pentaquark wave function. However, in order to obtain the complete wave function, it has to be combined with the space, spin, and colour wave function of the four quarks and the antiquark. Since the complete wavefunction has to be antisymmetric under the exchange of any two fermions, restrictions on the allowed flavour multiplets may apply.

This phenomenon is well known from the construction of the wave functions of baryons. In this case, the classification of the lowest baryon states based on flavour SU(3) can be improved by proceeding from flavour SU(3) to the combined spin-flavour group SU(6). This yields exactly one octet with spin $s = 1/2$ and one decuplet with spin $s = 3/2$. Even though the combination of three fundamental representations of SU(6) contains $6^3 = 216$ states, a strong restriction arises since the complete wave function of the three quarks, including space, flavour, spin, and colour degrees of freedom, has to be completely antisymmetric in order to fulfil the Pauli principle. However, the colour part of wave function is completely antisymmetric, since the baryon is colour neutral. The space part of the wave function is completely symmetric, if one assumes that for baryons in the ground state, the quarks are in relative s-wave states. Thus, the combined spin-flavour group part of the wave function must be completely symmetric!

We will start by discussing this example in more detail, before moving on to the construction of the wave functions of states of four quarks, and of four quarks and one antiquark. This will result in a more complete classification of pentaquark multiplets, which will include spin. However, we will always assume that the pentaquark states are s-wave states, thus that there are no excitations of orbital angular momentum.

C.1 Spin-flavour SU(6) and the classification of baryons

When three quarks combine to form a baryon, the colour part of their wave function has to be a colour singlet $\mathbf{1}_c$, in compliance with confinement. Thus, the colour part of the quark wave function is antisymmetric under the exchange of any two quarks. The space part of the wave function for baryons in the ground state is assumed to be a s-wave state for each quark: there is no orbital angular momentum in the ground state. Hence, the space part of the wave function is completely symmetric. Now, the total wave function for the three quarks,

$$|q \otimes q \otimes q\rangle_A \;=\; |\text{colour}\rangle_A \otimes |\text{space}\rangle_S \otimes |\text{spin, flavour}\rangle_S \tag{C.1}$$

has to be completely antisymmetric, as indicated by the index A, in order to fulfil the Pauli principle. This requires the combined spin-flavour wave function to be completely symmetric! Complete symmetry is indicated by the index S.

The classification of the combined spin-flavour wave function is best described by the representation theory of SU(6) [273, 274]. This method is an extension of the theory of supermultiplets created by Wigner, where spin and isospin are combined in the description of multi-nucleon states. In the application of SU(6) to spin-flavour, the six-dimensional fundamental representation operates on the vector space spanned by the six states $u_\uparrow$, $u_\downarrow$, $d_\uparrow$, $d_\downarrow$, $s_\uparrow$, and $s_\downarrow$, where the index indicates the orientation of spin. In the formalism of Young tables, a single box now depicts a quark with a well-defined orientation of spin. The decomposition of a SU(6) product representation corresponding to three quarks is described by the same Young tables as in the case of SU(3), (B.36), hence

$|q \otimes q \otimes q\rangle_{\text{SU(6)}} \;=\;$ 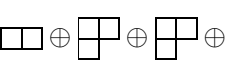 . (C.2)

However, one has to keep in mind that these Young tables now stand for the irreducible representations $D(3,0,0,0,0)$, $D(1,1,0,0,0)$, and $D(0,0,1,0,0)$, respectively, and that their dimensions can not be calculated according to (B.32), but that the general expression (B.22) has to be used instead. Denoting the irreducible representations by their dimensions, this yields

$$|q \otimes q \otimes q\rangle_{\text{SU(6)}} \;=\; \mathbf{56} \oplus \mathbf{70} \oplus \mathbf{70} \oplus \overline{\mathbf{20}}\,, \tag{C.3}$$

with $56+70+70+20 = 216 = 6^3$. Since the completely symmetric representation is depicted by the Young table with all boxes in one row, we see that the combined spin-flavour part of the state (C.1) is given by

$|\text{spin, flavour}\rangle_S \;=\;$ 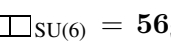 $\;=\; \mathbf{56}_{\text{SU(6)}}\,.$ (C.4)

Thus, among the four multiplets in the decomposition (C.2), only the multiplet corresponding to the representation $\mathbf{56}_{\text{SU(6)}}$ can occur in the description of baryons in the ground state.

Of course, it is interesting to know the flavour and spin content of the representation $\mathbf{56}_{\text{SU(6)}}$. Here, one can use the mathematical fact that any irreducible representation of SU(NM) can be decomposed in a unique way in a sum of combinations of irreducible representations of SU(M) and SU(N). Details of this

decomposition, along with tables for the lowest representations of SU(6), can be found in [234]. As an example, the fundamental representation $\mathbf{6}_{\mathrm{SU}(6)}$ of SU(6) decomposes into one fundamental representation $\mathbf{3}_{\mathrm{SU}(3)}$ of SU(3) and one fundamental representation $\mathbf{2}_{\mathrm{SU}(2)}$ of SU(2). Physically speaking, this means that a single quark can be either up, down, or strange, with spin up or down independent of flavour. This decomposition is written as

$$\begin{aligned} \square_{\mathrm{SU}(6)} &= (\square_{\mathrm{SU}(3)}; \square_{\mathrm{SU}(2)}) \\ \text{or} \qquad \mathbf{6}_{\mathrm{SU}(6)} &= (\mathbf{3}_{\mathrm{SU}(3)}; \mathbf{2}_{\mathrm{SU}(2)}) = (\mathbf{3}; 1/2) \,, \end{aligned} \tag{C.5}$$

where in the last notation, the subscripts indicating the group are omitted and the representation of SU(2) is denoted by its spin.

The spin-flavour part of the baryon wave function is described by the completely symmetric multiplet $\square\square\square_{\mathrm{SU}(6)} = \mathbf{56}$. In the decomposition in a sum of combinations of irreducible representations of SU(3) and SU(2), complete symmetry can only be achieved if both the SU(3) and the SU(2) factor have the same symmetry. Thus, they must be represented by the same Young tables. This means

$$\square\square\square_{\mathrm{SU}(6)} = \left(\square\square\square_{\mathrm{SU}(3)}; \square\square\square_{\mathrm{SU}(2)}\right) \oplus \left(\begin{array}{ll}\square&\square\\\square&\end{array}_{\mathrm{SU}(3)}; \square_{\mathrm{SU}(2)}\right) \,, \tag{C.6}$$

keeping in mind the equivalence $\begin{array}{ll}\square&\square\\\square&\end{array}_{\mathrm{SU}(2)} \equiv \square_{\mathrm{SU}(2)}$. Noting the dimensions,

$$\begin{aligned} \mathbf{56}_{\mathrm{SU}(6)} &= \left(\mathbf{10}_{\mathrm{SU}(3)}; \mathbf{4}_{\mathrm{SU}(2)}\right) \oplus \left(\mathbf{8}_{\mathrm{SU}(3)}; \mathbf{2}_{\mathrm{SU}(6)}\right) \\ &= (\mathbf{10}; 3/2) \oplus (\mathbf{8}; 1/2) \end{aligned} \tag{C.7}$$

and check that $56 = 10 \times 4 + 8 \times 2$. This decomposition means that the baryons in the ground state form a decuplet with spin $s = 3/2$ and an octet with spin $s = 1/2$. This is just the well-known octet of the nucleons, the hyperons, and the cascade particles, and the decuplet which contains the Δ quadruplet, the $\Sigma^\star$ triplet, the $\Xi^\star$ doublet, and the Ω.

Thus, the spin-flavour scheme of SU(6) can explain why there is only one octet for baryons in the ground state, although the decomposition (B.36) contains two octets. Furthermore, it accounts for the spins of the states in the flavour multiplets.

A similar decomposition is obtained when the classification according to spin-flavour SU(6) is applied to the pentaquark states (B.42). Unfortunately, there will be no restriction to the allowed flavour multiplets. However, we will obtain a definite series of flavour multiplets, along with their spin. Before constructing the states of $|qqqq\overline{q}\rangle$ for SU(6) in section C.3, we will discuss the decomposition of states made out of four quarks, $|qqqq\rangle$, in the next section.

C.2 States of four quarks in SU(6)

Using the technique of Young tables, we have already constructed the irreducible decomposition of the product of four fundamental representations in (B.39). However, we have to be careful, since (B.39) was concerned with the case of SU(3)

only. In general,

$$
\begin{aligned}
&|q\otimes q\otimes q\otimes q\rangle_{\mathrm{SU}(N)} \\
&\quad = \square\otimes\square\otimes\square\otimes\square = \Big(\square\!\square\oplus\begin{smallmatrix}\square\\\square\end{smallmatrix}\Big)\otimes\square\otimes\square \\
&\quad = \Big(\square\!\square\!\square\oplus\begin{smallmatrix}\square\square\\\square\end{smallmatrix}\oplus\begin{smallmatrix}\square\square\\\square\end{smallmatrix}\oplus\begin{smallmatrix}\square\\\square\\\square\end{smallmatrix}\Big)\otimes\square \\
&\quad = \square\!\square\!\square\!\square\oplus 3\cdot\begin{smallmatrix}\square\square\square\\\square\end{smallmatrix}\oplus 2\cdot\begin{smallmatrix}\square\square\\\square\square\end{smallmatrix}\oplus 3\cdot\begin{smallmatrix}\square\square\\\square\\\square\end{smallmatrix}\oplus\begin{smallmatrix}\square\\\square\\\square\\\square\end{smallmatrix},
\end{aligned}
\tag{C.8}
$$

and the completely antisymmetric term does not vanish for $N \geq 4$. However, for $N = 2$ (C.8) reduces to the well-known coupling of four spins,

$$
|q\otimes q\otimes q\otimes q\rangle_{\mathrm{SU}(2)} \;=\; \square\!\square\!\square\!\square\oplus 3\cdot\begin{smallmatrix}\square\square\square\square\\\square\square\end{smallmatrix}\oplus 2\cdot\begin{smallmatrix}\square\square\\\square\square\end{smallmatrix} \;=\; \mathbf{5}\oplus 3\cdot\mathbf{3}\oplus 2\cdot\mathbf{1}\;, \tag{C.9}
$$

corresponding to multiplets with spin $s = 2$, $s = 1$, and $S = 0$. In the case of $N = 3$, the decomposition yields the flavour structure (B.39),

$$
\begin{aligned}
|q\otimes q\otimes q\otimes q\rangle_{\mathrm{SU}(3)} \;&=\; \square\!\square\!\square\!\square\oplus 3\cdot\begin{smallmatrix}\square\square\square\square\\\square\end{smallmatrix}\oplus 2\cdot\begin{smallmatrix}\square\square\\\square\square\end{smallmatrix}\oplus 3\cdot\begin{smallmatrix}\square\square\\\square\\\square\end{smallmatrix} \\
&=\; \mathbf{15}\oplus 3\cdot\mathbf{15}\oplus 2\cdot\mathbf{6}\oplus 3\cdot\mathbf{3}\;.
\end{aligned}
\tag{C.10}
$$

the spin-flavour decomposition corresponding to $N = 6$ contains all five different Young tables, thus

$$
\begin{aligned}
&|q\otimes q\otimes q\otimes q\rangle_{\mathrm{SU}(6)} \\
&\quad = \square\!\square\!\square\!\square\oplus 3\cdot\begin{smallmatrix}\square\square\square\square\\\square\end{smallmatrix}\oplus 2\cdot\begin{smallmatrix}\square\square\\\square\square\end{smallmatrix}\oplus 3\cdot\begin{smallmatrix}\square\square\\\square\\\square\end{smallmatrix}\oplus\begin{smallmatrix}\square\\\square\\\square\\\square\end{smallmatrix} \\
&\quad = \mathbf{126}\oplus 3\cdot\mathbf{210}\oplus 2\cdot\mathbf{105}\oplus 3\cdot\mathbf{105}\oplus\mathbf{15}\;.
\end{aligned}
\tag{C.11}
$$

The decomposition (C.8) will be used in the next section, where it will be combined with an antiquark, given by the conjugate representation

$$
|\overline{q}\rangle_{\mathrm{SU}(N)} \;=\; D(\underbrace{0\ldots0}_{N-2}1)\;, \tag{C.12}
$$

which is depicted by $N-1$ boxes in a row.

C.3 Pentaquark classification in SU(6)

We now will apply the spin-flavour scheme to the analysis of pentaquark states and multiplicities. The necessary group theoretical considerations are not knew [235, 275, 276], and we will present here only a short account of the procedure and the underlying assumptions.

As in the case of the baryon, we assume that the four quarks and the antiquark in the pentaquark are all in a relative s-wave. Note that this implies that the parity

$$
P\left(q^4\bar{q}^1\right) \;=\; (1)^4(-1)^1(-1)^{(\ell=0)} \;=\; -1 \tag{C.13}
$$

of the pentaquark is negative, which is at odds with the Skyrme model of Diakonov [214], but also with the strongly correlated diquark-antiquark model of Jaffe and Wilczek [233], and with the diquark-triquark model with relative angular momentum $\ell = 1$ of Karliner and Lipkin [232]. The analysis along the lines of the spin-flavour SU(6) could be expanded to include orbital angular momentum, but this is much more involved.

Since the pentaquark is colour neutral, and the antiquark in the pentaquark corresponds to a conjugate representation of colour SU(3), the four quarks have to couple in such a way that they form a colour triplet. On the other hand, the Pauli principle requires the complete spin-flavour-colour state of the four quarks to be completely antisymmetric, keeping in mind that s-wave spatial wave functions are always symmetric. Hence, we have to apply the decomposition (C.8) to the case $N = 18$, corresponding to the combined spin-flavour-colour wave function. A completely antisymmetric state is represented by a Young tableau with four boxes in a column. Thus, the spin-flavour-colour state of the four quarks in the pentaquark is given by

$$|q \otimes q \otimes q \otimes q\rangle_{\text{s, f, c}} = \begin{array}{|c|}\hline\\\hline\\\hline\\\hline\end{array}_{\,\text{SU(18)}} = \mathbf{3060}\,, \tag{C.14}$$

where the indices c, f, and s stand for colour, flavour, and spin, respectively. The dimension is calculated using (B.22). This seems to be a terrible mess of states.

However, we can use again the break-down of representations of spin-flavour-colour SU(18) in a sum of products of representations of spin-flavour SU(6) and colour SU(3). There are two constraints which allow us to restrict the decomposition to a manageable complexity: First, we know that the colour part of the representation has to be a triplet. Second, we can use a general rule [277, §63] that restricts the terms occuring in the decomposition of a completely antisymmetric irreducible representation I_a into a sum of combinations of irreducible representations J_i and K_j, $I_\text{a} = \bigoplus_\alpha J_\alpha \otimes K_\alpha$: Such a decomposition has contributions only from combinations of irreducible representations J_α and K_α whose Young tables are dual to each other, which means that the tables of these factors are symmetric with respect to a diagonal axis through the upper left box of the tables.

Applying these constraints to the four quark spin-flavour-colour state (C.14), we find

$$\begin{aligned}\begin{array}{|c|}\hline\\\hline\\\hline\\\hline\end{array}_{\,\text{c,f,s}} &= \left(\begin{array}{|c|c|}\hline\\\hline\\\cline{1-1}\end{array}_{\,\text{c}}\,;\,\begin{array}{|c|c|c|}\hline\\\hline\end{array}_{\,\text{f,s}}\right) \oplus \left(\begin{array}{|c|c|}\hline\\\hline\\\hline\end{array}_{\,\text{c}}\,;\,\begin{array}{|c|c|}\hline\\\hline\\\hline\end{array}_{\,\text{f,s}}\right) \oplus \dots \\ &= \left(\mathbf{3}_\text{c}\,;\,\mathbf{210}_\text{f,s}\right) \oplus \dots\,.\end{aligned} \tag{C.15}$$

Since for the construction of the pentaquark states, the four quarks have to be in the colour triplet representation $\mathbf{3}_\text{c}$, only the first term of the sum will contribute. All other terms contain colour representations which can not be combined with the conjugate representation of the antiquark to form a colour singlet. Thus, they can be ignored, and we can obtain the complete multiplet structure of the pentaquark states by combining the representation $(\mathbf{3}_\text{c}; \mathbf{210}_\text{f,s})$ for the four quarks with the conjugate representation $(\overline{\mathbf{3}}_\text{c}; \overline{\mathbf{6}}_\text{f,s})$ of the antiquark. Focussing on the spin-flavour part of this product, it can be decomposed using Young tables for SU(6). This

decomposition reads

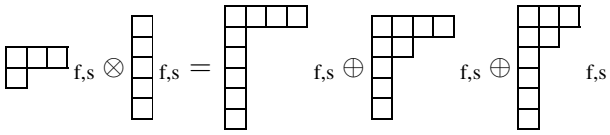

$$\mathbf{210}_{\text{f,s}} \otimes \overline{\mathbf{6}}_{\text{f,s}} = \mathbf{56}_{\text{f,s}} \oplus \mathbf{1134}_{\text{f,s}} \oplus \mathbf{70}_{\text{f,s}} \,. \tag{C.16}$$

There are 1260 states altogether. Unfortunately, not the same reduction of the plethora of states is attained as in case of the baryon. However, the decompositions of irreducible multiplets of SU(6) into combinations of SU(3) and SU(2) are known and tabulated [234]. Thus, the following classification of multiplets is obtained:

$$\begin{aligned}
&|q \otimes q \otimes q \otimes q \otimes \bar{q}\rangle_{\text{f,s}} \;= \\
&\quad 2 \cdot (\mathbf{1}; 1/2) \oplus 5 \cdot (\mathbf{8}; 1/2) \oplus 3 \cdot (\mathbf{10}; 1/2) \\
&\quad \oplus 1 \cdot \left(\overline{\mathbf{10}}; 1/2\right) \oplus 2 \cdot (\mathbf{27}; 1/2) \oplus 1 \cdot (\mathbf{35}; 1/2) \\
&\quad \oplus 1 \cdot (\mathbf{1}; 3/2) \oplus 4 \cdot (\mathbf{8}; 3/2) \oplus 3 \cdot (\mathbf{10}; 3/2) \\
&\quad \oplus 1 \cdot \left(\overline{\mathbf{10}}; 3/2\right) \oplus 2 \cdot (\mathbf{27}; 3/2) \oplus 1 \cdot (\mathbf{35}; 3/2) \\
&\quad \oplus 1 \cdot (\mathbf{8}; 5/2) \oplus 1 \cdot (\mathbf{10}; 5/2) \oplus 1 \cdot (\mathbf{27}; 5/2) \;\;.
\end{aligned} \tag{C.17}$$

We see that the SU(6) scheme yields exactly one antidecuplet with spin $s = 1/2$ and one antidecuplet with spin $s = 3/2$.

The multiplicities of pentaquark states, split according to hypercharge Y and isospin projection T_3 as derived from the spin-flavour SU(6) scheme, are shown in figure C.1. This decomposition should be compared to the simple flavour SU(3) multiplicities shown in figure 8.2. Note that the relative multiplicities for different strangeness S differ from the results derived from the SU(3) coupling scheme. The list on the right hand side of the figure shows which SU(3) multiplets will contribute to a given strangeness S. Note that the SU(3) multiplets can have different

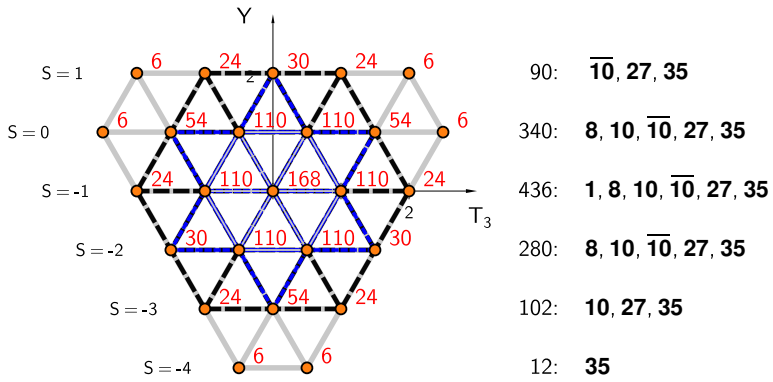

Figure C.1
Multiplicities of pentaquark states in the simple quark model as derived from the spin-flavour SU(6) scheme. The list on the right indicates the multiplicity of states for a given strangeness, together with the SU(3) multiplets contributing to this strangeness.

spins of $s = 1/2$, $s = 3/2$, or $s = 5/2$, corresponding to the allowed combinations from the decomposition (C.17), and that the spin multiplicites contribute to the multiplicites of the SU(3) states. For example, states of the multiplet **35** are populated by four states of the SU(6) multiplet $(\mathbf{35}; 3/2)$ and by two states of $(\mathbf{35}; 1/2)$, which results in the overall multiplicity of 6.

It should be noted that in recent work on pentaquarks and exotic hadrons, the SU(6) coupling scheme is often used to discuss not spin-flavour coupling, but colour-spin coupling. On the one hand, the mass spectrum of pentaquarks is thought to be determined to a large extent by colour-magnetic terms and colour-spin hyperfine interactions [230, 278, 279]. On the other hand, calculations using the MIT bag model hint at possible low mass baryonium states [246] which are classified best by the SU(6) colour-spin scheme. This means in both cases that the coupling of flavour and spin degrees of freedom should be considered independently, as is done in the qMD model, where isospin and spin are coupled independent of each other.

Bibliography

Chapter 1: From atoms to the QGP

[1] J. E. STACHEL: *Einstein's miraculous year. Five papers that changed the face of physics.* (Princeton University Press, Princeton, NJ, 1999), dt. Ausgabe: *Einsteins Annus mirabilis*; 224 Seiten; Rowohlt, Hamburg, 2001.

[2] H. KRAGH: *Quantum Generations: A History of Physics in the Twentieth Century* (Princeton University Press, Princeton, NJ, 1999).

[3] A. PAIS: *Inward Bound: Of Matter and Forces in the Physical World* (Oxford University Press, Oxford, UK, 1988).

[4] E. HODDESON, L., E. BROWN, L., E. RIORDAN, M., E. DRESDEN, M.: *The Rise of the standard model: Particle physics in the 1960s and 1970s* (Cambridge University Press, Cambridge, UK, 1997), proceedings of the 3rd International Symposium on the History of Particle Physics: The Rise of the Standard Model; Stanford, USA, June 24-27, 1992.

[5] A. PICKERING: *Constructing Quarks: A Sociological History of Particle Physics.* (Princeton University Press, Princeton, NJ, 1984).

[6] A. WATSON: *The Quantum Quark* (Cambridge University Press, Cambridge, UK, 2004).

[7] S. HEMBACHER, F. J. GIESSIBL, J. MANNHART, C. F. QUATE: "Revealing the hidden atom in graphite by low-temperature atomic force microscopy". *PNAS* **100** (22), (2003) 12539–12542.

[8] J. ITATANI, J. LEVESQUE, D. ZEIDLER, H. NIIKURA, H. PEPIN, J. C. KIEFFER, P. B. CORKUM, D. M. VILLENEUVE: "Tomographic imaging of molecular orbitals". *Nature* **432**, (2004) 867–871.

[9] W. GREINER, S. SCHRAMM, E. STEIN: *Quantum chromodynamics* (Springer-Verlag, Berlin; Heidelberg; London; etc., 2002).

[10] R. K. ELLIS, W. J. STIRLING, B. R. WEBBER: *QCD and collider physics* (Cambridge University Press, Cambridge, UK, 1996).

[11] N. ISGUR, J. PATON: "A flux tube model for hadrons in QCD". *Phys. Rev.* **D31**, (1985) 2910.

[12] K. SAILER, T. SCHÖNFELD, Z. SCHRAM, A. SCHÄFER, W. GREINER: "Strings and ropes in heavy ion collisions: Towards a semiclassical unified string flux tube model". *J. Phys.* **G17**, (1991) 1005–1057.

[13] J. MALDACENA: "Into the fifth dimension". *Nature* **423**, (2003) 695–696.

[14] K. D. BORN, E. LAERMANN, R. SOMMER, P. M. ZERWAS, T. F. WALSH: "The Interquark potential: A QCD lattice analysis". *Phys. Lett.* **B329**, (1994) 325–331.

[15] E. EICHTEN, K. GOTTFRIED, T. KINOSHITA, J. KOGUT, K. D. LANE, T.-M. YAN: "The spectrum of charmonium". *Phys. Rev. Lett.* **34**, (1975) 369–372.

[16] E. EICHTEN, K. GOTTFRIED, T. KINOSHITA, K. D. LANE, T.-M. YAN: "Charmonium: comparison with experiment". *Phys. Rev.* **D21**, (1980) 203.

[17] S. GODFREY, N. ISGUR: "Mesons in a relativized quark model with chromodynamics". *Phys. Rev.* **D32**, (1985) 189–231.

[18] S. CAPSTICK, S. GODFREY, N. ISGUR, J. PATON: "Taking the 'naive' and 'nonrelativistic' out of the quark potential model". *Phys. Lett.* **B175**, (1986) 457.

[19] R. L. JAFFE: "Multi-quark hadrons. 1. the phenomenology of (2 quark 2 anti-quark) mesons". *Phys. Rev.* **D15**, (1977) 267.

[20] R. L. JAFFE: "Multi-quark hadrons. 2. methods". *Phys. Rev.* **D15**, (1977) 281.

[21] D. STROTTMAN: "Multi-quark baryons and the MIT bag model". *Phys. Rev.* **D20**, (1979) 748–767.

[22] A. J. G. HEY, R. L. KELLY: "Baryon spectroscopy". *Phys. Rept.* **96**, (1983) 71.

[23] T. NAKANO, ET AL. (LEPS): "Evidence for a narrow $S = +1$ baryon resonance in photoproduction from the neutron". *Phys. Rev. Lett.* **91**, (2003) 012002, hep-ex/0301020.

[24] J. C. COLLINS, M. J. PERRY: "Superdense matter: neutrons or asymptotically free quarks?" *Phys. Rev. Lett.* **34**, (1975) 1353.

[25] P. PETRECZKY: "QCD thermodynamics on lattice". *Nucl. Phys. Proc. Suppl.* **140**, (2005) 78–91, hep-lat/0409139.

[26] Z. FODOR, S. D. KATZ: "Critical point of QCD at finite T and μ: lattice results for physical quark masses". *JHEP* **04**, (2004) 050, hep-lat/0402006.

[27] D. H. RISCHKE: "The quark-gluon plasma in equilibrium". *Prog. Part. Nucl. Phys.* **52**, (2004) 197–296, nucl-th/0305030.

[28] D. H. RISCHKE, M. I. GORENSTEIN, A. SCHÄFER, H. STÖCKER, W. GREINER: "Non-perturbative effects in the SU(3) gluon plasma". *Phys. Lett.* **B278**, (1992) 19–23.

[29] B. B. BACK, ET AL.: "The PHOBOS perspective on discoveries at RHIC". *Nucl. Phys.* **A757**, (2005) 28–101, nucl-ex/0410022.

[30] E. V. SHURYAK: "What RHIC experiments and theory tell us about properties of quark-gluon plasma?" *Nucl. Phys.* **A750**, (2005) 64–83, hep-ph/0405066.

[31] S. SCHERER, H. STÖCKER: "Multifragmentation, clustering, and coalescence in nuclear collisions". *Proceedings of the International Symposium "Atomic Cluster Collisions", St. Petersburg, Russia, July 18-21, 2003* 169–180, ed. by J.-P. Connerade and A.V. Solov'yov, nucl-th/0502069.

[32] D. J. SCHWARZ: "The first second of the universe". *Annalen Phys.* **12**, (2003) 220–270, astro-ph/0303574.

[33] N. K. GLENDENNING: *Compact stars: Nuclear physics, particle physics, and general relativity* (Springer-Verlag, Berlin; Heidelberg; London; etc., 2000).

[34] H. STÖCKER, W. GREINER: "High-energy heavy ion collisions: Probing the equation of state of highly excited hadronic matter". *Phys. Rept.* **137**, (1986) 277–392.

[35] H. STÖCKER: "Collective flow signals the quark-gluon plasma". *Nucl. Phys.* **A750**, (2005) 121–147, nucl-th/0406018.

[36] C. SPIELES, H. STOECKER, C. GREINER: "Phase transition of a finite quark-gluon plasma". *Phys. Rev.* **C57**, (1998) 908–915, hep-ph/9708280.

[37] J. CARDY: *Scaling and renormalization in statistical physics* (Cambridge University Press, Cambridge, UK, 1996).

[38] J. W. HARRIS, B. MÜLLER: "The search for the quark-gluon plasma". *Ann. Rev. Nucl. Part. Sci.* **46**, (1996) 71–107, hep-ph/9602235.

[39] S. A. BASS, M. GYULASSY, H. STÖCKER, W. GREINER: "Signatures of quark-gluon-plasma formation in high energy heavy-ion collisions: A critical review". *J. Phys. G* **G25**, (1999) R1, hep-ph/9810281.

[40] S. SCHERER, ET AL.: "Critical review of quark gluon plasma signatures". *Prog. Part. Nucl. Phys.* **42**, (1999) 279–293.

[41] H. STÖCKER, J. BERGER, U. EICHMANN, S. SALUR, S. SCHERER, D. ZSCHIESCHE: "Critical review of quark gluon plasma signatures". *AIP Conf. Proc.* **631**, (2003) 553–579.

[42] S.-Y. JEON, V. KOCH: "Event-by-event fluctuations". In "Quark-gluon plasma 3", edited by R. C. HWA (World Scientific Publishing Co., 2004), hep-ph/0304012.

[43] S. A. BASS, P. DANIELEWICZ, S. PRATT: "Clocking hadronization in relativistic heavy ion collisions with balance functions". *Phys. Rev. Lett.* **85**, (2000) 2689, nucl-th/0005044.

[44] J. RAFELSKI, B. MÜLLER: "Strangeness production in the quark-gluon plasma". *Phys. Rev. Lett.* **48**, (1982) 1066.

[45] C. GREINER, P. KOCH, H. STÖCKER: "Separation of strangeness from antistrangeness in the phase transition from quark to hadron matter: possible formation of strange quark matter in heavy ion collisions". *Phys. Rev. Lett.* **58**, (1987) 1825–1828.

[46] C. GREINER, D.-H. RISCHKE, H. STÖCKER, P. KOCH: "The creation of strange quark matter droplets as a unique signature for quark - gluon plasma formation in relativistic heavy ion collisions". *Phys. Rev.* **D38**, (1988) 2797–2807.

[47] M. GAZDZICKI, M. I. GORENSTEIN: "On the early stage of nucleus nucleus collisions". *Acta Phys. Polon.* **B30**, (1999) 2705, hep-ph/9803462.

[48] T. MATSUI, H. SATZ: "J/Ψ suppression by quark-gluon plasma formation". *Phys. Lett.* **B178**, (1986) 416.

[49] M. ASAKAWA, T. HATSUDA: "J/Ψ and eta_c in the deconfined plasma from lattice QCD". *Phys. Rev. Lett.* **92**, (2004) 012001, hep-lat/0308034.

[50] A. MOCSY, P. PETRECZKY: "Heavy quarkonia survival in potential model". *Eur. Phys. J.* **C43**, (2005) 77–80, hep-ph/0411262.

[51] S. GAO, C. GALE, C. ERNST, H. STÖCKER, W. GREINER: "ρ meson broadening and dilepton production in heavy ion collisions". *Nucl. Phys.* **A661**, (1999) 518–521, nucl-th/9906087.

[52] L. M. SATAROV, H. STÖCKER, I. N. MISHUSTIN: "Mach shocks induced by partonic jets in expanding quark-gluon plasma". *Phys. Lett.* **B627**, (2005) 64–70, hep-ph/0505245.

[53] R. J. FRIES, B. MULLER, C. NONAKA, S. A. BASS: "Hadronization in heavy ion collisions: Recombination and fragmentation of partons". *Phys. Rev. Lett.* **90**, (2003) 202303, nucl-th/0301087.

[54] R. J. FRIES, B. MULLER, C. NONAKA, S. A. BASS: "Hadron production in heavy ion collisions: Fragmentation and recombination from a dense parton phase". *Phys. Rev.* **C68**, (2003) 044902, nucl-th/0306027.

[55] V. GRECO, C. M. KO, P. LEVAI: "Parton coalescence and antiproton/pion anomaly at RHIC". *Phys. Rev. Lett.* **90**, (2003) 202302, nucl-th/0301093.

[56] V. GRECO, C. M. KO, P. LEVAI: "Parton coalescence at RHIC". *Phys. Rev.* **C68**, (2003) 034904, nucl-th/0305024.

[57] R. C. HWA, C. B. YANG: "Scaling behavior at high $p(T)$ and the p/π ratio". *Phys. Rev.* **C67**, (2003) 034902, nucl-th/0211010.

[58] R. C. HWA, C. B. YANG: "Scaling distributions of quarks, mesons and proton for all $p(T)$, energy and centrality". *Phys. Rev.* **C67**, (2003) 064902, nucl-th/0302006.

[59] S. A. VOLOSHIN: "Anisotropic flow". *Nucl. Phys.* **A715**, (2003) 379–388, nucl-ex/0210014.

[60] D. MOLNAR, S. A. VOLOSHIN: "Elliptic flow at large transverse momenta from quark coalescence". *Phys. Rev. Lett.* **91**, (2003) 092301, nucl-th/0302014.

Chapter 2: QCD and some of its models

[61] J. C. MAXWELL: "Experiments on colour as perceived by the eye". *Transactions of the Royal Society Edinburgh* **21**, (1855) 275–298.

[62] M. GELL-MANN: "Symmetries of baryons and mesons". *Phys. Rev.* **125**, (1962) 1067–1084.

[63] S. BETHKE: "alpha(s) at Zinnowitz 2004". *Nucl. Phys. Proc. Suppl.* **135**, (2004) 345–352, hep-ex/0407021.

[64] T. SCHÄFER, E. V. SHURYAK: "Instantons in QCD". *Rev. Mod. Phys.* **70**, (1998) 323–426, hep-ph/9610451.

[65] E. V. SHURYAK, T. SCHÄFER: "The QCD vacuum as an instanton liquid". *Ann. Rev. Nucl. Part. Sci.* **47**, (1997) 359–394.

[66] V. L. BEREZINSKY: "Destruction of long range order in one-dimensional and two-dimensional systems having a continuous symmetry group. 1. Classical systems". *Sov. Phys. JETP* **32**, (1971) 493–500.

[67] J. M. KOSTERLITZ: "The critical properties of the two-dimensional xy model". *J. Phys. C* **7**, (1974) 1046–1060.

[68] J. M. KOSTERLITZ, D. J. THOULESS: "Ordering, metastability and phase transitions in two-dimensional systems". *J. Phys.* **C6**, (1973) 1181–1203.

[69] G. 'T HOOFT: "Magnetic monopoles in unified gauge theories". *Nucl. Phys.* **B79**, (1974) 276–284.

[70] A. M. POLYAKOV: "Particle spectrum in quantum field theory". *JETP Lett.* **20**, (1974) 194–195.

[71] S. MANDELSTAM: "Vortices and quark confinement in non-Abelian gauge theories". *Phys. Rept.* **23**, (1976) 245–249.

[72] G. 'T HOOFT: "Topology of the gauge condition and new confinement phases in non-Abelian gauge theories". *Nucl. Phys.* **B190**, (1981) 455.

[73] Z. F. EZAWA, A. IWAZAKI: "Abelian dominance and quark confinement in Yang-Mills theories". *Phys. Rev.* **D25**, (1982) 2681.

[74] G. RIPKA: *Dual superconductor models of color confinement* (Springer-Verlag, Berlin; Heidelberg; London; etc., 2004), hep-ph/0310102.

[75] C. ITZYKSON, J. M. DROUFFE: *Statistical field theory. Vol. 1: From Brownian motion to renormalization and lattice gauge theory* (Cambridge University Press, Cambridge, UK, 1989).

[76] H. J. ROTHE: *Lattice gauge theories: An Introduction* (World Scientific Publishing Co., Singapore; Philadelphia; River Edge, NJ, 2005).

[77] K. AMEMIYA, H. SUGANUMA: "Effective mass generation of off-diagonal gluons as the origin of infrared Abelian dominance in the maximally Abelian gauge in QCD". *Phys. Rev.* **D60**, (1999) 114509, hep-lat/9811035.

[78] M. I. POLIKARPOV: "Recent results on the Abelian projection of lattice gluodynamics". *Nucl. Phys. Proc. Suppl.* **53**, (1997) 134–140, hep-lat/9609020.

[79] H. SUGANUMA, K. AMEMIYA, A. TANAKA, H. ICHIE: "Quark confinement physics from quantum chromodynamics". *Nucl. Phys.* **A670**, (2000) 40–47, hep-lat/0407017.

[80] Y. NAMBU, G. JONA-LASINIO: "Dynamical model of elementary particles based on an analogy with superconductivity. I". *Phys. Rev.* **122**, (1961) 345–358.

[81] Y. NAMBU, G. JONA-LASINIO: "Dynamical model of elementary particles based on an analogy with superconductivity. II". *Phys. Rev.* **124**, (1961) 246–254.

[82] S. P. KLEVANSKY: "The Nambu-Jona-Lasinio model of quantum chromodynamics". *Rev. Mod. Phys.* **64**, (1992) 649–708.

[83] R. FRIEDBERG, T. D. LEE: "Fermion field nontopological solitons. 1". *Phys. Rev.* **D15**, (1977) 1694.

[84] R. FRIEDBERG, T. D. LEE: "Fermion field nontopological solitons. 2. models for hadrons". *Phys. Rev.* **D16**, (1977) 1096.

[85] A. ABADA, J. AICHELIN: "Chiral phase transition in an expanding quark gluon plasma". *Phys. Rev. Lett.* **74**, (1995) 3130–3133, `hep-ph/9404303`.

[86] F. GASTINEAU, R. NEBAUER, J. AICHELIN: "Thermodynamics of the three-flavor Nambu-Jona-Lasinio model: Chiral symmetry breaking and color superconductivity". *Phys. Rev.* **C65**, (2002) 045204, `hep-ph/0101289`.

[87] C. T. TRAXLER, U. MOSEL, T. S. BIRO: "Hadronization of a quark-gluon plasma in the chromodielectric model". *Phys. Rev.* **C59**, (1999) 1620–1636, `hep-ph/9808298`.

[88] C. RATTI, M. A.. THALER, W. WEISE: "Phases of QCD: Lattice thermodynamics and a field theoretical model". *(arxive only)* `hep-ph/0506234`.

[89] P. REHBERG, S. P. KLEVANSKY, J. HUFNER: "Hadronization in the SU(3) Nambu-Jona-Lasinio model". *Phys. Rev.* **C53**, (1996) 410–429, `hep-ph/9506436`.

[90] G. MARTENS, C. GREINER, S. LEUPOLD, U. MOSEL: "Chromofields of strings and baryons". *Eur. Phys. J.* **A18**, (2003) 223–226, `hep-ph/0303017`.

[91] G. MARTENS, C. GREINER, S. LEUPOLD, U. MOSEL: "Two- and three-body color flux tubes in the chromo dielectric model". *Phys. Rev.* **D70**, (2004) 116010, `hep-ph/0407215`.

[92] W. LUCHA, F. F. SCHÖBERL: *Die starke Wechselwirkung: Eine Einführung in nichtrelativistische Potentialmodelle* (BI Wissenschaftsverlag, Mannheim, Wien, Zürich, 1989).

[93] S. CAPSTICK, N. ISGUR: "Baryons in a relativized quark model with chromodynamics". *Phys. Rev.* **D34**, (1986) 2809.

[94] M. CRAWFORD, D. N. SCHRAMM: "Spontaneous generation of density perturbations in the early universe". *Nature* **298**, (1982) 538–540.

Chapter 3: Model building to study heavy ion collisions

[95] S. A. BASS, M. BELKACEM, M. BLEICHER, M. BRANDSTETTER, L. BRAVINA, C. ERNST, L. GERLAND, M. HOFMANN, S. HOFMANN, J. KONOPKA, G. MAO, L. NEISE, S. SOFF, C. SPIELES, H. WEBER, L. A. WINCKELMANN, H. STOCKER, W. GREINER, C. HARTNACK, J. AICHELIN, N. AMELIN: "Microscopic models for ultrarelativistic heavy ion collisions". *Prog. Part. Nucl. Phys.* **41**, (1998) 225–370, `nucl-th/9803035`.

[96] M. BLEICHER, E. ZABRODIN, C. SPIELES, C. BASS, S.A.AND ERNST, S. SOFF, L. BRAVINA, M. BELKACEM, H. WEBER, H. STÖCKER, W. GREINER: "Relativistic hadron hadron collisions in the ultra-relativistic quantum molecular dynamics model". *J. Phys.* **G25**, (1999) 1859–1896, `hep-ph/9909407`.

[97] W. EHEHALT, W. CASSING: "Relativistic transport approach for nucleus nucleus collisions from SIS to SPS energies". *Nucl. Phys.* **A602**, (1996) 449–486.

[98] B. ANDERSSON, G. GUSTAFSON, B. SODERBERG: "A general model for jet fragmentation". *Z. Phys.* **C20**, (1983) 317.

[99] B. ANDERSSON, G. GUSTAFSON, G. INGELMAN, T. SJOSTRAND: "Parton fragmentation and string dynamics". *Phys. Rept.* **97**, (1983) 31.

[100] S. SOFF, ET AL.: "Strangeness enhancement in heavy ion collisions: Evidence for quark-gluon matter?" *Phys. Lett.* **B471**, (1999) 89–96, `nucl-th/9907026`.

[101] K. GEIGER: "Space-time description of ultrarelativistic nuclear collisions in the QCD parton picture". *Phys. Rept.* **258**, (1995) 237–376.

[102] D. MOLNAR, M. GYULASSY: "New solutions to covariant nonequilibrium dynamics". *Phys. Rev.* **C62**, (2000) 054907, nucl-th/0005051.

[103] Z. XU, C. GREINER: "Thermalization of gluons in ultrarelativistic heavy ion collisions by including three-body interactions in a parton cascade". *Phys. Rev.* **C71**, (2005) 064901, hep-ph/0406278.

[104] V. BÖRCHERS, J. MEYER, S. GIESEKE, G. MARTENS, C. C. NOACK: "A Poincaré covariant parton cascade model for ultrarelativistic heavy-ion reactions". *Phys. Rev.* **C62**, (2000) 064903, hep-ph/0006038.

[105] D. H. RISCHKE: "Hydrodynamics and collective behaviour in relativistic nuclear collisions". *Nucl. Phys.* **A610**, (1996) 88c–101c, nucl-th/9608024.

[106] J. BRACHMANN, A. DUMITRU, J. A. MARUHN, H. STOCKER, W. GREINER, D. H. RISCHKE: "Non-equilibrium fluid-dynamics in the early stage of ultrarelativistic heavy-ion collisions". *Nucl. Phys.* **A619**, (1997) 391, nucl-th/9703032.

[107] J. BRACHMANN, S. SOFF, A. DUMITRU, H. STOCKER, J. A. MARUHN, W. GREINER, D. H. RISCHKE: "Antiflow of nucleons at the softest point of the EoS". *Phys. Rev.* **C61**, (2000) 024909, nucl-th/9908010.

[108] K. PAECH, H. SÖCKER, A. DUMITRU: "Hydrodynamics near a chiral critical point". *Phys. Rev.* **C68**, (2003) 044907, nucl-th/0302013.

[109] K. PAECH, A. DUMITRU: "Density inhomogeneities in heavy ion collisions around the critical point". *Phys. Lett.* **B623**, (2005) 200–207, nucl-th/0504003.

[110] A. MURONGA: "Causal Theories of Dissipative Relativistic Fluid Dynamics for Nuclear Collisions". *Phys. Rev.* **C69**, (2004) 034903, nucl-th/0309055.

[111] A. MURONGA: "Viscous hydrodynamics". *J. Phys.* **G31**, (2005) S1035–S1039.

[112] S. A. BASS, M. HOFMANN, M. BLEICHER, L. BRAVINA, E. ZABRODIN, H. STOCKER, W. GREINER: "Analysis of reaction dynamics at ultrarelativistic energies in a combined parton hadron transport approach". *Phys. Rev.* **C60**, (1999) 021901, nucl-th/9902055.

[113] S. A. BASS, B. MULLER: "K-factors in parton cascades at RHIC and SPS". *Phys. Lett.* **B471**, (1999) 108, nucl-th/9908014.

[114] R. J. FRIES, B. MULLER, A. SCHAFER, E. STEIN: "Angular dependence of the nuclear enhancement of Drell-Yan pairs". *Phys. Rev. Lett.* **83**, (1999) 4261, hep-ph/9907567.

[115] T. S. BIRO, P. LEVAI, J. ZIMANYI: "ALCOR: A Dynamic model for hadronization". *Phys. Lett.* **B347**, (1995) 6–12.

[116] T. S. BIRO, P. LEVAI, J. ZIMANYI: "Hadronization with a confining equation of state". *Phys. Rev.* **C59**, (1999) 1574–1584.

[117] J. ZIMANYI, P. LEVAI, T. S. BIRO: "Faces of quark matter". *Heavy Ion Phys.* **17**, (2003) 205–217, hep-ph/0205192.

[118] J. ZIMANYI, P. LEVAI, T. S. BIRO: "Properties of quark matter produced in heavy ion collision". *J. Phys.* **G31**, (2005) 711–718, nucl-th/0502060.

[119] P. F. KOLB, L.-W. CHEN, V. GRECO, C. M. KO: "Momentum anisotropies in the quark coalescence model". *Phys. Rev.* **C69**, (2004) 051901, nucl-th/0402049.

[120] T. PEITZMANN: "Mass generation in coalescence: Effects on hadron spectra". *Acta Phys. Hung.* **A22/1**, (2005) to be publ., nucl-th/0511022.

[121] A. BONASERA: "Color dynamics on phase space". *Phys. Rev.* **C62**, (2000) 052202, nucl-th/0003020.

[122] A. BONASERA: "Color dynamics in phase space: The Balescu-Lenard-Vlasov approach". *Nucl. Phys.* **A681**, (2001) 64–71, hep-ph/0009056.

[123] T. MARUYAMA, T. HATSUDA: "Color molecular-dynamics for high density matter". *Phys. Rev.* **C61**, (2000) 062201, nucl-th/9908021.

[124] T. MARUYAMA, T. HATSUDA, S. CHIBA: "Color molecular dynamics simulation of nuclei and dense matter". *Nucl. Phys.* **A681**, (2001) 72–75.

[125] Y. AKIMURA, T. MARUYAMA, N. YOSHINAGA, S. CHIBA: "Stability and structure of quark matter in a molecular dynamics framework". *Nucl. Phys.* **A749**, (2005) 329–332, nucl-th/0411008.

[126] Y. AKIMURA, T. MARUYAMA, N. YOSHINAGA, S. CHIBA: "Molecular dynamics simulation for baryon - quark phase transition at finite temperature and density". *Eur. Phys. J.* **A25**, (2005) 405–411, nucl-th/0505029.

[127] S. SCHERER, ET AL.: "Microscopic coloured quark-dynamics in the soft non-perturbative regime: Description of hadron formation in relativistic S + Au collisions at CERN". *New J. Phys.* **3**, (2001) 8, nucl-th/0106036.

[128] S. A. BASS, A. DUMITRU, M. BLEICHER, L. BRAVINA, E. ZABRODIN, H. STOCKER, W. GREINER: "Hadronic freeze-out following a first order hadronization phase transition in ultrarelativistic heavy-ion collisions". *Phys. Rev.* **C60**, (1999) 021902, nucl-th/9902062.

[129] M. HOFMANN, S. SCHERER, M. BLEICHER, L. NEISE, H. STOCKER, W. GREINER: "Statistical mechanics of semi-classical colored objects". *Phys. Lett.* **B478**, (2000) 161–171, nucl-th/9908030.

[130] M. HOFMANN, S. SCHERER, M. BLEICHER, L. NEISE, H. STOCKER, W. GREINER: "Nonequilibrium dynamics of a hadronizing quark-gluon plasma". *(arxive only)* nucl-th/9908031.

[131] K. AMEMIYA, H. SUGANUMA: "Effective mass generation of off-diagonal gluons and Abelian dominance in the maximally Abelian gauge in QCD". *Nucl. Phys. Proc. Suppl.* **83**, (2000) 419–421, hep-lat/9909096.

[132] P. REHBERG, L. BOT, J. AICHELIN: "Expansion and hadronization of a chirally symmetric quark-meson plasma". *Nucl. Phys.* **A653**, (1999) 415–435, hep-ph/9809565.

[133] P. REHBERG, L. BOT, J. AICHELIN: "Expansion and hadronization of quark-meson plasma". *Prog. Part. Nucl. Phys.* **42**, (1999) 323–331.

Chapter 4: The quark molecular dynamics model qMD

[134] M. HOFMANN: *Mikroskopische Beschreibung des QCD-Phasenübergangs* (Ibidem-Verlag, Stuttgart, 1999).

[135] C. KITTEL: *Introduction to solid state physics* (John Wiley and Sons, New York; London; Sydney, 1996).

[136] C.-Y. WONG: *Introduction to High-Energy Heavy-Ion Collisions* (World Scientific Publishing Co., Singapore; Philadelphia; River Edge, NJ, 1994).

[137] S. EIDELMAN, ET AL. (Particle Data Group): "Review of particle physics". *Phys. Lett.* **B592**, (2004) 1.

[138] M. GYULASSY, L. MCLERRAN: "New forms of QCD matter discovered at RHIC". *Nucl. Phys.* **A750**, (2005) 30–63, nucl-th/0405013.

[139] H.-T. ELZE, U. W. HEINZ: "Quark-gluon transport theory". *Phys. Rept.* **183**, (1989) 81–135.

[140] W. THOMÉ, ET AL. (Aachen-CERN-Heidelberg-Munich): "Charged particle multiplicity distributions in pp collisions at ISR energies". *Nucl. Phys.* **B129**, (1977) 365.

[141] Y. KANADA-EN'YO, O. MORIMATSU, T. NISHIKAWA: "Prediction of narrow $J^\pi = 1/2^+$, $J^\pi = 3/2^+$, and $3/2^-$ states of Θ^+ in a quark model with antisymmetrized molecular dynamics". *Phys. Rev.* **C71**, (2005) 045202, hep-ph/0404144.

[142] P. VALTA, ET AL.: "Treatment of fermions in microscopic models". *Nucl. Phys.* **A538**, (1992) 417c–428c.

[143] G. PEILERT, J. RANDRUP, H. STÖCKER, W. GREINER: "Clustering in nuclear matter at subsaturation densities". *Phys. Lett.* **B260**, (1991) 271–277.

Chapter 5: Thermal properties of the qMD model

[144] K. HUANG: *Statistical mechanics* (John Wiley and Sons, New York; London; Sydney, 1987).

[145] F. JÜTTNER: "Das Maxwellsche Gesetz der Geschwindigkeitsverteilung in der Relativtheorie". *Ann. Physik (4. Folge)* **34**, (1911) 856–882.

[146] M. MÉZARD, G. PARISI, M. VIRASORO: *Spin glass theory and beyond* (World Scientific Publishing Co., Singapore; Philadelphia; River Edge, NJ, 1987).

[147] S. ELITZUR, R. B. PEARSON, J. SHIGEMITSU: "The phase structure of discrete abelian spin and gauge systems". *Phys. Rev.* **D19**, (1979) 3698.

[148] K.-I. KONDO: "Existence of confinement phase in quantum electrodynamics". *Phys. Rev.* **D58**, (1998) 085013, `hep-th/9803133`.

[149] J. V. JOSE, L. P. KADANOFF, S. KIRKPATRICK, D. R. NELSON: "Renormalization, vortices, and symmetry breaking perturbations on the two-dimensional planar model". *Phys. Rev.* **B16**, (1977) 1217–1241.

[150] N. METROPOLIS, A. W. ROSENBLUTH, M. N. ROSENBLUTH, A. H. TELLER, E. TELLER: "Equation of state calculations by fast computing machines". *J. Chem. Phys.* **21**, (1953) 1087–1092.

[151] D. P. LANDAU, K. BINDER: *A guide to Monte Carlo simulations in statistical physics* (Cambridge University Press, Cambridge, UK, 2000).

[152] K. BINDER, D. W. HEERMANN: *Monte Carlo simulation in statistical physics* (Springer-Verlag, Berlin; Heidelberg; London; etc., 1997).

[153] F. KARSCH, E. LAERMANN, A. PEIKERT: "The pressure in 2, 2+1 and 3 flavour QCD". *Phys. Lett.* **B478**, (2000) 447–455, `hep-lat/0002003`.

[154] M. ASAKAWA, T. HATSUDA: "What thermodynamics tells about QCD plasma near phase transition". *Phys. Rev.* **D55**, (1997) 4488–4491, `hep-ph/9508360`.

[155] P. P. EWALD: "Die Berechnung des optischen und elektrostatischen Gitterpotentials". *Ann. Physik (4. Folge)* **44**, (1921) 253–287.

[156] E. L. POLLOCK, J. GLOSLI: "Comments on P^3M, FMM, and the Ewald method for large periodic Coulombic systems". *Computer Physics Communications* **95**, (1996) 93–110.

[157] A. Y. TOUKMAJI, J. J. A. BOARD: "Ewald summation techniques in perspective: a survey". *Computer Physics Communications* **95**, (1996) 73–92.

[158] S. W. DE LEEUW, J. W. PERRAM, E. R. SMITH: "Simulation of Electrostatic Systems in Periodic Boundary Conditions. I. Lattice Sums and Dielectric Constants". *Proc. R. Soc. Lond. Ser. A, Math. Phys. Sci.* **373**, (1980) 27–56.

[159] S. W. DE LEEUW, J. W. PERRAM, E. R. SMITH: "Simulation of Electrostatic Systems in Periodic Boundary Conditions. II. Equivalence of Boundary Conditions". *Proc. R. Soc. Lond. Ser. A, Math. Phys. Sci.* **373**, (1980) 57–66.

[160] C. SAGUI, T. A. DARDEN: "Molecular Dynamics Simulations of Biomolecules: Long-Range Electrostatic Effects". *Annu. Rev. Biophys. Biomol. Struct.* **28**, (1999) 155–179.

[161] V. SPRINGEL, S. D. M. WHITE, A. JENKINS, C. S. FRENK, N. YOSHIDA, L. GAO, J. NAVARRO, R. THACKER, D. CROTON, J. HELLY, J. A. PEACOCK, S. COLE, P. THOMAS, H. COUCHMAN, A. EVRARD, J. COLBERG, F. PEARCE: "Simulations of the formation, evolution and clustering of galaxies and quasars". *Nature* **435**, (2005) 629–636.

[162] A. MOCSY: "Heavy quark correlators above deconfinement". *(arxive only)* hep-ph/0510135.

[163] N. W. ASHCROFT, N. D. MERMIN: *Solid state physics* (Brooks Cole, Belmont, 1976).

[164] S.-J. TU, E. FISCHBACH: "A new geometric probability technique for an N-dimensional sphere and its applications". *(arxive only)* math-ph/0004021.

[165] M. LAINE, O. PHILIPSEN: "The non-perturbative QCD Debye mass from a Wilson line operator". *Phys. Lett.* **B459**, (1999) 259–264, hep-lat/9905004.

[166] M. H. THOMA: "The quark-gluon plasma liquid". *J. Phys.* **G31**, (2005) L7, hep-ph/0409213.

[167] R. L. THEWS, M. SCHROEDTER, J. RAFELSKI: "Enhanced J/Ψ production in deconfined quark matter". *Phys. Rev.* **C63**, (2001) 054905, hep-ph/0007323.

[168] R. L. THEWS, J. RAFELSKI: "J/Ψ production at RHIC in a QGP". *Nucl. Phys.* **A698**, (2002) 575–578, hep-ph/0104025.

[169] M. CACCIARI, P. NASON, R. VOGT: "QCD predictions for charm and bottom production at RHIC". *Phys. Rev. Lett.* **95**, (2005) 122001, hep-ph/0502203.

[170] L. GRANDCHAMP, S. LUMPKINS, D. SUN, H. VAN HEES, R. RAPP: "Bottomonium production at RHIC and LHC". *(arxive only)* hep-ph/0507314.

[171] H. VAN HEES, V. GRECO, R. RAPP: "Heavy-quark probes of the quark-gluon plasma at RHIC". *(arxive only)* nucl-th/0508055.

Chapter 6: qMD in heavy ion collisions: Coupling to UrQMD

[172] M. OKAMOTO, ET AL. (CP-PACS): "Equation of state for pure SU(3) gauge theory with renormalization group improved action". *Phys. Rev.* **D60**, (1999) 094510, hep-lat/9905005.

[173] S. A. BASS, H. WEBER, C. ERNST, M. BLEICHER, M. BELKACEM, L. BRAVINA, S. SOFF, H. STÖCKER, W. GREINER, S. C.: "Reaction dynamics in Pb+Pb at the CERN/SPS: From partonic degrees of freedom to freeze-out". *Prog. Part. Nucl. Phys.* **42**, (1999) 313–322, nucl-th/9810077.

[174] D. ZSCHIESCHE, G. ZEEB, K. PAECH, H. STÖCKER, S. SCHRAMM: "Particle ratios from AGS to RHIC in an interacting hadronic model". *J. Phys.* **G30**, (2004) S381–S391.

[175] R. D. PISARSKI: "Phenomenology of the chiral phase transition". *Phys. Lett.* **B110**, (1982) 155.

[176] R. RAPP, J. WAMBACH: "Chiral symmetry restoration and dileptons in relativistic heavy-ion collisions". *Adv. Nucl. Phys.* **25**, (2000) 1, hep-ph/9909229.

[177] G. E. BROWN, M. RHO: "On the manifestation of chiral symmetry in nuclei and dense nuclear matter". *Phys. Rept.* **363**, (2002) 85–171, hep-ph/0103102.

[178] S. DAMJANOVIC, ET AL. (NA60): "First measurement of the ρ spectral function in nuclear collisions". *(arxive only)* nucl-ex/0510044.

[179] P. BRAUN-MUNZINGER, J. STACHEL, J. P. WESSELS, N. XU: "Thermal and hadrochemical equilibration in nucleus-nucleus collisions at the SPS". *Phys. Lett.* **B365**, (1996) 1–6, nucl-th/9508020.

[180] J. RAFELSKI, J. LETESSIER: "Hadron freeze-out and QGP hadronization". *(arxive only)* hep-ph/9902365.

[181] M. BLEICHER, C. SPIELES, C. ERNST, L. GERLAND, S. SOFF, H. STOCKER, W. GREINER, S. BASS: "The origin of transverse flow at the SPS". *Phys. Lett.* **B447**, (1999) 227, hep-ph/9803346.

Chapter 7: Charge fluctuations as a signal for the QGP

[182] S. SCHERER: "Exotic hadrons from dynamical clustering of quarks in ultra-relativistic heavy ion collisions". *J. Phys.* **G31**, (2005) S1199–S1202, hep-ph/0411296.

[183] S. JEON, V. KOCH: "Charged particle ratio fluctuation as a signal for QGP". *Phys. Rev. Lett.* **85**, (2000) 2076–2079, hep-ph/0003168.

[184] M. ASAKAWA, U. W. HEINZ, B. MULLER: "Fluctuation probes of quark deconfinement". *Phys. Rev. Lett.* **85**, (2000) 2072–2075, hep-ph/0003169.

[185] M. BLEICHER, S. JEON, V. KOCH: "Event-by-event fluctuations of the charged particle ratio from non-equilibrium transport theory". *Phys. Rev.* **C62**, (2000) 061902, hep-ph/0006201.

[186] E. V. SHURYAK, M. A. STEPHANOV: "Long-range charge fluctuations and search for a quark-gluon plasma signal". *Phys. Rev.* **C63**, (2001) 064903, hep-ph/0010100.

[187] J. ADAMS, ET AL. (STAR): "Net charge fluctuations in Au+Au collisions at $\sqrt{s_{(\mathrm{NN})}} =$ 130 GeV". *Phys. Rev.* **C68**, (2003) 044905, nucl-ex/0307007.

[188] C. A. PRUNEAU (STAR): "Event by event net charge fluctuations". *Heavy Ion Phys.* **21**, (2004) 261–266, nucl-ex/0304021.

[189] G. D. WESTFALL (STAR): "Correlations and fluctuations in STAR". *J. Phys.* **G30**, (2004) S1389, nucl-ex/0404004.

[190] K. ADCOX, ET AL. (PHENIX): "Net charge fluctuations in Au+Au interactions at $\sqrt{s_{NN}} =$ 130 GeV". *Phys. Rev. Lett.* **89**, (2002) 082301, nucl-ex/0203014.

[191] J. NYSTRAND (PHENIX): "Charge fluctuations at mid-rapidity in Au+Au collisions in the PHENIX experiment at RHIC". *Nucl. Phys.* **A715**, (2003) 603–606, nucl-ex/0209019.

[192] C. ALT, ET AL. (NA49): "Electric charge fluctuations in central Pb+Pb collisions at 20 AGeV, 30 AGeV, 40 AGeV, 80 AGeV, and 158 AGeV". *Phys. Rev.* **C70**, (2004) 064903, nucl-ex/0406013.

[193] H. SAKO, H. APPELSHAEUSER (CERES/NA45): "Event-by-event fluctuations at 40 A GeV/c, 80 A GeV/c, and 158 A GeV/c in Pb+Au collisions". *J. Phys.* **G30**, (2004) S1371–S1376, nucl-ex/0403037.

[194] S. MROWCZYNSKI: "Measuring charge fluctuations in high-energy nuclear collisions". *Phys. Rev.* **C66**, (2002) 024904, nucl-th/0112007.

[195] J. ZARANEK: "Measures of charge fluctuations in nuclear collisions". *Phys. Rev.* **C66**, (2002) 024905, hep-ph/0111228.

[196] C. NONAKA, B. MULLER, S. A. BASS, M. ASAKAWA: "Possible resolutions of the D-paradox". *Phys. Rev.* **C71**, (2005) 051901, nucl-th/0501028.

[197] A. BIALAS: "Charge fluctuations in a quark antiquark system". *Phys. Lett.* **B532**, (2002) 249–251, hep-ph/0203047.

[198] S. JEON, V. KOCH: "Fluctuations of particle ratios and the abundance of hadronic resonances". *Phys. Rev. Lett.* **83**, (1999) 5435–5438, nucl-th/9906074.

[199] W. GREINER, H. STÖCKER, L. NEISE: *Thermodynamik und Statistische Mechanik* (Wiss. Verlag Harri Deutsch, Frankfurt am Main, 1987 (1. Auflage)), engl. edition: *Thermodynamics and Statistical Mechanics*; xii + 463 pages; Springer-Verlag, Heidelberg, New York, 2001.

[200] L.-J. SHI, S. JEON: "Charge transfer fluctuations as a signal for QGP". *Phys. Rev.* **C72**, (2005) 034904, hep-ph/0503085.

[201] V. KOCH, A. MAJUMDER, J. RANDRUP: "Baryon-strangeness correlations: A diagnostic of strongly interacting matter". *Phys. Rev. Lett.* **95**, (2005) 182301, nucl-th/0505052.

Chapter 8: Exotic hadronic clusters and pentaquarks

[202] V. V. BARMIN, ET AL. (DIANA): "Observation of a baryon resonance with positive strangeness in K^+ collisions with Xe nuclei". *Phys. Atom. Nucl.* **66**, (2003) 1715–1718, hep-ex/0304040.

[203] V. KUBAROVSKY, ET AL. (CLAS): "Observation of an exotic baryon with $S = +1$ in photoproduction from the proton". *Phys. Rev. Lett.* **92**, (2004) 032001, hep-ex/0311046.

[204] S. STEPANYAN, ET AL. (CLAS): "Observation of an exotic $S = +1$ baryon in exclusive photoproduction from the deuteron". *Phys. Rev. Lett.* **91**, (2003) 252001, hep-ex/0307018.

[205] V. KUBAROVSKY, S. STEPANYAN (CLAS): "Evidence for an exotic baryon state, $\Theta(1540)^+$, in photoproduction reactions from protons and deuterons with CLAS". *AIP Conf. Proc.* **698**, (2004) 543–547, hep-ex/0307088.

[206] C. ALT, ET AL. (NA49): "Observation of an exotic $S = -2, Q = -2$ baryon resonance in proton proton collisions at the CERN SPS". *Phys. Rev. Lett.* **92**, (2004) 042003, hep-ex/0310014.

[207] A. AKTAS, ET AL. (H1): "Evidence for a narrow anti-charmed baryon state". *Phys. Lett.* **B588**, (2004) 17, hep-ex/0403017.

[208] H. Z. HUANG: "Recent results on searches for pentaquark states from STAR at RHIC". *(arxive only)* nucl-ex/0509037.

[209] C. SEIFE: "Scientific priority: CERN's gamble shows perils, rewards of playing the odds". *Science* **289**, (2000) 2260–2262.

[210] J. RANDRUP: "Production of the exotic Theta baryon in relativistic nuclear collisions". *Phys. Rev.* **C68**, (2003) 031903, nucl-th/0307042.

[211] J. LETESSIER, G. TORRIERI, S. STEINKE, J. RAFELSKI: "Strange Pentaquark Hadrons in Statistical Hadronization". *Phys. Rev.* **C68**, (2003) 061901, hep-ph/0310188.

[212] L. W. CHEN, V. GRECO, C. M. KO, S. H. LEE, W. LIU: "Pentaquark baryon production at the Relativistic Heavy Ion Collider". *Phys. Lett.* **B601**, (2004) 34–40, nucl-th/0308006.

[213] M. CHEMTOB: "Skyrme model of baryon octet and decuplet". *Nucl. Phys.* **B256**, (1985) 600–608.

[214] D. DIAKONOV, V. PETROV, M. V. POLYAKOV: "Exotic anti-decuplet of baryons: Prediction from chiral solitons". *Z. Phys.* **A359**, (1997) 305–314, hep-ph/9703373.

[215] J. BARTH, ET AL. (SAPHIR): "Evidence for the positive-strangeness pentaquark Θ^+ in photoproduction with the SAPHIR detector at ELSA". *Phys. Lett.* **B572**, (2003) 127–132.

[216] H. G. JUENGST (CLAS): "Search for a Θ^{++} pentaquark state". *Nucl. Phys.* **A754**, (2005) 265–271, nucl-ex/0312019.

[217] K. H. HICKS: "Experimental search for pentaquarks". *Prog. Part. Nucl. Phys.* **55**, (2005) 647–676, hep-ex/0504027.

[218] A. R. DZIERBA, C. A. MEYER, A. P. SZCZEPANIAK: "Reviewing the evidence for pentaquarks". *J. Phys. Conf. Ser.* **9**, (2005) 192–204, hep-ex/0412077.

[219] S. KABANA: "Pentaquarks: Review of the experimental evidence". *J. Phys.* **G31**, (2005) S1155–S1164, hep-ex/0503019.

[220] H. G. FISCHER, S. WENIG: "Are there $S = -2$ pentaquarks?" *Eur. Phys. J.* **C37**, (2004) 133–140, hep-ex/0401014.

[221] M. KARLINER, H. J. LIPKIN: "Why the Θ^+ is seen in some experiments and not in others: A possible explanation". *Phys. Lett.* **B597**, (2004) 309–313, hep-ph/0405002.

[222] S. SALUR (STAR): "Pentaquark Search in Relativistic Heavy Ion Collisions with STAR". *Poster presentation at Quark Matter 2004, Oakland* nucl-ex/0403009.

[223] S. SALUR (STAR): "$\Sigma(1385)$ results and status of the Θ^+ in STAR". *J. Phys.* **G31**, (2005) S179–S186, nucl-ex/0410039.

[224] S. KABANA (STAR): "Exotic particle searches with STAR at RHIC". *(arxive only)* hep-ex/0406032.

[225] I. I. STRAKOVSKY, R. A. ARNDT, Y. I. AZIMOV, M. V. POLYAKOV, R. L. WORKMAN: "Present status of the nonstrange and other flavor partners of the exotic Θ^+ baryon". *J. Phys. Conf. Ser.* **9**, (2005) 218, hep-ph/0501114.

[226] B. K. JENNINGS, K. MALTMAN: "Z^* resonances: Phenomenology and models". *Phys. Rev.* **D69**, (2004) 094020, hep-ph/0308286.

[227] S.-L. ZHU: "Pentaquarks". *Int. J. Mod. Phys.* **A19**, (2004) 3439–3469, hep-ph/0406204.

[228] M. OKA: "Theoretical overview of the pentaquark baryons". *Prog. Theor. Phys.* **112**, (2004) 1–19, hep-ph/0406211.

[229] R. L. JAFFE: "Exotica". *Phys. Rept.* **409**, (2005) 1–45, hep-ph/0409065.

[230] H. HOGAASEN, P. SORBA: "The systematics of possibly narrow quark states with baryon number one". *Nucl. Phys.* **B145**, (1978) 119.

[231] M. DE CROMBRUGGHE, H. HOGAASEN, P. SORBA: "Quantitative predictions for $4q - \bar{q}$ baryons". *Nucl. Phys.* **B156**, (1979) 347.

[232] M. KARLINER, H. J. LIPKIN: "A Diquark-Triquark Model for the KN Pentaquark". *Phys. Lett.* **B575**, (2003) 249–255, hep-ph/0402260.

[233] R. L. JAFFE, F. WILCZEK: "Diquarks and exotic spectroscopy". *Phys. Rev. Lett.* **91**, (2003) 232003, hep-ph/0307341.

[234] C. R. HAGEN, A. J. MACFARLANE: "Reduction of representations of $\mathrm{SU}(mn)$ with respect to the subgroup $\mathrm{SU}(m) \otimes \mathrm{SU}(n)$". *J. Math. Phys.* **6**, (1965) 1355.

[235] B. G. WYBOURNE: "S wave color singlet states of multi-quark configurations". *Australian J. Phys.* **31**, (1978) 117.

[236] A. ALOISIO, ET AL. (KLOE): "Study of the decay $\Phi \to \eta\pi_0\gamma$ with the KLOE detector". *Phys. Lett.* **B536**, (2002) 209–216, hep-ex/0204012.

[237] A. ALOISIO, ET AL. (KLOE): "Study of the decay $\Phi \to \pi_0\pi_0\gamma$ with the KLOE detector". *Phys. Lett.* **B537**, (2002) 21–27, hep-ex/0204013.

[238] P. KROKOVNY, ET AL. (Belle): "Observation of the $D_{sJ}(2317)$ and $D_{sJ}(2457)$ in B decays". *Phys. Rev. Lett.* **91**, (2003) 262002, hep-ex/0308019.

[239] B. AUBERT, ET AL. (BABAR): "Observation of a Narrow Meson Decaying to $D_s + \pi_0$ at a Mass of 2.32 GeV/c^2". *Phys. Rev. Lett.* **90**, (2003) 242001, hep-ex/0304021.

[240] D. BESSON, ET AL. (CLEO): "Observation of a narrow resonance of mass 2.46 GeV/c^2 decaying to $D_s^* + \pi 0$ and confirmation of the $D_{sJ}^*(2317)$ state". *Phys. Rev.* **D68**, (2003) 032002, hep-ex/0305100.

[241] T. BARNES, F. E. CLOSE, H. J. LIPKIN: "Implications of a DK molecule at 2.32 GeV". *Phys. Rev.* **D68**, (2003) 054006, hep-ph/0305025.

[242] H.-Y. CHENG, W.-S. HOU: "B decays as spectroscope for charmed four-quark states". *Phys. Lett.* **B566**, (2003) 193–200, hep-ph/0305038.

[243] C. AMSLER, N. A. TORNQVIST: "Mesons beyond the naive quark model". *Phys. Rept.* **389**, (2004) 61–117.

[244] J.-M. RICHARD: "Quasi-nuclear and quark model baryonium: Historical survey". *Nucl. Phys. Proc. Suppl.* **86**, (2000) 361–367, nucl-th/9909030.

[245] J. Z. BAI, ET AL. (BES): "Observation of a near-threshold enhancement in the $p\bar{p}$ mass spectrum from radiative $J/\Psi \to \gamma p\bar{p}$ decays". *Phys. Rev. Lett.* **91**, (2003) 022001, hep-ex/0303006.

[246] I. N. MISHUSTIN, L. M. SATAROV, D. STROTTMAN, W. GREINER: "Possible production of exotic baryonia in relativistic heavy-ion collisions". *J. Phys.* **G31**, (2005) 803–808, hep-ph/0406067.

[247] K. MALTMAN, N. ISGUR: "Nuclear physics and the quark model: Six quarks with chromodynamics". *Phys. Rev.* **D29**, (1984) 952.

[248] R. L. JAFFE: "Perhaps a stable dihyperon". *Phys. Rev. Lett.* **38**, (1977) 195–198.

[249] R. BILGER, H. A. CLEMENT, M. G. SHCHEPKIN: "Signature of a πNN resonance in pionic double charge exchange at low-energies". *Phys. Rev. Lett.* **71**, (1993) 42–45.

[250] T. GOLDMAN, K. MALTMAN, J. STEPHENSON, G. J., K. E. SCHMIDT, F. WANG: ""Inevitable" nonstrange dibaryon". *Phys. Rev.* **C39**, (1989) 1889–1895.

[251] V. B. KOPELIOVICH, B. E. STERN, B. SCHWESINGER: "SU(3) dibaryon configurations from chiral soliton models with explicit scalar mesons". *Phys. Lett.* **B242**, (1990) 145–150.

[252] S. M. KISELEV, M. I. KRIVORUCHENKO, B. V. MARTEMYANOV, A. FAESSLER, C. FUCHS: "d' production in heavy ion collisions". *Nucl. Phys.* **A650**, (1999) 78–96, nucl-th/9808019.

[253] J. SCHAFFNER-BIELICH, R. MATTIELLO, H. SORGE: "Dibaryons with strangeness: Their weak nonleptonic decay using SU(3) symmetry and how to find them in relativistic heavy-ion collisions". *Phys. Rev. Lett.* **84**, (2000) 4305–4308, nucl-th/9908043.

[254] M. BLEICHER, ET AL.: "A novel mechanism of H0 di-baryon production in proton proton interactions from parton based Gribov-Regge theory". *Phys. Rev. Lett.* **92**, (2004) 072301, hep-ph/0205182.

[255] Z. Y. ZHANG, Y. W. YU, C. R. CHING, T. H. HO, Z.-D. LU: "Suggesting a di-Ω dibaryon search in heavy ion collision experiments". *Phys. Rev.* **C61**, (2000) 065204.

[256] S. V. AFANASEV, ET AL. (NA49): "Deuteron production in central Pb+Pb collisions at 158 AGeV". *Phys. Lett.* **B486**, (2000) 22–28.

[257] T. ANTICIC, ET AL. (NA49): "Energy and centrality dependence of deuteron and proton production in Pb+Pb collisions at relativistic energies". *Phys. Rev.* **C69**, (2004) 024902.

[258] H. APPELSHÄUSER, ET AL. (NA49): "Baryon stopping and charged particle distributions in central Pb + Pb collisions at 158 GeV per nucleon". *Phys. Rev. Lett.* **82**, (1999) 2471–2475, nucl-ex/9810014.

[259] S. S. ADLER, ET AL. (PHENIX): "Deuteron and antideuteron production in Au+Au collisions at $\sqrt{s_{\rm (NN)}} = 200$ GeV". *Phys. Rev. Lett.* **94**, (2005) 122302, nucl-ex/0406004.

[260] B. B. BACK, ET AL.: "The significance of the fragmentation region in ultrarelativistic heavy ion collisions". *Phys. Rev. Lett.* **91**, (2003) 052303, nucl-ex/0210015.

[261] S. D. PAGANIS, ET AL.: "Can doubly strange dibaryon resonances be discovered at RHIC?" *Phys. Rev.* **C62**, (2000) 024906, nucl-ex/9910007.

[262] P. FACHINI (STAR): "$\rho(770)_0$ and $f_0(980)$ production in Au+Au and pp collisions at $\sqrt{s_{(NN)}} = 200$ GeV". *J. Phys.* **G30**, (2004) S565–S570, nucl-ex/0305034.

[263] C. GREINER, H. STÖCKER: "Distillation and survival of strange quark matter droplets in ultrarelativistic heavy ion collisions". *Phys. Rev.* **D44**, (1991) 3517–3529.

[264] S. SOFF: "News on strangeness at ultrarelativistic energies: Review of microscopic models". *J. Phys.* **G30**, (2004) S139–S150, nucl-th/0312085.

[265] G. APPELQUIST, ET AL. (NA52 (NEWMASS)): "Strangelet search in $Pb + Pb$ interactions at 158 GeV/c per nucleon". *Phys. Rev. Lett.* **76**, (1996) 3907–3910.

[266] T. A. ARMSTRONG, ET AL. (E864): "Search for strange quark matter produced in relativistic heavy ion collisions". *Phys. Rev.* **C63**, (2001) 054903, nucl-ex/0010017.

[267] A. H. TANG (STAR): "Strangelet search at RHIC". *J. Phys.* **G31**, (2005) S1187–S1190, nucl-ex/0412011.

Appendix

[268] K. HAGIWARA, ET AL. (Particle Data Group): "Review of particle physics". *Phys. Rev.* **D66**, (2002) 010001.

[269] M. GUIDRY: *Gauge field theories: an introduction with applications* (John Wiley and Sons, New York; London; Sydney, 1999).

[270] W. GREINER, B. MÜLLER: *Quantenmechanik – Symmetrien* (Wiss. Verlag Harri Deutsch, Frankfurt am Main, 2004), engl. edition: *Quantum Mechanics: Symmetries*; xviii + 526 pages; Springer-Verlag, Heidelberg, New York, 2001.

[271] P. DI FRANCESCO, P. MATHIEU, D. SENECHAL: *Conformal field theory* (Springer-Verlag, Berlin; Heidelberg; London; etc., 1999).

[272] E. VAN BEVEREN, G. RUPP: "Observed $D_s(2317)$ and tentative $D(2030)$ as the charmed cousins of the light scalar nonet". *Phys. Rev. Lett.* **91**, (2003) 012003, `hep-ph/0305035`.

[273] F. GÜRSEY, L. A. RADICATI: "Spin and Unitary Spin Independence of Strong Interactions". *Phys. Rev. Lett.* **13**, (1964) 173–175.

[274] A. PAIS: "Dynamical Symmetry in Particle Physics". *Rev. Mod. Phys.* **38**, (1966) 215–255.

[275] B. G. WYBOURNE: "Group theory and the Pentaquark". *(arxive only)* `hep-ph/0307170`.

[276] R. BIJKER, M. M. GIANNINI, E. SANTOPINTO: "Spectroscopy of pentaquark states". *Eur. Phys. J.* **A22**, (2004) 319–329, `hep-ph/0310281`.

[277] L. D. LANDAU, E. M. LIFSHITZ: *Quantum Mechanics: Non-Relativistic Theory* (Butterworth-Heinemann, Oxford, Burlington, 1981).

[278] H. HOGAASEN, P. SORBA: "The colour triplet $qq\bar{q}$ cluster and pentaquark models". *Mod. Phys. Lett.* **A19**, (2004) 2403–2410, `hep-ph/0406078`.

[279] S. K. MAJEE, A. RAYCHAUDHURI: "Pentaquark masses: Another look". *(arxive only)* `hep-ph/0407042`.

Publications of Stefan Scherer

Scientific Papers

[1] S. Scherer *et al.*: *Physics opportunities at RHIC and LHC*, in: "RHIC physics and beyond: Kay Kay Gee Day" (B. Müller and R. Pisarski, eds.), AIP Conf. Proc. **482** (1999) 121-141 [arXiv: hep-ph/9903392].

[2] S. Scherer *et al.*: *Critical Review Of Quark Gluon Plasma Signatures*, Prog. Part. Nucl. Phys. **42** (1999) 279.

[3] M. Hofmann, J. M. Eisenberg, S. Scherer, M. Bleicher, L. Neise, H. Stöcker, W. Greiner: *Nonequilibrium dynamics of a hadronizing quark-gluon plasma*, in: "Nuclear Matter, Hot and Cold" (J. Alster and D. Ashery, eds.), Tel Aviv (2000) 110-124 [arXiv: nucl-th/9908031].

[4] M. Hofmann, M. Bleicher, S. Scherer, L. Neise, H. Stöcker, W. Greiner: *Statistical mechanics of semi-classical colored objects*, Phys. Lett. B **478** (2000) 161 [arXiv: nucl-th/9908030].

[5] K. Paech, S. A. Bass, M. Belkacem, M. Bleicher, J. Brachmann, L. Bravina, D. Dietrich, A. Dumitru, C. Ernst, L. Gerland, M. Hofmann, L. Neise, M. Reiter, S. Scherer, S. Soff, C. Spieles, H. Weber, E. Zabrodin, D. Zschiesche, J. A. Maruhn, Horst Stöcker, W. Greiner: *Current status of heavy ion physics*, in "Advances in Nuclear Physics" (D. Poenaru and S. Stoica, eds.), Singapore: World Scientific (2000) 212-222.

[6] K. Paech, M. Bleicher, S. Scherer, D. Zschiesche, H. Stöcker, W. Greiner: *Hadron ratios: Chiral symmetry restauration versus nonequilibrium quark dynamics*, AIP Conf. Proc. **597** (2001) 45-53.

[7] D. Zschiesche, K. Paech, M. Bleicher, S. Scherer, D. Zschiesche, H. Stöcker: *Current status of quark gluon plasma signals*, Heavy Ion Phys. **14** (2001) 425 [arXiv: nucl-th/0101047].

[8] S. Scherer, M. Hofmann, M. Bleicher, L. Neise, H. Stöcker, W. Greiner: *Microscopic coloured quark-dynamics in the soft non-perturbative regime: Description of hadron formation in relativistic S+Au collisions at CERN*, New J. Phys. **3** (2001) 8 [arXiv: nucl-th/0106036].

[9] S. Agostinelli *et al.* [GEANT4 Collaboration]: *GEANT4: A simulation toolkit*, Nucl. Instrum. Meth. A **506** (2003) 250.

[10] S. Hossenfelder, M. Bleicher, S. Hofmann, J. Ruppert, S. Scherer, H. Stöcker: *Signatures in the Planck regime*, Phys. Lett. B **575** (2003) 85 [arXiv: hep-th/0305262].

[11] H. Stöcker, J. Berger, U. Eichmann, S. Salur, S. Scherer, D. Zschiesche: *Critical review of quark gluon plasma signatures*, AIP Conf. Proc. **631** (2003) 553.

[12] S. Scherer, H. Stöcker: *Multifragmentation, Clustering, and Coalescence in Nuclear Collisions*, in: "Latest Advances in Atomic Cluster Collisions: Fission, Fusion, Electron, Ion and Photon Impact" (J.-P. Connerade and A. Solov'yov, eds.) Singapore: World Scientific (2000) 169-180 [arXiv: hep-ph/0411296].

[13] S. Scherer: *Exotic hadrons from dynamical clustering of quarks in ultra-relativistic heavy ion collisions*, J. Phys. G **31** (2005) S1199 [arXiv: hep-ph/0411296].

While nearly all of my publications concern topics of quark matter as probed in heavy ion collisions, the paper [10] is about a completely different, and exciting new issue, which is not mentioned in my doctoral thesis:

We discuss possible consequences of the introduction of a minimal length scale in physics, as it can be motivated in several approaches to merge general relativity with the standard model of particle physics, such as quantum loop gravity, and string theory. We develop a model in which the wave vector of a particle is bounded by the inverse of the minimal length scale, corresponding to a minimal resolution of space-time, while the momentum is free to increase without limits. Thus, the de Broglie relation is generalized and recovered in its usual, linear form as a low-energy limit. Our model can be quantized using the canonical commutation relations $[\hat{x}_i, \hat{k}_j] = \mathrm{i}\delta_{ij}$ between position and wave vector. The new relation between momentum and wave vector then yields a modified commutation relation for position and momentum, and a generalized Heisenberg uncertainty principle for position Δx and momentum Δp.

In the first part of the paper, I develop the non-relativistic quantum mechanics of this model, including applications to the harmonic oscillator and the hydrogen atom. The modification of the commutator relations for momentum and position results in subtle modifications of the energy spectra of these systems, which are calculated using perturbation theory and the numerical evaluation of the corresponding eigenwert problems. Current data from high-precision spectroscopy of the hydrogen atom then allow to establish upper bounds for the size of a possible minimal length scale. The second part of the paper, written mostly by my coauthors, implements our idea into relativistic quantum field theory and high-energy scattering.

This paper is of high relevance in the ongoing debate about deformed special relativity (DSR) and effective models for phenomenological quantum gravity.

Talks and presentations

[1] Poster presentation at conference: *Topologischer finite-size-Effekt im XY-Modell auf dem Torus*, DPG-Frühjahrstagung des Fachverbandes Dynamik und Statistische Physik, Münster, March 1997.

[2] Talk at conference: *Hadronisierung eines Quark-Gluon-Plasmas in der mikroskopischen Quark-Dynamik*, DPG-Frühjahrstagung des Fachverbandes Hadronen und Kerne, Freiburg, March 1999.

[3] Poster presentation at conference: *Microscopic Description of the QCD Phase Transition*, Quark Matter 99, Turino, May 1999.

[4] Seminar talk: *Microscopic Description of the QCD Phase Transition*, Seminar, IReS Strasbourg, July 1999.

[5] Talk at conference: *Non-Equilibrium quark Molecular Dynamics*, Workshop RHIC 2000, Park City, Utah, March 2000.

[6] Seminar talk: *Hadronization in non-Equilibrium Quark Molecular Dynamics*, Workshop, Obernai, France, October 2000.

[7] Poster presentation at conference: *Quark non-equilibrium Molecular Dynamics: Correlation Studies*, Quark Matter 2001, Stony Brook, Long Island, January 2001.

[8] Seminar talk: *Correlations in Quark non-equilibrium Molecular Dynamics*, Seminar, Michigan State University, East Lansing, Michigan, January 2001.

[9] Poster presentation at conference: *Strangeness production in SIS/200 collisions*, Quark Matter 2002, Nantes, July 2002.

[10] Talk at conference: *Different Temperatures in Quark Molecular Dynamics at SPS energies*, DPG-Frühjahrstagung des Fachverbandes Hadronen und Kerne, Tübingen, March 22, 2003.

[11] Seminar talk: *Quark-Gluon-Plasma im Computer*, HHLR-Nutzerkolloquium, Darmstadt, July 10, 2003.

[12] Seminar talk: *Pentaquarks in Relativistic Heavy Ion Collisions with qMD*, Universität Frankfurt, May 3, 2004.

[13] Talk at conference: *Exotic hadrons from dynamical clustering of quarks*, Strange Quark Matter 2004, Cape Town, September 20, 2004.

[14] Poster presentation at conference: *Charge Fluctuations from cluster hadronization and the D puzzle*, Quark Matter 2005, Budapest, August 2005.

Danksagung

Die vorliegende Arbeit ist am Institut für Theoretische Physik der Johann Wolfgang Goethe-Universität in Frankfurt am Main bei Prof. Dr. Horst Stöcker angefertigt worden. Teilprojekte entstanden bei Aufenthalten bei der GEANT 4-Kollaboration am CERN, Genf, auf Einladung von Dr. H.-P. Wellisch, an der Michigan State University, East Lansing, auf Einladung von Prof. Dr. W. Bauer und mit Förderung durch DAAD und NSF, sowie an der Universität Bergen, Norwegen, auf Einladung von Prof. Dr. L. Csernai und mit Unterstützung durch das Marie-Curie-Programm der Europäischen Union. Für die bei allen diesen Gelegenheiten erfahrene Gastlichkeit danke ich herzlich. Rechenkapazität wurde bereitgestellt durch das Hochschulrechenzentrum der Johann Wolfgang Goethe-Universität, den Hessischer Hochleistungsrechner (HHLR) in Darmstadt, das Bergen Computational Physics Laboratory im NOTUR-Rechner-Verbund in Norwegen sowie das Center for Scientific Computing (CSC) in Frankfurt am Main. Auch hier gilt mein Dank den Administratoren für die immer reibungslose Zusammenarbeit.

Ich danke Herrn Prof. Dr. Horst Stöcker sehr herzlich dafür, daß er mir die Gelegenheit gegeben hat, mich in ein mir neues und, wie ich finde, äußerst spannendes Gebiet der Physik einzuarbeiten. Auch hat er immer wieder großes Verständnis gezeigt für die besonderen Umstände, die meine parallele berufliche Tätigkeit mit sich gebracht haben. Beides zusammenzubringen wäre ohne sein Unterstützung nicht möglich gewesen.

Zurückgehend vor allem auf den Einsatz von Prof. Dr. Walter Greiner, ist die theoretische Schwerionenphysik in Frankfurt fest eingebunden in die internationale Forschung auf diesem Gebiet. Von den sich daraus ergebenden Kontakten mit Forschern aus aller Welt habe ich sowohl fachlich als auch persönlich sehr profitieren können. Die einmalige Gelegenheit, Kontakte und Freundschaften mit Menschen aus buchstäblich allen Erdteilen zu schließen, kann ich kaum hoch genug bewerten. Die Atmosphäre unter meinen Kolleginnen und Kollegen, den jüngeren Wissenschaftler und Gästen am Institut habe ich als sehr angenehm in Erinnerung. Von Markus Hofmann, Ludwig Neise, Marcus Bleicher, Henning Weber, Detlef Zschiesche, Agnes Mocsy, Azwinndini Muronga und vielen anderen habe ich nicht nur Physik gelernt.

Wichtig war mir während all der Zeit der Anfertigung dieser Arbeit aber auch, durch meine Tätigkeit für den Verlag Harri Deutsch ein Gegengewicht zur Welt der Wissenschaft und einen andauernden Kontakt “zum richtigen Leben” zu erfahren. Dafür bin ich den Mitarbeiterinnen und Mitarbeitern im Verlag, vor allem Klaus Horn und Heike Schulze, sehr dankbar.

Das Einarbeiten in das Thema, die notwendige Forschung und das Schreiben dieser Dissertation haben eine längere Zeit gebraucht, als ich zuvor gedacht hätte. Ich bin allen von Herzen dankbar, die mich darin bestärkt und mich immer wieder dazu ermuntert haben, es trotzdem anzupacken und zu einem gelungenen Abschluß zu bringen. Für ihre immerwährende Unterstützung und Geduld danke ich vor allem meinen Eltern, Hubert und Marianne Scherer, und ganz besonders Sabine.

Frankfurt am Main, am 11. Dezember 2005 Stefan Scherer

Lebenslauf

Stefan Scherer
Hamburger Allee 46
60468 Frankfurt am Main

geboren am 30. August 1967 in Ottweiler (Saar), ledig

Schulausbildung:

1973-77	Grundschule Güdesweiler, Steinberg-Deckenhardt
1977-86	Gymnasium Wendalinum, St. Wendel – Abitur 1986

Wehrdienst:

1986-87	Grundwehrdienst

Studium:

1987-96	Studium der Physik an der Universität des Saarlandes; Vorlesungen in Mathematik bei Prof. Dr. G.-A. Brosamler, Prof. Dr. H.-G. Zimmer, Prof. Dr. D. Kröner, Prof. Dr. J. Bemelmans, Prof. Dr. E.-U. Gekeler, Prof. Dr. G. Wittstock; Vorlesungen und Praktika in Experimentalphysik Prof. Dr. G. Schulz, Prof. Dr. U. Kreibig, Dr. H. Schmidt, Prof. Dr. J. Petersson, PD Dr. J.-K. Krüger Prof. Dr. H.-G. Unruh, Prof. Dr. T. Wichert; Ausbildung in Theoretischer Physik bei PD. Dr. K.-H. Weyrich, Prof. Dr. A. Holz (†1995), PD. Dr. T. Filk
1989	Vordiplom
1989-90	Mitglied im Fachschaftsrat Physik
1990-92	studentisches Mitglied im Fachbereichsrat Physik
Dezember 1996	Abschluß als Diplom-Physiker, Gesamtnote “sehr gut”, Diplomarbeit zum Kosterlitz-Thouless-Phasenübergang auf dem Torus (Betreuer: Prof. Dr. Arno Holz, PD Dr. Thomas Filk)
seit Dezember 1997	Wissenschaftlicher Mitarbeiter am Lehrstuhl von Prof. Dr. Horst Stöcker, Arbeiten zur Simulation des Quark-Gluon-Plasmas; Vorlesungen und Seminare bei Prof. Dr. H. Stöcker, Prof. Dr. Dr. h. c. mult. W. Greiner, Prof. Dr. D. Rischke, Prof. Dr. H. F. de Groote, Prof. Dr. A. Dumitru, Prof. Dr. M. Bleicher, HD Dr. J. Schaffner-Bielich ↪

Betreuung der Lehrveranstaltung “Physik mit dem Computer” und des zugehörigen Internet-Auftritts;
mehrere Forschungsaufenthalte am CERN bei der GEANT 4-Kollaboration

Berufstätigkeit:

Oktober 1995-Juni 1996	Übersetzung von A. P. Sutton, *Electronic structure of materials*, OUP 1993, für VCH, Weinheim
seit Mai 1997	Praktikum im Fachverlag Harri Deutsch, Frankfurt/Main, anschließend Festanstellung bei Harri Deutsch (bis Dezember 2001), dann Tätigkeit als freier Mitarbeiter für Harri Deutsch; Betreuung und technische Leitung von Multimedia-Projekten (cliXX-Reihe: CDROM-Projekte zur Physik, Chemie, Biologie), Entwicklung und Betreuung des Internet-Auftritts des Verlages, Betreuung von Autoren und Buchprojekten, Betreuung der Neuedition der Reihe “Greiner: Theoretische Physik”.

Computerkenntnisse:

PC, Unix, Linux, Latex, HTML, JavaScript, Perl, C++

Sprachkenntnisse:

sehr gute Kenntnisse in Englisch, Französisch (Wort und Schrift), Grundkenntnisse in Italienisch, Niederländisch